

Reliable Downlink Transmission in Unsynchronized Coordinated Multipoint Transmission LTE Networks

Von der Fakultät für Ingenieurwissenschaften,
Abteilung Elektrotechnik und Informationstechnik
der Universität Duisburg-Essen

zur Erlangung des akademischen Grades

Doktor der Ingenieurwissenschaften (Dr.-Ing.)

genehmigte Dissertation

von

Stanislaus Michael Iwelski

aus

Danzig

Gutachter: Prof. Dr.-Ing. habil. Peter Jung

Gutachter: Prof. Dr.-Ing. Armin Dekorsy

Tag der mündlichen Prüfung: 22.11.2018

Danksagung

Die Zukunft beginnt heute, nicht morgen.
(PAPST JOHANNES PAUL II)

Diese vorliegende Dissertation ist im Rahmen meiner Tätigkeit als wissenschaftlicher Mitarbeiter am Lehrstuhl für Kommunikationstechnik der Fakultät für Ingenieurwissenschaften an der Universität Duisburg-Essen entstanden. Aus diesem Grund möchte ich zunächst dem Inhaber des Lehrstuhls Herrn Professor Dr.-Ing. habil. PETER JUNG meinen persönlichen und tiefen Dank aussprechen. Er hat mir die Möglichkeit gegeben diese Dissertation anzufertigen, mich fortlaufend betreut und dank seines Fachwissens wesentlich zum Gelingen dieser Arbeit beigetragen. Ebenso danke ich Herrn Professor Dr.-Ing. ARMIN DEKORSY, Institutsleiter des Arbeitsbereichs Nachrichtentechnik an der Universität Bremen, für die Bereitschaft zur Übernahme des Koreferates und den damit verbundenen zeitlichen Aufwand.

Für die angenehme Atmosphäre am Lehrstuhl danke ich allen aktuellen sowie ehemaligen Mitarbeitern, namentlich: HERIBERT ANNEN, Dr. ZIJIAN BAI, GERALD BAIER, Dr. GUIDO H. BRUCK, Dr. WEI CHEN, BÄRBEL CLAUSEN, SVEN DUDDA, ANDREAS FRIEDRICH, BARBARA FRISCHMEIER, LUKAS GRINWITSCHUS, Dr. CHRISTIAN KOCKS, Dr. LI LUO, ERFAN MAJEED, Dr. SEBASTIAN RICKERS, Dr. ERNEST SCHEIBER, ANDREY SKREBTSOV, Dr. CHRISTOPH SPIEGEL, PETER VAN DER WEL, Dr. ALEXANDER VIESSMANN, ANDREAS WAADT, Dr. SHANGBO WANG, LIU XUE, Dr. DONG XU und ZIAD YOUSSEF. Besonders hervorheben möchte ich die fachlichen Diskussionen mit meinen ehemaligen Kollegen Dr. ZIJIAN BAI und mich für die kritische Durchsicht meines Manuskriptes bei Dr. GUIDO H. BRUCK herzlich bedanken. Diese Zeit hat mich sehr geprägt und ich werde diese stets in Erinnerung behalten.

Ein weiterer herzlicher Dank gebührt den Mitarbeitern der Intel Mobile Communications, besonders Dr. BILJANA BADIC, Dr. TOBIAS SCHOLAND und Dr. RAJAJARAN BALRAJ, die zur Entstehung dieses Manuskriptes beigetragen haben.

Weiterhin möchte ich mich bei allen Studierenden bedanken, die mich während ihrer Bachelor- und Masterarbeiten unterstützt haben.

Meiner Frau KLAUDIA und unseren Kindern MAXIMILIAN und ALEXANDER möchte ich für die Motivation, Geduld und die für mich freigestellte Zeit an etlichen Wochenenden und Abenden, die zur Fertigstellung des Manuskriptes notwendig war, von ganzem Herzen danken. Ein herzlicher Dank gebührt meinen Schwiegereltern JOLANTA und BOGUSŁAW KRUŻYCKI.

Abschließend möchte ich meinen Eltern IRENE und HEINRICH IWELSKI für ihre unermüdliche Unterstützung vom ganzen Herzen danken. Sie haben mir das Studium und somit erst die Promotion ermöglicht.

Köln, im Februar 2019
Stanislaus Iwelski

Übersicht

Die Entwicklung im Bereich der mobilen Informations- und Kommunikationstechnologien ermöglicht es, trotz räumlicher Entfernungen schnell und flexibel Informationen zu erhalten, zu verarbeiten und auszutauschen und eröffnet somit vollkommen neue Potenziale des Privat- und Wirtschaftslebens [Rei02]. Der weltweit enorme Zuwachs an Mobilfunkteilnehmern und die Forderung nach flächendeckend wachsenden Übertragungsgeschwindigkeiten stellt besonders am Zellrand eine große Herausforderung dar. Die technische Lösung dieses Problems sind Methoden der koordinierten Signalverarbeitung, mit deren Hilfe der Einfluss von Interzellinterferenz unterdrückt und somit die Übertragungsgeschwindigkeit am Zellrand signifikant verbessert werden kann.

Die vorliegende Arbeit leistet einen Beitrag zu diesem Thema mit der Forderung, die Vorteile dieser koordinierten Methoden der Signalverarbeitung gegenüber konventionellen Methoden trotz nichtidealer Übertragungseigenschaften zu gewährleisten. Im ersten Kapitel dieser Arbeit wird auf Basis des *Long Term Evolution (LTE)* - Mobilfunkstandards der Einfluss von Interzellinterferenz untersucht und der Stand der Technik hinsichtlich interferenzlimitierender Maßnahmen untersucht. Darauf aufbauend werden die wesentlichen Ziele dieser Arbeit formuliert. Wesentliche Aspekte der physikalischen Übertragungsschicht von *LTE*, die zum Erreichen der formulierten Ziele notwendig sind, werden anschließend diskutiert. Die zur Interferenzreduktion notwendigen Methoden der Signalverarbeitung werden in einem eigenständigen Kapitel zunächst für idealisierte Übertragungseigenschaften hergeleitet. Auf Basis der optimalen koordinierten Methode wird eine komplexitätsreduzierte und dadurch implementierungsfreundlichere Methode hergeleitet, so dass der Einfluss von Interzellinterferenz am Zellrand wesentlich reduziert werden kann. Um nichtidealen Systemeigenschaften gerecht zu werden, wird der Einfluss von zeitlich veränderlichen Ankunftszeiten der empfangenen Nutzsignale analytisch untersucht und es werden darauf basierend Methoden entwickelt, um diese weitestgehend am Empfänger zu kompensieren. Somit wird die Möglichkeit geschaffen, die Vorteile der koordinierten Methoden der Signalverarbeitung trotz nichtidealer Systemeigenschaften zu gewährleisten und damit die Übertragungsgeschwindigkeiten am Zellrand signifikant zu verbessern. Dies wird durch Computersimulationen gezeigt. Die wesentlichen Ergebnisse werden abschließend zusammengefasst und ein Ausblick auf weiterführende Arbeiten wird gegeben.

Abstract

The development of mobile information and communication technologies allows fast and flexible ways of receiving, exchanging and processing information over long distances and, thus, opens up new potential for the private and economic life [Rei02]. The tremendous growth of subscribers worldwide and the demand for area-wide increasing transmission rates, however, pose new challenges, particularly in the cell-edge. Schemes making use of coordinated signal transmission provide a technical solution for this challenge and can be used to mitigate the impact of inter-cell interference to improve the transmission rates in the cell-edge.

The intention of this thesis is to provide a solution to maintain the advantages of coordinated signal transmission in non-ideal system conditions against conventional signal transmission. Based on the Long Term Evolution (LTE) mobile radio standard, the impact of inter-cell interference is investigated in Chapter 1 of this thesis, followed by a representation of state-of-the-art interference mitigation techniques. The main goals of this thesis are subsequently defined. Substantial physical layer aspects of LTE systems, which are necessary for achieving the defined main goals, are subsequently discussed. The necessary signal processing measures enabling interference mitigation are initially derived for ideal signal transmission in a chapter of their own. Based on the optimal coordination scheme for signal transmission, an implementation-friendly method is derived which enables to mitigate the impact of inter-cell interference in the cell-edge considerably, while keeping the computational complexity low. To consider non-ideal system conditions, the impact of varying delays among the desired receive signals is investigated analytically and, based on this, methods to compensate that impact in the receiver to the greatest possible extent are suggested. Numerical results will show that the advantages of coordinated signal transmission can be maintained in non-ideal system conditions and, as a result, the transmission rates in the cell-edge are considerably improved. The key findings will be summarized and an outlook on future work provided.

Contents

1	Introduction	1
1.1	Evolution of Wireless Communication	1
1.1.1	Introduction	1
1.1.2	Historical Background	4
1.1.3	Driving Forces Behind 4G LTE Systems	6
1.1.4	Evolution of 4G LTE Systems	7
1.2	Interference-Limited Cellular LTE Networks	14
1.2.1	Introduction	14
1.2.2	Cellular LTE Networks	14
1.2.3	Types of Interference	16
1.2.4	Inter-Cell Interference	17
1.2.5	Frame and Slot Structure	22
1.2.6	System Model	24
1.2.7	Restriction Through Inter-Cell Interference	33
1.3	State of the Art	37
1.3.1	Introduction	37
1.3.2	Enhanced Receivers	38
1.3.3	Signal Precoding	39
1.3.4	CoMP Transmission	41
1.4	Criticism of the State of the Art	46
1.5	Scope and Objective of this Thesis	48
1.5.1	Introduction	48
1.5.2	Cooperative Interference Mitigation Signal Precoding	49
1.5.3	Signal Reception Enhancements using CoMP Transmission	50
1.6	Organization of this Thesis	50
2	Physical Layer Aspects of LTE Systems	53
2.1	Introduction	53
2.2	Reference Signal Generation	54
2.2.1	Introduction	54
2.2.2	Cell Specific Reference Signal	56
2.2.3	Demodulation Reference Signal	59
2.2.4	Channel State Information Reference Signal	62
2.3	Transport Channel Processing	66

2.4	Physical Channel Processing	68
2.4.1	Introduction	68
2.4.2	Modulation Mapping	71
2.4.3	Precoding	75
2.4.4	Resource Mapping	81
2.5	OFDM	89
2.5.1	Modulation	89
2.5.2	Demodulation	93
2.6	Receiver Design	98
2.6.1	Introduction	98
2.6.2	Channel Estimation	100
2.6.3	Interference Suppression Receiver Implementation	103
2.6.4	Interference Cancellation Receiver Implementation	107
2.7	Aperiodic CSI Reporting	109
2.7.1	Introduction	109
2.7.2	Subband PMI Feedback	110
2.7.3	Aperiodic CSI Reporting in TM6, TM8 and TM9	112
2.7.4	Aperiodic CSI Reporting in TM 10	113
2.8	Signal Propagation	114
2.8.1	Introduction	114
2.8.2	Channel Model Properties	115
2.8.3	Interference Properties	117
2.9	Quality Criterion	119
2.10	Performance Evaluation	122
3	Implicit Feedback Generation for Synchronized CoMP Trans-	
	mission	135
3.1	Introduction	135
3.2	Network Configuration	137
3.2.1	Downlink Scenarios	137
3.2.2	Transmission Categories	139
3.3	Cooperative Interference Mitigation Signal Precoding	141
3.3.1	Introduction	141
3.3.2	Optimal Codebook-Based Cooperative Interference Mit-	
	igation Signal Precoding	144
3.3.3	Low-Complexity Codebook-Based Cooperative Interfer-	
	ence Mitigation Signal Precoding	146
3.3.4	Complexity Analysis	152
3.4	Performance Evaluation	156
4	Reliable Implicit Feedback Generation and Channel Estima-	
	tion for Unsynchronized CoMP Transmission	165
4.1	Introduction	165

4.2	Challenges of Asynchronous CoMP Transmission	166
4.2.1	Antenna Port Co-Location	166
4.2.2	Implicit Feedback Generation	168
4.2.3	Analysis of the Timing Offset on the Estimated CTF and IRC Performance	180
4.3	Timing Offset Estimation Techniques	189
4.4	Reliable Implicit Feedback Generation for CoMP Transmission .	197
4.5	Channel Equalization for Asynchronous CoMP Transmission . .	203
4.6	Performance Evaluation	212
5	Summary and Outlook	227
5.1	Summary	227
5.2	Outlook	229
A	Codebook and Characteristic Antenna Diagram	231
B	Derivation of the Code Rates	237
B.1	Introduction	237
B.2	Physical Time-Frequency Resources for Codeword Transmission	238
B.3	Numeric Results	244
C	Complexity Analysis of the CCIMP Schemes	249
C.1	O-CCIMP Scheme	249
C.2	LC-CCIMP Scheme	251
D	Timing Offset Estimation Accuracy in Flat Fading Channels	255
	List of Frequently used Symbols	257
	List of Acronyms	265
	Bibliography	269

List of Figures

1.1	Block diagram of a typical wireless transmission system	2
1.2	Overview of outstanding physical achievements of the 19th century for the development of modern wireless communication systems	4
1.3	Cutout for a macro cellular deployed LTE network	17
1.4	Frame structure type 1 for FDD mode	25
1.5	Simplified system model for single-layer transmission in TM6	34
1.6	Impact of inter-cell interference on the bandwidth efficiency loss	36
2.1	Overview of the physical and transport channel processing chain	69
2.2	Scatterplot of 64 QAM modulation mapped symbols	72
2.3	Code rate in dependency on the transmission mode and the transmitter configuration	82
2.4	Mapping of RS and symbols for signal transmission in TM9	85
2.5	Cutout of a PRB and subframe for signal transmission in TM9	87
2.6	Illustration of the impact of varying delays on the receive signals	93
2.7	Block diagram of the designed receiver	99
2.8	Performance for single-layer transmission in TM6 for (a) MCS4, (b) MCS14 and (c) MCS25	129
2.9	Performance for single-layer transmission in TM8 for (a) MCS4, (b) MCS14 and (c) MCS25	131
2.10	Performance for single-layer transmission in TM9 for (a) MCS4, (b) MCS14 and (c) MCS25	133
3.1	Code rate in dependency on the transmission mode and the transmitter configuration	138
3.2	Cutout for a macro cellular deployed LTE network of CoMP Scenario 4 with low-power RRHs	141
3.3	Cooperative interference mitigation precoding scenario	142
3.4	Block diagram of the O-CCIMP scheme	145
3.5	Block diagram of the LC-CCIMP scheme	151
3.6	Performance comparison of the O-CCIMP and LC-CCIMP scheme for (a) MCS4, (b) MCS14 and (c) MCS25 using the 2×2 MIMO antenna configuration	161

List of Figures

3.7	Performance comparison of the O-CCIMOP and LC-CCIMP scheme for (a) MCS4, (b) MCS14 and (c) MCS25 using the 4×2 MIMO antenna configuration	163
4.1	Mapping of the CSI-RS on physical time-frequency resources for two transmit AP groups	173
4.2	Distribution of the PMIs in dependence on the TO	176
4.3	Impact of the TO on the performance for the 4×2 MIMO antenna configuration for (a) MCS4, (b) MCS14 and (c) MCS25	178
4.4	Magnitude of the estimated CTF	182
4.5	Impact of the TO on the equalized signal using the 64QAM mapping scheme	183
4.6	Impact of the TO on signal equalization for CP-based OFDM	186
4.7	Impact of the TO on signal equalization for cyclic postfix based OFDM	187
4.8	Mapping of DMRSs on physical time-frequency resources in one subband and subframe	193
4.9	Accuracy for DMRS-based TO estimation	196
4.10	Channel estimation for unsynchronized CoMP transmission . . .	199
4.11	PMI error rate for (a) MCS4, (b) MCS14 and (c) MCS25	200
4.12	Normalized magnitude of the residual channel estimation error .	206
4.13	Magnitude of the estimated CTF after TO compensation	206
4.14	EVM of the equalized complex-valued modulation symbols for (a) MCS4, (b) MCS14 and (c) MCS25	210
4.15	Performance of the TO compensation schemes for unsynchronized CoMP transmission	220
4.16	Enlarged view of Figure 4.15 for (a) MCS25, (b) MCS14 and (c) MCS4	222
4.17	Impact of the TO on the performance for the 4×2 MIMO antenna configuration for (a) MCS4, (b) MCS14 and (c) MCS25	224
D.1	Accuracy for DMRS-based TO estimation	256

List of Tables

1.1	Selected key features of LTE systems	10
1.2	Relation between the channel bandwidth and the DL bandwidth configuration	22
1.3	Summary of components illustrating the receive signal	28
2.1	Properties of complex-valued modulation symbols	74
2.2	Codebook and characteristic antenna diagram for signal transmission from two AEs	78
2.3	Example of RS and symbols for signal transmission in TM9	90
2.4	Interference profile based on averaged set of unconditional median DIP values	117
2.5	Simulation Parameters	127
2.6	Legend for Figure 2.8 (a) – (c)	129
2.7	Legend for Figure 2.9 (a) – (c)	131
2.8	Legend for Figure 2.10 (a) – (c)	133
3.1	Restricted PMIs using the CCIMP scheme	143
3.2	Complexity of linear algebra operations	155
3.3	Complexity of the O-CCIMP and LC-CCIMP scheme	156
3.4	Simulation Parameters	159
3.5	Legend for Figure 3.6 (a) – (c)	161
3.6	Legend for Figure 3.7 (a) – (c)	163
4.1	Legend for Figure 4.3	179
4.2	Tolerable range of the TO for CP-based OFDM	186
4.3	Tolerable range of the TO for cyclic postfix based OFDM	187
4.4	Key values for DMRS-based TO estimation	192
4.5	Legend for Figure 4.11	201
4.6	Legend for Figure 4.14	211
4.7	Comparison of the lower EVMs in Figure 4.14	213
4.8	Simulation Parameters	219
4.9	Legend for Figure 4.15	221
4.10	Legend for Figure 4.16	223
4.11	Legend for Figure 4.17	225

List of Tables

A.1	Codebook and characteristic antenna diagram for signal transmission from four transmit AEs	233
B.1	Relation between the TM, the eNodeB configuration and the number of physical time-frequency resources	239
B.2	Relationship between MCS and code rate for TM6, TM8 and TM9	245
B.3	Relationship between the MCS, the modulation mapping scheme and the code rate for supported CoMP scenarios	246

Chapter 1

Introduction

1.1 Evolution of Wireless Communication

1.1.1 Introduction

The term *evolution* stems from the Latin word *evolvere*, where its present active infinitive *evolvo* can be translated as *to unroll* and *to develop* [Gla71]. In the linguistic context, the "development by natural process to a higher state" shall be conveyed [Gla71]. In his aphorisms on science, ALBERT EINSTEIN compares knowledge with imagination and comes to the conclusion that the former is limited, whereas the latter embraces the entire world and gives birth to evolution [Ein31]. Beside biological sciences, the evidence of evolution has gained significant importance in history and modern research areas including anthropology, astrophysics, chemistry, geology, physics and mathematics [SM08].

The term *communication* has its origins in the Latin word *communicare* and means *to share* and *to make things common* [Gla69]. The intention behind communication is thus to make things common by sharing knowledge [Ros00]. In the area of information theory, the communication model by CLAUDE E. SHANNON [Sha48] is widely-used to understand the fundamental communication problems [LC04, Section 1.1]. The block diagram of a typical wireless transmission system is depicted in Figure 1.1 on page 2. To enable communication, at least three components are necessary: a message, a transmitter and a receiver [LC04, Section 1.1]. The transmitter produces a signal that is suitable for transmission over a channel [Sha48] and consists of an information source, a source encoder, a channel encoder and a modulator [LC04, Section 1.1]. The receiver performs the inverse operation of the transmitter to reconstruct the message from the receive signal [Sha48]. The receiver consists of a demodulator, a channel decoder, a source decoder and the destination [LC04, Section 1.1]. The channel is a medium to transmit the signal from the

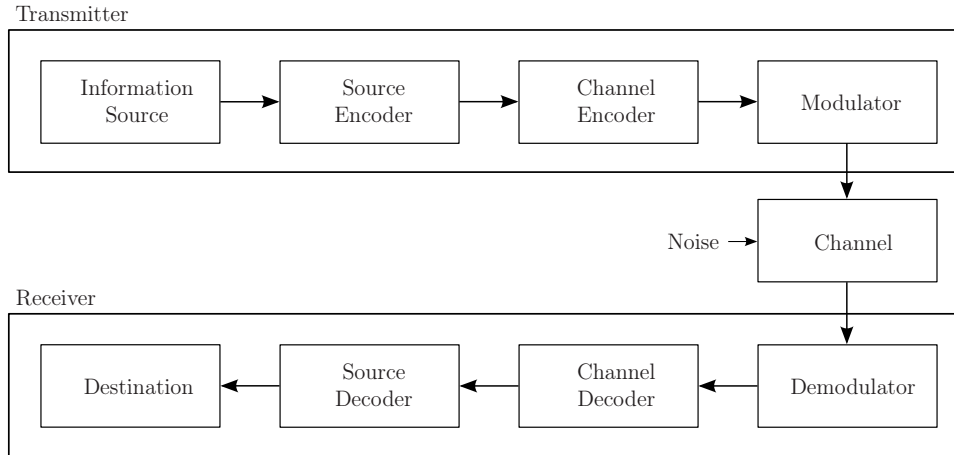


Figure 1.1. Block diagram of a typical wireless transmission system (according to [LC04, Figure 1.1]).

transmitter to the receiver [Sha48, Introduction]. In what follows, the individual elements of the transmitter and the receiver, as well as the channel are briefly discussed. The information source produces a message or a sequence of messages to be transmitted to the destination [Sha48]. To guarantee unambiguous communication among the communication entities, the message or sequence of messages to be transmitted must be constructed according to a syntax that is specified according to a fix communication protocol which is consistent throughout the communication entities [MS09, Section 1.2]. The area of communication protocols is not part of this thesis. Further information on communication protocols of wireless communication systems can be found in [Wal01] and references therein. The source encoder transforms each message into a sequence of binary digits, defined as the information sequence [LC04, Section 1.1]. The ideal source encoder is aimed to minimize the number of bits to represent each message and to unambiguously reconstruct the message of the information source [LC04, Section 1.1]. The aspect of source encoding is not discussed in this investigation. Extended reference literature can be found in [CT12] and references therein. The channel encoder transforms the information source into a codeword [LC04, Section 1.1]. The task of the channel encoder is to add redundancy to the information sequence to protect it against errors [Bos98, Chapter 1]. The aspect of channel coding is discussed in Section 2.3 of this thesis. The modulator transforms the codeword of the channel encoder into a signal form that is suitable for transmission over the channel [LC04, Section 1.3]. The aspect of modulation is discussed in Section 2.5.1 of this thesis. The signal form propagates through the channel and undergoes various types of disturbances [Jun97, Chapter 3]. In addition, the signal is perturbed by noise [Sha48, Section 11]. Further information on signal propagation is provided in Section 2.8.2 of this thesis. The demodulator processes the receive signal to recover the modulated signal form the transmitter

as precisely as possible [LC04, Section 1.1]. The output of the demodulator is denoted as the demodulated transmit signal form [LC04, Section 1.1]. Further information is provided in Section 2.5.2 of this thesis. The channel decoder transforms the demodulated transmit signal form into the estimated information sequence [LC04, Section 1.1]. Ideally, the estimated information sequence becomes a replica of the information sequence [LC04, Section 1.1]. The source decoder transforms the estimated information sequence into an estimate of the source output and delivers this information to the destination [LC04, Section 1.1]. The aspect of source decoding is not discussed in this thesis. Detail information on source decoding can be found in [CT12] and references therein. The destination has to interpret the estimated message or sequence of estimated messages following the defined protocol [MS09, Section 1.2].

Wireless communication can be divided into acoustic, optic and radio frequency based communication [AV10, Section 4.1.2]. In this thesis radio frequency based wireless communication is focused on. The aspect of acoustic and optic wireless communication is not addressed in this thesis. Further information on acoustic and optic wireless communication can be found in [Tru01] and [Agr10], respectively.

Radio frequency based wireless communication can be further subdivided into short-range [Mol05, Section 1.2] and mobile [Jun97, Chapter 2] communication. The purpose behind short-range communication is to provide wireless connectivity within the local sphere [KK09, Chapter 1]. Typical short-range communication systems include, among others, Radio Frequency Identification (RFID) [KK09, Chapter 1] with transmission path distances ranging from millimeters to centimeters, Wireless Person Area Networks (WPAN) [KK09, Chapter 1] providing wireless access in close vicinity of a person limited by a few meters, Wireless Body Area Networks (WBAN) [KK09, Chapter 1] serving users in surroundings of up to ten meters and Wireless Local Area Network (WLAN) [KK09, Chapter 1] providing local connectivity for indoor scenarios covering typically up to one hundred meters. Short-range communication is designed for fix and nomadic mobility, where seamless movement can only be guaranteed inside the coverage area of the corresponding system [KK09, Chapter 1]. High speed transmission is, however, not supported by short-range communication systems [KK09, Chapter 1]. The aspect of short-range communication is not considered in this thesis, Further information on short-range communication can be found in [KK09, Chapter 1].

Mobile communication on the other hand is designed to support fix, nomadic and high speed scenarios and thereby wireless communication over much larger distances [Mol05, Section 1.2.3]. With approximately 4.6 billion unique subscribers, as expected by 2020 [WD14], mobile communication is one of the big

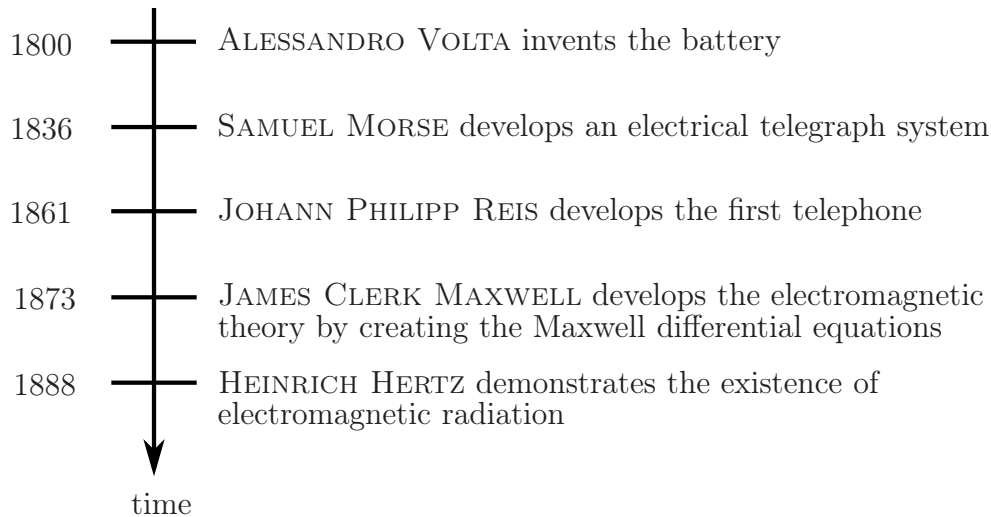


Figure 1.2. Overview of outstanding physical achievements of the 19th century for the development of modern wireless communication systems (created by the author of this thesis using [Bro86, Vol. 23, p. 436; Bro86, Vol. 15, p. 118; Bro86, Vol. 18, p. 245; Bro86, Vol. 14, p. 344; Bro86, Vol. 10, p. 14]).

engineering success stories of the last decades and the latest growing segment of the communication industry [Mol05, Section 1.4].

1.1.2 Historical Background

From the perspective of communication technology, the mathematical fundamentals of the 17th and 18th century [Kle12], the physical fundamentals of the 19th century [Bra95] and the technological progress of microcontrollers of the 20th century [Add+99] provide the essential preconditions for modern wireless communication.

Mathematical fundamentals are indispensable for modern wireless communication [Kle12]. Outstanding personalities providing non-negligible fundamental contribution include the French lawyer and mathematician PIERRE DE FERMAT [Bro86, Vol. 7, p. 200], the English statistician and philosopher THOMAS BAYES [Bro86, Vol. 2, p. 678] and the German mathematician and physicist JOHANN CARL FRIEDRICH GAUSS [Bro86, Vol. 8, p. 175]. PIERRE DE FERMAT, who is known as the founder of modern number theory, provided further fundamental contribution to analytical geometry, calculus and probability [Bro86, Vol. 7, p. 200]. THOMAS BAYES made outstanding contribution in the field of statistics and is famous for the Bayes' Theorem which was later named after him [Bro86, Vol. 2, p. 678]. JOHANN CARL FRIEDRICH GAUSS contributed significantly to many fields including number theory, statistics,

analysis, differential geometry and matrix theory [Bro86, Vol. 8, p. 175]. This list is not a complete one by far, but only contains selected contributions of outstanding personalities. A complete overview of outstanding mathematical contributors of the 17th and 18th century can be found in [Kle12] and references therein.

Outstanding physical achievements of the 19th century were essential for the development of modern wireless communication [Bra95]. Outstanding personalities providing non-negligible contribution include the Italian physicist and chemist ALESSANDRO VOLTA [Bro86, Vol. 23, p. 436], the American inventor SAMUEL MORSE [Bro86, Vol. 15, p. 118], the German physicist JOHANN PHILIPP REIS [Bro86, Vol. 18, p. 245], the Scottish scientist JAMES CLERK MAXWELL [Bro86, Vol. 14, p. 344] and the German physicist HEINRICH HERTZ [Bro86, Vol. 10, p. 14]. The chronological overview of the contribution of the outstanding personalities is depicted in Figure 1.2 on page 4. Around 1800, ALESSANDRO VOLTA invented the Voltaic pile which was the first chemical battery [Bro86, Vol. 23, p. 436]. The *Système International d'unités* (SI) unit for electrical voltage [SI08, Appendix 1, page 144] is named after him. In 1836, SAMUEL MORSE developed the Morse telegraph, known as the first telegraph system [Bro86, Vol. 15, p. 118]. In 1861, JOHANN PHILIPP REIS developed the first telephone, where tones were transmitted over electromagnetic signals [Bro86, Vol. 18, p. 245]. In 1873, JAMES CLERK MAXWELL published the work "A Treatise on Electricity and Magnetism" where MAXWELL has predicted the existence of radio waves which travel through the space with the speed of light [Max73]. In 1888, HEINRICH HERTZ was able to demonstrate the existence of electromagnetic radiation in laboratory experiments [Bro86, Vol. 10, p. 14]. The SI unit of frequency [SI08, Table 3] is named after him. Around 13 years after HEINRICH HERTZ's demonstration, the Italian engineer GUGLIELMO MARCONI became the first person who sent a transatlantic message from Cornwall, England to Newfoundland using Morse code [Bro86, Vol. 14, p. 189]. GUGLIELMO MARCONI received the Nobel Prize together with FERDINAND BRAUN in 1909 [Bro86, Vol. 14, p. 189]. This list is not a complete one by far, but only contains selected contributions of outstanding personalities. A complete overview of outstanding physical contributors of the 19th century can be found in [Bra95] and references therein.

The progress and development of microelectronics is the technical key enabler for modern wireless communication systems [Add+99]. Outstanding personalities providing non-negligible contribution include the American physicists JOHN BARDEEN [Bel56], WALTER BRATTAIN [Bel56] and WILLIAM SHOCKLEY [Bel56] as well as GORDON MOORE [Per08]. In 1947, JOHN BARDEEN, WALTER BRATTAIN and WILLIAM SHOCKLEY discovered the transistor effect which became the key enabler of modern electronics and microelectronics [LG06]. In 1956, they received the Nobel Prize in physics for the "investigation

on semiconductors and the discovery of the transistor effect" [Bel56]. GORDON MOORE, the co-founder of the Fairchild Semiconductors and Intel [Mol06], asserted in 1965 that "the number of components that could be placed in a chip could be expected to double every year" [Moo65] and revised his prediction 10 years later "that the new slope might approximate a doubling every two years, rather than every year [Mol06]. Comprehensive articles reviewing the development of semiconductors can be found in [Mac11; CK13] and references therein, whereas future trends of the development of semiconductors can be found in [Bea+08; Sch+13] and references therein. The list of outstanding personalities providing non-negligible contribution is not a complete one by far. A complete overview of outstanding technological contributors of microelectronics of the 20th century can be found in [SN07] and references therein.

1.1.3 Driving Forces Behind 4G LTE Systems

The growth of social media is the dominant force behind the development of mobile communication networks [WD14]. Internet-based multimedia services impose different requirements on the latency and data rate to guarantee the user requested Quality of Service (QoS) [Eri16]. Detail information on the data rate in Long Term Evolution (LTE) systems is provided in Section 1.1.4 and Section 2.9 of this thesis. Interactive real-time services, including video-telephony, impose stringent requirements on the latency, such that the preferred Round-Trip Time (RTT) should not exceed 150 ms [3GP99b, Section 2]. The preferred data rate for that interactive real-time services ranges up to 2 MBit/s [3GP99a, Section 5.3]. Real-time block transfer services, including video-streaming, are latency tolerant up to 10 s [3GP99b, Section 3], but impose stringent requirements on high data rates of approximately 15 MBit/s to enable High Definition Video (HDV) using the Moving Picture Experts Group (MPEG) compression [ITU96, Table 8-13]. Contemporary 3rd generation (3G) Universal Mobile Telecommunication System (UMTS) Release 99 systems were designed to support 2 MBit/s [Jun97, Section 1.2.4], as the *Elektronisches Wählsystem Digital* (EWS-D), developed by Siemens, was able to support 2 MBit/s per connection [Sie02]. Furthermore, the transport channels of the 3G UMTS Release 99 systems terminate at the Serving Resource Network Controller (SRNC) [WSA03, Section 4.4.7]. As the SRNC rather than the NodeB is responsible for the acknowledge of the packet data [WSA03, Section 4.4.7], RTTs of 3G UMTS Release 99 systems range from 20 ms to 300 ms [3GP99a, Section 5.4]. However, the data rates and RTTs experienced by the user average 1.5 MBit/s [Wes13] and 361 ms [Wes13], respectively, such that the requested QoS for the internet-based multimedia services cannot be guaranteed by 3G UMTS Release 99 systems [WD14].

To overcome this limitation, the 3rd Generation Partnership Project (3GPP) organized a workshop to initiate work on the radio interface of the 4th generation (4G) LTE system in November 2004 and approved the first specification in January 2006 [DPS14, Section 1.5.3]. As no backwards compatibility on legacy UMTS devices was required and data services rather than voice services were expected to dominate the resource utilization in the future, it was decided to establish a flat All Internet Protocol Network (AIPN) and migrate the UMTS circuit-switched services on the packet-switched core network [DPS14, Section 1.5.3]. To meet the required QoS for the evolving internet-based multimedia services [WD14], LTE was optimized for data services supporting

- short Transmission Time Intervals (TTIs),
- Media Access Control (MAC) termination in Enhanced Node B (eNodeB),
- flexible bandwidth utilization,
- Higher Order Modulation (HOM) and
- Multiple-Input and Multiple-Output (MIMO)

with the aim of reducing the network latency and increasing the bandwidth efficiency [3GP16n; 3GP16b; 3GP16f; 3GP16d; 3GP16g], where the eNodeB is defined as the stationary transmission unit for mobile communication in LTE networks in the Downlink (DL) [3GP16b, Chapter 1; 3GP16h, Section 4.4.1.1]. LTE systems are designed to provide latencies of less than 5 ms [Ast+09]. The aspect of network latencies in LTE systems is not discussed in this investigation. For further information on latencies in LTE networks see [3GP09c]. The aspect of bandwidth efficiency enhancements in LTE networks is discussed in Section 1.1.4 of this investigation.

1.1.4 Evolution of 4G LTE Systems

Since the first release of LTE, the 3GPP has continuously evolved the LTE specification to meet the changing requirements of internet-based multimedia services [3GPf; WD14]. A rough overview of selected key enhancements and parameters of LTE systems operating in the DL transmission is provided in Table 1.1 on page 10. Table 1.1 provides information on the standard, the end date of the release, the key enhancements being of particular importance for this thesis, the channel bandwidth, the supported modulation mapping schemes, the maximum data rate and the maximum bandwidth efficiency. A complete overview of features standardized in LTE Release 8, Release 9, Release 10, Release 11, Release 12 and Release 13 can be found in [3GP14c], [3GP14d], [3GP14a], [3GP14b], [3GP15a] and [3GP15b], respectively.

The name of the standard is provided in the first column of Table 1.1.

The end date of the release denotes the date from which no further changes on the specification can be carried out [3GPF]. The end date of the respective release is provided in the second column of Table 1.1.

The key enhancements of the respective release being of particular importance for this thesis are summarized in the third column of Table 1.1. Note that the presented key enhancements merely denote an excerpt of all enhancements. A complete list of enhancements of the respective release can be found in [3GP14c; 3GP14d; 3GP14a; 3GP14b; 3GP15a; 3GP15b].

The available transmission bandwidth LTE is designed to operate in, is divided into operating bands [3GP16n, Section 5.5]. The operating band denotes the frequency range LTE operates in [3GP15f, Section O]. Valid operating bands are tabularized in [3GP16n, Table 5.5-1]. Each operating band can be further subdivided into channel bandwidths [3GP16n, Section 5.6.1]. The assignment between operating band and channel bandwidth is tabularized in [3GP16n, Table 5.6.1-1]. The channel bandwidth denotes the range in frequency domain enabling signal transmission with acceptable attenuation [Kam08, Section 2.2]. The supported range of channel bandwidths is summarized in the fourth column of Table 1.1. Further information on the channel bandwidth is provided in Section 1.2.5 of this thesis.

The modulation mapping describes the process of mapping binary digits on modulation symbols [3GP16f, Section 7.1]. The supported modulation mapping schemes of the respective release are summarized in the fifth column of Table 1.1. Further information on modulation mapping schemes is provided in Section 2.4.2 of this thesis.

The data rate is defined as the number of transmitted bits per second [Mol05, Section 1.3.1]. In LTE systems, the number of information bits is determined by the Transport Block Size (TBS) and excludes the redundancy information of the channel encoder [3GP16g, Section 7.1]. However, overhead caused by higher layer signaling is included in the data rate [3GP16g]. The maximum achievable data rate of the respective release is denoted in the sixth column of Table 1.1.

The bandwidth efficiency is defined as the data rate per utilized bandwidth and is measured in bit/s/Hz [Stü11, Section 1.7.1]. The maximum achievable bandwidth efficiency of the respective release is denoted in the seventh column of Table 1.1. In this thesis the bandwidth efficiency is one of the quality criterion and is further explained in Section 2.9.

The standardization of LTE Release 8 ended on 2009-03-12 [3GPF]. The key enhancements being of particular importance for this thesis include the MIMO

support [3GP14c, Section 5.1.3], Orthogonal Frequency Division Multiplexing (OFDM) baseband signal generation [3GP14c, Section 5.1.3] and closed-loop transmission [3GP09b, Section 7.2]. A complete list of LTE Release 8 enhancements can be found in [3GP14c]. Since LTE Release 8, MIMO antenna configuration enabling signal transmission on up to four spatial layers is supported in the DL. Furthermore, the OFDM baseband signal generation technique [3GP09a, Section 6.12], introduced since LTE Release 8, is the core of the LTE radio interface in the DL transmission [Ast+09]. OFDM baseband signal generation is discussed in Section 2.5 of this thesis. Moreover, closed-loop transmission is supported since LTE Release 8 [3GP09b, Section 7.2]. To assist the eNodeB in the DL transmission, the User Equipment (UE) measures the DL channel and feeds quantized Channel State Information (CSI) back, such that the eNodeB can adapt the transmission signal on the varying channel conditions [Ast+09]. In this thesis, closed-loop transmission is an essential feature and is further discussed in Section 2.7. LTE Release 8 systems support variable bandwidth configuration [3GP16o, Section 5.6]. Supported bandwidth configuration include 1.4 MHz, 3 MHz, 5 MHz, 10 MHz, 15 MHz and 20 MHz [3GP16o, Section 5.6]. LTE Release 8 systems support four different modulation mapping schemes, including Binary Phase Shift Keying (BPSK), Quadrature Phase Shift Keying (QPSK), 16 Quadrature Amplitude Modulation (QAM) and 64 QAM [3GP09a, Section 7.1], whereas only the QPSK, the 16 QAM and the 64 QAM are used for data transmission in the DL [3GP09a, Section 6.3.2]. Note that stable support of MIMO, OFDM baseband signal generation, closed-loop transmission, variable bandwidth configuration and modulation mapping schemes in LTE can be guaranteed since freezing LTE Release 8 in December 2008 [3GPa] and remains in each LTE specification released by 3GPP [3GP16n, Section 5.6; 3GP16f, Section 6.3; 3GP16g, Section 7.2] until today. With a MIMO antenna configuration enabling signal transmission on four spatial layers, an allocated channel bandwidth of 20 MHz and the 64 QAM modulation mapping scheme, a maximum data rate of up to 300 MBit/s can be achieved for class 5 UEs in the DL [HTR16, Table 2.2]. Dividing the maximum data rate by the channel bandwidth [Stü11, Section 1.7.1] results in a maximum bandwidth efficiency of 15 bit/s/Hz.

The standardization on LTE Release 9 ended on 2010-03-05 [3GPf]. The key enhancement being of particular importance for this thesis includes the extended support of closed-loop CSI feedback for Demodulation Reference Signal (DMRS)-based transmission [3GP14d, Section 12.2], denoted as Transmission Mode (TM) 8 [3GP10b, Section 7.2.2]. A complete list of LTE Release 9 enhancements can be found in [3GP14d]. DMRS-based TMs are characterized by the fact that the transmitted Reference Signals (RSs) are precoded with the same precoder that is also used for precoding the data signal [3GP10a, Section 6.10.3]. Detail information on the DMRS generation is provided in

Table 1.1. Selected key features of LTE systems (created by the author of this thesis using [3GPP; 3GPP14c; 3GPP16o; 3GPP09a; 3GPP14d; 3GPP16o; 3GPP10a; 3GPP14a; 3GPP16k; 3GPP13b; 3GPP14b; 3GPP16l; 3GPP14e; 3GPP15a; 3GPP16m; 3GPP15c; 3GPP15b; 3GPP16n; 3GPP16f; HTR16]).

Standard	End Date of Release	Key Enhancements	Channel Bandwidth	Modulation Mapping Schemes	Maximum Data Rate	Maximum Bandwidth Efficiency
3GPP TS 36 series (Release 8)	2009-03-12	MIMO support, OFDM signal generation, closed-loop transmission	1.4 MHz,..., 20 MHz	QPSK, 16 QAM, 64 QAM	300 MBit/s	15 bit/s/Hz
3GPP TS 36 series (Release 9)	2010-03-25	extended closed-loop transmission support for DMRS-based TMs	1.4 MHz,..., 20 MHz	QPSK, 16 QAM, 64 QAM	300 MBit/s	15 bit/s/Hz
3GPP TS 36 series (Release 10)	2011-06-08	CSI feedback using CSI-RS in closed-loop transmission for DMRS- based TMs	1.4 MHz,..., 20 MHz, up to 100 MHz using CA	QPSK, 16 QAM, 64 QAM	3 GBit/s	30 bit/s/Hz
3GPP TS 36 series (Release 11)	2013-03-06	CoMP transmission	1.4 MHz,..., 20 MHz, up to 100 MHz using CA	QPSK, 16 QAM, 64 QAM	3 GBit/s	30 bit/s/Hz
3GPP TS 36 series (Release 12)	2015-05-13	NAICS	1.4 MHz,..., 20 MHz, up to 100 MHz using CA	QPSK, 16 QAM, 64 QAM, 256 QAM	3.9 GBit/s	39 bit/s/Hz

Continued on next page

Table 1.1. Selected key features of LTE systems (*Continued from previous page*).

Standard	End Date of Release	Key Enhancements	Channel Bandwidth	Modulation Mapping Schemes	Maximum Data Rate	Maximum Bandwidth Efficiency
3GPP TS 36 series (Release 13)	2016-03-11		1.4 MHz,..., 20 MHz, up to 100 MHz using CA	QPSK, 16 QAM, 64 QAM, 256 QAM	3.9 GBit/s	39 bit/s/Hz

3GPP: 3rd Generation Partnership Project, CA: Carrier Aggregation, CoMP: Coordinated Multipoint, CSI: Channel State Information, DMRS: Demodulation Reference Signal, MIMO: Multiple-Input and Multiple-Output, NAICS: Network-Assisted Interference Cancellation and Suppression, OFDM: Orthogonal Frequency Division Multiplexing, QAM: Quadrature Amplitude Modulation, QPSK: Quadrature Phase Shift Keying, RS: Reference Signal, TM: Transmission Mode, TS: Technical Specification

Section 2.2 of this thesis. The mapping of the DMRS on resources is discussed in Section 2.4.4 of this thesis. Detail information on CSI reporting in TM 8 is provided in Section 2.7 of this thesis. Note that stable support of closed-loop CSI feedback for DMRS-based transmission can be guaranteed since freezing LTE Release 9 in March 2010 [3GPb] and remains in each LTE specification released by 3GPP [3GP16f, Section 6.10.3; 3GP16g, Section 7.2] until today. Furthermore, no changes on the supported variable bandwidth configuration, introduced in LTE Release 8 [3GP16o, Section 5.6], have been made in LTE Release 9 [3GP16p, Section 5.6]. Moreover, no changes on the supported modulation mapping schemes introduced in LTE Release 8 [3GP09a, Section 7.1] have been made in LTE Release 9 [3GP10a, Section 7.1]. No enhancements in terms of maximum data rate nor bandwidth efficiency have been achieved in LTE Release 9 systems, compared with LTE Release 8 systems [HTR16, Table 2.2].

The standardization on LTE Release 10 ended on 2012-06-08 [3GPf]. The key enhancement being of particular importance for this thesis includes the CSI feedback using CSI-RSs in closed-loop transmission for DMRS-based TMs [3GP14a, Section 10.2], denoted as TM 9 [3GP15d, Section 7.2.2]. A complete list of LTE Release 10 enhancements can be found in [3GP14a]. The transmission of the CSI-RSs enables the UE to estimate the CSI for multiple cells rather than just for its serving cell [STB11, Section 29.1.2]. The generation of the DMRSs and the CSI-RSs is discussed in Section 2.2 of this thesis. The mapping of the DMRSs and the CSI-RSs on resources is discussed in Section 2.4.4 of this thesis. Detail information on the CSI reporting in TM 9 is provided in Section 2.7 of this thesis. It is worth adding that LTE Release 10 standardized of the MIMO antenna configuration enabling signal transmission on up to eight spatial layers in the DL [3GP14a, Section 10.2]. Furthermore, the support of Carrier Aggregation (CA) with up to five component carriers is supported in LTE Release 10 [3GP14a, Section 10.1]. Note that the stable support of CSI feedback using CSI-RSs in closed-loop transmission for DMRS-based TMs, the MIMO antenna configuration supporting signal transmission on up to eight spatial layers and CA can be guaranteed since freezing LTE Release 10 in September 2011 [3GPc] and remains in each LTE specification released by 3GPP [3GP16g, Section 7.2; 3GP16g, Section 7.1.5B; 3GP16n, Chapter 5-Chapter 7] until today. With a MIMO antenna configuration supporting signal transmission on eight spatial layers, an allocated channel bandwidth of 100 MHz using CA and the 64 QAM modulation mapping scheme, a maximum data rate of up to 3 GBit/s can be achieved for class 8 UEs in the DL [HTR16, Table 2.3]. Dividing the maximum data rate by the channel bandwidth [Stü11, Section 1.7.1] results in a maximum bandwidth efficiency of 30 bit/s/Hz. The properties of the MIMO antenna configuration supporting signal transmission on eight spatial layers are not discussed in this thesis. A de-

tailed overview of antenna configuration supporting signal transmission on up to eight spatial layers can be found in [3GP15d, Section 7.1.5B] and references therein. Furthermore, the properties of CA are not discussed in this thesis. A detailed overview of CA can be found in [3GP16k, Chapter 5-Chapter 7]. No changes on the supported modulation mapping schemes, introduced in LTE Release 8 [3GP09a, Section 7.1] have been made in LTE Release 10 [3GP13b, Section 7.1]. Moreover, no changes on the supported variable bandwidth configuration, introduced in LTE Release 8 [3GP16o, Section 5.6], have been made in LTE Release 10 [3GP16k, Section 5.6].

The standardization on LTE Release 11 ended on 2013-03-06 [3GPf]. The key enhancement being of particular importance for this thesis includes the support of Coordinated Multipoint (CoMP) transmission [3GP14b, Section 11.10]. A complete list of LTE Release 11 enhancements can be found in [3GP14b]. CoMP transmission enables coordinated signal transmission from multiple transmitters in the DL [3GP13a, Chapter 5] to improve the coverage of high data rates and cell-edge throughput [3GP14b, Section 21.1]. Further information on CoMP transmission is provided in Chapter 3 and Chapter 4 of this thesis. Note that the stable support of CoMP transmission in LTE can be guaranteed since freezing LTE Release 11 in March 2013 [3GPc] and remains in each LTE specification released by the 3GPP [3GP16g, Section 7.2.2] until today. Furthermore, no changes on the supported variable bandwidth configuration, introduced in LTE Release 8 [3GP16o, Section 5.6] have been made in LTE Release 11 [3GP16l, Section 5.6]. Moreover, no changes on the supported modulation mapping schemes, introduced in LTE Release 8, [3GP09a, Section 7.1] have been made in LTE Release 11 [3GP14e, Section 7.1]. No enhancements in terms of maximum data rate nor bandwidth efficiency have been achieved in LTE Release 11 systems compared with LTE Release 10 systems [HTR16, Table 2.2].

The standardization on LTE Release 12 ended on 2015-03-13 [3GPf]. The key enhancement being of particular importance for this thesis includes the support of Network-Assisted Interference Cancellation and Suppression (NAICS) receivers [3GP15a, Section 11.18]. A complete list of LTE Release 12 enhancements can be found in [3GP15a]. NAICS receivers are characterized by the fact that they obtain assistance from the network to enable improved interference cancellation and suppression properties over conventional LTE Release 11 receivers [3GP15a, Section 11.18; 3GP14f, Chapter 7]. Further information on NAICS receivers is provided in Section 2.6 of this thesis. It is worth adding that the 256 QAM modulation mapping scheme has been standardized in LTE Release 12 [3GP15c, Section 7.1]. Note that stable support of NAICS receivers and the 256 QAM can be guaranteed since freezing LTE Release 12 in March 2015 [3GPd] and remains in each LTE specification released by 3GPP [3GP16f, Section 7.1] until today. With a MIMO antenna configuration supporting sig-

nal transmission on eight spatial layers, an allocated channel bandwidth of 100 MHz using CA and the 256 QAM modulation mapping scheme, a maximum data rate of up to 3.9 GBit/s can be achieved for class 15 UEs in the DL [HTR16, Table 3.4]. Dividing the maximum data rate by the channel bandwidth [Stü11, Section 1.7.1] results in a maximum bandwidth efficiency of 39 bit/s/Hz. Furthermore, no changes on the supported variable bandwidth configuration, introduced in LTE Release 8 [3GP16o, Section 5.6], have been made in LTE Release 12 [3GP16m, Section 5.6].

The standardization on LTE Release 13 ended on 2016-03-11 [3GPf]. No key enhancements being of particular importance for this thesis have been identified in [3GP15b]. Note that stable usage of LTE Release 13 features can be guaranteed since freezing LTE Release 13 in March 2016 [3GPe]. No changes on the supported variable bandwidth configuration, introduced in LTE Release 8 [3GP16o, Section 5.6], have been made in LTE Release 13 [3GP16n, Section 5.6]. Furthermore, no changes on the modulation mapping schemes, extended in LTE Release 12 [3GP15c, Section 7.1], have been made in LTE Release 13 [3GP16f, Section 7.1]. Moreover, no enhancements in terms of maximum data rate nor bandwidth efficiency have been achieved in LTE Release 13 systems compared with LTE Release 12 systems [HTR16, Table 3.4].

1.2 Interference-Limited Cellular LTE Networks

1.2.1 Introduction

A network is defined as a graph which consists of a set of nodes, where the nodes are interconnected by edges [Mar08, Section P].

In the research field of cellular networks, a cell is defined as the area in which the eNodeB provides coverage and can be identified by a unique cell-ID [Mol05, Section 17.6.1]. Furthermore, a cluster is defined as a set of cells to be considered as a whole [Bro86, Vol. 4, p. 611]. The properties of cellular LTE networks are discussed in Section 1.2.2 of this thesis.

Interference is defined as the formation of a new signal pattern where two or more incident signal patterns overlap [Ren15, page 124]. A classification of types of interference is provided in Section 1.2.3 of this thesis.

1.2.2 Cellular LTE Networks

The properties of cellular LTE networks, being of particular importance for this thesis, are discussed in what follows. In LTE networks the cells are organized

hierarchically with four zones including [DPS14, Section 19.7.5]

- macro-cells,
- micro-cells,
- femto-cells and
- pico-cells.

In this thesis macro-cells are focused on. Further information on micro-cells, femto-cells and pico-cells can be found in [DPS14, Section 19.7.5]. In a macro cellular deployed LTE network, the base stations with three sectors per site are placed on a hexagonal grid with distance of $3 \cdot R_{\text{cell}}$, where R_{cell} denotes the radius of the cell [3GP16h, Section 4.4.1.1]. Each of the three sectors per site can be understood as a cell [3GP16h, Section 4.4.1.1]. A typical layout for a macro cellular deployed LTE network can be found in [3GP16h, Figure 4.2]. Furthermore, a distinct eNodeB Identified (eNodeB-ID) is used to identify the eNodeB providing coverage to a distinct cell [3GP16a, Section 8.2]. The eNodeB-ID is contained with the physical layer cell identity $N_{\text{cell}}^{\text{ID}}$ of its cell [3GP16a, Section 8.2; 3GP16f, Section 6.11]. The physical layer cell-identity $N_{\text{cell}}^{\text{ID}}$ is uniquely defined by a number $N_{\text{ID}}^{(1)}$ in the range of 0 to 167, representing the physical layer cell-identity group [3GP16f, Section 6.11] and a number $N_{\text{ID}}^{(2)}$ in the range of 0 to 2, representing the physical layer identity within the physical layer cell-identity group [3GP16f, Section 6.11] and reads [3GP16f, Section 6.11]

$$N_{\text{cell}}^{\text{ID}} = 3 \cdot N_{\text{cell}}^{(1)} + N_{\text{cell}}^{(2)}. \quad (1.1)$$

Valid physical layer cell-identity groups and physical layer identities can be found in [3GP16f, Table 6.11.2.1-1]. The physical layer cell-identity is used, among others, for reference signal generation and reference signal mapping. Further information on reference signal generation and reference signal mapping, respectively, is provided in Section 2.2 and Section 2.4.4 this thesis, respectively.

For the sake of completeness, it should be mentioned that the eNodeBs are interconnected with each other by means of the X2 interface [3GP16a, Chapter 4]. The X2 interface and the underlying X2 application protocol is specified in [3GP16a, Section 20.1] and [3GP16r], respectively. Furthermore, the eNodeBs are connected by means of the S1 interface protocol with the Evolved Packet Core (EPC) [3GP16a, Section 19.1]. Further information on the S1 interface protocol and the underlying S1 application protocol can be found in [3GP16a, Section 19.1] and [3GP16q], respectively.

LTE networks are designed to operate with a frequency reuse factor of one [STB11, Section 12.5]. The frequency reuse factor denotes the number of cells in a cluster that operate on disjoint frequency bands [Jun97, Section 2.2.7].

Hence, with a frequency reuse factor of one [STB11, Section 12.5], all specified frequency bands [3GP16n, Section 5.5] can be reused in each cell. The associated impact on signal reception is discussed in Section 1.2.3 of this thesis.

1.2.3 Types of Interference

Interference can be classified into [Jun97, Section 3.2; CT07, Section 4.3.1]

- Inter-Symbol Interference (ISI),
- Inter-Carrier Interference (ICI) and
- Multiple Access Interference (MAI).

ISI denotes the superposition of differently delayed and weighted replica of the transmit signal in the receiver [Jun97, Section 3.2.1]. These replicas are denoted as echoes of the transmit signal, result in frequency-selective fading and, thus in ISI [Jun97, Section 3.2.1]. ISI inherits from the inhomogeneities of the mobile communication channel [Jun97, Section 3.2.1]. The transmit waves do not propagate uniformly, but rather experience diffractions, reflections and scattering [Jun97, Section 3.2.1]. If no appropriate measures are carried out, ISI will considerably disturb the receive signal [Jun97, Section 3.2.1]. The impact of ISI can be eliminated by using a Cyclic Prefix (CP), where the tail of each OFDM symbol is copied and placed in front of the OFDM symbol [Mol05, Section 19.4]. The supported lengths of the CP in LTE systems are denoted in [3GP16f, Table 6.12-1]. Further information on CP generation is provided in Section 2.5.1 of this thesis. Moreover, the impact of frequency-selective fading can be eliminated by using single-tap equalization in the frequency domain [Kam08, Section 16.2.4]. Further information on single-tap equalization is provided in Section 2.6.2 of this thesis.

ICI denotes the superposition of non-orthogonal carriers [Pra04, Section 5.2.4.2; CT07, Section 4.3.2] that cause, among others, Carrier Frequency Offsets (CFOs) [CT07, Section 4.3.1], Sampling Clock Offsets (SCOs) [CT07, Section 4.3.2] and phase-offsets [CT07, Section 4.3.3]. ICI is attributed to two factors: frequency mismatch among the local transmitter and receiver oscillators [CT07, Section 4.3.1], and the time-selective mobile communication channel due to the Doppler effect [Mol05, Section 19.7]. If no appropriate measures are carried out, ICI will considerably disturb the receive signal [CT07, Section 5.2.1]. The aspect of ICI is not considered in this investigation. Detail information on the impact of CFO, SCO and phase-noise caused by ICI can be found in [CT07, Section 5.2.1]. Furthermore, CFO, SCO and phase-noise compensation techniques can be found in [CT07, Section 5.3 - Section 5.4] and references therein.

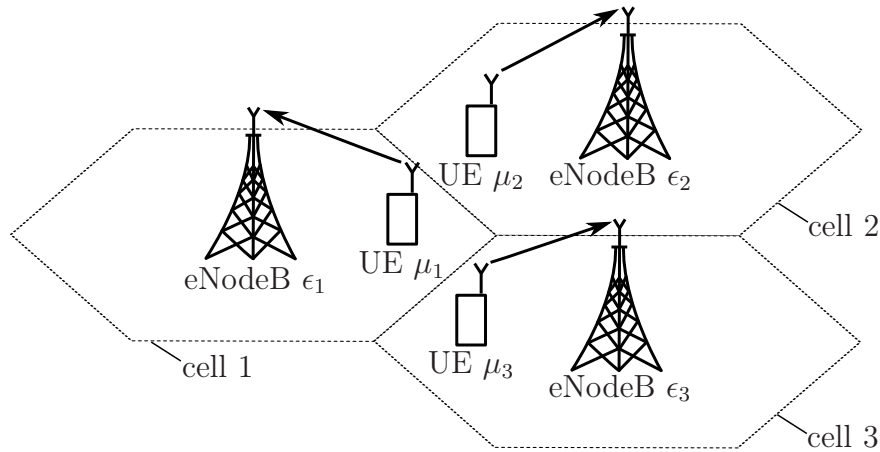


Figure 1.3. Cutout for a macro cellular deployed LTE network (created by the author of this thesis using [Mol05, Figure 20.7]).

MAI denotes the superposition of receive signals, which go back to different transmitters of the mobile communication system [Jun97, Table 3.1]. MAI can be further classified into intra-cell interference and inter-cell interference [Jun97, Section 3.2.2].

Intra-cell interference denotes the superposition of receive signals which go back to different transmitters of the mobile communication system, where the transmit signals arise from the same cell [Jun97, Section 3.2.2] and, thus, also from the same eNodeBs. The aspect of intra-cell interference is not discussed in this thesis. Further information on intra-cell interference can be found in [Jun97, Section 4.3 - Section 4.5].

Inter-cell interference denotes the superposition of receive signals which go back to different transmitters of the mobile communication system, where the transmit signals arise from different cells [Jun97, Section 3.3.2] and, thus, also from different eNodeBs. The aspect of inter-cell interference is further discussed in Section 1.2.4 of this thesis.

1.2.4 Inter-Cell Interference

The occurrence of inter-cell interference in LTE networks in the DL is explained by using Figure 1.3 on page 17. Figure 1.3 shows a cutout of a macro cellular deployed LTE network with three cells, three eNodeBs ϵ_1 to ϵ_3 and three UEs, μ_1 to μ_3 . Two variants of assignment between the UEs and eNodeBs are discussed. The assignment with respect to connection refers to the Radio Resource Control (RRC) connection establishment among the UEs and the eNodeBs [3GP16s, Section 4.1.1.2]. The assignment with respect to desired

signal transmission refers to the mapping of one or more of the eNodeBs transmitting the desired signal to each of the UEs [3GP16g, Section 7.1; 3GP13a, Section 5.1.3].

The assignment with respect to synchronization between the UEs μ_1 to μ_3 and the eNodeBs ϵ_1 to ϵ_3 is denoted by arrows beginning at each UE and ending at the respective eNodeB the UE is assigned with [Jun97, Section 4.4.1], as depicted in Figure 1.3. Furthermore, it is assumed that the UEs μ_1 to μ_3 are scheduled on the same frequency band in the DL transmission. To provide a precise formulation of the inter-cell interference issue arising in LTE networks [Ast+09], the eNodeBs and the UEs are considered as sets.

Let \mathbb{E} denote the set of all eNodeBs in the macro cellular deployed LTE network, where

$$\mathbb{E} \stackrel{\text{def}}{=} \{\epsilon_1, \dots, \epsilon_{|\mathbb{E}|}\} \quad (1.2)$$

holds [Jun97, Section 4.4.1]. The cardinality of the set \mathbb{E} is denoted by $|\mathbb{E}|$ and represents the number of eNodeBs in the macro cellular deployed LTE network [Jun97, Section 4.4.1]. The cutout of the macro cellular deployed LTE network, depicted in Figure 1.3, includes $|\mathbb{E}| = 3$ eNodeBs, such that $\{\epsilon_1, \epsilon_2, \epsilon_3\}$ holds for the set \mathbb{E} . The eNodeB ϵ_b is located in the middle of the b -th cell for $b = 1, \dots, 3$, as depicted in Figure 1.3.

Furthermore, let \mathbb{U} denote the set of UEs located in the macro cellular deployed LTE network, where

$$\mathbb{U} \stackrel{\text{def}}{=} \{\mu_1, \dots, \mu_{|\mathbb{U}|}\} \quad (1.3)$$

holds [Jun97, Section 4.4.1]. The cardinality of the set \mathbb{U} is denoted by $|\mathbb{U}|$ and represents the number of UEs located in the macro cellular deployed LTE network that operate in the same frequency band [Jun97, Section 4.4.1]. With respect to the cutout of the macro cellular deployed LTE network depicted in Figure 1.3, three UEs operate in the same frequency band, such that $|\mathbb{U}| = 3$ holds. Hence, the set \mathbb{U} includes $\{\mu_1, \mu_2, \mu_3\}$. The UE $\mu_m \in \mathbb{U}$ is located in the edge of the m -th cell, as depicted in the cutout of the macro cellular deployed LTE network in Figure 1.3 for $m = 1, \dots, 3$.

In the following step, the assignment with respect to synchronization between the UEs $\mu_m \in \mathbb{U}$, defined in (1.3) and the eNodeBs $\epsilon_b \in \mathbb{E}$, defined in (1.2) is discussed. Each UE μ_m , $m = 1, \dots, |\mathbb{U}|$ operating in the same frequency band is uniquely assigned with respect to synchronization by the mapping function

$$m \mapsto a_{\text{sync}}(m), \quad m = 1, \dots, |\mathbb{U}| \quad (1.4)$$

to the eNodeB $\epsilon_{a_{\text{sync}}(m)} \in \mathbb{E}$ [Jun97, Section 4.4.1]. With respect to the cutout

of the macro cellular deployed LTE network depicted in Figure 1.3

$$1 \mapsto 1, \quad (1.5a)$$

$$2 \mapsto 2, \quad (1.5b)$$

$$3 \mapsto 3 \quad (1.5c)$$

holds for the assignment with respect to synchronization in (1.4) among the UEs $\mu_m \in \mathbb{U}$ and the eNodeBs $\epsilon_{a_{\text{sync}}(m)} \in \mathbb{E}$ for $m = 1, \dots, |\mathbb{U}|$. Algorithms providing assignment with respect to synchronization among the UEs and the eNodeBs are not discussed in this thesis. Further information on assignment algorithms with respect to synchronization can be found in [STB11, Section 3.2.3.2, Section 7.2, Section 23.7.1; Mol05, Section 23.7.2].

In what follows, the assignment with respect to desired signal transmission is discussed. The eNodeBs $\epsilon_b \in \mathbb{E}$, transmitting the desired signal to the UE $\mu_{a_{\text{data}}(b)}$, are uniquely assigned by the mapping function

$$b \mapsto a_{\text{data}}(b), \quad b = 1, \dots, |\mathbb{E}|. \quad (1.6)$$

Usually, the UE $\mu_m \in \mathbb{U}$ receives the desired signal from the eNodeB $\epsilon_{a_{\text{sync}}(m)}$ it is synchronized with [3GP16g, Section 7.1]. Let \mathbb{A}_m denote the set of eNodeBs $\epsilon_b \in \mathbb{E}$ transmitting the desired signal to the UE $\mu_m \in \mathbb{U}$ with

$$\mathbb{A}_m \stackrel{\text{def}}{=} \{\epsilon_b | a_{\text{data}}(b) = m\}, \quad m = 1, \dots, |\mathbb{U}|. \quad (1.7)$$

The cardinality of \mathbb{A}_m is denoted by $|\mathbb{A}_m|$ and represents the number of eNodeBs $\epsilon_b \in \mathbb{E}$ that are simultaneously transmitting the desired signal on the same frequency band to the UE $\mu_m \in \mathbb{U}$. In CoMP transmission networks, operating in Joint Processing (JP) mode [3GP16g, Section 5.1.3], the cardinality of \mathbb{A}_m , $m = 1, \dots, |\mathbb{E}|$ is usually greater than or equal to one. CoMP transmission networks are discussed in Chapter 3 of this thesis. With respect to the cutout of the macro cellular deployed LTE networks depicted in Figure 1.3,

$$1 \mapsto 1, \quad (1.8a)$$

$$2 \mapsto 2, \quad (1.8b)$$

$$3 \mapsto 3 \quad (1.8c)$$

holds for the mapping function in (1.6). Furthermore,

$$\mathbb{A}_1 \mapsto \{\epsilon_1\}, \quad (1.9a)$$

$$\mathbb{A}_2 \mapsto \{\epsilon_2\}, \quad (1.9b)$$

$$\mathbb{A}_3 \mapsto \{\epsilon_3\} \quad (1.9c)$$

holds for each set \mathbb{A}_m , $m = 1, \dots, |\mathbb{U}|$ according to (1.7). Moreover,

$$\mathbb{A}_i \cap \mathbb{A}_j = \emptyset \quad (1.10)$$

holds for the intersection of two sets \mathbb{A}_i and \mathbb{A}_j , where $i = 1, \dots, |\mathbb{U}|$ and $j = 1, \dots, |\mathbb{U}|$ holds for $i \neq j$, such that one eNodeB does not transmit the desired signal to more than one UE.

Due to the inhomogeneities of the mobile communication channel [Jun97, Section 3.2.1], the UE $\mu_m \in \mathbb{U}$ experiences a superposition of receive signals which go back to the eNodeBs $\epsilon_b \in \mathbb{A}_m$ the UE $\mu_m \in \mathbb{U}$ is assigned to with respect to signal transmission and of receive signals which go back to the eNodeBs $\epsilon_{\tilde{b}} \in \mathbb{A}_{\tilde{m}}$ transmitting the desired signal to the UE $\mu_{\tilde{m}} \in \mathbb{U}$ that the UE $\mu_m \in \mathbb{U}$ experiences as inter-cell interference for $m = 1, \dots, |\mathbb{U}|$, $\tilde{m} = 1, \dots, |\mathbb{U}|$, where $m \neq \tilde{m}$ holds. Hence,

$$\mathbb{I}_m = \bigcup_{\substack{j=1 \\ j \neq m}}^{|\mathbb{U}|} \mathbb{A}_j \quad (1.11)$$

denotes the set of interfering eNodeBs imposing inter-cell interference on the desired signal received by the UE $\mu_m \in \mathbb{U}$. The cardinality of the set \mathbb{I}_m is denoted by $|\mathbb{I}_m|$ and represents the number of interfering eNodeBs operating in the same frequency band. With respect to the cutout of the macro cellular deployed LTE network, depicted in Figure 1.3,

$$\mathbb{I}_1 = \{\epsilon_2, \epsilon_3\}, \quad (1.12a)$$

$$\mathbb{I}_2 = \{\epsilon_1, \epsilon_3\}, \quad (1.12b)$$

$$\mathbb{I}_3 = \{\epsilon_1, \epsilon_2\} \quad (1.12c)$$

holds.

In LTE networks the relation between the average receive power of the desired signal, the average receive power of the interfering signals and the thermal noise power over the received bandwidth experienced by the UE $\mu_m \in \mathbb{U}$, is summarized under the term geometry $G^{(m)}$ [3GP12, Section 6.2] and reads

$$G^{(m)} \stackrel{\text{def}}{=} \frac{C^{(m)}}{I^{(m)} + \sigma_m^2}, \quad (1.13)$$

where $C^{(m)}$, $I^{(m)}$ and σ_m^2 denotes the accumulated average power of the receive signal, the accumulated average received power of the interfering signals and the thermal noise power over the received bandwidth, respectively [3GP12, Section 6.2] experienced by the UE $\mu_m \in \mathbb{U}$. The aforementioned powers including the average receive power of the receive signal, the average receive power of the interfering signals and the thermal noise power over the received

bandwidth are discussed in what follows.

Let $P^{(b)}$ denote the transmit power at the eNodeB $\epsilon_b \in \mathbb{E}$, $b = 1, \dots, |\mathbb{E}|$ [Jun97, Section 4.4.1]. The average receive power $C^{(m,b)}$ of the desired signal experienced by the UE $\mu_m \in \mathbb{U}$, is defined as the transmit power of the eNodeB $\epsilon_b \in \mathbb{E}$, denoted by $P^{(b)}$, weighted with the path-loss $\rho^{(m,b)}$ [Jun97, Section 4.4.1] and reads

$$C^{(m,b)} = \rho^{(m,b)} P^{(b)}. \quad (1.14)$$

In the general case of $|\mathbb{A}_m|$ eNodeBs transmitting the desired signal to the UE $\mu_m \in \mathbb{U}$, the average power of the receive signals in (1.14) accumulates to

$$C^{(m)} = \sum_{\{b|\epsilon_b \in \mathbb{A}_m\}} C^{(m,b)} = \sum_{\{b|\epsilon_b \in \mathbb{A}_m\}} \rho^{(m,b)} P^{(b)}. \quad (1.15)$$

The path-loss $\rho^{(m,b)}$ in (1.15) depends on the distance between transmitter and receiver, as well as on fast fading and slow fading [Jun97, Section 4.4.1]. Further information on fast fading and slow fading can be found in [Jun97, Section 3.3.1] and [Jun97, Section 3.3.2], respectively.

Analogously, the average receive power $C^{(m,\tilde{b})}$ of the interfering signal experienced by the UE $\mu_m \in \mathbb{U}$ is defined as the transmit power at each interfering eNodeB $\epsilon_{\tilde{b}} \in \mathbb{I}_m$, denoted as $P^{(\tilde{b})}$, weighted with the path-loss $\rho^{(m,\tilde{b})}$ [Jun97, Section 4.4.1] and reads

$$C^{(m,\tilde{b})} = \rho^{(m,\tilde{b})} P^{(\tilde{b})}. \quad (1.16)$$

In the general case of $|\mathbb{I}_m|$ interfering eNodeBs $\epsilon_{\tilde{b}} \in \mathbb{I}_m$, the average receive power of the interfering signals in (1.16) accumulates to

$$I^{(m)} = \sum_{\{\tilde{b}|\epsilon_{\tilde{b}} \in \mathbb{I}_m\}} C^{(m,\tilde{b})} = \sum_{\{\tilde{b}|\epsilon_{\tilde{b}} \in \mathbb{I}_m\}} \rho^{(m,\tilde{b})} P^{(\tilde{b})}. \quad (1.17)$$

The thermal noise power over the received bandwidth σ_m^2 in (1.13) experienced by the UE $\mu_m \in \mathbb{U}$ is defined by [Mol05, Section 3.2]

$$\begin{aligned} \sigma_m^2 &= N_0 f_{\text{BW}}^{(m)} F_m \\ &= k_{\text{B}} T_0 f_{\text{BW}}^{(m)} F_m. \end{aligned} \quad (1.18)$$

The noise spectral density N_0 in (1.18) denotes the noise power per unit bandwidth [Jun97, Section 2.3.3] and is defined by the multiplication of the BOLTZMANN constant k_{B} and the environmental temperature T_0 [Mol05, Section 3.2]. The BOLTZMANN constant k_{B} is equal to $1.380658 \cdot 10^{-23}$ J/K [Jun97, Section 3.4]. The environmental temperature T_0 is isotropically 300 K [Mol05, Section 3.2], which corresponds to a temperature of approximately 27°C. Hence,

Table 1.2. Relation between the channel bandwidth and the DL bandwidth configuration (created by the author of this thesis using [3GP16n, Table 5.6-1]).

Channel Bandwidth / MHz	Downlink Bandwidth Configuration / $N_{\text{RB}}^{\text{DL}}$	Resource elements per subframe
1.4	6	72
3	15	180
5	25	300
10	50	600
15	75	900
20	100	1200

the noise spectral density N_0 in logarithmic scale reads -174 dBm/Hz. This means that the noise power contained in a bandwidth of 1 Hz referenced to 1 mW is approximately equal to -174 dBm [Mol05, Section 3.2]. Furthermore, the channel bandwidth $f_{\text{BW}}^{(m)}$ denotes the bandwidth assigned to the UE $\mu_m \in \mathcal{U}$. Supported channel bandwidths of LTE networks are tabulated in the fourth column of Table 1.1. Moreover, the noise figure F_m considers the impact of thermal noise power enhancements caused by amplifiers and mixers at the UE $\mu_m \in \mathcal{U}$ [Mol05, Section 3.2].

1.2.5 Frame and Slot Structure

Despite all other assertions, LTE systems do not use OFDM in the classical sense. In the classical OFDM, the channel bandwidth is fix, such that the subcarrier spacing decreases as the number of subcarriers increases [OL07, Section 8.3.6]. To support a wide range of cellular deployment scenarios including inner, urban and rural situations, in LTE systems the subcarrier spacing is, however, fix and sufficiently large to tolerate the impact on the performance and to guarantee reliable signal detection at high user mobility and, thus, a high bandwidth efficiency [STB11, Section 5.4.1].

The relation between the subcarrier spacing and the channel bandwidth is explained using Figure 1.4 on page 25. In LTE systems, the DL transmission is organized in radio frames with a duration of

$$T_{\text{frame}} = 10 \text{ ms} \quad (1.19)$$

per radio frame [3GP16f, Section 4], as depicted in Figure 1.4. In this thesis, the frame structure type 1, considered for signal transmission in Frequency

Division Duplex (FDD) mode, consists of twenty slots $S_0, \dots, S_i, \dots, S_{19}$, as depicted in Figure 1.4, where each slot has a duration of [3GP16f, Section 4.1]

$$T_{\text{slot}} = 0.5 \text{ ms.} \quad (1.20)$$

Moreover, one subframe consists of two slots S_{2j} and S_{2j+1} , $0 \leq j \leq 4$, as depicted in Figure 1.4 and lasts [3GP16f, Section 4.1]

$$T_{\text{subframe}} = 1 \text{ ms.} \quad (1.21)$$

Each slot of the DL transmission signal is described by $N_{\text{sy mb}}^{\text{DL}}$ OFDM symbols $0 \leq \ell < N_{\text{sy mb}}^{\text{DL}}$ in time direction [3GP16f, Section 6.2.3] and $N_{\text{RB}}^{\text{DL}}$ Physical Resource Blocks (PRBs) $0 \leq n_{\text{PRB}} < N_{\text{RB}}^{\text{DL}}$ in frequency direction [3GP16f, Section 6.2.1], as depicted in Figure 1.4. LTE systems support two configuration for the subcarrier spacing f_{sc} , including 7.5 kHz and 15 kHz [3GP16f, Table 6.2.3-1]. In this thesis the subcarrier spacing f_{sc} equal to 15 kHz is focused on. The subcarrier spacing f_{sc} equal to 7.5 kHz is supported in the Multimedia Broadcast Multicast Service (MBMS) only [3GP16a, Section 5.1.1]. Detail information on the MBMS can be found in [3GP16a, Section 15] and references therein. In LTE systems, each OFDM symbol transmitted by the eNodeB in the DL is accompanied with a CP [3GP16f, Section 6.12]. The CP denotes the tail part of an OFDM symbol which is put in front of the OFDM symbol [Kam08, Section 16.2.1]. Further information on the CP in LTE systems is provided in Section 2.5.1 of this thesis. LTE systems support two CP configuration including the normal CP configuration [3GP16f, Table 6.2.3-1] and the extended CP configuration [3GP16f, Table 6.2.3-1]. In this thesis the normal CP configuration is focused on. Detail information on the extended CP configuration can be found in [3GP16f, Section 6.2.3; 3GP16f, Section 6.12]. The normal CP configuration in conjunction the the subcarrier spacing f_{sc} equal to 15 kHz results in a PRB configuration of $N_{\text{sy mb}}^{\text{DL}}$ equal to seven consecutive OFDM symbols transmitted in each slot of the radio frame structure type 1 [3GP16f, Section 6.2.3; 3GP16f, Table 6.2.3-1] and $N_{\text{sc}}^{\text{RB}}$ equal to twelve consecutive subcarriers in the frequency direction [3GP16f, Section 6.2.3; 3GP16f, Table 6.2.3-1], as depicted in Figure 1.4. Hence, the spacing of each PRB reads $N_{\text{sc}}^{\text{RB}} \cdot f_{\text{sc}}$ equal to 180 kHz, as depicted in Figure 1.4. The PRBs are numbered from 0 to $N_{\text{RB}}^{\text{DL}} - 1$ in frequency direction [3GP16f, Section 6.2.3]. The relation between the PRB number n_{PRB} and the subcarrier index k is given by [3GP16f, Section 6.2.3]

$$n_{\text{PRB}} = \left\lfloor \frac{k}{N_{\text{sc}}^{\text{RB}}} \right\rfloor, \quad (1.22)$$

for $0 \leq k < N_{\text{RB}}^{\text{DL}} \cdot N_{\text{sc}}^{\text{RB}}$, where $0 \leq n_{\text{PRB}} < N_{\text{RB}}^{\text{DL}}$ holds. Moreover, $\lfloor \cdot \rfloor$ denotes the largest integer smaller than or equal to \cdot . Moreover, the subcarriers of the n_{PRB} -th can be uniquely addressed such that

$n_{\text{PRB}} \cdot N_{\text{sc}}^{\text{RB}} \leq k < (n_{\text{PRB}} + 1) \cdot N_{\text{sc}}^{\text{RB}}$ holds for $0 \leq n_{\text{PRB}} < N_{\text{RB}}^{\text{DL}}$, as depicted in Figure 1.4. Furthermore, a Resource Element (RE) denotes the smallest physical time-frequency element that can be uniquely identified by the tuple (k, ℓ) [3GP16f, Section 6.2.2], as depicted in Figure 1.4, and is used to transmit a complex-valued modulation symbol. The index k corresponds to the subcarrier index for $0 \leq k < N_{\text{RB}}^{\text{DL}} \cdot N_{\text{sc}}^{\text{RB}}$, where the index ℓ corresponds to the OFDM symbol index within the slot with $0 \leq \ell < N_{\text{symp}}^{\text{DL}}$ [3GP16f, Section 6.2.2], as depicted in Figure 1.4. The mapping of complex-valued modulation symbols carrying RSs and data is discussed in Section 2.2 and Section 2.4.4 of this thesis, respectively.

The relation between the channel bandwidth and the DL bandwidth configuration is provided in Table 1.2 on page 22. In contrast to the classical OFDM, in LTE systems only six DL channel bandwidth configurations denoted in the second column of Table 1.2 are supported, such that

$$N_{\text{RB}}^{\text{min,DL}} \leq N_{\text{RB}}^{\text{DL}} \leq N_{\text{RB}}^{\text{max,DL}}, \quad (1.23)$$

holds, where $N_{\text{RB}}^{\text{min,DL}}$ and $N_{\text{RB}}^{\text{max,DL}}$ represents the smallest and largest DL bandwidth configuration [3GP16f, Section 6.2.1] and reads 6 and 100 PRBs, respectively [3GP16n, Table 5.6-1]. The DL bandwidth configuration is denoted by $N_{\text{RB}}^{\text{DL}}$ [3GP16f, Section 3.1] and is expressed in multiples of $N_{\text{sc}}^{\text{RB}}$, where $N_{\text{sc}}^{\text{RB}}$ denotes the PRB size in frequency direction and is expressed as a number of subcarriers [3GP16f, Section 3.1]. An illustration representing the relation between the channel bandwidth and the transmission bandwidth configuration can be found in [3GP16n, Figure 5.6-1]. Multiplying the transmission bandwidth configuration with the PRB size in frequency direction and the subcarrier spacing f_{sc} , the product denotes the active transmission bandwidth for signal transmission in the DL and is always smaller than the corresponding channel bandwidth [3GP16n, Section 5.6], denoted in the second column of Table 1.2. The corresponding number of resource elements in one subframe is denoted in the third column of Table 1.2.

1.2.6 System Model

To investigate the impact of inter-cell interference in macro cellular deployed LTE networks with $|\mathbb{U}|$ UEs receiving the desired signal in the same frequency band, a system function is provided. In this thesis the terms antenna, Antenna Port (AP) and Antenna Element (AE) are used at the transmitter and receiver. Each eNodeB $\epsilon_b \in \mathbb{A}_m$ and $\epsilon_{\bar{b}} \in \mathbb{I}_m$ is equipped with a transmit antenna which consists of one or multiple transmit APs [3GP16f, Section 6.4]. Each AP in turn may be implemented either as a single transmit AE or as a combination of multiple transmit AEs [STB11, Section 8.2]. Detail information regarding the

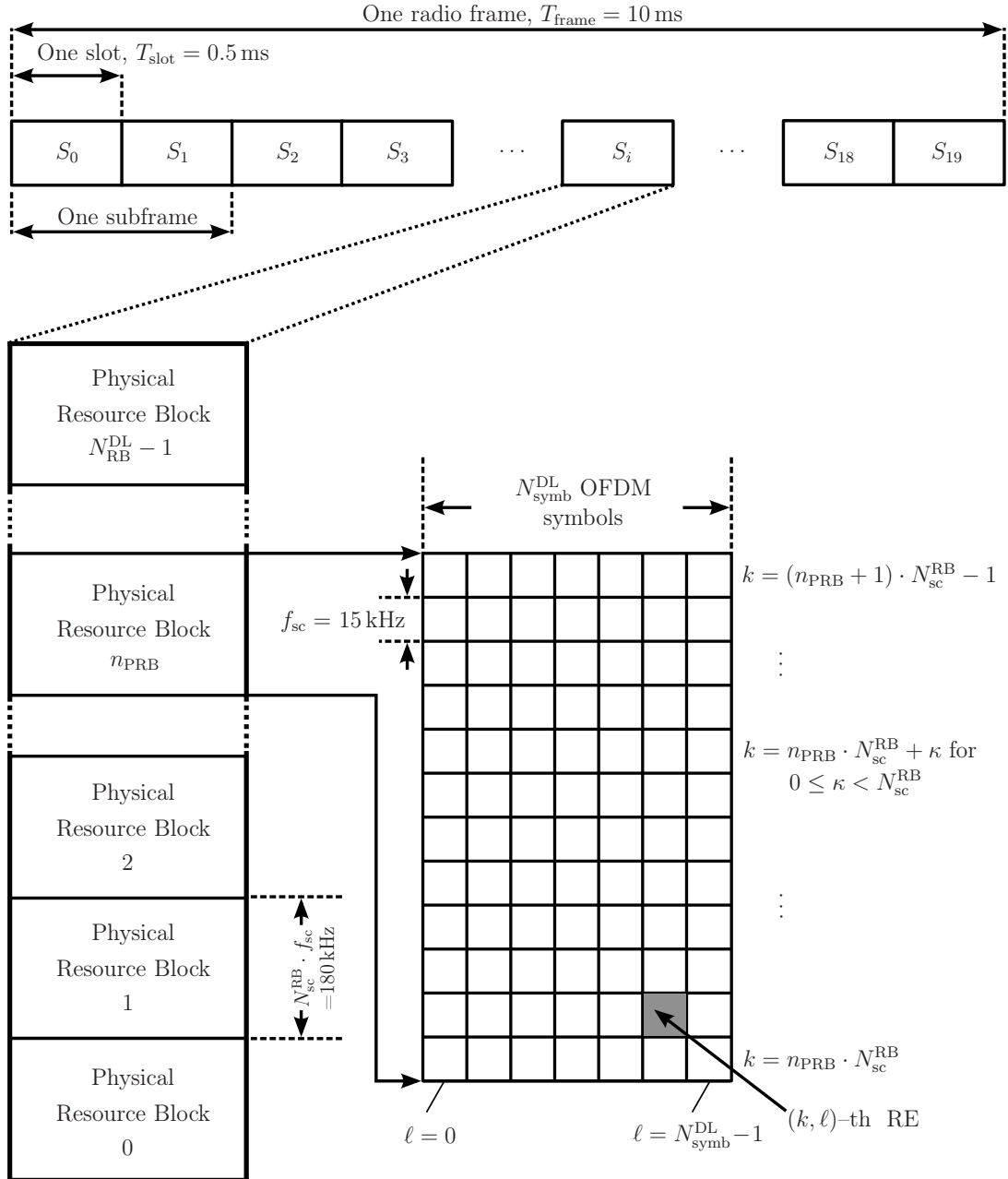


Figure 1.4. Frame structure type 1 for FDD mode (created by the author of this thesis using [3GP16f, Figure 4.1-1, Figure 6.2.2-1]).

relation between transmit APs and transmit AEs is provided in Section 2.2.1 of this thesis. Moreover, each UE $\mu_m \in \mathbb{U}$ is equipped with a receive antenna which consists of one or multiple receive APs. In this thesis it is assumed that each receive AP is uniquely assigned to a unique AE.

The complex-valued OFDM baseband signal representation [3GP16f, Section 6.12] of the receive signals experienced by the UE $\mu_m \in \mathbb{U}$ after OFDM demodulation for the Single-Input and Single-Output (SISO) antenna configuration, is denoted by

$$\underline{r}^{(m)} [k, \ell] = \sqrt{C^{(m,b)}} \underline{h}^{(m,b)} [k, \ell] \underline{d}^{(b)} [k, \ell] + \underline{n}^{(m)} [k, \ell] + \sum_{\{\tilde{b} | \epsilon_{\tilde{b}} \in \mathbb{I}_m\}} \sqrt{C^{(m,\tilde{b})}} \underline{h}^{(m,\tilde{b})} [k, \ell] \underline{d}^{(\tilde{b})} [k, \ell]. \quad (1.24)$$

The components in (1.24) are discussed in what follows. Moreover, the components in (1.24) are summarized in Table 1.3 on page 28.

The scalar value $\underline{r}^{(m)} [k, \ell] \in \mathbb{C}$ in (1.24) denotes the superposition of receive signals plus thermal noise the UE $\mu_m \in \mathbb{U}$ experiences in the DL transmission on the k -th subcarrier and ℓ -th OFDM symbol [3GP16f, Section 6.2.2], where $0 \leq k < N_{\text{RB}}^{\text{DL}} \cdot N_{\text{sc}}^{\text{RB}}$ and $0 \leq \ell < 2 \cdot N_{\text{symp}}^{\text{DL}}$ holds.

The Channel Transfer Function (CTF) representing the inhomogeneities of the mobile communication channel [Jun97, Section 3.2.1] between one receive AE at the UE $\mu_m \in \mathbb{U}$ and one transmit AP at the eNodeB $\epsilon_b \in \mathbb{A}_m$ transmitting the desired signal in the k -th subcarrier and ℓ -th OFDM symbol in (1.24), is denoted by the scalar value $\underline{h}^{(m,b)} [k, \ell] \in \mathbb{C}$. Furthermore, the CTF representing the inhomogeneities of the mobile communication channel [Jun97, Section 3.2.1] between one receive AE at the UE $\mu_m \in \mathbb{U}$ and one transmit AP of each interfering eNodeB $\epsilon_{\tilde{b}} \in \mathbb{I}_m$ in the k -th subcarrier and ℓ -th OFDM symbol in (1.24) is denoted by the scalar value $\underline{h}^{(m,\tilde{b})} [k, \ell] \in \mathbb{C}$. The mapping of transmit APs on transmit AEs is discussed in Section 2.2.1 of this thesis.

The complex-valued modulation symbol carrying the codewords and the RSs to be transmitted by the eNodeB $\epsilon_b \in \mathbb{A}_m$ to the UE $\mu_m \in \mathbb{U}$ on the k -th subcarrier and ℓ -th OFDM symbol in (1.24) is denoted by $\underline{d}^{(b)} [k, \ell] \in \mathbb{C}$ [3GP16f, Section 7.1]. Furthermore, the complex-valued modulation symbol carrying the codewords and the RSs [3GP16f, Section 6.10] to be transmitted by each eNodeB $\epsilon_{\tilde{b}} \in \mathbb{I}_m$ on the k -th subcarrier and ℓ -th OFDM symbol in (1.24) is denoted by $\underline{d}^{(\tilde{b})} [k, \ell] \in \mathbb{C}$ [3GP16f, Section 7.1]. The mapping of the complex-valued modulation symbols and the RSs on physical resources is discussed in Section 2.4.4 of this thesis.

The baseband representation of the complex-valued Additive White Gaussian Noise (AWGN) in the k -th subcarrier and the ℓ -th OFDM symbol in (1.24)

is denoted by $\underline{n}^{(m)} [k, \ell] \in \mathbb{C}$. The AWGN component $\underline{n}^{(m)} [k, \ell]$ is Zero Mean Circularly Symmetric Complex Gaussian (ZMCSCG) distributed with [Kay98, Section 13.3.1]

$$\underline{n}^{(m)} [k, \ell] \sim \mathcal{CN} (0, \sigma_m^2) \quad (1.25)$$

and can be subdivided into a real and imaginary component according to [Kam08, Section 5.2.1]

$$\underline{n}^{(m)} [k, \ell] = \Re \{ \underline{n}^{(m)} [k, \ell] \} + j \Im \{ \underline{n}^{(m)} [k, \ell] \}, \quad (1.26)$$

where j denotes the imaginary number and equals to $\sqrt{-1}$ [Bro+01, Section 1.5.1.1]. In this thesis the noise figure in (1.18) is set to one, such that the thermal noise power over the received bandwidth σ_m^2 is equal to the noise spectral density multiplied with the channel bandwidth. Moreover, $\Re \{ \cdot \}$ and $\Im \{ \cdot \}$ denotes the real and imaginary component of \cdot , respectively. The spectral noise power density N_0 is evenly spread over the real and imaginary frequency [Kam08, Section 5.2.1] such that both, the real and imaginary component of (1.26) are zero-mean normal distributed with variance $\sigma_m^2/2$. The real and imaginary component of (1.26) is stochastically independent [Kam08, Section 5.2.1], such that

$$\mathbb{E} \{ \Re \{ \underline{n}^{(m)} [k, \ell] \} \cdot \Im \{ \underline{n}^{(m)} [k, \ell] \} \} = 0 \quad (1.27)$$

holds for $0 \leq k < N_{\text{RB}}^{\text{DL}} \cdot N_{\text{sc}}^{\text{RB}}$ and $0 \leq \ell < 2 \cdot N_{\text{symp}}^{\text{DL}}$, where $\mathbb{E} \{ \cdot \}$ denotes the expectation operator. Note that the impact of ISI is not included in the complex-valued OFDM baseband signal representation of the receive signal experienced by the UE $\mu_m \in \mathbb{U}$ in (1.24). This restriction is dropped in Chapter 4 of this thesis. The complex-valued OFDM baseband signal representation of the receive signals experienced by the UE $\mu_m \in \mathbb{U}$ after OFDM demodulation for the MIMO antenna configuration in the k -th subcarrier and ℓ -th OFDM symbol can be extended from (1.24) for single-layer transmission according to

$$\begin{aligned} \underline{r}_{\nu}^{(m)} [k, \ell] = & \sqrt{C^{(m,b)}} \underbrace{\sum_{i=1}^{N_{\text{T}}^{(b)}} \underline{h}_{\nu, \omega_i}^{(m,b)} [k, \ell] \cdot \frac{p_{\omega_i}^{(b)} [k, \ell]}{\sqrt{N_{\text{T}}^{(b)}}}}_{\underline{g}_{\nu}^{(m,b)} [k, \ell]} \cdot \underline{d}^{(b)} [k, \ell] + \underline{n}_{\nu}^{(m)} [k, \ell] + \\ & \sum_{\{\bar{b} | \epsilon_{\bar{b}} \in \mathbb{I}_m\}} \sqrt{C^{(m,\bar{b})}} \underbrace{\sum_{i=1}^{N_{\text{T}}^{(\bar{b})}} \underline{h}_{\nu, \omega_i}^{(m,\bar{b})} [k, \ell] \cdot \frac{p_{\omega_i}^{(\bar{b})} [k, \ell]}{\sqrt{N_{\text{T}}^{(\bar{b})}}}}_{\underline{g}_{\nu}^{(m,\bar{b})} [k, \ell]} \cdot \underline{d}^{(\bar{b})} [k, \ell] \quad (1.28) \end{aligned}$$

for $1 \leq \nu \leq N_{\text{R}}^{(m)}$ and is explained using Figure 1.5 on page 34. Figure 1.5

Table 1.3. Summary of components illustrating the receive signal (created by the author of this thesis).

Component	Illustration
b	Index of the eNodeB $\epsilon_b \in \mathbb{A}_m$.
\tilde{b}	Index of the eNodeB $\epsilon_{\tilde{b}} \in \mathbb{I}_m$.
$C^{(m,b)}$	Average receiver power of the desired signal transmitted by the eNodeB $\epsilon_b \in \mathbb{A}_m$ that is experienced by the UE $\mu_m \in \mathbb{U}$. For the definition on $C^{(m,b)}$, see (1.14).
$C^{(m,\tilde{b})}$	Average receiver power of the interfering signal transmitted by the eNodeB $\epsilon_{\tilde{b}} \in \mathbb{I}_m$ that is experienced by the UE $\mu_m \in \mathbb{U}$. For the definition on $C^{(m,\tilde{b})}$, see (1.16).
$\underline{d}^{(b)} [k, \ell]$	Complex-valued modulation symbol carrying either the code-word or the RS [3GP16f, Section 6.10] to be transmitted by the eNodeB $\epsilon_b \in \mathbb{A}_m$ in the k -th subcarrier and ℓ -th OFDM symbol.
$\underline{d}^{(\tilde{b})} [k, \ell]$	Complex-valued modulation symbol carrying either the code-word or the RS [3GP16f, Section 6.10] to be transmitted by each eNodeB $\epsilon_{\tilde{b}} \in \mathbb{I}_m$ in the k -th subcarrier and ℓ -th OFDM symbol.
ϵ_b	eNodeB out of the set \mathbb{A}_m transmitting the desired signal to the UE $\mu_m \in \mathbb{U}$.
$\epsilon_{\tilde{b}}$	eNodeB out of the set \mathbb{I}_m transmitting the interfering signal to the UE $\mu_m \in \mathbb{U}$.
$\underline{h}^{(m,b)} [k, \ell]$	CTF representing the inhomogeneities of the mobile communication channel [Jun97, Section 3.2.1] between the UE $\mu_m \in \mathbb{U}$ and the eNodeB $\epsilon_b \in \mathbb{A}_m$ in the k -th subcarrier and ℓ -th OFDM symbol.

Continued on next page

Table 1.3. Summary of components illustrating the receive signal
(Continued from previous page).

Component	Illustration
$\underline{h}^{(m,\bar{b})}[k, \ell]$	CTF representing the inhomogeneities of the mobile communication channel [Jun97, Section 3.2.1] between the UE $\mu_m \in \mathbb{U}$ and the eNodeB $\epsilon_{\bar{b}} \in \mathbb{I}_m$ in the k -th subcarrier and ℓ -th OFDM symbol.
\mathbb{I}_m	Subset of eNodeBs out of the set \mathbb{E} transmitting the interfering signal to the UE $\mu_m \in \mathbb{U}$, defined in (1.11).
k	Subcarrier index.
ℓ	OFDM symbol index.
m	Index of the UE $\mu_m \in \mathbb{U}$.
$\underline{n}^{(m)}[k, \ell]$	Baseband representation of the complex-valued AWGN in the k -th subcarrier and ℓ -th OFDM symbol experienced by the UE $\mu_m \in \mathbb{U}$. For the definition on $\underline{n}^{(m)}[k, \ell]$, see (1.25).
$\underline{r}^{(m)}[k, \ell]$	Complex-valued OFDM baseband signal representation [3GP16f, Section 6.10] of the receive signals experienced by the UE $\mu_m \in \mathbb{U}$ in the k -th subcarrier and ℓ -th OFDM symbol after OFDM demodulation. For the definition on $\underline{r}^{(m)}[k, \ell]$, see (1.24).

shows a simplified system model for signal transmission in TM6 in frequency domain in the DL, where the UE $\mu_m \in \mathbb{U}$ experiences at the ν -th receive AE in the k -th subcarrier and the ℓ -th OFDM symbols a superposition of the

1. precoded representation of the desired complex-valued modulation symbol $\underline{d}^{(b)} [k, \ell]$ transmitted by the eNodeB $\epsilon_b \in \mathbb{A}_m$,
2. precoded representation of the interfering complex-valued modulation symbol $\underline{d}^{(b)} [k, \ell]$ transmitted by each eNodeB out of the set \mathbb{I}_m and the
3. complex-valued AWGN component $\underline{n}_\nu^{(m)} [k, \ell]$

for $1 \leq \nu \leq N_R^{(m)}$. For the sake of clarity the sum of the receive signals arising from the interfering eNodeBs out of the set \mathbb{I}_m experienced by the UE $\mu_m \in \mathbb{U}$ on the ν -th receive AE, is denoted by $\underline{n}'_\nu^{(m)} [k, \ell]$ for $1 \leq \nu \leq N_R^{(m)}$, as depicted in Figure 1.5. Signal transmission in TM6 is characterized by the fact that signal precoding for Spatial Multiplexing (SM) using APs with Cell Specific Reference Signal (CRS) is limited on one spatial layer [3GP16f, Section 6.3.4.2; 3GP16g, Section 7.1]. Detail information on CRS generation and resource mapping is provided in Section 2.2.2 and Section 2.4.4 of this thesis, respectively. The desired complex-valued modulation symbol $\underline{d}^{(b)} [k, \ell]$, transmitted simultaneously from the $N_T^{(b)}$ transmit APs, is weighted with the phase information $\underline{p}_{\omega_\zeta}^{(b)} / \sqrt{N_T^{(b)}}$ for $1 \leq \zeta \leq N_T^{(b)}$ prior to mapping on the transmit AEs to enable signal precoding, as depicted in Figure 1.5. The aspect of signal precoding is further discussed in Section 2.4.3 of this thesis, whereas the precoding vector selection for single-layer transmission in TM6 is discussed in Section 2.7.3 of this thesis. In a practical implementation a transmit AP may be implemented either as a single transmit AE or as a combination of multiple AEs [STB11, Section 8.2]. In the simplified system model for single-layer transmission in frequency domain in the DL it is assumed that each transmit AP is uniquely mapped on one transmit AE. Hence, the transmit AP with index ω_ζ equal to $\zeta - 1$ is mapped on the ζ -th transmit AE for $1 \leq \zeta \leq N_T^{(b)}$, as depicted in Figure 1.5. In that case the number of transmit APs is equal to the number of transmit AEs for TM 6 [3GP16f, Section 6.3.4.2; 3GP16g, Section 7.1; STB11, Section 8.2], as depicted in Figure 1.5. To address the index of the transmit AE the eNodeB $\epsilon_b \in \mathbb{A}_m$ transmits the desired signal from which is received by the UE $\mu_m \in \mathbb{U}$ on the ν -th receive AE, the CTF $\underline{h}^{(m,b)} [k, \ell]$ in (1.24) is extended by the two subscripts ν and ζ , respectively, as denoted in (1.28) and depicted in Figure 1.5. Moreover, the superposition of the CTFs $\underline{h}_{\nu,\zeta}^{(m,b)} [k, \ell]$ weighted with the phase information $\underline{p}_\zeta^{(b)} / \sqrt{N_T^{(b)}}$ over all $N_T^{(b)}$ transmit AEs at the eNodeB $\epsilon_b \in \mathbb{A}_m$ represents the desired effective channel $\underline{g}_\nu^{(m,b)} [k, \ell]$, experienced by the UE $\mu_m \in \mathbb{U}$ on the ν -th receive AE in the k -th subcarrier and the ℓ -th OFDM symbol for $1 \leq \nu \leq N_R^{(m)}$,

as denoted in (1.28). The respective interfering components in (1.28) can be explained analogously when replacing b by \tilde{b} .

The complex-valued OFDM baseband signal representation of the receive signals experienced by the UE $\mu_m \in \mathbb{U}$ after OFDM demodulation for MIMO antenna configuration in (1.28) comes up with a complicated notation making use of error-prone calculus with sigma signs [ZF92, Section 1.1]. Following [ZF92, Section 1.1], the complex-valued OFDM baseband signal representation of the receive signals in (1.28) can be represented by matrix-vector calculus according to

$$\begin{aligned} \underline{\mathbf{r}}^{(m)} [k, \ell] = & \sqrt{C^{(m,b)}} \underbrace{\underline{\mathbf{H}}^{(m,b)} [k, \ell] \underline{\mathbf{p}}^{(b)} [k, \ell] \underline{\mathbf{d}}^{(b)} [k, \ell]}_{\underline{\mathbf{g}}^{(m,b)} [k, \ell]} + \underline{\mathbf{n}}^{(m)} [k, \ell] + \\ & \sum_{\{\tilde{b} | \epsilon_{\tilde{b}} \in \mathbb{I}_m\}} \sqrt{C^{(m,\tilde{b})}} \underbrace{\underline{\mathbf{H}}^{(m,\tilde{b})} [k, \ell] \underline{\mathbf{p}}^{(\tilde{b})} [k, \ell] \underline{\mathbf{d}}^{(\tilde{b})} [k, \ell]}_{\underline{\mathbf{g}}^{(m,\tilde{b})} [k, \ell]}, \end{aligned} \quad (1.29)$$

as the computation with matrices and vectors is a well-understood mathematical tool [ZF92, Section 1.1].

The complex-valued vector $\underline{\mathbf{r}}^{(m)} [k, \ell] \in \mathbb{C}^{N_R^{(m)} \times 1}$ in (1.29) denotes the receive signal experienced by the UE $\mu_m \in \mathbb{U}$ in each receive AE in the k -th subcarrier and ℓ -th OFDM symbol and is defined as

$$\underline{\mathbf{r}}^{(m)} [k, \ell] = \left(\underline{r}_1^{(m)} [k, \ell], \dots, \underline{r}_{\nu}^{(m)} [k, \ell], \dots, \underline{r}_{N_R^{(m)}}^{(m)} [k, \ell] \right)^T, \quad (1.30)$$

where $\underline{r}_{\nu}^{(m)} [k, \ell] \in \mathbb{C}$ in (1.30) represents the receive signal experienced by the UE $\mu_m \in \mathbb{U}$ on the ν -th receive AE for $1 \leq \nu \leq N_R^{(m)}$ and is equal to (1.28).

The MIMO representation of the CTF $\underline{\mathbf{H}}^{(m,b)} [k, \ell] \in \mathbb{C}^{N_R^{(m)} \times N_T^{(b)}}$ in (1.29) is defined as [Kam08, Section 18.1.2]

$$\underline{\mathbf{H}}^{(m,b)} [k, \ell] = \begin{pmatrix} \underline{h}_{1,1}^{(m,b)} [k, \ell] & \dots & \underline{h}_{1,\zeta}^{(m,b)} [k, \ell] & \dots & \underline{h}_{1,N_T^{(b)}}^{(m,b)} [k, \ell] \\ \vdots & \ddots & \vdots & \ddots & \vdots \\ \underline{h}_{\nu,1}^{(m,b)} [k, \ell] & \dots & \underline{h}_{\nu,\zeta}^{(m,b)} [k, \ell] & \dots & \underline{h}_{\nu,N_T^{(b)}} [k, \ell] \\ \vdots & \ddots & \vdots & \ddots & \vdots \\ \underline{h}_{N_R^{(m)},1}^{(m,b)} [k, \ell] & \dots & \underline{h}_{N_R^{(m)},\zeta}^{(m,b)} [k, \ell] & \dots & \underline{h}_{N_R^{(m)},N_T^{(b)}} [k, \ell] \end{pmatrix}. \quad (1.31)$$

The MIMO representation of the CTF $\underline{\mathbf{H}}^{(m,\tilde{b})} [k, \ell] \in \mathbb{C}^{N_R^{(m)} \times N_T^{(\tilde{b})}}$ in (1.29) is defined analogously as (1.31) when replacing the superscript index b by \tilde{b} .

Further information regarding the correlation of the transmit and receive AEs is provided in Section 2.8.2 of this thesis.

The complex-valued vector $\underline{\mathbf{p}}^{(b)} [k, \ell] \in \mathbb{C}^{N_T^{(b)} \times 1}$ in (1.29) denotes the precoding vector used by the eNodeB $\epsilon_b \in \mathbb{A}_m$ to precode the complex-valued modulation symbols carrying the codewords and is defined as [3GP16f, Section 6.3.4.2.3]

$$\underline{\mathbf{p}}^{(b)} [k, \ell] = \frac{1}{\sqrt{N_T^{(b)}}} \left(\underline{p}_1^{(b)} [k, \ell], \dots, \underline{p}_\zeta^{(b)} [k, \ell], \dots, \underline{p}_{N_T^{(b)}}^{(b)} [k, \ell] \right)^T, \quad (1.32)$$

where $(\cdot)^T$ denotes the transpose operation of \cdot . The component $\underline{p}_\zeta^{(b)} [k, \ell] \in \mathbb{C}$ in (1.32) has unit magnitude and contains the phase information which is assigned on the respective transmit AP. The precoding vector used by the interfering eNodeBs out of the set \mathbb{I}_m , denoted in (1.29), is defined analogously as (1.32) when replacing the superscript index b by \tilde{b} . The characteristic antenna diagram for when making use of the signal precoding vectors is discussed in Section 2.4.3 of this thesis.

The desired effective channel $\underline{\mathbf{g}}^{(m,b)} [k, \ell] \in \mathbb{C}^{N_R^{(m)} \times 1}$ in (1.29) is defined by the multiplication of the CTF $\underline{\mathbf{H}}^{(m,b)} [k, \ell]$, defined in (1.31) and the precoding vector $\underline{\mathbf{p}}^{(b)} [k, \ell]$, defined in (1.32) for each eNodeB $\epsilon_b \in \mathbb{A}_m$ according to (1.29), where

$$\underline{\mathbf{g}}^{(m,b)} [k, \ell] = \left(\underline{g}_1^{(m,b)} [k, \ell], \dots, \underline{g}_\nu^{(m,b)} [k, \ell], \dots, \underline{g}_{N_R^{(m)}}^{(m,b)} [k, \ell] \right)^T \quad (1.33)$$

holds. The ν -th element of the desired effective channel in (1.33) represents the inhomogeneities of the mobile communication channel between the UE $\mu_m \in \mathbb{U}$ receiving the desired signal on the ν -th receive AE for $1 \leq \nu \leq N_R^{(m)}$ and each eNodeB $\epsilon_b \in \mathbb{A}_m$ transmitting the precoded desired signal in the k -th subcarrier and ℓ -th OFDM symbol. The effective channel $\underline{\mathbf{g}}^{(m,\tilde{b})} [k, \ell] \in \mathbb{C}^{N_R^{(m)} \times 1}$ in (1.29) is defined analogously as (1.33) when replacing the superscript index b by \tilde{b} . Hence, $\underline{g}_\nu^{(m,\tilde{b})} [k, \ell]$ represents the inhomogeneities of the mobile communication channel between the UE $\mu_m \in \mathbb{U}$, receiving the interfering signal on the ν -th receive antenna $1 \leq \nu \leq N_R^{(m)}$ and each eNodeB $\epsilon_{\tilde{b}} \in \mathbb{I}_m$, transmitting the precoded interfering signal on the k -th subcarrier and ℓ -th OFDM symbol.

The representation of the complex-valued AWGN component for multiple receive AEs in $\underline{\mathbf{n}}^{(m)} [k, \ell] \in \mathbb{C}^{N_R^{(m)} \times 1}$ in (1.29) is defined by [Kam08, Section 18.1.2]

$$\underline{\mathbf{n}}^{(m)} [k, \ell] = \left(\underline{n}_1^{(m)} [k, \ell], \dots, \underline{n}_\nu^{(m)} [k, \ell], \dots, \underline{n}_{N_R^{(m)}}^{(m)} [k, \ell] \right)^T, \quad (1.34)$$

where $\underline{n}_\nu^{(m)} [k, \ell] \in \mathbb{C}$ in (1.34) denotes the complex-valued AWGN component at the ν -th receive AE for $1 \leq \nu \leq N_R^{(m)}$ at the UE $\mu_m \in \mathbb{U}$ in the k -th subcarrier and ℓ -th OFDM symbol. The AWGN component $\underline{n}_\nu^{(m)} [k, \ell]$ in (1.34) follows the same distribution as (1.25) for $1 \leq \nu \leq N_R^{(m)}$ [Kam08, Section 18.1.2]. Furthermore, the AWGN components at the receive AEs are mutually uncorrelated, such that

$$\mathbb{E} \left\{ \underline{\mathbf{n}}^{(m)} [k, \ell] (\underline{\mathbf{n}}^{(m)} [k, \ell])^H \right\} = \sigma_m^2 \mathbf{I}_{N_R^{(m)}} \quad (1.35)$$

holds [Kam08, Section 18.1.2], where $\mathbf{I}_{N_R^{(m)}}$ and $(\cdot)^H$ denotes the $N_R^{(m)} \times N_R^{(m)}$ identity matrix and the Hermitian operation of \cdot [ZF92, Section 11.5], respectively.

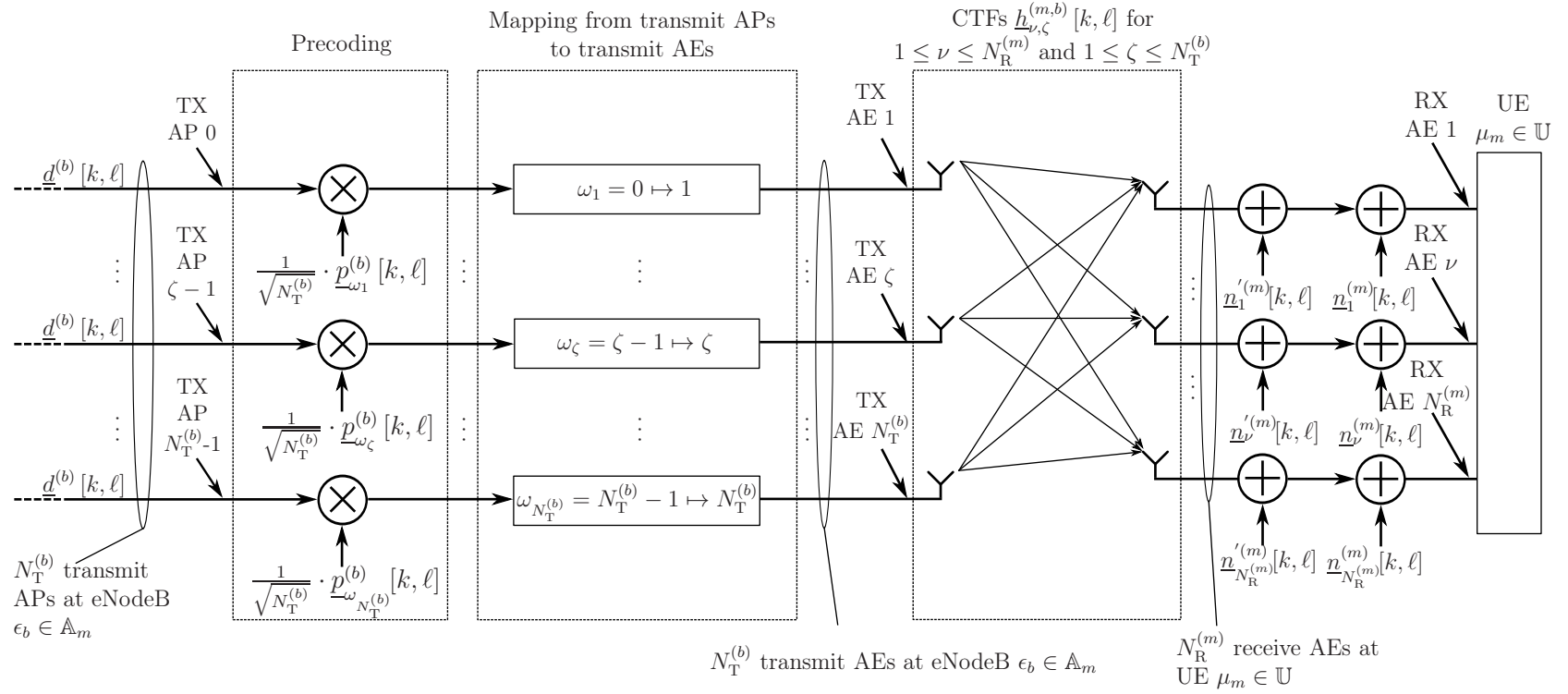
Note that the impact of ISI is not included in the complex-valued OFDM baseband signal representation of the receive signal experienced by the UE $\mu_m \in \mathbb{U}$ in (1.29). This restriction is dropped in Chapter 4 of this thesis.

1.2.7 Restriction Through Inter-Cell Interference

Inter-cell interference is the dominant limiting factor which prevents macro cellular deployed LTE networks from achieving the maximum bandwidth efficiency [STB11, Section 12.5]. To demonstrate the restriction caused by inter-cell interference, the Information Theoretic (IT) bandwidth efficiency of Noise Limited (NL) scenarios [STB11, Section 12.5] is compared with the IT bandwidth efficiency of Interference Limited (IL) scenarios [STB11, Section 12.5]. The IT bandwidth efficiency denotes the capacity of a wireless channel normalized by the channel bandwidth [TV05, Chapter 5]. The capacity of a wireless channel denotes the maximum data rate that can be guaranteed with arbitrary small error probability [TV05, Section 5.1]. As the OFDM technique enables to decompose the mobile communication channel into narrow-band subcarriers, such that each of the subcarriers approximately do not suffer from frequency selective fading [Kam08, Section 16.1.1], the impact of inter-cell interference is discussed based on subcarriers.

In absence of the interfering eNodeBs $\epsilon_{\bar{b}} \in \mathbb{I}_m$, the receive signal experienced by the UE $\mu_m \in \mathbb{U}$ is only influenced by the AWGN component [Mol05, Section 3.2]. The IT bandwidth efficiency for this NL single-layer transmission experienced by the UE $\mu_m \in \mathbb{U}$ in the k -th subcarrier and ℓ -th OFDM symbol reads [TV05, Section 5.1; STB11, Section 12.5]

$$\eta_{\text{IT,NL}}^{(m)} (k, \ell) = \frac{1}{f_{\text{sc}}} \frac{1}{T_{\text{OFDM}}} \log_2 \left(1 + \frac{C_{\text{chan}}^{(m)} (k, \ell)}{\sigma_m^2} \right), \quad (1.36)$$



AE: Antenna Element, AP: Antenna Port, eNodeB: Enhanced Node B, RX: Receive, TX: Transmit, UE: User Equipment

Figure 1.5. Simplified system model for single-layer transmission in TM6 (created by the author of this thesis using [AGR10, Figure 18; Kam08, Figure 18.1.2]).

where f_{sc} and T_{OFDM} in (1.36) denotes the subcarrier spacing [3GP16f, Section 3.1] and the duration of one OFDM symbol [3GP16f, Section 6.2.2], respectively. Furthermore, $C_{\text{chan}}^{(m)}(k, \ell)$ in (1.36) is defined by [TV05, Section 5.1]

$$C_{\text{chan}}^{(m)}(k, \ell) = C^{(m,b)} \cdot \left\| \underline{\mathbf{H}}^{(m,b)}[k, \ell] \underline{\mathbf{p}}^{(b)}[k, \ell] \right\|^2. \quad (1.37)$$

and represents the accumulated receive signal power of the desired signal experienced by the UE $\mu_m \in \mathbb{U}$ in the k -th subcarrier and ℓ -th OFDM symbol. For small ratios between $C_{\text{chan}}^{(m)}(k, \ell)$ and σ_m^2 , the IT bandwidth efficiency in (1.37) experienced by the UE $\mu_m \in \mathbb{U}$ increases linearly with the average receive power of the desired signal $C^{(m)}$ for arbitrary but fix CTFs $\underline{\mathbf{H}}^{(m,b)}[k, \ell]$ and precoding vectors $\underline{\mathbf{p}}^{(b)}$ for $\{b|\epsilon_b \in \mathbb{A}_m\}$ [TV05, Section 5.2.1]. For large ratios between $C_{\text{chan}}^{(m)}(k, \ell)$ and σ_m^2 , the IT bandwidth efficiency in (1.37) experienced by the UE $\mu_m \in \mathbb{U}$ increases logarithmically with the average receive power of the desired signal $C^{(m)}$ for arbitrary but fix CTFs $\underline{\mathbf{H}}^{(m,b)}[k, \ell]$ and precoding vectors $\underline{\mathbf{p}}^{(b)}$ for $\{b|\epsilon_b \in \mathbb{A}_m\}$ [TV05, Section 5.2.1].

In presence of the interfering eNodeBs $\epsilon_{\bar{b}} \in \mathbb{I}_m$, the receive signal experienced by the UE $\mu_m \in \mathbb{U}$ is influenced by inter-cell interference and the AWGN component [Mol05, Section 3.3]. Treating the impact of inter-cell interference as AWGN [TV05, Section 5.1], the IT bandwidth efficiency for IL single-layer transmission experienced by the UE $\mu_m \in \mathbb{U}$ in the k -th subcarrier and ℓ -th OFDM symbol reads [TV05, Section 5.1; STB11, Section 12.5]

$$\eta_{\text{IT, IL}}^{(m)}(k, \ell) = \frac{1}{f_{\text{sc}}} \frac{1}{T_{\text{OFDM}}} \log_2 \left(1 + \frac{C_{\text{chan}}^{(m)}(k, \ell)}{I_{\text{chan}}^{(m)}(k, \ell) + \sigma_m^2} \right), \quad (1.38)$$

where

$$I_{\text{chan}}^{(m)}(k, \ell) = \sum_{\{\bar{b}|\epsilon_{\bar{b}} \in \mathbb{I}_m\}} C^{(m,\bar{b})} \left\| \underline{\mathbf{H}}^{(m,\bar{b})}[k, \ell] \underline{\mathbf{p}}^{(\bar{b})}[k, \ell] \right\|^2 \quad (1.39)$$

represents the accumulated receive signal power of the interfering signals experienced by the UE $\mu_m \in \mathbb{U}$ in the k -th subcarrier and ℓ -th OFDM symbol. The presence of inter-cell interference decreases the argument of the logarithm in (1.38) and, thus the bandwidth efficiency experienced by the UE $\mu_m \in \mathbb{U}$ in the k -th subcarrier and ℓ -th OFDM symbol [TV05, Section 4.2.3].

To quantify the impact of inter-cell interference, the IT bandwidth efficiency loss is used [STB11, Section 12.5]. The IT bandwidth efficiency loss experienced by the UE $\mu_m \in \mathbb{U}$ in the k -th subcarrier and ℓ -th OFDM symbol is defined as the difference between the IT bandwidth efficiency of the NL scenario, calculated in (1.36) and the IT bandwidth efficiency of the IL scenario,

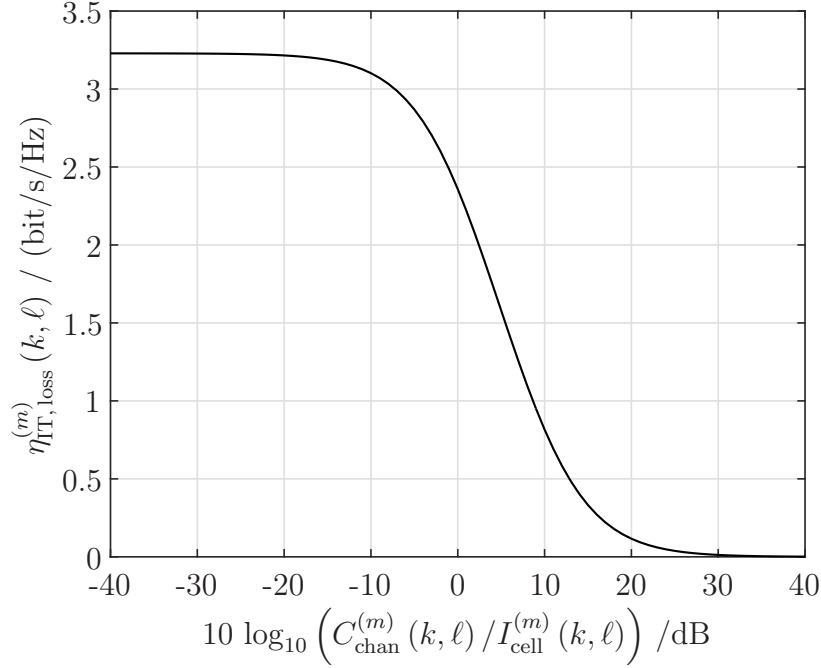


Figure 1.6. Impact of inter-cell interference on the bandwidth efficiency loss (created by the author of this thesis using [STB11, Figure 12.4]).

calculated in (1.38) and reads [STB11, Section 12.5]

$$\begin{aligned}
 \eta_{\text{IT,loss}}^{(m)}(k, \ell) &\stackrel{\text{def}}{=} \eta_{\text{IT,NL}}^{(m)}(k, \ell) - \eta_{\text{IT,IL}}^{(m)}(k, \ell) \\
 &= \frac{1}{f_{\text{sc}} \cdot T_{\text{OFDM}}} \log_2 \left(\frac{1 + C_{\text{chan}}^{(m)}(k, \ell) / \sigma_m^2}{1 + \left(\left(\frac{C_{\text{chan}}^{(m)}(k, \ell)}{\sigma_m^2} \right)^{-1} + \left(\frac{C_{\text{chan}}^{(m)}(k, \ell)}{I_{\text{chan}}^{(m)}(k, \ell)} \right)^{-1} \right)^{-1}} \right). \quad (1.40)
 \end{aligned}$$

To illustrate the impact of inter-cell interference, the IT bandwidth efficiency loss experienced by the UE $\mu_m \in \mathbb{U}$ in the k -th subcarrier and ℓ -th OFDM symbol is depicted in Figure 1.6 on page 36 as a function of the ratio of the accumulated receive signal power of the desired signal and the accumulated signal receive power of the interfering signals, denoted by $C_{\text{chan}}^{(m)}(k, \ell) / I_{\text{chan}}^{(m)}(k, \ell)$. Furthermore, the ratio of the accumulated receive signal power of the desired signal and the thermal noise power over the received bandwidth, denoted by the term $C_{\text{chan}}^{(m)}(k, \ell) / \sigma_m^2$, has been set to 10 dB. Moreover, the subcarrier spacing f_{sc} is equal to 15 kHz [3GP16f, Table 6.2.3-1], whereas the duration of the OFDM symbol T_{OFDM} is equal to 71.43 μs [3GP16f, Section 6.2.2].

A glance at Figure 1.6 shows that the larger the ratio $C_{\text{chan}}^{(m)}(k, \ell) / I_{\text{chan}}^{(m)}(k, \ell)$ becomes, the smaller the IT bandwidth efficiency loss experienced by the UE $\mu_m \in \mathbb{U}$ in the k -th subcarrier and ℓ -th OFDM symbol. For the asymptotic case, where the ratio $C_{\text{chan}}^{(m)}(k, \ell) / I_{\text{chan}}^{(m)}(k, \ell)$ tends to infinity, it can be shown that the IT bandwidth efficiency loss experienced by the UE $\mu_m \in \mathbb{U}$ in the k -th subcarrier and ℓ -th OFDM symbol tends to zero, as depicted in Figure 1.6. In that case the IT bandwidth efficiency experienced by the UE $\mu_m \in \mathbb{U}$ in the k -th subcarrier and ℓ -th OFDM symbol is only limited by the accumulated receive signal power of the desired signal $C_{\text{chan}}^{(m)}(k, \ell)$ and reads 3.2 bit/s/Hz, as can be calculated from (1.36). Note that the IT bandwidth efficiency in (1.36) changes as the ratio $C_{\text{chan}}^{(m)}(k, \ell) / \sigma_m^2$ changes.

Moreover, it can be observed that the smaller the ratio $C_{\text{chan}}^{(m)}(k, \ell) / I_{\text{chan}}^{(m)}(k, \ell)$ becomes, the larger the IT bandwidth efficiency loss experienced by the UE $\mu_m \in \mathbb{U}$ in the k -th subcarrier and ℓ -th OFDM symbol, as depicted in Figure 1.6. For the asymptotic case where the ratio $C_{\text{chan}}^{(m)}(k, \ell) / I_{\text{chan}}^{(m)}(k, \ell)$ tends to zero, the impact of thermal noise power over the received bandwidth in (1.38) can be ignored, such that the argument of the logarithm to the base of two in (1.38) tends to one. Hence, the IT bandwidth efficiency for IL single-layer transmission experienced by the UE $\mu_m \in \mathbb{U}$ in the k -th subcarrier and ℓ -th OFDM symbol tends to zero, such that the IT bandwidth efficiency loss in (1.40) tends to the IT bandwidth efficiency for NL single-layer transmission and reads 3.2 bit/s/Hz, as depicted in Figure 1.6.

The ratio $C_{\text{chan}}^{(m)}(k, \ell) / I_{\text{chan}}^{(m)}(k, \ell)$ is a random variable [Jun97, Section 4.4.2.1]. While the impact of inter-cell interference on the IT bandwidth efficiency loss is negligible for sufficiently high ratios of $C_{\text{chan}}^{(m)}(k, \ell) / I_{\text{chan}}^{(m)}(k, \ell)$, the UE $\mu_m \in \mathbb{U}$ suffers from severe bandwidth efficiency loss when the aforementioned ratio decreases and, hence, limits the expected performance of LTE networks [STB11, Section 12.5]. An overview of state-of-the-art techniques to alleviate the impact of inter-cell interference is discussed in Section 1.3 of this thesis.

1.3 State of the Art

1.3.1 Introduction

The presence of inter-cell interference, discussed in Section 1.2.7 of this thesis, is the dominant limiting factor which prevents cell-edge UEs from achieving the expected bandwidth efficiency [Him+10]. Therefore it is necessary to mitigate the impact of inter-cell interference to improve the bandwidth efficiency and the related throughput [Him+10]. To achieve this, state-of-the-art techniques

shall be discussed. The overview of state-of-the-art interference mitigation techniques is restricted on

- enhanced receivers [3GP14f, Chapter 7],
- signal precoding [3GP16g, Section 7.1] and
- CoMP transmission [3GP13a, Chapter 5]

in this thesis and is discussed in what follows.

1.3.2 Enhanced Receivers

The 3GPP investigated three types of enhanced receivers that take the presence of inter-cell interference into account, including Interference Suppression (IS) receivers [3GP14f, Section 7.2], Maximum Likelihood (ML) receivers [3GP14f, Section 7.3] and Interference Cancellation (IC) receivers [3GP14f, Section 7.4]. ML receivers are not discussed in this thesis. Further information on ML receivers can be found in [3GP14f, Section 7.3; Pro01, Section 5.1.3].

IS receivers apply linear filtering on the receive signal to suppress the impact of inter-cell interference [3GP14f, Section 7.2]. IS receivers are composed of a decorrelating filter and a matched filter which together form the Decorrelating Matched Filter (DMF) [Jun97, Section B.1.3]. The decorrelating filter is used to whiten the inter-cell interfering signals such that the inter-cell interference plus the AWGN component becomes white and zero-mean after applying the decorrelating filter [Jun97, Section B.1.3]. The matched filter is used to match the whitened receive signal on the properties of the mobile communication channel, such that the post processing Signal to Noise Ratio (SNR) is maximized [Jun97, Section B.1.3]. The post processing SNR of IS receivers is derived in Section 2.6.3 of this thesis. Three types of IS receivers are identified, including the Linear Minimum Mean Square Error (MMSE)-Interference Rejection Combining (IRC) (LMMSE-IRC) receiver, the Enhanced Linear MMSE-IRC (E-LMMSE-IRC) receiver and the Widely Linear MMSE-IRC (WLMMSE-IRC) receiver [3GP14f, Section 7.2]. The LMMSE-IRC receiver does not require explicit knowledge on the CTF nor the precoding vector of the interfering eNodeBs to calculate the decorrelating filter [3GP14f, Section 7.2]. The decorrelating filter is rather calculated based on subcarriers and OFDM symbols carrying either the CRS, DMRS or modulation mapped symbols [3GP12, Section 4.3]. The LMMSE-IRC receiver adapted for single-layer transmission is discussed in Section 2.6.3 of this thesis. The E-LMMSE-IRC receiver explicitly considers the CTF and precoding vector of each interfering eNodeBs to calculate the decorrelation filter [3GP14f, Section 7.2]. The E-LMMSE-IRC receiver adapted for single-layer transmission is discussed in

Section 2.6.3 of this thesis. The WMMSE-IRC receiver exploits additional degrees of freedom from the real and imaginary part of the receive signal to enhance the interference suppression capabilities [3GP14f, Section 7.2] and brings the most benefit when the codewords at the interfering eNodeBs are mapped on pulse amplitude modulated symbols instead of QPSK or QAM symbols [3GP14f, Section 7.5]. As pulse amplitude modulation is not considered for a modulation mapping scheme for data transmission in the DL [3GP16f, Section 6.3.2], the WMMSE-IRC receiver is not considered in this thesis. The shortcomings of IS receivers are discussed in Section 1.4 of this thesis.

IC receivers refer to non-linear receivers that aim for canceling inter-cell interference from the receive signal [Kam08, Section 17.1.5]. IC can be carried out on the codeword level and on the symbol level [3GP14f, Section 7.4]. Interference cancellation on the codeword level is not discussed in this thesis. Further information on codeword level interference cancellation can be found in [3GP14f, Section 7.4; 3GP15e, Section A.3.2, A.3.3]. Symbol Level IC (SLIC) receivers perform successive application of the LMMSE-IRC receiver or the E-LMMSE-IRC receiver to detect the strongest interfering signal, followed by signal reconstruction and cancellation [3GP14f, Section 7.4; Mol05, Section 18.4]. Signal detection means that the most probable modulation mapped symbol is determined [Jun97, Section 5.3.3]. The most probable modulation mapped symbol is multiplied with the CTF and precoding vector of the respective interfering eNodeB and subtracted from the receive signal [3GP14f, Section 7.4]. There are two possibilities for subtracting the inter-cell interfering signal [Mol05, Section 18.4]. In case of hard subtraction, the inter-cell interfering signal is subtracted completely [Mol05, Section 18.4]. In case of soft subtraction, only a scaled-down version of the inter-cell interfering signal is subtracted, such that a residual amount of inter-cell interference remains in the receive signal [Mol05, Section 18.4]. SLIC receivers performing soft subtraction of the inter-cell interfering signal are not considered in this thesis. Further information on SLIC receivers performing soft subtraction of inter-cell interference can be found in [Mol05, Section 18.4]. The SLIC receiver adapted for single-layer transmission and performing hard subtraction of inter-cell interference is discussed in Section 2.6.4 of this thesis. The shortcomings of SLIC receivers performing hard inter-cell interference subtraction are discussed in Section 1.4 of this thesis.

1.3.3 Signal Precoding

The support of closed-loop transmission, identified in Section 1.1.4 as one of the key features supported since LTE Release 8 [3GP09b, Section 7.2], is used to assist the eNodeB in the DL [Ast+09]. Closed-loop transmission enables the

UE to feed CSI back to the serving eNodeB [3GP16g, Section 7.2]. The CSI includes the Channel Quality Indication (CQI) [3GP16g, Section 7.2.3], the Precoding Matrix Index (PMI) [3GP16g, Section 7.2.4] and the Rank Indicator (RI) [3GP16g, Section 7.2]. The RI denotes the number of transmit layers the modulation mapped symbols and RSs are mapped on [3GP16f, Section 6.3.3]. The number of transmit layers is fixed to one throughout this thesis. The CQI refers to the modulation order of the complex-valued modulation symbols and the TBS [3GP16g, Section 7.2.3]. In case of single-layer transmission, the PMI refers to a precoding vector of a predefined codebook to precode the complex-valued modulation symbols at the eNodeB [3GP16f, Section 6.3.4.2.3; 3GP16f, Section 6.3.4]. For TMs supporting DMRS transmission, the precoding vector can, but does not need to be selected from a predefined codebook [3GP16g, Section 7.1]. Signal precoding schemes enabling interference mitigation precoding are discussed in what follows.

An inquiry for journal publications available in the IEEE-XPLORE with the search term *Interference Mitigation Precoding LTE* on the 13th July 2016 resulted in [EDL14; MDV13; Lan+15; XRS16].

ELSHERIF et al. focus on codebook-based interference mitigation precoding schemes to mitigate the impact of inter-cell interference arising in heterogeneous LTE networks [EDL14]. In this network scenario low power base stations, denoted as small cells, are deployed in presence of the overlaid macro cellular LTE network that operates in the same frequency band [3GP13c, Chapter 4]. The authors assume that each UE is either assigned with respect to synchronization to the eNodeB or one of the small cells [EDL14]. The same holds for the synchronization with respect to desired signal transmission [EDL14]. To mitigate the impact of inter-cell interference experienced by the UE that assigned to the eNodeB, three codebook-based interference mitigation precoding schemes that follow the concept of codebook subset restriction [3GP16g, Section 7.2] are suggested [EDL14]. The first codebook-based interference mitigation precoding scheme suggested in [EDL14] specifies that the UE assigned to the eNodeB sends a restricted codebook to the dominant interfering small cell such that the interference constraint can be satisfied. The dominant interfering small cell in turn selects the precoding vector from the restricted codebook which ensures maximum throughput at its serving UE [EDL14]. The second codebook-based interference mitigation precoding scheme, suggested in [EDL14], specifies that the dominant interfering small cell sends a codebook subset that satisfies the throughput requirements at its serving UE to the UE served by the eNodeB. The UE served by the eNodeB chooses the precoding vector from the restricted subset that minimizes the impact of inter-cell interference caused by the dominant interfering small cell [EDL14]. The third codebook-based interference mitigation precoding scheme suggested in [EDL14] specifies that the dominant interfering small cell esti-

mates the reciprocal channel to the UE that is assigned to the eNodeB and generates a subset of precoding vectors that satisfies the interference constraint at that UE. Next, the dominant interfering small cell selects the precoding vector which ensures maximum throughput at its serving UE [EDL14]. Further information on the suggested interference mitigation precoding schemes can be found in [EDL14]. The shortcomings of the suggested codebook-based interference mitigation precoding schemes suggested in [EDL14] are discussed in Section 1.4 of this thesis.

MASO et. al. suggest non codebook-based interference mitigation precoding schemes [MDV13]. The authors focus on heterogeneous LTE networks, as in [EDL14], and aim to precode the signals arising at each small cell such that the UE that is assigned to the eNodeB is able to mitigate the impact of inter-cell interference [MDV13]. Following the concept of Interference Alignment (IA) [Jaf11, Chapter 2], the authors in [MDV13] design the precoding vectors for the small cells such that the inter-cell interference signals experienced by the UE that is assigned to the eNodeB, are projected on one subspace which is different to the subspace for the desired signal [MDV13]. Further information can be found in [MDV13]. The shortcomings of the suggested non codebook-based interference mitigation precoding scheme are discussed in Section 1.4 of this thesis.

LAN et. al. focus on techniques to estimate the precoding vectors applied at the interfering eNodeBs to enhance the interference suppression capabilities of the receiver [Lan+15]. In contrast to [EDL14; MDV13], the aspect of interference mitigation precoding is not discussed in [Lan+15]. Therefore, [Lan+15] is not further considered in this thesis.

The investigation of XU et. al. in [XRS16] is based on CoMP transmission and is discussed in Section 1.3.4 of this thesis.

1.3.4 CoMP Transmission

The support of CoMP transmission in the DL has been identified in Section 1.1.4 of this thesis as one of the key enhancements in LTE Release 11 systems. LTE Release 11 systems support both, CoMP transmission in the DL [3GP13a, Section 5] and CoMP reception in the Uplink (UL) [3GP13a, Section 6]. CoMP reception in the UL is not considered in this thesis. Further information on CoMP reception in the UL can be found in [3GP13a, Section 6]. The idea behind CoMP transmission in the DL is to enable joint signal processing at geometrically distributed transmitters to improve coverage and bandwidth efficiency in the cell-edge [3GP13a, Section 4; Lee+12b]. The aspect of coverage improvements using CoMP transmission in the DL is not

considered in this thesis. Further information on coverage improvements using CoMP transmission in the DL can be found in [3GP13a, Section 4; Lee+12b]. One way forward to improve the bandwidth efficiency in the cell-edge is to increase the post-processing SNR at the UE $\mu_m \in \mathcal{U}$ by mitigating the impact of inter-cell interference and, thus, decreasing the accumulated received power of the interfering signals [Lee+12b].

An inquiry for journal publications available in the IEEE-XPLORE with the search term *Interference Mitigation CoMP* on the 14th July 2016 resulted in [Pat+13; Lee+12b; Irm+11; Huq+15; XRS16; HYA16; LL13; GAH11; Moo+13; Jan+11; YKS13; Zha+15b; Bas+16; Zha+15a; Bai+13a; HFK12; Pap+11; CPP13; Ann16; PBT12; Ros13; Mar+12].

An overview of CoMP transmission is provided in [Pat+13; Lee+12b; Irm+11], including benefits and limitations of CoMP transmission in practical LTE networks. The main advantage of CoMP transmission is the ability to mitigate the impact of inter-cell interference in the cell-edge and, thus improve the data rate and spectral efficiency at the cell-edge UE [Pat+13; Lee+12b; Irm+11]. The challenges and issues of practical CoMP transmission identified in [Pat+13; Lee+12b; Irm+11] include

- increased backhaul overhead,
- synchronization among the transmitters and
- feedback design for CSI reporting.

This list is not complete. For a complete list of challenges and issues of practical CoMP transmission, see [Pat+13; Lee+12b; Irm+11]. The aspect of backhaul overhead arising in CoMP transmission is not discussed in this thesis. Further information on backhaul overhead in CoMP transmission can be found in [Pat+13; Lee+12b; Irm+11]. The aspect of synchronization among transmitters and feedback design for CSI reporting is discussed in Chapter 3 and Chapter 4 of this thesis.

Inter-cell interference mitigation techniques via signal precoding in CoMP transmission are suggested in [Irm+11; Huq+15; HYA16; LL13; GAH11; Moo+13; Jan+11; YKS13].

IRMER et. al. suggest a codebook-based interference mitigation precoding scheme for CoMP transmission, where each UE determines a PMI for its eNodeB it is assigned to with respect to data transmission and, additionally, a set of PMIs for the interfering eNodeBs causing strong inter-cell interference [Irm+11]. Detail information on the suggested codebook-based interference mitigation precoding scheme can be found in [Irm+11]. The shortcomings of the suggested codebook-based interference mitigation precoding scheme are discussed in Section 1.4 of this thesis.

HUQ et. al. investigate cooperative codebook-based interference mitigation signal precoding schemes with a particular focus on power consumption of the backhaul [Huq+15]. Concerning the cooperative codebook-based interference mitigation precoding scheme, provided in [Huq+15], each UE suggests a set of PMIs that ensures the throughput constraints and a set of PMIs that ensures the interference constraints and feeds the sets back to its eNodeB it is assigned to with respect to synchronization. The eNodeBs exchange the information via the backhaul and determine the most suitable PMI to precode the desired signal for each UE. Detail information on the suggested cooperative codebook-based interference mitigation signal precoding scheme can be found in [Huq+15]. The shortcomings of the suggested cooperative codebook-based interference mitigation signal precoding scheme are discussed in Section 1.4 of this thesis.

XU et. al. combine CoMP transmission with non codebook-based interference mitigation precoding schemes to mitigate the impact of intra-cell and inter-cell interference at the cell-edge UE in a cooperative manner [XRS16]. The precoder design is carried out in two steps [XRS16]. In the first step, IA is suggested to project the inter-cell interference signals of each UE on one subspace [XRS16]. In the second step, the impact of intra-cell interference is suppressed through channel orthogonalization [XRS16]. Detail information on the non codebook-based interference mitigation precoding scheme using IA and channel orthogonalization can be found in [XRS16]. The shortcomings of the suggested non codebook-based interference mitigation precoding scheme using IA and channel orthogonalization are discussed in Section 1.4 of this thesis.

HOSSEINI et. al. discuss the fundamental limitations of Zero Forcing (ZF) signal precoding schemes in CoMP transmission [HYA16]. ZF signal precoding is a linear precoding technique which enables to project the signal to the zero-space [Kam08, Section 16.2.2]. It is shown that CoMP transmission in conjunction with ZF signal precoding enables to force the power of the inter-cell interfering signals to zero and, thus provides significant performance improvements as compared to uncoordinated transmission [HYA16]. Detail information on the suggested ZF signal precoding scheme can be found in [HYA16]. The shortcomings of the suggested ZF signal precoding scheme are discussed in Section 1.4 of this thesis.

LIU et. al. address the issue of inter-cell interference in media applications [LL13]. It is shown that non cooperative signal precoding schemes aiming at maximizing the local throughput at each UE fail in presence of multiple UEs operating in the same frequency band [LL13]. To overcome this limitation, cooperative non codebook-based interference mitigation precoding is suggested, where the eNodeBs jointly precode and transmit the desired signal [LL13]. De-

tail information on the suggested cooperative non codebook-based interference mitigation precoding scheme can be found in [LL13]. The shortcomings of the suggested cooperative non codebook-based interference mitigation precoding scheme are discussed in Section 1.4 of this thesis.

GHIMIRE et. al. propose a self organizing and decentralized approach to coordinate inter-cell interference [GAH11]. Each eNodeB exploits the RSs sent by the UEs in the UL and estimates the amount of inter-cell interference it would cause to each of the UEs [GAH11]. Based on this measurement, a protocol for user scheduling and non codebook-based interference mitigation precoding is suggested to keep the amount of inter-cell interference below a predefined level [GAH11]. Detail information can be found in [GAH11]. The shortcomings of the proposed self organizing and decentralized approach are discussed in Section 1.4 of this thesis.

Signal precoding schemes combined with user selection for CoMP transmission are suggested in [Moo+13; Jan+11; YKS13]. MOON et. al. suggest a non codebook-based signal precoding scheme combined with user selection to maximize the bandwidth efficiency in each cell [Moo+13]. Detail information can be found in [Moo+13]. JANG et. al. suggest to combine ZF signal precoding with user scheduling [Jan+11]. Detail information can be found in [Jan+11]. Moreover, YU et. al. extend the non codebook-based signal precoding scheme combined with user selection by power allocation at each eNodeB [YKS13]. Detail information can be found in [YKS13]. The shortcomings of the precoding schemes combined with user selection are discussed in Section 1.4 of this thesis.

Inter-cell interference mitigation by CoMP clustering is discussed in [Zha+15b; Bas+16; Zha+15a]. The aspect of CoMP clustering is not considered in this thesis. Further information on inter-cell interference mitigation by CoMP clustering can be found in [Zha+15b; Bas+16; Zha+15a] and references therein.

BAI et. al. focus on PMI feedback schemes for CoMP transmission to improve the diversity gain at the cell-edge UE [Bai+13a]. Two PMI feedback schemes are suggested and their performance versus complexity trade-off is investigated [Bai+13a]. The shortcomings of the suggested PMI feedback schemes are discussed in Section 1.4 of this thesis.

HASSAN et. al. investigate the impact of CSI quantization on signal precoding in CoMP transmission [HFK12]. To alleviate channel quantization errors, a phase pre-compensation scheme is suggested to compensate the resulting phase-offset among the estimated and quantized channel [HFK12]. Detail information on the channel quantization scheme and the suggested phase pre-compensation scheme can be found in [HFK12]. The shortcomings of the

suggested channel quantization and the phase pre-compensation scheme are discussed in Section 1.4 of this thesis.

PAPADOGIANNIS et. al. provide a framework to reduce the CSI feedback and backhaul overhead in CoMP transmission [Pap+11]. The aspect of overhead reduction in CoMP transmission is not discussed in this thesis. Further information on CSI feedback and backhaul overhead reduction can be found in [Pap+11] and references therein.

CHENG et. al. focus on power consumption optimization in CoMP transmission and provide a trade-off between power consumption adjustment at the eNodeBs and the QoS experienced by the UE [CPP13]. The aspect of power consumption optimization is not discussed in this thesis. Further information on power consumption optimization can be found in [CPP13] and references therein.

ANNAVAJJALA focuses on CoMP reception techniques to improve signal detection capabilities in the UL [Ann16]. UL CoMP reception is not considered in this thesis. Further information on UL CoMP reception can be found in [3GP13a, Chapter 6], whereas CoMP reception techniques enabling signal detection improvement can be found in [Ann16] and references therein.

PAPADOGIANNIS et. al. propose a cooperation scheme between relay nodes and eNodeBs to mitigate the impact of inter-cell interference [PBT12]. Relay nodes are network nodes designed to complement the macro cellular deployed LTE network by expanding coverage and increasing capacity [STB11, Section 30.1.1]. A two-way relaying strategy based on amplifying and forwarding the receive signal at the relay node combined with CoMP transmission is suggested to improve the signal detection capabilities in the cell-edge [PBT12]. Further information on the suggested two-way relaying strategy can be found in [PBT12]. The shortcomings of the suggested two-way relaying strategy are discussed in Section 1.4 of this thesis.

ROST suggests an inter-cell interference mitigation scheme based on asymmetric assignment of UL and DL resources to pairs of UEs and eNodeBs [Ros13]. The aim is to turn inter-cell interference into inter-eNodeB and inter-UE interference and, thus, improve the signal detection capabilities at the cell-edge UE. Detailed information on the suggested inter-cell interference mitigation scheme can be found in [Ros13]. The shortcomings of the suggested inter-cell interference mitigation scheme are discussed in Section 1.4 of this thesis.

MARTIN et. al. address the issue of localization in cooperative wireless sensor networks [Mar+12]. The aspect of localization is not discussed in this thesis. Further information on localization on cooperative wireless sensor networks can be found in [Mar+12] and references therein.

1.4 Criticism of the State of the Art

As discussed in Section 1.3.2 of this thesis, IS receivers apply the DMF to suppress the impact of inter-cell interference in presence of single-layer transmission and maximize the post processing SNR [Jun97, Section B.1.3]. Theoretically, it is possible to suppress $N_{\text{R}}^{(m)} - 1$ inter-cell interfering signals at the UE $\mu_m \in \mathbb{U}$ by projecting the interfering signals to a subspace that is orthogonal to the subspace the desired signal is projected on [Léo+12]. However, IS receivers fail to project the interfering signals to a subspace that is orthogonal to the subspace the desired signal is projected on when the number of receive AEs at the UE $\mu_m \in \mathbb{U}$ is smaller than the number of spatial layers, experienced by the UE $\mu_m \in \mathbb{U}$ [Léo+12]. As a result, the impact of inter-cell interference cannot be entirely suppressed after applying the DMF, such that reliable signal detection at the UE $\mu_m \in \mathbb{U}$ cannot be guaranteed [Léo+12]. A solution to improve signal detection at the UE $\mu_m \in \mathbb{U}$ in that case is motivated in Section 1.5.2 of this thesis and discussed in detail in Section 3.3 of this thesis.

The concept of SLIC receivers has been discussed in Section 1.3.2 of this thesis. SLIC receivers enable remarkable improvements over IS receivers when the impact of inter-cell interference can be reliably removed from the receive signal experienced by the UE $\mu_m \in \mathbb{U}$ [LTY11]. However, to enable interference cancellation on symbol level, the UE $\mu_m \in \mathbb{U}$ needs to know the CTF and the precoding vector of each interfering eNodeB $\epsilon_{\bar{j}} \in \mathbb{I}_m$ [3GP14f, Section 7.5]. For DMRS-based TMs the desired effective channel among the UE $\mu_m \in \mathbb{U}$ and the eNodeB $\epsilon_b \in \mathbb{A}_m$ in (1.29) can be jointly estimated with the interfering effective channels among the UE $\mu_m \in \mathbb{U}$ and each eNodeB $\epsilon_{\bar{j}} \in \mathbb{I}_m$ in (1.29) [Iwe+15a]. Therefore, the UE $\mu_m \in \mathbb{U}$ needs information on the physical layer cell-identities $N_{\text{cell}}^{\text{ID}}$ and the scrambling identity field of each interfering eNodeB $\epsilon_{\bar{j}} \in \mathbb{I}_m$ [3GP14f, Section 7.5]. For single-layer transmission the scrambling identity field is set to zero [3GP16f, Section 6.10.3.1]. This information can be either provided by the network or is blindly detected by the UE $\mu_m \in \mathbb{U}$ [3GP14f, Section 7.6]. In this thesis it is assumed that the physical layer cell-identity of the interfering eNodeBs $\epsilon_{\bar{j}} \in \mathbb{I}_m$ is provided to the UE $\mu_m \in \mathbb{U}$ through the network. Further information on blind detection of the physical layer cell-identity of the interfering eNodeBs $\epsilon_{\bar{j}} \in \mathbb{I}_m$ can be found in [3GP14f, Section 7.6]. Moreover, the UE $\mu_m \in \mathbb{U}$ needs information about the modulation order of the complex-valued modulation symbols transmitted by each interfering eNodeB $\epsilon_{\bar{j}} \in \mathbb{I}_m$ [3GP14f, Section 7.5]. The modulation order of the complex-valued modulation symbols transmitted by each interfering eNodeB $\epsilon_{\bar{j}} \in \mathbb{I}_m$ can be either provided through the network or is detected blindly by the UE $\mu_m \in \mathbb{U}$ [3GP14f, Section 7.5]. In this thesis it is assumed that the modulation order of the complex-valued modulation symbols

transmitted by each interfering eNodeB $\epsilon_b \in \mathbb{I}_m$ is provided to the UE $\mu_m \in \mathbb{U}$ through the network. Further information on blind modulation order detection can be found in [3GP14f, Section 7.5]. Reliable inter-cell interference cancellation on symbol level can be guaranteed when the average receive power of the interfering signal is significantly larger than the average receive power of the desired signal [LTY11]. However, inter-cell interference cancellation on symbol level fails when the average receive power of the interfering signal is approximately equal to or even smaller than the average receive power of the desired signal [LTY11]. In that case the SLIC receiver suffers from error propagation and performs considerably worse than the IS receiver [LTY11]. A solution to dynamically switch between IS and SLIC is provided in Section 2.6.4 of this thesis.

The codebook-based signal precoding schemes suggested by ELSHERIF et. al. in [EDL14] enable inter-cell interference mitigation through codebook restriction. However, the provided codebook-based interference mitigation precoding schemes are limited on one interfering small cell [EDL14]. Furthermore, the number of receive AEs at each UE in the investigated heterogeneous LTE network is fixed to one [EDL14], such that the advantages of enhanced receivers discussed in Section 1.3.2 of this thesis have not been exploited. A signal precoding scheme enabling interference mitigation precoding for arbitrary number of interfering eNodeBs and arbitrary number of receive AEs at the UE $\mu_m \in \mathbb{U}$ is motivated in Section 1.5.2 of this thesis and discussed in detail in Section 3.3 of this thesis.

The non codebook-based signal precoding schemes suggested by MASO et. al. in [MDV13] enable inter-cell interference mitigation precoding by projecting the inter-cell interference signals on one subspace which is different to the subspace used for the desired signal. The precoding vector calculation is limited on LTE networks operating in Time Division Duplex (TDD) mode [MDV13]. In LTE networks operating in TDD mode, the same operating band is used in the UL and DL [3GP16n, Section 5.5; STB11, Section 6.2]. Valid operating bands for LTE networks operating in TDD mode are denoted in [3GP16n, Table 5.5-1] for duplex mode TDD. One property of communication systems operating in TDD mode is channel reciprocity, where both, transmitter and receiver have knowledge on the CTF [Mol05, Section 17.5]. In LTE networks operating in FDD mode, the operating band for UL and DL is different [3GP16n, Section 5.5; STB11, Section 6.2]. Valid operating bands for LTE networks operating in FDD mode are denoted in [3GP16n, Table 5.5-1]. One property of communication systems operating in FDD mode is that only the receiver can estimate the CTF in the DL [Mol05, Section 17.5]. Following the concept of LTE networks operating in TDD mode, MASO et. al. assume that each eNodeB has knowledge on the CTF to each UE and, based on this, is able to design a precoding vector which projects the inter-cell interference signals

on one subspace which is different to the subspace used for the desired signal [MDV13]. In this thesis LTE networks operating in FDD mode are focused on. In FDD systems the UE can feed quantized CSI back to its eNodeB it is assigned to with respect to synchronization [3GP16g, Section 7.2]. However, the knowledge on the CTF estimated by each UE is not included in the CSI feedback [3GP16g, Section 7.2]. Although the CTFs of the interfering eNodeBs can be estimated in LTE networks operating in FDD mode [Iwe+15b], non codebook-based signal precoding schemes come at the expense of high feedback overhead and are therefore not preferred in practical LTE networks operating on FDD mode.

Practical CoMP transmission suffers from unsynchronized signal reception, where the desired signals and the interfering signals reach the UE $\mu_m \in \mathbb{U}$ with varying delays [KRF12]. To achieve the anticipated gains of CoMP transmission, the impact of Timing Offsets (TOs) among the receive signals experienced by the UE $\mu_m \in \mathbb{U}$ has to be considered [KF10], where the TO is defined as the difference of the eNodeB time alignment errors plus the difference of the propagation delay between transmitter and receiver [3GP13a, Section 5.1.2A]. However, the relevant state-of-the-art CoMP transmission schemes discussed in Section 1.3.4 of this thesis do not consider the impact of TOs among the desired and the interfering signals [Irm+11; Huq+15; XRS16; HYA16; LL13; GAH11; Moo+13; Bai+13a; HFK12; PBT12; Ros13]. Ignoring the impact of TOs among the receive signals experienced by the UE $\mu_m \in \mathbb{U}$ can significantly degrade the performance of CoMP transmission, especially at high data rates [Zha+07]. Reliable PMI selection to maximize the accumulated receive power of the desired signals fails if the impact of TOs arising in practical CoMP transmission schemes is neglected [Iwe+14b]. Moreover, reliable signal precoding to minimize the accumulated received power of the interfering signals is considerably limited when the impact of TOs arising in practical CoMP transmission schemes is neglected [Iwe+15b]. The impact of TOs among the receive signals, caused by unsynchronized CoMP transmission, is the core aspect of this thesis. A solution to mitigate the impact of TOs among the receive signals experienced by the UE $\mu_m \in \mathbb{U}$ is motivated in Section 1.5.3 of this thesis and discussed in detail in Chapter 4 of this thesis.

1.5 Scope and Objective of this Thesis

1.5.1 Introduction

The major goal of this thesis is to provide reliable implicit feedback generation and ensure reliable channel estimation to improve the DL transmission performance in unsynchronized CoMP transmission LTE networks. To reach this

goal, a cooperative interference mitigation signal precoding scheme [Iwe+15b; Iwe+15a; Iwe+14a] is motivated in Section 1.5.2 of this thesis and, based on this, techniques to enhance the desired signal reception using CoMP transmission [3GP13a, Section 5.1.2] are motivated in Section 1.5.3 of this thesis.

Parts of this work have been achieved in cooperation with industrial partners. In the scope of this work, numerous scientific contributions have been published, which fit in the context of this thesis, including conference contributions [Bai+13c; Iwe+13c; Iwe+14a; Iwe+14e; Iwe+14f; Iwe+14g; Iwe+14h; Iwe+15a; Iwe+15b; Iwe+15c; Iwe+16] and articles [Bai+11a; Bai+13a; Bai+14a; Iwe+14b]. All publications of this author can be found in the Section "Publications of the Author". Furthermore, in the scope of this work patents have been filed which are provided in Section "Filed Patents of the Author". Moreover, the author of this thesis has co-supervised various theses, including Bachelor's and Master's theses at the Lehrstuhl für Kommunikationstechnik at the University of Duisburg-Essen that fit in the context of this thesis [Lu13; Tar13; Teh13; Zho13; Fan14; Mos16; Wan16; Che17; Bao17; Li18]. All theses the author of this thesis has co-supervised can be found in the Section "Co-Supervised Theses by the Author".

1.5.2 Cooperative Interference Mitigation Signal Precoding

To improve the signal detection capabilities of IS receivers, discussed in Section 1.3.2 of this thesis, the following approach has been chosen to assist the UE $\mu_m \in \mathbb{U}$ [Iwe+14a]: Assuming that the UEs $\mu_{\tilde{m}} \in \mathbb{U}$ with $\tilde{m} \neq m$ do not need to operate at high data rates, unlike the UE $\mu_m \in \mathbb{U}$, the UE $\mu_m \in \mathbb{U}$ is empowered to select the precoding vector for each interfering eNodeB $\epsilon_{\tilde{b}} \in \mathbb{I}_m$ from a predefined codebook, restricted by each UE $\mu_{\tilde{m}} \in \mathbb{U}$, where $\tilde{m} \neq m$ holds [Iwe+14a]. To enable Codebook-Based Cooperative Interference Mitigation Precoding (CCIMP), the following goals have been defined and will be reached in this thesis:

1. Develop a cooperative signal precoding scheme to mitigate the impact of inter-cell interference at the UE $\mu_m \in \mathbb{U}$.
2. Provide an Optimal CCIMP (O-CCIMP) scheme to maximize the global post-processing SNR of the IS receiver at the UE $\mu_m \in \mathbb{U}$.
3. Derive a low-complexity implementation following the concept of the O-CCIMP scheme to decouple signal precoding of the desired and the interfering signals.
4. Performance evaluation with numerical results at the link level.

1.5.3 Signal Reception Enhancements using CoMP Transmission

To further enhance the signal detection capabilities at the UE $\mu_m \in \mathbb{U}$, the accumulated received power of the desired signal needs to be increased. Following the concept of CoMP transmission, low-power Remote Radio Heads (RRHs) are deployed within the coverage area of the macro cellular deployed LTE network to reduce the geometrical distance to the UE $\mu_m \in \mathbb{U}$ [3GP13a, Section 5.1.2].

Among the supported CoMP categories [3GP13a, Section 5.1.3] in this thesis the CoMP JP-Dynamic Point Selection (DPS) is considered. Further information on JP in CoMP transmission is provided in Section 3.2 of this thesis. As discussed in Section 1.4 of this thesis, the UEs operating in practical CoMP transmission schemes might suffer from unsynchronized signal reception such that reliable signal detection of the desired signal is limited. To maintain the promised advantages of CoMP transmission, reliable implicit feedback generation and channel estimation techniques for unsynchronized CoMP JP-DPS are of particular importance. The following goals have been defined and will be reached in this thesis.

1. Analytic derivation of the impact of TOs on PMI selection for particular antenna configuration at the RRHs.
2. TO estimation and compensation schemes based on reference signals.
3. Reliable PMI feedback.
4. Reliable channel estimation.
5. Performance evaluation with numerical results at the link level.

1.6 Organization of this Thesis

Following up on the introduction, the physical layer aspects of LTE systems being of particular importance for this thesis are discussed in Chapter 2 of this thesis. The generation of the RSs for DL signal transmission is discussed in Section 2.2 of this thesis. Furthermore, the transport channel processing and the physical channel processing schemes are discussed in Section 2.3 and Section 2.4 of this thesis, respectively. The support of OFDM baseband signal generation has already been identified in Section 1.1.4 of this thesis as one of the key enhancements in LTE systems. The aspect of OFDM baseband signal modulation and OFDM baseband signal demodulation is discussed in Section 2.5 of this thesis. Channel estimation schemes that are essential for the

IS and for the SLIC receiver implementation are discussed in Section 2.6 of this thesis. Moreover, two practical IS receiver implementation schemes adapted for single-layer transmission are discussed. Furthermore, a practical implementation for the SLIC receiver adapted for single-layer transmission is provided. The aspect of aperiodic CSI reporting with a particular focus in closed-loop PMI feedback, supported in TM 6, TM 8, TM 9 and TM 10, is discussed in Section 2.7 of this thesis. The emphasis is on the PMI selection based on the transmitted RSs. The properties of the selected channel and interference model are discussed in Section 2.8 of this thesis. The quality criterion for LTE systems are defined in Section 2.9 of this thesis. In this context, the key terms, such as throughput, bandwidth efficiency, Bit Error Rate (BER) and SNR are explained. Numerical results at the link level are provided in Section 2.10 of this thesis to demonstrate the impact of inter-cell interference. Moreover, the limitation of selected state-of-the-art interference mitigation techniques, including IS and SLIC receivers, as well as signal precoding is provided.

Opportunities to improve signal detection capabilities in the cell-edge using implicit feedback generation in CoMP transmission in synchronized LTE networks are discussed in Chapter 3 of this thesis. The network configuration for CoMP transmission including the supported transmission categories and network deployment scenarios is discussed in Section 3.2 of this thesis. Cooperative signal precoding schemes enabling interference mitigation are discussed in Section 3.3 of this thesis. Following the concept of codebook-based signal precoding, an O-CCIMP scheme is suggested to alleviate the impact of inter-cell interference at the cell-edge UE $\mu_m \in \mathbb{U}$. Moreover, a low-complexity implementation of the O-CCIMP scheme is derived. A complexity analysis of the O-CCIMP scheme and the Low-Complexity CCIMP (LC-CCIMP) scheme is provided, followed by a detailed complexity analysis. Numerical results at the link level are provided in Section 3.4 of this thesis to demonstrate the improved signal detection capabilities at the cell-edge UE $\mu_m \in \mathbb{U}$, which became possible by cooperative interference mitigation precoding in conjunction with enhanced CSI feedback reporting schemes.

Opportunities to provide reliable implicit feedback generation and channel estimation for unsynchronized CoMP transmission are derived in Chapter 4 of this thesis. The challenges arising in practical CoMP transmission are derived in Section 4.2 of this thesis. In this context it is shown that the PMI reporting schemes for synchronized CoMP transmission fail in unsynchronized CoMP transmission. Therefore, the impact of varying TOs on PMI selection for CoMP JP-DPS in unsynchronized CoMP transmission is investigated analytically for arbitrary antenna configuration. Moreover, the impact of the low-complexity channel estimation and interpolation scheme, discussed in Section 2.6.2 of this thesis, is analyzed. TO estimation techniques based on the precoded DMRSs are discussed in Section 4.3 of this thesis. To maintain the

promised advantages of CoMP transmission, reliable implicit feedback generation and channel estimation schemes are of particular importance in a practical implementation and are discussed in Section 4.4 and Section 4.5 of this thesis, respectively. The impact of TOs on the DL performance is demonstrated with numerical results at the link level in Section 4.6 of this thesis. Moreover, the DL performance after applying the suggested compensation methods to ensure reliable implicit feedback generation and channel estimation is verified with numerical results at the link level.

Conclusions are drawn in Chapter 5 of this thesis, where the key findings are summarized. Moreover, an outlook of possible further investigation of implicit feedback generation in unsynchronized CoMP transmission is provided.

Chapter 2

Physical Layer Aspects of LTE Systems

2.1 Introduction

In LTE networks, the radio architecture is divided into layers [3GP16a, Section 4.3], where each layer takes on special, largely defined tasks in order to provide service to the layer directly above it [WSA03, Section 5.1]. Each layer in the transmitter has a corresponding layer in the receiver with a logical connection between the two [WSA03, Section 5.1]. In LTE networks, the radio architecture is defined for the user-plane protocol stack [3GP16a, Section 4.3.1] and the control-plane protocol stack [3GP16a, Section 4.3.2]. In this thesis the radio architecture for the user-plane protocol stack is focused on. Detail information on the radio architecture for the control-plane protocol stack can be found in [3GP16a, Section 4.3.2; 3GP16a, Section 23.10.2.2]. The user-plane protocol stack consists of four layers including the Physical (PHY) layer, the MAC layer, the Radio Link Control (RLC) layer and the Packet Data Convergence Protocol (PDCP) layer [3GP16a, Section 4.3.1]. In this thesis the PHY layer of the user-plane protocol stack is focused on. Detail information on the MAC layer, the RLC layer and the PDCP layer can be found in [3GP16c], [3GP16i] and [3GP16e], respectively. The PHY layer of the user-plane protocol can be further subdivided into transport channel processing, physical channel processing and analog processing [Cox14, Section 6.1; Cox14, Figure 6.1]. Despite the transport channel processing and the physical channel processing, the analog processing is not discussed in this thesis. Further information on analog processing, included in the PHY layer of the user-plane protocol stack, can be found in [3GP16b].

The purpose of Chapter 2 of this thesis is to provide the necessary background information of the physical layer aspects of the user-plane protocol stack which is used throughout Chapter 3 and Chapter 4. Chapter 2 of this thesis is organized as follows: The sequence generation and the mapping to REs for the

CRS, for the DMRS and for the CSI-RS is discussed in Section 2.2 of this thesis. The transport channel processing and the physical channel processing is addressed in Section 2.3 and Section 2.4 of this thesis, respectively. In this context, the aspect of modulation mapping, precoding and resource element mapping is discussed in detail. The aspect of OFDM baseband signal modulation and demodulation is discussed in Section 2.5 of this thesis. Practical receiver design schemes are provided in Section 2.6 of this thesis. In this context, the Least Square Channel Estimation (LSCE) and Joint Least Square Channel Estimation (JLSCE) scheme which is essential for practical receiver design is provided. Following the concept of IS receivers, a practical implementation of the LMMSE-IRC receiver adapted for single-layer transmission is suggested, where the LSCE scheme is used. Moreover, a practical implementation of the E-LMMSE-IRC receiver adapted for single-layer transmission is suggested, where the JLSCE scheme is used. Furthermore, a practical implementation of the SLIC receiver adapted for single-layer transmission is suggested, where the JLSCE scheme is used. The aspect of closed-loop transmission with a particular focus on PMI feedback generation supported in TM 6, TM 8, TM 9 and TM 10, is discussed in Section 2.7 of this thesis. In detail, practical PMI feedback schemes based on the transmitted RSs are provided for single-layer transmission. Signal propagation and channel modeling is discussed in Section 2.8 of this thesis. In this context, the interference model is explained. The quality criterion for LTE systems are defined in Section 2.9 of this thesis. In this context, the key terms such as throughput, bandwidth efficiency, BER and SNR are explained. Numerical results at the link level are provided in Section 2.10 of this thesis to demonstrate the impact of inter-cell interference. In this context, the performance of the practical implementation of the LMMSE-IRC receiver adapted for single-layer transmission that makes use of the LSCE scheme is provided. Moreover, the performance of the practical implementation of the E-LMMSE-IRC receiver adapted for single-layer transmission that makes use of the JLSCE scheme is provided. Furthermore, the performance of the SLIC receiver adapted for single-layer transmission that makes use of the JLSCE scheme is provided.

2.2 Reference Signal Generation

2.2.1 Introduction

In LTE systems, RSs denote complex-valued modulation symbols that are known to both, transmitter and receiver [3GP16g, Section 6.10] and are transmitted together with the precoded complex-valued modulation symbols carrying the codewords [3GP16g, Section 6.3.5]. To revert the impact caused by the

inhomogeneities of the mobile communication channel, the receiver at the UE has to equalize the receive signal [CT07, Section 6.1; Kam08, Section 16.2.4]. However, to enable signal equalization, a precise channel estimation for each subcarrier is necessary [CT07, Section 6.1]. A sufficient number of RSs must be inserted accordingly to the degree of channel variation, including the coherence bandwidth and coherence time of the mobile communication channel [CT07, Section 6.1]. The coherence bandwidth of the mobile communication channel denotes the range of frequencies over which the mobile communication channel can be considered as spectrally flat [Jun97, Section 3.3.3]. Moreover, the coherence time of the mobile communication channel denotes the time that must elapse such that the state of the mobile communication channel changes completely [Jun97, Section 3.3.3]. Therefore, to enable signal equalization, the spacing of RSs in frequency domain and in time domain, respectively, must be smaller than the coherence bandwidth and the coherence time of the mobile communication channel. Obviously, the more RSs are transmitted by the eNodeB, the more precisely the UE can estimate the mobile communication channel, but the less physical time-frequency resources remain for the actual data transmission [HH03]. The trade-off between the quantity of RSs and data is not discussed in this thesis. Detail information can be found in [HH03] and references therein.

Each eNodeB $e_b \in \mathbb{E}$ is equipped with a transmit antenna that consists of a set of transmit APs the RS pattern and data is transmitted from [3GP16f, Section 6.10; 3GP16f, Section 6.3.5]. A transmit AP is defined such that the mobile communication channel over which a modulation symbol on the transmit AP is transmitted can be inferred from the mobile communication channel over which another modulation symbol is transmitted from the same transmit AP [3GP16f, Section 6.2.1]. In a practical implementation, a transmit AP may be implemented either as a single transmit AE or as a combination of multiple transmit AEs [STB11, Section 8.2]. In both cases, the signal transmitted from each transmit AP is not designed to be further deconstructed by the UE [STB11, Section 8.2]. Hence, the transmitted RS pattern and data corresponding to a given transmit AP denote the transmit AP from the point of view of the UE and enables the UE to estimate the mobile communication channel regardless of whether a single transmit AE or a composition of multiple transmit AEs is present at the eNodeB [STB11, Section 8.2]. The way in which the transmit APs are assigned to the transmit AEs is up to the eNodeB [TA11]. To guarantee a unique assignment between transmit APs and transmit AEs [TA11], the mapping function

$$\pi_{\text{AP}} \mapsto a_{\text{AE}}(\pi_{\text{AP}}) \quad (2.1)$$

is used, where π_{AP} and $a_{\text{AE}}(\pi_{\text{AP}})$, denotes the π_{AP} -th transmit AP and the ζ -th transmit AE at the eNodeB $e_b \in \mathbb{E}$, respectively. In this thesis it is

assumed that the number of transmit AEs at each eNodeB $\epsilon_b \in \mathbb{E}$ is equal to either two or four.

In LTE systems, six types of RSs are defined for the DL transmission [3GP16f, Section 6.10], including

- CRS [3GP16f, Section 6.10.1],
- Multimedia Broadcast Service Single Frequency Network (MBSFN) RS [3GP16f, Section 6.10.2],
- DMRS associated with Physical Downlink Shared Channel (PDSCH) [3GP16f, Section 6.10.3],
- DMRS associated with Enhanced Physical Downlink Control Channel (EPDCCH) or Machine Type Communication Physical Downlink Control Channel (MPDCCH) [3GP16f, Section 6.10.3A],
- Positioning Reference Signal (PRS) [3GP16f, Section 6.10.4] and
- CSI-RS [3GP16f, Section 6.10.5].

In this thesis CRS, DMRS associated with PDSCH (hereinafter DMRS) and CSI-RS are focused on. Detail information on MBSFN RS and PRS can be found in [3GP16f, Section 6.10.2] and [3GP16f, Section 6.10.4], respectively. Moreover, detail information on DMRS associated with EPDCCH or MPDCCH can be found in [3GP16f, Section 6.10.3A]. In what follows the properties of the CRS, the DMRS and the CSI-RS are provided in Section 2.2.2, Section 2.2.3 and Section 2.2.4 of this thesis, respectively.

2.2.2 Cell Specific Reference Signal

The CRSs are transmitted on one or several transmit APs 0 to 3 [3GP16f, Section 6.10.1], denoted by the set \mathcal{A}_{CRS} , and enable the UE $\mu_m \in \mathbb{U}$ to estimate the mobile communication channel between each pair of the transmit AP $\pi_{\text{AP}} \in \mathcal{A}_{\text{CRS}}$ and the ν -th receive AE for $1 \leq \nu \leq N_{\text{R}}^{(m)}$ [STB11, Section 8.2.1] to provide signal equalization and CSI reporting for selected TMs including TM6 and TM8 [3GP16f, Section 7.2.3 - 7.2.4]. The aspect of CSI reporting in TM6 and TM8 is discussed in Section 2.7.3 of this thesis. In case of one, two or four transmit APs at the eNodeB $\epsilon_b \in \mathbb{E}$, $\mathcal{A}_{\text{CRS}} = \{0\}$, $\mathcal{A}_{\text{CRS}} = \{0, 1\}$ and $\mathcal{A}_{\text{CRS}} = \{0, 1, 2, 3\}$ holds, respectively [3GP16f, Section 6.10.1]. Each CRS denotes a complex-valued modulation symbol following the QPSK modulation mapping scheme that originates from a pseudo-random sequence [3GP16f, Section 6.10.1.1]. Detail information on the pseudo-random sequence generation can be found in [3GP16f, Section 6.10.1.1].

The CRSs are transmitted by each eNodeB $\epsilon_b \in \mathbb{E}$ in all cells supporting PDSCH transmission [3GP16f, Section 6.10.1], where the PDSCH denotes the main physical channel in LTE systems enabling data transmission [3GP16f, Section 6.4; STB11, Section 9.2.2]. The REs used for the transmission of CRSs at the eNodeB $\epsilon_b \in \mathbb{E}$ on any of the APs in a slot are not used for any transmission on any transmit AP in the same slot by the same eNodeB $\epsilon_b \in \mathbb{E}$ [3GP16f, Section 6.10.1.2]. Detail information on the mapping of CRSs on physical time-frequency resources can be found in [3GP16f, Section 6.10.1.2].

Following the mapping of CRS on physical time-frequency resources [3GP16f, Section 6.10.1.2], let $\mathcal{S}_{i, n_{\text{PRB}}, \text{CRS}}^{(b, \pi_{\text{AP}})}$ denote the set of REs in terms of subcarriers and OFDM symbols carrying the CRS transmitted by the eNodeB $\epsilon_b \in \mathbb{E}$ on the transmit AP $\pi_{\text{AP}} \in \mathcal{A}_{\text{CRS}}$ in the i -th subframe which consists of two slots, S_{2i} and S_{2i+1} , and the n_{PRB} -th PRB, where $0 \leq i \leq 9$ [3GP16f, Section 4.1] and $0 \leq n_{\text{PRB}} < N_{\text{RB}}^{\text{DL}}$ [3GP16f, Section 6.2.3] holds.

For the eNodeBs $\epsilon_b \in \mathbb{E}$ equipped with two transmit AEs

$$0 \mapsto 1, \quad (2.2a)$$

$$1 \mapsto 2 \quad (2.2b)$$

holds for the mapping function in (2.1) for $\pi_{\text{AP}} \in \mathcal{A}_{\text{CRS}} = \{0, 1\}$. Each CRS transmitted by the eNodeB $\epsilon_b \in \mathbb{E}$ from the transmit AP0 and the transmit AP1 is mapped on the first and second transmit AE, respectively. The mapping of CRS transmitted by the eNodeB $\epsilon_b \in \mathbb{E}$ on the transmit AP0 and on the transmit AP1 on physical time-frequency resources, is depicted in the center part of [3GP16f, Figure 6.10.1.2-1] for the physical layer cell-identity modulo six equal to zero. Either of the figures shows a cutout of the DL resource grid of the i -th subframe which consists of two consecutive slots S_{2i} and S_{2i+1} for $0 \leq i \leq 9$ [3GP16f, Section 4.1] that carry the CRS transmitted by the eNodeB $\epsilon_b \in \mathbb{E}$ on the n_{PRB} -th PRB for $0 \leq n_{\text{PRB}} < N_{\text{RB}}^{\text{DL}}$ [3GP16f, Section 6.2.3] on the respective transmit AP. Following the properties of the CRS [3GP16f, Section 6.10.1.2]

$$\bigcap_{\pi_{\text{AP}} \in \mathcal{A}_{\text{CRS}} = \{0, 1\}} \mathcal{S}_{i, n_{\text{PRB}}, \text{CRS}}^{(b, \pi_{\text{AP}})} = \emptyset \quad (2.3)$$

holds for $0 \leq i \leq 9$ and $0 \leq n_{\text{PRB}} < N_{\text{RB}}^{\text{DL}}$ such that the UE $\mu_m \in \mathbb{U}$ is able to estimate the mobile communication channel between each pair of the transmit AP $\pi_{\text{AP}} \in \mathcal{A}_{\text{CRS}} = \{0, 1\}$ and the ν -th receive AE for $1 \leq \nu \leq N_{\text{R}}^{(m)}$ [STB11, Section 8.2.1]. For each eNodeB $\epsilon_b \in \mathbb{E}$ transmitting the CRS on the transmit AP0 and on the transmit AP1 [3GP16f, Section 6.10.1.2]

$$N_{\text{CRS}, 1} = \left| \mathcal{S}_{i, n_{\text{PRB}}, \text{CRS}}^{(b, 0)} \right| = \left| \mathcal{S}_{i, n_{\text{PRB}}, \text{CRS}}^{(b, 1)} \right| = 8 \quad (2.4)$$

holds for $0 \leq i \leq 9$ [3GP16f, Section 4.1] and $0 \leq n_{\text{PRB}} < N_{\text{RB}}^{\text{DL}}$ [3GP16f, Section 6.2.3]. Furthermore, for each eNodeB $\epsilon_b \in \mathbb{E}$ transmitting the CRSs on the transmit AP0 and on the transmit AP1

$$N_{\text{CRS},2} = \left| \bigcup_{\pi_{\text{AP}} \in \mathcal{A}_{\text{CRS}} = \{0,1\}} \mathcal{S}_{i, n_{\text{PRB}}, \text{CRS}}^{(b, \pi_{\text{AP}})} \right| = 16 \quad (2.5)$$

holds, such that sixteen out of $N_{\text{RE}}^{\text{SF,PRB}}$ equal to 168 REs are occupied to transmit the CRSs in one subframe and PRB. The number of REs in one subframe and PRB is represented by [3GP16f, Section 4.1; 3GP16f, Section 6.2.2]

$$N_{\text{RE}}^{\text{SF,PRB}} = 2 \cdot N_{\text{ymb}}^{\text{DL}} \cdot N_{\text{sc}}^{\text{RB}} = 168. \quad (2.6)$$

For the eNodeBs $\epsilon_b \in \mathbb{E}$ equipped with four transmit AEs

$$0 \mapsto 1, \quad (2.7a)$$

$$1 \mapsto 2, \quad (2.7b)$$

$$2 \mapsto 3, \quad (2.7c)$$

$$3 \mapsto 4 \quad (2.7d)$$

holds for the mapping function in (2.1). Each CRS transmitted by the eNodeB $\epsilon_b \in \mathbb{E}$ from the transmit AP0, the transmit AP1, the transmit AP2 and the transmit AP3 is mapped on the first, second, third and fourth transmit AE, respectively. The mapping of the CRS transmitted by the eNodeB $\epsilon_b \in \mathbb{E}$ from the transmit AP0, the transmit AP1, the transmit AP2 and the transmit AP3 is depicted in the lower part of [3GP16f, Figure 6.10.1.2-1] for the physical layer cell-identity modulo six equal to zero. Either of the figures shows a cutout of the DL resource grid of the i -th subframe which consists of two consecutive slots S_{2i} and S_{2i+1} for $0 \leq i \leq 9$ [3GP16f, Section 4.1] that carry the CRS transmitted by the eNodeB $\epsilon_b \in \mathbb{E}$ on the n_{PRB} -th PRB for $0 \leq n_{\text{PRB}} < N_{\text{RB}}^{\text{DL}}$ [3GP16f, Section 6.2.3] on the respective transmit AP. Following the properties of the CRS [3GP16f, Section 6.10.1.2]

$$\bigcap_{\pi_{\text{AP}} \in \mathcal{A}_{\text{CRS}} = \{0, \dots, 3\}} \mathcal{S}_{i, n_{\text{PRB}}, \text{CRS}}^{(b, \pi_{\text{AP}})} = \emptyset \quad (2.8)$$

holds for $0 \leq i \leq 9$ [3GP16f, Section 4.1] and $0 \leq n_{\text{PRB}} < N_{\text{RB}}^{\text{DL}}$ [3GP16f, Section 6.2.3], such that the UE $\mu_m \in \mathbb{U}$ is able to estimate the mobile communication channel between each pair of the transmit AP $\pi_{\text{AP}} \in \mathcal{A}_{\text{CRS}} = \{0, \dots, 3\}$ and the ν -th receive AE for $1 \leq \nu \leq N_{\text{R}}^{(m)}$ [STB11, Section 8.2.1]. The granularity of the CRSs transmitted by the eNodeB $\epsilon_b \in \mathbb{E}$ from the transmit AP0 and the transmit AP1 is denoted in (2.4) for the i -th subframe and

n_{PRB} -th PRB for $0 \leq i \leq 9$ [3GP16f, Section 4.1] and $0 \leq n_{\text{PRB}} < N_{\text{RB}}^{\text{DL}}$ [3GP16f, Section 6.2.3]. Moreover,

$$\left| \mathcal{S}_{i, n_{\text{PRB}}, \text{CRS}}^{(b, 2)} \right| = \left| \mathcal{S}_{i, n_{\text{PRB}}, \text{CRS}}^{(b, 3)} \right| = 4 \quad (2.9)$$

holds for $0 \leq i \leq 9$ [3GP16f, Section 4.1] and $0 \leq n_{\text{PRB}} < N_{\text{RB}}^{\text{DL}}$ [3GP16f, Section 6.2.3] when the eNodeB $\epsilon_b \in \mathbb{E}$ is transmitting the CRS additionally on the transmit AP2 and the transmit AP3 [3GP16f, Figure 6.10.1.2-1]. Hence,

$$N_{\text{CRS}, 4} = \left| \bigcup_{\pi_{\text{AP}} \in \mathcal{A}_{\text{CRS}} = \{0, \dots, 3\}} \mathcal{S}_{i, n_{\text{PRB}}, \text{CRS}}^{(b, \pi_{\text{AP}})} \right| = 24 \quad (2.10)$$

out of $N_{\text{RE}}^{\text{SF, PRB}}$ equal to 168 REs are occupied to transmit the CRSs in each subframe and PRB when the eNodeB $\epsilon_b \in \mathbb{E}$ is transmitting the CRSs from the transmit AP0, the transmit AP1, the transmit AP2 and the transmit AP3.

A cell-specific frequency shift

$$v_{\text{shift}} = N_{\text{cell}}^{\text{ID}} \bmod 6 \quad (2.11)$$

is applied to the pattern of the CRSs [3GP16f, Section 6.10.1.2] to avoid time-frequency collision between the CRSs from up to six adjacent cells [STB11, Section 8.2.1].

The mapping of the CRSs on physical time-frequency resources to be transmitted from the eNodeB $\epsilon_b \in \mathbb{A}_m$ on the transmit AP0 for the physical layer cell-identity equal to zero is depicted in Figure 2.4 on page 85 for one radio frame and a channel bandwidth equal to 10 MHz together with the precoded DMRSs, the CSI-RSs and the precoded complex-valued modulation symbols carrying the codewords for TM9 and signal transmission from the first AE. Moreover, the value of the aforementioned CRSs transmitted on the first subframe and zeroth PRB is denoted in Table 2.3 on page 90 for TM9 and signal transmission from the first transmit AE at the eNodeB $\epsilon_b \in \mathbb{A}_m$.

2.2.3 Demodulation Reference Signal

Among the various combination of transmit AP candidates carrying the DMRSs used for PDSCH transmission on up to eight spatial layers [3GP16f, Section 6.10.3; 3GP16f, Table 6.10.3.2-1], in this thesis single-layer transmission on the transmit AP7 is focused on for DMRSs-based TMs. Hence, $\mathcal{A}_{\text{DMRS}} = \{7\}$ holds for the set of transmit APs the DMRSs are transmitted from. Detail information on signal transmission from multiple spatial layers for DMRSs-based transmission can be found in [3GP16f, Section 6.10.3].

Each DMRS denotes a complex-valued modulation symbol following the QPSK modulation mapping scheme [3GP16f, Section 6.10.3.1] which originates from a pseudo-random sequence where the pseudo-random sequence generation is initialized at the beginning of each subframe. Detail information on the pseudo-random number generation can be found in [3GP16f, Section 6.10.3.1].

Following the assignment for transmit APs to transmit AEs in DMRS-based TMs for single-layer transmission [TA11],

$$7 \mapsto \left\{ 1, \dots, \zeta, \dots, N_T^{(b)} \right\} \quad (2.12)$$

holds for the mapping function (2.1) for $\pi_{\text{AP}} \in \mathcal{A}_{\text{DMRS}}$ and $N_T^{(b)} \in \{2, 4\}$, where each DMRS transmitted from the transmit AP7 is multiplied with a complex-valued scalar value $\underline{p}_\zeta^{(b)} / \sqrt{N_T^{(b)}}$ and a real-valued scalar value of the WALSH-sequence prior to transmission from the ζ -th transmit AE at each eNodeB $\epsilon_b \in \mathbb{E}$ for $1 \leq \zeta \leq N_T^{(b)}$. Multiplying each DMRS with the complex-valued scalar value $\underline{p}_\zeta^{(b)} / N_T^{(b)}$ is used to adjust the phase of the DMRS at each transmit AE in order to enable signal precoding at the eNodeB $\epsilon_b \in \mathbb{E}$. The properties of the precoding vectors with respect to the antenna gain and the characteristic antenna diagram are discussed in Section 2.4.3 of this thesis, whereas precoding vector selection schemes are discussed in Section 2.7.2 of this thesis. Moreover, WALSH-sequences are pairwise orthogonal sequences [Bro+01, Section 15.6.2] to enable spatial separation of the effective channels at the UE $\mu_m \in \mathbb{U}$ in case of signal transmission on more than one spatial layer. For single-layer transmission on the transmit AP7, the WALSH-sequence is defined by the all-ones vector [3GP16f, Table 6.10.3.2-1] such that each of the precoded complex-valued modulation symbols carrying the DMRSs are multiplied with one. Further information on WALSH-sequences used for multi-layer transmission can be found in [3GP16f, Table 6.10.3.2-1], where channel and interference estimation schemes for multi-layer transmission in practical LTE networks can be found in [Bai+12, Section II-III] and references therein.

If transmitted by the eNodeB $\epsilon_b \in \mathbb{E}$, the UE $\mu_m \in \mathbb{U}$ is expected to exploit the DMRSs in order to estimate the mobile communication channel between the transmit AP7 and each receive AE ν for $1 \leq \nu \leq N_R^{(m)}$ [STB11, Section 8.2.2] to perform signal equalization of the receive signal. Note that in non DMRS-based TMs, such as for example in TM6, the precoding vector the complex-valued modulation symbols carrying the codewords are precoded with, must be explicitly signaled to the UE $\mu_m \in \mathbb{U}$ to enable reliable signal equalization. In DMRS-based TMs, however, the complex-valued modulation symbols carrying the codewords and the DMRSs make use of the same precoding vector for signal precoding for the duration of at least one subframe in time domain and one subband in frequency domain in case of subband PMI feedback [3GP16g, Section 7.2.1] considered in this thesis. Further information

on subband PMI feedback is provided in Section 2.7.2 of this thesis. Hence, explicit signalization of the precoding vector is not necessary in DMRS-based TMs, as the precoding vector is implicitly included in the estimate of the effective channel in each subframe and subband. Further information on the channel estimation and interpolation schemes selected for DMRS-based TMs can be found in Section 2.6.2 of this thesis.

The mapping the the precoded DMRSs on physical time-frequency resources is specified in [3GP16f, Section 6.10.3.2]. Let $\mathcal{S}_{i, n_{\text{PRB}}, \text{DMRS}}^{(b, \tau)}$ denote the set of tuples in terms of subcarriers and OFDM symbols carrying the DMRSs that are transmitted by the eNodeB $\epsilon_b \in \mathbb{E}$ from the transmit AP7 in the i -th subframe and the n_{PRB} -th PRB, respectively, where $0 \leq i \leq 9$ [3GP16f, Section 4.1] and $0 \leq n_{\text{PRB}} < N_{\text{RB}}^{\text{DL}}$ [3GP16f, Section 6.2.3] holds. The mapping of the precoded DMRSs on physical time-frequency resources to be transmitted from the eNodeB $\epsilon_b \in \mathbb{A}_m$ on the transmit AP7 is depicted in Figure 2.4 on page 85 for one radio frame and a channel bandwidth equal to 10 MHz together with the CRSs, the CSI-RSs and the precoded complex-valued modulation symbols carrying the codewords for TM9 and signal transmission from the first transmit AE. Moreover, the value of the aforementioned precoded DMRSs transmitted on the first subframe and zeroth PRB is denoted in Table 2.3 on page 90 for TM9 and signal transmission from the first transmit AE at the eNodeB $\epsilon_b \in \mathbb{A}_m$.

Following the properties of DMRS [3GP16f, Section 6.10.3.2], each eNodeB $\epsilon_b \in \mathbb{E}$ occupies

$$N_{\text{DMRS}} = \left| \mathcal{S}_{i, n_{\text{PRB}}, \text{DMRS}}^{(b, \tau)} \right| = 12 \quad (2.13)$$

out of $N_{\text{RE}}^{\text{SF, PRB}}$ equal to 168 REs to transmit the DMRS from the transmit AP7 in the i -th subframe and n_{PRB} -th PRB for $0 \leq i \leq 9$ [3GP16f, Section 4.1] and $0 \leq n_{\text{PRB}} < N_{\text{RB}}^{\text{DL}}$, respectively. Note that, despite the CRS [3GP16f, Section 6.10.1.2], the DMRSs transmitted on the transmit AP7 do not support a cell-specific frequency shift to avoid frequency collision between adjacent cells [3GP16f, Section 6.10.3.2]. Hence, the eNodeB $\epsilon_b \in \mathbb{E}$ uses the same REs to transmit the DMRSs as the eNodeB $\epsilon_{\tilde{b}} \in \mathbb{E}$, such that

$$\mathcal{S}_{i, n_{\text{PRB}}, \text{DMRS}}^{(b, \tau)} = \mathcal{S}_{i, n_{\text{PRB}}, \text{DMRS}}^{(\tilde{b}, \tau)} \quad (2.14)$$

holds for $0 \leq i \leq 9$ [3GP16f, Section 4.1], $0 \leq n_{\text{PRB}} < N_{\text{RB}}^{\text{DL}}$ [3GP16f, Section 6.2.3] and $b \neq \tilde{b}$, when the same subframe configuration is used [3GP16f, Section 6.10.3.2]. Moreover, the DMRS transmitted from the transmit AP $\pi_{\text{AP}} \in \mathcal{A}_{\text{DMRS}}$ are mapped on REs different to the REs used for CRS transmission from the transmit AP $\pi_{\text{AP}} \in \mathcal{A}_{\text{CRS}}$ [3GP16f, Section 6.10.1.2; 3GP16f,

Section 6.10.3.2] such that

$$\left(\bigcup_{\pi_{\text{AP}} \in \mathcal{A}_{\text{DMRS}}} \mathcal{S}_{i, n_{\text{PRB}}, \text{DMRS}}^{(b, \tau)} \right) \cap \left(\bigcup_{\pi_{\text{AP}} \in \mathcal{A}_{\text{CRS}}} \mathcal{S}_{i, n_{\text{PRB}}, \text{CRS}}^{(b, \pi_{\text{AP}})} \right) = \emptyset \quad (2.15)$$

holds for $\{b | \epsilon_b \in \mathbb{E}\}$, $0 \leq i \leq 9$ [3GP16f, Section 4.1] and $0 \leq n_{\text{PRB}} < N_{\text{RB}}^{\text{DL}}$ [3GP16f, Section 6.2.3].

2.2.4 Channel State Information Reference Signal

The transmission of the CSI-RSs by the eNodeB $\epsilon_b \in \mathbb{E}$ is used to acquire CSI at the UE $\mu_m \in \mathbb{U}$ and feed quantized CSI back to the transmitter [STB11, Section 29.1.2] with the aim of improving the signal detection capabilities in a closed-loop manner [Bai+11b, Section II-B]. Moreover, the transmission of the CSI-RSs enables the UE $\mu_m \in \mathbb{U}$ to estimate the CSI from multiple eNodeBs rather than just one eNodeB the UE $\mu_m \in \mathbb{U}$ is assigned to with respect to synchronization or signal transmission [STB11, Section 29.1.2].

The supported transmit APs used for CSI-RS transmission are provided in [3GP16f, Section 6.10.5]. As mentioned in Section 1.3.3 of this thesis, the number of transmit AEs at each eNodeB is set to either two or four. In case of two and four transmit AEs at the eNodeB $\epsilon_b \in \mathbb{E}$, respectively, the CSI-RS are transmitted from the transmit APs $\pi_{\text{AP}} \in \mathcal{A}_{\text{CSI-RS}} = \{15, 16\}$ and the transmit APs $\pi_{\text{AP}} \in \mathcal{A}_{\text{CSI-RS}} = \{15, \dots, 18\}$. Detail information on the CSI-RS transmission from more than four transmit APs can be found in [3GP16f, Section 6.10.5]. Each CSI-RS denotes a complex-valued modulation symbol following the QPSK modulation mapping scheme which originates from a pseudo-random sequence [3GP16f, Section 6.10.5.1]. Detail information on the pseudo-random number generation can be found in [3GP16f, Section 6.10.5.1].

The mapping of the CSI-RSs on physical time-frequency resources is specified in [3GP16f, Section 6.10.5.2]. Following the mapping of the CSI-RS on physical time-frequency resources [3GP16f, Section 6.10.5.2], let $\mathcal{S}_{i, n_{\text{PRB}}, \text{CSI-RS}}^{(b, \pi_{\text{AP}})}$ denote the set of REs in terms of subcarriers and OFDM symbols carrying the CSI-RS transmitted by the eNodeB $\epsilon_b \in \mathbb{E}$ on the transmit AP $\pi_{\text{AP}} \in \mathcal{A}_{\text{CSI-RS}}$ in the i -th subframe and the n_{PRB} -th PRB, where $0 \leq i \leq 9$ [3GP16f, Section 4.1] and $0 \leq n_{\text{PRB}} < N_{\text{RB}}^{\text{DL}}$ [3GP16f, Section 6.2.3] holds. The CSI-RSs transmitted on each transmit AP $\pi_{\text{AP}} \in \mathcal{A}_{\text{CSI-RS}}$ have a uniform spacing in frequency domain with one CSI-RS per PRB [3GP16f, Section 6.10.5.2; STB11, Section 29.1.2]. Moreover, the spacing in time domain for the CSI-RS transmitted from the transmit AP $\pi_{\text{AP}} \in \mathcal{A}_{\text{CSI-RS}}$ is configurable [3GP16f, Section 6.10.5.3]. Valid CSI-RS subframe configuration are tabularized in

[3GP16f, Table 6.10.5.3-1]. The intention behind different CSI-RS configuration [3GP16f, Table 6.10.5.2-1] and different CSI-RS subframe configuration [3GP16f, Section 6.10.5.3-1] is to ensure orthogonal CSI-RS transmission among the eNodeBs, such that accurate CSI estimation at each UE can be guaranteed [STB11, Section 29.1.2].

For each eNodeB equipped with two transmit AEs

$$15 \mapsto 1, \quad (2.16a)$$

$$16 \mapsto 2 \quad (2.16b)$$

holds for the mapping function in (2.1) for each transmit $\pi_{\text{AP}} \in \mathcal{A}_{\text{CSI-RS}} = \{15, 16\}$. Each CSI-RS transmitted from the transmit AP15 and the transmit AP16 is mapped on the first and second transmit AE, respectively.

The mapping of the CSI-RSs transmitted by the eNodeB $\epsilon_b \in \mathbb{E}$ from the transmit AP15 and the transmit AP16 on physical time-frequency resources is depicted for the CSI-RS configuration 0 in the first two figures from the top-left to the top-right in [3GP16f, Figure 6.10.5.2-1]. Either of the figures shows a cutout of the DL resource grid of the i -th subframe configured for CSI-RS transmission [3GP16f, Section 6.10.5.2] which consists of two consecutive slots S_{2i} and S_{2i+1} for $0 \leq i \leq 9$ [3GP16f, Section 4.1] that carry the CSI-RS transmitted from the transmit AP15 and the transmit AP16 on the n_{PRB} -th PRB for $0 \leq n_{\text{PRB}} < N_{\text{RB}}^{\text{DL}}$ [3GP16f, Section 6.2.3]. Following the properties of the CSI-RSs

$$\mathcal{S}_{i, n_{\text{PRB}}, \text{CSI-RS}}^{(b, 15)} = \mathcal{S}_{i, n_{\text{PRB}}, \text{CSI-RS}}^{(b, 16)} \quad (2.17)$$

holds [3GP16f, Section 6.10.5.2] such that each eNodeB $\epsilon_b \in \mathbb{E}$ uses the same physical time-frequency resources to transmit the CSI-RS on the i -th subframe configured for CSI-RS transmission [3GP16f, Section 6.10.5.2] for $0 \leq n_{\text{PRB}} < N_{\text{RB}}^{\text{DL}}$ [3GP16f, Section 6.2.3] on the transmit AP15 and the transmit AP16. Moreover,

$$N_{\text{CSI-RS}, 2} = \left| \mathcal{S}_{i, n_{\text{PRB}}, \text{CSI-RS}}^{(b, 15)} \right| = \left| \mathcal{S}_{i, n_{\text{PRB}}, \text{CSI-RS}}^{(b, 16)} \right| = 2 \quad (2.18)$$

holds for the i -th subframe configured for CSI-RS transmission [3GP16f, Section 6.10.5.2] for $0 \leq n_{\text{PRB}} < N_{\text{RB}}^{\text{DL}}$ [3GP16f, Section 6.2.3], such that two out of $N_{\text{RE}}^{\text{SF, PRB}}$ equal to 168 REs are occupied by the eNodeB $\epsilon_b \in \mathbb{E}$ for CSI-RS transmission from the transmit AP15 and the transmit AP16 [3GP16f, Figure 6.10.5.2-2]. As a result, the UE $\mu_m \in \mathbb{U}$ experiences a superposition of the mobile communication channel among the transmit AP15 and the transmit AP16 at the ν -th receive AE for $1 \leq \nu \leq N_{\text{R}}^{(m)}$ [STB11, Section 29.1.2] at each RE of the set (2.17) on the i -th subframe used for CSI-RS transmission

[3GP16f, Section 6.10.5.2] and n_{PRB} -th PRB for $0 \leq n_{\text{PRB}} < N_{\text{RB}}^{\text{DL}}$ for each eNodeB $\epsilon_b \in \mathbb{E}$. Spatial separation techniques exploiting the properties of the WALSH-function are discussed in Section 2.6.2 of this thesis.

For each eNodeB $\epsilon_b \in \mathbb{E}$ equipped with four transmit AEs,

$$15 \mapsto 1, \quad (2.19a)$$

$$16 \mapsto 2, \quad (2.19b)$$

$$17 \mapsto 3, \quad (2.19c)$$

$$18 \mapsto 4 \quad (2.19d)$$

holds for the mapping function in (2.1) for each transmit $\pi_{\text{AP}} \in \mathcal{A}_{\text{CSI-RS}} = \{15, \dots, 18\}$. Each CSI-RS transmitted from the transmit AP15, the transmit AP16, the transmit AP17 and the transmit AP18 is mapped on the first, second, third and fourth transmit AE, respectively.

The mapping of the CSI-RSs, transmitted by the eNodeB $\epsilon_b \in \mathbb{E}$ from the transmit AP15, the transmit AP16, the transmit AP17 and the transmit AP18 on physical time-frequency resources is depicted in the upper half in [3GP16f, Figure 6.10.5.2-1]. Each of the figures shows a cutout of the DL resource grid of the i -th subframe configured for CSI-RS transmission which consists of the consecutive slots S_{2i} and S_{2i+1} for $0 \leq i \leq 9$ [3GP16f, Section 4.1] that carry the CSI-RS transmitted from the transmit AP15, the transmit AP16, the transmit AP17 and the transmit AP18 on the n_{PRB} -th PRB for $0 \leq n_{\text{PRB}} < N_{\text{RB}}^{\text{DL}}$ [3GP16f, Section 6.2.3]. The properties of CSI-RS transmitted by the eNodeB $\epsilon_b \in \mathbb{E}$ from the transmit AP15 and the transmit AP16 are provided in (2.17) and (2.18). Moreover, considering CSI-RS transmission from the transmit AP17 and the transmit AP18,

$$\mathcal{S}_{i, n_{\text{PRB}}, \text{CSI-RS}}^{(b, 17)} = \mathcal{S}_{i, n_{\text{PRB}}, \text{CSI-RS}}^{(b, 18)} \quad (2.20)$$

holds [3GP16f, Section 6.10.5.2], such that each eNodeB $\epsilon_b \in \mathbb{E}$ uses the same physical time-frequency resources to transmit the CSI-RS on the i -th subframe configured for CSI-RS transmission [3GP16f, Section 6.10.5.2] for $0 \leq n_{\text{PRB}} < N_{\text{RB}}^{\text{DL}}$ [3GP16f, Section 6.2.3]. Following the properties of the CSI-RSs

$$\bigcap_{\pi_{\text{AP}} \in \mathcal{A}_{\text{CSI-RS}} = \{15, \dots, 18\}} \mathcal{S}_{i, n_{\text{PRB}}, \text{CSI-RS}}^{(b, \pi_{\text{AP}})} = \emptyset \quad (2.21)$$

holds for each eNodeB $\epsilon_b \in \mathbb{E}$ transmitting the CSI-RS from the transmit AP15, the transmit AP16, the transmit AP17 and the transmit AP18 on the i -th subframe configured for CSI-RS transmission [3GP16f, Section 6.10.5.2] for $0 \leq n_{\text{PRB}} < N_{\text{RB}}^{\text{DL}}$ [3GP16f, Section 6.2.3]. Consequently, the CSI-RSs transmitted from the transmit AP15 and the transmit AP16 are mapped on the physical time-frequency resources that are orthogonal to the physical time-

frequency resources used for the CSI-RS transmission from the transmit AP17 and the transmit AP18 [3GP16f, Section 6.10.5.2]. Moreover,

$$N_{\text{CSI-RS},4} = \left| \bigcup_{\pi_{\text{AP}} \in \mathcal{A}_{\text{CSI-RS}} = \{15, \dots, 18\}} \mathcal{S}_{i, n_{\text{PRB}}, \text{CSI-RS}}^{(b, \pi_{\text{AP}})} \right| = 4 \quad (2.22)$$

holds for the i -th subframe configured for CSI-RS transmission [3GP16f, Section 6.10.5.2] for $0 \leq n_{\text{PRB}} < N_{\text{RB}}^{\text{DL}}$ [3GP16f, Section 6.2.3] such that four out of $N_{\text{RE}}^{\text{SF, PRB}}$ equal to 168 REs are occupied by the eNodeB $\epsilon_b \in \mathbb{E}$ for CSI-RS transmission from the transmit AP15, the transmit AP16, the transmit AP17 and the transmit AP18 [3GP16f, Figure 6.10.5.2-2]. As a result, the UE $\mu_m \in \mathbb{U}$ experiences a superposition of the mobile communication channel among the transmit AP15 and the transmit AP16 at the ν -th receive AE for $1 \leq \nu \leq N_{\text{R}}^{(m)}$ [STB11, Section 29.1.2] at each RE out of the set (2.17) on the i -th subframe used for the CSI-RS transmission [3GP16f, Section 6.10.5.2] and $n_{\text{PRB}} - \text{th}$ PRB $0 \leq n_{\text{PRB}} < N_{\text{RB}}^{\text{DL}}$ for each $\{b | \epsilon_b \in \mathbb{E}\}$. Moreover, the UE $\mu_m \in \mathbb{U}$ experiences a superposition of the mobile communication channel among the transmit AP17 and the transmit AP18 at the ν -th receive AE for $1 \leq \nu \leq N_{\text{R}}^{(m)}$ [STB11, Section 29.1.2] at each RE out of the set (2.20) on the i -th subframe used for CSI-RS transmission [3GP16f, Section 6.10.5.2] and $n_{\text{PRB}} - \text{th}$ PRB $0 \leq n_{\text{PRB}} < N_{\text{RB}}^{\text{DL}}$ for each $\{b | \epsilon_b \in \mathbb{E}\}$. Spatial separation techniques, exploiting the properties of the WALSH-function, are discussed in Section 2.6.2 of this thesis.

The CSI-RS transmitted from the transmit AP $\pi_{\text{AP}} \in \mathcal{A}_{\text{CSI-RS}}$ [3GP16f, Section 6.10.5.2] are mapped on physical time-frequency resources different to the physical time-frequency resources used for CRS transmission from the transmit APs $\pi_{\text{AP}} \in \mathcal{A}_{\text{CRS}}$ [3GP16f, Section 6.10.1.2] and different to the physical time-frequency resources used for DMRS transmission from the transmit APs $\pi_{\text{AP}} \in \mathcal{A}_{\text{DMRS}}$ [3GP16f, Section 6.10.3.2], such that

$$\left(\bigcup_{\pi_{\text{AP}} \in \mathcal{A}_{\text{CSI-RS}}} \mathcal{S}_{i, n_{\text{PRB}}, \text{CSI-RS}}^{(b, \pi_{\text{AP}})} \right) \cap \left(\bigcup_{\pi_{\text{AP}} \in \mathcal{A}_{\text{CRS}}} \mathcal{S}_{i, n_{\text{PRB}}, \text{CRS}}^{(b, \pi_{\text{AP}})} \right) = \emptyset \quad (2.23)$$

and

$$\left(\bigcup_{\pi_{\text{AP}} \in \mathcal{A}_{\text{CSI-RS}}} \mathcal{S}_{i, n_{\text{PRB}}, \text{CSI-RS}}^{(b, \pi_{\text{AP}})} \right) \cap \left(\bigcup_{\pi_{\text{AP}} \in \mathcal{A}_{\text{DMRS}}} \mathcal{S}_{i, n_{\text{PRB}}, \text{DMRS}}^{(b, 7)} \right) = \emptyset \quad (2.24)$$

holds for $\{b | \epsilon_b \in \mathbb{E}\}$, $0 \leq i \leq 9$ [3GP16f, Section 4.1] and $0 \leq n_{\text{PRB}} < N_{\text{RB}}^{\text{DL}}$ [3GP16f, Section 6.2.3].

The mapping of the CSI-RSs on physical time-frequency resources to be trans-

mitted from the eNodeB $\epsilon_b \in \mathbb{A}_m$ on the transmit AP15 for CSI-RS configuration 0 is depicted in Figure 2.4 on page 85 for one radio frame and a channel bandwidth equal to 10 MHz together with the CRSs, the precoded DMRSs and the precoded complex-valued modulation symbols carrying the codewords for TM9 and signal transmission from the first transmit AE. Moreover, the value of the aforementioned CSI-RSs transmitted on the first subframe and zeroth PRB are denoted in Table 2.3 on page 90 for TM9 and signal transmission from the first transmit AE at the eNodeB $\epsilon_b \in \mathbb{A}_m$.

2.3 Transport Channel Processing

The transport channel processing unit of the PHY layer is used to transform the data from the MAC layer suitable for physical channel processing [3GP16d, Section 5.3.2; DPS14, Section 10.1.1] and to protect the Transport Block (TB) against transmission errors [3GP16d, Section 5.3.2.1]. The transport channel processing unit of the PHY layer receives data from the MAC layer in terms of TBs every TTI [3GP16d, Section 5.3.2]. A TB is defined as the basic data unit exchanged between the PHY layer and the MAC layer [3GP15f, Section 3]. Moreover, the TTI is defined as the inter-arrival time of TB sets, i.e. the time it shall take to transmit a TB set [3GP15f, Section 3.1]. Each TTI corresponds to the length of one subframe [DPS14, Section 10.1.1]. The TBS denotes the number of bits of a TB [3GP15f, Section 3] and depends on the TBS index I_{TBS} and the number of PRBs allocated for the DL transmission [3GP16g, Section 7.1.7.2.1], where $0 \leq I_{\text{TBS}} \leq 26$ [3GP16g, Table 7.1.7.1-1] and $0 \leq n_{\text{PRB}} \leq 110$ holds for TBs not mapped to two-layer SM [3GP16g, Section 7.1.7.2.1] which is used for single-layer transmission. Hence, the number of bits in each TB denoted by N_{TBS} is given by the tuple $(I_{\text{TBS}}, N_{\text{PRB}})$ in [3GP16g, Table 7.1.7.2.1-1]. The visualization of one radio frame which is composed of ten subframes [3GP16f, Section 4.1] is provided in Figure 2.4 on page 85 for N_{PRB} equal to fifty PRBs and is discussed in Section 2.4.4 of this thesis.

The following processing subunits can be identified for each TB in the DL transmission [3GP16d, Section 5.3.2]

- Transport block Cyclic Redundancy Check (CRC) attachment,
- Code block segmentation and code block CRC attachment,
- Channel coding,
- Rate matching and
- Code block concatenation,

as depicted in Figure 2.1 on page 69. The main function of the aforementioned subunits, being part of the transport channel processing unit, is discussed in what follows. References to further information for each of the subunits are being provided at the appropriate place.

The transport block CRC attachment subunit is used to enable error detection in each TB through a CRC [3GP16d, Section 5.3.2.1]. The CRC allows the UE $\mu_m \in \mathbb{U}$ to detect errors in the decoded TB [DPS14, Section 10.1.1.1]. General information on CRC coding can be found in [LC04, Chapter 5]. Detail information on parity bit computation within the transport block CRC attachment subunit can be found in [3GP16d, Section 5.3.2.1]. The TB together with the attached CRC is delivered to the code block segmentation and code block CRC attachment subunit [3GP16d, Figure 5.3.2-1], as depicted in Figure 2.1.

The code block segmentation and code block CRC attachment subunit is used to segment the TB with the CRC into code blocks attached with a CRC if the TB together with the CRC exceeds the maximum block size. The maximum block size is denoted by $N_{\text{BS}}^{\text{max}}$ equal to 6144 [3GP16d, Table 5.1.3.3] and corresponds to the number of bits the turbo code interleaver can process [3GP16d, Section 5.3.2.2]. The CRC of each code block allows the UE $\mu_m \in \mathbb{U}$ for early detection of the early decoded code block and correspondingly early termination of the iteratively decoding of that code block [DPS14, Section 10.1.1.2]. An illustration of the code block segmentation and code block CRC attachment subunit can be found in [DPS14, Figure 10.2]. Further information on the code block segmentation and code block CRC attachment subunit can be found in [3GP16d, Section 2.4.3]. The code blocks with the attached CRCs are forwarded to the channel coding subunit [3GP16d, Section 5.3.2.2], as depicted in Figure 2.1.

The channel coding subunit is used to add redundancy information on each code block and CRC and, thus, protect the information sequence against transmission errors [Bos98, Chapter 1]. LTE systems use turbo-coding to encode the information sequence [3GP16d, Section 5.3.2.3; 3GP16d, Section 5.1.3.2.1] which is transmitted over the PDSCH [3GP16d, Table 5.1.3-1]. The core idea of turbo-codes is the parallel concatenation of convolutional codes by using a turbo-code internal interleaver [Jun97, Section E.2.1]. Turbo-codes have exceptionally good performance in terms of error protection for large code block lengths [Jun97, Section E.1; LC04, Section 16.1] and operate close to the SHANNON limit [LC04, Section 16.1]. The structure of the turbo encoder is depicted in [3GP16d, Figure 5.1.3-2]. Further information on the turbo-encoder which is represented by a parallel concatenated convolutional code with two eight-state constituent encoders and one turbo-code internal interleaver can be found in [3GP16d, Section 5.1.3.2.1]. The turbo-encoded code blocks and CRCs are

delivered to the rate matching subunit [3GP16d, Section 5.3.2.4], as depicted in Figure 2.1.

The rate matching subunit is used to interleave each codeword [3GP16d, Section 5.1.4.1.1] and to select bits for transmission over the PDSCH [3GP16d, Section 5.1.4.1.2; STB11, Section 10.3.2.4]. Since the number of bits for transmission over the PDSCH is determined on the available physical time-frequency resources, the rate matching unit is used to generate puncturing patterns for arbitrary size, resulting in arbitrary code rates [STB11, Section 10.3.2.4]. For further information on rate matching see [3GP16d, Section 5.1.4.1]. The bits at the output of the rate matching subunit are delivered to the code block concatenation subunit [3GP16d, Section 5.3.2.5], as depicted in Figure 2.1.

The code block concatenation subunit is used to sequentially concatenate the rate matched code blocks [3GP16d, Section 5.1.5]. The collection of bits of the sequentially concatenated code blocks refers to one codeword [3GP16d, Section 5.3.2.5] and is delivered to the physical channel processing unit [3GP16f, Section 6.3], as depicted in Figure 2.1.

2.4 Physical Channel Processing

2.4.1 Introduction

The physical channel processing unit of the PHY layer is used to transform the codewords at the output of the transport channel processing chain, discussed in Section 2.3 of this thesis, into a representation that is suitable for OFDM baseband signal generation [3GP16f, Section 6.3; 3GP16d, Section 5.3.2]. The physical channel processing unit consists of [3GP16f, Section 6.3]

- Scrambling,
- Modulation mapping,
- Layer mapping,
- Precoding,
- Resource mapping and
- OFDM baseband signal generation,

as depicted in Figure 2.1. The main function of the aforementioned subunits is discussed in what follows, where a detailed discussion on modulation mapping, precoding, resource mapping and OFDM signal generation is provided in Section 2.4.2, Section 2.4.3, Section 2.4.4 and Section 2.5.1 of this thesis,

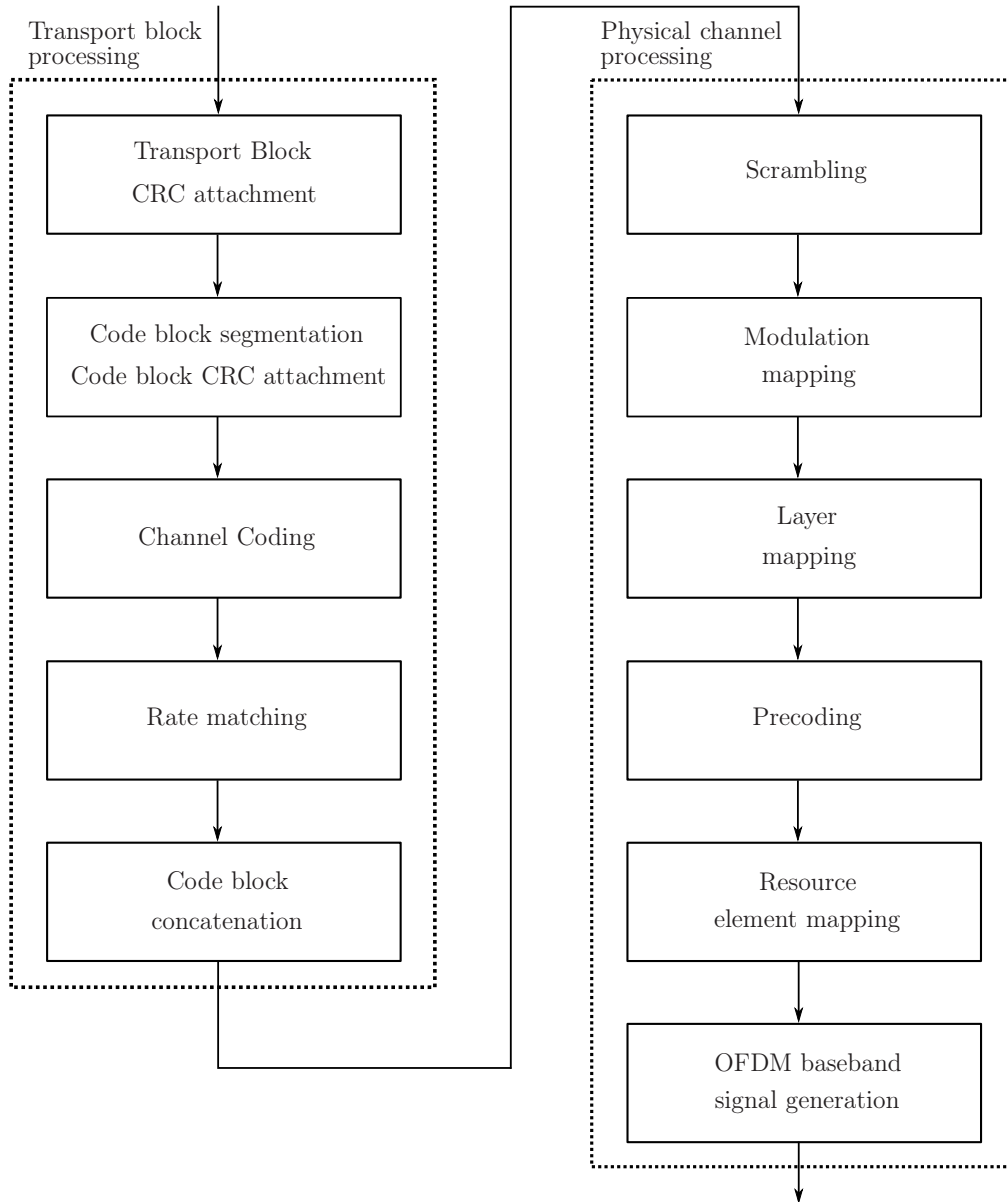


Figure 2.1. Overview of the physical and transport channel processing chain (created by the author of this thesis using [3GP16d, Figure 5.3.2-1; 3GP16f, Figure 6.3-1]).

respectively. References to further information for each of the subunits are being provided at the appropriate place.

The scrambling subunit is used to scramble the bits of each codeword to be transmitted over the PDSCH prior to modulation mapping with the aim of reducing the error concentration effects at the UE $\mu_m \in \mathbb{U}$ [3GP16f, Section 6.3; BL89, Section IV]. The bits of each codeword are added in the GF(2) [Bro+01, Section 5.4.3] with a scrambling sequence that is defined by a GOLD sequence [3GP16f, Section 6.3.1; Gho+11, Section 7.1.2]. For general information on GOLD sequences, see [Kam08, Section 17.6.1]. Detail information on GOLD sequence generation used in the scrambling subunit can be found in [3GP16f, Section 6.3.1]. The scrambled bits of each codeword are delivered to the modulation mapping subunit [3GP16f, Section 6.3.2], as depicted in Figure 2.1.

The modulation mapping subunit is used to map the bits of the scrambled codewords on complex-valued modulation symbols [3GP16f, Section 6.3.2]. For PDSCH signal transmission, LTE systems support the QPSK, 16QAM, 64QAM and 256QAM mapping scheme [3GP16f, Table 6.3.2-1]. In this thesis the QPSK, 16QAM and 64QAM mapping scheme is considered. Detail information on the 256QAM mapping scheme can be found in [3GP16f, Section 7.1.5]. The properties of the 64QAM mapping scheme are discussed as an example in Section 2.4.2 of this thesis. The complex-valued modulation symbols are delivered to the layer mapping subunit [3GP16f, Section 6.3.3], as depicted in Figure 2.1.

The layer mapping subunit is used to map the complex-valued modulation symbols on one or several layers [3GP16f, Section 6.3.3]. As mentioned in Section 1.2.6 of this thesis, single-layer transmission is focused on. Hence, the complex-valued modulation symbols are mapped on one layer [3GP16f, Section 6.3.3.2]. Detail information on mapping of complex-valued modulation symbols on two up to eight layers to enable SM can be found in [3GP16f, Table 6.3.3.2-1]. The complex-valued modulation symbols mapped on one layer are delivered to the precoding subunit [3GP16f, Section 6.3.4], as depicted in Figure 2.1.

The precoding subunit is used to precode the complex-valued modulation symbols carrying the codewords and - if transmitted - the DMRSs [3GP16f, Section 6.3.4] to control the directionality of the antenna pattern and, thus the antenna gain along the direction of the eNodeB $\epsilon_b \in \mathbb{A}_m$ the UE $\mu_m \in \mathbb{U}$ receives the desired signal from. Detail information on codebook-based signal precoding for single-layer transmission is provided in Section 2.4.3 of this thesis. The precoded complex-valued modulation symbols are delivered to the resource element mapping subunit [3GP16f, Section 6.3.5], as depicted in Figure 2.1.

The resource element mapping subunit is used to map the precoded complex-valued modulation symbols carrying the codewords on physical time-frequency resources of the respective transmit AP [3GP16f, Section 6.3.5]. The aspect of resource mapping is further discussed in Section 2.4.4 of this thesis. In detail, the impact of the selected TM and transmit antenna configuration on the code rate and the associated Modulation and Coding Scheme (MCS) is discussed. Moreover, the mapping on physical time-frequency resources is illustrated for signal transmission in TM9 and the eNodeB $\epsilon_b \in \mathbb{A}_m$ equipped with four transmit AEs for a channel bandwidth equal to 10 MHz. The complex-valued modulation symbols mapped on time-frequency resources are delivered to the OFDM baseband signal generation subunit [3GP16f, Figure 6.3.1], as depicted in Figure 2.1.

The OFDM baseband signal generation subunit is used to transform the complex-valued modulation symbols into a time-continuous baseband signal representation [3GP16f, Section 6.12] with the aim of decoupling the frequency selective fading channel into narrowband subchannels such that each of the subchannels is approximately non-selective [Kam08, Section 16.1.1]. Further information on OFDM modulation and OFDM demodulation is provided in Section 2.5 of this thesis.

2.4.2 Modulation Mapping

In case of the 64 QAM scheme, hexuples of bits are mapped on complex-valued modulation symbols [3GP16f, Section 7.1.4], defined in [3GP16f, Table 7.1.4-1]. Let

$$\mathbb{V}_{64\text{QAM}} = A_{64\text{QAM}} \cdot \{a + jb \in \mathbb{C} \mid a = 2i - 1, b = 2j - 1, -3 \leq i, j \leq 4\} \quad (2.25)$$

denote the set of complex-valued modulation symbols following the 64 QAM scheme, defined in [3GP16f, Table 7.1.4-1], where $A_{64\text{QAM}}$ equals to $1/\sqrt{42}$. As a result, the mean energy of the 64 QAM symbols reads

$$\frac{1}{|\mathbb{V}_{64\text{QAM}}|} \cdot \sum_{\underline{d}^{(b)}[k, \ell] \in \mathbb{V}_{64\text{QAM}}} \left| \underline{d}^{(b)}[k, \ell] \right|^2 = 1, \quad (2.26)$$

where $|\mathbb{V}_{64\text{QAM}}|$ denotes the cardinality of the set $\mathbb{V}_{64\text{QAM}}$ and equals to 64 [3GP16f, Table 7.1.4-1]. The complex-valued modulation symbols $\underline{d}^{(b)}[k, \ell]$ out of the set $\mathbb{V}_{64\text{QAM}}$ are depicted in Figure 2.2 on page 72. Figure 2.2 shows the complex-valued modulation symbols $\underline{d}^{(b)}[k, \ell]$ out of the set $\mathbb{V}_{64\text{QAM}}$ in Cartesian coordinates, such that the abscissa and ordinate in Figure 2.2 represents the real and imaginary component of $\underline{d}^{(b)}[k, \ell] \in \mathbb{V}_{64\text{QAM}}$, respectively. Moreover, the associated bit pattern is denoted under each complex-valued

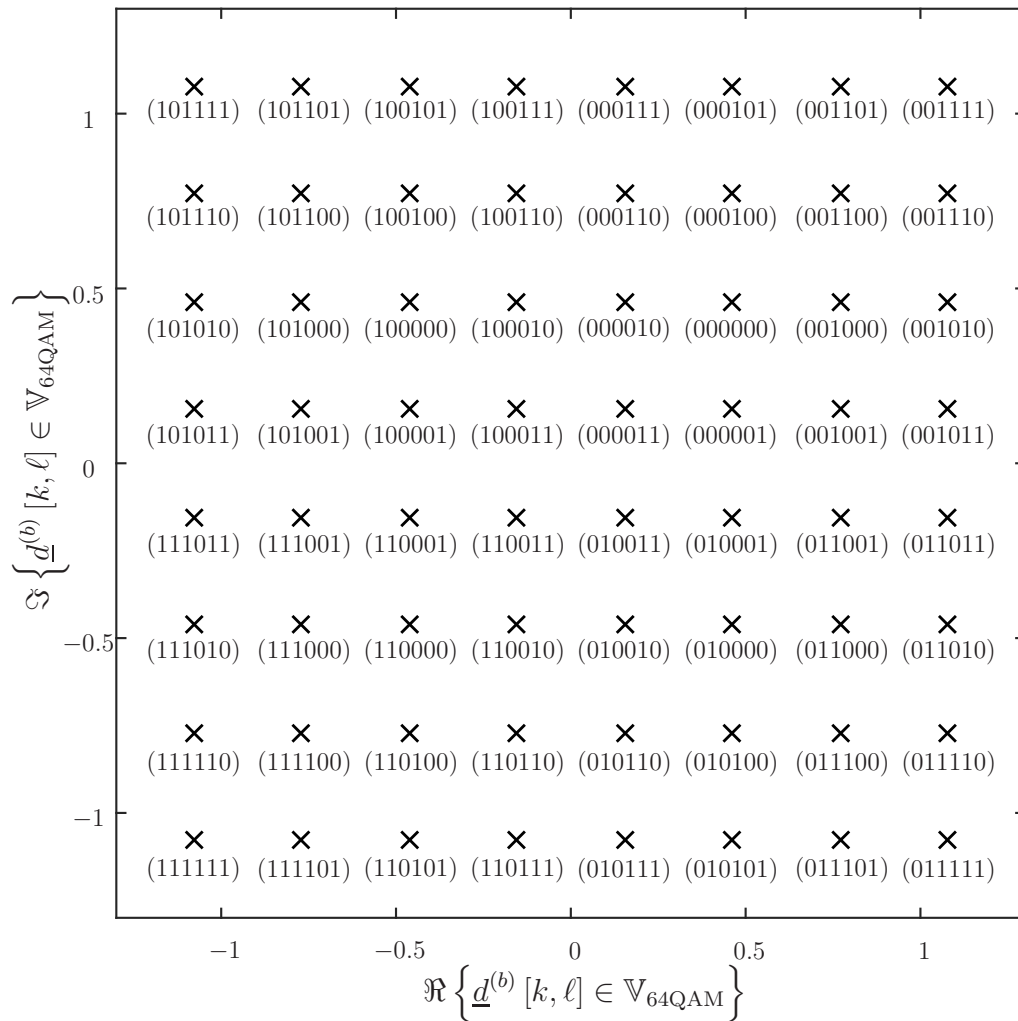


Figure 2.2. Scatterplot of 64 QAM modulation mapped symbols (created by the author of this thesis using [3GP16f, Table 7.1.4-1]).

modulation symbol $\underline{d}^{(b)}[k, \ell] \in \mathbb{V}_{64\text{QAM}}$ following [3GP16f, Table 7.1.4-1], as depicted in Figure 2.2.

The set of complex-valued modulation symbols in (2.25) can be subdivided into ten subsets

$$\mathbb{V}_{64\text{QAM}}^{(1)} = A_{64\text{QAM}} \cdot \{a + jb \in \mathbb{C} | a = 2i - 1, b = 2j - 1, 0 \leq i, j \leq 1\} \quad (2.27a)$$

$$\begin{aligned} \mathbb{V}_{64\text{QAM}}^{(2)} = & A_{64\text{QAM}} \cdot \{a + jb \in \mathbb{C} | a = 2i - 1, b = 6j - 3, 0 \leq i, j \leq 1\} \cup \\ & A_{64\text{QAM}} \cdot \{a + jb \in \mathbb{C} | a = 6i - 3, b = 2j - 1, 0 \leq i, j \leq 1\} \end{aligned} \quad (2.27b)$$

$$\mathbb{V}_{64\text{QAM}}^{(3)} = A_{64\text{QAM}} \cdot \{a + jb \in \mathbb{C} | a = 6i - 3, b = 6j - 3, 0 \leq i, j \leq 1\} \quad (2.27c)$$

$$\begin{aligned} \mathbb{V}_{64\text{QAM}}^{(4)} = & A_{64\text{QAM}} \cdot \{a + jb \in \mathbb{C} | a = 2i - 1, b = 10j - 5, 0 \leq i, j \leq 1\} \cup \\ & A_{64\text{QAM}} \cdot \{a + jb \in \mathbb{C} | a = 10i - 5, b = 2j - 1, 0 \leq i, j \leq 1\} \end{aligned} \quad (2.27d)$$

$$\begin{aligned} \mathbb{V}_{64\text{QAM}}^{(5)} = & A_{64\text{QAM}} \cdot \{a + jb \in \mathbb{C} | a = 6i - 3, b = 10j - 5, 0 \leq i, j \leq 1\} \cup \\ & A_{64\text{QAM}} \cdot \{a + jb \in \mathbb{C} | a = 10i - 5, b = 6j - 3, 0 \leq i, j \leq 1\} \end{aligned} \quad (2.27e)$$

$$\mathbb{V}_{64\text{QAM}}^{(6)} = A_{64\text{QAM}} \cdot \{a + jb \in \mathbb{C} | a = 10i - 5, b = 10j - 5, 0 \leq i, j \leq 1\} \quad (2.27f)$$

$$\begin{aligned} \mathbb{V}_{64\text{QAM}}^{(7)} = & A_{64\text{QAM}} \cdot \{a + jb \in \mathbb{C} | a = 2i - 1, b = 14j - 7, 0 \leq i, j \leq 1\} \cup \\ & A_{64\text{QAM}} \cdot \{a + jb \in \mathbb{C} | a = 14i - 7, b = 2j - 1, 0 \leq i, j \leq 1\} \end{aligned} \quad (2.27g)$$

$$\begin{aligned} \mathbb{V}_{64\text{QAM}}^{(8)} = & A_{64\text{QAM}} \cdot \{a + jb \in \mathbb{C} | a = 6i - 3, b = 14j - 7, 0 \leq i, j \leq 1\} \cup \\ & A_{64\text{QAM}} \cdot \{a + jb \in \mathbb{C} | a = 14i - 7, b = 6j - 3, 0 \leq i, j \leq 1\} \end{aligned} \quad (2.27h)$$

$$\begin{aligned} \mathbb{V}_{64\text{QAM}}^{(9)} = & A_{64\text{QAM}} \cdot \{a + jb \in \mathbb{C} | a = 10i - 5, b = 14j - 7, 0 \leq i, j \leq 1\} \cup \\ & A_{64\text{QAM}} \cdot \{a + jb \in \mathbb{C} | a = 14i - 7, b = 10j - 5, 0 \leq i, j \leq 1\} \end{aligned} \quad (2.27i)$$

$$\mathbb{V}_{64\text{QAM}}^{(10)} = A_{64\text{QAM}} \cdot \{a + jb \in \mathbb{C} | a = 14i - 7, b = 14j - 7, 0 \leq i, j \leq 1\}, \quad (2.27j)$$

representing the complex-valued modulation symbols of one amplitude level each. The properties of the complex-valued modulation symbols out of the set $\mathbb{V}_{64\text{QAM}}^{(i)}$ after transmission from Cartesian coordinates to polar coordinates [Bro+01, Section 3.5.2.1] are summarized in Table 2.1 on page 74 for $1 \leq i \leq 10$. The first, second and third column in Table 2.1 denotes the index, the i -th subset $\mathbb{V}_{64\text{QAM}}^{(i)}$ and the reference of the definition of the respective subset, respectively, where $1 \leq i \leq 10$ holds. The amplitude and set of discrete phases of the complex-valued modulation symbols out of the set $\mathbb{V}_{64\text{QAM}}^{(i)}$ is denoted in the fourth and fifth column of Table 2.1, respectively, for $1 \leq i \leq 10$. The set of discrete phases for the complex-valued modulation symbols out of

Table 2.1. Properties of complex-valued modulation symbols (created by the author of this thesis using [3GP16f, Table 7.1.4-1; Bro+01, Section 3.5.2.1; Kam08, Section 9.1.1]).

Index i	Subset $\mathbb{V}_{64\text{QAM}}^{(i)}$	Subset definition	Amplitude of $\underline{d}^{(b)} [k, \ell] \in \mathbb{V}_{64\text{QAM}}^{(i)}$	Discrete phases of $\underline{d}^{(b)} [k, \ell] \in \mathbb{V}_{64\text{QAM}}^{(i)}$
1	$\mathbb{V}_{64\text{QAM}}^{(1)}$	(2.27a)	$\sqrt{2/42}$	ϕ_i acc. (2.29a) in (2.28)
2	$\mathbb{V}_{64\text{QAM}}^{(2)}$	(2.27b)	$\sqrt{10/42}$	ϕ_i acc. (2.29d) in (2.28)
3	$\mathbb{V}_{64\text{QAM}}^{(3)}$	(2.27c)	$\sqrt{18/42}$	ϕ_i acc. (2.29a) in (2.28)
4	$\mathbb{V}_{64\text{QAM}}^{(4)}$	(2.27d)	$\sqrt{20/42}$	ϕ_i acc. (2.29c) in (2.28)
5	$\mathbb{V}_{64\text{QAM}}^{(5)}$	(2.27e)	$\sqrt{34/42}$	ϕ_i acc. (2.29f) in (2.28)
6	$\mathbb{V}_{64\text{QAM}}^{(6)}$	(2.27f)	$\sqrt{50/42}$	ϕ_i acc. (2.29a) in (2.28)
7	$\mathbb{V}_{64\text{QAM}}^{(7)}$	(2.27g)	$\sqrt{50/42}$	ϕ_i acc. (2.29b) in (2.28)
8	$\mathbb{V}_{64\text{QAM}}^{(8)}$	(2.27h)	$\sqrt{58/42}$	ϕ_i acc. (2.29e) in (2.28)
9	$\mathbb{V}_{64\text{QAM}}^{(9)}$	(2.27i)	$\sqrt{74/42}$	ϕ_i acc. (2.29g) in (2.28)
10	$\mathbb{V}_{64\text{QAM}}^{(10)}$	(2.27j)	$\sqrt{98/42}$	ϕ_i acc. (2.29a) in (2.28)

the set $\mathbb{V}_{64\text{QAM}}^{(i)}$ is denoted by

$$\angle \left(\underline{d}^{(b)} [k, \ell] \in \mathbb{V}_{64\text{QAM}}^{(i)} \right) \in \left\{ \varphi \mid \varphi = \frac{\pi}{2} \cdot \mu \pm \phi_i, \mu \in \{0, \dots, 3\} \right\} \quad (2.28)$$

where

$$\phi_i = \begin{cases} \frac{\pi}{4} & i \in \{1, 3, 6, 10\} & (2.29a) \\ \arctan \left(\frac{1}{7} \right) & i = 7 & (2.29b) \\ \arctan \left(\frac{1}{5} \right) & i = 4 & (2.29c) \\ \arctan \left(\frac{1}{3} \right) & i = 2 & (2.29d) \\ \arctan \left(\frac{3}{7} \right) & i = 8 & (2.29e) \\ \arctan \left(\frac{3}{5} \right) & i = 5 & (2.29f) \\ \arctan \left(\frac{5}{7} \right) & i = 9 & (2.29g) \end{cases}$$

holds.

The modulation mapping schemes, including the QPSK scheme [3GP16f, Section 7.1.2], the 16QAM scheme [3GP16f, Section 7.1.3] and the 64QAM scheme [3GP16f, Section 7.1.4] make use of the GRAY code, where the bit pattern of adjacent complex-valued modulation symbols differs in at most one bit [Kam08, Section 11.4.3]. It is assumed that a wrong decision occurs with higher probability on adjacent complex-valued modulation symbols, rather than on complex-valued modulation symbols being far away from each other [Kam08, Section 11.4.3]. Therefore, in case of a wrong decision, a single bit error is more probable than multiple bit errors [Kam08, Section 11.4.3].

2.4.3 Precoding

The precoding unit processes each complex-valued modulation symbol carrying data and - if transmitted - DMRS and generates a vector to be mapped onto resources on each of the transmit APs [3GP16f, Section 6.3.4]. In case of single-layer transmission, discussed throughout this thesis, each complex-valued modulation symbol carrying data and DMRS to be transmitted by the eNodeB $\epsilon_b \in \mathbb{E}$ is linearly combined with a precoding vector [DPS14, Section 10.3.3] according to

$$\underline{\mathbf{d}}_{\text{prec}}^{(b)} [k, \ell] = \underline{\mathbf{p}}^{(b)} [k, \ell] \underline{\mathbf{d}}^{(b)} [k, \ell], \quad (2.30)$$

where

$$\underline{\mathbf{d}}_{\text{prec}}^{(b)} [k, \ell] = \left(\underline{\mathbf{d}}_{1, \text{prec}}^{(b)} [k, \ell], \dots, \underline{\mathbf{d}}_{\zeta, \text{prec}}^{(b)} [k, \ell], \dots, \underline{\mathbf{d}}_{N_{\text{T}}^{(b)}, \text{prec}}^{(b)} [k, \ell] \right)^{\text{T}} \quad (2.31)$$

holds. The ζ -th element of the vector $\underline{\mathbf{d}}_{\text{prec}}^{(b)} [k, \ell]$ in (2.31) is denoted by $\underline{\mathbf{d}}_{\zeta, \text{prec}}^{(b)} [k, \ell]$ and represents the precoded complex-valued modulation symbol to be transmitted from the ζ -th transmit AE of eNodeB $\epsilon_b \in \mathbb{E}$.

In LTE systems, signal precoding is defined for

- Transmission on a single transmit AP [3GP16f, Section 6.3.4.1],
- SM using transmit APs with CRSs [3GP16f, Section 6.3.4.2],
- Transmit diversity [3GP16f, Section 6.3.4.3] and
- SM using transmit APs with DMRSs [3GP16f, Section 6.3.4.4].

In this thesis signal precoding for transmit diversity is not discussed. Detail information on signal precoding for transmit diversity can be found in [3GP16f, Section 6.3.4.3].

Precoding for SM using the transmit APs with the CRSs is only used for CRSs transmitted on two or four transmit APs [3GP16f, Section 6.3.4.2] denoted by the set $\mathcal{A}_{\text{CRS}} = \{0, 1\}$ and $\mathcal{A}_{\text{CRS}} = \{0, 1, 2, 3\}$, respectively [3GP16f, Section 6.10.1]. Precoding for SM using transmit APs with CRS can be further subdivided into precoding without Cyclic Delay Diversity (CDD) [3GP16f, Section 6.3.4.2.1] and precoding for large delay CDD [3GP16f, Section 6.3.4.2.2]. For the sake of completeness, it should be mentioned that in case of TM3, making use of the large delay CDD, two TBs are transmitted per TTI and pass through the transport processing chain [3GP16d, Section 5.3.3.1.5]. Depending on the number of transmit APs at the eNodeB $\epsilon_b \in \mathbb{E}$, in TM3 the codewords at the output of the modulation mapping subunit are mapped on two, three and four spatial layers [3GP16f, Section 6.3.4.2.2]. In this thesis, however, single-layer transmission is focused on. Detail information on signal transmission in TM3 and precoding for large delay CDD can be found in [3GP16g, Section 7.1.3] and [3GP16f, Section 6.3.4.2.2], respectively.

In case of single-layer transmission based signal precoding without CDD for SM using transmit APs with the CRS, each complex-valued modulation symbol carrying data is precoded by the eNodeB $\epsilon_b \in \mathbb{E}$ with a precoding vector from a predefined codebook [3GP16f, Section 6.3.4.2.1] according to (2.31). For the eNodeBs $\epsilon_b \in \mathbb{E}$ transmitting the CRS from two transmit APs, the relation between the PMI, the precoding vector, the maximum achievable antenna gain and the characteristic antenna diagram of the transmit AEs for the respective precoding vector is summarized in Table 2.2 on page 78 for single-layer transmission. The PMI is denoted in the first column of Table 2.2, where the set of PMIs is defined by the set $\mathcal{S}_{\text{PMI}, N_{\text{T}}^{(b)}}$ for $N_{\text{T}}^{(b)}$ equal to two and reads

$$\mathcal{S}_{\text{PMI}, 2} = \{0, \dots, 3\} \quad (2.32)$$

for the eNodeBs $\epsilon_b \in \mathbb{E}$ equipped with $N_{\text{T}}^{(b)}$ equal to two transmit AEs [3GP16f, Table 6.3.4.2.3-1]. The respective precoding vector, associated with the PMI out of the set $\mathcal{S}_{\text{PMI}, 2}$ is denoted in the second column of Table 2.2. The maximum achievable antenna gain over an isotropic radiator [Mol05, Section 4.1] in logarithmic scale is denoted in the third column of Table 2.2. Moreover, the equivalent characteristic antenna diagram in logarithmic scale for two horizontally placed transmit AEs with a spacing of a half of the wavelength [3GP06, Table A.1.3-3] is depicted in the fourth column in Table 2.2 for the respective precoding vector. A detailed discussion on the resulting antenna gain is provided in the end part of Section 2.4.3 of this thesis. Moreover, for the eNodeBs $\epsilon_b \in \mathbb{E}$, transmitting the CRSs from four transmit APs, the relation between each PMI, defined by the set $\mathcal{S}_{\text{PMI}, N_{\text{T}}^{(b)}}$ for $N_{\text{T}}^{(b)}$ equal to four and reads

$$\mathcal{S}_{\text{PMI}, 4} = \{0, \dots, 15\}, \quad (2.33)$$

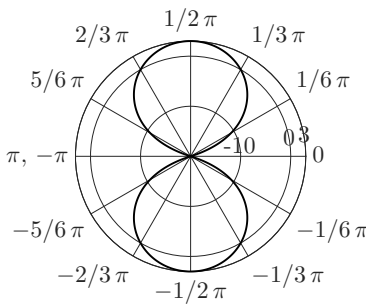
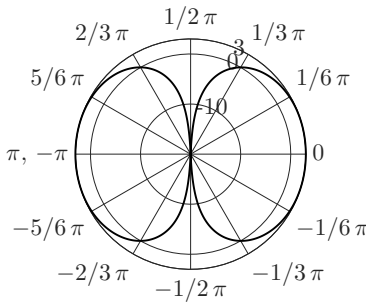
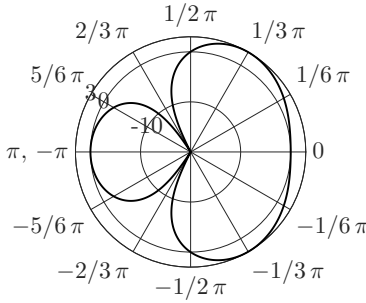
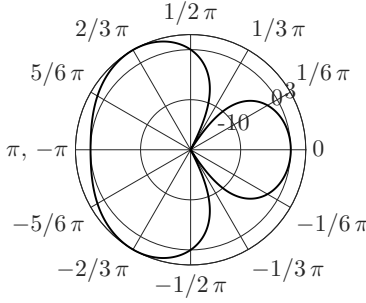
for the eNodeB $\epsilon_b \in \mathbb{E}$ with $N_T^{(b)}$ equal to four transmit AEs [3GP16f, Table 6.3.4.2.3-2]. The respective precoding vector, the maximum achievable antenna gain [Mol05, Section 4.1] and the characteristic antenna diagrams of the transmit antenna for the respective precoding vector are summarized in Table A.1 in Appendix A on page 233 of this thesis. Note that, despite the complex-valued modulation symbols carrying data, the CRSs are not precoded [3GP16f, Section 6.10.1; 3GP16f, Section 6.3.4.2.1].

In case of DMRS-based single-layer transmission, each complex-valued modulation symbol carrying the codewords and the DMRS is precoded by the eNodeB $\epsilon_b \in \mathbb{E}$ with a precoding vector [3GP16f, Section 6.3.4.4]. As mentioned in Section 1.3.3 of this thesis, the precoding vector can but does not need to be selected from a predefined codebook [3GP16g, Section 7.1]. In this thesis codebook-based signal precoding is focused on. Detail information on non codebook-based signal precoding can be found in [3GP16g, Section 7.1; STB11, Section 11.2.2.3]. For the eNodeBs $\epsilon_b \in \mathbb{E}$ transmitting the CRS or the CSI-RS from two transmit APs to enable CSI reporting, the precoding vectors for single-layer transmission are selected from the same codebook as in case of single-layer transmission based signal precoding without CDD for SM using transmit APs with the CRSs [3GP16f, Section 6.3.4.2.1; 3GP16f, Section 6.3.4.2.3; 3GP16f, Table 6.3.4.2.3-1], denoted on the second column of Table 2.2. Moreover, for the eNodeBs $\epsilon_b \in \mathbb{E}$ transmitting the CRS or the CSI-RS from four transmit AP to enable CSI reporting, the precoding vectors for single-layer transmission are selected from the same codebook as in case of single-layer transmission based signal precoding without CDD for SM using the transmit APs with the CRSs [3GP16f, Section 6.3.4.2.1; 3GP16f, Section 6.3.4.2.3; 3GP16f, Table 6.3.4.2.3-2], denoted on the second column of Table A.1 in Appendix A of this thesis. Note that despite the complex-valued modulation symbols carrying the codewords and the DMRS, neither the CRS nor the CSI-RS are precoded [3GP16f, Section 6.10.1; 3GP16f, Section 6.10.5; 3GP16f, Section 6.3.4.4]. Moreover, note that for the special case of single-layer transmission, signal precoding for SM using the transmit APs with the DMRSs [3GP16f, Section 6.3.4.4] is equivalent to precoding for transmission on a single transmit AP [3GP16f, Section 6.3.4.1], when the transmit AP7 is selected for DMRS transmission, as specified in Section 2.2.3 of this thesis.

Referring to the characteristic antenna diagram for the respective precoding vector, let ϱ_{TX} denote the antenna gain. The antenna gain ϱ_{TX} depends on the given transmit direction ϕ and the precoding vector $\underline{\mathbf{p}}^{(b)}[k, \ell]$ and reads [End07, Section 4.2.1]

$$\varrho_{\text{TX}}(\phi, \underline{\mathbf{p}}^{(b)}[k, \ell]) = \frac{\left| \underline{\mathbf{e}}(\phi)^T \underline{\mathbf{p}}^{(b)}[k, \ell] \right|^2}{\left\| \underline{\mathbf{p}}^{(b)}[k, \ell] \right\|^2}, \quad (2.34)$$

Table 2.2. Codebook and characteristic antenna diagram for signal transmission from two AEs (created by the author of this thesis using [3GP16f, Table 6.3.4.2.3-2]).

Precoding matrix index	Precoding vector $\underline{\mathbf{p}}^{(b)} [k, \ell]$	Maximum antenna gain	Characteristic antenna diagram
0	$\frac{1}{\sqrt{2}} \begin{pmatrix} 1 \\ 1 \end{pmatrix}$	3 dBi	
1	$\frac{1}{\sqrt{2}} \begin{pmatrix} 1 \\ -1 \end{pmatrix}$	3 dBi	
2	$\frac{1}{\sqrt{2}} \begin{pmatrix} 1 \\ j \end{pmatrix}$	3 dBi	
3	$\frac{1}{\sqrt{2}} \begin{pmatrix} 1 \\ -j \end{pmatrix}$	3 dBi	

where $\underline{\mathbf{e}}(\phi)$ denotes the steering vector which represents the unit spatial signature in a given transmit direction ϕ [End07, Section 4.2.1; TV05, Section 7.2.2]. The steering vector $\underline{\mathbf{e}}(\phi)$ in (2.34) is defined by [End07, Section 4.2.1; TV05, Section 7.2.2]

$$\underline{\mathbf{e}}(\phi) = \begin{pmatrix} 1 \\ \exp\left(-j2\pi \cdot \frac{d_{\text{TX}}^{(b)}}{\lambda_c} \cdot \cos(\phi)\right) \\ \vdots \\ \exp\left(-j2\pi \cdot (\zeta - 1) \cdot \frac{d_{\text{TX}}^{(b)}}{\lambda_c} \cdot \cos(\phi)\right) \\ \vdots \\ \exp\left(-j2\pi \cdot (N_{\text{T}}^{(b)} - 1) \cdot \frac{d_{\text{TX}}^{(b)}}{\lambda_c} \cdot \cos(\phi)\right) \end{pmatrix}, \quad (2.35)$$

where $d_{\text{TX}}^{(b)}$ denotes the spacing among the transmit AEs at the eNodeB $\epsilon_b \in \mathbb{E}$, which are arranged in an Uniform Linear Array (ULA) of $N_{\text{T}}^{(b)}$ transmit AEs. Moreover, λ_c in (2.35) denotes the wavelength of the OFDM baseband signal upconverted to carrier frequency f_c [3GP16f, Section 6.13]. The relation between wavelength and carrier frequency of a signal is given by [Kam08, Section 18.2.1]

$$\lambda_c = \frac{c_0}{f_c}, \quad (2.36)$$

where c_0 denotes the speed of light which is approximately equal to $3 \cdot 10^9$ m/s [Bro+01, Section 21.2]. Moreover, $\|\underline{\mathbf{p}}^{(b)}[k, \ell]\|^2$ in the denominator on the right hand side of (2.34) denotes the squared Euclidean norm of the precoding vector $\underline{\mathbf{p}}^{(b)}[k, \ell]$ [Bro+01, Section 5.3.7.5] and is equal to one for each precoding vector with corresponding PMI out of the set $\mathcal{S}_{\text{PMI},2}$ [3GP16f, Table 6.3.4.2.3-1] and $\mathcal{S}_{\text{PMI},4}$ [3GP16f, Table 6.3.4.2.3-2]. Hence, the antenna gain in (2.34) can be simplified to

$$\varrho_{\text{TX}} = \left| \underline{\mathbf{e}}(\phi)^{\text{T}} \underline{\mathbf{p}}^{(b)}[k, \ell] \right|^2, \quad (2.37)$$

where

$$10 \log_{10}(\varrho_{\text{TX}}) = 20 \log_{10} \left(\left| \underline{\mathbf{e}}(\phi)^{\text{T}} \underline{\mathbf{p}}^{(b)}[k, \ell] \right| \right) \quad (2.38)$$

holds for the antenna gain is logarithmic scale.

Calculating the antenna gain for the eNodeBs $\epsilon_b \in \mathbb{E}$ equipped with two trans-

mit AEs, ϱ_{TX} in (2.37) turns to

$$\begin{aligned}\varrho_{\text{TX}} &= \left| \left(\exp \left(-j2\pi \cdot \frac{d_{\text{TX}}^{(b)}}{\lambda_c} \cdot \cos(\phi) \right) \right)^T \cdot \frac{1}{\sqrt{2}} \begin{pmatrix} 1 \\ \nu \end{pmatrix} \right|^2 \\ &= \frac{1}{2} |1 + \nu \cdot \exp(-j2\pi \cos \phi)|^2 \\ &= 1 + \Re \{ \nu \cdot \exp(-j\pi \cos \phi) \}\end{aligned}\quad (2.39)$$

for a transmit AE spacing $d_{\text{TX}}^{(b)}$ at the eNodeB $\epsilon_b \in \mathbb{E}$ equal to one half of the wavelength [3GP06, Table A.1.3-3] of the OFDM baseband signal upconverted to carrier frequency f_c [3GP16f, Section 6.13]. Moreover, $\nu \in \{-1, 1, -j, j\}$ holds [3GP16f, Table 6.3.4.2.3-1].

For ν equal to one, the antenna gain in (2.39) for the precoding vector with PMI equal to zero reads

$$\varrho_{\text{TX}} \left(\phi, \underline{\mathbf{p}}^{(b)}[k, \ell] = \frac{1}{\sqrt{2}} \begin{pmatrix} 1 \\ 1 \end{pmatrix} \right) = 1 + \cos(\pi \cos \phi), \quad (2.40)$$

where $-1 \leq \cos(\pi \cos \phi) \leq 1$ [Bro+01, Section 2.7.1.1] holds. Hence, (2.40) is maximal when the second summand on the right hand side in (2.40) is equal to zero. The second summand on the right hand side in (2.40) is one, when the argument of the outer cosine function of the second summand on the right hand side in (2.40) is equal to zero [Bro+01, Section 2.7.1.1], such that the directional cosine $\cos \phi$ is equal to zero. As a result, (2.40) is maximal for

$$\phi \in \left\{ \varphi \mid \varphi = \frac{2n+1}{2}\pi, n \in \mathbb{Z} \right\}, \quad (2.41)$$

where \mathbb{Z} denotes the set of integer values [Bro+01, Section 1.1.1.1]. On the interval within $-\pi, \dots, \pi$ this is fulfilled for $\phi \in \{-\pi/2, \pi/2\}$. Obviously, for $\phi \in \{-\pi/2, \pi/2\}$ the antenna gain is maximal and reads 3 dBi over an isotropic radiator, as depicted in the characteristic antenna diagram for the transmit antenna for the precoding vector with PMI equal to zero, provided in Table 2.2. Moreover, the antenna gain when using the precoding vector with PMI equal to zero is greater than 0 dBi for $1/3\pi < \phi < 2/3\pi$ and $-2/3\pi < \phi < -1/3\pi$ and less or equal to 0 dBi for the remaining transmit directions ϕ .

Valid values for the transmit direction ϕ providing an antenna gain of 3 dBi, greater than 0 dBi and less or equal to 0 dBi over an isotropic radiator can be determined analogously for precoding vectors with PMI equal to one, two and three.

The precoded complex-valued modulation symbols are delivered to the resource element mapping unit [3GP16f, Section 6.3.5].

2.4.4 Resource Mapping

As initially mentioned, the resource mapping subunit is used to map the precoded complex-valued modulation symbols carrying the codewords on physical time-frequency resources of the respective transmit AP [3GP16f, Section 6.3.5]. The physical time-frequency resources used for the precoded complex-valued modulation symbols carrying the codewords on the respective transmit AP are not used for transmission of [3GP16f, Section 6.3.5]

- CRSs,
- DMRSs and
- CSI-RSs,

on the PDSCH, where the transmission of DMRSs and CSI-RSs depends on the selected TM [3GP16g, Section 7.1; 3GP16g, Table 7.1-5]. In this thesis it is assumed that the number of transmit AEs at each eNodeB $\epsilon_b \in \mathbb{E}$ is always constant. Hence, the number of the transmit AEs at the eNodeB $\epsilon_b \in \mathbb{A}_m$ transmitting the desired signal to the UE $\mu_m \in \mathbb{U}$ is equal to the number of transmit AEs at the interfering eNodeBs $\epsilon_{\bar{b}} \in \mathbb{I}_m$ and equals to either two or four, as already mentioned in Section 2.2.1 of this thesis. Let

- $\mathcal{S}_{i, n_{\text{PRB}}, \text{TM6}}^{(b, N_{\text{T}}^{(b)})}$,
- $\mathcal{S}_{i, n_{\text{PRB}}, \text{TM8}}^{(b, N_{\text{T}}^{(b)})}$,
- $\mathcal{S}_{i, n_{\text{PRB}}, \text{TM9}}^{(b, N_{\text{T}}^{(b)})}$ and
- $\mathcal{S}_{i, n_{\text{PRB}}, \text{TM10}}^{(b, N_{\text{T}}^{(b)})}$

denote the set of physical time-frequency resources used to transmit the precoded complex-valued modulation symbol carrying the codewords in the i -th subframe and n_{PRB} -th PRB for $1 \leq i \leq 9$ [3GP14e, Section 4.1] and $0 \leq n_{\text{PRB}} < N_{\text{RB}}^{\text{DL}}$ [3GP14e, Section 6.2.3], respectively, for the eNodeBs $\epsilon_b \in \mathbb{A}_m$ equipped with $N_{\text{T}}^{(b)}$ transmit AEs operating in TM6, TM8, TM9 and TM10, respectively. The derivation of the aforementioned sets of the physical time-frequency resources used to transmit the precoded complex-valued modulation symbols carrying the codewords for TM6, TM8, TM9 and TM10 is provided in Appendix B of this thesis, for $N_{\text{T}}^{(b)}$ equal to two and four transmit AEs at the eNodeB $\epsilon_b \in \mathbb{A}_m$. The cardinality of each of the aforementioned

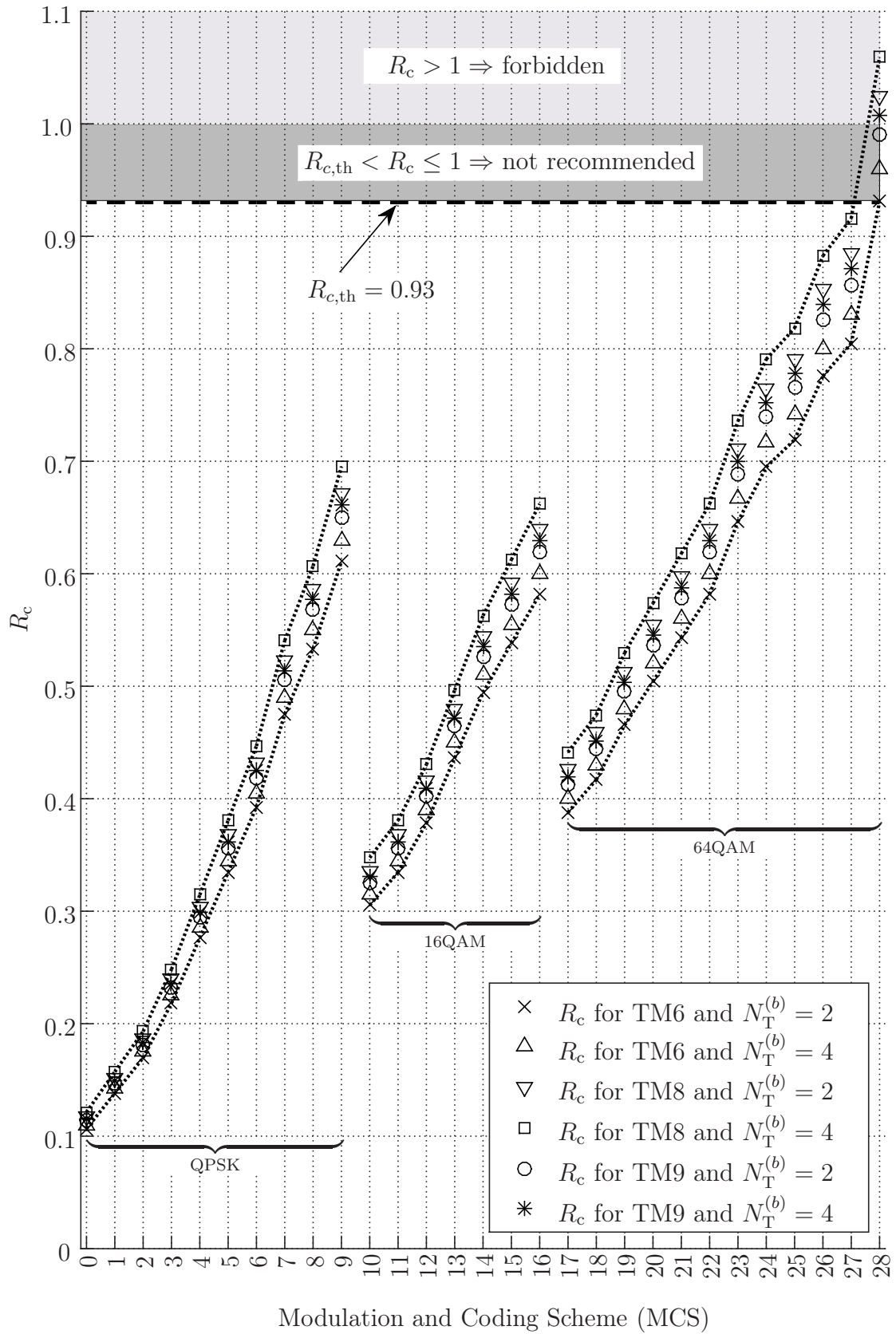


Figure 2.3. Code rate in dependency on the transmission mode and the transmitter configuration (created by the author of this thesis).

sets represents the number of physical time-frequency resources carrying the precoded complex-valued modulation symbols for codeword transmission and is provided in Table B.1 on page 239 for the first subframe and one PRB.

In LTE systems the code rate represents the ratio of the number of bits at the output of the code rate block segmentation and code block CRC attachment subunit and the number of bits that can be transmitted on the appropriate complex-valued modulation symbols carrying the codewords in one subframe [3GP16j, Section A.3.1]. The code rate for each MCS in dependence on the TM and the number of transmit AEs at the eNodeB $\epsilon_b \in \mathbb{A}_m$, denoted by $N_T^{(b)}$, is depicted in Figure 2.3 on page 82 for the first subframe and a channel bandwidth equal to 10 MHz, where the respective numerical code rates are summarized in Table B.2 on page 245. In that case, the code rate R_c reads [3GP16j, Section A.3.1]

$$R_c = \frac{N_{\text{seg}}(I_{\text{MCS}})}{\left| \mathcal{S}_{1, n_{\text{PRB}}, \text{TM}}^{(b, N_T^{(b)})} \right| \cdot N_{\text{RB}}^{\text{DL}} \cdot \log_2(|\mathbb{V}_{M\text{QAM}}|)}, \quad (2.42)$$

where $N_{\text{seg}}(I_{\text{MCS}})$ denotes the number of bits after code block segmentation and code block CRC attachment [3GP16d, Section 5.1.2] and reads [3GP16j, Section A.3.1]

$$N_{\text{seg}}(I_{\text{MCS}}) = N_{\text{TBS}} + 24 \cdot (N'_{\text{CB}} + 1) \quad (2.43)$$

for

$$N'_{\text{CB}} = \begin{cases} 0 & \text{for } N_{\text{CB}} = 1 \\ N_{\text{CB}} & \text{for } N_{\text{CB}} > 1 \end{cases} \quad (2.44)$$

and $0 \leq I_{\text{MCS}} \leq 28$. The component N_{CB} in (2.44) denotes the total number of code blocks after code block segmentation and reads [3GP16d, Section 5.1.2]

$$N_{\text{CB}} = \left\lceil \frac{N_{\text{TBS}} + N_{\text{CRC24A}}}{N_{\text{BS}}^{\text{max}} - N_{\text{CRC24B}}} \right\rceil, \quad (2.45)$$

where N_{CRC24A} and N_{CRC24B} denotes the number of bits for transport block CRC attachment [3GP16d, Section 5.3.2.1] and code block CRC attachment [3GP16d, Section 5.3.2.2] and reads 24bit each. Furthermore, $\mathbb{V}_{M\text{QAM}}$ in (2.42) is defined by

$$\mathbb{V}_{M\text{QAM}} = \begin{cases} \mathbb{V}_{\text{QPSK}} & \text{for } M = 4 \\ \mathbb{V}_{16\text{QAM}} & \text{for } M = 16 \\ \mathbb{V}_{64\text{QAM}} & \text{for } M = 64 \end{cases}, \quad (2.46)$$

where the cardinality of $\mathbb{V}_{M\text{QAM}}$ is denoted by $|\mathbb{V}_{M\text{QAM}}|$ and represents the number of modulation symbols within the set that is equal to M . Moreover, the logarithm to the base of two of the cardinality of $\mathbb{V}_{M\text{QAM}}$ represents the number of bits each modulation symbols out of the set $\mathbb{V}_{M\text{QAM}}$ is carrying. As

a result, the denominator of (2.42) represents the number of bits that can be transmitted on the complex-valued modulation symbols carrying the codeword in one subframe. The corridor in Figure 2.3 provides a graphical illustration of the lowest and highest code rate that can be achieved for the QPSK, the 16QAM and the 64QAM mapping scheme. The lowest code rate for each modulation mapping scheme is achieved for signal transmission in TM6 with two transmit AEs at the eNodeB $\epsilon_b \in \mathbb{A}_m$, whereas the highest code rate for each modulation mapping scheme is achieved for signal transmission in TM8 with four transmit AEs at the eNodeB $\epsilon_b \in \mathbb{A}_m$, as depicted in Figure 2.3. Following (2.42), a code rate greater than one implies that the number of bits at the output of the code rate block segmentation and code block CRC attachment subunit exceeds the number of resources the bits are intended to be transmitted on. Consequently, it is not possible to use TM8 with two and four transmit AEs as well as TM9 with four transmit AEs for single-layer transmission for the MCS with index 28, as depicted in Figure 2.3. On the other hand the code rate for single-layer transmission for the MCS with index 28 in TM6 for two and four transmit AEs as well as in TM9 for two transmit AEs is smaller than one, but greater than R_c , as depicted in Figure 2.3. Following [3GP16j, Section A.3.1], $R_{c,th}$ equal to 0.93 denotes the code rate that should not be exceeded and is represented by a dashed line in Figure 2.3. As a result, the MCS with index 27 represents the highest MCS that can be selected for single-layer transmission in TM6, TM8 and TM9, as depicted in Figure 2.3.

A statement on the best choice of the TM and antenna configuration at the transmitter to provide the highest bandwidth efficiency cannot be limited solely on the code rate for IL single-layer transmission. Rather it is important to investigate the interference mitigation capabilities of the respective receivers in each TM in conjunction with the antenna configuration at the transmitter and the code rates. This requires an analysis of the numerical results at the link level, provided in Section 2.10 of this thesis.

In what follows, the signal at the output of the resource element mapping subunit is illustrated for single-layer transmission in TM9 with the eNodeB $\epsilon_b \in \mathbb{E}$ equipped with four transmit AEs, where the physical layer cell-identity is assumed to be equal to zero. Following the reference measurement channel in [3GP16j, Table A.3.3.3.2-1] for verifying the demodulation performance for DMRS-based TMs with four CSI-RS transmit APs, the mapping of complex-valued symbols for single-layer transmission in TM9 is depicted in Figure 2.4 on page 85 for one radio frame and a channel bandwidth equal to 10 MHz, corresponding to N_{RB}^{DL} equal to 50 PRBs. Beside signal transmission of the DMRSs and the precoded complex-valued modulation symbols used for code-word transmission over the PDSCH as well as the CRSs and the CSI-RSs, the physical time-frequency resources carrying the information transmitted over the

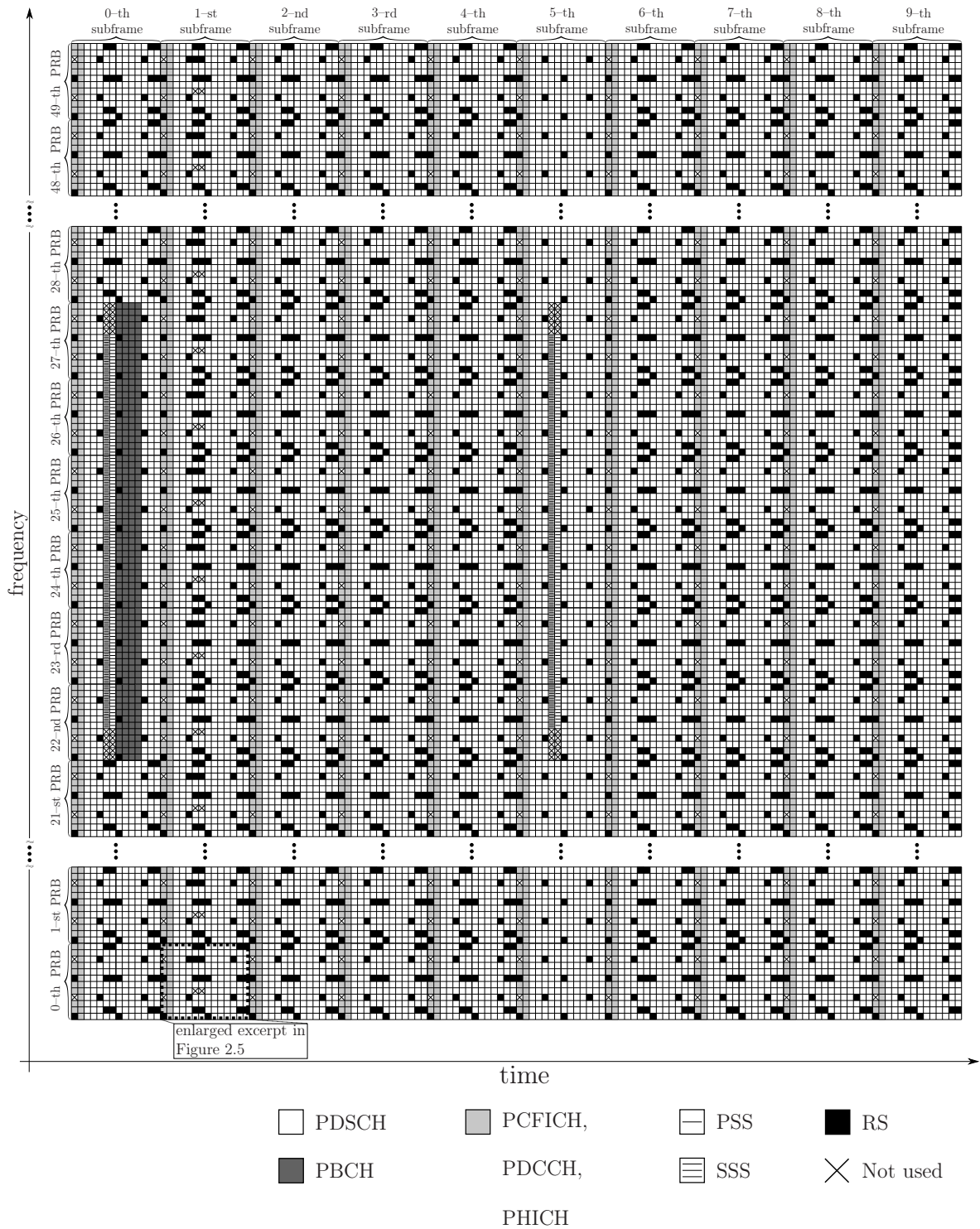


Figure 2.4. Mapping of RS and symbols for signal transmission in TM9 (created by the author of this thesis using [3GP16f, Figure 6.10.1.2-1, Figure 6.10.3.2-3, Figure 6.10.5.2-1]).

- Physical Broadcast Channel (PBCH) [3GP16f, Section 6.6],
- Physical Control Format Indicator Channel (PCFICH) [3GP16f, Section 6.7],
- Physical Hybrid ARQ Indicator Channel (PHICH) [3GP16f, Section 6.9] and
- Physical Downlink Control Channel (PDCCH) [3GP16f, Section 6.8],

as well as the

- Primary Synchronization Signal (PSS) [3GP16f, Section 6.11.1] and
- Secondary Synchronization Signal (SSS) [3GP16f, Section 6.11.2],

are also included, as depicted in Figure 2.4 and their main task is discussed.

The PBCH carries the system information for the UE $\mu_m \in \mathbb{U}$ which is necessary to access the network [STB11, Section 9.2.1]. This system information is transmitted in the first four OFDM symbols of the first slot on the 72 subcarriers around the Discrete Current (DC) subcarrier, excluding the physical time-frequency resources for the CRS transmission [3GP16f, Section 6.6.4], as depicted in Figure 2.4. Further information on the PBCH can be found in [3GP16f, Section 6.6; STB11, Section 9.2.1].

The PCFICH carries the control information that indicates the number of OFDM symbols used for the PDCCH [STB11, Section 9.3.3]. The complex-valued modulation symbols transmitted on the PCFICH are transmitted within the first OFDM symbol of every subframe [3GP16f, Section 6.7.4], as depicted in Figure 2.4. Further information on the PCFICH can be found in [3GP16f, Section 6.7; STB11, Section 9.3.3].

The PHICH carries the information that indicates whether the eNodeB has correctly received a transmission [STB11, Section 9.3.4]. The binary information is mapped on QPSK modulation symbols [3GP16f, Section 7.11] which are transmitted on the PHICH within the first OFDM symbol of each subframe [3GP16f, Section 6.9.2], as depicted in Figure 2.4. Further information on the PHICH can be found in [3GP16f, Section 6.9; STB11, Section 9.3.4].

The PDCCH carries the information that includes the resource assignment and other control information for the UE $\mu_m \in \mathbb{U}$ [STB11, Section 9.3.5]. The complex-valued modulation symbols are transmitted within the first L OFDM symbols in every subframe, where the number L for PDCCH transmission is indicated by the PCFICH [STB11, Section 9.3.5]. Following [3GP16j, Section A.3.3], in this thesis it is assumed that L is equal to two for single-layer transmission. As a result, the first two OFDM symbols of each subframe are reserved for signal transmission on the PCFICH, the PHICH and the PDCCH,

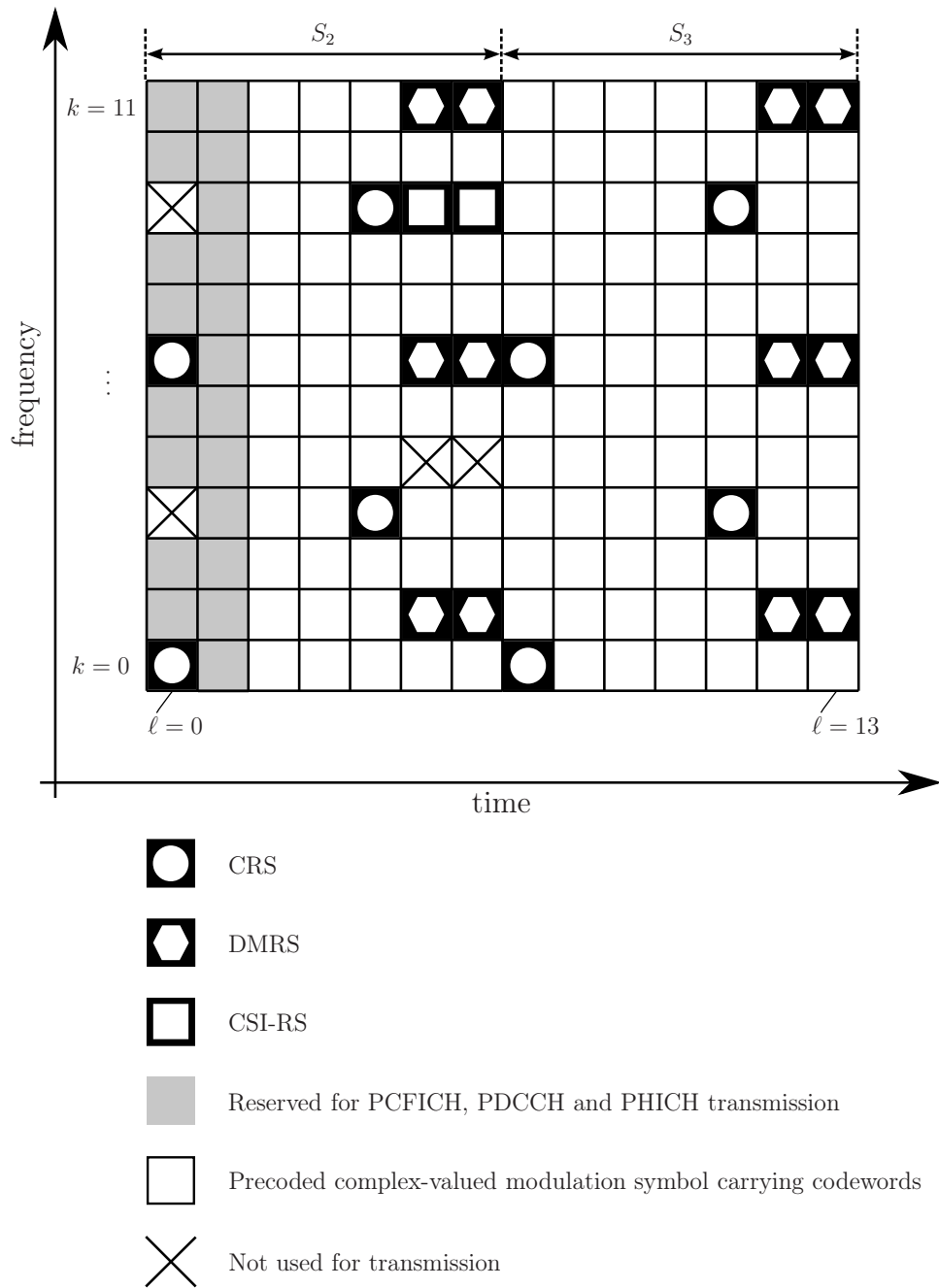


Figure 2.5. Cutout of a PRB and subframe for signal transmission in TM9 (created by the author of this thesis).

excluding the physical time-frequency resources for CRS transmission, as depicted in Figure 2.4. For further information on the PDCCH, see [3GP16f, Section 6.8; STB11, Section 9.3.5].

The PSS and SSS are used to enable time and frequency synchronization among the UE $\mu_m \in \mathbb{U}$ and the eNodeB $\epsilon_b \in \mathbb{A}_m$ including the [STB11, Section 7.2]

- Symbol and radio frame timing acquisition to set the Discrete Fourier Transform (DFT) window,
- Carrier frequency synchronization to reduce or eliminate the effect of CFOs and the
- Sampling clock synchronization to reduce or eliminate the effect of SCOs.

As already mentioned in Section 1.2.3 of this thesis, the impact of CFOs and SCOs is not discussed in this thesis. References for further information on the impact of CFOs and SCOs are provided in Section 1.2.3 of this thesis. Moreover, the synchronization signals provide the UE $\mu_m \in \mathbb{U}$ with the physical layer cell-identity, the CP length and inform the UE $\mu_m \in \mathbb{U}$ whether the FDD or TDD mode is used [STB11, Section 7.2]. The synchronization signals are transmitted twice per radio frame [3GP16f, Section 6.11.1.2, Section 6.11.2.2], as depicted in Figure 2.4. The PSS is always located in the last OFDM symbol of the zeroth and tenth slot of each radio frame and is transmitted in the 62 central subcarriers around the DC subcarrier [3GP16f, Section 6.11.1.2; STB11, Section 7.2], as depicted in Figure 2.4. Moreover, the SSS is always located in the last but one OFDM symbol of the zeroth and tenth slot of each radio frame and is transmitted in the central 62 subcarriers around the DC subcarrier [3GP16f, Section 6.11.2.2; STB11, Section 7.2], as depicted in Figure 2.4. Following [3GP16f, Section 6.11.1.2, Section 6.11.2.2], five REs at each extremity of each synchronization sequence are not used, as depicted in Figure 2.4. Further information on the PSS and SSS can be found in [3GP16f, Section 6.11.1; STB11, Section 7.2] and [3GP16f, Section 6.11.2; STB11, Section 7.2], respectively.

The enlarged cutout of the zeroth PRB and first subframe of the radio frame in Figure 2.4 is depicted in Figure 2.5 on page 87. Furthermore, the modulation symbols that are transmitted within the zeroth PRB and first subframe, where the respective physical time-frequency resources are denoted by the (k, ℓ) -th RE, are summarized in Table 2.3 on page 90 for $0 \leq k \leq 11$ and $0 \leq \ell \leq 13$. Following the findings achieved in this section, the (k, ℓ) -th RE for $0 \leq \ell \leq 1$ and $0 \leq k \leq 11$, excluding the $(0, 0)$ -th RE and the $(0, 6)$ -th RE which denotes the physical time-frequency resources carrying the CRSs from the transmit AP0 as well as the $(0, 3)$ -th RE and the $(0, 9)$ -th RE which denotes the physical time-frequency resources carrying the CRSs for a

possible transmission from the transmit AP1, are shared for signal transmission on the PCFICH, the PHICH and the PDCCH, as depicted in Figure 2.5. The respective complex-valued modulation symbols transmitted on the PCFICH, the PHICH and the PDCCH are denoted in Table 2.3 and are marked with a rounded single rectangular box. Note that since the CRSs are transmitted only from the transmit AP0, the same transmit AP is used for signal transmission on the PCFICH, the PHICH and the PDCCH [3GP16f, Section 6.3.4.1, Section 6.7.3, Section 6.8.4, Section 6.9.3]. The complex-valued modulation symbols carrying the CRSs and the complex-valued modulation symbols carrying the CSI-RSs are transmitted on the physical time-frequency resources out of the set $\mathcal{S}_{0,1,\text{CRS}}^{(b,0)}$ and $\mathcal{S}_{0,1,\text{CSI-RS}}^{(b,14)}$, respectively, where the former RSs in Table 2.3 are marked with a single rectangular solid box, while the latter RSs are marked with a double rectangular solid box. Moreover, the precoded complex-valued modulation symbols carrying the precoded DMRSs are transmitted on the physical time-frequency resources out of the set $\mathcal{S}_{0,1,\text{DMRS}}^{(b,7)}$ and are marked with a single rectangular dashed box, as denoted in Table 2.3. Following the findings achieved in this section, $\mathcal{S}_{0,1,\text{TM9}}^{(b,4)}$ denotes the set of physical time-frequency resources used to transmit the precoded complex-valued modulation symbols carrying the codewords on the PDSCH, as depicted in Figure 2.5. The precoded complex-valued modulation symbols on the physical time-frequency resources out of the set $\mathcal{S}_{0,1,\text{TM9}}^{(b,4)}$ are denoted in Table 2.3, where each precoded complex-valued modulation symbol represents a complex-valued modulation symbol out of set $\mathbb{V}_{64\text{QAM}}$, denoted in (2.27) and is weighted with the factor of one half which represents the first component of each precoding vector according to Table A.1.

2.5 OFDM

2.5.1 Modulation

In this section, the OFDM baseband signal generation is described. A presentation that resembles a textbook is not included on purpose. General information on the OFDM principle can be found in [CT07, Section 2.2; Kam08, Chapter 16; Mol05, Chapter 19; OL07, Section 8.3.6; STB11, Chapter 5; Stü11, Section 10.1]. The focus of Section 2.5 of this thesis is to discuss the OFDM baseband signal generation at each eNodeB $\epsilon_b \in \mathbb{E}$ operating in LTE networks for signal transmission in the DL and discuss the impact of varying delays among the receive signals, experienced by the UE $\mu_m \in \mathbb{U}$.

The time-continuous OFDM baseband signal of the ℓ -th OFDM symbol for $0 \leq \ell < N_{\text{symb}}^{\text{DL}}$ [3GP16f, Section 6.2.2; 3GP16f, Table 6.2.3-1] to be transmitted

Table 2.3. Example of RS and symbols for signal transmission in TM9 (created by the author of this thesis).

$\uparrow k/\ell \rightarrow$	0	1	2	3	4	5	6	7	8	9	10	11	12	13
11	$\frac{+1+j}{2}$	$\frac{-1-j}{2}$	$\frac{+1+j\cdot 3}{2\cdot\sqrt{42}}$	$\frac{-7+j\cdot 3}{2\cdot\sqrt{42}}$	$\frac{+1-j\cdot 3}{2\cdot\sqrt{42}}$	$\frac{+1-j}{2\cdot\sqrt{2}}$	$\frac{+1+j}{2\cdot\sqrt{2}}$	$\frac{+3+j\cdot 3}{2\cdot\sqrt{42}}$	$\frac{-7-j\cdot 3}{2\cdot\sqrt{42}}$	$\frac{-1+j\cdot 3}{2\cdot\sqrt{42}}$	$\frac{+1+j\cdot 3}{2\cdot\sqrt{42}}$	$\frac{-1+j\cdot 3}{2\cdot\sqrt{42}}$	$\frac{-1+j}{2\cdot\sqrt{2}}$	$\frac{+1+j}{2\cdot\sqrt{2}}$
10	$\frac{-1-j}{2}$	$\frac{+1+j}{2}$	$\frac{+5-j\cdot 3}{2\cdot\sqrt{42}}$	$\frac{-7-j\cdot 3}{2\cdot\sqrt{42}}$	$\frac{+7-j\cdot 3}{2\cdot\sqrt{42}}$	$\frac{+5+j\cdot 3}{2\cdot\sqrt{42}}$	$\frac{+7+j\cdot 3}{2\cdot\sqrt{42}}$	$\frac{-3-j\cdot 3}{2\cdot\sqrt{42}}$	$\frac{+1+j\cdot 3}{2\cdot\sqrt{42}}$	$\frac{-1-j}{2\cdot\sqrt{42}}$	$\frac{-1-j}{2\cdot\sqrt{42}}$	$\frac{-7+j}{2\cdot\sqrt{42}}$	$\frac{+1+j\cdot 3}{2\cdot\sqrt{42}}$	$\frac{-1+j\cdot 3}{2\cdot\sqrt{42}}$
9	0	$\frac{+1-j}{2}$	$\frac{-3-j\cdot 3}{2\cdot\sqrt{42}}$	$\frac{+5+j\cdot 3}{2\cdot\sqrt{42}}$	$\frac{+1+j}{2}$	$\frac{+1-j}{\sqrt{2}}$	$\frac{-1-j}{\sqrt{2}}$	$\frac{-3+j\cdot 3}{2\cdot\sqrt{42}}$	$\frac{-3+j}{2\cdot\sqrt{42}}$	$\frac{+1+j\cdot 3}{2\cdot\sqrt{42}}$	$\frac{+1+j\cdot 3}{2\cdot\sqrt{42}}$	$\frac{+1-j}{2}$	$\frac{+1-j}{2\cdot\sqrt{42}}$	$\frac{-1-j\cdot 3}{2\cdot\sqrt{42}}$
8	$\frac{+1+j}{2}$	$\frac{+1+j}{2}$	$\frac{+7+j}{2\cdot\sqrt{42}}$	$\frac{-1-j}{2\cdot\sqrt{42}}$	$\frac{-1-j\cdot 3}{2\cdot\sqrt{42}}$	$\frac{-1+j}{2\cdot\sqrt{42}}$	$\frac{+7-j\cdot 3}{2\cdot\sqrt{42}}$	$\frac{-3-j\cdot 3}{2\cdot\sqrt{42}}$	$\frac{+7+j\cdot 3}{2\cdot\sqrt{42}}$	$\frac{-5-j\cdot 3}{2\cdot\sqrt{42}}$	$\frac{+7-j}{2\cdot\sqrt{42}}$	$\frac{+3+j\cdot 3}{2\cdot\sqrt{42}}$	$\frac{+7-j\cdot 3}{2\cdot\sqrt{42}}$	$\frac{+1-j}{2\cdot\sqrt{42}}$
7	$\frac{+1+j}{2}$	$\frac{+1+j}{2}$	$\frac{+3+j\cdot 3}{2\cdot\sqrt{42}}$	$\frac{+5+j\cdot 3}{2\cdot\sqrt{42}}$	$\frac{-5-j\cdot 3}{2\cdot\sqrt{42}}$	$\frac{-5+j}{2\cdot\sqrt{42}}$	$\frac{+3+j\cdot 3}{2\cdot\sqrt{42}}$	$\frac{+1-j\cdot 3}{2\cdot\sqrt{42}}$	$\frac{+7+j\cdot 3}{2\cdot\sqrt{42}}$	$\frac{+5+j\cdot 3}{2\cdot\sqrt{42}}$	$\frac{+5-j\cdot 3}{2\cdot\sqrt{42}}$	$\frac{-5+j\cdot 3}{2\cdot\sqrt{42}}$	$\frac{-3+j\cdot 3}{2\cdot\sqrt{42}}$	$\frac{+7+j\cdot 3}{2\cdot\sqrt{42}}$
6	$\frac{+1+j}{2}$	$\frac{+1+j}{2}$	$\frac{-1-j\cdot 3}{2\cdot\sqrt{42}}$	$\frac{-3+j\cdot 3}{2\cdot\sqrt{42}}$	$\frac{+3-j\cdot 3}{2\cdot\sqrt{42}}$	$\frac{+1+j}{2\cdot\sqrt{2}}$	$\frac{+1+j}{2\cdot\sqrt{2}}$	$\frac{+1+j}{2}$	$\frac{+1-j}{2\cdot\sqrt{42}}$	$\frac{-7-j\cdot 3}{2\cdot\sqrt{42}}$	$\frac{+7-j\cdot 3}{2\cdot\sqrt{42}}$	$\frac{+7+j\cdot 3}{2\cdot\sqrt{42}}$	$\frac{-1+j}{2\cdot\sqrt{2}}$	$\frac{+1+j}{2\cdot\sqrt{2}}$
5	$\frac{-1-j}{2}$	$\frac{+1+j}{2}$	$\frac{+7+j}{2\cdot\sqrt{42}}$	$\frac{-1-j\cdot 3}{2\cdot\sqrt{42}}$	$\frac{-7+j\cdot 3}{2\cdot\sqrt{42}}$	$\frac{+7-j}{2\cdot\sqrt{42}}$	$\frac{+1-j\cdot 3}{2\cdot\sqrt{42}}$	$\frac{+7-j}{2\cdot\sqrt{42}}$	$\frac{-7-j\cdot 3}{2\cdot\sqrt{42}}$	$\frac{+1+j\cdot 3}{2\cdot\sqrt{42}}$	$\frac{+7+j\cdot 3}{2\cdot\sqrt{42}}$	$\frac{+7-j\cdot 3}{2\cdot\sqrt{42}}$	$\frac{-1+j\cdot 3}{2\cdot\sqrt{42}}$	$\frac{-7-j\cdot 3}{2\cdot\sqrt{42}}$
4	$\frac{+1+j}{2}$	$\frac{+1+j}{2}$	$\frac{+3+j\cdot 3}{2\cdot\sqrt{42}}$	$\frac{+5+j\cdot 3}{2\cdot\sqrt{42}}$	$\frac{-3+j\cdot 3}{2\cdot\sqrt{42}}$	0	0	$\frac{+7+j\cdot 3}{2\cdot\sqrt{42}}$	$\frac{+1+j\cdot 3}{2\cdot\sqrt{42}}$	$\frac{+7+j\cdot 3}{2\cdot\sqrt{42}}$	$\frac{-7-j\cdot 3}{2\cdot\sqrt{42}}$	$\frac{+1-j\cdot 3}{2\cdot\sqrt{42}}$	$\frac{-7-j}{2\cdot\sqrt{42}}$	$\frac{-7-j\cdot 3}{2\cdot\sqrt{42}}$
3	0	$\frac{-1-j}{2}$	$\frac{+1-j}{2\cdot\sqrt{42}}$	$\frac{-7+j}{2\cdot\sqrt{42}}$	$\frac{+1+j}{2}$	$\frac{+1-j\cdot 3}{2\cdot\sqrt{42}}$	$\frac{+1+j\cdot 3}{2\cdot\sqrt{42}}$	$\frac{+7+j\cdot 3}{2\cdot\sqrt{42}}$	$\frac{-7+j\cdot 3}{2\cdot\sqrt{42}}$	$\frac{+1+j\cdot 3}{2\cdot\sqrt{42}}$	$\frac{-5+j\cdot 3}{2\cdot\sqrt{42}}$	$\frac{+1+j}{2}$	$\frac{-7-j}{2\cdot\sqrt{42}}$	$\frac{+1+j}{2\cdot\sqrt{42}}$
2	$\frac{+1+j}{2}$	$\frac{+1-j}{2}$	$\frac{+1+j}{2\cdot\sqrt{42}}$	$\frac{-7-j\cdot 3}{2\cdot\sqrt{42}}$	$\frac{-7-j\cdot 3}{2\cdot\sqrt{42}}$	$\frac{+1-j\cdot 3}{2\cdot\sqrt{42}}$	$\frac{-7+j}{2\cdot\sqrt{42}}$	$\frac{-7-j}{2\cdot\sqrt{42}}$	$\frac{+1+j\cdot 3}{2\cdot\sqrt{42}}$	$\frac{+7+j}{2\cdot\sqrt{42}}$	$\frac{+7+j\cdot 3}{2\cdot\sqrt{42}}$	$\frac{-1+j}{2\cdot\sqrt{42}}$	$\frac{-7+j\cdot 3}{2\cdot\sqrt{42}}$	$\frac{+7-j\cdot 3}{2\cdot\sqrt{42}}$
1	$\frac{+1+j}{2}$	$\frac{+1-j}{2}$	$\frac{+1+j}{2\cdot\sqrt{42}}$	$\frac{-7+j\cdot 3}{2\cdot\sqrt{42}}$	$\frac{+7-j\cdot 3}{2\cdot\sqrt{42}}$	$\frac{-1-j}{2\cdot\sqrt{2}}$	$\frac{-1-j}{2\cdot\sqrt{2}}$	$\frac{-7-j\cdot 3}{2\cdot\sqrt{42}}$	$\frac{-3+j\cdot 3}{2\cdot\sqrt{42}}$	$\frac{-1-j\cdot 3}{2\cdot\sqrt{42}}$	$\frac{+1-j\cdot 3}{2\cdot\sqrt{42}}$	$\frac{-5+j\cdot 3}{2\cdot\sqrt{42}}$	$\frac{-1+j}{2\cdot\sqrt{2}}$	$\frac{+1+j}{2\cdot\sqrt{2}}$
0	$\frac{-1-j}{2}$	$\frac{+1-j}{2}$	$\frac{+7-j\cdot 3}{2\cdot\sqrt{42}}$	$\frac{+1+j\cdot 3}{2\cdot\sqrt{42}}$	$\frac{-3-j}{2\cdot\sqrt{42}}$	$\frac{-1-j\cdot 3}{2\cdot\sqrt{42}}$	$\frac{+5-j\cdot 3}{2\cdot\sqrt{42}}$	$\frac{+1+j}{2}$	$\frac{+5-j\cdot 3}{2\cdot\sqrt{42}}$	$\frac{-3+j\cdot 3}{2\cdot\sqrt{42}}$	$\frac{+1+j}{2\cdot\sqrt{42}}$	$\frac{+1+j}{2\cdot\sqrt{42}}$	$\frac{-1+j}{2\cdot\sqrt{42}}$	$\frac{-5-j\cdot 3}{2\cdot\sqrt{42}}$

from the eNodeB $\epsilon_b \in \mathbb{E}$ on the ζ -th transmit AE for $1 \leq \zeta \leq N_T^{(b)}$ is denoted by [3GP16f, Section 6.12]

$$\begin{aligned} \underline{s}_{\ell, \zeta}^{(b)}(t) = & \sum_{k'=-\lfloor N_{\text{RB}}^{\text{DL}} N_{\text{sc}}^{\text{RB}} / 2 \rfloor}^{-1} \underline{y}_{\zeta}^{(b)}[k^{(-)}, \ell] \cdot \exp(j2\pi k' f_{\text{sc}}(t - N_{\text{CP}, \ell} T_s)) + \\ & \sum_{k'=1}^{\lceil N_{\text{RB}}^{\text{DL}} N_{\text{sc}}^{\text{RB}} / 2 \rceil} \underline{y}_{\zeta}^{(b)}[k^{(+)}, \ell] \cdot \exp(j2\pi k' f_{\text{sc}}(t - N_{\text{CP}, \ell} T_s)) \end{aligned} \quad (2.47)$$

for $0 \leq t < (N_{\text{CP}, \ell} + N_{\text{OFDM}}) \cdot T_s$, where $\lceil \cdot \rceil$ denotes the smallest integer greater than or equal to \cdot . For single-layer transmission, considered throughout this thesis, the complex-valued scalar value $\underline{y}_{\zeta}^{(b)}[k, \ell] \in \mathbb{C}$ in (2.47) is defined by

$$\underline{y}_{\zeta}^{(b)}[k, \ell] = \begin{cases} \underline{d}^{(b)}[k, \ell] & \text{for transmission of the CRSs and,} \\ & \text{if supported, the CSI-RSs} \\ \underline{d}_{\zeta, \text{prec}}^{(b)}[k, \ell] & \text{for transmission of, if supported, the DMRSS} \\ & \text{and the precoded complex-valued modulation} \\ & \text{symbols carrying the codewords.} \end{cases} \quad (2.48)$$

Moreover, $k^{(-)}$ and $k^{(+)}$ in (2.47) is defined by [3GP16f, Section 6.12]

$$k^{(-)} = k + \lfloor N_{\text{RB}}^{\text{DL}} N_{\text{sc}}^{\text{RB}} / 2 \rfloor \quad \text{and} \quad (2.49a)$$

$$k^{(+)} = k + \lfloor N_{\text{RB}}^{\text{DL}} N_{\text{sc}}^{\text{RB}} / 2 \rfloor - 1, \quad (2.49b)$$

respectively. In addition, the duration of the ℓ -th CP reads [3GP16f, Section 6.12]

$$\tau_{\text{CP}, \ell} = N_{\text{CP}, \ell} T_s, \quad (2.50)$$

where

$$N_{\text{CP}, \ell} = \begin{cases} 160 & \text{for } l = 0 \\ 144 & \text{for } l = 1, 2, \dots, 6 \end{cases} \quad (2.51)$$

denotes the number of samples [3GP16f, Table 6.12-1] with sample interval T_s defined by [3GP16f, Section 6.12]

$$T_s = \frac{1}{N_{\text{OFDM}} \cdot f_{\text{sc}}}, \quad (2.52)$$

where N_{OFDM} is equal to 2048 [3GP16f, Section 6.12]. The inverse of the sample interval T_s in (2.52) denotes the sampling frequency f_s and reads 30.72 MHz [STB11, Section 5.4.1].

The time-continuous OFDM baseband signal in (2.47) is generated by a set of $N_{\text{RB}}^{\text{DL}} N_{\text{sc}}^{\text{RB}}$ modulators which assign each complex-valued scalar value $\underline{y}_{\zeta}^{(b)}[k, \ell]$

in (2.47) at subcarrier k , $0 \leq k < N_{\text{RB}}^{\text{DL}} N_{\text{sc}}^{\text{RB}}$ [3GP16f, Section 6.2.2] a carrier with carrier frequency $k' \cdot f_{\text{sc}}$. The parameter k' is denoted by the range $-\lfloor N_{\text{RB}}^{\text{DL}} N_{\text{sc}}^{\text{RB}} / 2 \rfloor, \dots, -1, 1, \dots, \lceil N_{\text{RB}}^{\text{DL}} N_{\text{sc}}^{\text{RB}} / 2 \rceil$, where k' equal zero is excluded [3GP16f, Section 6.12] to evade the unwanted DC offset [CT07, Section 2.2.2].

Each time-continuous OFDM baseband signal $\underline{s}_{\ell, \zeta}^{(b)}(t)$ transmitted by the eNodeB $\epsilon_b \in \mathbb{E}$ on the ζ -th transmit AE for $1 \leq \zeta \leq N_{\text{T}}^{(b)}$ denotes a composition of a CP and the OFDM symbol [3GP16f, Section 6.12]. The CP is located in the forefront of the time-continuous OFDM baseband signal $0 \leq t < N_{\text{CP}, \ell} \cdot T_{\text{s}}$ and represents an exact copy of the rear part of the time-continuous OFDM baseband signal $N_{\text{OFDM}} \cdot T_{\text{s}} \leq t < (N_{\text{CP}, \ell} + N_{\text{OFDM}}) \cdot T_{\text{s}}$ for each $0 \leq \ell < N_{\text{sy mb}}^{\text{DL}}$ [3GP16f, Section 6.12]. The CP is used to eliminate ICI and ISI which occurs during the transient state at the beginning and decay process at the end of each OFDM symbol, respectively [Kam08, Section 16.2.1]. A detailed illustration can be found in [3GP16f, Figure 16.2.1]. One condition to guarantee ICI and ISI free transmission is that the length of the CP has to be larger than the length of the Channel Impulse Response (CIR) of the mobile communication channel [Kam08, Section 16.2.1]. The aspect of ICI is not discussed in this thesis. Detail information on ICI can be found in [Kam08, Section 16.2.1; CT07, Section 5.2.2; Mol05, Section 19.7].

Extending the time-continuous OFDM baseband signal of the ℓ -th OFDM symbol in (2.47) on the time-continuous OFDM baseband signal in one DL slot, $\underline{s}_{\zeta}^{(b)}(t)$ denotes a compilation of $N_{\text{sy mb}}^{\text{DL}}$ consecutive OFDM symbols $0 \leq \ell < N_{\text{sy mb}}^{\text{DL}}$ [3GP16f, Section 6.2.2] transmitted by the eNodeB $\epsilon_b \in \mathbb{E}$ on the ζ -th transmit AE for $1 \leq \zeta \leq N_{\text{T}}^{(b)}$. The time-continuous OFDM baseband signal in a DL slot is defined for [3GP16f, Section 6.2.2; 3GP16f, Section 6.12; STB11, Section 5.4.1]

$$0 \leq t < \underbrace{\left(N_{\text{sy mb}}^{\text{DL}} \cdot N_{\text{OFDM}} + \sum_{\ell'=0}^{N_{\text{sy mb}}^{\text{DL}}-1} N_{\text{CP}, \ell'} \right)}_{=T_{\text{slot}}} \cdot T_{\text{s}}. \quad (2.53)$$

Moreover, $n_{\text{shift}}(\ell - 1) \cdot T_{\text{s}} \leq t < n_{\text{shift}}(\ell) \cdot T_{\text{s}}$ denotes the excerpt of the ℓ -th OFDM symbol and CP within the DL slot, where

$$n_{\text{shift}}(\ell) = \ell \cdot N_{\text{OFDM}} + \sum_{\ell'=0}^{\ell-1} N_{\text{CP}, \ell'} \quad (2.54)$$

denotes the accumulated number of samples of the previous ℓ OFDM symbols and CPs at sampling frequency f_{s} [3GP16f, Section 6.12].

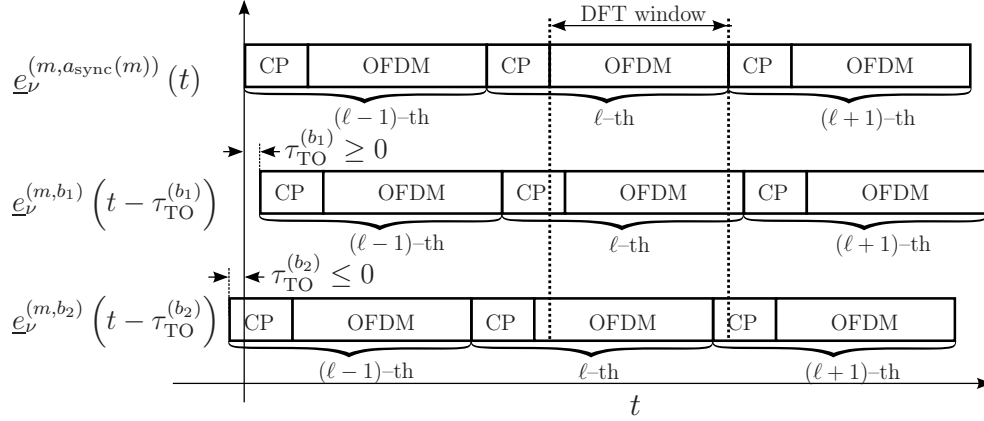


Figure 2.6. Illustration of the impact of varying delays on the receive signals (created by the author of this thesis using [CT07, Figure 5.3]).

CP: Cyclic Prefix, DFT: Discrete Fourier Transform, OFDM: Orthogonal Frequency Division Multiplexing

2.5.2 Demodulation

OFDM demodulation is carried out by the UE $\mu_m \in \mathbb{U}$ to disassemble the receive signal into subchannels [Kam08, Section 16.1.1]. Let $\underline{e}_\nu^{(m,b)}(t)$ denote the baseband representation of the time-continuous receive signal in one slot at the output of the mobile communication channel [Jun97, Section 3.5.3] for $1 \leq \nu \leq N_R^{(m)}$ when the eNodeB $\epsilon_b \in \mathbb{E}$ transmits the time-continuous OFDM baseband signal on $N_T^{(b)}$ transmit AEs. Hence, the baseband representation of the time-continuous receive signal $\underline{e}_\nu^{(m,b)}(t)$ at the output of the mobile communication channel represents the convolution of the time-continuous OFDM baseband signal $\underline{s}_\zeta^{(b)}(t)$ transmitted by the eNodeB $\epsilon_b \in \mathbb{E}$ and the CIR $\underline{h}'_{\nu,\zeta}{}^{(m,b)}(\tau, t)$ of the mobile communication channel [Jun97, Section 3.5.3] summed up over all $N_T^{(b)}$ transmit AEs according to

$$\underline{e}_\nu^{(m,b)}(t) = \sqrt{C^{(m,b)}} \sum_{\zeta=1}^{N_T^{(b)}} \underline{s}_\zeta^{(b)}(t) * \underline{h}'_{\nu,\zeta}{}^{(m,b)}(\tau, t), \quad (2.55)$$

where $*$ denotes the linear convolution operation [Bro+01, Section 15.3.1.3]. The CIR $\underline{h}'_{\nu,\zeta}{}^{(m,b)}(\tau, t)$ in (2.55) denotes the complex-valued baseband representation of the real-valued bandpass signal which describes the channel response at the ν -th receive AE for $1 \leq \nu \leq N_R^{(m)}$ at the UE $\mu_m \in \mathbb{U}$ at time t when transmitting a DIRAC impulse at time $t - \tau$ at the ζ -th transmit AE with $1 \leq \zeta \leq N_T^{(b)}$ at the eNodeB $\epsilon_b \in \mathbb{E}$ [Jun97, Section 3.5.3].

Generalizing (2.55) for individually delayed desired and interfering signals transmitted by the eNodeB $\epsilon_b \in \mathbb{A}_m$ and the eNodeBs $\epsilon_{\bar{b}} \in \mathbb{I}_m$, respectively

[3GP13a, Section 5.1.2A], (2.55) turns to

$$\begin{aligned} \underline{e}_\nu^{(m)}(t) = & \sqrt{C^{(m,b)}} \sum_{\zeta=1}^{N_T^{(b)}} \underline{s}_\zeta^{(b)}(t) * \delta\left(t - \tau_{\text{TO}}^{(b)}\right) * \underline{h}_{\nu,\zeta}^{(m,b)}(\tau, t) + \\ & \sum_{\{\tilde{b} | \epsilon_{\tilde{b}} \in \mathbb{I}_m\}} \sqrt{C^{(m,\tilde{b})}} \sum_{\zeta=1}^{N_T^{(\tilde{b})}} \underline{s}_\zeta^{(\tilde{b})}(t) * \delta\left(t - \tau_{\text{TO}}^{(\tilde{b})}\right) * \underline{h}_{\nu,\zeta}^{(m,\tilde{b})}(\tau, t), \end{aligned} \quad (2.56)$$

for the UE $\mu_m \in \mathbb{U}$ and $1 \leq \nu \leq N_R^{(m)}$. Furthermore, $\delta(t)$ in (2.56) denotes the DIRAC delta function [Bro+01, Section 12.9.5.3]. Hence, the desired signal, transmitted by the eNodeB $\epsilon_b \in \mathbb{A}_m$ is experienced by the UE $\mu_m \in \mathbb{U}$ with a delay denoted by $\tau_{\text{TO}}^{(b)}$ in (2.56) [3GP13a, Section 5.1.2A]. The delay of the interfering signals transmitted by each eNodeB $\epsilon_{\tilde{b}} \in \mathbb{I}_m$ is defined analogously in (2.56) when replacing the superscript index b in $\tau_{\text{TO}}^{(b)}$ by \tilde{b} .

To illustrate the impact of the varying delays among the receive signals, Figure 2.6 on page 93 is used. Figure 2.6 shows a cutout of the DL slot of the baseband representation of the time-continuous receive signal (2.56) which is assumed to consist of three superposed time-continuous baseband signals

$$\underline{e}_\nu^{(m, a_{\text{sync}}(m))}\left(t - \tau_{\text{TO}}^{(a_{\text{sync}}(m))}\right) = \underline{e}_\nu^{(m, a_{\text{sync}}(m))}(t) * \delta\left(t - \tau_{\text{TO}}^{(a_{\text{sync}}(m))}\right), \quad (2.57a)$$

$$\underline{e}_\nu^{(m, b_1)}\left(t - \tau_{\text{TO}}^{(b_1)}\right) = \underline{e}_\nu^{(m, b_1)}(t) * \delta\left(t - \tau_{\text{TO}}^{(b_1)}\right), \quad (2.57b)$$

$$\underline{e}_\nu^{(m, b_2)}\left(t - \tau_{\text{TO}}^{(b_2)}\right) = \underline{e}_\nu^{(m, b_2)}(t) * \delta\left(t - \tau_{\text{TO}}^{(b_2)}\right), \quad (2.57c)$$

received by the UE $\mu_m \in \mathbb{U}$ on the ν -th receive AE for $1 \leq \nu \leq N_R^{(m)}$, where $a_{\text{sync}}(m) \neq b_1 \neq b_2$ holds. Moreover, the $(l-1)$ -th, l -th and $(l+1)$ -th CP and OFDM symbol of each of the three time-continuous baseband signals (2.57a), (2.57b) and (2.57c) is depicted in Figure 2.6. Note that each of the time-continuous baseband signals (2.57b) and (2.57c) may carry either the desired or the interfering signals. As the UE $\mu_m \in \mathbb{U}$ is assigned to the eNodeB $\epsilon_{a_{\text{sync}}(m)}$ with respect to synchronization [3GP16f, Section 7.1], $\tau_{\text{TO}}^{(a_{\text{sync}}(m))}$ is set to zero. In that case, the time continuous signal (2.57b) reaches the UE $\mu_m \in \mathbb{U}$ by $|\tau_{\text{TO}}^{(b_1)}|$ later than the time-continuous baseband signal (2.57a), as depicted in Figure 2.6. Furthermore, the time-continuous baseband signal (2.57c) reaches the UE μ_m by $|\tau_{\text{TO}}^{(b_2)}|$ earlier than the time-continuous baseband signal (2.57a), as depicted in Figure 2.6. Hence, in the former case the delay is defined as positive with $\tau_{\text{TO}}^{(b_1)}$ greater than or equal to zero, whereas in the latter case the delay is defined as negative with $\tau_{\text{TO}}^{(b_2)}$ less than or equal to zero, as depicted in Figure 2.6.

To disassemble the receive signal into subchannels [Kam08, Section 16.1.1], the UE $\mu_m \in \mathbb{U}$ samples the baseband representation of the time-continuous receive signal with sampling frequency f_s , assigns the DFT window and calculates the DFT transform [Kam08, Section 16.1.2]. Following the findings within Section 1.2.4 of this thesis, $\epsilon_{a_{\text{sync}}(m)} \in \mathbb{A}_m$ denotes the eNodeB the UE $\mu_m \in \mathbb{U}$ is assigned to with respect to synchronization [Jun97, Section 4.4.1]. Hence, the UE $\mu_m \in \mathbb{A}_m$ assigns the DFT window on each OFDM symbol transmitted by eNodeB $\epsilon_{a_{\text{sync}}(m)} \in \mathbb{A}_m$ [3GP16g, Section 7.1].

In what follows the complex-valued OFDM baseband signal representation of (2.57b) and (2.57c) after sampling and OFDM demodulation is calculated when the UE $\mu_m \in \mathbb{U}$ is assigned to eNodeB $\epsilon_{a_{\text{sync}}(m)}$ with respect to synchronization [3GP16f, Section 7.1] with the aim to generalize the system model introduced in Section 1.2.4 of this thesis for varying delays among the receive signals.

Let

$$n_{\text{shift}}(\ell - 1) + N_{\text{CP},\ell} - \tau_{\text{TO}}^{(b_1)} \cdot f_s \leq v < n_{\text{shift}}(\ell - 1) + N_{\text{OFDM}} - \tau_{\text{TO}}^{(b_1)} \cdot f_s \quad (2.58)$$

denote the N_{OFDM} samples of the sampled time-continuous baseband signal (2.57b) when the UE $\mu_m \in \mathbb{U}$ assigns the DFT window on the ℓ -th OFDM symbol of the sampled baseband signal (2.57a). For the sake of simplicity it is assumed that $\tau_{\text{TO}}^{(b_1)} \cdot f_s \in \mathbb{Z}$ holds. The DFT transform of the N_{OFDM} samples (2.58) in absence of the AWGN component reads [CT07, Section 5.2.2]

$$\begin{aligned} r_{\nu}^{(m,b_1)}[k, \ell] &= \sum_{v=0}^{N_{\text{OFDM}}-1} \underline{e}_{\nu}^{(m,b_1)} \left[v + n_{\text{shift}}(\ell - 1) + N_{\text{CP},\ell} - \tau_{\text{TO}}^{(b_1)} \cdot f_s \right] \cdot \\ &\quad \exp \left(-j2\pi \frac{k'' v}{N_{\text{OFDM}}} \right) \\ &= \sqrt{C^{(m,b_1)}} \sum_{\zeta=1}^{N_{\text{T}}^{(b)}} \underline{h}_{\nu,\zeta}^{(m,b_1)}[k, \ell] \underline{y}_{\zeta}^{(b_1)}[k, \ell] \cdot \exp \left(-j2\pi k \frac{\tau_{\text{TO}}^{(b_1)} \cdot f_s}{N_{\text{OFDM}}} \right) \end{aligned} \quad (2.59)$$

when the length of the CP reduced by the length of the delay $\tau_{\text{TO}}^{(b_1)}$ is larger than the CIR of $\underline{h}_{\nu,\zeta}^{(m,b_1)}(\tau, t)$ for each $1 \leq \nu \leq N_{\text{R}}^{(m)}$ and $1 \leq \zeta \leq N_{\text{T}}^{(b)}$. The parameter k'' in (2.59) is defined by [3GP16f, Section 6.12]

$$k'' = \begin{cases} k - \lceil N_{\text{RB}}^{\text{DL}} N_{\text{sc}}^{\text{RB}} / 2 \rceil & \text{for } 0 \leq k < \lceil N_{\text{RB}}^{\text{DL}} N_{\text{sc}}^{\text{RB}} / 2 \rceil \\ k - \lceil N_{\text{RB}}^{\text{DL}} N_{\text{sc}}^{\text{RB}} / 2 \rceil + 1 & \text{for } \lceil N_{\text{RB}}^{\text{DL}} N_{\text{sc}}^{\text{RB}} / 2 \rceil \leq k < N_{\text{RB}}^{\text{DL}} N_{\text{sc}}^{\text{RB}} - 1 \end{cases} \quad (2.60)$$

The complex-valued OFDM baseband signal representation after OFDM de-

modulation in (2.59) is affected by the subcarrier specific phase shift denoted by $\exp(-j2\pi k\tau_{\text{TO}}^{(b_1)}f_s/N_{\text{OFDM}})$ in each subcarrier $0 \leq k < N_{\text{RB}}^{\text{DL}} N_{\text{sc}}^{\text{RB}}$ [CT07, Section 5.2.2] and is ISI-free [CT07, Section 5.2.2]. In that case the impact of the aforementioned subcarrier specific phase shift can be reverted when $\tau_{\text{TO}}^{(b_1)}$ in (2.59) is reliably determined [CT07, Section 5.2.2].

The N_{OFDM} samples of the sampled time-continuous baseband signal (2.57c) can be obtained from (2.58) when replacing b_1 by b_2 . Here again, for the sake of simplicity it is assumed that $\tau_{\text{TO}}^{(b_2)} \cdot f_s \in \mathbb{Z}$ holds. The DFT transform of the N_{OFDM} samples in absence of the AWGN component reads [CT07, Section 5.2.2]

$$\begin{aligned} \underline{r}_{\nu}^{(m,b_2)}[k, \ell] &= \sum_{v=0}^{N_{\text{OFDM}}-1} \underline{e}_{\nu}^{(m,b_2)} \left[v + n_{\text{shift}}(\ell - 1) + N_{\text{CP},\ell} - \tau_{\text{TO}}^{(b_2)} \cdot f_s \right] \cdot \\ &\quad \exp\left(-j2\pi \frac{k'' v}{N_{\text{OFDM}}}\right) \\ &= \sqrt{C^{(m,b_2)}} \sum_{\zeta=1}^{N_{\text{T}}^{(b)}} \underline{h}_{\nu,\zeta}^{(m,b_2)}[k, \ell] \underline{y}_{\zeta}^{(b_2)}[k, \ell] \cdot \frac{N_{\text{OFDM}} - |\tau_{\text{TO}}^{(b_2)}| \cdot f_s}{N_{\text{OFDM}}} \cdot \\ &\quad \exp\left(-j2\pi k \frac{\tau_{\text{TO}}^{(b_2)} \cdot f_s}{N_{\text{OFDM}}}\right) + \underline{n}_{\text{ISI}}^{(b_2)}[k, \ell]. \end{aligned} \tag{2.61}$$

Note that there exists a slight decrease in the signal magnitude by the factor of $(N_{\text{OFDM}} - |\tau_{\text{TO}}^{(b_2)}| \cdot f_s)/N_{\text{OFDM}}$ [CT07, Section 5.2.2], as denoted in (2.61). This is because only $N_{\text{OFDM}} - |\tau_{\text{TO}}^{(b_2)}|$ out of N_{OFDM} samples of the desired signal are covered by the DFT window [CT07, Section 5.2.2]. The contribution of the $|\tau_{\text{TO}}^{(b_2)}| \cdot f_s$ samples that belong to the $(\ell + 1)$ -th CP rather than to the desired signal introduce ISI [CT07, Section 5.2.2] which is indicated in (2.61) by $\underline{n}_{\text{ISI}}^{(b_2)}[k, \ell]$. A detailed description of $\underline{n}_{\text{ISI}}^{(b_2)}[k, \ell]$ can be found in [CT07, Section 5.2.2] and references therein.

The complex-valued OFDM baseband signal representation of the receive signal experienced by UE $\mu_m \in \mathbb{U}$ after OFDM demodulation for MIMO in (1.28) can be generalized for varying delays of the receive signals by making use of

(2.59) and (2.61) according to

$$\begin{aligned}
\mathbf{r}^{(m)} [k, \ell] = & \sqrt{C^{(m,b)}} \left(\underline{\mathbf{H}}^{(m,b)} [k, \ell] \underline{\mathbf{p}}^{(b)} [k, \ell] \underline{\mathbf{d}}^{(b)} [k, \ell] \cdot \right. \\
& \left. \exp \left(-j2\pi k \frac{\tau_{\text{TO}}^{(b)} f_s}{N_{\text{OFDM}}} \right) \chi_{\text{DTF}} \left(\tau_{\text{TO}}^{(b)} \right) + \chi_{\text{ISI}} \left(\tau_{\text{TO}}^{(b)} \right) \right) + \\
& \sum_{\{\tilde{b} | \epsilon_{\tilde{b}} \in \mathbb{I}_m\}} \sqrt{C^{(m,\tilde{b})}} \left(\underline{\mathbf{H}}^{(m,\tilde{b})} [k, \ell] \underline{\mathbf{p}}^{(\tilde{b})} [k, \ell] \underline{\mathbf{d}}^{(\tilde{b})} [k, \ell] \cdot \right. \\
& \left. \exp \left(-j2\pi k \frac{\tau_{\text{TO}}^{(\tilde{b})} f_s}{N_{\text{OFDM}}} \right) \chi_{\text{DTF}} \left(\tau_{\text{TO}}^{(\tilde{b})} \right) + \chi_{\text{ISI}} \left(\tau_{\text{TO}}^{(\tilde{b})} \right) \right) + \\
& \mathbf{n}^{(m)} [k, \ell].
\end{aligned} \tag{2.62}$$

The component $\chi_{\text{DTF}}(\tau_{\text{TO}}^{(b)})$ in (2.62) is used to adjust the signal magnitude and is defined by [CT07, Section 5.3]

$$\chi_{\text{DTF}} \left(\tau_{\text{TO}}^{(b)} \right) = \begin{cases} 1 & \text{for } 0 \leq \tau_{\text{TO}}^{(b)} \leq \tau_{\text{CP},\ell} \\ \frac{N_{\text{OFDM}} - |\tau_{\text{TO}}^{(b)}| \cdot f_s}{N_{\text{OFDM}}} & \text{for } \tau_{\text{TO}}^{(b)} < 0 \end{cases}, \tag{2.63}$$

where in case of $\tau_{\text{TO}}^{(b)}$ less than zero only $N_{\text{OFDM}} - |\tau_{\text{TO}}^{(b)}| \cdot f_s$ samples belong to the desired OFDM symbol. Moreover, the component $\chi_{\text{ISI}}(\tau_{\text{TO}}^{(b)})$ in (2.62) is defined by

$$\chi_{\text{ISI}} \left(\tau_{\text{TO}}^{(b)} \right) = \begin{cases} \mathbf{0}_{N_{\text{R}}^{(m)}} & \text{for } \tau_{\text{CP},\ell} - \tau_{\text{TO}}^{(b)} \leq \tau_{\text{CIR}} \left(\underline{\mathbf{h}}'_{\nu,\zeta}{}^{(m,b)} (\tau, t) \right) \\ & \text{fulfilled for } 1 \leq \nu \leq N_{\text{R}}^{(m)}, 1 \leq \zeta \leq N_{\text{T}}^{(b)} \\ \underline{\mathbf{n}}_{\text{ISI}}^{(m,b)} [k, \ell] & \text{for } \tau_{\text{TO}}^{(b)} < 0 \vee \tau_{\text{CP},\ell} - \tau_{\text{TO}}^{(b)} > \tau_{\text{CIR}} \left(\underline{\mathbf{h}}'_{\nu,\zeta}{}^{(m,b)} (\tau, t) \right) \\ & \text{fulfilled for } 1 \leq \nu \leq N_{\text{R}}^{(m)}, 1 \leq \zeta \leq N_{\text{T}}^{(b)} \end{cases}, \tag{2.64}$$

where $\tau_{\text{CIR}}(\cdot)$ in (2.64) denotes the length of the CIR of \cdot and $\mathbf{0}_{N_{\text{R}}^{(m)}}$ represents the Null vector of dimension $N_{\text{R}}^{(m)} \times 1$ [Bro+01, Section 3.5.1.1]. The component $\chi_{\text{DFT}}(\tau_{\text{TO}}^{(\tilde{b})})$ and $\chi_{\text{ISI}}(\tau_{\text{TO}}^{(\tilde{b})})$, respectively, is defined analogously as in (2.63) and (2.64) when replacing b by \tilde{b} .

For the special case $\tau_{\text{TO}}^{(b)}$ equal zero for the eNodeB $\epsilon_b \in \mathbb{A}_m$ and $\tau_{\text{TO}}^{(\tilde{b})}$ equal zero for each eNodeB $\epsilon_{\tilde{b}} \in \mathbb{I}_m$, the equality of the complex-valued OFDM baseband signal representation of the receive signals experienced by the UE $\mu_m \in \mathbb{U}$ in the k -th subcarrier for $0 \leq k < N_{\text{RB}}^{\text{DL}} N_{\text{sc}}^{\text{RB}}$ [3GP16f, Section 6.2.2]

and ℓ -th OFDM symbol for $0 \leq \ell < N_{\text{symb}}^{\text{DL}}$ [3GP16f, Section 6.2.2] after OFDM demodulation for MIMO antenna configuration of (1.29) and (2.62) is ensured.

The impact of varying delays among the receive signals with a particular focus on implicit feedback generation and channel estimation is discussed in Chapter 4 of this thesis.

2.6 Receiver Design

2.6.1 Introduction

The receiver implementation aspects to transform the complex-valued OFDM baseband signal representation of the receive signals experienced by the UE $\mu_m \in \mathbb{U}$ into bits within the TB is discussed in this section. Therefore, the following steps are carried out [Cox14, Section 5.2.4]

- OFDM demodulation,
- channel estimation,
- signal equalization,
- PMI feedback and
- channel decoding,

as depicted in Figure 2.7 on page 99. The aspect of OFDM demodulation is discussed in Section 2.5.2 of this thesis. Channel estimation schemes for CRSs, DMRSs and CSI-RSs are discussed in Section 2.6.2 of this thesis. To equalize the complex-valued OFDM baseband signal of the receive signal after OFDM demodulation, signal equalization is carried out [Kam08, Section 16.2.2]. To enable signal equalization at the UE $\mu_m \in \mathbb{U}$, two receiver types including the IS receiver [3GP14f, Section 7.2] and Adaptive SLIC (ASLIC) receiver [Iwe+16, Section III-C] including practical implementation aspects are discussed in Section 2.6.3 and Section 2.6.4 of this thesis, respectively. The aspect of PMI feedback depends on the currently selected TM [3GP16g, Section 7.2.1] and is discussed in Section 2.7 of this thesis. In this thesis iterative decoding of the turbo-codes is used. A detailed discussion is not provided in this thesis. Detail information on iterative decoding of turbo-codes can be found in [Jun97, Section E.3].

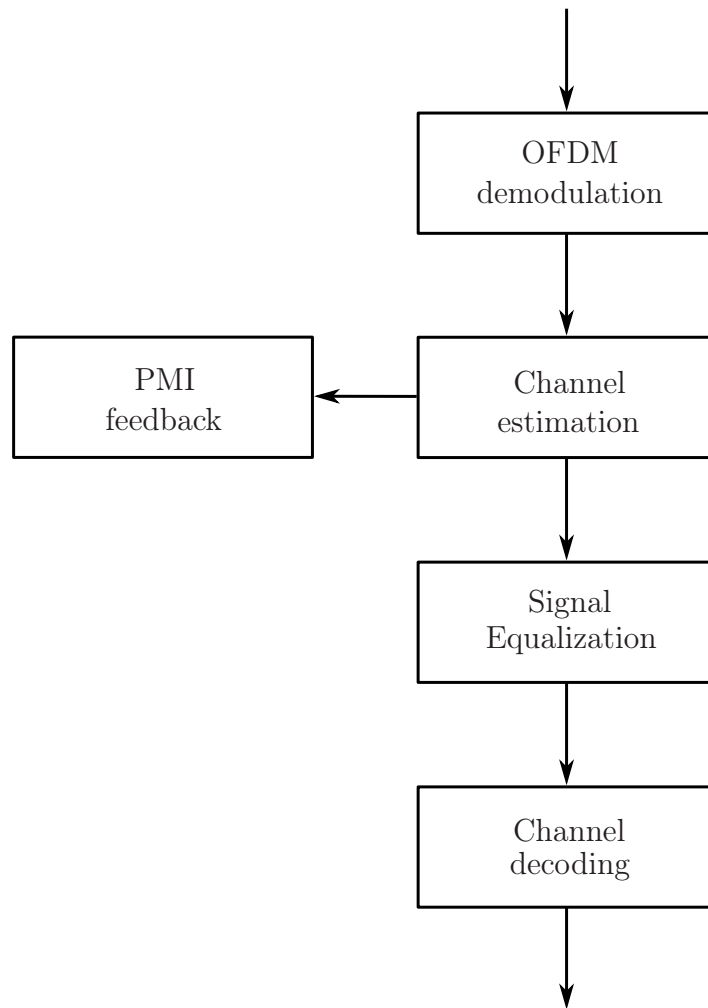


Figure 2.7. Block diagram of the designed receiver (created by the author of this thesis using [Cox14, Figure 5.7]).

2.6.2 Channel Estimation

Channel estimation provides information about the distortion of the transmission signal when it propagates through the mobile communication channel [CT07, Chapter 6]. This information is used by equalizers so that the fading effect, phase distortion and inter-cell interference can be mitigated to recover the desired signal at the UE $\mu_m \in \mathbb{U}$ [CT07, Chapter 6]. Channel estimation can be categorized into non-data-aided and data-aided [CT07, Section 6.1]. The aspect of non-data-aided channel estimation is not discussed in this thesis. Detail information on non-data-aided channel estimation can be found in [Mol05, Section 16.7] and references therein. In this thesis data-aided channel estimation based on pilot signals is considered to obtain precise channel estimation for equalizing each subcarrier [CT07, Section 6.1] and to acquire CSI at the UE $\mu_m \in \mathbb{U}$ [STB11, Section 29.1.2] to feed quantized CSI back to the respective eNodeB [3GP16g, Section 7.2]. General information on channel estimation can be found in [Jun97, Chapter 5]. The knowledge of the pilot signals transmitted by the respective eNodeB $\epsilon_b \in \mathbb{E}$ is absolutely necessary at the UE $\mu_m \in \mathbb{U}$ [Jun97, Section 5.2.2]. In this thesis a low-complexity channel estimation and interpolation scheme is used for the CRSs, DMRSs and CSI-RSs and is discussed in what follows. Detail information on optimal channel estimation and interpolation schemes can be found in [CT07, Chapter 6] and references therein.

In this thesis, channel estimation based on CRSs that are transmitted by each eNodeBs $\epsilon_b \in \mathbb{E}$ [3GP16f, Section 6.10.1] is divided into LSCE [CT07, Section 6.3] and double one-dimensional interpolation [CT07, Section 6.3.2]. Let $\hat{\mathbf{H}}_{\text{CRS}}^{(m,b)} [k, \ell]$ denote the estimate of the CTF $\mathbf{H}^{(m,b)} [k, \ell]$, defined in (1.31), when evaluating the CRSs. To calculate $\hat{\mathbf{H}}_{\text{CRS}}^{(m,b)} [k, \ell]$, the following three steps are carried out.

1. UE $\mu_m \in \mathbb{U}$ estimates the CTF $\underline{h}_{\nu, \zeta}^{(m,b)} [k, \ell]$, representing the inhomogeneities of the mobile communication channel [Jun97, Section 3.2.1] between the ν -th receive AE for $1 \leq \nu \leq N_{\text{R}}^{(m)}$ and the ζ -th transmit AE for $1 \leq \zeta \leq N_{\text{T}}^{(b)}$ at the eNodeB $\epsilon_b \in \mathbb{E}$ at the physical time-frequency resources carrying the CRSs out of the set $\mathcal{S}_{i, n_{\text{PRB}}, \text{CRS}}^{(b, \pi_{\text{AP}})}$ using the LSCE scheme [CT07, Section 6.3] for each subframe $0 \leq i \leq 9$ [3GP16f, Section 4.1], each PRB $0 \leq n_{\text{PRB}} < N_{\text{RB}}^{\text{DL}}$ [3GP16f, Section 6.2.3] and each transmit AP $\pi_{\text{AP}} \in \mathcal{A}_{\text{CRS}}$ [3GP16f, Section 6.10.1] from the complex-valued OFDM baseband signal representation of the receive signal after OFDM demodulation.
2. UE $\mu_m \in \mathbb{U}$ interpolates through all subcarriers in frequency direction [CT07, Section 6.3.2] using linear channel interpolation separated into the real and imaginary component [TG11, Section III-C] for each OFDM

symbol out of the set $\mathcal{S}_{i, n_{\text{PRB}}, \text{CRS}}^{(b, \pi_{\text{AP}})}$ for $0 \leq i \leq 9$ [3GP16f, Section 4.1], $0 \leq n_{\text{PRB}} < N_{\text{RB}}^{\text{DL}}$ [3GP16f, Section 6.2.3] and each transmit $\pi_{\text{AP}} \in \mathcal{A}_{\text{CRS}}$ [3GP16f, Section 6.10.1].

3. UE $\mu_m \in \mathbb{U}$ interpolates through all OFDM symbols in time direction [CT07, Section 6.3.2] using linear channel interpolation separated into the real and imaginary component [TG11, Section III-C] for each sub-carrier [3GP16f, Section 6.2.2].

Channel estimation based on DMRSs which are transmitted by each eNodeB $\epsilon_b \in \mathbb{E}$ operating in TM8, TM9 and TM10 [3GP16g, Table 7.1-5] is divided into either LSCE [CT07, Section 6.3] or JLSCE [Iwe+16, Section IV-A] in this thesis. Following the aperiodic CSI reporting [3GP16g, Section 7.2.1], in this thesis Mode 1-2 is selected for PMI feedback for the considered TMs. Detail information on PMI selection for the considered TMs is provided in Section 2.7 in this thesis. One property of multiple PMI feedback supported in Mode 1-2 [3GP16g, Table 7.2.1-1] that is of particular importance for channel estimation and interpolation for DMRS-based TMs is that the precoding vector might change from subband to subband and from subframe to subframe [3GP16g, Section 7.2.1], where a subband denotes a set of predefined contiguous PRBs [3GP16g, Section 7.2] which depends on the bandwidth configuration [3GP16g, Table 7.2.1-3]. Let $\hat{\underline{g}}_{\text{DMRS}}^{(m,b)}[k, \ell]$ denote the estimate of the CTF $\underline{g}^{(m,b)}[k, \ell]$, defined in (1.33), when evaluating the DMRSs. To calculate $\hat{\underline{g}}_{\text{DMRS}}^{(m,b)}[k, \ell]$, the following three steps are carried out.

1. In case of the LSCE scheme [CT07, Section 6.3], the UE $\mu_m \in \mathbb{U}$ estimates the CTF $\underline{g}_{\nu}^{(m,b)}[k, \ell]$ representing the inhomogeneities of the mobile communication channel [Jun97, Section 3.2.1] between the ν -th receive AE for $1 \leq \nu \leq N_{\text{R}}^{(m)}$ and the transmit AP7 represented by the $N_{\text{T}}^{(b)}$ transmit AEs at the eNodeB $\epsilon_b \in \mathbb{E}$ [3GP16f, Section 6.10.3] at the physical time-frequency resources carrying the DMRSs, denoted by the set $\mathcal{S}_{i, n_{\text{PRB}}, \text{DMRS}}^{(b, 7)}$ for each subframe $0 \leq i \leq 9$ [3GP16f, Section 4.1] and each PRB for $0 \leq n_{\text{PRB}} < N_{\text{RB}}^{\text{DL}}$ [3GP16f, Section 6.2.3] from the complex-valued OFDM baseband signal representation of the receive signal after OFDM demodulation. In case of the JLSCE scheme, the UE $\mu_m \in \mathbb{U}$ estimates the CTF $\underline{g}_{\nu}^{(m,b)}[k, \ell]$ between the ν -th receive AE for $1 \leq \nu \leq N_{\text{R}}^{(m)}$ and the transmit AP7 at a subset of the eNodeBs out of the set \mathbb{E} [Iwe+16, Section IV-A]. To enable the JLSCE scheme, the UE $\mu_m \in \mathbb{U}$ receives knowledge on the cell-ID $N_{\text{cell}}^{\text{ID}}$ of the interfering eNodeBs [3GP14f, Section 7.5]. Detail information on a practical implementation of the JLSCE scheme can be found in [Iwe+16, Section IV-A].
2. UE $\mu_m \in \mathbb{U}$ interpolates through all subcarriers in frequency direction [CT07, Section 6.3.2] within the subband the precoding vector remains

unchanged [3GP16g, Section 7.2.1] using linear channel interpolation separated into the real and imaginary component [TG11, Section III-C] for each OFDM symbol out of the set $\mathcal{S}_{i, n_{\text{PRB}}, \text{DMRS}}^{(b, 7)}$ for $0 \leq i \leq 9$ [3GP16f, Section 4.1] and $0 \leq n_{\text{PRB}} < N_{\text{RB}}^{\text{DL}}$ [3GP16f, Section 6.2.3].

3. UE $\mu_m \in \mathbb{U}$ interpolates through all OFDM symbols in time direction [CT07, Section 6.3.2] within the subframe the precoding vector remains unchanged [3GP16g, Section 7.2.1] using linear channel interpolation, separated into the real and imaginary component [TG11, Section III-C] for each subcarrier within the subband the precoding vector remains unchanged [3GP16g, Section 7.2.1]

In what follows, the channel estimation scheme for CSI-RSs used in this thesis is discussed. Following the findings achieved in Section 2.2.4 of this thesis, the transmission of CSI-RSs is used to acquire CSI information at the UE $\mu_m \in \mathbb{U}$ [STB11, Section 29.1.2] and feed quantized CSI back to the eNodeB [3GP16g, Section 7.2]. Let $\hat{\mathbf{H}}_{\text{CSI-RS}}^{(m, b)} [n_{\text{PRB}}]$ denote the estimated channel between the UE $\mu_m \in \mathbb{U}$ in the n_{PRB} -th PRB for $0 \leq n_{\text{PRB}} < N_{\text{RB}}^{\text{DL}}$ [3GP16f, Section 6.2.3]. The (ν, ζ) -th element of the MIMO representation $\hat{\mathbf{H}}_{\text{CSI-RS}}^{(m, b)} [n_{\text{PRB}}]$ is characterized by the CTF $h_{\nu, \zeta}^{(m, b)} [k_{14+\zeta}, \ell_{14+\zeta}]$ and represents the inhomogeneities of the mobile communication channel among the ν -th receive AE at the UE $\mu_m \in \mathbb{U}$ for $1 \leq \nu \leq N_{\text{R}}^{(m)}$ and the ζ -th transmit AE at the eNodeB $\epsilon_b \in \mathbb{E}$ in the $k_{14+\zeta}$ -th subcarrier and $\ell_{14+\zeta}$ -th OFDM symbol for $1 \leq \zeta \leq N_{\text{T}}^{(b)}$. The tuple $(k_{14+\zeta}, \ell_{14+\zeta}) \in \mathcal{S}_{i, n_{\text{PRB}}, \text{CSI-RS}}^{(b, 14+\zeta)}$ denotes the physical time-frequency resources carrying the CSI-RSs transmitted from the transmit AP π_{AP} equal to $14 + \zeta$ out of the set $\mathcal{A}_{\text{CSI-RS}}$ which is mapped on the ζ -th transmit AE according to (2.16) and (2.19) for two and four transmit AEs at the eNodeB $\epsilon_b \in \mathbb{E}$, respectively, in the i -th subframe for $0 \leq i \leq 9$ [3GP16f, Section 4.1] and n_{PRB} -th PRB for $0 \leq n_{\text{PRB}} < N_{\text{RB}}^{\text{DL}}$ [3GP16f, Section 6.2.3], where $n_{\text{PRB}} \cdot N_{\text{sc}}^{\text{RB}} \leq k_{\pi_{\text{AP}}} < (n_{\text{PRB}} + 1) \cdot N_{\text{sc}}^{\text{RB}}$ and $0 \leq \ell_{\pi_{\text{AP}}} < 2 \cdot N_{\text{symb}}^{\text{DL}} - 1$ holds. For the eNodeB $\epsilon_b \in \mathbb{E}$ equipped with two and four transmit AEs, the CTF representing the inhomogeneities of the mobile communication channel [Jun97, Section 3.2.1] between the ν -th receive AE at the UE $\mu_m \in \mathbb{U}$ for $1 \leq \nu \leq N_{\text{R}}^{(m)}$ and transmit the AP15 assigned to the first transmit AE according to the mapping function in (2.16a) and (2.19a), respectively, in the n_{PRB} -th for $0 \leq n_{\text{PRB}} < N_{\text{RB}}^{\text{DL}}$ [3GP16f, Section 6.2.3] is calculated in this thesis by adding the receive signal at the ν -th receive AE at the UE $\mu_m \in \mathbb{U}$ at the physical time-frequency resource defined by the tuple (k_{15}, ℓ_{15}) after LSCE [CT07, Section 6.3] to the signal received by the same receive AE at the UE $\mu_m \in \mathbb{U}$ at the physical time-frequency resource defined by the tuple (k_{16}, ℓ_{16}) after LSCE [CT07, Section 6.3] and dividing the sum by two to revert the WALSH function [3GP16f, Section 6.10.5.2]. Moreover, the CTF representing the inhomogeneities of the mobile communication channel

[Jun97, Section 3.2.1] between the ν -th receive AE at the UE $\mu_m \in \mathbb{U}$ for $1 \leq \nu \leq N_R^{(m)}$ and the transmit AP16 assigned to the second transmit AE according to the mapping function in (2.16b) and (2.19b), respectively, in the n_{PRB} -th for $0 \leq n_{\text{PRB}} < N_{\text{RB}}^{\text{DL}}$ [3GP16f, Section 6.2.3] is calculated in this thesis by subtracting the receive signal at the ν -th receive AE at the UE $\mu_m \in \mathbb{U}$ at the physical time-frequency resource defined by the tuple (k_{15}, ℓ_{15}) after LSCE [CT07, Section 6.3] from the signal received by the same receive AE at the UE $\mu_m \in \mathbb{U}$ at the physical time-frequency resource defined by the tuple (k_{16}, ℓ_{16}) after LSCE [CT07, Section 6.3] and dividing the sum by two to revert the WALSH function [3GP16f, Section 6.10.5.2]. Furthermore, in case of the eNodeB $\epsilon_b \in \mathbb{E}$ is equipped with four transmit AEs, the CTF representing the inhomogeneities of the mobile communication channel [Jun97, Section 3.2.1] between the ν -th receive AE at the UE $\mu_m \in \mathbb{U}$ for $1 \leq \nu \leq N_R^{(m)}$ and the transmit AP17 assigned to the third transmit AE according to the mapping function (2.19c) can be calculated analogously to the CTF between the ν -th receive AE at the UE $\mu_m \in \mathbb{U}$ and the transmit AP15 assigned to the first transmit AE at the eNodeB $\epsilon_b \in \mathbb{E}$ when replacing the tuple (k_{15}, ℓ_{15}) and (k_{16}, ℓ_{16}) by (k_{17}, ℓ_{17}) and (k_{18}, ℓ_{18}) , respectively. Moreover, the CTF representing the inhomogeneities of the mobile communication channel [Jun97, Section 3.2.1] between the ν -th receive AE at the UE $\mu_m \in \mathbb{U}$ for $1 \leq \nu \leq N_R^{(m)}$ and the transmit AP18 assigned to the fourth transmit AE according to the mapping function (2.19d) can be calculated analogously to the CTF between the ν -th receive AE at the UE $\mu_m \in \mathbb{U}$ and the transmit AP16 assigned to the second transmit AE at the eNodeB $\epsilon_b \in \mathbb{E}$ when replacing the tuple (k_{15}, ℓ_{15}) and (k_{16}, ℓ_{16}) by (k_{17}, ℓ_{17}) and (k_{18}, ℓ_{18}) , respectively.

2.6.3 Interference Suppression Receiver Implementation

The implementation of IS receivers, including the LMMSE-IRC and E-LMMSE-IRC receiver, both adapted for single-layer transmission, is discussed in this section when the desired signal is transmitted from the eNodeB $\epsilon_b \in \mathbb{A}_m$, whereas the interfering signals may be transmitted from one or multiple eNodeBs $\epsilon_{\tilde{b}} \in \mathbb{I}_m$. Both, the LMMSE-IRC and E-LMMSE-IRC receiver can suppress not only inter-stream interference, but also inter-cell interference when the number of receive AEs at the UE $\mu_m \in \mathbb{U}$ is higher than the number of desired streams [3GP12, Section 4.3]. For single-layer transmission, however, the MMSE component used to suppress inter-stream interference is not necessary [3GP12, Section 4.3]. Hence, the LMMSE-IRC and E-LMMSE-IRC receiver turns to the IRC and Enhanced IRC (E-IRC) receiver, respectively, with the aim to suppress the impact of inter-cell interference at the UE $\mu_m \in \mathbb{U}$ arising from the interfering eNodeBs $\epsilon_{\tilde{b}} \in \mathbb{I}_m$.

Following the concept of linear IS receivers [3GP14f, Section 7.2], the weight vector of the IS receiver is composed of a Decorrelating Filter (DF) and a Matched Filter (MF) which together form the DMF [Jun97, Section B.1.3], as discussed in Section 1.3.2 of this thesis. The weight vector of the IS receiver used to equalize the desired signal in the k -th subcarrier and ℓ -th OFDM symbol is denoted by $\underline{\mathbf{m}}_{\text{IS}} [k, \ell] \in \mathbb{C}^{N_{\text{R}}^{(m)} \times 1}$ and reads [Bai+11a, Section III]

$$\underline{\mathbf{m}}_{\text{IS}}^{\text{T}} [k, \ell] = \frac{(\underline{\mathbf{g}}^{(m,b)} [k, \ell])^{\text{H}} \left(\underline{\mathbf{R}}_{\Sigma}^{(m)} [k, \ell] \right)^{-\frac{1}{2}} \exp \left(j2\pi k \tau_{\text{TO}}^{(b)} f_s / N_{\text{OFDM}} \right)}{\sqrt{C^{(m,b)}} (\underline{\mathbf{g}}^{(m,b)} [k, \ell])^{\text{H}} \underline{\mathbf{g}}^{(m,b)} [k, \ell]}, \quad (2.65)$$

where $\underline{\mathbf{g}}^{(m,b)} [k, \ell] \in \mathbb{C}^{N_{\text{R}}^{(m)} \times 1}$ denotes the DMF [Jun97, Section B.1.3] and reads [Bai+11a, Section III]

$$\underline{\mathbf{g}}^{(m,b)} [k, \ell] = \left(\underline{\mathbf{R}}_{\Sigma}^{(m)} [k, \ell] \right)^{-\frac{1}{2}} \underline{\mathbf{g}}^{(m,b)} [k, \ell]. \quad (2.66)$$

Hence, the weight vector of the IS receiver $\underline{\mathbf{m}}_{\text{IS}} [k, \ell]$ in (2.65) can be simplified according to [Bai+11a, Section III]

$$\underline{\mathbf{m}}_{\text{IS}}^{\text{T}} [k, \ell] = \frac{(\underline{\mathbf{g}}^{(m,b)} [k, \ell])^{\text{H}} \left(\underline{\mathbf{R}}_{\Sigma}^{(m)} [k, \ell] \right)^{-1} \exp \left(j2\pi k \tau_{\text{TO}}^{(b)} f_s / N_{\text{OFDM}} \right)}{\sqrt{C^{(m,b)}} (\underline{\mathbf{g}}^{(m,b)} [k, \ell])^{\text{H}} \left(\underline{\mathbf{R}}_{\Sigma}^{(m)} [k, \ell] \right)^{-1} \underline{\mathbf{g}}^{(m,b)} [k, \ell]}, \quad (2.67)$$

where the covariance matrix $\underline{\mathbf{R}}_{\Sigma}^{(m)} [k, \ell]$ is always positive semi-definite and singular with probability equal to zero [Jun97, Section B.1.3] and reads

$$\underline{\mathbf{R}}_{\Sigma}^{(m)} [k, \ell] = \sum_{\{\bar{b} | \epsilon_{\bar{b}} \in \mathbb{I}_m\}} C^{(m,\bar{b})} \underline{\mathbf{g}}^{(m,\bar{b})} [k, \ell] \left(\underline{\mathbf{g}}^{(m,\bar{b})} [k, \ell] \right)^{\text{H}} + \sigma_m^2 \mathbf{I}_{N_{\text{R}}^{(m)}}. \quad (2.68)$$

Hence, the inverse of the covariance matrix $\underline{\mathbf{R}}_{\Sigma}^{(m)} [k, \ell]$ exists [Jun97, Section B.1.3]. Detail information on the properties of the covariance matrix $\underline{\mathbf{R}}_{\Sigma}^{(m)} [k, \ell]$ can be found in [Jun97, Section B.1.3]. Applying the IS receiver expressed by the weight vector $\underline{\mathbf{m}}_{\text{IS}} [k, \ell]$ in (2.67), the UE $\mu_m \in \mathbb{U}$ can theoretically suppress $N_{\text{R}}^{(m)} - 1$ interfering layers by projecting the interfering signals to a subspace that is orthogonal to the subspace the desired signal is projected on [Léo+12]. Equalizing the receive signal (2.62) with the IS receiver (2.67), the post-SNR $\gamma_{\text{post}}^{(m,b)} [k, \ell] \in \mathbb{R}$ of the complex-valued modulation symbol $\underline{\mathbf{d}}^{(b)} [k, \ell]$ transmitted by the eNodeB $\epsilon_b \in \mathbb{A}_m$ in the k -th subcarrier and ℓ -th OFDM symbol reads [Bai+11a, Section III]

$$\gamma_{\text{post}}^{(m,b)} [k, \ell] = C^{(m,b)} (\underline{\mathbf{g}}^{(m,b)} [k, \ell])^{\text{H}} \left(\underline{\mathbf{R}}_{\Sigma}^{(m)} [k, \ell] \right)^{-1} \underline{\mathbf{g}}^{(m,b)} [k, \ell], \quad (2.69)$$

when the impact of varying delays at the interfering eNodeBs $\epsilon_{\bar{i}} \in \mathbb{I}_m$ can be reverted. In what follows, the practical implementation of IS receivers is provided.

Following the concept of IRC receivers [3GP14f, Section 7.2], the covariance matrix including the sources of interference needs to be estimated [3GP12, Section 4.3]. Making use of the DMRSs transmitted in TM8, TM9 and TM10 [3GP16f, Table 7.1-5], the covariance matrix including the sources of inter-cell interference (2.68) is estimated at the UE $\mu_m \in \mathbb{U}$ according to [3GP12, Section 4.3]

$$\hat{\mathbf{R}}_{\Sigma, \text{DMRS}}^{(m)} [k, \ell] = \frac{1}{|\mathcal{S}_{i, n_{\text{PRB}}, \text{DMRS}}^{(b, 7)}|} \cdot \sum_{(k', \ell') \in \mathcal{S}_{i, n_{\text{PRB}}, \text{DMRS}}^{(b, 7)}} \tilde{\mathbf{r}}^{(m)} [k', \ell'] \left(\tilde{\mathbf{r}}^{(m)} [k', \ell'] \right)^{\text{H}}, \quad (2.70)$$

where of $\tilde{\mathbf{r}}^{(m)} [k', \ell']$ is defined by [3GP12, Section 4.3]

$$\tilde{\mathbf{r}}^{(m)} [k', \ell'] = \mathbf{r}^{(m)} [k', \ell'] - \hat{\mathbf{g}}_{\text{DMRS}}^{(m, b)} [k, \ell] \mathbf{d}^{(b)} [k', \ell'], \quad (2.71)$$

while the ν -th element of $\hat{\mathbf{g}}_{\text{DMRS}}^{(m, b)} [k, \ell]$ represents the estimated and precoded CTF among the ν -th receive AE at the UE $\mu_m \in \mathbb{U}$ and $N_{\text{T}}^{(b)}$ transmit AEs at the eNodeB $\epsilon_b \in \mathbb{E}$ in the k -th subcarrier and ℓ -th OFDM symbol weighted with the average receive power (1.14) and the subcarrier specific phase shift $\exp(j2\pi k \tau_{\text{TO}}^{(b)} f_s / N_{\text{OFDM}})$ for $1 \leq \nu \leq N_{\text{R}}^{(m)}$ when making use of the LSCE scheme discussed in Section 2.6.2 of this thesis. To ensure the best trade-off between low cross correlation among the components of $\tilde{\mathbf{r}}^{(m)} [k', \ell']$ in (2.71) and frequency selective fading [Iwe+14g, Section III-B], the covariance matrix (2.70) remains unchanged for the subframe and PRB the (ℓ', k') -th RE out of the set $\mathcal{S}_{i, n_{\text{PRB}}, \text{DMRS}}^{(b, 7)}$ are transmitted on, such that

$$\left\lfloor \frac{k'}{N_{\text{sc}}^{\text{RB}}} \right\rfloor \cdot N_{\text{sc}}^{\text{RB}} \leq k < \left(\left\lfloor \frac{k'}{N_{\text{sc}}^{\text{RB}}} \right\rfloor + 1 \right) \cdot N_{\text{sc}}^{\text{RB}} \quad (2.72)$$

holds. Detail information on the covariance matrix estimation using the DMRSs can be found in [Bai+12, Section III-C]. Hence, the weight vector for the practical implementation of the IRC receiver making use of the DMRS-based covariance matrix estimation is denoted by $\mathbf{m}_{\text{IRC}} [k, \ell]$ and reads [3GP12, Section 4.3]

$$\mathbf{m}_{\text{IRC}}^{\text{T}} [k, \ell] = \frac{\left(\hat{\mathbf{g}}_{\text{DMRS}}^{(m, b)} [k, \ell] \right)^{\text{H}} \left(\hat{\mathbf{R}}_{\Sigma, \text{DMRS}}^{(m)} [k, \ell] \right)^{-1}}{\left(\hat{\mathbf{g}}_{\text{DMRS}}^{(m, b)} [k, \ell] \right)^{\text{H}} \left(\hat{\mathbf{R}}_{\Sigma, \text{DMRS}}^{(m)} [k, \ell] \right)^{-1} \hat{\mathbf{g}}_{\text{DMRS}}^{(m, b)} [k, \ell]}. \quad (2.73)$$

The performance of the IRC receiver with weight vector (2.73) is discussed in Section 2.10 of this thesis.

In case of TM6 where the DMRSs are not transmitted [3GP16g, Table 7.1-5], the covariance matrix including the desired effective channel and the sources of inter-cell interference is estimated at the UE $\mu_m \in \mathbb{U}$ for each subcarrier k within the respective PRB for $0 \leq n_{\text{PRB}} < N_{\text{RB}}^{\text{DL}}$ [3GP16f, Section 6.2.3] and OFDM symbol ℓ within the respective subframe for $0 \leq \ell < 2 \cdot N_{\text{symb}}^{\text{DL}}$ [3GP16f, Section 4.1] by evaluating the physical time-frequency resources carrying the PDSCH according to [3GP12, Section 4.3]

$$\hat{\mathbf{R}}_{\Sigma, \text{PDSCH}}^{(m)} [k, \ell] = \frac{1}{\left| \mathcal{S}_{i, n_{\text{PRB}}, \text{TM6}}^{(b, N_{\text{T}}^{(b)})} \right|} \cdot \sum_{(k', \ell') \in \mathcal{S}_{i, n_{\text{PRB}}, \text{TM6}}^{(b, N_{\text{T}}^{(b)})}} \mathbf{r}^{(m)} [k', \ell'] \left(\mathbf{r}^{(m)} [k', \ell'] \right)^{\text{H}} \quad (2.74)$$

to ensure the best trade-off the cross correlation among the components of $\mathbf{r}^{(m)} [k', \ell']$ and distortion caused by frequency selective fading [Jun97, Section 3.3.2]. Detail information on the covariance matrix estimated from the physical time-frequency resources used for PDSCH transmission can be found in [3GP12, Section 4.3]. Making use of the equivalence of the IRC and MMSE receiver for single-layer transmission [Bai+11a, Section III], for the sake of lower implementation complexity the MMSE receiver adapted for single-layer transmission making use of PDSCH physical time-frequency resource based covariance matrix estimation (2.74), denoted by $\mathbf{m}_{\text{MMSE}} [k, \ell]$, is used to equalize the receive signal and reads [3GP12, Section 4.3]

$$\mathbf{m}_{\text{MMSE}}^{\text{T}} [k, \ell] = \left(\hat{\mathbf{H}}_{\text{CRS}}^{(m, b)} [k, \ell] \cdot \underline{\mathbf{p}}^{(b)} [k, \ell] \right)^{\text{H}} \left(\hat{\mathbf{R}}_{\Sigma, \text{PDSCH}}^{(m)} [k, \ell] \right)^{-1}. \quad (2.75)$$

The performance of the MMSE receiver with weight vector (2.75) is discussed in Section 2.10 of this thesis.

Following the concept of the E-IRC receiver [3GP14f, Section 7.2], the covariance matrix including the sources of inter-cell interference is determined by making use of explicit knowledge of the CTF of the interfering effective channels and reads [3GP14f, Section 7.2; Iwe+16, Section III-B]

$$\hat{\mathbf{R}}_{\Sigma, \text{expl.}}^{(m)} [k, \ell] = \sum_{\{\tilde{b} | \epsilon_{\tilde{b}} \in \mathbb{I}_m\}} \hat{\mathbf{g}}_{\text{DMRS}}^{(m, \tilde{b})} [k, \ell] \left(\hat{\mathbf{g}}_{\text{DMRS}}^{(m, \tilde{b})} [k, \ell] \right)^{\text{H}} + \mathbf{R}_{\Delta}^{(m)} [k, \ell], \quad (2.76)$$

where

$$\mathbf{R}_{\Delta}^{(m)} [k, \ell] = \frac{1}{\left| \mathcal{S}_{i, n_{\text{PRB}}, \text{DMRS}}^{(b, \gamma)} \right|} \cdot \sum_{(k', \ell') \in \mathcal{S}_{i, n_{\text{PRB}}, \text{DMRS}}^{(b, \gamma)}} \check{\mathbf{r}}^{(m)} [k', \ell'] \left(\check{\mathbf{r}}^{(m)} [k', \ell'] \right)^{\text{H}}, \quad (2.77)$$

and

$$\underline{\mathbf{r}}^{(m)} [k', \ell'] = \mathbf{r}^{(m)} [k', \ell'] - \sum_{\{\tilde{b} | \epsilon_{\tilde{b}} \in \mathbb{I}_m\}} \hat{\mathbf{g}}_{\text{DMRS}}^{(m, \tilde{b})} [k', \ell'] \underline{d}^{(\tilde{b})} [k', \ell'] \quad (2.78)$$

holds for the i -th subframe for $0 \leq i \leq 9$ [3GP16f, Section 4.1] and n_{PRB} -th PRB for $0 \leq n_{\text{PRB}} < N_{\text{RB}}^{\text{DL}}$ [3GP16f, Section 6.2.3], assuming that the UE $\mu_m \in \mathbb{U}$ has knowledge on the complex-valued modulation symbol $\underline{d}^{(\tilde{b})} [k', \ell']$ transmitted by the interfering eNodeB $\epsilon_b \in \mathbb{I}_m$. The desired effective CTF $\hat{\mathbf{g}}_{\text{DMRS}}^{(m, b)} [k, \ell]$ among the UE $\mu_m \in \mathbb{U}$ and the eNodeB $\epsilon_b \in \mathbb{A}_m$, as well as the interfering effective CTFs $\hat{\mathbf{g}}_{\text{DMRS}}^{(m, \tilde{b})} [k, \ell]$ among the UE $\mu_m \in \mathbb{U}$ and the eNodeBs $\epsilon_{\tilde{b}} \in \mathbb{I}_m$ can be estimated using the JLSCE scheme, discussed in Section 2.6.2 of this thesis. The practical implementation of the E-IRC receiver making use of explicit knowledge of the interfering effective channels can be obtained from (2.73) when replacing $\hat{\mathbf{R}}_{\Sigma, \text{DMRS}}^{(m)} [k, \ell]$ by $\hat{\mathbf{R}}_{\Sigma, \text{expl.}}^{(m)} [k, \ell]$. As a result, the weight vector for the practical implementation of the E-IRC receiver making use of explicit knowledge of the interfering effective channels is denoted by $\underline{\mathbf{m}}_{\text{E-IRC}} [k, \ell]$ and reads [3GP14f, Section 7.2; Iwe+16, Section III-B]

$$\underline{\mathbf{m}}_{\text{E-IRC}}^{\text{T}} [k, \ell] = \frac{\left(\hat{\mathbf{g}}_{\text{DMRS}}^{(m, b)} [k, \ell] \right)^{\text{H}} \left(\hat{\mathbf{R}}_{\Sigma, \text{expl.}}^{(m)} [k, \ell] \right)^{-1}}{\left(\hat{\mathbf{g}}_{\text{DMRS}}^{(m, b)} [k, \ell] \right)^{\text{H}} \left(\hat{\mathbf{R}}_{\Sigma, \text{expl.}}^{(m)} [k, \ell] \right)^{-1} \hat{\mathbf{g}}_{\text{DMRS}}^{(m, b)} [k, \ell]}. \quad (2.79)$$

The performance of the E-IRC receiver with weight vector (2.79) is discussed in Section 2.10 of this thesis.

2.6.4 Interference Cancellation Receiver Implementation

The implementation of the ASLIC receiver adapted for single-layer transmission which enables dynamic switching between IS and SLIC is discussed in this section when the desired signal is transmitted from the eNodeB $\epsilon_b \in \mathbb{A}_m$, whereas the interfering signals may be transmitted from one or multiple eNodeBs $\epsilon_{\tilde{b}} \in \mathbb{I}_m$.

Equalizing the desired and interfering signal using the linear IS receiver, the post-SNR of the desired and interfering complex-valued modulation symbol, respectively, changes constantly due to the movement of the UE and the inhomogeneities of the mobile communication channel [Jun97, Section 3.2.1]. Hence, the post-SNR of the desired complex-valued modulation symbol in an arbitrary but fix physical time-frequency resource used for PDSCH transmission might be greater than the post-SNR of the interfering complex-valued modulation symbol in the same physical time-frequency resource or vice versa [Mol05,

Section 18.4]. According to this, the conventional SLIC receiver [3GP14f, Section 7.4] is extended to the ASLIC receiver [Iwe+16, Section III-C].

Following the concept of the optimal detection ordering [Wol+98, Section 3.1], the UE $\mu_m \in \mathbb{U}$ calculates the post-SNR of the complex-valued modulation symbol $\underline{d}^{(b)} [k, \ell]$ transmitted by the eNodeB $\epsilon_b \in \mathbb{A}_m$ and the post-SNR of each of the complex-valued modulation symbol $\underline{d}^{(\tilde{b})} [k, \ell]$ transmitted by the eNodeB $\epsilon_{\tilde{b}} \in \mathbb{I}_m$ by exploiting the estimated CTFs $\hat{\underline{g}}_{\text{DMRS}}^{(m,b)} [k, \ell]$ and $\hat{\underline{g}}_{\text{DMRS}}^{(m,\tilde{b})} [k, \ell]$ after JLSCE [Iwe+16, Section III-C], discussed in Section 2.6.2 of this thesis with subsequent covariance matrix computation in the k -th subcarrier and ℓ -th OFDM symbol [3GP14f, Section 7.5]. The information on the physical layer cell-identities of each interfering eNodeB $\epsilon_b \in \mathbb{I}_m$, being mandatory to perform the JLSCE at the UE $\mu_m \in \mathbb{U}$, is provided through the network [3GP14f, Section 7.6]. If the complex-valued modulation symbol $\underline{d}^{(b)} [k, \ell]$ transmitted by the eNodeB $\epsilon_b \in \mathbb{A}_m$ has the largest post-SNR, $\underline{d}^{(b)} [k, \ell]$ is equalized using the E-IRC receiver [Iwe+16, Section III-C]. In the other case, if the complex-valued modulation symbol $\underline{d}^{(\tilde{b})} [k, \ell]$ has the largest post-SNR, IC on symbol level is carried out [Iwe+16, Section III-C], as specified in the next three steps.

- (1) The complex-valued modulation symbol $\underline{d}^{(\tilde{b})} [k, \ell]$, transmitted by the eNodeB $\epsilon_{\tilde{b}} \in \mathbb{I}_m$, is mapped on the closest constellation point out of the set \mathbb{V}_{QPSK} , $\mathbb{V}_{16\text{QAM}}$, or $\mathbb{V}_{64\text{QAM}}$ after equalization, depending on the modulation mapping scheme applied at the interfering eNodeB [Iwe+16, Section III-C]. The information on the modulation mapping scheme at the eNodeB $\epsilon_{\tilde{b}} \in \mathbb{I}_m$ is provided to the UE $\mu_m \in \mathbb{U}$ through the network [3GP14f, Section 7.5].
- (2) The de-mapped complex-valued modulation symbol is multiplied with the estimated interfering effective channel $\hat{\underline{g}}_{\text{DMRS}}^{(m,\tilde{b})} [k, \ell]$ and subtracted from the complex-valued OFDM baseband signal representation of the receive signal after OFDM demodulation [Iwe+16, Section III-C]. The cleaned-up complex-valued OFDM baseband signal representation of the receive signal after OFDM demodulation is updated by [Iwe+16, Section III-C] $\underline{\mathbf{r}}^{(m)} [k, \ell] - \hat{\underline{g}}_{\text{DMRS}}^{(m,\tilde{b})} [k, \ell] \hat{\underline{d}}^{(\tilde{b})} [k, \ell]$.
- (3) Assuming the impact of inter-cell interference caused by the eNodeB $\epsilon_{\tilde{b}} \in \mathbb{I}_m$ has been reliably canceled, the post-SNR of the remaining complex-valued modulation symbols is recalculated [Iwe+16, Section III-C]. The process is repeated from (1) if the complex-valued modulation symbol $\underline{d}^{(\tilde{b})} [k, \ell]$, transmitted by the eNodeB $\epsilon_{\tilde{b}} \in \mathbb{I}_m$ has largest post-SNR and terminates if the complex-valued modulation symbol $\underline{d}^{(b)} [k, \ell]$, transmitted by eNodeB $\epsilon_b \in \mathbb{A}_m$ has largest post-SNR [Iwe+16, Section III-C]. In the latter case the possibly remaining impact of inter-cell

interference is aimed to be suppressed by the E-IRC receiver [Iwe+16, Section III-C].

An error while mapping the equalized complex-valued modulation symbol $\underline{d}^{(b)}[k, \ell]$ on the closest constellation point results in the fact that the cleaned-up OFDM baseband signal representation of the receive signal after OFDM demodulation is updated incorrectly and this error propagates through all further iterations in the ASLIC receiver [TV05, Section 8.3.2]. Consequently, the mistakenly considered cleaned-up OFDM baseband signal of the receive signal after OFDM demodulation suffers from more instead of less inter-cell interference [Mol05, Section 18.4]. Further information on error propagation can be found in [Mol05, Section 18.4; TV05, Section 8.3.2]. The performance of the ASLIC receiver is discussed in Section 2.10 of this thesis.

2.7 Aperiodic CSI Reporting

2.7.1 Introduction

LTE systems enable the support of ten TMs [3GP16g, Section 7.1], including TM1 to TM10 [3GP16g, Table 7.1-5] when the PDSCH transmission is configured by the Cell - Radio Network Temporary Identifier (RNTI) (C-RNTI). The C-RNTI is an UE identifier allocated by a controlling Radio Network Controller (RNC) [3GP15f, Section C]. Detail information on the C-RNTI can be found in [3GP16g, Section 7.1]. To enable cooperative interference mitigation signal precoding and signal reception enhancements, identified in Section 1.5.2 and Section 1.5.3 of this thesis, respectively, the properties of TM6, TM8, TM9 and TM10 with respect to implicit feedback generation are focused on. The properties of TM1 to TM5 and TM7 are not discussed in this thesis. Detail information on TM1 to TM5 and TM7 can be found in [3GP16g, Chapter 7].

LTE systems support aperiodic CSI reporting [3GP16g, Section 7.2.1] and periodic CSI reporting [3GP16g, Section 7.2.2]. Aperiodic CSI reports are delivered when explicitly requested by the network, whereas periodic CSI reports are configured by the network to be delivered within a certain period [DPS14, Section 13.7.3.1]. In this thesis aperiodic CSI reporting is focused on. Detail information on periodic CSI reporting can be found in [3GP16g, Section 7.2.2]. Aperiodic CSI reporting is further subdivided into reporting modes for CQI and PMI feedback [3GP16g, Section 7.2.1; 3GP16g, Table 7.2.1-1]. In this thesis Mode 1-2 for CSI reporting is focused on. The properties of the other supported reporting modes for CQI and PMI feedback, tabularized in [3GP16g, Table 7.2.1-1] can be found in [3GP16g, Section 7.2.1]. CSI reporting Mode 1-2 is characterized by the multiple PMI and the wideband CQI feedback type

[3GP16g, Section 7.2.1-1]. The multiple PMI feedback type in turn is characterized by the fact that for each subband a preferred PMI is selected by the UE $\mu_m \in \mathbb{U}$ from the codebook which is aimed to be used by the eNodeB $\epsilon_b \in \mathbb{A}_m$ [3GP16g, Section 7.2.1]. The report of the selected PMI for each subband depends on the TM. The subband PMI selection criterion used in this thesis is discussed in Section 2.7.2 of this thesis. Subband PMI reporting schemes adapted for TM6, TM8 and TM9 are discussed in Section 2.7.3, whereas the benefits of subband PMI reporting in TM10 are discussed in Section 2.7.4 of this thesis. Moreover, the wideband CQI feedback type is characterized by the fact that the UE $\mu_m \in \mathbb{U}$ is aimed to report one CQI per codeword which is calculated assuming the use of the corresponding selected PMI in each subband [3GP16g, Section 7.2.1]. The aspect of CQI feedback is not discussed in this thesis. Detail information on CQI feedback can be found in [3GP16g, Section 7.2; STB11, Section 10.2; Gho+11, Section 9.2]. A practical implementation for the wideband CQI feedback scheme is discussed in [Gho+11, Section 9.2.1].

2.7.2 Subband PMI Feedback

To alleviate the antenna specific fading, the UE $\mu_m \in \mathbb{U}$ measures the instantaneous channel condition and, based on this, selects a precoding vector with corresponding PMI from the codebook [Bai+10, Section III]. Among the investigated PMI selection criteria in [Bai+10, Section III], the maximum post-SNR based PMI selection has been found to be the most suitable one [Bai+10, Section III-C]. Following the concept of the maximum post-SNR based PMI selection criterion, the UE $\mu_m \in \mathbb{U}$ selects the precoding vector with corresponding PMI which maximizes the post-SNR of the complex-valued modulation symbol $\underline{d}^{(b)} [k, \ell]$ after equalization with the IS receiver [Bai+10, Section III-C]. Extending the maximum post-SNR based PMI selection criterion of [Bai+10, Section III-C] to meet the requirements for subband PMI reporting and single-layer transmission, the UE $\mu_m \in \mathbb{U}$ selects the precoding vector with corresponding PMI which maximizes the average post-SNR per subframe in the w -th subband, defined by

$$\bar{\gamma}_{\text{post}}^{(m,b)} [w] = \frac{1}{N_{\text{syb}}^{\text{DL}}} \sum_{\ell=0}^{2N_{\text{syb}}^{\text{DL}}-1} \sum_{k \in \mathcal{S}_{\text{SB}}^{(w)}} \gamma_{\text{post}}^{(m,b)} [k, \ell], \quad (2.80)$$

where $\mathcal{S}_{\text{SB}}^{(w)}$ denotes the set of subcarriers in the w -th subband [3GP16g, Table 7.2.1-3] for $0 \leq w < N_{\text{SB}}$, where N_{SB} represents the number of subbands [3GP16g, Section 7.2.1]. The precoding vector with corresponding PMI, maximizing the average post-SNR in the respective subband and subframe, is

determined by [Bai+13a, Section III]

$$\underline{\mathbf{p}}^{(b)} [k, \ell] = \arg \max_{\underline{\mathbf{q}}_j^{(b)} [k, \ell], j \in \mathcal{S}_{\text{PMI}, N_T^{(b)}}} \overline{\gamma}_{\text{post}}^{(m,b)} [w], \quad (2.81)$$

where the set of indices is equal to $\mathcal{S}_{\text{PMI}, 2}$ and $\mathcal{S}_{\text{PMI}, 4}$ for $N_T^{(b)}$ equal to two and four is defined in (2.32) and (2.33), respectively. Moreover, $\underline{\mathbf{q}}_j^{(b)} [k, \ell]$ in (2.81) denotes the precoding vector with corresponding PMI equal to j out of one of the aforementioned sets to be used by the eNodeB $\epsilon_b \in \mathbb{A}_m$ in the k -th subcarrier and ℓ -th OFDM symbol [3GP16g, Section 7.2.1]. Replacing $\overline{\gamma}_{\text{post}}^{(m,b)} [w]$ in (2.81) by (2.80) and using the definition of the post-SNR in (2.69), the precoding vector selection in (2.81) turns to

$$\underline{\mathbf{p}}^{(b)} [k, \ell] = \arg \max_{\underline{\mathbf{q}}_j^{(b)} [k, \ell], j \in \mathcal{S}_{\text{PMI}, N_T^{(b)}}} \left(\underline{\mathbf{q}}_j^{(b)} [k, \ell] \right)^{\text{H}} \cdot \left(\underbrace{\sum_{\ell=0}^{2N_{\text{synd}}^{\text{DL}}-1} \sum_{k \in \mathcal{S}_{\text{SB}}^{(w)}} \left(\left(\underline{\mathbf{H}}^{(m,b)} [k, \ell] \right)^{\text{H}} \left(\underline{\mathbf{R}}_{\Sigma}^{(m)} [k, \ell] \right)^{-1} \underline{\mathbf{H}}^{(m,b)} [k, \ell] \right)}_{\underline{\mathbf{R}}_{\text{T}}^{(m)}}} \right) \underline{\mathbf{q}}_j^{(b)} [k, \ell], \quad (2.82)$$

where $\underline{\mathbf{R}}_{\text{T}}^{(m)} \in \mathbb{C}^{N_T^{(b)} \times N_T^{(b)}}$ denotes the transmit covariance matrix [Bai+13a, Section III] experienced by the UE $\mu_m \in \mathbb{U}$ in the w -th subband for $0 \leq w < N_{\text{SB}}$ [3GP16g, Table 7.2.1-3] and i -th subframe for $0 \leq i \leq 9$ [3GP16f, Section 4.1]. Following the properties of multiple PMI selection [3GP16g, Section 7.2.1], the UE $\mu_m \in \mathbb{U}$ feeds the PMI of the corresponding precoding vector in (2.82) back to the eNodeB, where the complex-valued modulation symbols carrying data and - if transmitted - DMRSs within the respective subband and subframe are aimed to be precoded with that precoding vector, as described in Section 2.4.3 of this thesis.

Note that for the precoding vector selection scheme in (2.82) it is assumed that the covariance matrix $\underline{\mathbf{R}}_{\Sigma}^{(m)} [k, \ell]$ is known to the UE $\mu_m \in \mathbb{U}$. As the covariance matrix $\underline{\mathbf{R}}_{\Sigma}^{(m)} [k, \ell]$ in (2.82) depends on the interfering effective channels $\underline{\mathbf{g}}^{(m, \tilde{b})} [k, \ell]$ which in turn depend on the precoding vectors $\underline{\mathbf{p}}^{(\tilde{b})} [k, \ell]$ selected by the interfering eNodeBs out of the set \mathbb{I}_m , in a practical implementation, however, the UE $\mu_m \in \mathbb{U}$ has no knowledge on the instantaneous realization of the covariance matrix $\underline{\mathbf{R}}_{\Sigma}^{(m)} [k, \ell]$. Practical precoding vector selection schemes exploiting the RSs transmitted in TM6, TM8, TM9 and TM10 are discussed in what follows.

2.7.3 Aperiodic CSI Reporting in TM6, TM8 and TM9

Practical subband PMI selection schemes in TM6, TM8 and TM9 have in common that the impact of inter-cell interference is not considered during the precoding vector selection [Bad+12b, Section III-B]. The reason is that the UE $\mu_m \in \mathbb{U}$ has no knowledge on the precoding vectors for subband PMI selection the UE $\mu_{\tilde{m}} \in \mathbb{U}$ is intended to select for the upcoming subframes and vice versa for $m \neq \tilde{m}$. As the precoding vectors might change from subframe to subframe [3GP16g, Section 7.2.1], the knowledge on the covariance matrix of the previous subframe might be outdated and, thus cannot be used for $\underline{\mathbf{R}}_{\Sigma}^{(m)} [k, \ell]$ in (2.82). Following [Bad+12b, Section III-B], in this thesis the covariance matrix $\underline{\mathbf{R}}_{\Sigma}^{(m)} [k, \ell]$ is set to the thermal noise power over the received bandwidth multiplied with the $N_{\text{R}}^{(m)} \times N_{\text{R}}^{(m)}$ identity matrix for signal transmission in TM6, TM8 and TM9. In that case the UE $\mu_m \in \mathbb{U}$ tries to maximize the receive signal power of the desired signal regardless the choice of the precoding vectors for subband PMI selection among the interfering eNodeBs $\epsilon_{\tilde{b}} \in \mathbb{I}_m$ what is equivalent in maximizing the post-SNR at the output of the MF receiver without taking the impact of inter-cell interference into account [Bad+12b, Section III-B].

In TM6 and TM8 the CSI reporting shall derive the channel measurement for computing the PMI per subband based on the CRSs, whereas in TM9 the CSI-RSs shall be exploited [3GP16g, Section 7.2.3, Section 7.2.4]. As a result, the transmit covariance matrix $\underline{\mathbf{R}}_{\text{T}}^{(m)}$ in (2.82) turns to

$$\underline{\mathbf{R}}_{\text{T}}^{(m)} = \frac{1}{\sigma_m^2} \cdot \begin{cases} \sum_{\ell=0}^{2N_{\text{symp}}^{\text{DL}}-1} \sum_{k \in \mathcal{S}_{\text{SB}}^{(w)}} \left(\hat{\underline{\mathbf{H}}}_{\text{CRS}}^{(m,b)} [k, \ell] \right)^{\text{H}} \hat{\underline{\mathbf{H}}}_{\text{CRS}}^{(m,b)} [k, \ell] & \text{for TM6, TM8} \\ \sum_{\ell=0}^{2N_{\text{symp}}^{\text{DL}}-1} \sum_{k \in \mathcal{S}_{\text{SB}}^{(w)}} \left(\hat{\underline{\mathbf{H}}}_{\text{CSI-RS}}^{(m,b)} [k, \ell] \right)^{\text{H}} \hat{\underline{\mathbf{H}}}_{\text{CSI-RS}}^{(m,b)} [k, \ell] & \text{for TM9} \end{cases}, \quad (2.83)$$

where the CTF $\hat{\underline{\mathbf{H}}}_{\text{CSI-RS}}^{(m,b)} [k, \ell]$ is equal to the estimated CTF $\hat{\underline{\mathbf{H}}}_{\text{CSI-RS}}^{(m,b)} [n_{\text{PRB}}]$ for $n_{\text{PRB}} \cdot N_{\text{sc}}^{\text{RB}} \leq k < (n_{\text{PRB}} + 1) \cdot N_{\text{sc}}^{\text{RB}}$, $0 \leq n_{\text{PRB}} < N_{\text{RB}}^{\text{DL}}$ [3GP16g, Section 6.2.3] and $0 \leq \ell < 2 \cdot N_{\text{symp}}^{\text{DL}}$ [3GP16f, Section 4.1]. Inserting (2.83) into (2.82), the post-SNR at the output of the MF receiver is typically larger than the post-SNR at the output of the IS receiver.

If the physical layer cell-identity modulo six of the eNodeB $\epsilon_b \in \mathbb{A}_m$ is equal to the physical layer cell-identity modulo six of the interfering eNodeB $\epsilon_{\tilde{b}} \in \mathbb{I}_m$,

the CRSs transmitted by the eNodeB $\epsilon_b \in \mathbb{A}_m$ and $\epsilon_{\tilde{b}} \in \mathbb{I}_m$ are transmitted on the same physical time-frequency resources for $b \neq \tilde{b}$. On the other hand, if the physical layer cell-identity modulo six of the eNodeB $\epsilon_b \in \mathbb{A}_m$ is not equal to the physical layer cell-identity modulo six of the interfering eNodeB $\epsilon_{\tilde{b}} \in \mathbb{I}_m$, the CRSs transmitted by the eNodeB $\epsilon_b \in \mathbb{A}_m$ are transmitted on the same physical time-frequency resources the interfering eNodeB $\epsilon_{\tilde{b}} \in \mathbb{I}_m$ uses to transmit the complex-valued modulation symbols carrying the codewords for $b \neq \tilde{b}$. Obviously, in a practical LTE network the estimate $\hat{\mathbf{H}}_{\text{CRS}}^{(m,b)}[k, \ell]$ is not free of inter-cell interference, such that reliable aperiodic CSI reporting in TM6 and TM8 might be limited.

Furthermore, in case of CSI reporting in TM9, in this thesis it is assumed that the CSI configuration at the eNodeB $\epsilon_b \in \mathbb{A}_m$ is different to the CSI configuration at the interfering eNodeB $\epsilon_{\tilde{b}} \in \mathbb{I}_m$ for $b \neq \tilde{b}$. Hence, the CSI-RSs for aperiodic CSI reporting transmitted by eNodeB $\epsilon_b \in \mathbb{A}_m$ are transmitted on the same physical time-frequency resources as the interfering complex-valued modulation symbols carrying the codewords that are transmitted by eNodeB $\epsilon_{\tilde{b}} \in \mathbb{I}_m$ for $b \neq \tilde{b}$. Hence, despite the different CSI configuration among the eNodeB $\epsilon_b \in \mathbb{A}_m$ and $\epsilon_{\tilde{b}} \in \mathbb{I}_m$, the estimate $\hat{\mathbf{H}}_{\text{CSI-RS}}^{(m,b)}[k, \ell]$ is not free of inter-cell interference. Consequently, reliable aperiodic CSI reporting in TM9 might be limited. Note that the transmission of the CSI-RSs in TM9 makes it possible to limit the transmission of the CRSs on one transmit AP, rather than on $N_{\text{T}}^{(b)}$ transmit APs and, hence, one transmit AE rather than $N_{\text{T}}^{(b)}$ transmit AEs for $N_{\text{T}}^{(b)}$ equal to two and four. Displacing the CSI reporting from CRSs to CSI-RSs for signal transmission in TM9 enables to decrease the code rate for both, two and four transmit AEs, as denoted in Table B.2.

2.7.4 Aperiodic CSI Reporting in TM 10

To enable aperiodic CSI reporting in TM10, the UE $\mu_m \in \mathbb{U}$ shall derive the channel measurements for computing the PMI based on the CSI-RSs [3GP16g, Section 7.2.4; 3GP16g, Section 7.2.3]. Two major enhancements compared with TM6, TM8 and TM9 that are of particular importance for this thesis are supported in TM10 and enable the UE $\mu_m \in \mathbb{U}$ to

- estimate the CTF $\hat{\mathbf{H}}_{\text{CSI-RS}}^{(m,\tilde{b})}[n_{\text{PRB}}]$ among itself and the interfering eNodeBs by making use of the CSI-Interference Measurement (IM) [3GP16g, Section 7.2.6] and to
- receive the desired complex-valued modulation symbols from multiple eNodeBs $\epsilon_b \in \mathbb{A}_m$ [3GP16g, Section 7.2.1; 3GP13a, Section 5.1.3].

Following the concept of the CSI-IM, the CTF $\hat{\mathbf{H}}_{\text{CSI-RS}}^{(m,\bar{b})}[n_{\text{PRB}}]$, representing the inhomogeneities of the mobile communication channel between the UE $\mu_m \in \mathbb{U}$ and the interfering eNodeB $\epsilon_{\bar{b}} \in \mathbb{I}_m$ in the n_{PRB} -th PRB, can be estimated if the UE $\mu_m \in \mathbb{U}$ is configured with multiple CSI-IM configurations [3GP16g, Section 7.2.6; DPS14, Section 15.2.1.1]. Detail information on CSI-IM can be found in [3GP16g, Section 7.2.6; DPS14, Section 15.2.1.1]. As a result, the covariance matrix in (2.82) turns to

$$\begin{aligned} \hat{\mathbf{R}}_{\Sigma, \text{CSI-RS}}^{(m)}[k, \ell] = & \\ & \sum_{\{\bar{b} | \epsilon_{\bar{b}} \in \mathbb{I}_m\}} \left(\hat{\mathbf{H}}_{\text{CSI-RS}}^{(m,\bar{b})}[k, \ell] \underline{\mathbf{p}}^{(\bar{b})}[k, \ell] \left(\hat{\mathbf{H}}_{\text{CSI-RS}}^{(m,\bar{b})}[k, \ell] \underline{\mathbf{p}}^{(\bar{b})}[k, \ell] \right)^{\text{H}} \right) + \sigma_m^2 \mathbf{I}_{N_{\text{R}}}^{(m)}. \end{aligned} \quad (2.84)$$

The major difference to the covariance matrix used in TM6, TM8 and TM9 is that the UE $\mu_m \in \mathbb{U}$ may calculate the aperiodic CSI feedback in TM10 based on the CTFs of the current subframe rather than the CTFs of the previous subframe by making assumptions on the precoding vector selected by the interfering eNodeBs $\epsilon_{\bar{b}} \in \mathbb{I}_m$ [Bad+12b, Section III-B] and, thus, enable cooperative interference mitigation signal precoding [Iwe+15b, Section III-A]. A detailed discussion on cooperative interference mitigation signal precoding is provided in Section 3.3 of this thesis.

2.8 Signal Propagation

2.8.1 Introduction

The transmit waves traveling from each eNodeB $\epsilon_b \in \mathbb{E}$ to the UE $\mu_m \in \mathbb{U}$ do not propagate uniformly but experience different modification including diffractions, reflections and scattering [Jun97, Section 3.2.1]. Moreover, besides the desired signal transmitted by the eNodeB $\epsilon_b \in \mathbb{A}_m$, the UE $\mu_m \in \mathbb{U}$ receives the interfering signal from each eNodeB $\epsilon_{\bar{b}} \in \mathbb{I}_m$ [Jun97, Section 3.2.2]. To evaluate the performance of mobile communication systems in presence of inter-cell interference, the mobile communication channel and the interference profile needs to be modeled [Mol05, Section 7.1]. Following [3GP06, Section A.1.3] and [3GP12, Section 6.2], respectively, channel models for the MIMO antenna configuration and the interference profiles are provided. In what follows the properties of one selected channel model for MIMO antenna configuration and interference profile used in this thesis is discussed in Section 2.8.2 and Section 2.8.3, respectively. Detail information on channel modeling for mobile communication systems is not provided in this thesis. Detail

information on channel modeling for mobile communication can be found in [Jun97, Chapter 3; Mol05, Chapter 7; SL05, Chapter 2; Stü11, Chapter 2].

2.8.2 Channel Model Properties

The MIMO channel models in [3GP06, Section A.1.3] denote tapped delay-line models for multiple antennas with correlation parameters derived from fixed angular parameters and assumed antenna pattern [Eri06]. Among the four MIMO channel models in [3GP06, Section A.1.3], in this thesis the Spatial Channel Model (SCM) Type B (SCM-B) is selected. The SCM-B is a geometry-based channel model for the urban macro scenario where the UE $\mu_m \in \mathbb{U}$ is represented by a handset in data position [3GP06, Table A.1.3-1]. An illustration of the UE $\mu_m \in \mathbb{U}$ used in data position can be found in [Eri06, Figure 2]. Detail information in the remaining MIMO channel models including the SCM Type A, SCM Type C and SCM Type D can be found in [3GP06, Table A.1.3-2], [3GP06, Table A.1.3-4] and [3GP06, Table A.1.3-5], respectively.

The SCM-B is modeled by six main taps where each of the six main taps contains three mid paths [3GP06, Table A.1.3-3]. The total per-tap covariance matrix for the SCM-B is defined by the KRONECKER multiplication [Bro+01, Section 4.1.5.9] of the spatial correlation matrix at the eNodeB $\epsilon_b \in \mathbb{E}$ and the polarization covariance matrix, weighted with the mean power of the time dependent coefficient for the respective tap [Eri06]. Following the properties of the total per-tap covariance matrix for the SCM-B in [3GP06, Section A.1.3], the eNodeB $\epsilon_b \in \mathbb{E}$ and the UE $\mu_m \in \mathbb{U}$ is assumed to be equipped with $N_T^{(b)}$ equal to four transmit AEs and $N_R^{(m)}$ equal to two receive AEs, respectively. To enable signal transmission from two transmit AEs at eNodeB $\epsilon_b \in \mathbb{E}$, the spatial correlation matrix for the SCM-B in [3GP06, Section A.1.3] has to be replaced by the scalar value one [3GP16n, Section B.2.3.1]. The mean power of the time-dependent coefficient and delay is denoted in the second and third column of [3GP06, Table A.1.3-3], respectively. Moreover, as the spatial correlation per mid path is very similar to the spatial correlation of the respective main tap, the spatial correlation of the respective main tap shall be used for the corresponding three mid paths [Eri06, Section A] and is denoted in the fourth column of [3GP06, Table A.1.3-3]. The polarization matrix of the respective tap is denoted in the fifth column of [3GP06, Table A.1.3-3].

Characteristic parameters to describe the short-term statistic of mobile communication channels include the [Jun97, Chapter 3]

- multipath spread,
- Power Delay Profile (PDP),

- delay spread,
- coherence bandwidth and the
- coherence time.

The multipath spread denotes the maximum time difference among two different paths [Jun97, Section 3.2.1]. The multipath spread is denoted by τ_{MS} and reads

$$\tau_{\text{MS}} = 4.625 \mu\text{s} \quad (2.85)$$

for the SCM-B [3GP06, Table A.1.3-3]. Comparing the multipath spread of the SCM-B in (2.85) with the length of the CP (2.50), it becomes obvious that $\tau_{\text{MS}} < \tau_{\text{CP},\ell}$ holds for $0 \leq \ell \leq 6$ such that the impact of ISI can be averted by the CP. However, taking the practical limitations including unsynchronized signal transmission discussed in Chapter 4 of this thesis into account, a TO larger than the difference of the length of the CP and the multipath spread resulting in 583.3 ns and 63.5 ns will introduce ISI on the signal received by the UE $\mu_m \in \mathbb{U}$ for the zeroth and the remaining six OFDM symbols in each slot, respectively.

The PDP represents the average power of the waves received by the UE $\mu_m \in \mathbb{U}$ with a delay τ . The average power of the waves and the delay is denoted in the second and third column of [3GP06, Table A.1.3-3], respectively for the SCM-B.

The delay spread is defined by the square root of the normalized second-order central moment of the PDP multiplied by two [Jun97, Section 3.5.9] and denotes the average time spread of a dirac impulse transmitted over the mobile communication channel [Jun97, Section 3.2.1]. The delay spread is denoted by τ_{DS} and reads [Jun97, Section 3.5.9]

$$\tau_{\text{DS}} = 0.52 \mu\text{s} \quad (2.86)$$

for the SCM-B [3GP06, Table A.1.3-3].

The coherence bandwidth of the mobile communication channel denotes the range of frequencies over which the mobile communication channel can be considered as spectrally flat [Jun97, Section 3.3.3]. The coherence bandwidth of the mobile communication channel is smaller than or equal to the inverse of the multipath spread [Jun97, Section 3.3.3]. Moreover, the coherence bandwidth of the mobile communication channel is approximately equal to the inverse of the eightfold delay spread [Jun97, Section 3.3.3] and reads

$$B_c = 240.3 \text{ kHz} \quad (2.87)$$

Table 2.4. Interference profile based on averaged set of unconditional median DIP values (created by the author of this thesis using [3GP12, Table 6.3-1]).

Index i	Average unconditional DIP value $z_{\text{DIP},i}/\text{dB}$	Interference to Noise Ratio $\gamma_{\text{INR}}^{(m,\tilde{b}_i)}/\text{dB}$
1	-3.2	3.2
2	-7.0	1.3
3	-11.6	0.5
4	-14.1	0.2
5	-16.1	0.2
6	-17.5	0.1
7	-19.3	0.1
8	-20.7	0.1

for the SCM-B [3GP06, Table A.1.3-3]. Following the findings achieved in Section 1.2.5 of this thesis, the next-lowest integer number of PRBs smaller than or equal to the coherence bandwidth of the SCM-B (2.87) is equal to one. For this reason, the covariance matrix (2.71) and (2.74) is determined by evaluating the respective precoded DMRSs and the precoded complex-valued modulation symbols carrying the codewords in that PRB, respectively.

The coherence time of the mobile communication channel denotes the time that must elapse such that the state of the mobile communication channel changes completely [Jun97, Section 3.3.3]. The coherence time of the mobile communication channel is approximately equal to the inverse of the DOPPLER spread [Jun97, Section 3.5.11].

2.8.3 Interference Properties

To investigate the impact of inter-cell interference on the DL performance, an interference model has to be determined [3GP12, Section 6.1]. The interference model suggested in [3GP12, Section 6] is developed to assess the performance of IS receivers in the DL and defines two types of interference profiles including the interference profile based on median values [3GP12, Section 6.3] and the interference profile based on the weighted average throughput gain [3GP12, Section 6.4]. The former interference profile can be further subdivided into

the interference profile based on averaged unconditional median Dominant Interferer Proportion (DIP) values [3GP12, Section 6.3.1] and the interference profile based on the averaged conditional median DIP values [3GP12, Section 6.3.2].

Both, the interference profile based on averaged unconditional median DIP values [3GP12, Section 6.3.2] and the interference profile based on weighted average throughput gain [3GP12, Section 6.4] are defined for dedicated geometries $G^{(m)}$. In contrast to this, the interference profile based on averaged unconditional median DIP values does not impose any restriction on the geometry $G^{(m)}$ and is therefore considered in this thesis to investigate the impact of inter-cell interference for cooperative interference mitigation signal precoding and signal reception enhancements using CoMP transmission. Neither the interference profile based on averaged conditional median DIP values nor the interference profile based on weighted average throughput gain is considered in this thesis. Detail information on the former and latter interference profile can be found in [3GP12, Section 6.3.2] and [3GP12, Section 6.4], respectively. In what follows, the properties of the interference profile based on the averaged unconditional median DIP values are discussed.

The DIP is defined as the ratio of the average power of the interfering signal of a given interfering eNodeB (1.16) over the accumulated average power of the interfering signals transmitted by the eNodeBs out of the set \mathbb{I}_m (1.17) plus the thermal noise power over the received bandwidth (1.18) [3GP12, Section 6.2]. The DIP of the interfering eNodeB $\epsilon_{\tilde{b}_i} \in \mathbb{I}_m$ is denoted by $z_{\text{DIP},i}$ and reads [3GP12, Section 6.2]

$$z_{\text{DIP},i} = \frac{C^{(m,\tilde{b}_i)}}{\sum_{j=1}^{|\mathbb{I}_m|} C^{(m,\tilde{b}_j)} + \sigma_m^2} \quad (2.88)$$

for $1 \leq i \leq |\mathbb{I}_m|$. To investigate the impact of inter-cell interference on the DL performance, the average power of the interfering signal of a given interfering eNodeB out of the set \mathbb{I}_m has to be determined from (2.88). Making use of matrix-vector calculus [ZF92, Section 5.10], the average power of the interfering signal transmitted by the interfering eNodeB out of the set \mathbb{I}_m reads

$$\begin{pmatrix} C^{(m,\tilde{b}_1)} \\ \vdots \\ C^{(m,\tilde{b}_i)} \\ \vdots \\ C^{(m,\tilde{b}_{|\mathbb{I}_m|})} \end{pmatrix} = -\sigma_m^2 \left(\left(\underbrace{\begin{pmatrix} \underline{z}_{\text{DIP}} & \cdots & \underline{z}_{\text{DIP}} \end{pmatrix}_{|\mathbb{I}_m| \text{-times}} \right) - \mathbf{I}_{|\mathbb{I}_m|} \right)^{-1} \cdot \underline{z}_{\text{DIP}}, \quad (2.89)$$

where $\mathbf{I}_{|\mathbb{I}_m|}$ denotes the $|\mathbb{I}_m| \times |\mathbb{I}_m|$ identity matrix. Moreover, $\underline{z}_{\text{DIP}}$ in (2.89) is

defined by

$$\underline{z}_{\text{DIP}} = (z_{\text{DIP},1}, \dots, z_{\text{DIP},i}, \dots, z_{\text{DIP},|\mathbb{I}_m|})^T, \quad (2.90)$$

with the DIP values in descending order such that

$$C^{(m,\tilde{b}_1)} \geq \dots \geq C^{(m,\tilde{b}_i)} \geq \dots \geq C^{(m,\tilde{b}_{|\mathbb{I}_m|})} \quad (2.91)$$

holds.

The interference profile based on the average set of unconditional median DIP values is tabularized in Table 2.4 on page 117. The first column of Table 2.4 denotes the index i of the respective interfering eNodeB out of the set \mathbb{I}_m . The second column of Table 2.4 represents the average unconditional DIP values in logarithmic scale in descending order. The third column denotes the Interference Noise Ratio (INR) in logarithmic scale. The INR is defined by the average power of the interfering signal of a given interfering eNodeB (1.16) divided by the thermal noise power over the received bandwidth (1.18) [Lap05, page 358] and reads

$$\gamma_{\text{INR}}^{(m,\tilde{b}_i)} = \frac{C^{(m,\tilde{b}_i)}}{\sigma_m^2} \quad (2.92)$$

for $1 \leq i \leq |\mathbb{I}_m|$. Following [3GP12, Section 9], two interfering eNodeBs causing strongest inter-cell interference shall be considered. Taking $|\mathbb{I}_m|$ equal to eight interfering eNodeBs [3GP12, Table 6.3-1], the impact of inter-cell interference arising from the last six interfering eNodeBs in Table 2.4 can therefore be ignored. As a result, the cutout of the macro cellular deployed LTE network, depicted in Figure 1.3 and discussed in Section 1.2.4 of this thesis can continue to be used.

2.9 Quality Criterion

Mobile communication systems are designed to enable reliable and efficient signal transmission [Jun97, Section 2.2.5]. To verify the performance of LTE systems, performance metrics such as power consumption, sensitivity, BER, Block Error Rate (BLER), throughput, bandwidth efficiency and handover success can be measured [STB11, Section 20.4.1]. In this thesis, the DL performance of LTE systems is measured by its probability of decoding errors, such that the performance metrics including the BER, BLER, throughput and bandwidth efficiency are discussed in what follows. Performance metrics including power consumption, sensitivity and handover success are not discussed in this thesis.

The probability of a bit error is the BER [LC04, Section 1.7] and can be further subdivided into coded BER and uncoded BER. The coded BER is defined as

the probability that a decoded information bit at the output of the channel decoder is in error [LC04, Section 1.7] and is denoted by $P_{b,\text{coded}}$. The coded BER is calculated by putting the number of faulty decoded information bits at the output of the channel decoder in relation with the number of transmitted information bits [LC04, Section 1.7]. Analogously, the uncoded BER is defined as the probability that an information bit is in error without passing the channel decoding chain and is denoted by $P_{b,\text{uncoded}}$. The uncoded BER is calculated by putting the number of faulty decoded information bits that did not pass the channel decoding chain into relation with the number of transmitted information bits. A closed form expression to calculate the uncoded BER for any QAM with GRAY coding for AWGN channels can be found in [Kam08, Section 11.4.6]. The respective performance in terms of uncoded BER over SNR for QPSK, 16QAM and 64QAM symbols transmitted over AWGN channels can be found in [Stü11, Figure 5.13].

The BLER is defined as the probability that a decoded TB at the output of the channel decoder is in error [LC04, Section 1.7] and is defined by P_B . The BLER is calculated by putting the number of faulty decoded TBs into relation with the number of transmitted TBs [LC04, Section 1.7]. As the error detection is provided in each TB through a CRC [3GP16d, Section 5.3.2.1], the UE $\mu_m \in \mathbb{U}$ is able to determine whether the TB is decoded correctly or not by evaluating the attached CRC [LC04, Section 5.10]. The TB is assumed to be correctly decoded by the UE $\mu_m \in \mathbb{U}$ if all N_{TBS} bits of the TB and the N_{CRC24A} bits attached to the TB are decoded correctly, such that

$$P_B = 1 - (1 - P_{b,\text{coded}})^{(N_{\text{TBS}} + N_{\text{CRC24A}})} \quad (2.93)$$

holds for the BLER [TSS10, Section II]. The TB is decoded erroneously if at least one bit within the TB or CRC is decoded erroneously [TSS10, Section II].

The throughput is defined as the number of information bits transferred in one direction from the eNodeB $\epsilon_b \in \mathbb{A}_m$ to the UE $\mu_m \in \mathbb{U}$ per unit time [3GP15f, Section T] and is denoted by $\mathcal{G}^{(m)}$. The throughput can be calculated from the complementary BLER weighted with the TBS for the selected MCS for the duration of one subframe and reads [3GP15f, Section T]

$$\mathcal{G}^{(m)} = \frac{(1 - P_B) \cdot N_{\text{TBS}}}{T_{\text{subframe}}} \quad (2.94)$$

The bandwidth efficiency mentioned in Section 1.1.4 of this thesis is defined as the throughput (2.94) per channel bandwidth assigned to the UE $\mu_m \in \mathbb{U}$

and reads [Stü11, Section 1.7.1]

$$\eta_{\text{eff}}^{(m)} = \frac{\mathcal{G}^{(m)}}{f_{\text{BW}}^{(m)}}. \quad (2.95)$$

In a NL and ideal communication system the DL performance experienced by the UE $\mu_m \in \mathbb{U}$ in terms of BER, BLER, throughput and spectral efficiency, depends on the average SNR when the signal transmission is not affected by systematic perturbation such as signal distortion and channel estimation errors [Jun97, Section 2.3.3]. Motivated by the fact that the bandwidth efficiency (2.95) represents the number of information bits per unit time and bandwidth [Stü11, Section 1.7.1; 3GP16g, Section 7.1.7.2.1], in this thesis the SNR is defined as the accumulated average receive power of the desired signal over the thermal noise power over the received bandwidth [TV05, Section 3.1.1] and reads

$$\gamma_{\text{SNR}}^{(m)} = \frac{C^{(m)}}{\sigma_m^2}. \quad (2.96)$$

Note that the SNR (2.96) can be derived from the geometry $G^{(m)}$ (1.13) when setting the accumulated receive power of the interfering signals experienced by the UE $\mu_m \in \mathbb{U}$ equal to zero. As the accumulated average receive power of the desired signal differs from the thermal noise over the received bandwidth by several orders of magnitude, the SNR in logarithmic scale is selected, such that [Jun97, Section 2.3.3]

$$\gamma_{\text{SNR}}'^{(m)} = 10 \log_{10} \left(\gamma_{\text{SNR}}^{(m)} \right) = 10 \log_{10} \left(\frac{C^{(m)}}{\sigma_m^2} \right) \quad (2.97)$$

holds. As the throughput is proportional to the complementary BLER (2.93), which in turn depends on the SNR, increasing the SNR (2.96) will reduce the BER and BLER and, hence, increase the throughput (2.94) while keeping the channel bandwidth assigned to the UE $\mu_m \in \mathbb{U}$ unchanged. The bandwidth efficiency (2.95) increases analogously. Note that the throughput is upper-bounded by the maximum number of information bits within a TB [3GP16g, Table 7.1.7.2.1-1].

The SNR to guarantee an arbitrary but fix bandwidth efficiency in an ideal communication system has to be enlarged to guarantee the same bandwidth efficiency in a practical communication system due to signal distortion caused by, amongst others, inter-cell interference and channel estimation effects [Jun97, Section 2.3.3]. Analogously, for an arbitrary but fix SNR, the expected bandwidth efficiency in an ideal communication system is typically larger than in a practical communication system.

To take the impact of the code rate (2.42) and the channel bandwidth into

account, the bandwidth efficiency (2.95) is considered as the most meaningful metric to evaluate the different interference mitigation capabilities throughout this thesis.

2.10 Performance Evaluation

Numerical results at the link level are carried out to demonstrate the impact of inter-cell interference on the DL performance at the UE $\mu_m \in \mathbb{U}$ operating in TM6, TM8 and TM9 and to investigate the interference mitigation capabilities of the IS and ASLIC receiver, discussed in Section 2.6.3 and Section 2.6.4 of this thesis, respectively. The assumed simulation parameters are summarized in Table 2.5 on page 127. Among all MCSs, in this thesis the numerical results at the link level are carried out for three MCSs including MCS4, MCS14 and MCS25 making use of the QPSK, the 16 QAM and the 64 QAM mapping scheme with a code rate R_c of approximately equal to 1/3, 1/2 and 3/4, respectively, as denoted in Table B.2 on page 245. The obtained simulation results in terms of SNR over bandwidth efficiency for the investigated TMs and receiver configuration are depicted in Figure 2.8 – Figure 2.10 on page 128 – 133. The performance is evaluated at 90% of the maximum bandwidth efficiency of each MCS and reads

$$\eta_{\text{BW}, 90\%, x}^{(m)} = 0.9 \cdot \eta_{\text{BW}, \text{max}, x}^{(m)} \approx \begin{cases} 0.33 \text{ bit/s/Hz} & \text{for } x = 4 & (2.98a) \\ 1.17 \text{ bit/s/Hz} & \text{for } x = 14, & (2.98b) \\ 2.55 \text{ bit/s/Hz} & \text{for } x = 25 & (2.98c) \end{cases}$$

where $\eta_{\text{BW}, \text{max}, x}^{(m)}$ denotes the maximum bandwidth efficiency for single-layer transmission for a channel bandwidth equal to 10 MHz and is determined by 0.36 bit/s/Hz, 1.29 bit/s/Hz and 2.83 bit/s/Hz for the MCS with index x equal to 4, 14 and 25, respectively [3GP16g, Table 7.1.7.2.1-1].

The performance of the interference mitigation capabilities in IL single-layer transmission in TM6 for the 4×2 and the 2×2 MIMO antenna configuration is depicted in Figure 2.8 for MCS4, MCS14 and MCS25, where the receive signal is equalized using the MCS and the MMSE receiver (2.75). The Maximum Ratio Combining (MRC) receiver is a special form of the IS receiver, where the covariance matrix $\underline{\mathbf{R}}_y^{(m)}[k, \ell]$ is set to the thermal noise power over the received bandwidth multiplied with the $N_R^{(m)} \times N_R^{(m)}$ identity matrix [Jun97, Section B.1.2 - B.1.3]. Hence, the weight vector of the MRC receiver is matched to the receive signal transmitted over the mobile communication channel with desired effective channel $\underline{\mathbf{g}}^{(m,b)}[k, \ell]$ to maximize the post-SNR in the k -th subcarrier and ℓ -th OFDM symbol [Jun97, Section B.1.2]. The upper bound

in terms of SNR over bandwidth efficiency is represented by the NL single-layer transmission for the 4×2 and the 2×2 MIMO antenna configuration, as depicted in Figure 2.8 for MCS4, MCS14 and MCS25. It should be pointed out that the 4×2 MIMO antenna configuration provides a performance gain of 1.7 dB, 1.7 dB and 1.5 dB over the respective 2×2 MIMO antenna configuration for MCS4, MCS14 and MCS25, respectively, although the code rate for the former antenna configuration is higher than the code rate for the latter configuration, as denoted in Table B.2 on page 245 for any MCS. The reason for this is that the number of CRSs transmitted per PRB increases from 16 to 24 when increasing the number of transmit AEs at the eNodeB $\epsilon_b \in \mathbb{A}_m$ from two to four [3GP16f, Section 6.10.1.2]. As a result, the number of REs carrying the complex-valued modulation symbols to be transmitted, represented by (B.2), decreases, as denoted in Table B.1 on page 239 for TM6. Hence, the performance gain results from the improved beamforming capabilities when doubling the number of transmit AEs at the eNodeB $\epsilon_b \in \mathbb{A}_m$ from two to four, as discussed in Section 2.4.3 and Appendix A of this thesis. The previously mentioned beamforming gain can be hardly observed in the IL single-layer transmission in TM6, when signal equalization is carried out with the MRC receiver or the MMSE receiver (2.75). In case of IL single-layer transmission in TM6 with signal equalization using the MRC receiver, the bandwidth efficiency $\eta_{\text{BW}, 90\%, x}^{(m)}$ for the 4×2 MIMO antenna configuration is almost equal to the 2×2 MIMO antenna configuration for the MCS with index x equal to 4, 14 and 25, as depicted in Figure 2.8. In that case, the enhanced beamforming gain of the 4×2 MIMO antenna configuration does not predominate the lower error protection. Regarding the SNR over bandwidth efficiency for the investigated MCSs for IL single-layer transmission in TM6, the MMSE receiver (2.75) outperforms the MRC receiver only in case of MCS4 for both, the 4×2 and the 2×2 MIMO antenna configuration. Following the structure of the covariance matrix $\hat{\mathbf{R}}_{\Sigma, \text{PDSCCH}}^{(m)}[k, \ell]$ in (2.75) and the interference properties discussed in Section 2.8.3 of this thesis, the condition number [ZF86, Section 25.5] of that covariance matrix increases as the SNR increases. In that case the covariance matrix might get ill-conditioned such that equalizing the receive signal with the MMSE receiver (2.75) might introduce a scaling on the equalized modulation symbols. Regarding the signal detection capabilities, in contrast to the 16 QAM and the 64 QAM mapping scheme, the QPSK modulation mapping scheme is not susceptible to scaling [Kam08, Section 9.1.1], such that despite the practical limitations of the MMSE receiver (2.75), the advantages over the MRC receiver can be exploited for IL single-layer transmission in TM6, as depicted in Figure 2.8 (a). However, in case of the 16 QAM and the 64 QAM mapping scheme, used for MCS14 and MCS25, respectively, the advantages of the MMSE receiver (2.75) can no longer be observed for single-layer transmission in TM6, as depicted in Figure 2.8 (b) and Figure 2.8 (c). Note that the impact of signal scaling becomes so crucial for

MCS25 such that in case of signal equalization for IL single-layer transmission in TM6 using the MMSE receiver (2.75), the bandwidth efficiency is equal to zero for both, the 4×2 and the 2×2 MIMO antenna configuration, as depicted in Figure 2.8 (c).

The performance of the interference mitigation capabilities in IL single-layer transmission in TM8 for the 4×2 and the 2×2 MIMO antenna configuration is depicted in Figure 2.9 for MCS4, MCS14 and MCS25, where the receive signal is equalized using the MRC receiver and the IRC receiver (2.73). The properties for the upper bound, represented by the NL single-layer transmission in TM8 can be taken over analogously to the previously discussed NL single-layer transmission in TM6. In contrast to the limited interference suppression capabilities in the IL single-layer transmission in TM6 using the MMSE receiver (2.75), the impact of inter-cell interference can be reliably mitigated in IL single-layer transmission in TM8 by making use of the IRC receiver (2.73). Compared with the MRC receiver, making use of the aforementioned IRC receiver provides a gain of 7.9 dB, 7.7 dB and 5.5 dB for MCS4, MCS14 and MCS25, as depicted in Figure 2.9 (a), Figure 2.9 (b) and Figure 2.9 (c), respectively, for the 4×2 MIMO antenna configuration. The major reason for the performance gain of the IRC receiver is that the covariance matrix including the sources of interference can be estimated more reliably when evaluating the complex-valued modulation symbols carrying the precoded DMRSs rather than the precoded complex-valued modulation symbols carrying the codewords, such that the weight vector enabling to project the interfering signals to a subspace that is orthogonal to the subspace the desired signal is projected on, can be determined more reliably. Moreover, in contrast to interference mitigation in IL single-layer transmission in TM6 using the MMSE receiver (2.75), the covariance matrix (2.68) and its estimate (2.70) strive towards a diagonal matrix for high SNR values, as the receive power of the interfering signals decreases. Consequently, the covariance matrix is not ill-conditioned and the IRC receiver (2.73) turns to the MRC receiver for $\gamma_{\text{SNR}}^{(m)} \rightarrow \infty$, such that reliable signal detection for the investigated MCSs supporting the QPSK, the 16 QAM and the 64 QAM mapping scheme can be guaranteed, as depicted in Figure 2.9. However, the beamforming gain which can be observed for the NL single-layer transmission in TM8 for any of the investigated MCSs when doubling the number of transmit AEs from two to four at eNodeB $\epsilon_b \in \mathbb{A}_m$ can be slightly observed in case of IL single-layer transmission in TM8 only for MCS4 and MCS14, but not in case of MCS25 for signal equalization using the IRC receiver (2.73), as depicted in Figure 2.9.

The performance of the interference mitigation capabilities in IL single-layer transmission in TM9 for the 4×2 and the 2×2 MIMO antenna configuration is depicted in Figure 2.10 for MCS4, MCS14 and MCS25, where the receive signal is equalized using the MRC receiver, the IRC receiver (2.73), the E-IRC

receiver (2.79) and the ASLIC receiver, discussed in Section 2.6.4 of this thesis. The properties for the upper bound, represented by the NL single-layer transmission in TM9 can be taken over analogously to the previously discussed NL single-layer transmission in TM6. The ASLIC receiver outperforms the E-IRC receiver, the IRC receiver and the MRC receiver in the IL single-layer transmission in TM9 by 2.1 dB, 1.5 dB and 10.5 dB, respectively, for the 4×2 MIMO antenna configuration, as depicted in Figure 2.10 (a). The respective gain for the 2×2 MIMO antenna configuration can be inferred from Figure 2.10 (a) analogously. Due to the low code rate of MCS4 of approximately equal to $1/3$, the error protection is high, such that the maximum bandwidth efficiency of the IRC receiver can be reached at comparatively low SNR values compared with the required SNR to reach the maximum bandwidth efficiency for MCS14 and MCS25, as depicted in Figure 2.10. Following the findings achieved in Section 2.8.3 of this thesis, the respective average power of the interfering signal is much larger than the average power of the desired signal, such that the interfering signal can be reliably detected and subtracted from the receive signal on the symbol level. Analogously, regarding the SNR over bandwidth efficiency for IL single-layer transmission for MCS14 and MCS25, depicted in Figure 2.10 (b) and Figure 2.10 (c), respectively, the gain of the ASLIC receiver vanishes as reliable signal detection of the interfering signals with subsequent interference cancellation cannot be guaranteed and turns to error propagation at the symbol level. As a result, making use of the ASLIC receiver for signal equalization is only advantageous for low MCSs such that the impact of inter-cell interference can be canceled out reliably at the symbol level. Comparing the performance of the E-IRC receiver and the IRC receiver for signal equalization for IL single-layer transmission in TM9, it can be observed that the IRC receiver performs approximately equal to the E-IRC receiver in case of MCS14 for both, the 4×2 and the 2×2 MIMO antenna configuration, as depicted in Figure 2.10 (b) and outperforms the E-IRC receiver in case of MCS4 and MCS25, as depicted in Figure 2.10 (a) and Figure 2.10 (c), respectively, for the 4×2 and the 2×2 MIMO antenna configuration. Following the achieved numerical results for IL single-layer transmission in TM9 when the receive signal is equalized with the E-IRC receiver, it can be observed that the maximum bandwidth efficiency cannot be reached for MCS25 for neither the 4×2 nor the 2×2 MIMO antenna configuration, as depicted in Figure 2.10 (c). Obviously, the impact of frequency selective fading of the selected SCM-B is too crucial, such that making use of the JLSCE scheme for channel estimation and linear channel interpolation, discussed in Section 2.6.2 of this thesis, is not accurate enough to estimate the desired and interfering effective CTF to set the receive filter (2.79) up and equalize the receive signal for a code rate of approximately equal to $3/4$.

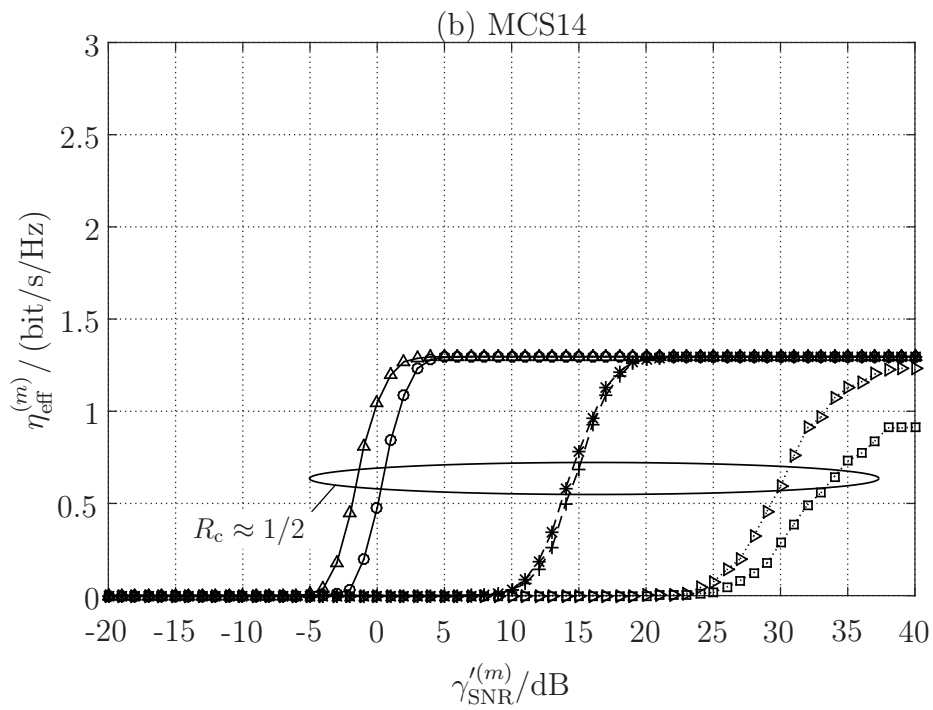
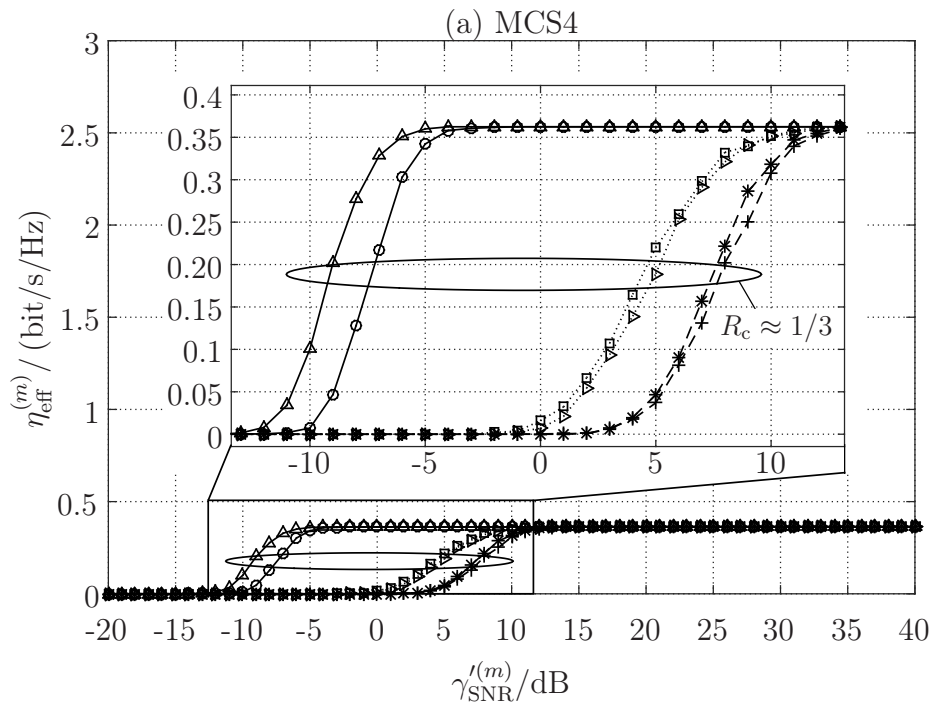
Although in contrast to IL single-layer transmission in TM6 the impact of inter-

cell interference can be considerably limited by any of the investigated MCSs and MIMO antenna configuration for IL single-layer transmission in TM8 and TM9 when making use of the IRC receiver (2.73), the gap to the upper bound is still remarkable and reads e.g. 9.6 dB and 8.1 dB for MCS25, as depicted in Figure 2.10 (c) for the 4×2 MIMO antenna configuration, respectively. Opportunities to improve the signal detection capabilities at the UE $\mu_m \in \mathbb{U}$ by making use of cooperative signal precoding schemes and CoMP transmission to further limit the impact of inter-cell interference in synchronized LTE networks are discussed in the next chapter of this thesis.

Following the findings achieved in this section, it is sufficient to limit the investigation on the IRC receiver (2.73), rather than the E-IRC receiver (2.79), as the former one provides the same or even better performance than the latter one without any side information on the interfering eNodeBs $\epsilon_{\bar{b}} \in \mathbb{I}_m$.

Table 2.5. Simulation Parameters (created by the author of this thesis).

Parameter	Value
General Parameters:	
Channel Bandwidth	$f_{\text{BW}}^{(m)} = 10 \text{ MHz}$
Channel Model	SCM-B
Transmission Mode	TM6, TM8, and TM9
Interference Profile	according to Section 2.8.3 with $\gamma_{\text{INR}}^{(m, \tilde{b}_1)} = 3.2 \text{ dB}$, $\gamma_{\text{INR}}^{(m, \tilde{b}_2)} = 1.3 \text{ dB}$
Timing Offset	Synchronized transmission with $\tau_{\text{TO}}^{(m, b_1)} = \tau_{\text{TO}}^{(m, \tilde{b}_1)} = \tau_{\text{TO}}^{(m, \tilde{b}_2)} = 0 \text{ }\mu\text{s}$
Base Stations:	
Set of base stations the desired signal is transmitted from	$\mathbb{A}_m = \{\epsilon_{b_1}\}$
Set of base stations the interfering signal is transmitted from	$\mathbb{I}_m = \{\epsilon_{\tilde{b}_1}, \epsilon_{\tilde{b}_2}\}$
Number of transmit AEs at the base stations	$N_{\text{T}}^{(b_1)} = N_{\text{T}}^{(\tilde{b}_1)} = N_{\text{T}}^{(\tilde{b}_2)} \in \{4, 2\}$
MCS	4, 14 and 25 at eNodeB $\epsilon_{b_1} \in \mathbb{A}_m$, random MCS selection at eNodeBs $\epsilon_{\tilde{b}_1}$ and $\epsilon_{\tilde{b}_2}$
Channel Coding	Turbo Coding [3GP16d, Section 5]
UE:	
Channel Estimation	LSCE, JLSCE
Receiver	MRC, IRC, E-IRC, ASLIC
Channel Decoding	Turbo Decoding [Jun97, Section E.3]
Number of Receive AEs	$N_{\text{R}}^{(m)} = 2$
CSI Reporting	Subband PMI Feedback



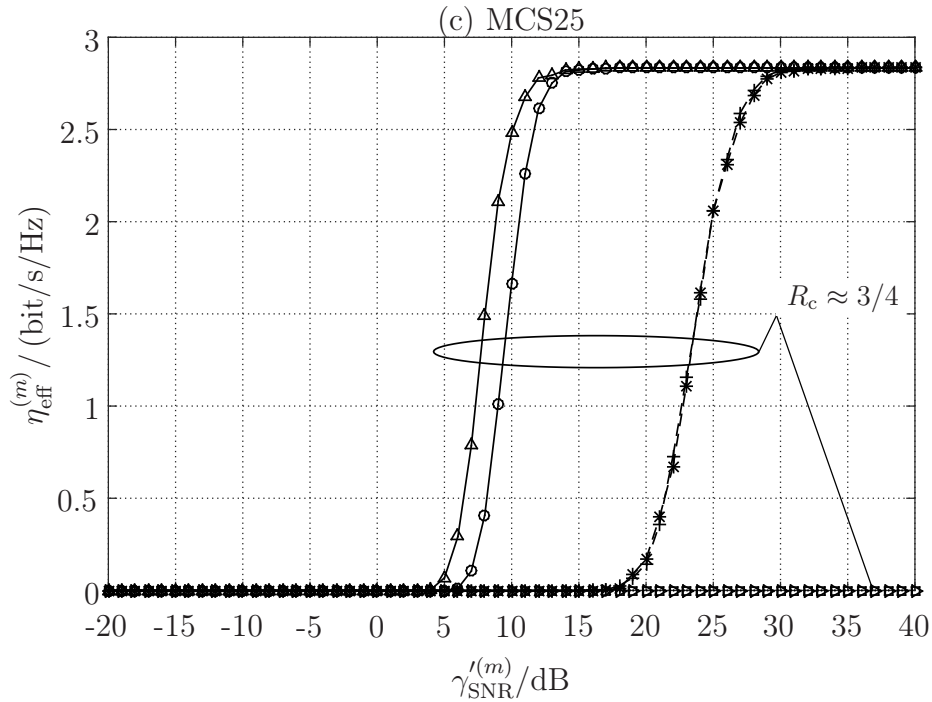
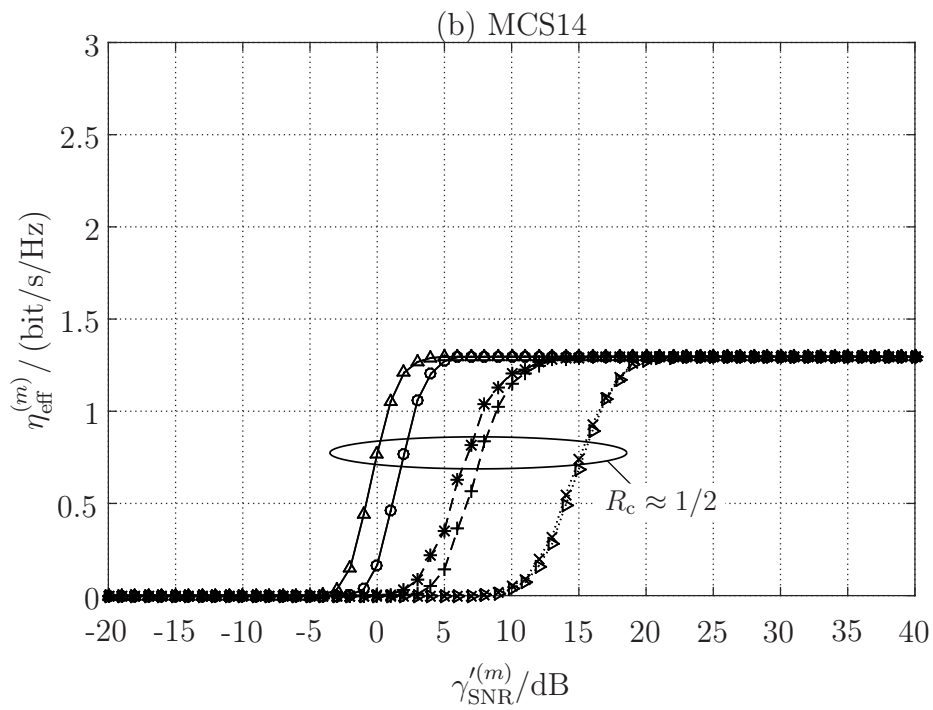
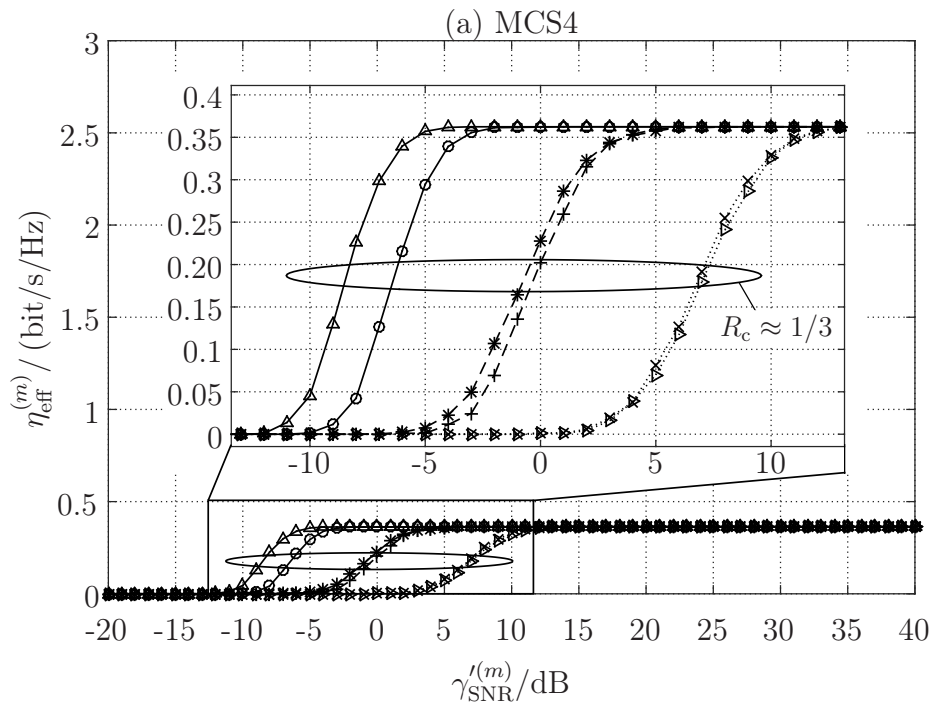


Figure 2.8. Performance for single-layer transmission in TM6 for (a) MCS4, (b) MCS14 and (c) MCS25 (legend see Table 2.6; created by the author of this thesis).

Table 2.6. Legend for Figure 2.8 (a) – (c).

<ul style="list-style-type: none"> —△— 4 × 2 MIMO —○— 2 × 2 MIMO 	NL single-layer transmission with the $N_T^{(b)} \times N_R^{(m)}$ MIMO antenna configuration and signal equalization using the MRC receiver
<ul style="list-style-type: none"> -*- 4 × 2 MIMO -+- 2 × 2 MIMO 	IL single-layer transmission with the $N_T^{(b)} \times N_R^{(m)}$ MIMO antenna configuration and signal equalization using the MRC receiver
<ul style="list-style-type: none"> ⋯□⋯ 4 × 2 MIMO ⋯▷⋯ 2 × 2 MIMO 	IL single-layer transmission with the $N_T^{(b)} \times N_R^{(m)}$ MIMO antenna configuration and signal equalization using the MMSE receiver (2.75)



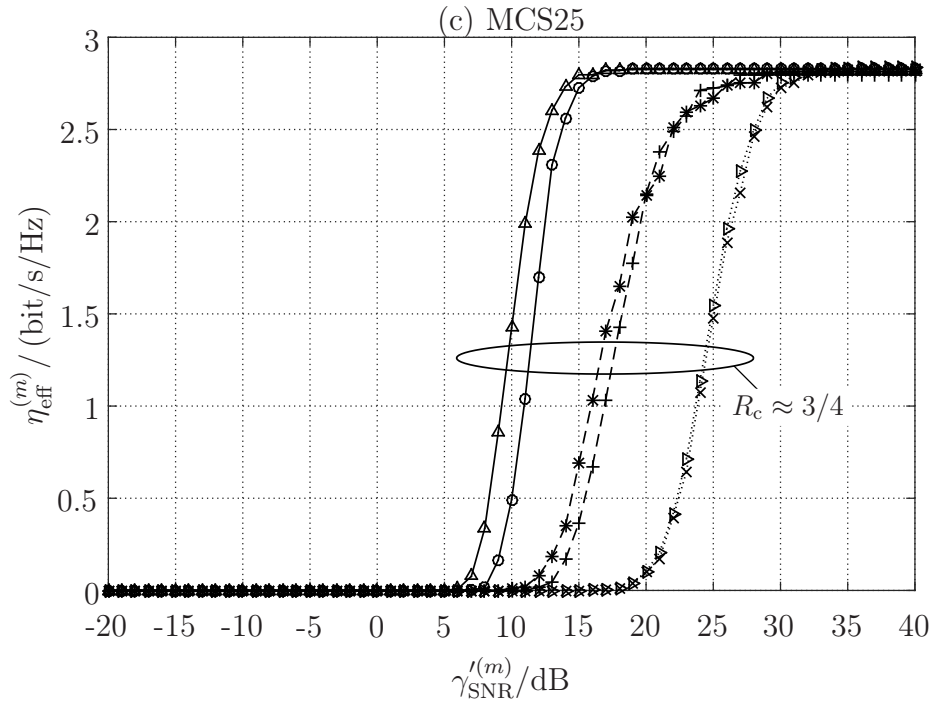
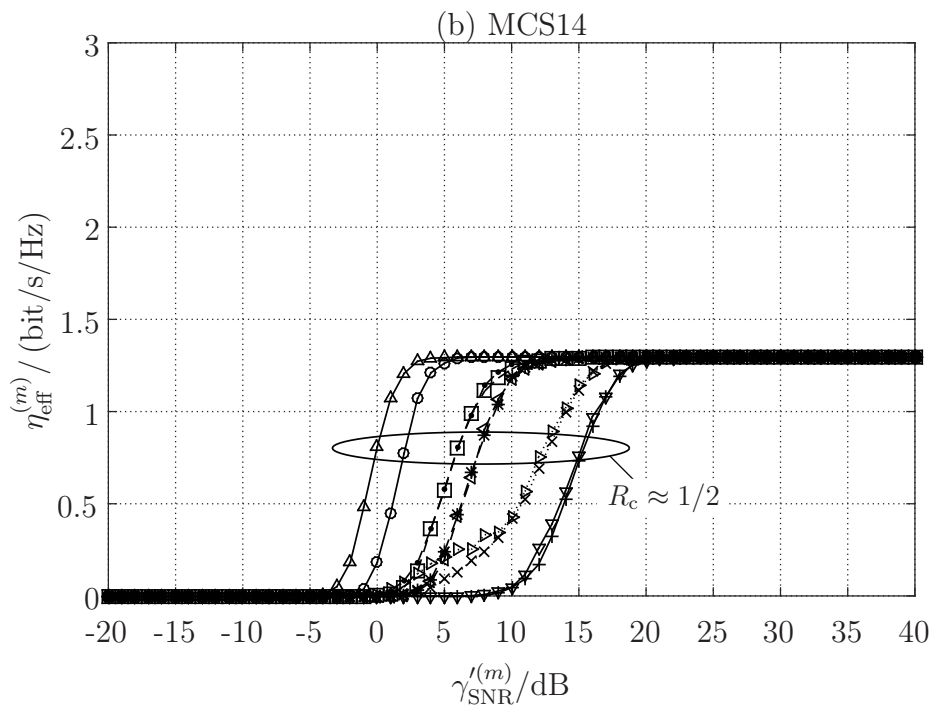
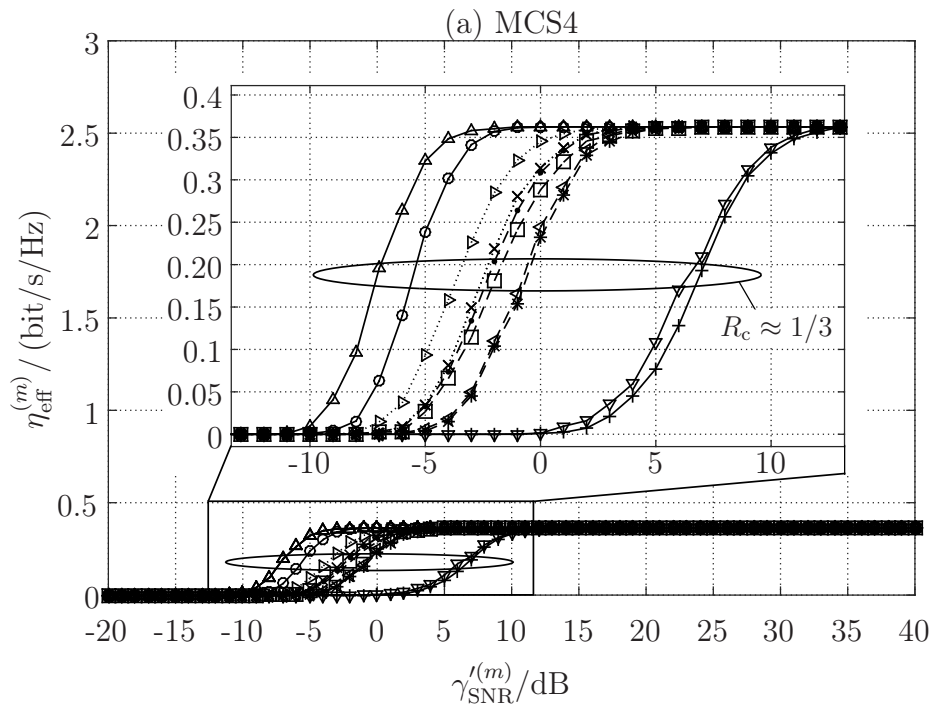


Figure 2.9. Performance for single-layer transmission in TM8 for (a) MCS4, (b) MCS14 and (c) MCS25 (legend see Table 2.7; created by the author of this thesis).

Table 2.7. Legend for Figure 2.9 (a) – (c).

$\text{---}\triangle\text{---}$ 4 × 2 MIMO $\text{---}\circ\text{---}$ 2 × 2 MIMO	NL single-layer transmission with the $N_T^{(b)} \times N_R^{(m)}$ MIMO antenna configuration and signal equalization using the MRC receiver
$\cdots\times\cdots$ 4 × 2 MIMO $\cdots\triangleright\cdots$ 2 × 2 MIMO	IL single-layer transmission with the $N_T^{(b)} \times N_R^{(m)}$ MIMO antenna configuration and signal equalization using the MRC receiver
$\text{---}\ast\text{---}$ 4 × 2 MIMO $\text{---}+\text{---}$ 2 × 2 MIMO	IL single-layer transmission with the $N_T^{(b)} \times N_R^{(m)}$ MIMO antenna configuration and signal equalization using the IRC receiver (2.73)



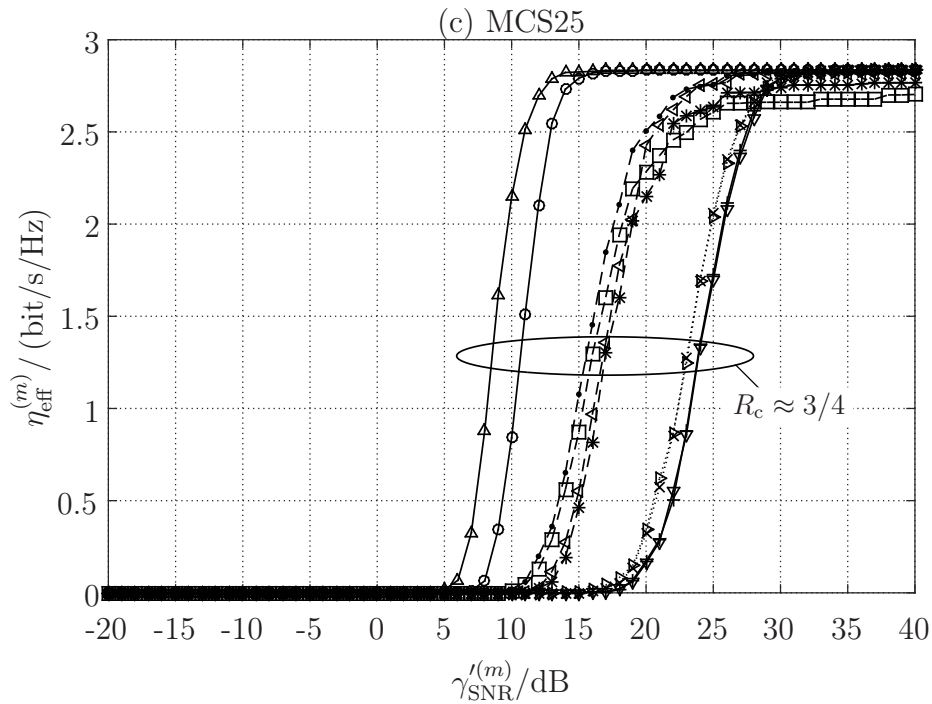


Figure 2.10. Performance for single-layer transmission in TM9 for (a) MCS4, (b) MCS14 and (c) MCS25 (legend see Table 2.8; created by the author of this thesis).

Table 2.8. Legend for Figure 2.10 (a) – (c).

<ul style="list-style-type: none"> —△— 4 × 2 MIMO —○— 2 × 2 MIMO 	NL single-layer transmission with the $N_T^{(b)} \times N_R^{(m)}$ MIMO antenna configuration and signal equalization using the MRC receiver
<ul style="list-style-type: none"> —▽— 4 × 2 MIMO —+— 2 × 2 MIMO 	IL single-layer transmission with the $N_T^{(b)} \times N_R^{(m)}$ MIMO antenna configuration and signal equalization using the MRC receiver
<ul style="list-style-type: none"> —●— 4 × 2 MIMO —▲— 2 × 2 MIMO 	IL single-layer transmission with the $N_T^{(b)} \times N_R^{(m)}$ MIMO antenna configuration and signal equalization using the IRC receiver (2.73)
<ul style="list-style-type: none"> —■— 4 × 2 MIMO —*— 2 × 2 MIMO 	IL single-layer transmission with the $N_T^{(b)} \times N_R^{(m)}$ MIMO antenna configuration and signal equalization using the E-IRC receiver (2.79)
<ul style="list-style-type: none"> ⋯▷⋯ 4 × 2 MIMO ⋯×⋯ 2 × 2 MIMO 	IL single-layer transmission with the $N_T^{(b)} \times N_R^{(m)}$ MIMO antenna configuration and signal equalization using the ASLIC receiver (Section 2.6.4)

Chapter 3

Implicit Feedback Generation for Synchronized CoMP Transmission

3.1 Introduction

In the area of CoMP transmission, the CoMP cooperating set denotes a set of geometrically separated Transmission Points (TPs) which directly and/or indirectly participate in signal transmission to the UE $\mu_m \in \mathbb{U}$ in a time-frequency resource [3GP13a, Section 5.1.4]. Moreover, in the area of CoMP transmission the transmitter transmitting the desired or interfering signal to the UE $\mu_m \in \mathbb{U}$ is referred to as a TP, rather than an eNodeB [3GP13a, Section 5.1.4]. A TP is defined by a transmitter with a set of geographically co-located transmit AEs [3GP13a, Section 5.1.1], where the set of geometrically separated TPs may or may not be transparent to the UE $\mu_m \in \mathbb{U}$ [3GP13a, Section 5.1.4]. As the desired signal may be transmitted from one or multiple TPs of the CoMP cooperating set [3GP13a, Section 5.1.4], different transmission categories for CoMP transmission are defined in [3GP13a, Section 5.1.4] and discussed in Section 3.2.2 of this thesis. Moreover, four different CoMP scenarios are defined for CoMP transmission [3GP13a, Section 5.1.2]. Detail information on the four CoMP scenarios with respect to channel estimation and resource allocation is provided in Section 3.2.1 of this thesis. General information on the CoMP scenarios can be found in [Lee+12b; Lee+12a] and references therein.

The term *synchronous* stems from the sequence of the two Greek words *syn* and *chronos* which can be translated as *with* and *time*, respectively [Bro86, Vol. 21, p. 527], where the latter one in turn represents the personification of time in the Greek mythology [Bro86, Vol. 4, p. 572]. In the context of synchronized CoMP transmission, the simultaneous reception of the desired and interfering signals, transmitted by one or multiple TPs shall be conveyed. As a result, the UE $\mu_m \in \mathbb{U}$ can assign the DFT window such that all samples of the OFDM symbols of the signals transmitted by the TPs of the CoMP

cooperating set are covered [KRF12, Section I]. The restriction on synchronous CoMP transmission is dropped in Chapter 4 of this thesis.

Following the CSI feedback for CoMP transmission, three main categories of feedback have been defined, including [3GP13a, Section 5.2.2]

- implicit CSI feedback,
- explicit CSI feedback and
- Sounding Reference Signal (SRS) based CSI feedback.

The transmission of SRS by the UE $\mu_m \in \mathbb{U}$ for CSI estimation at one or multiple TPs by exploiting channel reciprocity is limited on TDD-based LTE systems [3GP13a, Section 5.2.2.3] and can therefore not be used in this thesis. Detail information on SRS based CSI estimation can be found in [3GP13a, Section 5.2.2.3]. In FDD-based LTE systems implicit CSI feedback [3GP13a, Section 5.2.2.2] and explicit CSI feedback [3GP13a, Section 5.2.2.1] can be used for CoMP transmission. In this thesis implicit CSI feedback generation for CoMP transmission is used. Detail information on explicit CSI feedback generation can be found in [3GP13a, Section 5.2.2.1].

In CoMP transmission, implicit feedback generation is based on one or a combination of two or more options that are summarized in [3GP13a, Section 5.2.2.2]. In this thesis a combination of interference based processing [3GP13a, Section 5.2.2.2] and coordinated JP transmission [3GP13a, Section 5.2.2.2] is used to improve the signal detection capabilities at the cell-edge UE $\mu_m \in \mathbb{U}$. The interference based processing and coordinated JP transmission is achieved by CSI reporting to enable cooperative interference mitigation signal precoding. In detail, aperiodic CSI reporting for subband PMI is discussed for cooperative signal transmission in TM10. Based on the IS receiver implementation, an O-CCIMP scheme with respect to subband PMI selection enabling post-SNR maximization is suggested in Section 3.3.2 of this thesis. With simple but extremely powerful matrix manipulations the complexity of the aforementioned O-CCIMP scheme can be considerably reduced [Iwe+15b, Section III-B]. The complexity of the two CCIMP schemes is discussed in Section 3.3.4 of this thesis.

Numerical results at the link level to compare the performance of the suggested cooperative interference mitigation precoding schemes for synchronized CoMP transmission with conventional IS receivers are provided in Section 3.4 of this thesis.

3.2 Network Configuration

3.2.1 Downlink Scenarios

In CoMP transmission, four scenarios for signal transmission are supported, including CoMP Scenario 1, 2, 3 and 4 [3GP13a, Section 5.1.2]. CoMP Scenarios 1, 2 and 3 have in common that the physical layer cell-identities of the TPs within the coordination area are not equal [3GP13a, Section 5.1.2]. Consequently, the pseudo random sequence used for the DMRS transmission is different for any TP within the coordination area, as each pseudo-random sequence generator is initialized with, amongst others, the scrambling identity which is set to the physical layer cell-identity of the respective TP. Hence, to equalize the complex-valued OFDM baseband signal of the receive signal after OFDM demodulation, the information of the physical layer cell-identity of the TP the OFDM baseband signal is transmitted from, needs to be forwarded to the UE $\mu_m \in \mathbb{U}$ via higher-layer signaling. In case of desired signal transmission from a single TP, the LSCE scheme discussed in Section 2.6.2 of this thesis in conjunction with the IS receiver discussed in Section 2.6.3 of this thesis can be used for signal equalization. However, in case of signal transmission from multiple TPs, the desired effective channels have to be spatially separated at the UE $\mu_m \in \mathbb{U}$ to provide an appropriate implementation of the IS receiver. Spatial separation of the desired effective channels can be carried out by following the concept of the JLSCE scheme discussed in Section 2.6.2 of this thesis in conjunction with the IS receiver implementation provided in [Bai+13a, Section II-B]. As the TP or set of TPs transmitting the desired signal to the UE $\mu_m \in \mathbb{U}$ might change from subframe to subframe [3GP13a, Section 5.1.4], signal transmission with a transparent configuration of TPs within the coordination area in any of the CoMP Scenarios 1, 2 and 3 is not possible at the UE $\mu_m \in \mathbb{U}$. On the other hand, CoMP Scenario 4 is characterized by the fact that the TPs within the CoMP operating set share the same physical layer cell-identity [3GP13a, Section 5.1.2]. Hence, in CoMP Scenario 4 the UE experiences a transparent signal transmission from dynamically changing TPs within the CoMP operating set. Hence, in case of synchronized CoMP transmission, the necessity of higher layer signaling to enable reliable signal demodulation is not necessary.

The code rate for each MCS for signal transmission in TM10 in dependence on the CoMP operating set and the number of transmit AEs at each TP within the CoMP operating set is depicted in Figure 3.1 on page 138 for the first subframe and a channel bandwidth equal to 10 MHz, where the respective numerical code rates are summarized in Table B.3 on page 246. The code rate for single-layer transmission in TM9, the CoMP system is to be compared with, is also provided in Figure 3.1. The respective numerical code rates are summarized

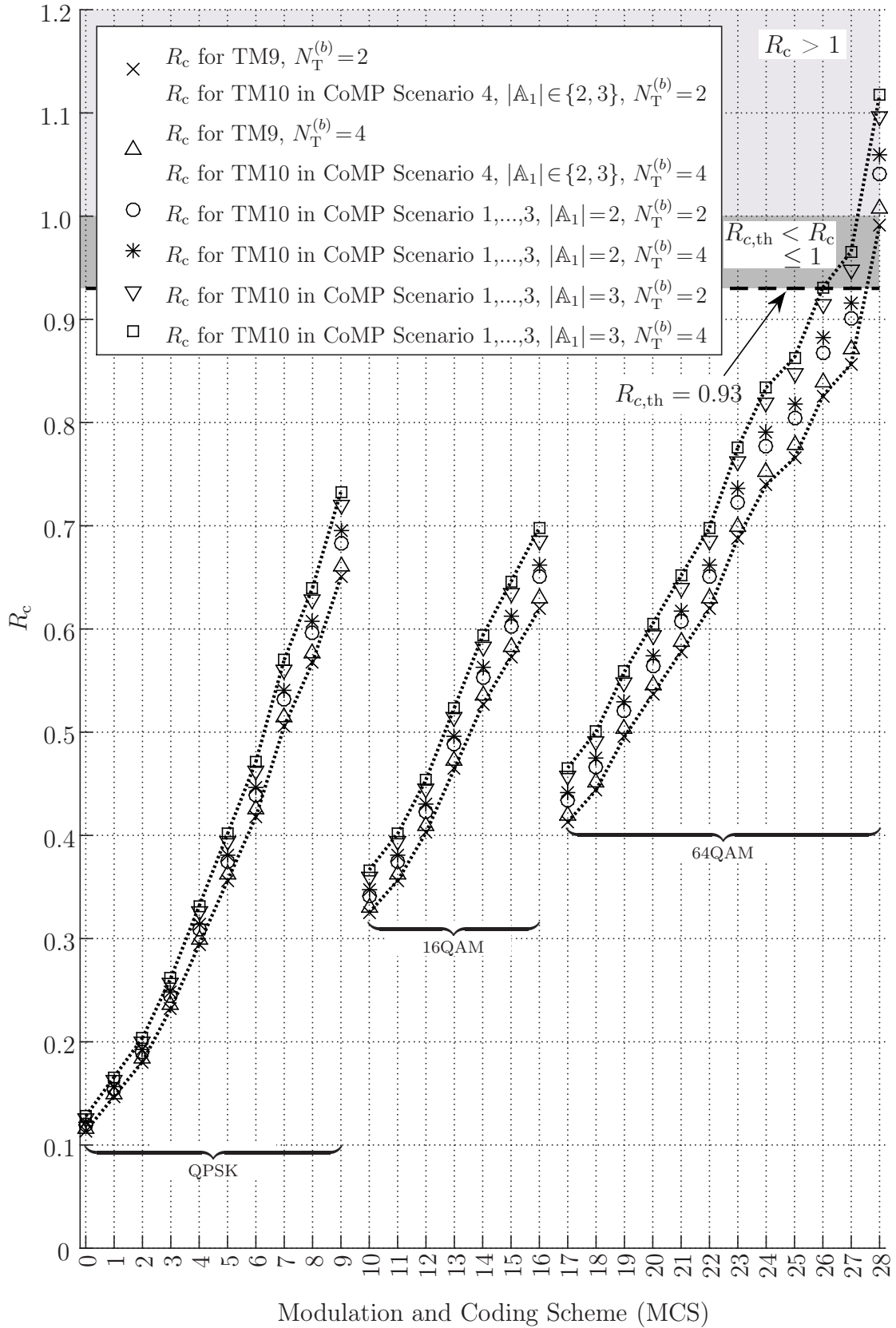


Figure 3.1. Code rate in dependency on the transmission mode and the transmitter configuration (created by the author of this thesis).

in the seventh and eighth column of Table B.2 on page 245 for the eNodeB $\epsilon_b \in \mathbb{A}_m$ equipped with two and four transmit AEs, respectively, as discussed in Section 2.4.4 of this thesis. Analogously to Figure 2.3 on page 82, the corridor in Figure 3.1 provides a graphical illustration of the lowest and the highest code rate that can be achieved for the QPSK, the 16 QAM and the 64 QAM mapping scheme. As the CSI-RSs transmitted by the TPs within the CoMP operating set are assumed to be transmitted on different subframes, the code rate for signal transmission in TM9 is equal to the code rate in TM10 in case of CoMP Scenario 4 for the first subframe for $N_T^{(b)}$ equal to two transmit AEs, as depicted in Figure 3.1. The same holds for the case of four transmit AEs, as depicted in Figure 3.1. Following the findings on the three ranges of the code rate discussed in Section 2.4.4 of this thesis in conjunction with the illustration of the code rates depicted in Figure 3.1, the MCS with index 27 represents the highest MCS index that can be selected for single-layer transmission in TM10 in CoMP Scenario 4 for two and three TPs within the CoMP operating set such that the maximum code rate equal to 0.93 is not exceeded. For single-layer transmission in CoMP Scenario 1,...,3 in TM10, however, the code rate increases as the physical time-frequency resources carrying the CRSs among the TPs within the CoMP operating set have to be excluded from the set $\mathcal{S}_{i, n_{\text{PRB}}}$, according to (2.42), such that the denominator in (2.42) decreases and (2.42) increases. While the MCS with index 27 can be supported for single-layer transmission in CoMP Scenario 1,...,3 in TM10 only for two TPs within the CoMP operating set for both, two and four transmit AEs at each TP, the code rate exceeds 0.93 in case of single-layer transmission in CoMP Scenario 1,...,3 in TM10 for three TPs within the CoMP operating set for both, two and four transmit AEs at each TP, as depicted in Figure 3.1 and can therefore not be supported in that case.

For the sake of transparent signal transmission from dynamically changing TPs within the CoMP operating set and no restriction on the maximum bandwidth efficiency compared with single-layer transmission in TM9, among the supported CoMP scenarios in this thesis single-layer transmission in TM10 in CoMP Scenario 4 is considered as a practical implementation to further improve the bandwidth efficiency in the cell-edge.

3.2.2 Transmission Categories

As the desired signal can be transmitted from one or multiple geometrically separated TPs, in CoMP Scenario 4 the signal transmission is categorized into different modes including [3GP13a, Section 5.1.3]

- JP,
- Coordinated Scheduling (CS)/Coordinated Beamforming (CB),

- Dynamic and semi-static muting in JP and CS/CB and
- Hybrid category of JP and CS/CB.

In this thesis the JP signal transmission in CoMP Scenario 4 is focused on. Detail information on signal transmission using CS/CB, dynamic and semi-dynamic muting in JP and CS/CB as well as a hybrid category of JP and CS/CB can be found in [3GP13a, Section 5.1.3]. An overview of practical implementation of the aforementioned CoMP categories can be found in [Lee+12b; Lee+12a; Yan+13] and references therein. The JP signal transmission scheme can be further subdivided into [3GP13a, Section 5.1.3]

- DPS,
- Joint Transmission (JT) and a
- Combination of JT and DPS.

For the reason of limited knowledge extraction with respect to reliable implicit feedback generation for unsynchronized CoMP transmission discussed in Chapter 4 of this thesis, in this thesis the JP-DPS signal transmission in CoMP Scenario 4 is focused on. The aspect of implicit feedback generation for synchronized and unsynchronized JP-JT signal transmission in CoMP Scenario 4 has also been investigated by the author of this thesis and can be found in [Bai+13a] and [Iwe+15c], respectively.

The properties of the JP-DPS signal transmission scheme in CoMP Scenario 4 are explained using Figure 3.2 on page 141. Figure 3.2 represents a cutout of a macro cellular deployed LTE network of CoMP Scenario 4 with three sectors per site, one eNodeB ϵ_1 , six low power RRHs $\epsilon'_1, \dots, \epsilon'_6$ and one UE μ_1 . Two low power RRHs are placed in the edge of each of the three sectors, also referred to as cells and are connected by a low latency backhaul to the eNodeB ϵ_1 [3GP13a, Section 5.5], as indicated by the dash-dotted line between each low power RRH ϵ'_i and eNodeB ϵ_1 for $1 \leq i \leq 6$ in Figure 3.2. The CoMP cooperating set for the UE μ_1 is denoted by \mathbb{A}_1 and includes the TPs $\{\epsilon_1, \epsilon'_1, \epsilon'_2\}$. In CoMP Scenario 4 the CRSs may be transmitted from the eNodeB or both, the eNodeB and all of the low power RRHs within the CoMP cooperating set [Gei+12, Note [0065]]. Following [Int12b, Section 1] and [Int12a, Section 1], in this thesis it is assumed that the CRSs are transmitted only from the eNodeB such that $\{\epsilon_1\}$ holds for the set $\mathbb{A}_1^{\text{CRS}}$. Hence, the UE μ_1 is assigned to the eNodeB ϵ_1 with respect to synchronization, as denoted by the solid arrow beginning at the UE μ_1 and ending at the eNodeB ϵ_1 , as depicted in Figure 3.2. The CSI-RSs are transmitted by each of the TP within the CoMP cooperating set \mathbb{A}_1 , as denoted by the dotted arrow beginning at the TP and ending at the UE, as depicted in Figure 3.2. To enable reliable CSI feedback, each TP uses orthogonal physical time-frequency resources to transmit the CSI-RSs [3GP13a, Section 5.2.4]. Following the properties of the CSI-RSs discussed

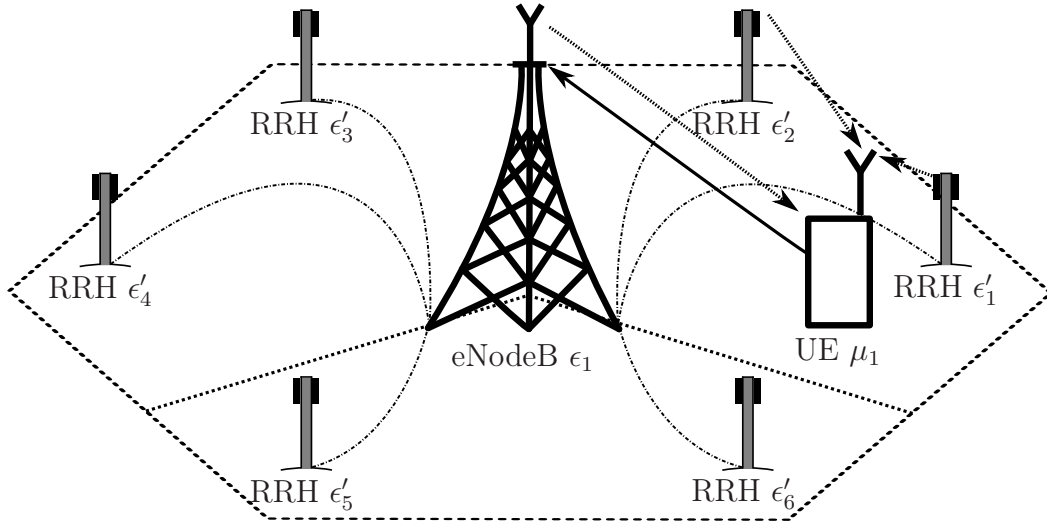


Figure 3.2. Cutout for a macro cellular deployed LTE network of CoMP Scenario 4 with low-power RRHs (created by the author of this thesis using [3GP13a, Figure A.1-4]).

in Section 2.2.4 of this thesis, each TP carrying the CSI-RSs is assigned with a distinct CSI-RS configuration, such that mutual interference between the CSI-RSs is avoided. Making use of the CSI-RS transmission on orthogonal physical time-frequency resources enables the UE μ_1 to select the TP out of the CoMP cooperating set aimed to transmit the DMRSs and complex-valued modulation symbols carrying the codewords in order to mitigate the impact of inter-cell interference. Following the concept of the JP-DPS signal transmission [3GP13a, Section 5.1.3], one TP out of the set $\mathbb{A}_1^{\text{data}}$ equal to $\{\epsilon_1, \epsilon'_1, \epsilon'_2\}$ is used to transmit the complex-valued modulation symbols carrying the codewords and the DMRSs, where the respective TP is selected by the UE $\mu_1 \in \mathbb{U}$ as discussed in Section 3.3 of this thesis.

3.3 Cooperative Interference Mitigation Signal Precoding

3.3.1 Introduction

Although the impact of inter-cell interference can be considerably mitigated by making use of the IS receivers in DMRS-based TMs, the gap to the NL single-layer transmission is still remarkable, as discussed in Section 2.10 of this thesis. From the point of view of signal processing, the major reason for this limitation is that the number of receive AEs at the UE $\mu_1 \in \mathbb{U}$ is smaller than the number of spatial layers experienced by the UE $\mu_1 \in \mathbb{U}$, such that the IS

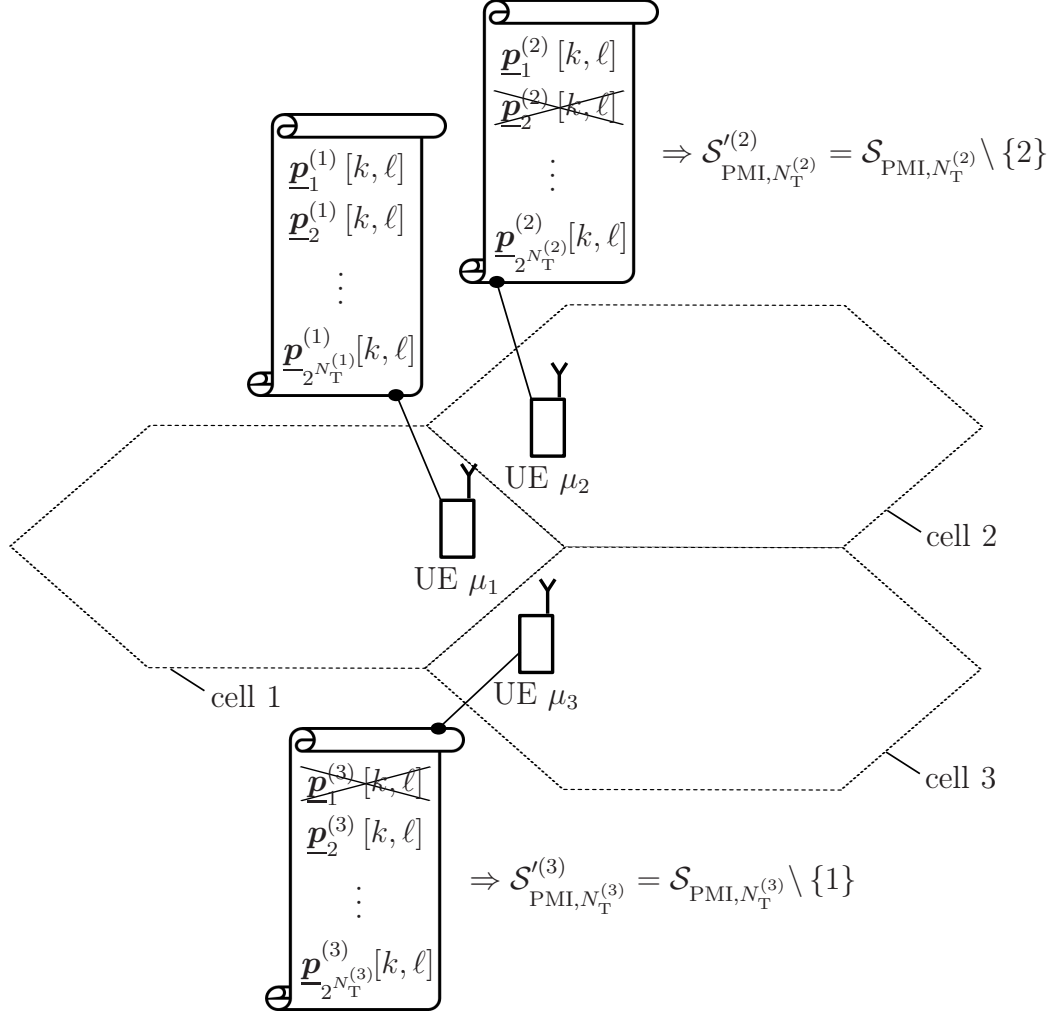


Figure 3.3. Cooperative interference mitigation precoding scenario (created by the author of this thesis).

receiver fails to project the interfering signals to a subspace that is orthogonal to the subspace the desired signal to projected on. One way forward to improve the bandwidth efficiency experienced by the UE $\mu_1 \in \mathcal{U}$ in IL single-layer transmission can be achieved by making use of interference based processing and coordinated JP transmission [3GP13a, Section 5.2.2.2]. Following the concept of subset restriction supported in TM10 [3GP16g, Section 7.2], in this thesis it is assumed that despite the UE $\mu_1 \in \mathcal{U}$, the UEs $\mu_{\tilde{m}} \in \mathcal{U}$ do not need to operate at high data rates for $\tilde{m} \neq 1$, such that the UE $\mu_1 \in \mathcal{U}$ is empowered to select the precoding vectors for the interfering TPs $\epsilon_b \in \mathbb{I}_1$ from a codebook restricted by each UE $\mu_{\tilde{m}} \in \mathcal{U}$ for $\tilde{m} \neq 1$. Each UE $\mu_{\tilde{m}} \in \mathcal{U}$ restricts the codebook by one precoding vector, typically the precoding vector causing smallest average post-SNR per subframe and subband. Hence, the set of PMIs representing the respective index of all but one precoding vector to

Table 3.1. Restricted PMIs using the CCIMP scheme (created by the author of this thesis).

UE	PMI				
μ_1	1	2	3	...	$2^{N_T^{(1)}}$
μ_2	1	2	3	...	$2^{N_T^{(2)}}$
μ_3	1	2	3	...	$2^{N_T^{(3)}}$

be used to precode the signal at each TP $\epsilon_{\tilde{b}} \in \mathbb{I}_1$ is denoted by

$$\mathcal{S}'_{\text{PMI}, N_T^{(\tilde{b})}}^{(\tilde{b})} = \mathcal{S}_{\text{PMI}, N_T^{(\tilde{b})}} \setminus \{u_{\tilde{m}}\}, \quad (3.1)$$

where $u_{\tilde{m}}$ denotes the index of the precoding vector which is restricted by the UE $\mu_{\tilde{m}} \in \mathbb{U}$ for each $\tilde{m} \neq 1$. Thus, the UE $\mu_1 \in \mathbb{U}$ is empowered to provide implicit feedback to precode the complex-valued modulation symbols carrying the codewords and the DMRSs at both, the TP $\epsilon_{\tilde{b}} \in \mathbb{A}_1^{\text{data}}$ the desired signal is transmitted from and each TP $\epsilon_{\tilde{b}} \in \mathbb{I}_1$ the interfering signal is transmitted from in order to improve the post-SNR (2.69) [Iwe+15b, Section III-A] and, thus the bandwidth efficiency experienced by the UE $\mu_1 \in \mathbb{U}$.

To illustrate the concept of the CCIMP scheme, Figure 3.3 on page 142 is used. In that scenario UE $\mu_1 \in \mathbb{U}$ restricts the set of PMIs by the index of the second precoding vector, as depicted in Figure 3.3. The restricted set of PMIs (3.1) UE $\mu_2 \in \mathbb{U}$ allows the target UE $\mu_1 \in \mathbb{U}$ to select the index of the precoding vector from, is depicted in Figure 3.3. UE $\mu_3 \in \mathbb{U}$ proceeds analogously and restricts the set of PMIs by the index of the first precoding vector, as depicted in Figure 3.3. The final set of PMIs, UE $\mu_1 \in \mathbb{U}$ can use the precode its own and the signals transmitted to UE $\mu_2 \in \mathbb{U}$ and UE $\mu_3 \in \mathbb{U}$ is summarized in Table 3.1 on page 143.

As already stated in Section 3.2.1 of this thesis, the TP transmitting the precoded complex-valued modulation symbols carrying the codewords and the precoded DMRSs might change from subframe to subframe. However, a change of the TP within one subframe is not allowed. The reason is that transparent signal transmission might not be guaranteed in unsynchronized CoMP transmission in case of positive and negative TOs among the receive signals such that a DFT window relocation might be necessary to turn the negative TO to a positive TO [Iwe+14h, Section III]. Hence, the UE μ_1 selects the TP out of the set $\mathbb{A}_1^{\text{data}}$ for the duration of at least one subframe, denoted by T_{subframe} in (1.21).

Two CCIMP schemes including the O-CCIMP scheme and the LC-CCIMP scheme used to improve the post-SNR and, thus the bandwidth efficiency at

the UE $\mu_1 \in \mathbb{U}$ are discussed in what follows.

3.3.2 Optimal Codebook-Based Cooperative Interference Mitigation Signal Precoding

The O-CCIMP scheme enables the optimal selection of the TP out of the CoMP cooperating set together with the precoding vectors with corresponding PMI out of the set $\mathcal{S}_{\text{PMI}, N_T^{(b)}}$ to be used to precode the complex-valued modulation symbols carrying the desired codewords and DMRSs at that TP in each subband and the precoding vector with corresponding PMI out of the subset (3.1) to be used to precode the complex-valued modulation symbols carrying the interfering codewords and DMRSs transmitted by each TP $\epsilon_{\bar{b}} \in \mathbb{I}_1$ in each subband, such that the maximum of the post-SNR over all N_{SB} subbands is found.

Following the findings achieved in [EDL14, Section III-A], the CCIMP scheme is derived based on signal equalization using the MRC receiver. Following the findings achieved in Section 2.10 of this thesis, equalizing the receive signal in presence of inter-cell interference in DMRS-based TMs with the MRC receiver rather than with the IS receiver does not project the interfering signals to a subspace that is orthogonal to the subspace the desired signal is projected on. However, the assumption in [EDL14] that the mutual impact of the desired and the interfering signals can be neglected is helpful to illustrate the concept of the CCIMP scheme. Neglecting the impact of inter-cell interference, the UE $\mu_1 \in \mathbb{U}$ selects the precoding vector with corresponding PMI out of the set $\mathcal{S}_{\text{PMI}, N_T^{(b)}}$ for each TP $\epsilon_b \in \mathbb{A}_1^{\text{data}}$ according to (2.81) with the simplification that the covariance matrix within the post-SNR in (2.81) is set to the thermal noise power over the received bandwidth multiplied with the $N_R^{(1)} \times N_R^{(1)}$ identity matrix. The TP with largest post-SNR in all N_{SB} subbands is selected to transmit the complex-valued modulation symbols carrying the desired codewords and DMRSs. Analogously, the UE $\mu_1 \in \mathbb{U}$ selects the precoding vector with corresponding PMI out of the subset (3.1) for each TP $\epsilon_{\bar{b}} \in \mathbb{I}_1$, such that the average post-SNR in the respective subband is minimized. This is intended to maximize the contribution of the desired signal while simultaneously minimizing the contribution of the inter-cell interfering signal. However, as the mutual impact of the desired and interfering signals cannot be neglected in presence of a practical cellular LTE network due to the inhomogeneities of the mobile communication channel, the CCIMP scheme suggested in [EDL14, Section III-A] does not provide the global maximum of the average post-SNR and is therefore not optimal in that sense. To overcome this limitation, in this section the O-CCIMP scheme is derived based on the post-SNR calculation of the IS receiver.

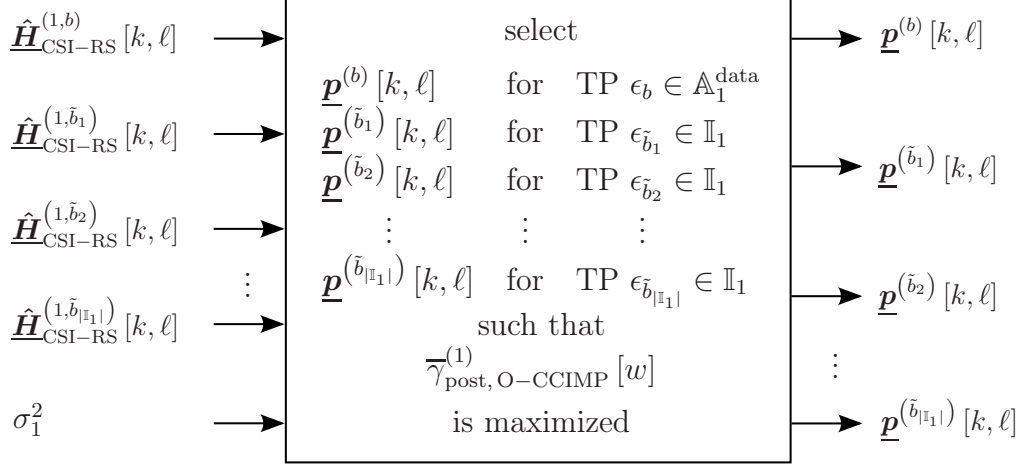


Figure 3.4. Block diagram of the O-CCIMP scheme (created by the author of this thesis).

The block diagram of the O-CCIMP scheme is depicted in Figure 3.4 on page 145. Following the properties of the channel estimation in TM10, discussed in Section 2.7.4 of this thesis, the UE $\mu_1 \in \mathbb{U}$ has knowledge on the estimated CTFs $\hat{\mathbf{H}}_{\text{CSI-RS}}^{(1,b)} [k, \ell]$ and $\hat{\mathbf{H}}_{\text{CSI-RS}}^{(1,\tilde{b}_i)} [k, \ell]$ for $1 \leq i \leq |\mathbb{I}_1|$, such that these parameters as well as the thermal noise power over the received bandwidth are considered as the input parameters to calculate the precoding vectors using the O-CCIMP scheme, as depicted in Figure 3.4. The precoding vectors $\underline{\mathbf{p}}^{(b)} [k, \ell]$ and $\underline{\mathbf{p}}^{(\tilde{b}_i)} [k, \ell]$ represent the output parameters for $1 \leq i \leq |\mathbb{I}_1|$, as depicted in Figure 3.4 to be used to precode the complex-valued modulation symbols carrying the codewords as well as the DMRSs at the target and interfering TPs, respectively, such that the global maximum of the average post-SNR, denoted by $\overline{\gamma}_{\text{post, O-CCIMP}}^{(1)} [w]$ is found by the UE $\mu_m \in \mathbb{U}$ in each subband $0 \leq w < N_{\text{SB}}$. The average post-SNR experienced by the UE $\mu_1 \in \mathbb{U}$ in the w -th subband for the O-CCIMP scheme is defined by

$$\overline{\gamma}_{\text{post, O-CCIMP}}^{(1)} [w] = \frac{1}{2 N_{\text{symp}}^{\text{DL}}} \sum_{\ell=0}^{2 N_{\text{symp}}^{\text{DL}}} \sum_{k \in \mathcal{S}_{\text{SB}}^{(w)}} \left(\left(\hat{\mathbf{H}}_{\text{CSI-RS}}^{(1,b)} [k, \ell] \underline{\mathbf{p}}^{(b)} [k, \ell] \right)^{\text{H}} \cdot \left(\underline{\mathbf{R}}_{\Sigma, \text{CSI-RS}}^{(1)} [k, \ell] \right)^{-1} \left(\hat{\mathbf{H}}_{\text{CSI-RS}}^{(1,b)} [k, \ell] \underline{\mathbf{p}}^{(b)} [k, \ell] \right) \right), \quad (3.2)$$

where the covariance matrix $\underline{\mathbf{R}}_{\Sigma, \text{CSI-RS}}^{(1)} [k, \ell]$ is defined for signal transmission in TM10 in (2.84) when setting m equal to one. To guarantee the conformity of aperiodic CSI reporting for Mode 1-2, the O-CCIMP scheme for subband PMI selection reads

$$\left[\underline{\mathbf{p}}^{(b)} [k, \ell], \underline{\mathbf{p}}^{(\tilde{b}_1)} [k, \ell], \dots, \underline{\mathbf{p}}^{(\tilde{b}_{|\mathbb{I}_1|})} [k, \ell] \right] = \arg \max_{\mathcal{A} \times \mathcal{I}_1 \times \dots \times \mathcal{I}_{|\mathbb{I}_1|}} \left\{ \overline{\gamma}_{\text{post, O-CCIMP}}^{(1)} [w] \right\} \quad (3.3)$$

where the set of candidate precoding vectors, the desired and interfering signal is to be precoded with, is denoted by

$$\mathcal{A} = \left\{ \underline{\mathbf{p}}^{(b)} [k, \ell] \mid \underline{\mathbf{p}}^{(b)} [k, \ell] = \underline{\mathbf{q}}_j [k, \ell], j \in \mathcal{S}_{\text{PMI}, N_T^{(b)}} \right\} \quad \text{and} \quad (3.4a)$$

$$\mathcal{I}_i = \left\{ \underline{\mathbf{p}}^{(\tilde{b}_i)} [k, \ell] \mid \underline{\mathbf{p}}^{(\tilde{b}_i)} [k, \ell] = \underline{\mathbf{q}}_j [k, \ell], j \in \mathcal{S}'_{\text{PMI}, N_T^{(\tilde{b}_i)}} \right\}, \quad (3.4b)$$

respectively, for $1 \leq i \leq |\mathbb{I}_1|$. Being informed by the network, the UE $\mu_1 \in \mathbb{U}$ has knowledge of the UEs scheduled on the same frequency band in the DL transmission. Evaluating the CSI-RSs, the UE $\mu_1 \in \mathbb{U}$ is able to determine the dominant interfering TPs, denoted by the set \mathbb{I}_1 . Moreover, $\underline{\mathbf{q}}_j [k, \ell]$ in (3.4) represents the precoding vector with PMI equal to j , denoted in the second column of Table 2.2 and Table A.1 for the TP equipped with two and four transmit AEs, respectively. Obviously, a full-blown search is carried out in (3.3) to ensure that the set of precoding vectors is determined such that the global maximum of the average post-SNR (3.2) is found in each subband for $0 \leq w < N_{\text{SB}}$.

The complexity of the O-CCIMP scheme is analyzed in Section 3.3.4, whereas the performance is discussed in Section 3.4 of this thesis.

3.3.3 Low-Complexity Codebook-Based Cooperative Interference Mitigation Signal Precoding

The goal of the LC-CCIMP scheme discussed in this section is to turn the full-blown search of the precoding vectors for subband PMI selection of the O-CCIMP scheme in (3.3) to an iterative search of the precoding vectors for subband PMI selection [Iwe+15b, Section III-A]. The Sherman-Morrison formula [ZF92, Section 22.5] enables to rewrite the inverse of the covariance matrix $\underline{\mathbf{R}}_{\Sigma, \text{CSI-RS}}^{(1)} [k, \ell]$ in (3.2), such that the covariance matrix and, hence the choice of precoding vectors can be computed in an iterative manner [Iwe+15b, Section III-A]. However, to rewrite the inverse of the covariance matrix $\underline{\mathbf{R}}_{\Sigma, \text{CSI-RS}}^{(1)} [k, \ell]$ using the Sherman-Morrison formula, the covariance matrix has to have full rank [ZF92, Section 22.5]. The covariance matrix $\underline{\mathbf{R}}_{\Sigma, \text{CSI-RS}}^{(1)} [k, \ell]$ consists of $|\mathbb{I}_1|$ matrices plus a diagonal matrix, represented by the thermal noise over the received bandwidth multiplied with the $N_{\text{R}}^{(1)} \times N_{\text{R}}^{(1)}$ identity matrix. Following (2.84), each of the $|\mathbb{I}_1|$ matrices is defined by

$$\hat{\underline{\mathbf{H}}}_{\text{CSI-RS}}^{(1, \tilde{b}_i)} [k, \ell] \underline{\mathbf{p}}^{(\tilde{b}_i)} [k, \ell] \left(\underline{\mathbf{p}}^{(\tilde{b}_i)} [k, \ell] \right)^{\text{H}} \left(\hat{\underline{\mathbf{H}}}_{\text{CSI-RS}}^{(1, \tilde{b}_i)} [k, \ell] \right)^{\text{H}} \quad (3.5)$$

$$\left(\underline{\mathbf{v}}_1 \underline{\mathbf{v}}_1^H + \underbrace{\underline{\mathbf{v}}_2 \underline{\mathbf{v}}_2^H + \underline{\mathbf{v}}_3 \underline{\mathbf{v}}_3^H + \cdots + \underline{\mathbf{v}}_{L-1} \underline{\mathbf{v}}_{L-1}^H + \underline{\mathbf{v}}_L \underline{\mathbf{v}}_L^H}_{=\underline{\mathbf{M}}_1} + \sigma_m^2 \underline{\mathbf{I}}_{N_R^{(m)}} \right)^{-1} = \underline{\mathbf{M}}_1^{-1} - \frac{\underline{\mathbf{M}}_1^{-1} \underline{\mathbf{v}}_1 \underline{\mathbf{v}}_1^H \underline{\mathbf{M}}_1^{-1}}{1 + \underline{\mathbf{v}}_1^H \underline{\mathbf{M}}_1^{-1} \underline{\mathbf{v}}_1} \quad (3.6a)$$

$$\left(\underline{\mathbf{v}}_2 \underline{\mathbf{v}}_2^H + \underbrace{\underline{\mathbf{v}}_3 \underline{\mathbf{v}}_3^H + \cdots + \underline{\mathbf{v}}_{L-1} \underline{\mathbf{v}}_{L-1}^H + \underline{\mathbf{v}}_L \underline{\mathbf{v}}_L^H}_{=\underline{\mathbf{M}}_2} + \sigma_m^2 \underline{\mathbf{I}}_{N_R^{(m)}} \right)^{-1} = \underline{\mathbf{M}}_2^{-1} - \frac{\underline{\mathbf{M}}_2^{-1} \underline{\mathbf{v}}_2 \underline{\mathbf{v}}_2^H \underline{\mathbf{M}}_2^{-1}}{1 + \underline{\mathbf{v}}_2^H \underline{\mathbf{M}}_2^{-1} \underline{\mathbf{v}}_2} \quad (3.6b)$$

$$\begin{array}{c} \dots \\ \left(\underline{\mathbf{v}}_{L-1} \underline{\mathbf{v}}_{L-1}^H + \underbrace{\underline{\mathbf{v}}_L \underline{\mathbf{v}}_L^H + \sigma_m^2 \underline{\mathbf{I}}_{N_R^{(m)}}}_{=\underline{\mathbf{M}}_{L-1}} \right)^{-1} = \underline{\mathbf{M}}_{L-1}^{-1} - \frac{\underline{\mathbf{M}}_{L-1}^{-1} \underline{\mathbf{v}}_{L-1} \underline{\mathbf{v}}_{L-1}^H \underline{\mathbf{M}}_{L-1}^{-1}}{1 + \underline{\mathbf{v}}_{L-1}^H \underline{\mathbf{M}}_{L-1}^{-1} \underline{\mathbf{v}}_{L-1}} \end{array} \quad (3.6c)$$

$$\left(\underline{\mathbf{v}}_L \underline{\mathbf{v}}_L^H + \sigma_m^2 \underline{\mathbf{I}}_{N_R^{(m)}} \right)^{-1} = \sigma_m^2 \underline{\mathbf{I}}_{N_R^{(m)}} - \frac{\sigma_m^{-4} \underline{\mathbf{v}}_L \underline{\mathbf{v}}_L^H}{1 + \sigma_m^{-4} \underline{\mathbf{v}}_L^H \underline{\mathbf{I}}_{N_R^{(m)}} \underline{\mathbf{v}}_L} \quad (3.6d)$$

for $1 \leq i \leq |\mathbb{I}_1|$. The product of the precoding vector $\underline{\mathbf{p}}^{(\tilde{b}_i)} [k, \ell]$ in (3.5) with the Hermitian representation of the same precoding vector denotes the outer product of two vectors with rank equal to one [ZF86, Section 40.1]. As the rank of a product of matrices is smaller than or equal to the smallest rank of each of the matrices [ZF92, Section 9.6], the rank of the matrix product in (3.5) is equal to one for any vector $\underline{\mathbf{p}}^{(\tilde{b}_i)} [k, \ell]$ including the precoding vectors denoted in Table 2.2 and Table A.1 on page 78 and 233, respectively. Moreover, following the subadditivity property of matrices, the rank of the sum of two or more matrices is smaller than or equal to the sum of the rank of these matrices [Tan17, Section 1.5] such that

$$\begin{aligned} \text{rank} \left(\hat{\mathbf{R}}_{\Sigma, \text{CSI-RS}}^{(1)} [k, \ell] \right) &\leq \text{rank} \left(\sigma_1^2 \mathbf{I}_{N_{\text{R}}^{(1)}} \right) + \\ &\sum_{i=1}^{|\mathbb{I}_1|} \text{rank} \left(\hat{\mathbf{H}}_{\text{CSI-RS}}^{(1, \tilde{b}_i)} [k, \ell] \underline{\mathbf{p}}^{(\tilde{b}_i)} [k, \ell] \left(\underline{\mathbf{p}}^{(\tilde{b}_i)} [k, \ell] \right)^{\text{H}} \left(\hat{\mathbf{H}}_{\text{CSI-RS}}^{(1, \tilde{b}_i)} [k, \ell] \right)^{\text{H}} \right) \end{aligned} \quad (3.7)$$

holds. As the rank of an arbitrary matrix is upper bounded by the minimum of the number of rows and columns [ZF92, Section 1.6] and the covariance matrix $\hat{\mathbf{R}}_{\Sigma, \text{CSI-RS}}^{(1)} [k, \ell]$ is a square matrix,

$$\text{rank} \left(\hat{\mathbf{R}}_{\Sigma, \text{CSI-RS}}^{(1)} [k, \ell] \right) \leq N_{\text{R}}^{(1)} \quad (3.8)$$

holds. Moreover, as the noise power over the received bandwidth multiplied with the $N_{\text{R}}^{(1)} \times N_{\text{R}}^{(1)}$ identity matrix, being part of the covariance matrix $\hat{\mathbf{R}}_{\Sigma, \text{CSI-RS}}^{(1)} [k, \ell]$ in (2.84), represents a diagonal matrix, the inequality in (3.8) is fulfilled with the equality sign. Consequently, the covariance matrix $\hat{\mathbf{R}}_{\Sigma, \text{CSI-RS}}^{(1)} [k, \ell]$ has full rank, such that its inverse exists. The covariance matrix can be rewritten as a sum of a rank one matrix and a full rank matrix according to (3.6a), such that the inverse of the covariance matrix can be determined using the Sherman-Morrison formula [ZF92, Section 22.5]. However, (3.6a) does not represent a closed-form expression, as the inverse of $\underline{\mathbf{M}}_1$ needs to be determined in advance. Regarding (3.6), the inverse of $\underline{\mathbf{M}}_j$ depends on $\underline{\mathbf{M}}_{j+1}$ for $j = 1, \dots, L-1$. For j equal to $L-1$, a closed-form expression of the matrix inverse $\underline{\mathbf{M}}_{L-1}^{-1}$ can be found according to (3.6d) and represents the starting point of the LC-CCIMP scheme.

To illustrate the concept of the LC-CCIMP scheme, Figure 3.5 on page 151 is used, where the precoding vectors are calculated in $|\mathbb{I}_1| + 1$ steps in an iterative manner. As in the O-CCIMP scheme, discussed in Section 3.3.2 of this thesis, the UE $\mu_1 \in \mathbb{U}$ has knowledge on the CTFs $\hat{\mathbf{H}}_{\text{CSI-RS}}^{(1, b)}$ and $\hat{\mathbf{H}}_{\text{CSI-RS}}^{(1, \tilde{b}_i)}$ for $1 \leq i \leq |\mathbb{I}_1|$ as well as the thermal noise power over the received bandwidth. These parameters represent the input parameters of the LC-CCIMP scheme, as depicted in Figure 3.5.

3.3 Cooperative Interference Mitigation Signal Precoding

Neglecting the second matrix on the right hand side of (3.6d) and making use of the definition of $\underline{\mathbf{v}}_{\tilde{b}}$ equal to $\hat{\mathbf{H}}_{\text{CSI-RS}}^{(1,b)} [k, \ell] \underline{\mathbf{p}}^{(\tilde{b})} [k, \ell]$, the UE $\mu_1 \in \mathbb{U}$ can determine the precoding vector used to precode the desired complex-valued modulation symbols carrying the codewords and the DMRSs transmitted by the TP $\epsilon_b \in$ according to

$$\underline{\mathbf{p}}^{(b)} [k, \ell] = \arg \max_A \underbrace{\frac{1}{\sigma_m^2} \sum_{\ell=0}^{2N_{\text{symp}}^{\text{DL}}-1} \sum_{k \in \mathcal{S}_{\text{SB}}^{(w)}} \left\| \hat{\mathbf{H}}_{\text{CSI-RS}}^{(m,b)} [k, \ell] \underline{\mathbf{q}}_j^{(b)} [k, \ell] \right\|^2}_{=2 \cdot N_{\text{symp}}^{\text{DL}} \cdot \overline{\gamma}_{\text{post, LC-CCIMP}}^{(1,b)} [w]} \quad (3.9)$$

assuming no inter-cell interference from the TPs out of the set \mathbb{I}_1 , such that the local post-SNR denoted by $\overline{\gamma}_{\text{post, LC-CCIMP}}^{(1,b)} [w]$ is maximized in each subband.

Following the concept of the Greedy algorithm [Cor+01, Section 16], the precoding vectors used to precode the interfering complex-valued modulation symbols carrying the codewords and DMRSs are subsequently computed in an iterative manner according to

$$\underline{\mathbf{p}}^{(\tilde{b}_i)} [k, \ell] = \arg \min_{\mathcal{I}_i} \underbrace{\sum_{\ell=0}^{2N_{\text{symp}}^{\text{DL}}-1} \sum_{k \in \mathcal{S}_{\text{SB}}^{(w)}} \frac{\left(\underline{\mathbf{q}}_j^{(\tilde{b}_i)} [k, \ell] \right)^{\text{H}} \mathbf{V}_i^{(m, \tilde{b}_i)} [k, \ell] \underline{\mathbf{q}}_j^{(\tilde{b}_i)} [k, \ell]}{1 + \left(\underline{\mathbf{q}}_j^{(\tilde{b}_i)} [k, \ell] \right)^{\text{H}} \mathbf{Q}_i^{(m, \tilde{b}_i)} [k, \ell] \underline{\mathbf{q}}_j^{(\tilde{b}_i)} [k, \ell]}}_{=2 \cdot N_{\text{symp}}^{\text{DL}} \cdot \overline{\gamma}_{\text{post, LC-CCIMP}}^{(1, \tilde{b}_i)} [w]}, \quad (3.10)$$

where

$$\mathbf{V}_i^{(m, \tilde{b}_i)} [k, \ell] = \underline{\mathbf{v}}_i^{(m, \tilde{b}_i)} [k, \ell] \left(\underline{\mathbf{v}}_i^{(m, \tilde{b}_i)} [k, \ell] \right)^{\text{H}} \quad (3.11a)$$

$$\underline{\mathbf{v}}_i^{(m, \tilde{b}_i)} [k, \ell] = \left(\hat{\mathbf{H}}_{\text{CSI-RS}}^{(m, \tilde{b}_i)} [k, \ell] \right)^{\text{H}} \left(\mathbf{R}_{i-1}^{(m)} [k, \ell] \right)^{-1} \hat{\mathbf{H}}_{\text{CSI-RS}}^{(m,b)} [k, \ell] \underline{\mathbf{p}}^{(b)} [k, \ell] \quad (3.11b)$$

$$\mathbf{Q}_i^{(m, \tilde{b}_i)} [k, \ell] = \left(\hat{\mathbf{H}}_{\text{CSI-RS}}^{(m, \tilde{b}_i)} [k, \ell] \right)^{\text{H}} \left(\mathbf{R}_{i-1}^{(m)} [k, \ell] \right)^{-1} \hat{\mathbf{H}}_{\text{CSI-RS}}^{(m, \tilde{b}_i)} [k, \ell] \quad (3.11c)$$

$$\mathbf{R}_n^{(m)} [k, \ell] = \sum_{u=1}^{n-1} \left(\hat{\mathbf{H}}_{\text{CSI-RS}}^{(m, \tilde{b}_u)} [k, \ell] \underline{\mathbf{p}}^{(\tilde{b}_u)} [k, \ell] \left(\hat{\mathbf{H}}_{\text{CSI-RS}}^{(m, \tilde{b}_u)} [k, \ell] \underline{\mathbf{p}}^{(\tilde{b}_u)} [k, \ell] \right)^{\text{H}} \right) + \sigma_m^2 \mathbf{I}_{N_{\text{R}}^{(m)}} \quad (3.11d)$$

holds, such that the average post-SNR denoted by $\overline{\gamma}_{\text{post, LC-CCIMP}}^{(1, \tilde{b}_i)} [w]$ is minimized in each subband at the interfering TP for $i = 1, \dots, |\mathbb{I}_1|$, as depicted in Figure 3.5. Inserting the two complex-valued matrices $\mathbf{V}_i^{(m, \tilde{b}_i)} [k, \ell]$ and $\mathbf{Q}_i^{(m, \tilde{b}_i)} [k, \ell]$, defined in (3.11a) and (3.11c), respectively, into (3.10), it becomes

obvious that the aforementioned average post-SNR $\bar{\gamma}_{\text{post, LC-CCIMP}}^{(1, \tilde{b}_i)} [w]$ in (3.10) is a function of the

- estimated CTFs $\hat{\mathbf{H}}_{\text{CSI-RS}}^{(1, b)} [k, \ell]$ and $\hat{\mathbf{H}}_{\text{CSI-RS}}^{(1, \tilde{b}_i)} [k, \ell]$ for $1 \leq i \leq n$,
- precoding vectors $\underline{\mathbf{p}}^{(b)} [k, \ell]$ and $\underline{\mathbf{p}}^{(\tilde{b}_i)} [k, \ell]$ for $1 \leq i < n$ and the
- thermal noise power over the received bandwidth,

as depicted in Figure 3.5. Consequently, to determine the precoding vector $\underline{\mathbf{p}}^{(\tilde{b}_n)} [k, \ell]$ minimizing the average post-SNR $\bar{\gamma}_{\text{post, LC-CCIMP}}^{(1, \tilde{b}_n)} [w]$ in the respective subband, the precoding vectors minimizing the average post-SNR $\bar{\gamma}_{\text{post, LC-CCIMP}}^{(1, \tilde{b}_i)} [w]$ have to be already determined for $1 \leq i < n$, as depicted in Figure 3.5. The resulting average post-SNR experienced by the UE $\mu_1 \in \mathbb{U}$ when using the iteratively computed precoding vectors reads

$$\bar{\gamma}_{\text{post, LC-CCIMP}}^{(1)} [w] = \bar{\gamma}_{\text{post, LC-CCIMP}}^{(1, b)} [w] - \sum_{i=1}^{|\mathbb{I}_1|} \bar{\gamma}_{\text{post, LC-CCIMP}}^{(1, \tilde{b}_i)} [w] \quad (3.12)$$

for each subband, where $0 \leq w < N_{\text{SB}}$ holds. Using the same TP $\epsilon_b \in \mathbb{A}_1^{\text{data}}$ and the same precoding vectors $\underline{\mathbf{p}}^{(b)} [k, \ell]$ and $\underline{\mathbf{p}}^{(\tilde{b}_i)} [k, \ell]$ for $1 \leq i \leq |\mathbb{I}_1|$, the equality between the average post-SNR (3.2) and (3.12) holds, as the transform of the inverse of the covariance matrix $\mathbf{R}_{\Sigma, \text{CSI-RS}}^{(1)} [k, \ell]$ using the Sherman-Morrison formula is a linear operation. Following the properties of the Greedy algorithm [Cor+01, Section 16], the LC-CCIMP scheme results in general in a lower average post-SNR, compared with the post-SNR when using the O-CCIMP scheme, such that

$$\bar{\gamma}_{\text{post, LC-CCIMP}}^{(1)} [w] \leq \bar{\gamma}_{\text{post, O-CCIMP}}^{(1)} [w] \quad (3.13)$$

holds for $0 \leq w < N_{\text{SB}}$. The inequality in (3.13) is fulfilled with the equality sign if the TP and precoding vectors selected by the O-CCIMP scheme and the LC-CCIMP scheme are equal. The major reason for the inequality in (3.13) is that, despite the O-CCIMP scheme where the global maximum of the average post-SNR in each subband is found by performing a full-blown search over all combinations of precoding vectors, the LC-CCIMP scheme only evaluates a subset of all combinations of the precoding vectors, such that only a local maximum rather than the global maximum of the average post-SNR is found.

The complexity of the LC-CCIMP scheme is analyzed in Section 3.3.4 of this thesis, whereas the performance of the LC-CCIMP scheme is discussed in Section 3.4 of this thesis.

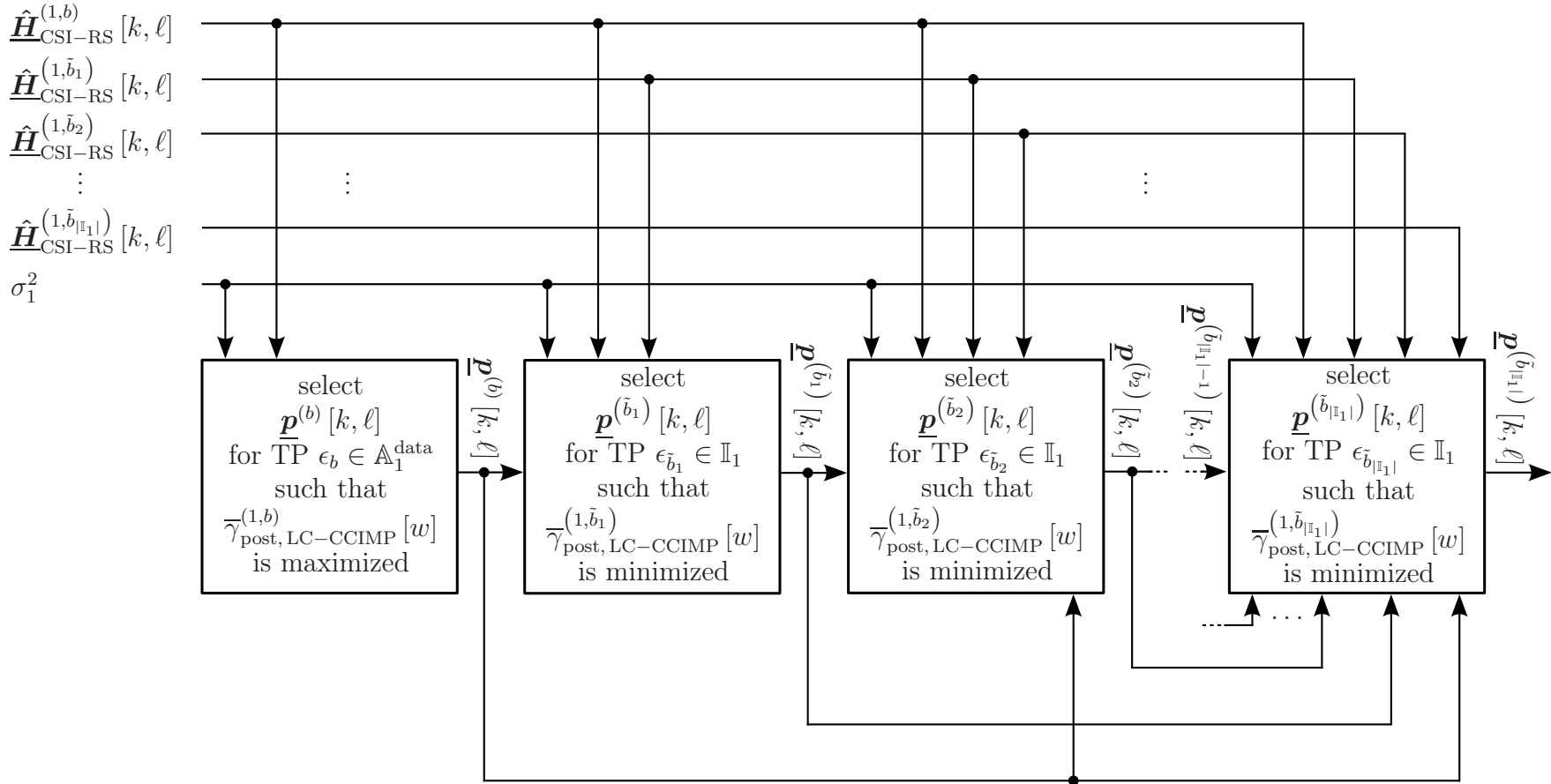


Figure 3.5. Block diagram of the LC-CCIMP scheme (created by the author of this thesis).

3.3.4 Complexity Analysis

To calculate the complexity of the O-CCIMP and the LC-CCIMP scheme, discussed in Section 3.3.2 and Section 3.3.3 of this thesis, respectively, the number of complex-valued additions and multiplications which have to be carried out in order to determine the precoding vectors $\underline{\mathbf{p}}^{(b)} [k, \ell]$ and $\underline{\mathbf{p}}^{(b_i)} [k, \ell]$ for $1 \leq i \leq |\mathbb{I}_1|$ is determined. The complexity of the linear operations used to calculate the average post-SNR experienced by the UE $\mu_1 \in \mathbb{U}$ in the w -th subband is denoted in Table 3.2 on page 155. Note that the complexity for the arg max, the arg min and the Hermitian operation is not included in this thesis. Furthermore, the memory requirement is not considered in this thesis.

The average post-SNR experienced by the UE $\mu_1 \in \mathbb{U}$ in the w -th subband of the O-CCIMP and LC-CCIMP scheme can be determined using an appropriate combination of linear algebra operations including the

- inverse of a matrix,
- sum of two matrices,
- product of two matrices,
- product of a matrix and a vector,
- scalar product of two vectors,
- outer product of two vectors and the
- product of the diagonal matrix with a scalar value,

denoted in the first column of Table 3.2. The complexity of the respective linear algebraic operation is denoted in the second column of Table 3.2 in terms of complex-valued additions and multiplications, denoted by $\Omega(\text{ADD})$ and $\Omega(\text{MUL})$, respectively. The dimension of the respective matrices and vectors is denoted in the third column of Table 3.2. Following [3GP06, Section A.1.3-3], in this thesis it is assumed that the UE $\mu_1 \in \mathbb{U}$ is equipped with two receive AEs, as already mentioned in Section 2.8.2 of this thesis. In that case, the covariance matrix $\underline{\mathbf{R}}_{\Sigma, \text{CSI-RS}}^{(1)} [k, \ell]$ in (3.2) and (3.11d) denotes a Hermitian square matrix with two rows and two columns and has full rank. Let

$$\underline{\mathbf{M}} = \begin{pmatrix} m_{11} & m_{21} \\ m_{21}^* & m_{22} \end{pmatrix} \quad (3.14)$$

denote the symbolic representation of that Hermitian square matrix. As (3.14) is Hermitian, the diagonal elements of $\underline{\mathbf{M}}$ in (3.14) are real valued, whereas the off-diagonal elements of $\underline{\mathbf{M}}$ in (3.14) are complex-valued and conjugate complex relative to each other [ZF92, Section 4.2]. The inverse of (3.14) can

be calculated using the adjugate matrix formula [ZF92, Section 3.2; Bro+01, Section 4.1.4.8] and reads

$$\underline{\mathbf{M}}^{-1} = \frac{1}{\underbrace{m_{11} \cdot m_{22} - |m_{21}|^2}_{=m_\zeta}} \cdot \begin{pmatrix} m_{22} & -m_{21} \\ -m_{21}^* & m_{11} \end{pmatrix} \quad (3.15)$$

for $m_{11} \cdot m_{22} \neq |m_{21}|^2$. To calculate the difference m_ζ in the denominator of (3.15), two products including the product of m_{11} and m_{22} as well as the product of m_{21} and m_{21}^* have to be determined followed by a subtraction. As the complexity of a subtraction is assumed to be equivalent to the complexity of an addition, the complexity to calculate the difference in the denominator of m_ζ reads $2 \cdot \Omega$ (MUL) and Ω (ADD). Furthermore, as the complexity of a division is assumed to be equivalent to the complexity of a multiplication, the complexity to calculate m_ζ in (3.15) reads $3 \cdot \Omega$ (MUL) and Ω (ADD).

As the off-diagonal elements of the 2×2 matrix $\underline{\mathbf{M}}$ in (3.14) are assigned with the negative preceding sign, what corresponds to the multiplication with minus one and each of the four elements of the 2×2 matrix in (3.14) needs to be weighted with m_ζ , the overall complexity to calculate the inverse of $\underline{\mathbf{M}}$ is denoted by $\Omega(\underline{\mathbf{M}}^{-1})$ and is equal to Ω (ADD) plus $9 \cdot \Omega$ (MUL), as denoted in Table 3.2. The complexity of the remaining linear algebra operations, denoted in Table 3.2 can be determined analogously.

Let $\Omega_{\text{O-CCIMP,ADD}}$ and $\Omega_{\text{O-CCIMP,MUL}}$ denote the complexity of the O-CCIMP scheme for subband PMI selection in terms of complex-valued additions and multiplications, respectively, assuming that the number of transmit AEs at the TP $\epsilon_b \in \mathbb{A}_1^{\text{data}}$ is equal to the number of transmit AEs at the interfering TPs out of the set \mathbb{I}_1 . Following the derivation of $\Omega_{\text{O-CCIMP,ADD}}$ and $\Omega_{\text{O-CCIMP,MUL}}$, discussed in the Appendix C.1 of this thesis,

$$\begin{aligned} \Omega_{\text{O-CCIMP,ADD}} = & \\ & 2^{N_{\text{T}}^{(b)}} \cdot \left(2^{N_{\text{T}}^{(b)}} - 1\right)^{|\mathbb{I}_1|} \left(2 N_{\text{symp}}^{\text{DL}} \left| \mathcal{S}_{\text{SB}}^{(w)} \right| \left(N_{\text{R}}^{(1)} (1 + |\mathbb{I}_1|) (3 N_{\text{R}}^{(1)} - 2)\right)\right) \end{aligned} \quad (3.16)$$

and

$$\begin{aligned} \Omega_{\text{O-CCIMP,MUL}} = & \\ & 2^{N_{\text{T}}^{(b)}} \left(2^{N_{\text{T}}^{(b)}} - 1\right)^{|\mathbb{I}_1|} \cdot 2 N_{\text{symp}}^{\text{DL}} \left| \mathcal{S}_{\text{SB}}^{(w)} \right| \left(N_{\text{R}}^{(1)} \left(|\mathbb{I}_1| N_{\text{R}}^{(1)} + \left(N_{\text{T}}^{(b)} (3 + 2 |\mathbb{I}_1|) + 2\right) + 9\right)\right) \end{aligned} \quad (3.17)$$

holds.

Moreover, let $\Omega_{\text{LC-CCIMP,ADD}}$ and $\Omega_{\text{LC-CCIMP,MUL}}$ denote the complexity of the LC-CCIMP scheme in terms of complex-valued additions and multiplications,

respectively, assuming that the number of transmit AEs at the TP $\epsilon_b \in \mathbb{A}_1^{\text{data}}$ is equal to the number of transmit AEs at the interfering TPs out of the set \mathbb{I}_1 . Following the derivation of $\Omega_{\text{LC-CCIMP,ADD}}$ and $\Omega_{\text{LC-CCIMP,MUL}}$, discussed in the Appendix C.2 of this thesis,

$$\begin{aligned} \Omega_{\text{LC-CCIMP,ADD}} = & \\ & 2 N_{\text{sy mb}}^{\text{DL}} \left| \mathcal{S}_{\text{SB}}^{(w)} \right| \left(|\mathbb{I}_1| \cdot \left(2^{N_{\text{T}}^{(b)}} - 1 \right) \cdot \left(N_{\text{R}}^{(1)} N_{\text{R}}^{(1)} \left(1 + 3 \cdot |\mathbb{I}_1| + 3 \cdot N_{\text{T}}^{(b)} \right) - \right. \right. \\ & \left. \left. N_{\text{R}}^{(1)} \left(2 \cdot |\mathbb{I}_1| + 3 \cdot N_{\text{T}}^{(b)} \right) + 2 \right) + 2^{N_{\text{T}}^{(b)}} \cdot \left(2 \cdot N_{\text{R}}^{(1)} N_{\text{R}}^{(1)} - N_{\text{R}}^{(1)} + 1 \right) - 1 \right) + \\ & \left(1 - 2^{N_{\text{T}}^{(b)}} \right) (2 + |\mathbb{I}_1|) \end{aligned} \quad (3.18)$$

and

$$\begin{aligned} \Omega_{\text{LC-CCIMP,MUL}} = & \\ & 2 N_{\text{sy mb}}^{\text{DL}} \left| \mathcal{S}_{\text{SB}}^{(w)} \right| \left(|\mathbb{I}_1| \cdot \left(2^{N_{\text{T}}^{(b)}} - 1 \right) \cdot \left(N_{\text{R}}^{(1)} N_{\text{R}}^{(1)} \left(|\mathbb{I}_1| + 3 \cdot N_{\text{T}}^{(b)} \right) + \right. \right. \\ & \left. \left. 2 \cdot N_{\text{R}}^{(1)} \cdot \left(N_{\text{T}}^{(b)} \cdot (|\mathbb{I}_1| + 1) + 2 \right) + 19 \right) + 2^{N_{\text{T}}^{(b)}} \cdot N_{\text{R}}^{(1)} \cdot \left(2 \cdot N_{\text{T}}^{(b)} + 1 \right) \right) + \\ & 2^{(N_{\text{T}}^{(b)}+1)}, \end{aligned} \quad (3.19)$$

holds.

The complexity of the O-CCIMP scheme and the LC-CCIMP scheme for subband PMI selection in terms of complex-valued additions and multiplications is denoted in Table 3.3 on page 156 for two and four transmit AEs at the TP $\epsilon_b \in \mathbb{A}_1^{\text{data}}$ and each interfering TP out of the set \mathbb{I}_1 . Moreover, following the findings achieved in Section 2.8.3 of this thesis, the number of interfering TPs causing strongest inter-cell interference is set to two, such that $|\mathbb{I}_1|$ in (3.16), (3.17), (3.18) and (3.19) is set to two. Moreover, the cardinality of the set of subcarriers in the respective subband, denoted by $|\mathcal{S}_{\text{SB}}^{(w)}|$ in (3.16), (3.17), (3.18) and (3.19) is set equal to six, corresponding to the channel bandwidth equal to 10 MHz [3GP16g, Table 7.2.1-3]. In case of two transmit AEs at the TP $\epsilon_b \in \mathbb{A}_1^{\text{data}}$ and the TPs out of the set \mathbb{I}_1 , making use of the LC-CCIMP scheme enables a complexity reduction over the O-CCIMP scheme in terms of complex-valued additions and multiplications of 74.5 % and 69.5 %, respectively. Increasing the number of transmit AEs from two to four and making use of the LC-CCIMP scheme enables a complexity reduction over the O-CCIMP scheme in terms of complex-valued additions and multiplications of 98.3 % and 98.5 %, respectively. Another interesting observation is that the complexity of both, complex-valued additions and multiplications increases approximately for one hundred times when doubling the number of transmit

Table 3.2. Complexity of linear algebra operations (created by the author of this thesis).

Operation	Complexity	Remark
Matrix inverse	$\Omega(\underline{\mathbf{M}}^{-1}) =$ $1 \cdot \Omega(\text{ADD}) +$ $9 \cdot \Omega(\text{MUL})$	$\underline{\mathbf{M}} \in \mathbb{C}^{N_{\text{R}}^{(1)} \times N_{\text{R}}^{(1)}}$ is a Hermitian square matrix with full rank; the inverse of $\underline{\mathbf{M}}$ is denoted in (3.15) for $N_{\text{R}}^{(1)}$ equal to two receive AEs at the UE $\mu_1 \in \mathbb{U}$
Sum of two matrices	$\Omega(\underline{\mathbf{M}}_1 + \underline{\mathbf{M}}_2) =$ $N_{\text{R}}^{(1)} \cdot N_{\text{R}}^{(1)} \cdot$ $\Omega(\text{ADD})$	$\underline{\mathbf{M}}_i \in \mathbb{C}^{N_{\text{R}}^{(1)} \times N_{\text{R}}^{(1)}}$ for $i = \{1, 2\}$
Product of two matrices	$\Omega(\underline{\mathbf{M}}_1 \cdot \underline{\mathbf{M}}_2) =$ $N_{\text{R}}^{(1)} \cdot N_{\text{T}}^{(b)} \cdot$ $\left(N_{\text{T}}^{(b)} \cdot \Omega(\text{MUL}) + \right.$ $\left. \left(N_{\text{R}}^{(1)} - 1 \right) \cdot \Omega(\text{ADD}) \right)$	$\underline{\mathbf{M}}_1 \in \mathbb{C}^{N_{\text{R}}^{(1)} \times N_{\text{R}}^{(1)}}$ and $\underline{\mathbf{M}}_2 \in \mathbb{C}^{N_{\text{R}}^{(1)} \times N_{\text{T}}^{(b)}}$
Product of matrix and a vector	$\Omega(\underline{\mathbf{M}} \underline{\mathbf{v}}) = N_{\text{R}}^{(1)} \cdot$ $\left(N_{\text{T}}^{(b)} \cdot \Omega(\text{MUL}) + \right.$ $\left. \left(N_{\text{R}}^{(1)} - 1 \right) \cdot \Omega(\text{ADD}) \right)$	$\underline{\mathbf{M}} \in \mathbb{C}^{N_{\text{R}}^{(1)} \times N_{\text{T}}^{(b)}}$ and $\underline{\mathbf{v}} \in \mathbb{C}^{N_{\text{T}}^{(b)} \times 1}$
Scalar product of two vectors	$\Omega(\underline{\mathbf{v}}^{\text{H}} \underline{\mathbf{v}}) =$ $N_{\text{R}}^{(1)} \cdot \Omega(\text{MUL}) +$ $\left(N_{\text{R}}^{(1)} - 1 \right) \cdot \Omega(\text{ADD})$	$\underline{\mathbf{v}} \in \mathbb{C}^{N_{\text{R}}^{(1)} \times 1}$
Outer product of two vectors	$\Omega(\underline{\mathbf{v}} \underline{\mathbf{v}}^{\text{H}}) =$ $N_{\text{R}}^{(1)} \cdot N_{\text{R}}^{(1)} \cdot$ $\Omega(\text{MUL})$	$\underline{\mathbf{v}} \in \mathbb{C}^{N_{\text{R}}^{(1)} \times 1}$
Product of the diagonal matrix with a scalar value	$\Omega\left(\alpha \cdot \underline{\mathbf{I}}_{N_{\text{R}}^{(1)}}\right) =$ $N_{\text{R}}^{(1)} \cdot \Omega(\text{MUL})$	$\alpha \in \mathbb{R}$ and $\underline{\mathbf{I}}_{N_{\text{R}}^{(1)}} \in \mathbb{R}^{N_{\text{R}}^{(1)} \times N_{\text{R}}^{(1)}}$

Table 3.3. Complexity of the O-CCIMP and LC-CCIMP scheme (created by the author of this thesis).

Complexity	$N_T^{(b)} = N_T^{(\tilde{b}_i)} = 2$ for $i \in \{1, 2\}$	$N_T^{(b)} = N_T^{(\tilde{b}_i)} = 4$ for $i \in \{1, 2\}$
$\Omega_{\text{O-CCIMP,ADD}} / \Omega(\text{ADD})$	$7.56 \cdot 10^4$	$7.56 \cdot 10^6$
$\Omega_{\text{LC-CCIMP,ADD}} / \Omega(\text{ADD})$	$1.93 \cdot 10^4$	$1.24 \cdot 10^5$
$\Omega_{\text{O-CCIMP,MUL}} / \Omega(\text{MUL})$	$1.48 \cdot 10^5$	$2.32 \cdot 10^7$
$\Omega_{\text{LC-CCIMP,MUL}} / \Omega(\text{MUL})$	$4.52 \cdot 10^4$	$3.54 \cdot 10^5$

AEs at the TP $\epsilon_b \in \mathbb{A}_1^{\text{data}}$ and the interfering TPs out of the set \mathbb{I}_1 for the O-CCIMP scheme from two to four. On the other hand, the complexity of the LC-CCIMP scheme in terms of complex-valued additions and multiplications increases approximately by a factor or less than ten when doubling the number of transmit AEs at the TP $\epsilon_b \in \mathbb{A}_1^{\text{data}}$ and the interfering TPs out of the set \mathbb{I}_1 from two to four.

3.4 Performance Evaluation

Numerical results at the link level are carried out to demonstrate the advantages of the O-CCIMP and the LC-CCIMP scheme for subband PMI selection, discussed in Section 3.3.2 and Section 3.3.3 of this thesis, respectively. The assumed simulation parameters are summarized in Table 3.4 on page 159. As already mentioned in Section 2.10 of this thesis, the numerical results at the link level are carried out for MCS4, MCS14 and MCS25, where the performance is evaluated at 90 % of the maximum bandwidth efficiency of the respective MCS according to (2.98a), (2.98b) and (2.98c), respectively. The performance of the IL single-layer transmission in TM10 in CoMP Scenario 4 in terms of SNR over bandwidth efficiency with signal equalization using the IRC receiver (2.73) is provided for both, the O-CCIMP as well as the LC-CCIMP scheme for subband PMI selection for the 2×2 MIMO antenna configuration in Figure 3.6 on page 160 - 161 for MCS4, MCS14 and MCS25. In addition, the reference performance for the upper bound in terms of SNR over bandwidth efficiency is represented by the NL single-layer transmission in TM9 for the 2×2 MIMO antenna configuration, where signal equalization is carried out using the MRC receiver and is depicted in Figure 3.6 for MCS4, MCS14 and MCS25. Moreover, the reference performance for the lower bound in terms of SNR over bandwidth efficiency is represented by the IL single-layer transmission in TM9 for the 2×2 MIMO antenna configuration, where signal

equalization is carried out using the IRC receiver (2.73) and is depicted in Figure 3.6 for MCS4, MCS14 and MCS25. The respective performance in terms of SNR over bandwidth efficiency for the 4×2 MIMO antenna configuration when making use of the O-CCIMP and the LC-CCIMP scheme for subband PMI selection, as well as the upper and lower bound is provided in Figure 3.7 on page 162 - 163 for MCS4, MCS14 and MCS25.

Making use of the O-CCIMP scheme for subband PMI selection for IL single-layer transmission in TM10 in CoMP Scenario 4, a gain of 2.9 dB compared with the subband PMI selection scheme (2.81) for the IL single-layer transmission in TM9 can be achieved, as depicted in Figure 3.6 (c) for the 2×2 MIMO antenna configuration for MCS25. Doubling the number of transmit AEs at each TP from two to four, the aforementioned gain increases to 5.6 dB, as depicted in Figure 3.7 (c) for the 4×2 MIMO antenna configuration. Furthermore, note that doubling the number of transmit AEs from two to four comes at the expense of a hundredfold increase of the computational complexity in terms of complex-valued additions and multiplications for subband PMI selection using the O-CCIMP scheme, as discussed in Section 3.3.4 of this thesis. Following the codebook and characteristic antenna diagram for signal transmission for two and four transmit AEs, denoted in Table 2.2 and Table A.1 on page 78 and 233, respectively, doubling the number of transmit AEs from two to four enables an increase of the maximum antenna gain from 3 dBi to 6 dBi over an isotropic radiator as well as a quadruplication of the number of precoding vectors. Hence, on the one hand a more precise precoding vector selection used to precode the desired complex-valued modulation symbols carrying the codewords and the DMRSs can be provided, resulting in a higher accumulated receiver power experienced by the UE $\mu_1 \in \mathbb{U}$ and, thus a higher bandwidth efficiency, as observed for the NL single-layer transmission in e.g. TM9. Furthermore, on the other hand a more precise precoding vector selection used to precode the interfering complex-valued modulation symbols carrying the codewords and DMRSs can be guaranteed with the aim of averting the main lobe of the interfering signal in order to decrease the accumulated receive signal power of the interfering signals experienced by the UE $\mu_1 \in \mathbb{U}$. The respective gain when making use of the O-CCIMP scheme for subband PMI selection for IL single-layer transmission in TM10, compared with the subband PMI selection scheme for IL single-layer transmission in TM9 reads 1.7 dB and 3.4 dB for MCS4 for the 2×2 and the 4×2 MIMO antenna configuration, as depicted in Figure 3.6 (a) and Figure 3.7 (a), respectively and 1.3 dB and 3.8 dB for MCS14 for the 2×2 and the 4×2 MIMO antenna configuration, as depicted in Figure 3.6 (b) and Figure 3.7 (b), respectively.

Making use of the LC-CCIMP scheme for subband PMI selection for IL single-layer transmission in TM10 in CoMP Scenario 4, a gain of 2.2 dB and 5.5 dB compared with the subband PMI selection (2.81) in for the IL single-layer

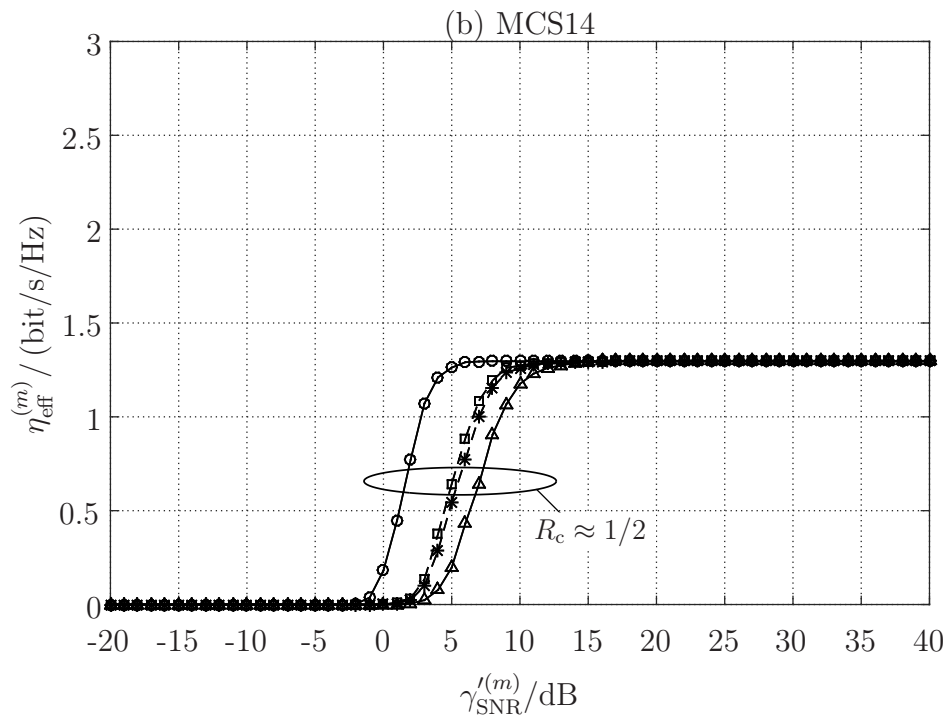
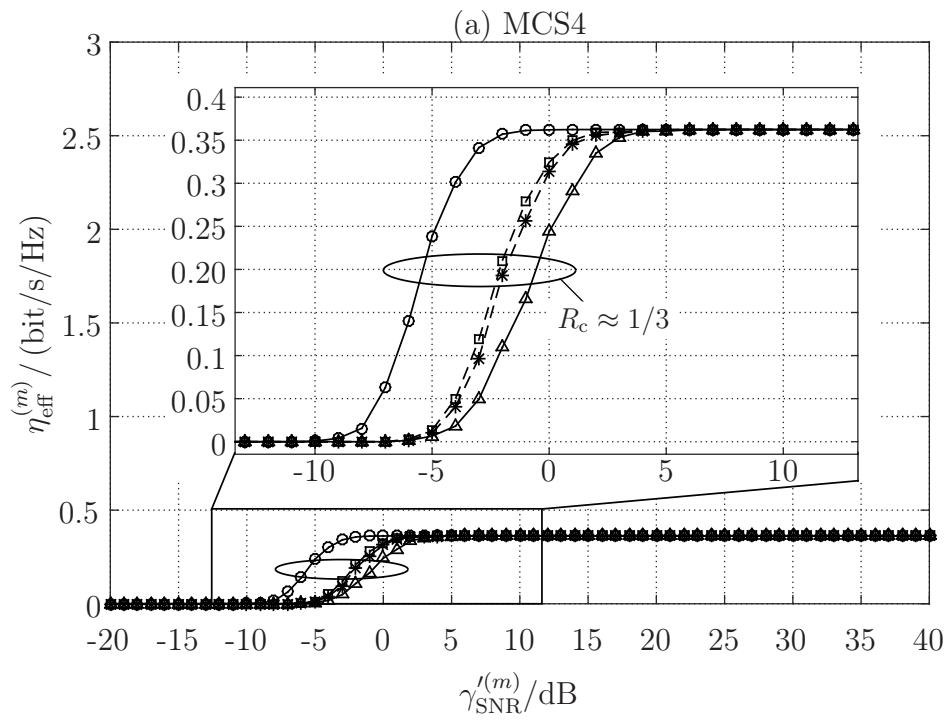
transmission in TM9 can be achieved for the 2×2 and the 4×2 MIMO antenna configuration, as depicted in Figure 3.6 (c) and Figure 3.7 (c), respectively, for MCS25. The respective gain when making use of the LC-CCIMP scheme for subband PMI selection for IL single-layer transmission in TM10 in CoMP Scenario 4, compared with the subband PMI selection scheme for IL single-layer transmission in TM9 reads 1.5 dB and 3.2 dB for MCS4 for the 2×2 and the 4×2 MIMO antenna configuration, as depicted in Figure 3.6 (a) and Figure 3.6 (a), respectively and 1.1 dB and 3.6 dB for MCS14 for the 2×2 and the 4×2 MIMO antenna configuration, as depicted in Figure 3.6 (b) and Figure 3.7 (b), respectively. Following the findings achieved in Section 3.3.3 of this thesis, the average post-SNR for the subband PMI selection using the LC-CCIMP scheme is smaller than or equal to the average post-SNR resulting for subband PMI selection using the O-CCIMP scheme. This observation is reflected by numerical results when comparing the performance of the O-CCIMP and the LC-CCIMP scheme for subband PMI selection for single-layer transmission in TM10 in CoMP Scenario 4. Making use of the LC-CCIMP scheme for subband PMI selection performs 0.7 dB and 0.2 dB close the the O-CCIMP scheme for subband PMI selection for single-layer transmission in TM10, as depicted in Figure 3.6 (c) and Figure 3.7 (c) for the 2×2 and the 4×2 MIMO antenna configuration, respectively for MCS25. The respective difference in terms of SNR of the performance of the O-CCIMP and the LC-CCIMP scheme for subband PMI selection reads 0.2 dB for both, the 2×2 and the 4×2 MIMO antenna configuration and the MCS4 and MCS14, as depicted in Figure 3.6 (a), Figure 3.6 (b), Figure 3.7 (a) and Figure 3.7 (b).

The investigation of the O-CCIMP and the LC-CCIMP scheme for subband PMI selection for single-layer transmission in TM10 in CoMP Scenario 4 represents a trade-off between the performance in terms of SNR over bandwidth efficiency and the computational complexity in terms of complex-valued additions and multiplications. While the O-CCIMP scheme for subband PMI selection outperforms the LC-CCIMP scheme for subband PMI selection in terms of SNR over bandwidth efficiency by 0.7 dB for the 2×2 MIMO antenna configuration and single-layer transmission in TM10, as depicted in Figure 3.6 (c) for MCS25, the latter scheme provides a complexity gain of 74.5 % and 69.5 % in terms of complex-valued additions and multiplications, respectively, over the former scheme. For the 4×2 MIMO antenna configuration the aforementioned gain reads 0.1 dB, while making use of the LC-CCIMP scheme for subband PMI selection provides a gain of 98.3 % and 98.5 % in terms of complex-valued additions and multiplications, respectively, compared with the O-CCIMP scheme for subband PMI selection for single-layer transmission in TM10 in CoMP Scenario 4.

Following the findings achieved in this section, it is sufficient to limit the investigation in Chapter 4 on the LC-CCIMP scheme for subband PMI selection.

Table 3.4. Simulation Parameters (created by the author of this thesis).

Parameter	Value
General Parameters:	
Channel Bandwidth	$f_{\text{BW}}^{(m)} = 10 \text{ MHz}$
Channel Model	SCM-B
Transmission Mode	TM9 and TM10
Interference Profile	according to Section 2.8.3 with $\gamma_{\text{INR}}^{(m, \tilde{b}_1)} = 3.2 \text{ dB}$, $\gamma_{\text{INR}}^{(m, \tilde{b}_2)} = 1.3 \text{ dB}$
Timing Offset	Synchronized transmission with $\tau_{\text{TO}}^{(x)} = 0 \text{ } \mu\text{s}$ for $x \in \{b_1, b'_1, b'_2, \tilde{b}_1, \tilde{b}_2\}$
CoMP Operating Set:	
Set of TPs the desired signal is transmitted from	$\mathbb{A}_1 = \mathbb{A}_1^{\text{data}} = \{\epsilon_{b_1}, \epsilon'_{b_1}, \epsilon'_{b_2}\}$ and $\mathbb{A}_1^{\text{CRS}} = \{\epsilon_{b_1}\}$
Set of TPs the interfering signal is transmitted from	$\mathbb{I}_1 = \{\epsilon_{\tilde{b}_1}, \epsilon_{\tilde{b}_2}\}$
Number of transmit AEs at the TPs	$N_{\text{T}}^{(x)} = 4 \vee N_{\text{T}}^{(x)} = 2$ for $x \in \{b_1, b'_1, b'_2, \tilde{b}_1, \tilde{b}_2\}$
MCS	4, 14 and 25 at TP $\epsilon_b \in \mathbb{A}_1^{\text{data}}$, random MCS selection at TPs $\epsilon_{\tilde{b}_1}$ and $\epsilon_{\tilde{b}_2}$
Channel Coding	Turbo Coding [3GP16d, Section 5]
UE:	
Channel Estimation	LSCE
Receiver	IRC
Channel Decoding	Turbo Decoding [Jun97, Section E.3]
Number of Receive AEs	$N_{\text{R}}^{(m)} = 2$
CSI Reporting	Subband PMI Feedback, O-CCIMP scheme (Section 3.3.2), LC-CCIMP scheme (Section 3.3.3)



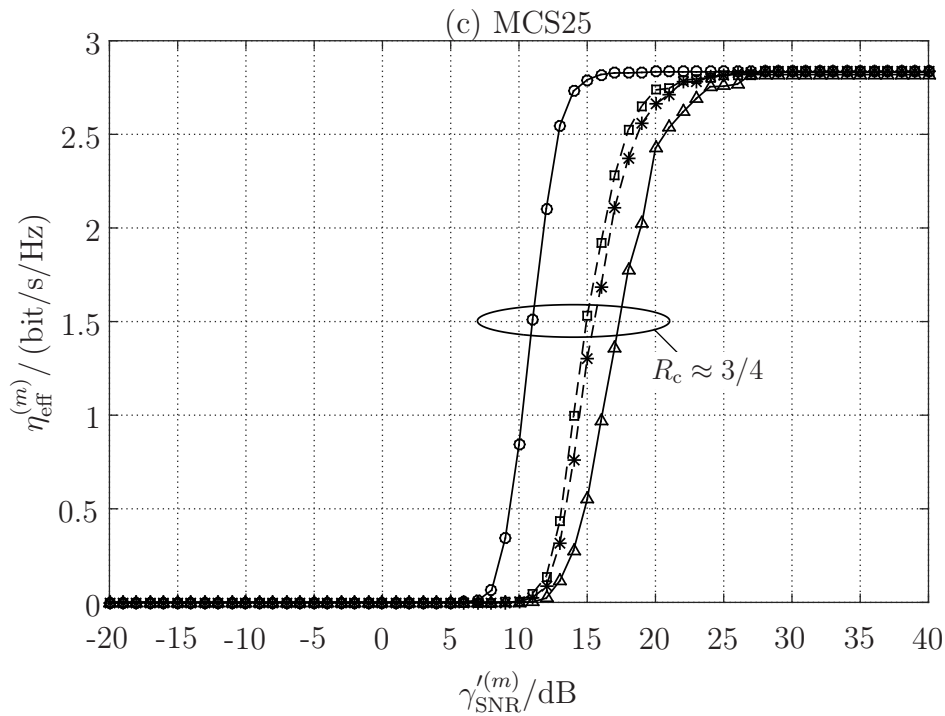
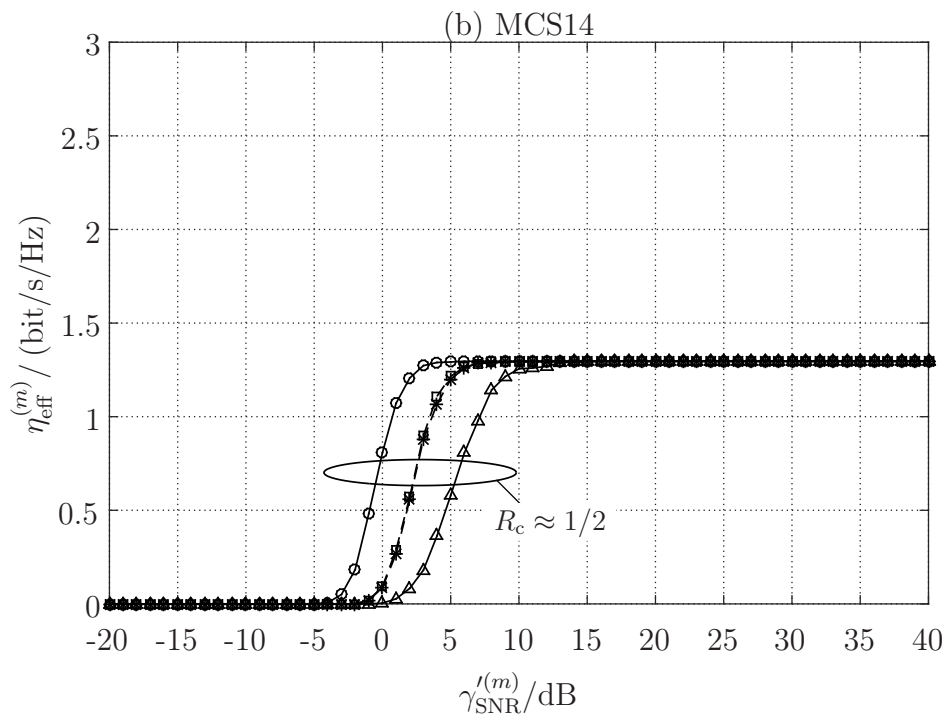
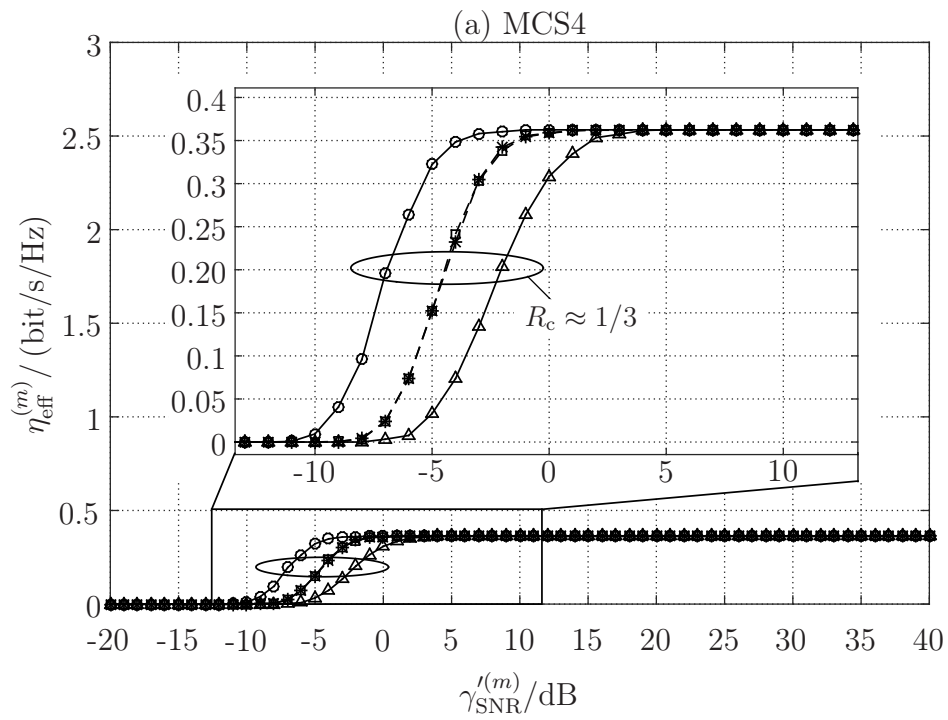


Figure 3.6. Performance comparison of the O-CCIMOP and LC-CCIMP scheme for (a) MCS4, (b) MCS14 and (c) MCS25 using the 2×2 MIMO antenna configuration (legend in Table 3.5; created by the author of this thesis).

Table 3.5. Legend for Figure 3.6 (a) – (c).

—○—	NL single-layer transmission in TM9 with the $N_T^{(b)} \times N_R^{(1)} = 2 \times 2$ MIMO antenna configuration and signal equalization using the MRC receiver; PMI selection according to (2.81) assuming no inter-cell interference
—△—	IL single-layer transmission in TM9 with the $N_T^{(b)} \times N_R^{(1)} = 2 \times 2$ MIMO antenna configuration and signal equalization using the IRC receiver (2.73); PMI selection according to (2.82) with $\underline{\mathbf{R}}_{\Sigma}^{(1)}[k, \ell] = \sigma_1^2 \cdot \mathbf{I}_{N_R^{(1)}}$
—■—	IL single-layer transmission in TM10 with the $N_T^{(b)} \times N_R^{(1)} = 2 \times 2$ MIMO antenna configuration and signal equalization using the IRC receiver (2.73); PMI selection using the O-CCIMP scheme according to (3.3)
—*—	IL single-layer transmission in TM10 with the $N_T^{(b)} \times N_R^{(1)} = 2 \times 2$ MIMO antenna configuration and signal equalization using the IRC receiver (2.73); PMI selection using the LC-CCIMP scheme according to (3.9) – (3.10)



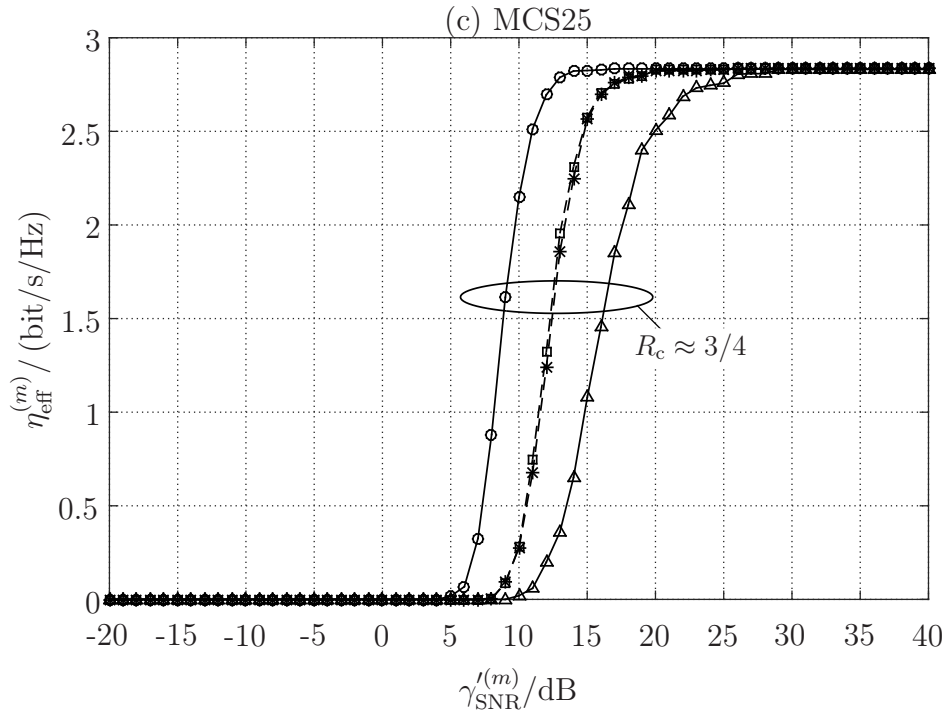


Figure 3.7. Performance comparison of the O-CCIMOP and LC-CCIMP scheme for (a) MCS4, (b) MCS14 and (c) MCS25 using the 4×2 MIMO antenna configuration (legend in Table 3.5; created by the author of this thesis).

Table 3.6. Legend for Figure 3.7 (a) – (c).

—○—	NL single-layer transmission in TM9 with the $N_T^{(b)} \times N_R^{(1)} = 4 \times 2$ MIMO antenna configuration and signal equalization using the MRC receiver; PMI selection according to (2.81) assuming no inter-cell interference
—△—	IL single-layer transmission in TM9 with the $N_T^{(b)} \times N_R^{(1)} = 4 \times 2$ MIMO antenna configuration and signal equalization using the IRC receiver (2.73); PMI selection according to (2.82) with $\underline{\mathbf{R}}_{\Sigma}^{(1)}[k, \ell] = \sigma_1^2 \cdot \mathbf{I}_{N_R^{(1)}}$
—■—	IL single-layer transmission in TM10 with the $N_T^{(b)} \times N_R^{(1)} = 4 \times 2$ MIMO antenna configuration and signal equalization using the IRC receiver (2.73); PMI selection using the O-CCIMOP scheme according to (3.3)
—*—	IL single-layer transmission in TM10 with the $N_T^{(b)} \times N_R^{(1)} = 4 \times 2$ MIMO antenna configuration and signal equalization using the IRC receiver (2.73); PMI selection using the LC-CCIMP scheme according to (3.9) – (3.10)

Chapter 4

Reliable Implicit Feedback Generation and Channel Estimation for Unsynchronized CoMP Transmission

4.1 Introduction

The restriction on synchronous CoMP transmission enables to determine the upper bound performance in terms of SNR over bandwidth efficiency for the implementation-friendly LC-CCIMP scheme discussed in Section 3.3.3 of this thesis. However, due to the geometrically separated TPs in the CoMP operating set, the simultaneous arrival of signals at the UE $\mu_m \in \mathbb{U}$ is fundamentally unrealizable [Zha+07, Section I; Iwe+14g, Section II-A]. Hence, it is not possible to find a DFT window that aligns all samples of the OFDM symbols arriving within the varying delays [KRF12, Section I]. In this thesis, the aspect of unsynchronized JP transmission with respect to implicit feedback generation and channel estimation is focused on. Therefore, it is assumed that the interfering signals reach the UE $\mu_m \in \mathbb{U}$ at the same time as the signals from the TP the UE is assigned to with respect to synchronization. Detail information on unsynchronized interference based processing can be found in [KRF12; Zha+07] and references therein.

Following the definition of the TO provided in Section 1.4 of this thesis, the TO occurs due to the time alignment error and the difference of the propagation delays [3GP13a, Section 5.1.2A]. The time alignment error inherits as the transmit APs are not perfectly aligned in time, such that the radio frequency signals at the APs experience certain differences in relation to each other [3GP16b, Section 6.5.3]. Moreover, the difference of the propagation delay denotes the distance between the TP out of the CoMP operating set the UE $\mu_m \in \mathbb{U}$ is assigned to with respect to synchronization and the TP

out of the CoMP operating set the UE receives the precoded DMRSs, the CSI-RSs and the precoded complex-valued modulation symbols carrying the codewords from, divided by the speed of the light [3GP13a, Section 5.1.2A]. Hence, the signal transmission in JP-DPS is said to be unsynchronized for any TO difference different from zero.

The presence of the TO among the desired signals is the major issue of practical CoMP transmission, leading to significant performance degradation if not appropriately compensated [Int12b, Section I; Int12c, Section 2; Hua12, Section 1.2]. The challenges of asynchronous CoMP transmission caused by non-ideal signal transmission are discussed in Section 4.2 of this thesis. In this context the aspect of the transmit AP co-location is discussed and the impact of the TO on implicit feedback generation and channel estimation is derived and illustrated. Frequency domain TO estimation techniques are discussed in Section 4.3 of this thesis. To enable reliable implicit feedback generation in practical CoMP transmission, the impact of the TO with respect to PMI selection has to be compensated [Iwe+14g, Section I]. Reliable implicit feedback generation schemes after OFDM signal demodulation are discussed in Section 4.4 of this thesis. Moreover, to enable reliable channel estimation in practical CoMP transmission, the impact of the TO with respect to channel estimation and piecewise linear interpolation has to be compensated. Therefore, a reliable channel estimation scheme is suggested and discussed in Section 4.5 of this thesis. In this content, the performance when making use of the TO estimation and compensation scheme with respect to PMI selection and channel estimation in conjunction with piecewise linear interpolation is discussed in Section 4.6 of this thesis.

4.2 Challenges of Asynchronous CoMP Transmission

4.2.1 Antenna Port Co-Location

To investigate the limitation of practical CoMP transmission, the co-location of the geometrically separated transmit APs out of the CoMP operating set has to be considered. Two transmit APs are said to be Quasi Co-Location (QCL) if the large scale properties of the mobile communication channel over which the complex-valued modulation symbols on one transmit AP is conveyed can be inferred from the mobile communication channel over which the complex-valued modulation symbols on the other transmit AP is conveyed, where the large properties include one or more of the [3GP16f, Section 6.2.1]

- delay spread,
- DOPPLER spread,
- DOPPLER shift,
- average delay and the
- average gain.

When applying the definition on the QCL on the TMs considered in this thesis, it becomes obvious that the transmit APs out of the set \mathcal{A}_{CRS} and, if available, the transmit APs out of the set $\mathcal{A}_{\text{DMRS}}$ and $\mathcal{A}_{\text{CSI-RS}}$ are jointly QCL for a serving cell for single-layer transmission in TM6, TM8 and TM9 [3GP16g, Section 7.1.10]. As a result, the UE $\mu_m \in \mathbb{U}$ can expect that the complex-valued modulation symbols transmitted from the transmit APs out of the set \mathcal{A}_{CRS} and, if available, the transmit APs out of the set $\mathcal{A}_{\text{DMRS}}$ and $\mathcal{A}_{\text{CSI-RS}}$ reach the UE with the same average delay, such that the timing is the same as derived from the PSS and SSS. Hence, in a practical implementation of single-layer transmission in TM6, TM8 and TM9 the UE $\mu_m \in \mathbb{U}$ is expected to receive the desired signals within the OFDM symbols covered by the DFT window.

In case of TM10 two QCL types are defined, including the QCL type A and the QCL Type B [3GP16g, Section 7.1.10] and explained in what follows for single-layer transmission in CoMP Scenario 4. To enable reliable switching between the TPs out of the CoMP operating set, aimed to transmit the precoded complex-valued modulation symbols, the QCL assumption for the transmit APs out of the set \mathcal{A}_{CRS} , $\mathcal{A}_{\text{DMRS}}$ and $\mathcal{A}_{\text{CSI-RS}}$ is only valid within one sub-frame. Note that it is up to the implementation of the UE to take advantage of the QCL assumption information [ZTE12, Section 2].

Following the properties of the QCL Type A [3GP16g, Section 7.1.10], the UE $\mu_m \in \mathbb{U}$ may assume that the transmit APs out of the set \mathcal{A}_{CRS} , $\mathcal{A}_{\text{DMRS}}$ and $\mathcal{A}_{\text{CSI-RS}}$ of a serving cell are QCL. In a practical implementation of single-layer transmission in CoMP Scenario 4 using JP-DPS, the QCL Type A is used to indicate that the signals transmitted from the transmit APs out of the set \mathcal{A}_{CRS} , $\mathcal{A}_{\text{DMRS}}$ and $\mathcal{A}_{\text{CSI-RS}}$ origin from one transmit AP out of the CoMP operating set, typically the TP the UE $\mu_m \in \mathbb{U}$ is assigned to with respect to synchronization. Hence, the UE $\mu_m \in \mathbb{U}$ receives the precoded DMRS, the precoded complex-valued modulation symbols carrying the codewords and the CSI-RSs with the same average delay as derived from the PSS and SSS transmitted from the transmit APs out of the set \mathcal{A}_{CRS} . Hence, the $\mu_m \in \mathbb{U}$ is expected to receive the desired signals within the OFDM symbols covered by the DFT window.

In case of QCL Type B, the UE $\mu_m \in \mathbb{U}$ cannot assume that the transmit APs out of the set \mathcal{A}_{CRS} , $\mathcal{A}_{\text{DMRS}}$ and $\mathcal{A}_{\text{CSI-RS}}$ are jointly QCL [3GP16g, Section 7.1.10]. However, the UE $\mu_m \in \mathbb{U}$ can definitely assume that the transmit APs out of the set $\mathcal{A}_{\text{DMRS}}$ and $\mathcal{A}_{\text{CSI-RS}}$ are QCL within a particular resource [3GP16g, Section 7.1.10]. In a practical implementation of single-layer transmission in CoMP Scenario 4 using JP-DPS, the former assumption is of major importance, as the UE $\mu_m \in \mathbb{U}$ might receive the signal transmitted from each transmit AP out of the set \mathcal{A}_{CRS} with a temporal delay to the signal transmitted from each transmit AP out of the set $\mathcal{A}_{\text{DMRS}}$ and $\mathcal{A}_{\text{CSI-RS}}$. In that case the TO among the signals is typically different from zero, such that the OFDM symbols carrying the precoded DMRSs, the precoded complex-valued modulation symbols carrying the codewords and the CSI-RSs are outside the DFT window, as depicted in Figure 2.6 on page 93. The latter assumption is mandatory to ensure that the precoding vector is selected from the same TP out of the CoMP operating set the codewords are transmitted from. The impact of unsynchronized signal transmission in presence of varying delays on implicit feedback generation and channel estimation is discussed in Section 4.2.2 and Section 4.2.3 of this thesis, respectively.

4.2.2 Implicit Feedback Generation

Following the findings achieved in Section 2.2.4 of this thesis, the CSI-RSs are transmitted in general on different subcarriers within a PRB and subframe for arbitrary transmit antenna configuration [3GP16f, Section 6.10.5.2]. As a delay in the time domain corresponds to a phase shift in the frequency domain [OL07, Section 2.7.1], the phase shift experienced at subcarrier k carrying a CSI-RS is in general different to the phase shift experienced at subcarrier k' carrying another CSI-RS within the same PRB after OFDM demodulation for $k \neq k'$. Hence, to investigate the impact of TOs on PMI selection, it is necessary to further break down the estimate $\hat{\mathbf{H}}_{\text{CSI-RS}}^{(m,b)} [n_{\text{PRB}}]$ into the transmit AP groups the CSI-RSs are transmitted from.

In case of unsynchronized CoMP transmission the estimate $\hat{\mathbf{H}}_{\text{CSI-RS}}^{(m,b)} [n_{\text{PRB}}]$ turns to

$$\begin{aligned} \hat{\mathbf{H}}_{\text{CSI-RS}}^{(m,b)} [n_{\text{PRB}}] = & \sqrt{C^{(m,b)}} \cdot \left(\mathbf{H}_{\text{CSI-RS}}^{(m,b)} [n_{\text{PRB}}] \odot \mathbf{\Phi}^{(m,b)} [n_{\text{PRB}}] \right) \cdot \chi_{\text{DFT}} \left(\tau_{\text{TO}}^{(b)} \right) + \\ & \mathbf{N}^{(m)} [n_{\text{PRB}}] + \mathbf{N}_{\text{ISI}}^{(m)} [n_{\text{PRB}}] \end{aligned} \quad (4.1)$$

with

$$\underline{\mathbf{H}}_{\text{CSI-RS}}^{(m,b)} [n_{\text{PRB}}] = \begin{pmatrix} \left[\underline{\mathbf{h}}_{1,1}^{(m,b)} [n_{\text{PRB}}] \right]^{\text{T}} & \cdots & \left[\underline{\mathbf{h}}_{1,u}^{(m,b)} [n_{\text{PRB}}] \right]^{\text{T}} & \cdots & \left[\underline{\mathbf{h}}_{1,U}^{(m,b)} [n_{\text{PRB}}] \right]^{\text{T}} \\ \vdots & \ddots & \vdots & \ddots & \vdots \\ \left[\underline{\mathbf{h}}_{\nu,1}^{(m,b)} [n_{\text{PRB}}] \right]^{\text{T}} & \cdots & \left[\underline{\mathbf{h}}_{\nu,u}^{(m,b)} [n_{\text{PRB}}] \right]^{\text{T}} & \cdots & \left[\underline{\mathbf{h}}_{\nu,U}^{(m,b)} [n_{\text{PRB}}] \right]^{\text{T}} \\ \vdots & \ddots & \vdots & \ddots & \vdots \\ \left[\underline{\mathbf{h}}_{N_{\text{R}}^{(m)},1}^{(m,b)} [n_{\text{PRB}}] \right]^{\text{T}} & \cdots & \left[\underline{\mathbf{h}}_{N_{\text{R}}^{(m)},u}^{(m,b)} [n_{\text{PRB}}] \right]^{\text{T}} & \cdots & \left[\underline{\mathbf{h}}_{N_{\text{R}}^{(m)},U}^{(m,b)} [n_{\text{PRB}}] \right]^{\text{T}} \end{pmatrix}, \quad (4.2)$$

where \odot in (4.1) corresponds to the SCHUR product [VA12, Section 1.2.7]. The vector $\underline{\mathbf{h}}_{\nu,u}^{(m,b)}$ in (4.2) is defined by [Iwe+14b, Section III-B]

$$\underline{\mathbf{h}}_{\nu,u}^{(m,b)} [n_{\text{PRB}}] = \begin{pmatrix} \underline{h}_{\nu,2u-1}^{(m,b)} [k_{14+(2u-1)}, \ell_{14+(2u-1)}] \\ \underline{h}_{\nu,2u}^{(m,b)} [k_{14+2u}, \ell_{14+2u}] \end{pmatrix} \quad (4.3)$$

and denotes the CTF between the ν -th receive AE at the UE $\mu_m \in \mathbb{U}$ and the u -th transmit AP group at the TP $\epsilon_b \in \mathbb{A}_m$ out of the CoMP operating set for $1 \leq \nu \leq N_{\text{R}}^{(m)}$ and $1 \leq u \leq U = N_{\text{T}}^{(b)}/2$, where $(k_{14+\zeta}, \ell_{14+\zeta}) \in \mathcal{S}_{i,n_{\text{PRB}},\text{CSI-RS}}^{(b,14+\zeta)}$ denotes the tuple of physical time-frequency resources carrying the CSI-RS for ζ being either equal to $2u - 1$ or $2u$. Note that the number of transmit AEs is assumed to be even and larger than or equal to two. Moreover, the matrix carrying the phase shift for each subcarrier the CSI-RSs are transmitted on in the n_{PRB} -th PRB is denoted by $\underline{\Phi}^{(m,b)} [n_{\text{PRB}}]$ in (4.1) and reads [Iwe+14b, Section III-B]

$$\underline{\Phi}^{(m,b)} [n_{\text{PRB}}] = \left[\mathbf{1}_{N_{\text{R}}^{(m)} \times 2} \cdot \exp(-j\phi(k_{15})), \dots, \mathbf{1}_{N_{\text{R}}^{(m)} \times 2} \cdot \exp(-j\phi(k_{15+(2u-1)})), \dots, \mathbf{1}_{N_{\text{R}}^{(m)} \times 2} \cdot \exp(-j\phi(k_{15+(2U-1)})) \right], \quad (4.4)$$

where $\mathbf{1}_{N_{\text{R}}^{(m)} \times 2}$ denotes the matrix of ones of dimension $N_{\text{R}}^{(m)} \times 2$ and $k_{15+(2u-1)}$ denotes the subcarrier index carrying the CSI-RS on the respective transmit AP group. For u equal to one, the CSI-RSs are transmitted from the first AP group, denoted by AP15 and AP16 on the subcarrier k_{15} . Furthermore, the baseband representation of the complex-valued AWGN for each physical time-frequency resource carrying the CSI-RS in the n_{PRB} -th PRB is denoted by the matrix $\underline{\mathbf{N}}^{(m)} [n_{\text{PRB}}] \in \mathbb{C}^{N_{\text{R}}^{(m)} \times N_{\text{T}}^{(b)}}$ in (4.1). The definition on the (ν, ζ) -th element of $\underline{\mathbf{N}}^{(m)} [n_{\text{PRB}}]$ can be found in (1.25) for $1 \leq \nu \leq N_{\text{R}}^{(m)}$ and $1 \leq \zeta \leq N_{\text{T}}^{(b)}$. Moreover, the matrix $\underline{\mathbf{N}}_{\text{ISI}}^{(m)} [n_{\text{PRB}}] \in \mathbb{C}^{N_{\text{R}}^{(m)} \times N_{\text{T}}^{(b)}}$ in (4.1) denotes the baseband representation of the complex-valued ISI component, where the (ν, ζ) -th el-

ement of $\underline{\mathbf{N}}_{\text{ISI}}^{(m)} [n_{\text{PRB}}]$ is different from zero in case of negative TOs and if the length of the CP minus the TO is smaller than or equal to the multipath spread of the mobile communication channel.

Following the iterative search of the precoding vectors for subband PMI selection of the LC-CCIMP scheme (3.9) - (3.10) discussed in Section 3.3.3 of this thesis and making use of (4.1), the transmit covariance matrix the PMI used to precode the DMRSs and the complex-valued modulation symbols carrying the codewords to be transmitted from a TP out of the CoMP operating set is selected upon, turns to

$$\underline{\mathbf{R}}_{\text{T}}^{(m)} = \frac{1}{\sigma_m^2} \cdot \sum_{k \in \mathcal{S}_{\text{SB}}^{(w)}} \hat{\underline{\mathbf{R}}}_{\text{T}}^{(m)} \left[\left\lfloor \frac{k}{N_{\text{sc}}^{\text{RB}}} \right\rfloor \right] = \frac{1}{\sigma_m^2} \cdot \sum_{k \in \mathcal{S}_{\text{SB}}^{(w)}} \hat{\underline{\mathbf{R}}}_{\text{T}}^{(m)} [n_{\text{PRB}}], \quad (4.5)$$

where

$$\begin{aligned} & \hat{\underline{\mathbf{R}}}_{\text{T}}^{(m)} [n_{\text{PRB}}] \\ &= \left(\hat{\underline{\mathbf{H}}}_{\text{CSI-RS}}^{(m,b)} [n_{\text{PRB}}] \right)^{\text{H}} \hat{\underline{\mathbf{H}}}_{\text{CSI-RS}}^{(m,b)} [n_{\text{PRB}}] \\ &= C^{(m,b)} \cdot \chi_{\text{DTF}}^2 \left(\tau_{\text{TO}}^{(b)} \right) \cdot \underline{\mathbf{\Gamma}}^{(m)} [n_{\text{PRB}}] + \\ & \quad \sqrt{C^{(m,b)}} \cdot \chi_{\text{DTF}} \left(\tau_{\text{TO}}^{(b)} \right) \cdot \left(\left(\underline{\mathbf{H}}_{\text{CSI-RS}}^{(m,b)} [n_{\text{PRB}}] \odot \underline{\mathbf{\Phi}}^{(m,b)} [n_{\text{PRB}}] \right)^{\text{H}} \cdot \right. \\ & \quad \left. \left(\underline{\mathbf{N}}^{(m)} [n_{\text{PRB}}] + \underline{\mathbf{N}}_{\text{ISI}}^{(m)} [n_{\text{PRB}}] \right) \right) + \\ & \quad \sqrt{C^{(m,b)}} \cdot \chi_{\text{DTF}} \left(\tau_{\text{TO}}^{(b)} \right) \cdot \left(\left(\underline{\mathbf{N}}^{(m)} [n_{\text{PRB}}] \right)^{\text{H}} + \left(\underline{\mathbf{N}}_{\text{ISI}}^{(m)} [n_{\text{PRB}}] \right)^{\text{H}} \cdot \right. \\ & \quad \left. \left(\underline{\mathbf{H}}_{\text{CSI-RS}}^{(m,b)} [n_{\text{PRB}}] \odot \underline{\mathbf{\Phi}}^{(m,b)} [n_{\text{PRB}}] \right) \right) + \\ & \quad \left(\left(\underline{\mathbf{N}}^{(m)} [n_{\text{PRB}}] \right)^{\text{H}} + \left(\underline{\mathbf{N}}_{\text{ISI}}^{(m)} [n_{\text{PRB}}] \right)^{\text{H}} \right) \cdot \\ & \quad \left(\left(\underline{\mathbf{N}}^{(m)} [n_{\text{PRB}}] \right) + \left(\underline{\mathbf{N}}_{\text{ISI}}^{(m)} [n_{\text{PRB}}] \right) \right) \end{aligned} \quad (4.6)$$

holds. The matrix $\underline{\mathbf{\Gamma}}^{(m)} [n_{\text{PRB}}] \in \mathbb{C}^{N_{\text{T}}^{(b)} \times N_{\text{T}}^{(b)}}$ in (4.6) denotes the transmit covariance matrix in absence of AWGN and ISI and reads [Iwe+14b, III-B]

$$\begin{aligned} \underline{\mathbf{\Gamma}}^{(m)} [n_{\text{PRB}}] &= \left(\underline{\mathbf{H}}_{\text{CSI-RS}}^{(m,b)} [n_{\text{PRB}}] \odot \underline{\mathbf{\Phi}}^{(m,b)} [n_{\text{PRB}}] \right)^{\text{H}} \cdot \\ & \quad \left(\underline{\mathbf{H}}_{\text{CSI-RS}}^{(m,b)} [n_{\text{PRB}}] \odot \underline{\mathbf{\Phi}}^{(m,b)} [n_{\text{PRB}}] \right). \end{aligned} \quad (4.7)$$

Exploiting the structure of the matrices $\underline{\mathbf{H}}_{\text{CSI-RS}}^{(m,b)} [n_{\text{PRB}}]$ and $\underline{\mathbf{\Phi}}^{(m,b)} [n_{\text{PRB}}]$, provided in (4.2) and (4.4), respectively, the matrix $\underline{\mathbf{\Gamma}}^{(m)} [n_{\text{PRB}}]$ can be simplified as provided in (4.8) on page 171 of this thesis. Obviously, the matrix $\underline{\mathbf{\Gamma}}^{(m)} [n_{\text{PRB}}]$ is divided into U^2 sub-matrices, where each sub-cross covariance

$$\underline{\mathbf{\Gamma}}^{(m)} [n_{\text{PRB}}] = \begin{bmatrix} \underline{\Xi}_{1,1}^{(m,b)} [n_{\text{PRB}}] & \dots & \underline{\Xi}_{1,u}^{(m,b)} [n_{\text{PRB}}] \cdot \exp(j\phi_{\Delta}(1,u)) & \dots & \underline{\Xi}_{1,U}^{(m,b)} [n_{\text{PRB}}] \cdot \exp(j\phi_{\Delta}(1,U)) \\ \vdots & \ddots & \vdots & \ddots & \vdots \\ \underline{\Xi}_{u,1}^{(m,b)} [n_{\text{PRB}}] \cdot \exp(j\phi_{\Delta}(u,1)) & \dots & \underline{\Xi}_{u,u}^{(m,b)} [n_{\text{PRB}}] & \dots & \underline{\Xi}_{u,U}^{(m,b)} [n_{\text{PRB}}] \cdot \exp(j\phi_{\Delta}(u,U)) \\ \vdots & \ddots & \vdots & \ddots & \vdots \\ \underline{\Xi}_{U,1}^{(m,b)} [n_{\text{PRB}}] \cdot \exp(j\phi_{\Delta}(U,1)) & \dots & \underline{\Xi}_{U,u}^{(m,b)} [n_{\text{PRB}}] \cdot \exp(j\phi_{\Delta}(U,u)) & \dots & \underline{\Xi}_{U,U}^{(m,b)} [n_{\text{PRB}}] \end{bmatrix} \quad (4.8)$$

matrix $\Xi_{i,j}^{(m,b)} [n_{\text{PRB}}] \in \mathbb{C}^{2 \times 2}$ in (4.8) is Hermitian and reads [Iwe+14b, Section III-B]

$$\Xi_{i,j}^{(m,b)} [n_{\text{PRB}}] = \sum_{\nu=1}^{N_{\text{R}}^{(m)}} \left(\left[\mathbf{h}_{\nu,i}^{(m,b)} [n_{\text{PRB}}] \right] \cdot \left[\mathbf{h}_{\nu,j}^{(m,b)} [n_{\text{PRB}}] \right]^{\text{H}} \right)^* \quad (4.9)$$

for $1 \leq i, j \leq U$. The phase offset $\phi_{\Delta}(i, j)$ in (4.8) can only be observed at the off-diagonal sub-matrices $\Xi_{i,j}^{(m,b)} [n_{\text{PRB}}]$ for $i \neq j$ [Iwe+14b, Section III-B]. Calculating the transmit covariance matrix, the presence of the TO results in a phase de-rotation caused by the $(\cdot)^{\text{H}}$ operation in (4.7) and a subsequent phase rotation in (4.7) [Iwe+14b, Section III-B]. The phase offset in (4.8) vanishes for the CSI-RSs transmitted from the same transmit AP group, as the CSI-RSs are transmitted on the same subcarrier and experience the same phase shift after OFDM demodulation for $i = j$. However, in any other case the amount of de-rotation and rotation is not balanced, leading to a phase offset $\phi_{\Delta}(i, j)$ and reads [Iwe+14b, Section III-B]

$$\phi_{\Delta}(i, j) = \frac{2\pi k_{\Delta}(i, j) \tau_{\text{TO}}^{(b)} f_s}{N_{\text{OFDM}}}, \quad (4.10)$$

as denoted in (4.8) for $i \neq j$. For each submatrix $\Xi_{i,j}^{(m,b)} [n_{\text{PRB}}]$ in (4.8), the phase offset $\phi_{\Delta}(i, j)$ depends linearly on the spacing between the subcarriers carrying the CSI-RSs transmitted from different transmit AP groups the mobile communication channel (4.3) is estimated from, where the spacing is represented by $k_{\Delta}(i, j)$ and reads [Iwe+14b, Section III-B]

$$k_{\Delta}(i, j) = k_{14+(2i-1)} - k_{14+(2j-1)} = k_{14+2i} - k_{14+2j} \quad (4.11)$$

for $1 \leq i, j \leq U$. Hence, for unsynchronized CoMP transmission with any TO different from zero, the phase offset (4.10) is equal to zero for $k_{\Delta}(i, j)$ equal to zero, corresponding to CSI-RS transmission from the same transmit AP group. Moreover, for unsynchronized CoMP transmission with any TO different from zero, the phase offset (4.10) is different from zero for $k_{\Delta}(i, j)$, corresponding to CSI-RS transmission from different transmit AP groups.

In what follows, the matrix $\mathbf{\Gamma}^{(m)} [n_{\text{PRB}}]$ in (4.6) is further analyzed to investigate the impact of the TO on the PMI selection for the 4×2 and the 2×2 MIMO antenna configuration, considered throughout this thesis.

In case of the TP $\epsilon_b \in \mathbb{A}_m$ equipped with four transmit AEs, the matrix

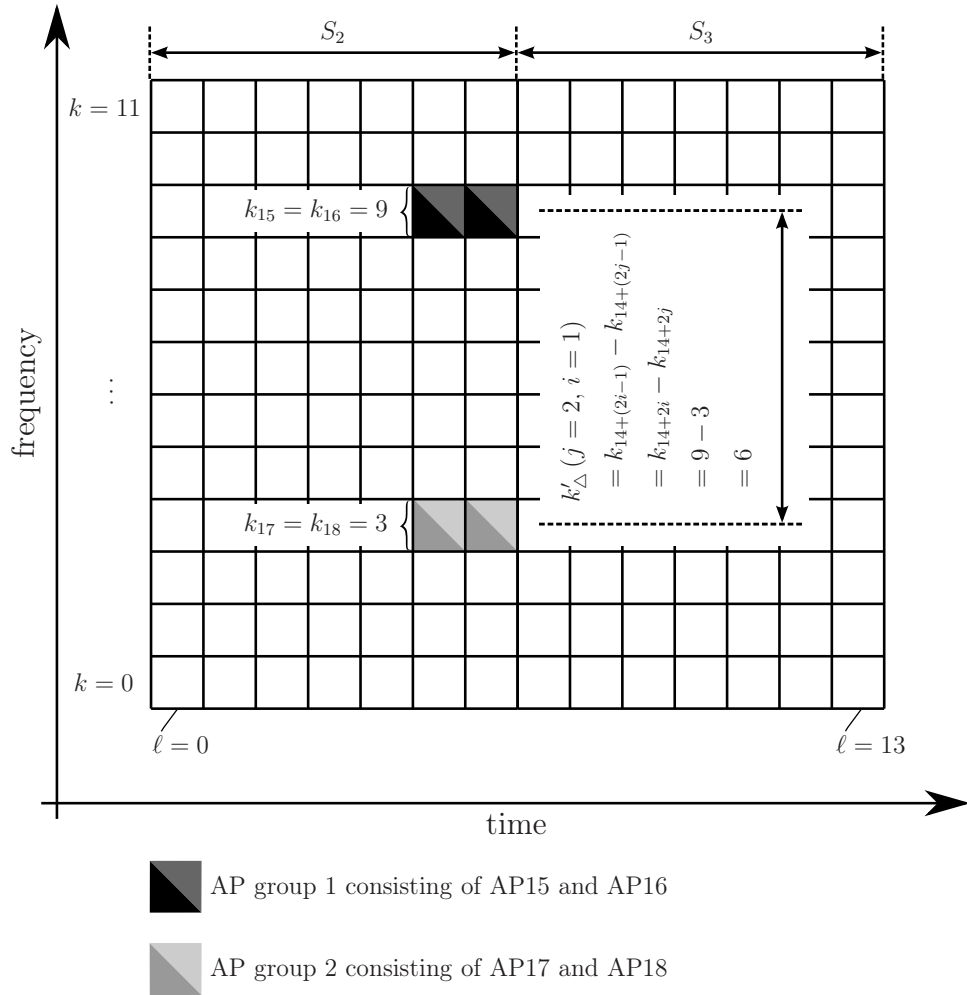


Figure 4.1. Mapping of the CSI-RS on physical time-frequency resources for two transmit AP groups (created by the author of this thesis using [Iwe+14b, Figure 3]).

$\underline{\Gamma}^{(m)} [n_{\text{PRB}}]$ in (4.8) turns to

$$\underline{\Gamma}^{(m)} [n_{\text{PRB}}] = \begin{bmatrix} \underline{\Xi}_{1,1}^{(m,b)} [n_{\text{PRB}}] & \underline{\Xi}_{1,2}^{(m,b)} [n_{\text{PRB}}] \cdot \exp(j\phi_{\Delta}(2,1)) \\ \underline{\Xi}_{2,1}^{(m,b)} [n_{\text{PRB}}] \cdot \exp(j\phi_{\Delta}(1,2)) & \underline{\Xi}_{2,2}^{(m,b)} [n_{\text{PRB}}] \end{bmatrix}, \quad (4.12)$$

where the spacing (4.11) of the phase offset (4.10) is illustrated in Figure 4.1 on page 173. Figure 4.1 shows a cutout of the zeroth PRB and the first subframe with a particular focus on the CSI-RSs transmitted from the transmit AP15, the transmit AP16, the transmit AP17 and the transmit AP18 using CSI configuration 0, where the former two transmit APs and the latter two transmit APs belong to the first and second transmit AP group, respectively. For the sake of clarity, the remaining physical time-frequency resources carrying the CRSs, the precoded DMRSs, the precoded complex-valued modulation symbols carrying the codewords and the complex-valued modulation symbols carrying the control information are not explicitly highlighted. Following [3GP16f, Table 6.10.5.2-1] for CSI configuration 0, the CSI-RSs transmitted from the first and second transmit AP group are scheduled in the ninth and the ninth subcarrier in each PRB, respectively. Following the mapping of CSI-RSs to resources [3GP16f, Section 6.10.5.2], the spacing $k_{\Delta}(i=1, j=2)$ is always equal to six for the normal CP configuration if the RSs are transmitted from transmit AP15 to transmit AP18, as depicted in Figure 4.1.

Let

$$p_{\text{PMI}, N_{\text{T}}^{(b)}}(i | \tau_{\text{TO}}^{(b)}), \quad i \in \mathcal{S}_{\text{PMI}, N_{\text{T}}^{(b)}} \quad (4.13)$$

denote the conditional probability to select the i -th PMI for subband PMI selection to precode the DMRSs and the complex-valued modulation symbols carrying the codewords in presence of the TO $\tau_{\text{TO}}^{(b)}$ for the TP $\epsilon_b \in \mathbb{A}_m^{\text{data}}$ equipped with $N_{\text{T}}^{(b)}$ transmit AEs. Making use of the LC-CCIMP scheme for subband PMI selection, discussed in Section 3.3.3 of this thesis, the conditional probability for each PMI used to precode the DMRSs and the complex-valued modulation symbols carrying the codewords, transmitted by the TP $\epsilon_b \in \mathbb{A}_m^{\text{data}}$ in dependence on the TO is depicted in Figure 4.2 on page 176 for $-6 \mu\text{s} \leq \tau_{\text{TO}}^{(b)} \leq 6 \mu\text{s}$. Regarding Figure 4.2, the conditional probability to select PMI1 is approximately equal to the conditional probability for PMI3, PMI10 and PMI12 for the investigated TO range, as indicated by the solid line. Moreover, the same holds for PMI2, PMI4, PMI9 and PMI11, as indicated by the dashed line, for PMI5 and PMI7, as indicated by the dotted line and for PMI6 and PMI8, as indicated by the dash-dotted line. As the maximum antenna gain for the precoding vectors with corresponding PMI13 to PMI16 is considerably smaller than the maximum antenna gain of the remaining precoding vectors, denoted in the third column of Table A.1 on page

233, the conditional probability for PMI13 to PMI16 is smaller than 0.1% for $-6\ \mu\text{s} \leq \tau_{\text{TO}}^{(b)} \leq 6\ \mu\text{s}$ and can therefore be neglected. It can be observed that the conditional probability (4.13) of selecting a PMI depends to a large extent on the TO and the associated phase offset (4.10), denoted on the off-diagonal sub-matrices in (4.12). While for instance the PMI6 and the PMI8 have an occurrence probability of approximately 42% each in case of a TO equal to zero, corresponding to synchronized CoMP transmission, the occurrence probability of the two aforementioned PMIs decreases to less than 1% for a TO equal to $2.6\ \mu\text{s}$, as depicted in Figure 4.2. Simultaneously, the occurrence probability of the PMI2, the PMI4, the PMI9 and the PMI11 increases to approximately 24% each for the TO equal to $2.6\ \mu\text{s}$, as depicted in Figure 4.2. Hence, the selected precoding vector does no longer maximize the local post-SNR $\bar{\gamma}_{\text{post, LC-CCIMP}}^{(1)}[w]$ in the respective subband in case of a DFT window mismatch, such that the main lobe of the desired signal is steered in another direction and, hence, the expected performance of CoMP transmission is reduced.

Following the findings achieved in Section 4.1 of this thesis, the presence of varying TOs arising in practical CoMP transmission results in general in improper PMI selection [Iwe+14b, Section III-B], improper channel estimation and ISI [TG11, Section I]. To provide the performance loss in terms of SNR caused by improper PMI selection, the impact on the former two effects must be decoupled. To enable reliable channel estimation in unsynchronized CoMP transmission, one way forward is to de-rotate the subcarrier specific phase shift prior to interpolating all subcarriers in frequency direction within the subband and all OFDM symbols in time direction within the subframe the precoding vector remains unchanged and, subsequently, re-rotate the subcarrier specific phase shift [HW98, Section IV-C] assuming perfect knowledge on the TO. Further information on reliable channel estimation in unsynchronized CoMP transmission is provided in Section 4.5 of this thesis.

Let $10 \log_{10}(\Delta)$ denote the performance loss in terms of SNR caused by the practical limitations of unsynchronized CoMP transmission compared to synchronized CoMP transmission, evaluated at 90% of the maximum bandwidth efficiency of the respective MCS. The performance loss over the TO is depicted in Figure 4.3 on page 178 for the 4×2 MIMO antenna configuration for the three MCSs including MCS4, MCS14 and MCS25. In detail the performance loss is provided for

- ignoring the impact of the TO with respect to both, PMI selection and channel estimation,
- compensating the impact of the TO with respect to PMI selection using a phase offset correction scheme provided in Section 4.4 of this thesis and ignoring the impact of the TO with respect to channel estimation,

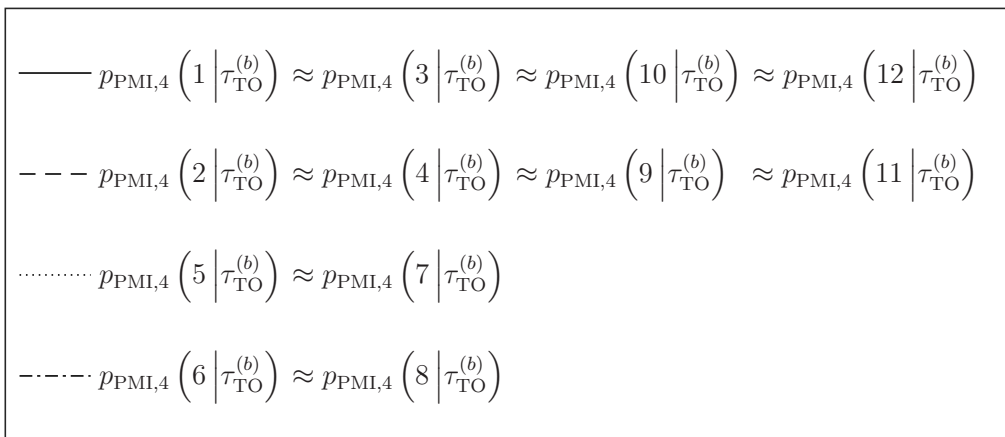
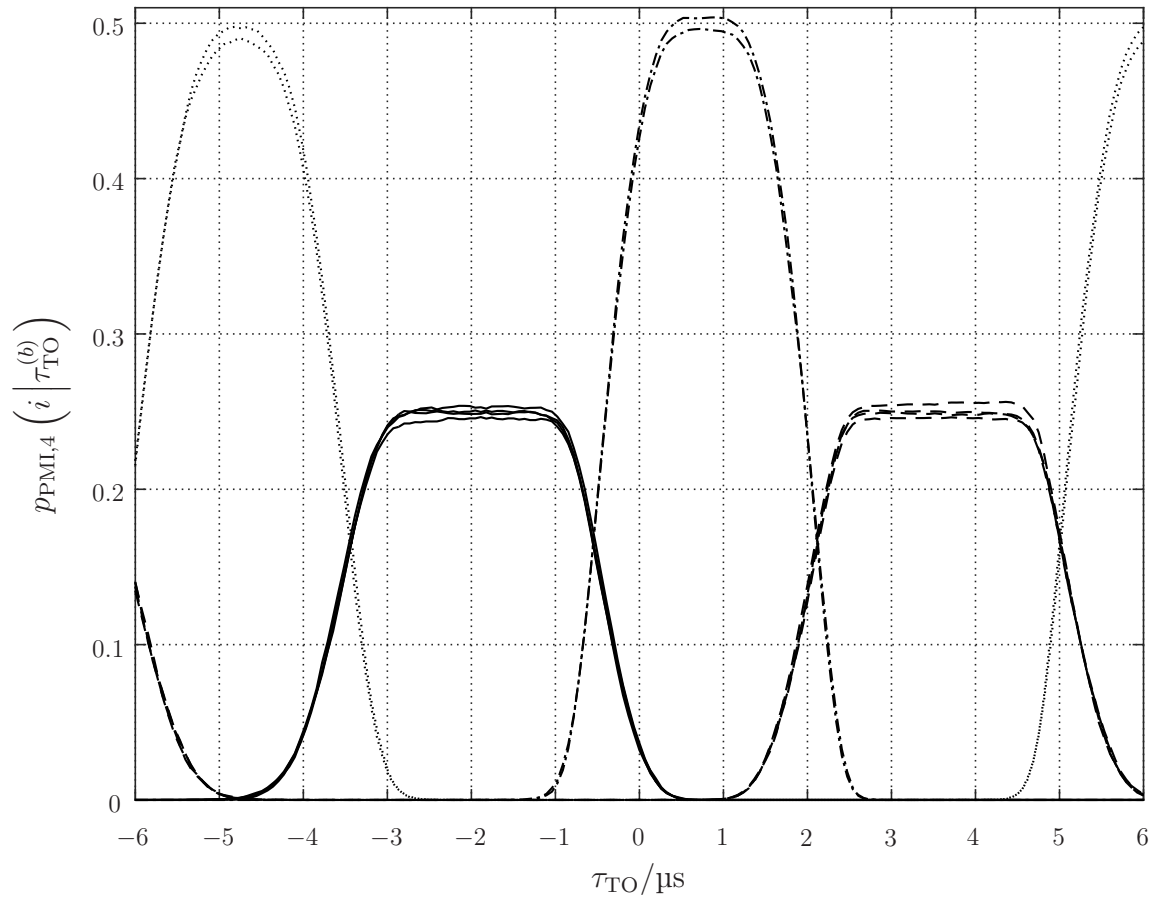


Figure 4.2. Distribution of the PMIs in dependence on the TO (created by the author of this thesis using).

- ignoring the impact of the TO with respect to PMI selection and compensating the impact of the TO with respect to channel estimation using a combined phase shift compensation and channel interpolation scheme provided in Section 4.5 of this thesis and for
- compensating the impact of the TO with respect to PMI selection and channel estimation using the aforementioned schemes provided in Section 4.4 and Section 4.5, respectively.

Hence, the first case provides the worst-case scenario for the performance loss, as depicted in Figure 4.3, as the post-SNR is not maximized due to improper PMI selection, reliable channel estimation is limited and the receive signal is additionally superimposed with ISI if the TO is larger than the difference between the length of the CP and the multipath spread. Compensating the impact of the TO with respect to PMI selection and channel estimation assuming perfect knowledge on the TO, the performance loss can be considerably limited such that the last case provides the best-case scenario for the performance loss, as depicted in Figure 4.3. In that case the receive signal is faced with ISI if the TO is larger than the difference between the length of the CP and the multipath spread (2.85), resulting in 583.3 ns and 63.5 ns for the zeroth and the remaining six OFDM symbols in each slot, respectively. However, the impact of ISI can be tolerated up to 4.7 μ s, 5.8 μ s and more than 6 μ s for MCS25, MCS14 and MCS4, respectively, such that the performance loss caused by the TO remains smaller than the performance difference provided in what follows.

For reference purpose, the performance difference between IL single-layer transmission in TM10 in CoMP Scenario 4 using the LC-CCIMP scheme for sub-band PMI selection and IL single-layer transmission in TM9, derived in Section 3.4 of this thesis for the 4×2 MIMO antenna configuration is depicted in Figure 4.3 (a), Figure 4.3 (b) and Figure 4.3 (c) for MCS4, MCS14 and MCS25 and reads 3.2 dB, 3.6 dB and 5.5 dB respectively, as indicated by the dashed line. Consequently, to exploit the advantages of practical CoMP transmission, the performance loss caused by the TO must be below the dashed line.

Ignoring the impact of the TO with respect to both, PMI selection and channel estimation, the advantages of CoMP transmission vanish for a TO larger than 2.1 μ s, 1.9 μ s and 1.8 μ s for MCS4, MCS14 and MCS25, respectively, as depicted in Figure 4.3. Furthermore, considering the findings achieved by LEE et. al. [Lee+12b], no significant performance loss caused by CSI feedback should be observed when deploying practical CoMP transmission with a TO up to 3 μ s [Lee+12b, 4-th sentence in the 3-rd paragraph of the right column on page 46]. However, although the impact of the TO with respect to channel estimation is compensated, a performance loss of approximately

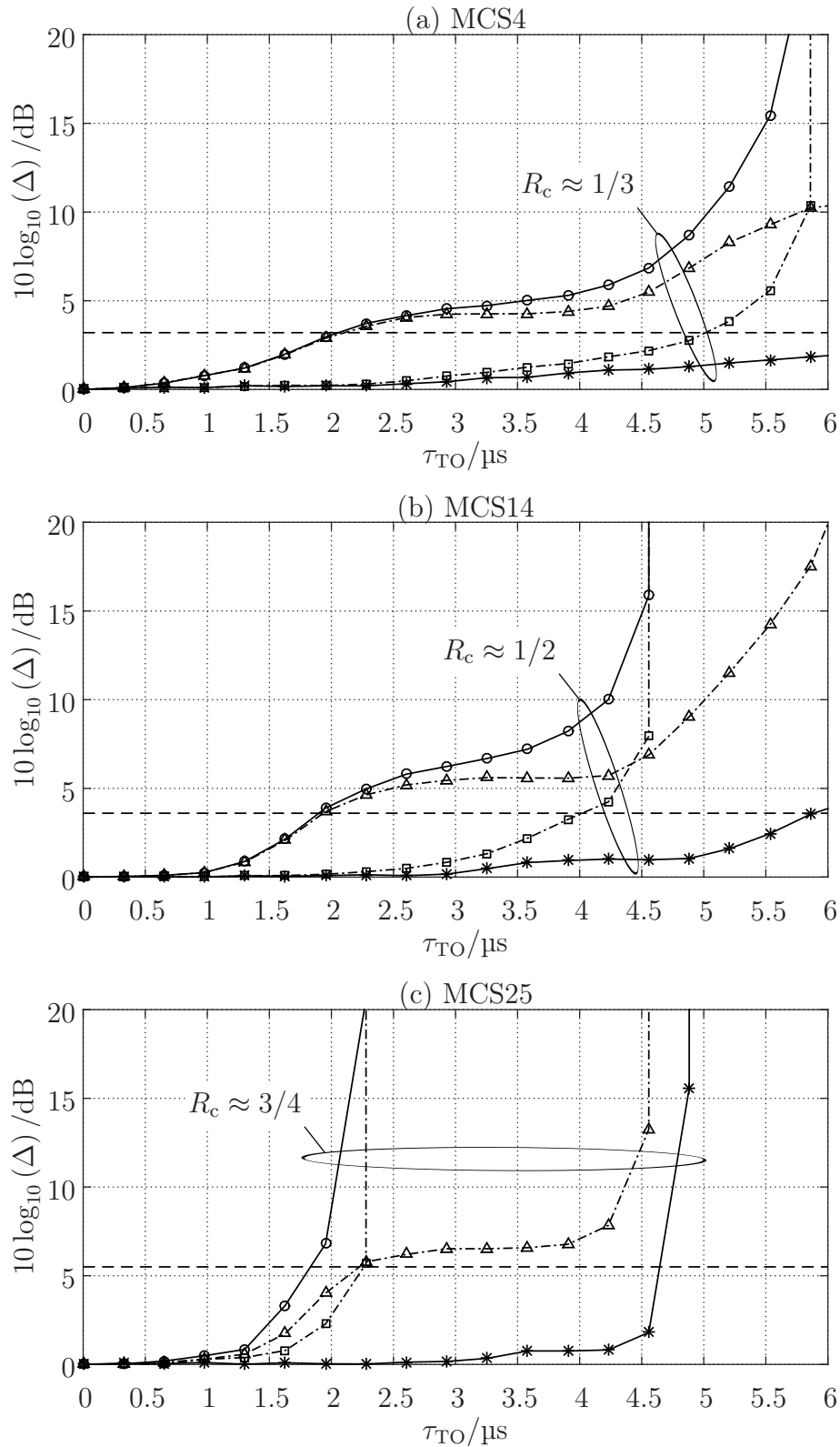


Figure 4.3. Impact of the TO on the performance for the 4×2 MIMO antenna configuration for (a) MCS4, (b) MCS14 and (c) MCS25 (legend see Table 4.11; created by the author of this thesis).

Table 4.1. Legend for Figure 4.3.

—○—	Ignore impact of the TO with respect to both, PMI selection and channel estimation in unsynchronized IL single-layer transmission in TM10
--△--	Ignore the impact of the TO with respect to PMI selection and compensate the impact of the TO with respect to channel estimation according to Section 4.5 assuming perfect knowledge of the TO in unsynchronized IL single-layer transmission in TM10
--■--	Compensate the impact of the TO with respect to PMI selection according to Section 4.4 assuming perfect knowledge of the TO and ignore the impact of the TO with respect to channel estimation in unsynchronized IL single-layer transmission in TM10
—*—	Compensate the impact of the TO with respect to PMI selection according to Section 4.4 and compensate the impact of the TO with respect to channel estimation according to Section 4.5 assuming perfect knowledge of the TO in unsynchronized IL single-layer transmission in TM10
---	Performance difference between synchronized IL single-layer transmission in TM10 and IL single-layer transmission in TM9

3.8 dB, 5.3 dB and 6.4 dB can be observed for IL single-layer transmission in TM10 in CoMP Scenario 4 when ignoring the impact of the TO with respect to PMI selection for the 4×2 MIMO antenna configuration, as depicted in Figure 4.3 (a), Figure 4.3 (b) and Figure 4.3 (c) for MCS4, MCS14 and MCS25, respectively. Schemes to enable reliable implicit feedback generation in unsynchronized CoMP transmission are discussed in Section 4.4 of this thesis.

In case of TP $\epsilon_b \in \mathbb{A}_m$ equipped with two transmit AEs, the matrix $\underline{\mathbf{I}}^{(m)} [n_{\text{PRB}}]$ in (4.8) turns to $\underline{\Xi}_{1,1}^{(m,b)} [n_{\text{PRB}}]$ for the 2×2 MIMO antenna configuration, as the CSI-RSs are transmitted from one transmit AP group. Hence, the phase offset (4.10) vanishes, such that the PMI selection is not affected by the TO as in the case of four transmit AEs. However, the impact of the TO with respect to channel estimation and ISI still persists.

The impact of the TO with respect to channel estimation and signal equalization is discussed in Section 4.2.3 of this thesis. In this context, Figure 4.3 is taken up. Moreover, in a practical implementation, however, perfect knowledge on the TO cannot be assumed. Practical TO estimation schemes are discussed in Section 4.3 of this thesis.

4.2.3 Analysis of the Timing Offset on the Estimated CTF and IRC Performance

Following the findings achieved in Section 4.1 of this thesis, the TO has two main effects, including ISI and the subcarrier specific phase shift [TG11, Section I], where the latter one is investigated in this section with respect to channel estimation and interpolation to enable reliable signal equalization of the receive signal at UE $\mu_m \in \mathbb{U}$. Let

$$\hat{g}_{\nu, \text{DMRS}}^{(m,b)} [\kappa, \ell] \in \mathbb{C}, \quad (\kappa, \ell) \in \mathcal{S}_{i, n_{\text{PRB}}, \text{DMRS}}^{(b,7)} \quad \text{and} \quad (4.14a)$$

$$\hat{g}_{\nu, \text{DMRS}}^{(m,b)} [\kappa + \kappa_{\Delta}, \ell] \in \mathbb{C}, \quad (\kappa + \kappa_{\Delta}, \ell) \in \mathcal{S}_{i, n_{\text{PRB}}, \text{DMRS}}^{(b,7)} \quad (4.14b)$$

denote the estimated CTF at the ν -th receive AE for $1 \leq \nu \leq N_{\text{R}}^{(m)}$ from the two adjacent REs represented by the tuple (κ, ℓ) and $(\kappa + \kappa_{\Delta}, \ell)$, respectively, the precoded DMRSs are transmitted from, where κ_{Δ} represents the spacing between the physical time-frequency resources in frequency domain and is either equal to two or five [3GP16f, Section 6.10.3.2]. Making use of the piecewise linear channel interpolation scheme [HW98, Section IV-A], in presence of unsynchronized CoMP transmission the magnitude of the linear

interpolant $\hat{\underline{g}}_{\nu, \text{DMRS}}^{(m,b)} [k, \ell]$ reads

$$\begin{aligned} \left| \hat{\underline{g}}_{\nu, \text{DMRS}}^{(m,b)} [k, \ell] \right| = & \\ \frac{1}{\kappa_{\Delta}} \left((k - \kappa)^2 \cdot \left| \hat{\underline{g}}_{\nu, \text{DMRS}}^{(m,b)} [\kappa + \kappa_{\Delta}, \ell] \right|^2 + (\kappa + \kappa_{\Delta} - k)^2 \cdot \left| \hat{\underline{g}}_{\nu, \text{DMRS}}^{(m,b)} [k, \ell] \right|^2 + \right. & \\ 2(k - \kappa)(\kappa + \kappa_{\Delta} - k) \cdot \left| \hat{\underline{g}}_{\nu, \text{DMRS}}^{(m,b)} [k, \ell] \right| \cdot \left| \hat{\underline{g}}_{\nu, \text{DMRS}}^{(m,b)} [\kappa + \kappa_{\Delta}, \ell] \right| \cdot & \\ \left. \cos \left(\Theta(\kappa, \kappa + \kappa_{\Delta}) + \Psi(\kappa_{\Delta}) \right) \right)^{\frac{1}{2}} & \quad (4.15) \end{aligned}$$

for $\kappa < k < \kappa + \kappa_{\Delta}$ and $1 \leq \nu \leq N_{\text{R}}^{(m)}$. The phase $\Theta(\kappa, \kappa + \kappa_{\Delta})$ in (4.15) represents the phase difference of the estimated CTF (4.14a) and (4.14b) and reads

$$\Theta(\kappa, \kappa + \kappa_{\Delta}) = \angle \left(\hat{\underline{g}}_{\nu, \text{DMRS}}^{(m,b)} [\kappa + \kappa_{\Delta}, \ell] \right) - \angle \left(\hat{\underline{g}}_{\nu, \text{DMRS}}^{(m,b)} [k, \ell] \right), \quad (4.16)$$

where $\angle(z)$ denotes the angle of $z \in \mathbb{C}$. Moreover, $\Psi(\kappa_{\Delta})$ in (4.15) represents the phase offset between the $(\kappa + \kappa_{\Delta})$ -th and the κ_{Δ} -th subcarrier and reads

$$\Psi(\kappa_{\Delta}) = \frac{2\pi\tau_{\text{TO}}^{(b)}f_s\kappa_{\Delta}}{N_{\text{OFDM}}}. \quad (4.17)$$

Comparing the largest spacing of adjacent subcarriers carrying the precoded DMRSs with the coherence bandwidth of the SCM-B, discussed in Section 2.8.2 of this thesis,

$$\kappa_{\Delta} \cdot f_{\text{sc}} \ll B_c \quad (4.18)$$

holds, such that the impact of the phase offset $\Theta(\kappa + \kappa_{\Delta})$ in (4.15) can be neglected compared a the large phase offset $\Psi(\kappa_{\Delta})$. Moreover, as the root function is strictly monotonic increasing for a positive radicand different from zero, the second and third factor of the second sum on the right hand side of (4.15) are both greater than zero for $\kappa < k < \kappa + \kappa_{\Delta}$ and the cosine function takes values between zero and one if the argument of the cosine function lies between $-\pi/2$ and $\pi/2$, corresponding to a TO between $-3.33 \mu\text{s}$ and $3.33 \mu\text{s}$ when resolving (4.10) to $\tau_{\text{TO}}^{(b)}$ and replacing $k_{\Delta}(i, j)$ by κ_{Δ} equal to five. Consequently, the magnitude in (4.15) decreases as the TO increases for $|\tau_{\text{TO}}^{(b)}| \leq 3.33 \mu\text{s}$. To illustrate the impact of the TO with respect to channel estimation, the magnitude (4.15) experienced by the UE $\mu_m \in \mathbb{U}$ at the first receive AE is depicted in Figure 4.4 on page 182 for 600 subcarriers around the DC subcarrier for a TO equal to $0 \mu\text{s}$, $1 \mu\text{s}$ and $2 \mu\text{s}$, where the SNR has been set to 40 dB in order to be able to disregard the impact of both, the AWGN and the inter-cell interference. Note that the average receive power of the interfering signals is connected to the thermal noise power over the received

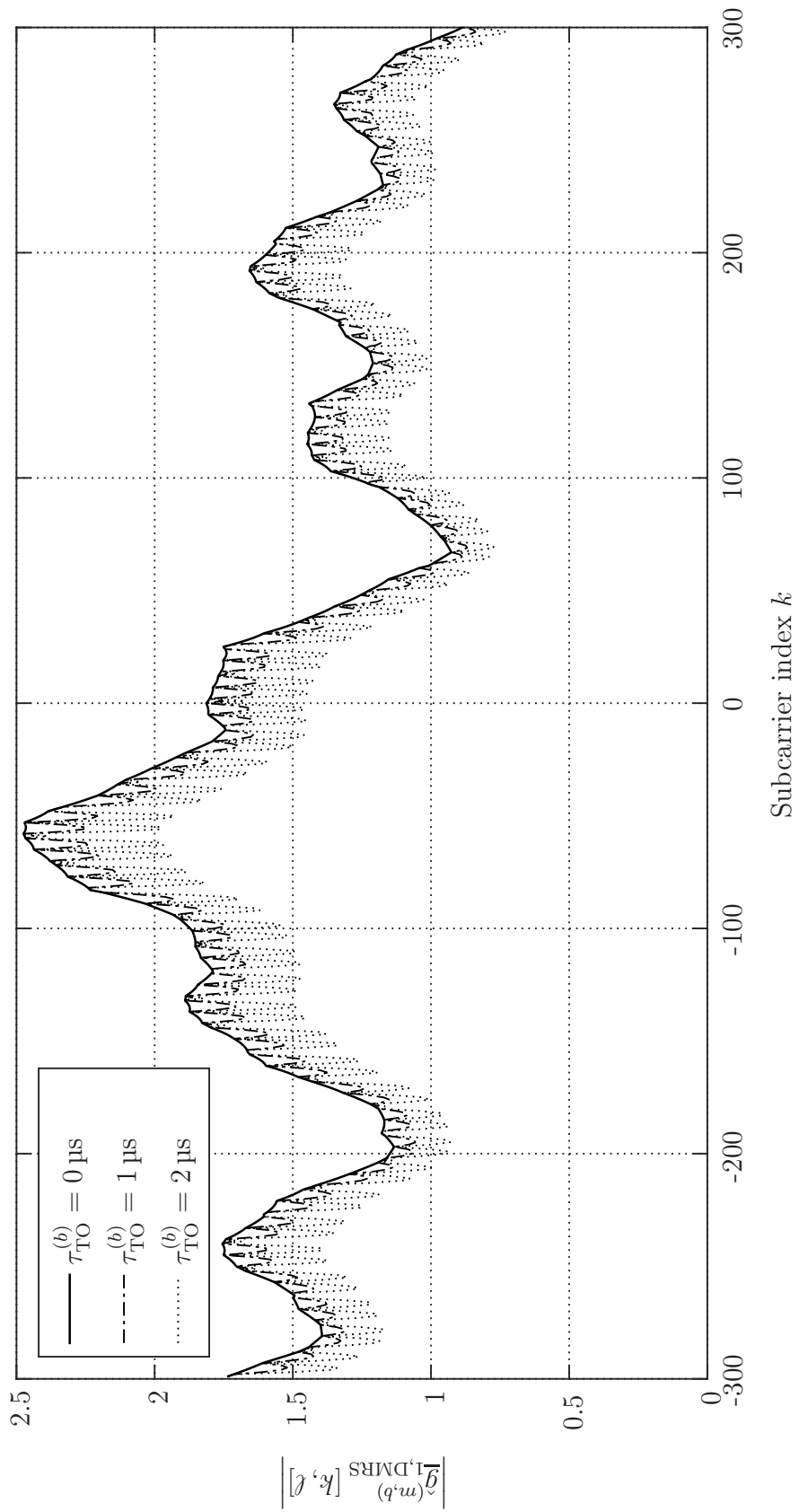


Figure 4.4. Magnitude of the estimated CTF (created by the author of this thesis).

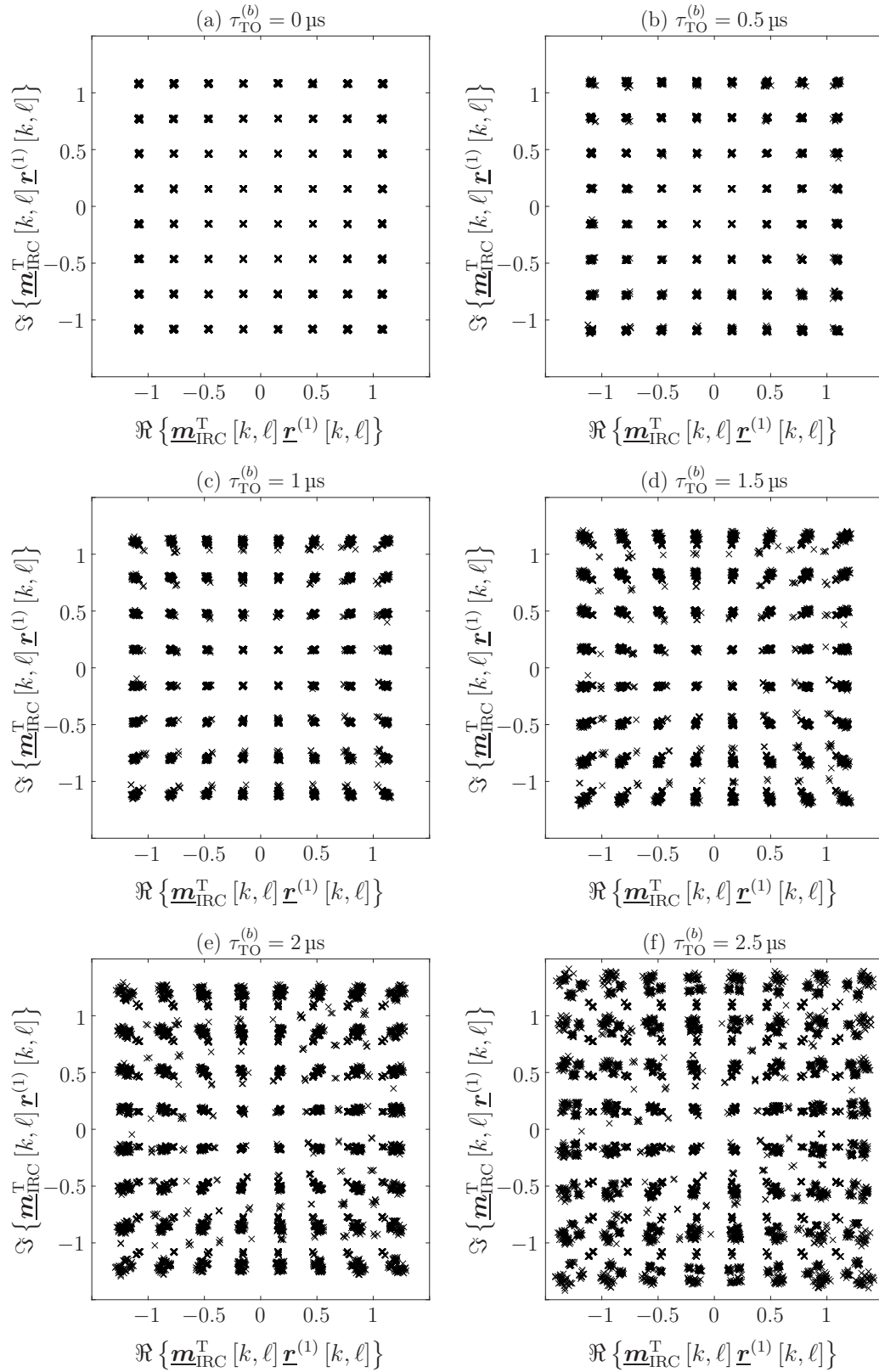


Figure 4.5. Impact of the TO on the equalized signal using the 64QAM mapping scheme (created by the author of this thesis).

bandwidth, as discussed in Section 2.8.3 of this thesis for the selected interference model. Regarding Figure 4.4, it can be observed that the magnitude (4.15) decreases as the TO increases. As the magnitude (4.15) decreases, the denominator on the right hand side of (2.73) decreases, such that the magnitude of the IRC receiver the signal is equalized with, increases, leading to an amplification of the equalized complex-valued modulation symbols carrying the codewords. To visualize the impact of the TO on signal equalization using the practical implementation of the IRC receiver (2.73), the scatterplot of the equalized complex-valued modulation symbols using the 64 QAM scheme is depicted in Figure 4.5 on page 183 for a TO equal to 0 μ s, 0.5 μ s, 1 μ s, 1.5 μ s, 2 μ s and 2.5 μ s. Regarding Figure 4.5, it can be observed that the equalized complex-valued modulation symbols are expanded towards the corner as the TO increases. Hence, the symbols do no longer lie in the designated detection area, such that the signal detection capabilities might be limited as the TO increases. In addition, the impact of ISI impairs the signal detection as the TO increases.

To determine the largest tolerable TO when neglecting the impact of the TO with respect to channel estimation, the performance of the TO over bandwidth efficiency is illustrated in Figure 4.6 on page 186 for MCS4, MCS14 and MCS25 for both, the 4×2 and the 2×2 MIMO antenna configuration for a SNR equal to 40 dB, such that improper PMI selection has no impact of the bandwidth efficiency. The impact of the TO is defined as tolerable if 90 % of the maximum bandwidth efficiency of each MCS can be reached according to (2.98a), (2.98b) and (2.98c) for MCS4, MCS14 and MCS25, respectively. The tolerable TO, resulting from Figure 4.6, is denoted in Table 4.2 on page 186. The first column of Table 4.2 represents the index of the MCS, where the second and third column represents the tolerable TO for the 2×2 and the 4×2 MIMO antenna configuration, respectively. The magnitude of the smallest tolerable TO for an arbitrary but fix MCS and antenna configuration is smaller than the respective magnitude of the largest tolerable TO, as denoted in Table 4.2. As the tail part of the OFDM symbol which is not covered by the DFT in case of positive TOs is included in the CP, as illustrated in Figure 2.6 for the signal transmitted by the eNodeB $\epsilon_{b_1} \in \mathbb{E}$, a decrease in the signal magnitude does not exist and the receive signal is in addition ISI-free if the TO is smaller than the difference of the length of the CP and the multipath spread, such that a higher positive TO can be tolerated compared with the negative TO. In case of negative TOs, illustrated in Figure 2.6 for the signal transmitted by the eNodeB $\epsilon_{b_2} \in \mathbb{E}$, the signal magnitude decreases from the first sample and the receive signal is accompanied by ISI arising from the next CP or OFDM symbol. Therefore, the tolerance region for positive and negative TOs is not symmetric around the TO equal to zero, as depicted in Figure 4.6 for any MCS and antenna configuration. This aspect is further taken up in the following of

this section.

The tolerable TO depends on the MCS which in turn depends on the code rate (2.42). Regarding Figure 4.6, it can be observed that the higher the MCS is, the higher the code rate and the lower the tolerable TO becomes. While for instance a TO of at most $2.5 \mu\text{s}$ can be tolerated for MCS25 in conjunction with the 4×2 MIMO antenna configuration when neglecting the impact of the TO with respect to channel estimation, making use of MCS14 and MCS4 enables to extend the tolerable range of the TO up to $4.81 \mu\text{s}$ and $5.91 \mu\text{s}$, respectively, at the cost of reduced bandwidth efficiency, as depicted in Figure 4.6 and denoted in Table 4.2. However, although the impact of the TO with respect to PMI selection is compensated assuming perfect knowledge on the TO, the advantages of CoMP transmission vanish when the TO is larger than $5 \mu\text{s}$, $4.1 \mu\text{s}$ and $2.3 \mu\text{s}$ for MCS4, MCS14 and MCS25, respectively, as depicted in Figure 4.3. Furthermore, it can be observed that the tolerable range of the TO for the 2×2 MIMO antenna configuration, denoted in the second column of Table 4.2 is larger than the tolerable range of the TO for the 4×2 MIMO antenna configuration, denoted in the third column of Table 4.2 for any of the investigated MCSs. Following the findings achieved in Section 2.2.4 of this thesis, in case of two transmit AEs at the TP, the CSI-RSs are transmitted in the respective subframe on two physical time-frequency resources in each PRB rather than on four physical time-frequency resources. Hence, as the code rate for the TP $\epsilon_b \in \mathbb{A}_m$ equipped with two transmit AEs is slightly lower than the code rate for the TP $\epsilon_b \in \mathbb{A}_m$ equipped with four transmit AEs, as depicted in Figure 3.1 on page 138 for TM10 in CoMP Scenario 4, the error protection and, thus the tolerable TO is slightly larger in the former case than in the latter case, as depicted in Figure 4.6 for any of the investigated MCSs.

To illustrate that the asymmetric tolerance range of the TO, denoted and depicted in Table 4.2 and Figure 4.6, respectively, inherits from the arrangement of the OFDM symbol and the prefixed CP, the CP carrying the tail part of the respective OFDM symbol is replaced by a cyclic postfix carrying the front part of the OFDM symbol and is arranged at the end of the OFDM symbol. Further modifications have not been carried out. Analogously to Figure 4.6 and Table 4.2, the performance of the TO over the bandwidth efficiency is illustrated in Figure 4.7 and the tolerable TO is denoted in Table 4.3, respectively, on page 187. Making use of the cyclic postfix OFDM, it can be observed that the tolerance range for negative TOs increases compared with the CP based OFDM for each MCS and MIMO antenna configuration, as denoted in Table 4.3. On the other hand, the tolerance range for positive TOs decreases for the cyclic postfix based OFDM over the CP based OFDM, as can be concluded from Table 4.2 and Table 4.3, such that To illustrate that the asymmetric tolerance range of the TO, denoted and depicted in Table 4.2 and Figure 4.6, respectively, inherits from the arrangement of the OFDM symbol and the pre-

Table 4.2. Tolerable range of the TO for CP-based OFDM (created by the author of this thesis).

MCS index	$N_T^{(b)} = 2$	$N_T^{(b)} = 4$
4	$-5.84 \mu\text{s} \leq \tau_{\text{TO,tol}} \leq 5.98 \mu\text{s}$	$-5.01 \mu\text{s} \leq \tau_{\text{TO,tol}} \leq 5.91 \mu\text{s}$
14	$-3.04 \mu\text{s} \leq \tau_{\text{TO,tol}} \leq 4.71 \mu\text{s}$	$-3.64 \mu\text{s} \leq \tau_{\text{TO,tol}} \leq 4.81 \mu\text{s}$
25	$-0.63 \mu\text{s} \leq \tau_{\text{TO,tol}} \leq 2.61 \mu\text{s}$	$-0.59 \mu\text{s} \leq \tau_{\text{TO,tol}} \leq 2.54 \mu\text{s}$

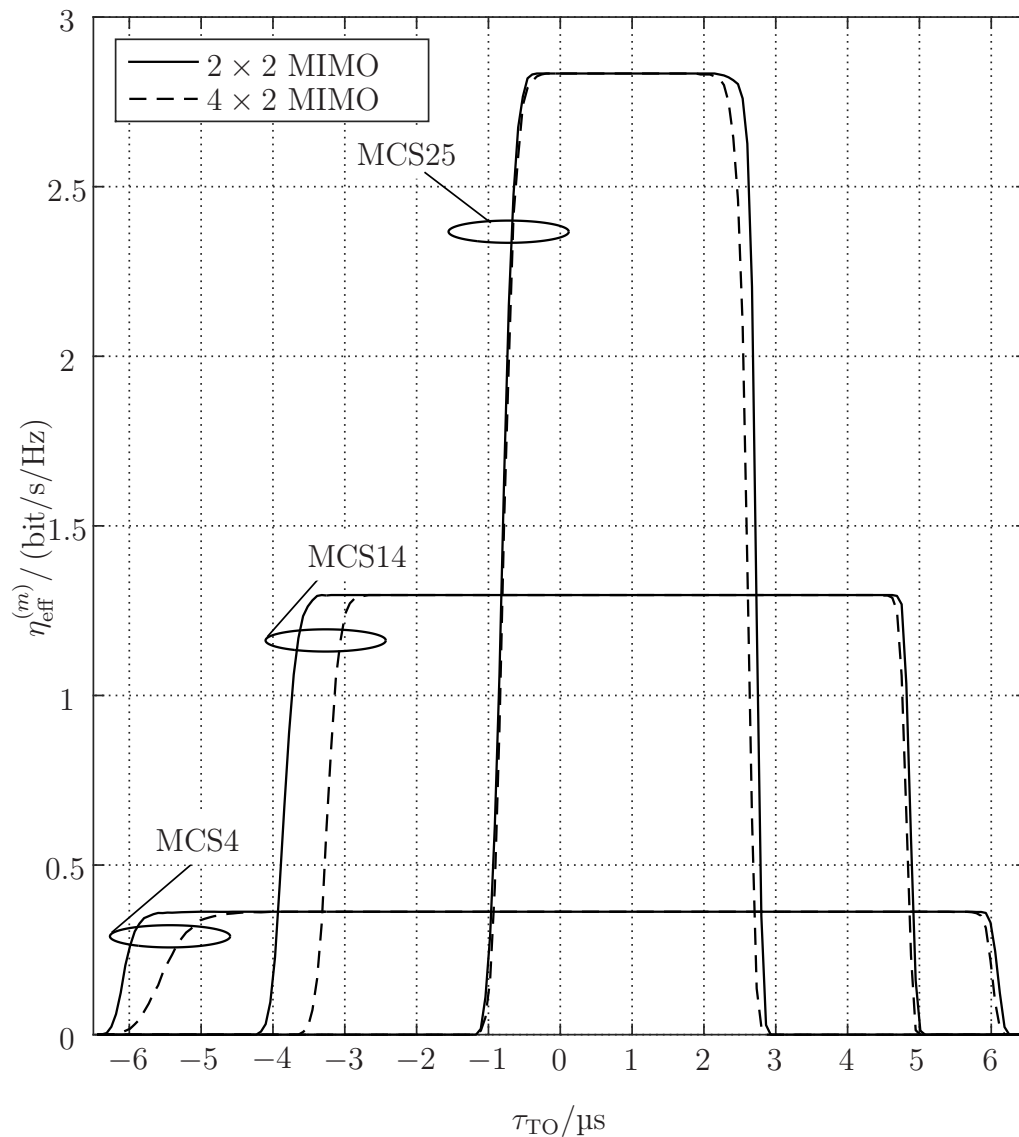
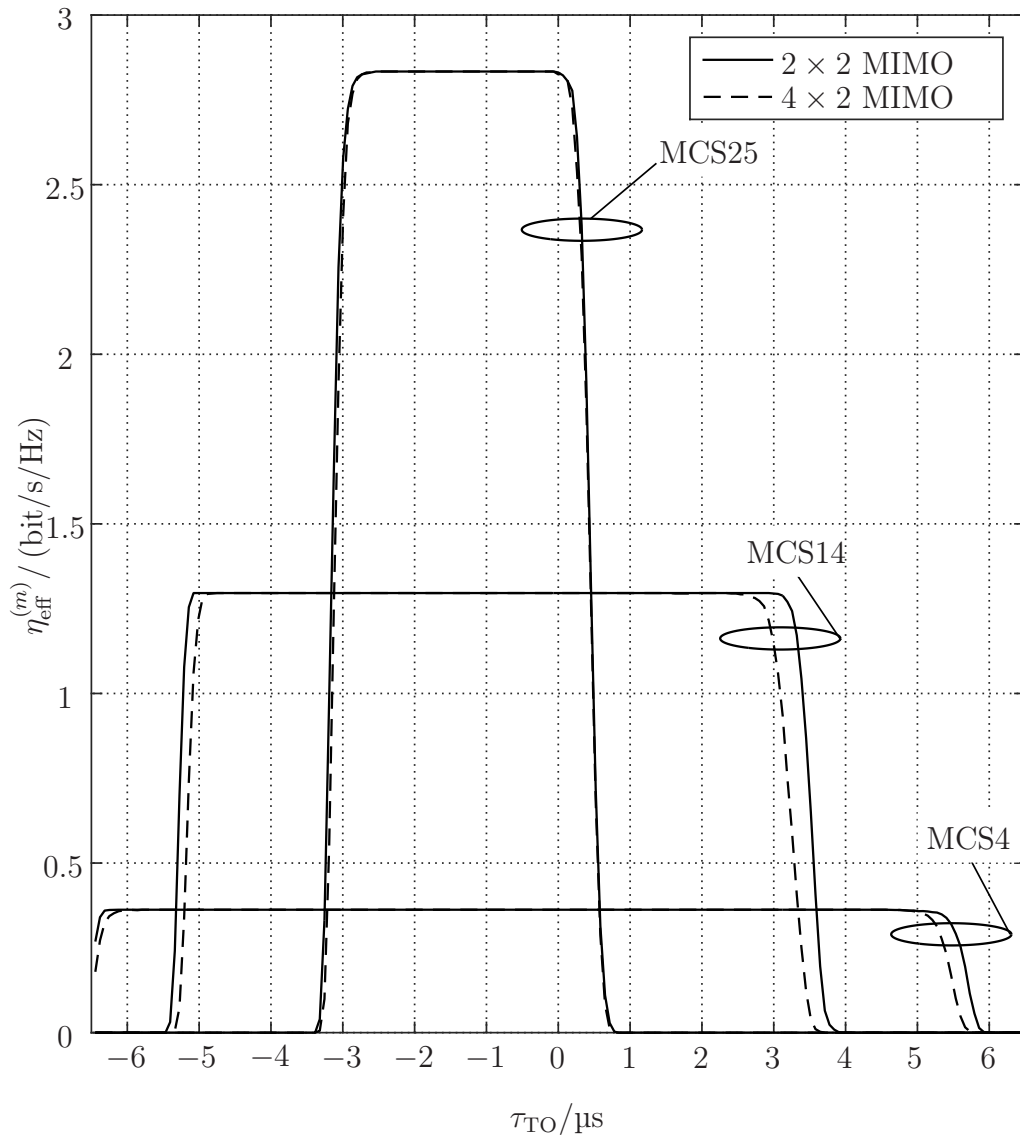


Figure 4.6. Impact of the TO on signal equalization for CP-based OFDM (created by the author of this thesis).

Table 4.3. Tolerable range of the TO for cyclic postfix based OFDM (created by the author of this thesis).

MCS index	$N_T^{(b)} = 2$	$N_T^{(b)} = 4$
4	$-6.41 \mu\text{s} \leq \tau_{\text{TO,tol}} \leq 5.44 \mu\text{s}$	$-6.31 \mu\text{s} \leq \tau_{\text{TO,tol}} \leq 5.21 \mu\text{s}$
14	$-5.17 \mu\text{s} \leq \tau_{\text{TO,tol}} \leq 3.34 \mu\text{s}$	$-5.04 \mu\text{s} \leq \tau_{\text{TO,tol}} \leq 2.97 \mu\text{s}$
25	$-3.14 \mu\text{s} \leq \tau_{\text{TO,tol}} \leq 0.27 \mu\text{s}$	$-2.97 \mu\text{s} \leq \tau_{\text{TO,tol}} \leq 0.27 \mu\text{s}$


Figure 4.7. Impact of the TO on signal equalization for cyclic postfix based OFDM (created by the author of this thesis).

fixed CP, the CP carrying the tail part of the respective OFDM symbol is replaced by a cyclic postfix carrying the front part of the OFDM symbol and is arranged at the end of the OFDM symbol. Further modifications have not been carried out. Analogously to Figure 4.6 and Table 4.2, the performance of the TO over the bandwidth efficiency is illustrated in Figure 4.7 and the tolerable TO is denoted in Table 4.3, respectively, on page 187. Making use of the cyclic postfix OFDM, it can be observed that the tolerance range for negative TOs increases compared with the CP based OFDM for each MCS and MIMO antenna configuration, as denoted in Table 4.3. On the other hand, the tolerance range for positive TOs decreases for the cyclic postfix based OFDM over the CP based OFDM, as can be concluded from Table 4.2 and Table 4.3, such that

$$|\min(\tau_{\text{TO,tol}})| \underset{\substack{\text{cyclic postfix} \\ \text{based OFDM}}}{\geq} \underset{\substack{\text{CP based} \\ \text{OFDM}}}{\leq} |\max(\tau_{\text{TO,tol}})| \quad (4.19)$$

holds. The situation of the cyclic postfix based OFDM for positive TOs is analogous to the situation of the CP based OFDM for negative TOs with respect to signal magnitude attenuation, but not with respect to the amount of ISI. Due to the PDP of the SCM-B, in case of positive TOs in the cyclic postfix based OFDM the $\tau_{\text{TO}}^{(b)} \cdot f_s$ samples of the CIR mirrored along the τ -axis extend into the desired OFDM symbol, where the residual samples are located in the cyclic postfix which belongs to the previous OFDM symbol. On the other hand, in case of a negative TO in the CP based OFDM, the $|\tau_{\text{TO}}^{(b)}| \cdot f_s$ samples of the CIR mirrored along the τ -axis extend into the CP of the next OFDM symbol, while the residual samples are located in the current OFDM symbol. Hence, the amount of ISI in the former case is more severe, resulting in a smaller tolerable positive TO in case of cyclic postfix based OFDM compared with the tolerable TO in case of CP based OFDM, as denoted in Table 4.2 and Table 4.3 for any of the investigated MCSs and MIMO antenna configuration. While e.g. the largest tolerable TO for cyclic postfix based OFDM reads $0.27 \mu\text{s}$, as denoted in Table 4.3 for MCS25 and the 4×2 MIMO antenna configuration, the smallest tolerable TO in CP based OFDM reads $-0.59 \mu\text{s}$, as denoted in Table 4.3 for the same MCS and MIMO antenna configuration.

In what follows the performance loss when neglecting the impact of the TO with respect to channel estimation is analyzed for CP based OFDM rather than for cyclic postfix based OFDM. The aspect of cyclic postfix based OFDM is not considered in the future course of this thesis.

Although the impact of improper PMI selection is compensated assuming perfect knowledge on the TO, the advantages of practical CoMP transmission vanish when ignoring the impact of the TO with respect to channel estimation if the TO exceeds $5 \mu\text{s}$, $4.1 \mu\text{s}$ and $2.3 \mu\text{s}$ for MCS4, MCS14 and MCS25,

respectively, as depicted in Figure 4.3 for the 4×2 MIMO antenna configuration. The value of the abscissa at the intersection of the two dash-dotted lines in each of the three subfigures in Figure 4.3 denotes the TO up to which the impact of improper PMI selection causes higher performance loss than the impact of improper channel estimation and reads $5.8 \mu\text{s}$, $4.4 \mu\text{s}$ and $2.3 \mu\text{s}$ for MCS4, MCS14 and MCS25, respectively. Obviously, the value of the abscissa decreases as the index of the MCS increases. The reason is that due to the large Euclidean distance of the complex-valued modulation symbols out of the set \mathbb{V}_{MQAM} with M equal to four and the four quadrants used for signal detection, MCS4 is largely robust against the amplification of the equalized complex-valued modulation symbols, denoted and depicted in Table 4.2 and Figure 4.6, respectively, while the selected precoding vector does not maximize the local post-SNR in the respective subband for the 4×2 MIMO antenna configuration for any TO different from zero, as discussed in Section 4.2.2 of this thesis. On the other hand, in case of MCS25 the Euclidean distance of two adjacent complex-valued modulation symbols out of the set \mathbb{V}_{MQAM} for M equal to 64 is much smaller than to that for M equal to four, such that reliable channel estimation to overcome the unwanted signal amplification is more important than reliable PMI selection as the TO increases, as depicted in Figure 4.3 (c) for the 4×2 MIMO antenna configuration.

Note that while improper PMI selection merely results in a finite performance loss, meaning that the desired bandwidth efficiency will be reached at higher SNRs in absence of ISI, the performance loss caused by improper channel estimation might not be reversible when increasing the SNR. A reliable channel estimation scheme for unsynchronized CoMP transmission is discussed in Section 4.5 of this thesis.

4.3 Timing Offset Estimation Techniques

Based on the findings achieved in Section 4.2.2 and Section 4.2.3 of this thesis, it is necessary to mitigate the impact of the TO to guarantee reliable PMI selection and channel estimation in order to limit the performance degradation and error floor, where the demand for reliable PMI selection is of particular importance for TPs equipped with more than two transmit AEs.

Particularly, the precoded DMRSs and the CSI-RSs can be exploited for TO estimation [Nok12, Section 2]. As the density of RSs and the theoretical TO estimation range is larger for the precoded DMRSs than for the CSI-RSs [Iwe+14g, Section III-C], the former RSs are considered for TO estimation in this thesis. Detail information on TO estimation schemes based on the CSI-RSs can be

found in [Iwe+14h, Section III-A]. In what follows, the DMRS-based TO estimation scheme is provided and its properties discussed, followed by a practical implementation scheme. The performance of the practical implementation scheme is evaluated and discussed.

Following the findings achieved in Section 2.5.2 of this thesis, the subcarrier specific phase shift is linearly proportional to the TO. Hence, taking the average phase of the ratio of each pair of estimated CTFs with a predefined spacing in frequency direction to mitigate the impact of the AWGN component, the channel phase component, the MAI and, if present, the ISI component, the TO can be estimated [CT07, Section 5.3.1]. Moreover, as the TP out of the CoMP operating set selected for signal transmission remains unchanged for the duration of at least one subframe in JP-DPS signal transmission in CoMP Scenario 4 [3GP13a, Section 5.1.3], the UE $\mu_m \in \mathbb{U}$ can assume that the TO remains unchanged, too. To provide an estimate of the TO, let $\underline{z}_\nu(k_j, k_i) \in \mathbb{C}$ denote the ratio of the estimated CTFs $\hat{g}_{\nu, \text{DMRS}}^{(m,b)}[k_j, \ell_j]$ and $\hat{g}_{\nu, \text{DMRS}}^{(m,b)}[k_i, \ell_i]$, where the tuple (k_j, ℓ_j) and (k_i, ℓ_i) represents the physical time-frequency resources carrying the precoded DMRSs in the same subband, where $k_i, k_j \in \mathcal{S}_{\text{SB}}^{(w)}$ and $k_i < k_j$ holds for $0 \leq w < N_{\text{SB}}$. Transforming the estimated CTFs into polar coordinates, the ratio $\underline{z}_\nu(k_j, k_i)$ turns to

$$\begin{aligned} \underline{z}_\nu(k_j, k_i) = & \frac{\left| \underline{g}_{\nu, \text{DMRS}}^{(m,b)}[k_j, \ell_j] \right|}{\left| \underline{g}_{\nu, \text{DMRS}}^{(m,b)}[k_i, \ell_i] \right|} \cdot \frac{|1 + \underline{w}[k_j, \ell_j]|}{|1 + \underline{w}[k_i, \ell_i]|} \cdot \exp\left(-j \frac{2\pi \tau_{\text{TO}}^{(b)}(k_j - k_i) f_s}{N_{\text{OFDM}}}\right) \cdot \\ & \exp\left(j \left(\angle \left(\underline{g}_{\nu, \text{DMRS}}^{(m,b)}[k_j, \ell_j] \right) - \angle \left(\underline{g}_{\nu, \text{DMRS}}^{(m,b)}[k_i, \ell_i] \right) \right)\right) \cdot \\ & \exp\left(j \left(\xi_\nu(k_j, \ell_j) - \xi_\nu(k_i, \ell_i) \right)\right), \end{aligned} \quad (4.20)$$

where

$$\underline{w}[k_j, \ell_j] = \frac{\exp\left(j \left(\frac{2\pi \tau_{\text{TO}}^{(b)} f_s k_j}{N_{\text{OFDM}}} - \angle \left(\underline{g}_{\nu, \text{DMRS}}^{(m,b)}[k_j, \ell_j] \right) \right)\right)}{\sqrt{C^{(m,b)}} \cdot \left| \underline{g}_{\nu, \text{DMRS}}^{(m,b)}[k_j, \ell_j] \right| \cdot \chi\left(\tau_{\text{TO}}^{(b)}\right)} \quad (4.21)$$

holds. The respective value $\underline{w}[k_i, \ell_i]$ in (4.20) can be obtained from (4.21) when replacing the index j by the index i . Moreover, $\xi_\nu(k_j, \ell_j)$ in (4.20) represents the sum of the phases of the AWGN, the MAI and, if present, the ISI component of the (k_j, ℓ_j) -th RE, experienced by the ν -th receive AE at the UE $\mu_m \in \mathbb{U}$ and is assumed to be uniformly distributed within $[-\pi, \pi]$ [Sal68, p. 564] for $1 \leq \nu \leq N_{\text{R}}^{(m)}$. The component $\xi_\nu(k_i, \ell_i)$ in (4.20) is defined analogously when replacing the index j by the index i . Obviously, the phase of $\underline{z}_\nu(k_j, k_i)$ gives information of the TO, such that the TO can be estimated by calculating the average phase of (4.20) [CT07, Section 5.3.1] and resolving

it with respect to $\tau_{\text{TO}}^{(b)}$ according to [Iwe+14h, Section III-A]

$$\begin{aligned}
 \hat{\tau}_{\text{TO}}^{(b)} &= -\frac{N_{\text{OFDM}}}{2\pi k'_{\Delta} f_s} \cdot \frac{1}{N_{\text{R}}^{(m)} \cdot \sum_{w=0}^{N_{\text{SB}}-1} |\mathcal{S}_{k'_{\Delta}}^{(w)}|} \cdot \sum_{\nu=1}^{N_{\text{R}}^{(m)}} \sum_{w=0}^{N_{\text{SB}}-1} \sum_{(k_i, k_j) \in \mathcal{S}_{k'_{\Delta}}^{(w)}} \angle(\underline{z}_{\nu}(k_j, k_i)) \\
 &= \tau_{\text{TO}}^{(b)} + \frac{N_{\text{OFDM}}}{2\pi k'_{\Delta} f_s} \cdot \frac{1}{N_{\text{R}}^{(m)} \cdot \sum_{w=0}^{N_{\text{SB}}-1} |\mathcal{S}_{k'_{\Delta}}^{(w)}|} \cdot \\
 &\quad \sum_{\nu=1}^{N_{\text{R}}^{(m)}} \sum_{w=0}^{N_{\text{SB}}-1} \sum_{(k_i, k_j) \in \mathcal{S}_{k'_{\Delta}}^{(w)}} \left(\angle\left(\underline{g}_{\nu, \text{DMRS}}^{(m, b)}[k_j, \ell_j]\right) - \angle\left(\underline{g}_{\nu, \text{DMRS}}^{(m, b)}[k_i, \ell_i]\right) \right) + \\
 &\quad \frac{N_{\text{OFDM}}}{2\pi k'_{\Delta} f_s} \cdot \frac{1}{N_{\text{R}}^{(m)} \cdot \sum_{w=0}^{N_{\text{SB}}-1} |\mathcal{S}_{k'_{\Delta}}^{(w)}|} \cdot \\
 &\quad \sum_{\nu=1}^{N_{\text{R}}^{(m)}} \sum_{w=0}^{N_{\text{SB}}-1} \sum_{(k_i, k_j) \in \mathcal{S}_{k'_{\Delta}}^{(w)}} \left(\xi_{\nu}(k_j, \ell_j) - \xi_{\nu}(k_i, \ell_i) \right), \tag{4.22}
 \end{aligned}$$

where

$$\mathcal{S}_{k'_{\Delta}}^{(w)} = \left\{ (k_i, k_j) \mid k'_{\Delta} = k_j - k_i, k_i \in \mathcal{S}_{\text{SB}}^{(w)}, k_j \in \mathcal{S}_{\text{SB}}^{(w)}, k_i < k_j \right\} \tag{4.23}$$

denotes the set of tuples where each tuple consists of two different subcarriers out of the set $\mathcal{S}_{\text{SB}}^{(w)}$, such that the difference of the subcarriers is equal to k'_{Δ} for each tuple.

Asymptotically the estimated TO in (4.22) represents a Gaussian distributed random variable with mean value equal to $\tau_{\text{TO}}^{(b)}$ and a variance equal to the sum of the variances representing the impact of the channel phase, the phase of the AWGN plus the MAI component and the phase of the ISI component. As the channel phase is subcarrier specific, the channel phase difference $\angle(\underline{g}_{\nu, \text{DMRS}}^{(m, b)}[k_j, \ell_j]) - \angle(\underline{g}_{\nu, \text{DMRS}}^{(m, b)}[k_i, \ell_i])$ in (4.22) is different from zero for any mobile communication channel with finite coherence bandwidth [Jun97, Section 3.3.3] and $k_i \neq k_j$, where each channel phase approximates to a uniformly distributed random variable within $[-\pi, \pi)$. Considering the central limit theorem [Pro01, Section 2.1.6], the sum of $N_{\text{R}}^{(m)} \cdot \sum_{w=0}^{N_{\text{SB}}-1} |\mathcal{S}_{k'_{\Delta}}^{(w)}|$ uniformly distributed random variables approximates to a zero mean Gaussian random variable and, hence, the difference of the sums is also zero mean Gaussian distributed, where the variance depends on the spacing k'_{Δ} and the PDP of the mobile communication channel. For a mobile communication channel with arbitrary but fix and finite coherence bandwidth the channel phase difference in (4.22) becomes

Table 4.4. Key values for DMRS-based TO estimation (created by the author of this thesis).

k'_Δ	$ \mathcal{S}_{k'_\Delta}^{(0)} $	Theoretical TO estimation range
2	5	$-16.67 \mu\text{s} \leq \hat{\tau}_{\text{TO}}^{(b)} \leq 16.67 \mu\text{s}$
5	12	$-6.67 \mu\text{s} \leq \hat{\tau}_{\text{TO}}^{(b)} \leq 6.67 \mu\text{s}$
7	10	$-4.76 \mu\text{s} \leq \hat{\tau}_{\text{TO}}^{(b)} \leq 4.76 \mu\text{s}$
10	6	$-3.33 \mu\text{s} \leq \hat{\tau}_{\text{TO}}^{(b)} \leq 3.33 \mu\text{s}$
12	15	$-2.78 \mu\text{s} \leq \hat{\tau}_{\text{TO}}^{(b)} \leq 2.78 \mu\text{s}$
14	4	$-2.38 \mu\text{s} \leq \hat{\tau}_{\text{TO}}^{(b)} \leq 2.38 \mu\text{s}$
17	10	$-1.96 \mu\text{s} \leq \hat{\tau}_{\text{TO}}^{(b)} \leq 1.96 \mu\text{s}$
19	8	$-1.75 \mu\text{s} \leq \hat{\tau}_{\text{TO}}^{(b)} \leq 1.75 \mu\text{s}$
22	5	$-1.52 \mu\text{s} \leq \hat{\tau}_{\text{TO}}^{(b)} \leq 1.52 \mu\text{s}$
24	12	$-1.39 \mu\text{s} \leq \hat{\tau}_{\text{TO}}^{(b)} \leq 1.39 \mu\text{s}$
29	8	$-1.15 \mu\text{s} \leq \hat{\tau}_{\text{TO}}^{(b)} \leq 1.15 \mu\text{s}$
31	6	$-1.08 \mu\text{s} \leq \hat{\tau}_{\text{TO}}^{(b)} \leq 1.08 \mu\text{s}$
34	4	$-0.98 \mu\text{s} \leq \hat{\tau}_{\text{TO}}^{(b)} \leq 0.98 \mu\text{s}$
36	9	$-0.93 \mu\text{s} \leq \hat{\tau}_{\text{TO}}^{(b)} \leq 0.93 \mu\text{s}$
38	6	$-0.88 \mu\text{s} \leq \hat{\tau}_{\text{TO}}^{(b)} \leq 0.88 \mu\text{s}$
41	6	$-0.81 \mu\text{s} \leq \hat{\tau}_{\text{TO}}^{(b)} \leq 0.81 \mu\text{s}$
43	4	$-0.78 \mu\text{s} \leq \hat{\tau}_{\text{TO}}^{(b)} \leq 0.78 \mu\text{s}$
46	3	$-0.72 \mu\text{s} \leq \hat{\tau}_{\text{TO}}^{(b)} \leq 0.72 \mu\text{s}$
48	6	$-0.69 \mu\text{s} \leq \hat{\tau}_{\text{TO}}^{(b)} \leq 0.69 \mu\text{s}$
50	1	$-0.67 \mu\text{s} \leq \hat{\tau}_{\text{TO}}^{(b)} \leq 0.67 \mu\text{s}$
53	4	$-0.63 \mu\text{s} \leq \hat{\tau}_{\text{TO}}^{(b)} \leq 0.63 \mu\text{s}$
55	2	$-0.61 \mu\text{s} \leq \hat{\tau}_{\text{TO}}^{(b)} \leq 0.61 \mu\text{s}$
58	2	$-0.57 \mu\text{s} \leq \hat{\tau}_{\text{TO}}^{(b)} \leq 0.57 \mu\text{s}$
60	3	$-0.56 \mu\text{s} \leq \hat{\tau}_{\text{TO}}^{(b)} \leq 0.56 \mu\text{s}$
65	2	$-0.51 \mu\text{s} \leq \hat{\tau}_{\text{TO}}^{(b)} \leq 0.51 \mu\text{s}$
70	1	$-0.48 \mu\text{s} \leq \hat{\tau}_{\text{TO}}^{(b)} \leq 0.48 \mu\text{s}$

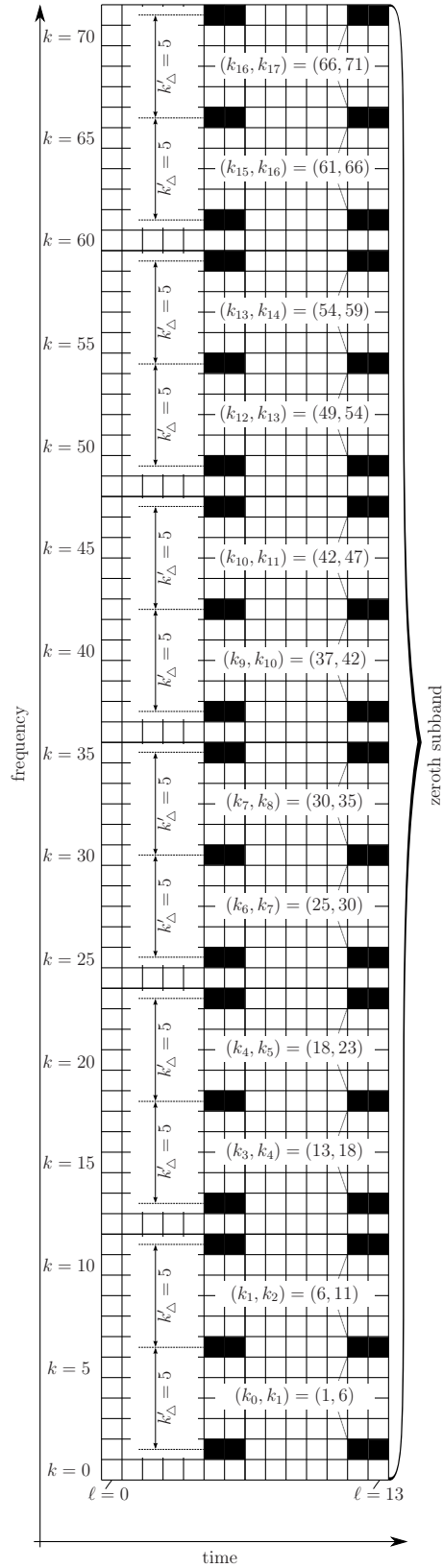


Figure 4.8. Mapping of DMRs on physical time-frequency resources in one subband and subframe (created by the author of this thesis).

the smaller, the smaller the spacing k'_Δ is. Furthermore, impinging the phase of the MAI component on the phase of the AWGN component and making use of the central limit theorem [Pro01, Section 2.1.6], the sum of the respective $N_{\text{R}}^{(m)} \cdot \sum_{w=0}^{N_{\text{SB}}-1} |\mathcal{S}_{k'_\Delta}^{(w)}|$ phase differences in (4.22) approximates to a zero-mean Gaussian random variable. Moreover, following the assumption of Gaussian distributed ISI [Sal68, p. 564], the respective phase is uniformly distributed within $[-\pi, \pi)$, such that the sum of the $N_{\text{R}}^{(m)} \cdot \sum_{w=0}^{N_{\text{SB}}-1} |\mathcal{S}_{k'_\Delta}^{(w)}|$ phase differences of the ISI component in (4.22) approximates to a zero mean Gaussian random variable.

The spacing k'_Δ in (4.22) is inversely proportional to the largest magnitude of the TO which can be theoretically estimated, such that

$$|\hat{\tau}_{\text{TO}}| \leq \frac{N_{\text{OFDM}}}{2k'_\Delta f_s} \quad (4.24)$$

holds. Valid values for k'_Δ which fulfill the requirements of (4.23) are summarized in Table 4.4 on page 192, together with the cardinality of the resulting set for the zeroth subband, denoted by $|\mathcal{S}_{k'_\Delta}^{(0)}|$ and the magnitude of the largest TO which can be estimated in absence of the distortion caused by the channel phase, the AWGN, the MAI and, if present, the ISI component. To provide an example, consider Figure 4.8 on page 193, where a cutout of the first subframe and zeroth subband for $0 \leq k \leq 71$ with a particular focus on the precoded DMRSs, transmitted from one of the low-power RRH, is depicted. For the sake of clarity, the physical time-frequency resources carrying the precoded complex-valued modulation symbols carrying the codewords and the CSI-RSs are not explicitly highlighted. Let (k_i, k_j) denote the tuple of subcarriers where both, k_i and k_j are out of the set $\mathcal{S}_{\text{SB}}^{(0)}$ which carry the precoded DMRSs and are equal to one and six, respectively, as depicted in Figure 4.8. Obviously, the spacing between k_i and k_j in frequency direction denoted by k'_Δ is equal to five subcarriers. Regarding Figure 4.8, in total twelve tuples with a spacing k'_Δ equal to five subcarriers in frequency direction can be found, such that

$$\begin{aligned} \mathcal{S}_5^{(0)} = \{ & (1, 6), (6, 11), (13, 18), (18, 23), (25, 30), (30, 35) \\ & (37, 42), (42, 47), (49, 54), (54, 59), (61, 66), (66, 71) \} \end{aligned} \quad (4.25)$$

holds. The respective set $\mathcal{S}_{k'_\Delta}^{(w)}$ for the remaining values of k'_Δ , denoted in the first column of Table 4.4, can be found analogously for $0 \leq w < N_{\text{SB}}$. The choice of the value k'_Δ provides a trade-off between the TO estimation range and the TO estimation accuracy. On the one hand, small values k'_Δ enable the estimation of large TOs up to $\pm 16.67 \mu\text{s}$ for k'_Δ equal to two and enable to keep the channel phase difference small. On the other hand, however, the impact of the channel phase difference, as well as the impact of the AWGN, the MAI and, if present, the ISI component can be suppressed the more reliably

the larger the value k'_{Δ} is selected, as can be derived from (4.22). Moreover, the larger the cardinality of $\mathcal{S}_{k'_{\Delta}}^{(w)}$ in (4.22), the more reliable the impact of the channel phase difference, the AWGN, the MAI and, if present, the ISI component can be suppressed. In this thesis, the value k'_{Δ} is set to five for DMRS-based TO estimation. The resulting TO estimation accuracy when evaluating the precoded DMRSs in terms of TO over Root-Mean-Square Error (RMSE) is provided in Figure 4.9 on page 196 for both, the 4×2 and the 2×2 MIMO antenna configuration, where for the sake of better readability the range of the SNR is selected between -10 dB and 40 dB with a step size of 10 dB. Regarding Figure 4.9, it can be observed that the RMSE decreases for both, the 4×2 and the 2×2 MIMO antenna configuration, if the SNR increases, as long as the TO does not approximate the the TO which can be theoretically estimated, as the impact of the phase difference of the AWGN component and the MAI component decreases. However, due to the non-negligible impact of the channel phase difference in (4.22), the DMRS-based TO estimation is biased, such that the RMSE does not decrease to zero and saturates at approximately $0.25 \mu\text{s}$ for positive TOs smaller than or equal to $4 \mu\text{s}$ for both, the 4×2 and the 2×2 MIMO antenna configuration when the SNR is sufficiently large, as depicted in Figure 4.9. Furthermore, the RMSE increases considerably if the TO approximates to the TO which can be theoretically estimated, as the probability of phase ambiguities and the impact of the phase difference caused by the ISI component in (4.22) increases. To show that the biased TO estimation error is due to the non-negligible channel phase difference of the SCM-B, the PDP of the SCM-B is modified accordingly and further discussed in Appendix D of this thesis.

The impact of the TO with respect to PMI selection identified and discussed in Section 4.2.2 of this thesis is reflected by the DMRS-based TO estimation when comparing the RMSE of the 4×2 and the 2×2 MIMO antenna configuration. While, due to the enhanced beamforming gain for a TO equal to zero, the local post-SNR (3.12) for the 4×2 MIMO antenna configuration is larger than the local post-SNR for the 2×2 MIMO antenna configuration, discussed in Section 3.4 of this thesis, the TO for the 4×2 MIMO antenna configuration can be estimated more reliable than for the 2×2 MIMO antenna configuration, as depicted in Figure 4.9 of this thesis. Following the findings achieved in Section 4.2.2 of this thesis, the conditional probability of the PMI selection for the 4×2 MIMO antenna configuration changes as the TO changes, such that the local post-SNR (3.12) for the 4×2 MIMO antenna configuration becomes smaller than the local post-SNR of the 2×2 MIMO antenna configuration [Iwe+14e, Section IV]. Hence, increasing to TO, the RMSE of the estimated TO for the 2×2 MIMO antenna configuration becomes smaller than the RMSE of the estimated TO for the 4×2 MIMO antenna configuration, as depicted in Figure 4.9.

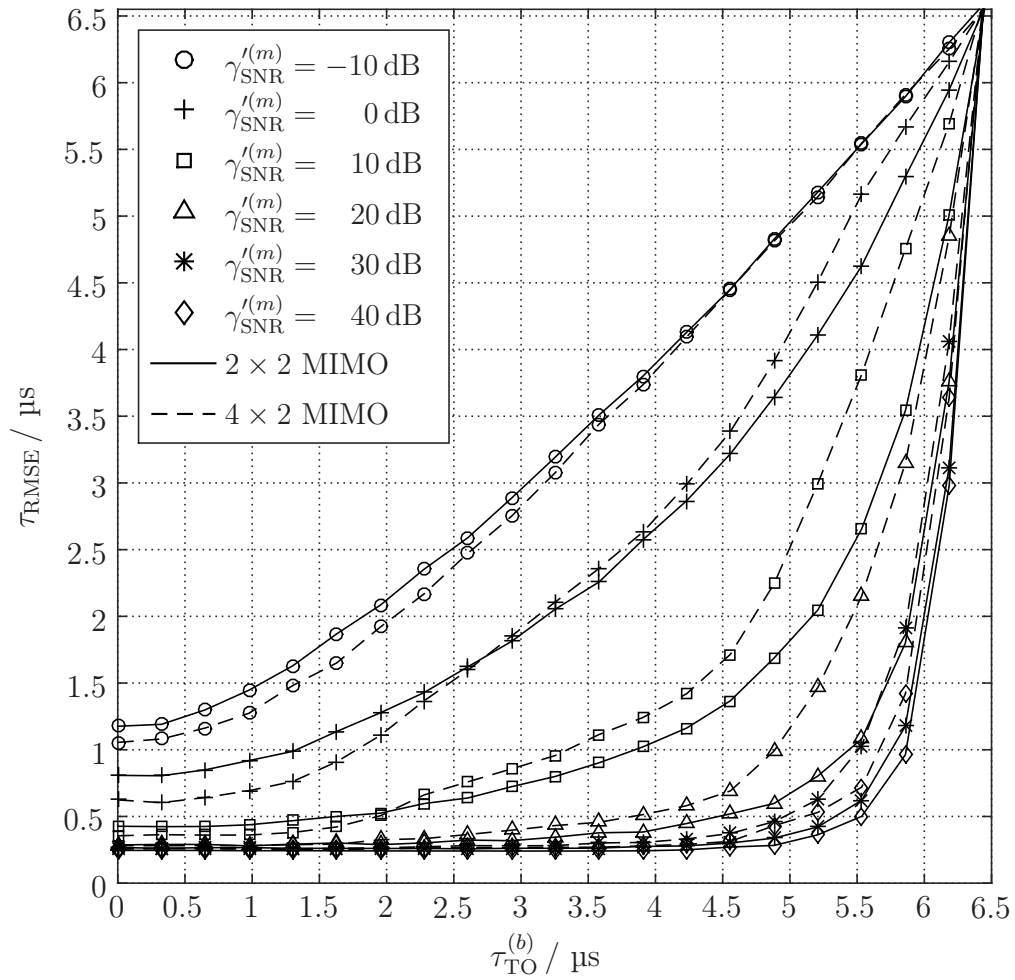


Figure 4.9. Accuracy for DMRS-based TO estimation (created by the author of this thesis).

4.4 Reliable Implicit Feedback Generation for CoMP Transmission

The presence of the TO imposes a phase offset (4.10) on the transmit covariance matrix (4.6) for a TP equipped with more than two transmit AEs and, hence, limits reliable PMI selection, as discussed in Section 4.2.2 of this thesis. As the phase offset (4.10) affecting each submatrix $\underline{\Xi}_{i,j}^{(m,b)} [n_{\text{PRB}}]$ in (4.9) for $i \neq j$ is linearly proportional to the TO and remains unchanged for the duration of at least one subframe, it can be compensated by multiplying the transmit covariance matrix (4.6) with $\underline{\Upsilon}(\hat{\tau}_{\text{TO}}^{(b)}) \in \mathbb{C}^{N_{\text{T}}^{(b)} \times N_{\text{T}}^{(b)}}$, denoted in (4.26) on page 198 using the SCHUR product, where the estimated phase offset $\hat{\phi}_{\Delta}(i, j)$ can be obtained from (4.10) when replacing $\tau_{\text{TO}}^{(b)}$ by $\hat{\tau}_{\text{TO}}^{(b)}$. As a result, the transmit covariance matrix in absence of the AWGN and the ISI component denoted by $\underline{\Gamma}^{(m)} [n_{\text{PRB}}]$ in (4.6) turns to $\underline{\Gamma}'^{(m)} [n_{\text{PRB}}]$ and is denoted in (4.27) on page 198 for the 4×2 MIMO antenna configuration, when replacing the phase offset $\phi_{\Delta}(i, j)$ by its definition (4.10), as well as the estimated phase offset $\hat{\phi}_{\Delta}(i, j)$. The impact of the phase offset in (4.27) is linearly proportional to the TO difference between the present TO and the estimated TO, denoted by $\tau_{\text{TO}}^{(b)}$ and $\hat{\tau}_{\text{TO}}^{(b)}$, respectively.

To investigate the impact of the TO on PMI selection, let $i' \in \mathcal{S}_{\text{PMI}, N_{\text{T}}^{(b)}}$ denote the PMI selected by the UE $\mu_m \in \mathbb{U}$, to be used to precode the DMRSs and the complex-valued modulation symbols carrying the codewords in one subband using the LC-CCIMP scheme, discussed in Section 3.3.3 of this thesis, assuming synchronized signal transmission. Analogously, let $j' \in \mathcal{S}_{\text{PMI}, N_{\text{T}}^{(b)}}$ denote the selected PMI in case of unsynchronized signal transmission. A PMI error is defined to occur if $i' \neq j'$ holds. Hence, the PMI Error Rate (PER) is defined as the ratio of the number of PMI errors over the number of subbands. The TO over PER is depicted in Figure 4.11 on page 200 for the 4×2 MIMO antenna configuration for MCS4, MCS14 and MCS25. In detail the PER is provided when

- ignoring the impact of the TO with respect to PMI selection,
- compensating the impact of the TO with respect to PMI selection, assuming perfect knowledge on the TO and
- compensating the impact of the TO with respect to PMI selection using the DMRS-based TO estimation scheme (4.22).

$$\underline{\mathbf{r}} \left(\hat{\tau}_{\text{TO}}^{(b)} \right) = \begin{pmatrix} \mathbf{1}_{2 \times 2} & \cdots & \mathbf{1}_{2 \times 2} \cdot \exp(-j\hat{\varphi}_{\Delta}(1, u)) & \cdots & \mathbf{1}_{2 \times 2} \cdot \exp(-j\hat{\varphi}_{\Delta}(1, U)) \\ \vdots & \ddots & \vdots & \ddots & \vdots \\ \mathbf{1}_{2 \times 2} \cdot \exp(-j\hat{\varphi}_{\Delta}(u, 1)) & \cdots & \mathbf{1}_{2 \times 2} & \cdots & \mathbf{1}_{2 \times 2} \cdot \exp(-j\hat{\varphi}_{\Delta}(u, U)) \\ \vdots & \ddots & \vdots & \ddots & \vdots \\ \mathbf{1}_{2 \times 2} \cdot \exp(-j\hat{\varphi}_{\Delta}(U, 1)) & \cdots & \mathbf{1}_{2 \times 2} \cdot \exp(-j\hat{\varphi}_{\Delta}(U, u)) & \cdots & \mathbf{1}_{2 \times 2} \end{pmatrix} \quad (4.26)$$

$$\underline{\mathbf{I}}'^{(m)} [n_{\text{PRB}}] = \begin{pmatrix} \underline{\Xi}_{1,1}^{(m,b)} [n_{\text{PRB}}] & \underline{\Xi}_{1,2}^{(m,b)} [n_{\text{PRB}}] \cdot \exp \left(\frac{j2\pi f_s k_{\Delta} (\tau_{\text{TO}}^{(b)} - \hat{\tau}_{\text{TO}}^{(b)})}{N_{\text{OFDM}}} \right) \\ \underline{\Xi}_{2,1}^{(m,b)} [n_{\text{PRB}}] \cdot \exp \left(-\frac{j2\pi f_s k_{\Delta} (\tau_{\text{TO}}^{(b)} - \hat{\tau}_{\text{TO}}^{(b)})}{N_{\text{OFDM}}} \right) & \underline{\Xi}_{2,2}^{(m,b)} [n_{\text{PRB}}] \end{pmatrix} \quad (4.27)$$

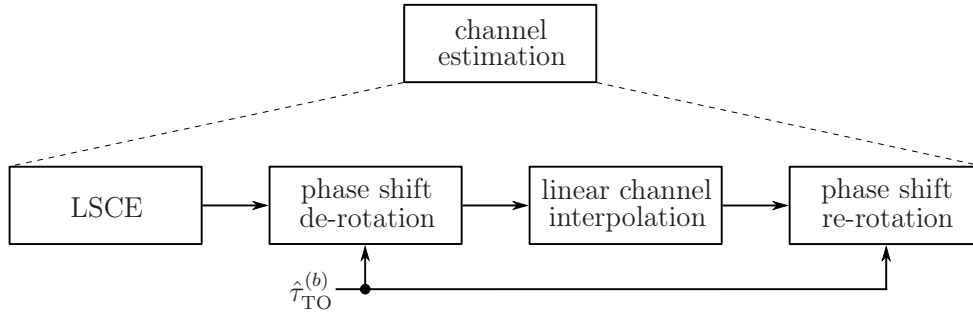


Figure 4.10. Channel estimation for unsynchronized CoMP transmission (created by the author of this thesis using [HW98, Figure 6]).

Following the findings achieved in Section 4.3 of this thesis, the TO estimation scheme (4.22) depends to a great extent on the SNR. As the operating range, the bandwidth efficiency becomes different from zero until it reaches the maximum bandwidth efficiency for an arbitrary but fix MCS depends on the SNR, which in turn has impact on the RMSE for DMRS-based TO estimation, as discussed in Section 4.3 of this thesis, an upper and a lower PER when compensating the impact of the TO with respect to PMI selection can be determined for each MCS, as indicated by the dashed lines in Figure 4.11. The upper PER is determined for the smallest SNR the IL single-layer transmission in TM10 using the 4×2 MIMO antenna configuration provides for a bandwidth efficiency different from zero and reads -9 dB, -1 dB and 8 dB for MCS4, MCS14 and MCS25, respectively, as depicted in Figure 3.7. Motivated by the fact that the advantages of unsynchronized CoMP IL single-layer transmission predominate as long as the achieved bandwidth efficiency exceeds the bandwidth efficiency of the IL single-layer transmission in TM9 for an arbitrary but fix SNR, the lower PER is determined for the SNR the IL single-layer transmission equals to 90 % of the maximum bandwidth efficiency of the respective MCS and reads -1 dB, 8 dB and 21 dB for MCS4, MCS14 and MCS25, respectively, as depicted in Figure 3.7.

Neglecting the impact of the TO with respect to PMI selection, the PER does not depend on the MCS and is therefore equal for MCS4, MCS14 and MCS25, as depicted in Figure 4.11. In that case, the PER is different from zero for any TO different from zero and reaches its maximum value equal to one for a TO greater than or equal to $2.9 \mu\text{s}$, as depicted in Figure 4.11. Hence, for a TO greater than or equal to $2.9 \mu\text{s}$, the average local post-SNR $\bar{\gamma}_{\text{post, LC-CCIMP}}^{(m,b)} [w]$ is no longer maximized for $0 \leq w < N_{\text{SB}}$. Analogously, the PER does not depend on the MCS when compensating the impact of the TO with respect to PMI selection when assuming perfect knowledge on the TO and is therefore equal for MCS4, MCS14 and MCS25, as depicted in Figure 4.11. However, despite compensating the impact of the TO with respect to PMI selection assuming perfect knowledge on the TO, the PER increases slightly up to a TO

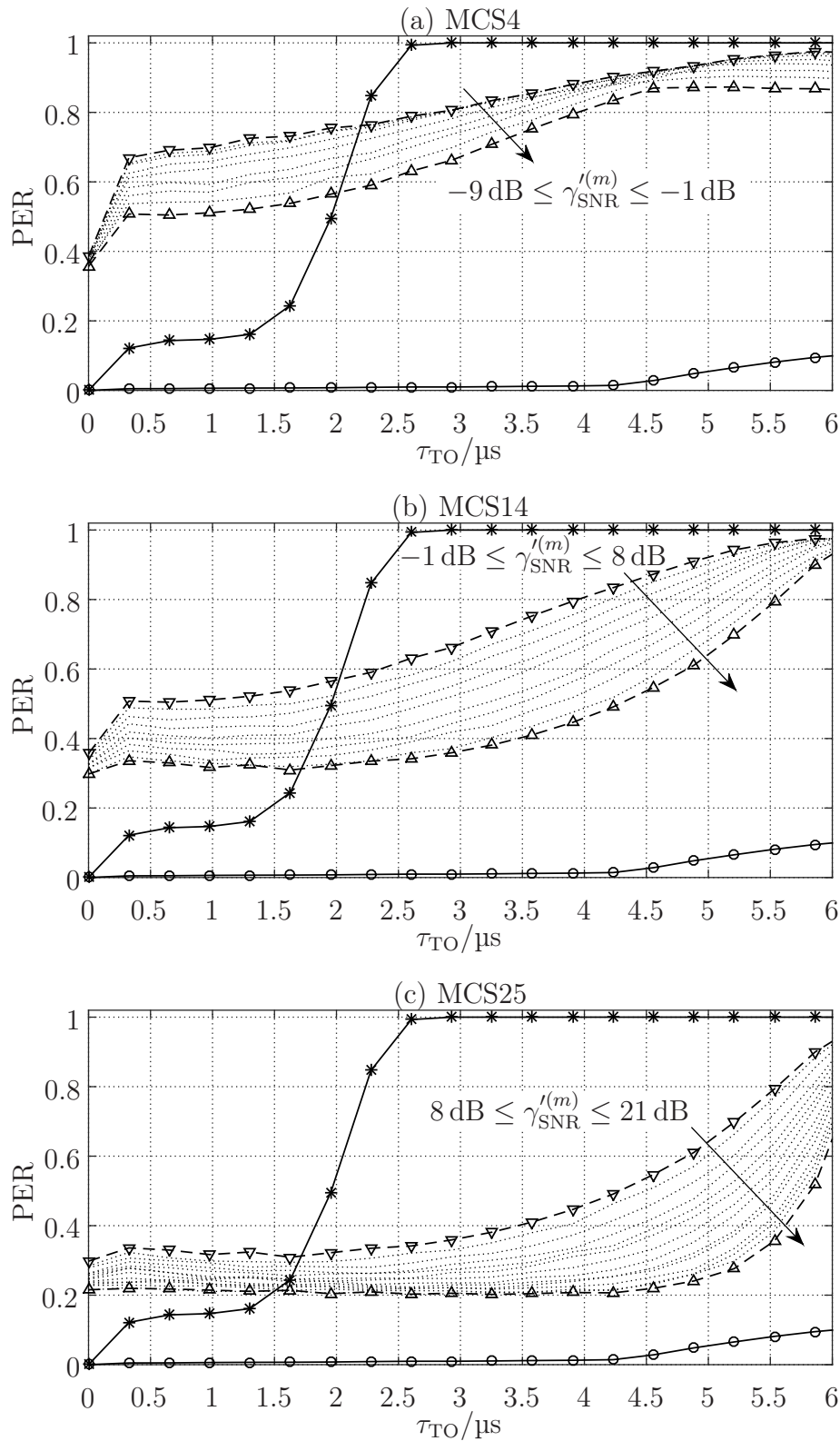


Figure 4.11. PMI error rate for (a) MCS4, (b) MCS14 and (c) MCS25 (legend see Table 4.5; created by the author of this thesis).

Table 4.5. Legend for Figure 4.11.

—*—	PER when ignoring the impact of the TO with respect to PMI selection
—▽—	Upper PER when compensating the impact of the TO with respect to PMI selection, making use of DMRS-based TO estimation according to (4.22)
.....	Intermediate PER when compensating the impact of the TO with respect to PMI selection, making use of DMRS-based TO estimation according to (4.22)
—△—	Lower PER when compensating the impact of the TO with respect to PMI selection, making use of DMRS-based TO estimation according to (4.22)
—○—	PER when compensating the impact of the TO with respect to PMI selection, assuming perfect knowledge on the TO

equal to $4.25 \mu\text{s}$ and noticeable for a TO greater than $4.25 \mu\text{s}$, as depicted in Figure 4.11. The reason is that the receive signal including the CSI-RSs on which basis the transmit covariance matrix (4.6) is determined, is faced with ISI if the TO is larger than the difference between the length of the CP and the multipath spread.

Due to the biased TO estimation error discussed in Section 4.3 of this thesis, the PER is different from zero for a TO equal to zero, as depicted in Figure 4.11 for MCS4, MCS14 and MCS25, as the TO difference in (4.27) is different from zero and so is the residual phase offset. However, the higher the SNR, the lower the RMSE of the TO estimation, resulting in a lower TO difference in (4.27) and, hence a lower residual phase offset, such that a lower PER can be achieved, as depicted in Figure 4.11. Following the findings achieved in Section 4.2.2 and Section 4.2.3 of this thesis, MCS4, making use of the QPSK mapping scheme is widely robust against signal amplification errors of the equalized complex-valued modulation symbols carrying the codewords when neglecting the impact of the TO with respect to channel estimation, while improper PMI selection results in a comparatively large performance loss. In accordance with the high RMSE experienced at comparatively low values of the SNR when making use of the DMRS-based TO estimation (4.22), applying the phase offset compensation scheme, the lowest possible PER reads 37 % for a SNR equal to -1 dB and increases to 50 % and more as the TO increases, as depicted in Figure 4.11(a). Hence, for TOs not exceeding $2.05 \mu\text{s}$ it is more beneficial to neglect rather than to compensate the impact of the TO with respect to PMI selection, as depicted in Figure 4.11(a) for MCS4.

The performance of the TO over the PER for MCS14 and MCS25 can be discussed analogously. As the operating range for MCS14 and MCS25 is at higher values of the SNR than the operating range for MCS4, the TO can be estimated more reliably, resulting in lower values of the PER, as depicted in Figure 4.11(b) and Figure 4.11(c). Particularly for MCS25, the RMSE for a SNR equal to 20 dB remains unchanged at approximately $0.25 \mu\text{s}$, as depicted in Figure 4.9, such that a PER of approximately 20 % can be maintained for $0 \mu\text{s} \leq \hat{\tau}_{\text{TO}}^{(b)} \leq 4.25 \mu\text{s}$, as depicted in Figure 4.11(c).

The performance of the TO compensation scheme with respect to PMI selection using the DMRS-based TO estimation scheme is further investigated in Section 4.6 of this thesis.

4.5 Channel Equalization for Asynchronous CoMP Transmission

Neglecting the impact of the TO with respect to channel estimation introduces an amplification of the equalized complex-valued modulation symbols carrying the codewords, such that the equalized symbols might not lie in the designated detection areas for HOMs when the TO increases, leading to limited signal detection capabilities, as discussed in Section 4.2.3 of this thesis. One way forward to mitigate the unwanted effect of the aforementioned amplification derived in (4.15) is to exploit the information of the TO for channel estimation [HW98, Section IV-C], as depicted in Figure 4.10 on page 199. The phase shift of the LSCE of the estimated CTF at each two adjacent subcarriers in frequency direction carrying the DMRSs denoted in (4.14a) and (4.14a) is de-rotated by $\exp(j\hat{\phi}(\kappa))$ and $\exp(j\hat{\phi}(\kappa + \kappa_\Delta))$, respectively, where the TO is estimated using the precoded DMRS-based TO estimation scheme (4.22). Subsequently, after piecewise linear channel interpolation the phase shift at each subcarrier carrying the complex-valued modulation symbol the codewords are transmitted on, is re-rotated by $\exp(j\hat{\phi}(k))$ [HW98, Section IV-C], as depicted in Figure 4.10 for $\kappa < k < \kappa + \kappa_\Delta$. Analogously to (4.15), $|\hat{g}'_{\nu, \text{DMRS}}(m, b)[k, \ell]|$ represents the magnitude of the linear interpolant at the (k, ℓ) -th RE and can be obtained from (4.15) when replacing $\Psi(\kappa_\Delta)$ by $2\pi(\tau_{\text{TO}}^{(b)} - \hat{\tau}_{\text{TO}}^{(b)})f_s\kappa_\Delta/N_{\text{OFDM}}$ for $\kappa < k < \kappa + \kappa_\Delta$ and $1 \leq \nu \leq N_{\text{R}}^{(m)}$. Obviously, the argument of the cosine function of the magnitude of the linear interpolant $|\hat{g}'_{\nu, \text{DMRS}}(m, b)[k, \ell]|$ approximates to the phase difference of the estimated CTF denoted in (4.16) when the estimated TO approximates to the experienced TO, denoted by $\hat{\tau}_{\text{TO}}^{(b)}$ and $\tau_{\text{TO}}^{(b)}$, respectively. In other word, the impact of the amplification of the equalized complex-valued symbols carrying the codewords can be theoretically reverted if the estimated TO matches perfectly to the experienced TO. Note that the impact of ISI will not be compensated in that way and persists if the TO is larger than the difference between the length of the CP and the multipath spread of the mobile communication channel. For that reason, the performance loss in terms of SNR over bandwidth efficiency caused by the practical limitations of the unsynchronized CoMP transmission, discussed in Section 4.2.2 and Section 4.2.3 of this thesis, cannot be entirely reverted despite perfect knowledge on the TO when making use of single-tap signal equalization.

The magnitude of the difference of (4.15) for synchronized CoMP transmission referring to a TO equal to zero and $|\hat{g}'_{\nu, \text{DMRS}}(m, b)[k, \ell]|$ represents the residual magnitude of the channel estimation error when making use of the channel

estimation scheme depicted in Figure 4.10 and reads

$$\begin{aligned}
 & \left| \underline{g}_{\nu, \text{err}}^{(m,b)} [k, \ell] \right| \\
 &= \left| \left| \hat{\underline{g}}_{\nu, \text{DMRS}}^{(m,b)} [k, \ell] \Big|_{\tau_{\text{TO}}^{(b)}=0} - \left| \hat{\underline{g}}_{\nu, \text{DMRS}}^{\prime(m,b)} [k, \ell] \right| \right| \\
 &= \left| \frac{1}{\kappa_{\Delta}} \sqrt{x_1^2 + x_2^2 + 2x_1x_2 \cos(\Theta(\kappa, \kappa + \kappa_{\Delta}))} - \right. \\
 & \quad \left. \frac{1}{\kappa_{\Delta}} \sqrt{x_1^2 + x_2^2 + 2x_1x_2 \cos\left(\Theta(\kappa, \kappa + \kappa_{\Delta}) - \frac{2\pi(\tau_{\text{TO}}^{(b)} - \hat{\tau}_{\text{TO}}^{(b)})f_s\kappa_{\Delta}}{N_{\text{OFDM}}}\right)} \right|, \tag{4.28}
 \end{aligned}$$

where

$$x_1 = (k - \kappa) \cdot \left| \hat{\underline{g}}_{\nu, \text{DMRS}}^{(m,b)} [\kappa + \kappa_{\Delta}, \ell] \right| > 0 \quad \text{and} \tag{4.29a}$$

$$x_2 = (\kappa + \kappa_{\Delta} - k) \cdot \left| \hat{\underline{g}}_{\nu, \text{DMRS}}^{(m,b)} [k, \ell] \right| > 0 \tag{4.29b}$$

holds. For the theoretic case when the coherence bandwidth of the mobile communication channel approximates to infinity, (4.28) turns to

$$\left| \underline{g}_{\nu, \text{err}}^{(m,b)} [k, \ell] \right| = \frac{1}{\kappa_{\Delta}} \cdot \left| x_1 + x_2 - \sqrt{x_1^2 + x_2^2 + 2x_1x_2 \cos\left(\frac{2\pi(\tau_{\text{TO}}^{(b)} - \hat{\tau}_{\text{TO}}^{(b)})f_s\kappa_{\Delta}}{N_{\text{OFDM}}}\right)} \right|, \tag{4.30}$$

as the phase difference $\Theta(\kappa, \kappa + \kappa_{\Delta})$ within the cosine function in (4.28) approximates to zero. Making use of the series expansion of the cosine function [MW02, Section 14.32a]

$$\cos(\alpha) = \sum_{i=0}^{\infty} (-1)^i \cdot \frac{\alpha^{2i}}{(2i)!} = 1 + \sum_{i=1}^{\infty} (-1)^i \cdot \frac{\alpha^{2i}}{(2i)!} \tag{4.31}$$

holds, such that (4.30) can be further simplified according to

$$\begin{aligned}
 & \left| \underline{g}_{\nu, \text{err}}^{(m,b)} [k, \ell] \right| = \\
 & \left| \hat{\underline{g}}_{\nu, \text{DMRS}}^{(m,b)} [\cdot, \ell] \right| \cdot \left(1 - \sqrt{1 + \omega \cdot \sum_{i=1}^{\infty} (-1)^i \frac{\left(2\pi f_s \kappa_{\Delta} (\tau_{\text{TO}}^{(b)} - \hat{\tau}_{\text{TO}}^{(b)}) / N_{\text{OFDM}}\right)^{2i}}{(2i)!}} \right), \tag{4.32}
 \end{aligned}$$

where

$$\omega = \left\{ \frac{2x_1x_2}{(x_1+x_2)^2} = \frac{2(k-\kappa)(\kappa+\kappa_\Delta-k)}{\kappa_\Delta^2} \middle| \kappa < k < \kappa + \kappa_\Delta, \kappa \in \mathcal{S}_{\text{SB}}^{(w)} \right\} \quad (4.33)$$

holds. For any $x_1 \in \mathbb{R}_+$ and $x_2 \in \mathbb{R}_+$, defined in (4.29a) and (4.29b), respectively, $\omega \in (0, \frac{1}{2}]$ holds. Note that ω equal to zero in (4.33) can only be reached for either k equal to κ or $\kappa + \kappa_\Delta$, corresponding to the subcarrier carrying the precoded DMRSs, where the respective LSCE is inherently provided in (4.14a) and (4.14a), respectively and is therefore not of any practical importance for signal equalization. Furthermore, the series in (4.30) is even and reaches the values on the interval $[-2, 0]$ for any TO difference $\tau_{\text{TO}}^{(b)} - \hat{\tau}_{\text{TO}}^{(b)} \in \mathbb{R}$. Hence, the discriminant in (4.30) reaches the values on the interval $[0, 1]$, which are mapped on the interval $[0, 1]$ after calculating the square root. As a result, (4.32) is greater than or equal to zero for any TO difference $\tau_{\text{TO}}^{(b)} - \hat{\tau}_{\text{TO}}^{(b)} \in \mathbb{R}$. The magnitude (4.32) normalized by the magnitude of the estimated CTF provides the relative channel estimation error when making use of the channel estimation scheme illustrated in Figure 4.10 and is depicted in Figure 4.12 on page 206 over the RMSE of the estimated TO for $\omega = \{\frac{4}{25}, \frac{6}{25}, \frac{1}{2}\}$, corresponding to the two valid values in (4.33) for κ_Δ equal to five and the one valid value equal to one half for κ_Δ equal to two. Regarding Figure 4.12, it can be observed that the larger the RMSE of the estimated TO becomes, the larger the relative estimation error becomes for any value ω . On the other hand, with a RMSE equal to zero, the residual channel estimation error approximates to zero, as depicted in Figure 4.12. Moreover, the larger the value ω , the larger the relative TO estimation error for an arbitrary but fix RMSE of the estimated TO excluding zero, as depicted in Figure 4.12. The reason is that the Euclidean distance to the closest subcarrier carrying the precoded DMRS increases for an arbitrary but fix κ_Δ as the value ω increases and, thus, the channel estimation error for any TO different from zero.

To provide an example, the cutout of the magnitude of the estimated CTF determined by making use of the LSCE and piecewise linear channel interpolation, is depicted in Figure 4.13 on page 206 for the first three PRBs out of the zeroth subband for synchronized CoMP transmission, where the SNR has been set to 40 dB in order to be able to disregard the impact of both, the AWGN and the inter-cell interference. Note that for a SNR equal to 40 dB the RMSE of the estimated TO is typically much lower than $2 \mu\text{s}$, as depicted in Figure D.1 on page 256, as long as the TO is smaller than the difference of the length of the CP and the multipath spread of the mobile communication channel. Therefore the RMSE equal to $2 \mu\text{s}$ as well as the choice of the coherence bandwidth of the mobile communication channel, assumed to approximate to infinity, are selected for illustration purposes only. Moreover, the magnitude

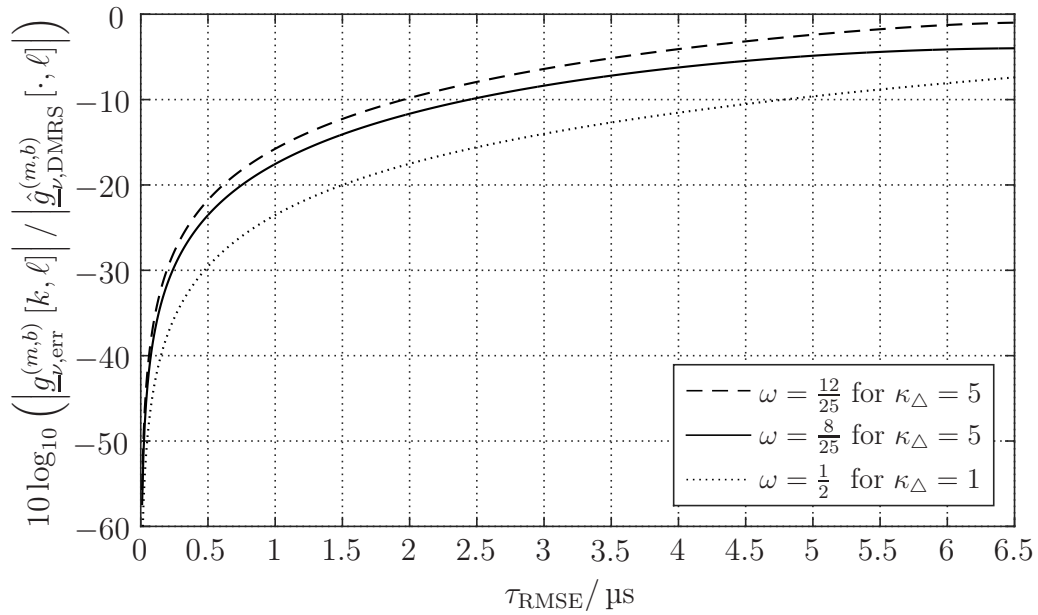


Figure 4.12. Normalized magnitude of the residual channel estimation error (created by the author of this thesis).

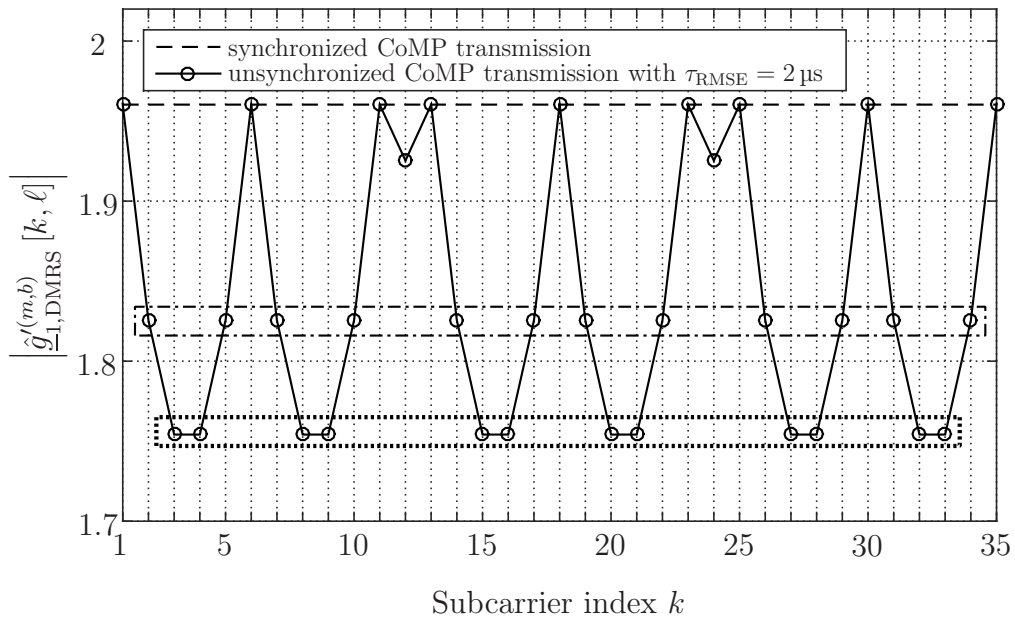


Figure 4.13. Magnitude of the estimated CTF after TO compensation (created by the author of this thesis).

of the estimated CTF, following the channel estimation scheme illustrated in Figure 4.10, is provided for the case of unsynchronized CoMP transmission, where the RMSE of the estimated TO is assumed to be equal to $2\ \mu\text{s}$. For the theoretic case when the coherence bandwidth of the mobile communication channel approximates to infinity, the magnitude of the estimated CTF in the k_i -th subcarrier is equal to the magnitude of the estimated CTF in the k_j -th subcarrier for synchronized CoMP transmission, as indicated by the dotted line in Figure 4.13 and reads

$$\left| \hat{\underline{g}}_{1,\text{DMRS}}^{(m,b)} [k, \ell] \right| = 1.94 \quad (4.34)$$

in this example. Following the findings achieved in Section 4.2.3 of this thesis, the magnitude of the estimated CTF at the subcarriers the complex-valued modulation symbols the codewords are transmitted on decreases as the TO increases. Replacing the TO by the RMSE of the estimated TO which is assumed to be equal to $2\ \mu\text{s}$, the magnitude of the estimated CTF depends on the subcarrier index and reads

$$\left| \hat{\underline{g}}_{1,\text{DMRS}}^{(m,b)} [k, \ell] \right| = \begin{cases} 1.94 & \text{for } k \in \mathcal{S}_{\text{SB}}^{(0)} & (4.35\text{a}) \\ 1.91 & \text{for } k \in \{12, 24, \dots\}, \\ & \kappa_{\Delta} = 2 \text{ and } \omega = 1/2 & (4.35\text{b}) \end{cases}$$

$$\left| \hat{\underline{g}}_{1,\text{DMRS}}^{(m,b)} [k, \ell] \right| = \begin{cases} 1.81 & \text{for } k \in \{2, 5, 7, 10, 14, 17, 19, \\ & 22, 26, 29, 31, 34, \dots\}, \\ & \kappa_{\Delta} = 5 \text{ and } \omega = 12/25 & (4.35\text{c}) \end{cases}$$

$$\left| \hat{\underline{g}}_{1,\text{DMRS}}^{(m,b)} [k, \ell] \right| = \begin{cases} 1.73 & \text{for } k \in \{3, 4, 8, 9, 15, 16, 20, \\ & 21, 27, 28, 32, 33, \dots\}, \\ & \kappa_{\Delta} = 5 \text{ and } \omega = 8/25 & (4.35\text{d}) \end{cases}$$

as depicted in Figure 4.13. The subcarriers in (4.35c) and (4.35d) in Figure 4.13 are marked with the dash-dotted and the dotted rectangular, respectively. The difference of (4.34) and (4.35b) normalized by (4.34) denotes the relative channel estimation error and is equal to $-18.1\ \text{dB}$ for a RMSE equal to $2\ \mu\text{s}$ and matches the theoretically expected relative channel estimation error, depicted in Figure 4.12. Moreover, the difference of (4.34) and (4.35c) normalized by (4.34) is approximately equal to $-11.7\ \text{dB}$ and the difference of (4.34) and (4.35d) normalized by (4.34) is approximately equal to $-9.66\ \text{dB}$ and, thus, matches to the theoretically expected relative channel estimation errors, depicted in Figure 4.12.

To measure the distortion introduced by the practical limitations such as the TO without taking the symbol detection and decoding capabilities into account, the Error Vector Magnitude (EVM) is used [STB11, Section 21.3.1.1]. The EVM is a measure of the difference between the reference waveform and

the measured waveform [3GP16n, Section 6.5.2.1], for example the root mean square of the difference between the transmitted complex-valued modulation symbols carrying the codewords and the equalized receive signal [STB11, Section 21.3.1.1] and is denoted by ϵ_{EVM} . To evaluate the suggested channel equalization scheme for unsynchronized CoMP transmission, the TO over EVM of the equalized complex-valued modulation symbols carrying the codewords is depicted in Figure 4.14 on page 210 for the 4×2 MIMO antenna configuration for MCS4, MCS14 and MCS25, making use of the QPSK, the 16QAM and the 64QAM mapping scheme, respectively. Each upper EVM is provided for a SNR $\gamma_{\text{SNR}}^{(m)}$ equal to -9 dB, -1 dB and 8 dB for MCS4, MCS14 and MCS25, respectively, while the upper EVM is provided for a SNR $\gamma_{\text{SNR}}^{(m)}$ equal to -1 dB, 8 dB and 21 dB for MCS4, MCS14 and MCS25, respectively, analogously to the PER discussed in Section 4.4 of this thesis. The upper and the lower EVM is provided for every of the three cases, where the impact of the TO with respect to channel estimation is

- neglected,
- compensated assuming perfect knowledge on the TO and
- compensated using the DMRS-based TO estimation scheme (4.22).

Obviously the smaller the EVM, the smaller the difference between the transmitted complex-valued modulation symbols carrying the codewords and the equalized receive signal. As the EVM depends on, amongst others, the SNR which in turn changes with the operating range of each MCS for an arbitrary but fix TO, it can be observed that the higher the MCS, the higher the required SNR and, hence, the lower the EVM, as depicted in Figure 4.14. Making use of the suggested channel estimation scheme for unsynchronized CoMP transmission in conjunction with the assumption of perfect knowledge on the TO, the impact of the amplification of the equalized complex-valued modulation symbols carrying the codewords can be reverted, such that the slight increase of the EVM is subject to the non-negligible impact of ISI as long as the TO remains smaller than the length of the CP, as depicted in Figure 4.14 (a), Figure 4.14 (b) and Figure 4.14 (c) for MCS4, MCS14 and MCS25, respectively. Following the findings achieved in Section 4.3 of this thesis, the TO estimation accuracy depends to a great extent on the SNR. Therefore, making use of the suggested channel estimation scheme for unsynchronized CoMP transmission in conjunction with DMRS-based TO estimation (4.22) is more reliable the higher the MCS and, hence the higher operating range in terms of SNR is, as depicted in Figure 4.14. Neglecting the impact of the TO with respect to channel estimation is, with a few minor exceptions, not beneficial. Regarding Figure 4.14, the upper and the lower EVM of MCS4, as well as the upper EVM of MCS14 results in a lower EVM when neglecting the impact of

the TO with respect to the suggested channel estimation scheme for unsynchronized CoMP transmission, compared with the respective EVM when compensating it by making use of the DMRS-bases TO estimation scheme (4.22) for TOs not exceeding approximately $1.2\mu\text{s}$. Here again, due to the large RMSE of the estimated TO for comparatively small values of the SNR, the suggested channel estimation scheme for unsynchronized CoMP transmission is not beneficial. However, as the TO increases, making use of the suggested channel estimation scheme for unsynchronized CoMP transmission is, despite the non-negligible RMSE of the estimated TO in terms of EVM reduction of major importance for each MCS, as depicted in Figure 4.14.

To discuss the gain of the suggested channel estimation scheme for unsynchronized CoMP transmission, the lower EVMs for MCS4, MCS14 and MCS25, provided in Figure 4.14 (a), Figure 4.14 (b) and Figure 4.14 (c), respectively, which are experienced at a TO equal to $3\mu\text{s}$ are considered and summarized in Table 4.7 on page 213 of this thesis. The gain is defined as the difference of the reference EVM, experienced for synchronized CoMP transmission for a TO equal to zero and the experienced EVM for unsynchronized CoMP transmission where the impact of the TO for channel estimation is either neglected or compensated, where the latter case is further subdivided into perfect knowledge on the TO and the DMRS-bases TO estimation (4.22). The reference EVM is primarily influenced by the AWGN and the residual impact of inter-cell interference after cooperative interference mitigation signal precoding. As the required SNR to guarantee 90 % of the maximum bandwidth efficiency of the respective MCS increases as the MCS increases, the impact of the AWGN and the related average power of the interfering signal decreases, such that the EVM decreases accordingly and reads -1.8 dB , -6.5 dB and -11.4 dB for MCS4, MCS14 and MCS25, respectively, as denoted in Table 4.7. Following the findings achieved in Section 4.2.3 of this thesis, the complex-valued modulation symbols carrying the codewords experience an amplification after channel estimation for any TO different from zero if the impact of the TO is neglected during the channel estimation process. Descriptively spoken, the equalized complex-valued modulation symbols carrying the codewords are expanded towards the corner of the scatterplot as the TO increases, leading to a gain of the EVM equal to -3.1 dB , -3.9 dB and -6.1 dB for MCS4, MCS14 and MCS25, respectively, as denoted in Table 4.7. Making use of the suggested channel estimation scheme for unsynchronized CoMP transmission in conjunction with perfect knowledge on the TO, the residual magnitude of the channel estimation error (4.28) approximates to zero such that the complex-valued modulation symbols carrying the codewords are no longer influenced by the aforementioned amplification. However, as the impact of ISI cannot be mitigated by making use of a single-tap equalizer, the resulting gain is limited by -0.2 dB for each MCS, as depicted in Table 4.7. In a practical scenario,

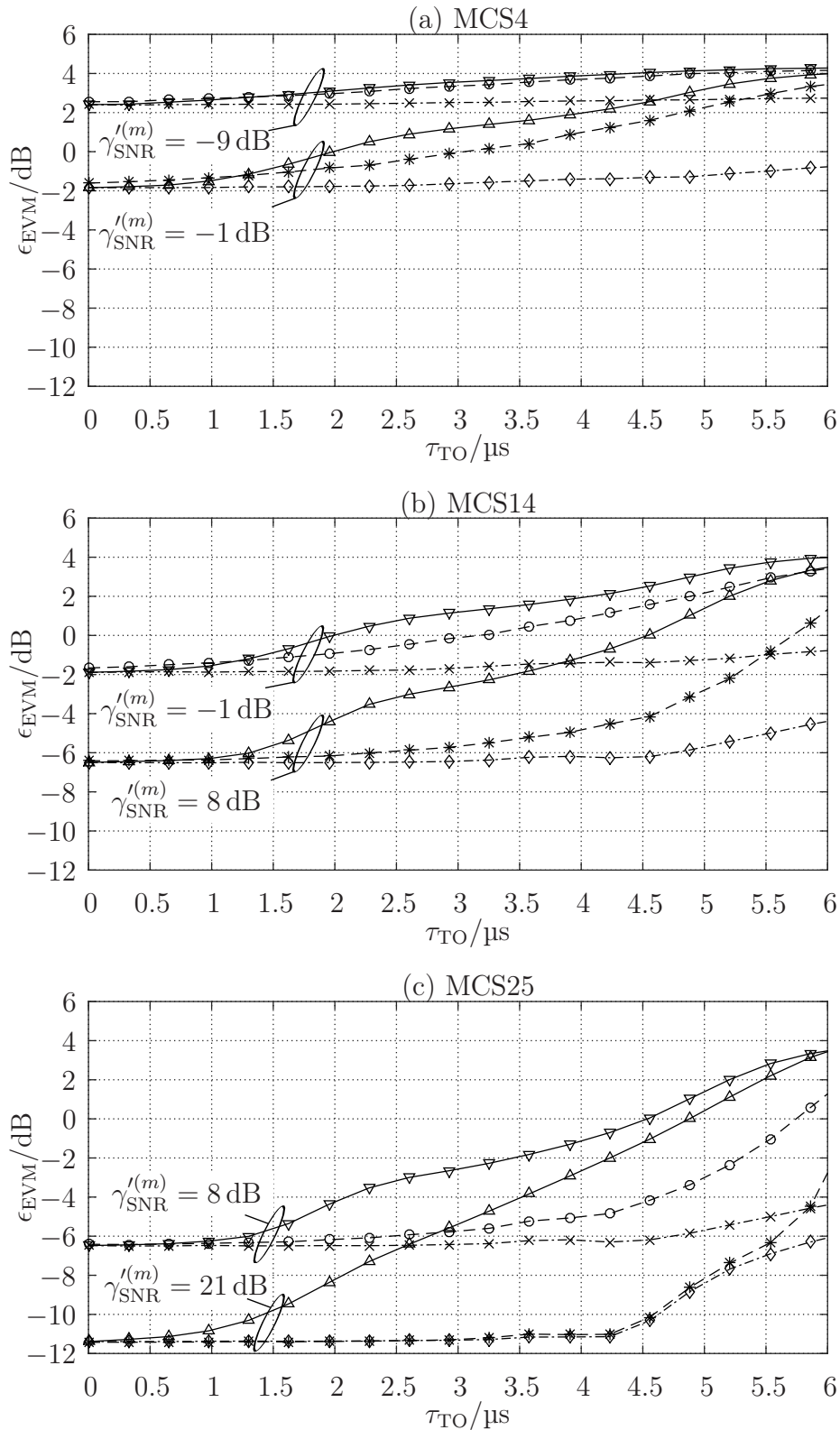


Figure 4.14. EVM of the equalized complex-valued modulation symbols for (a) MCS4, (b) MCS14 and (c) MCS25 (legend see Table 4.6; created by the author of this thesis).

Table 4.6. Legend for Figure 4.14.

—▽—	Upper EVM when neglecting the impact of the TO with respect to both, PMI selection and channel estimation
—△—	Lower EVM when neglecting the impact of the TO with respect to both, PMI selection and channel estimation
--×--	Upper EVM when compensating the impact of the TO with respect to PMI selection and channel estimation assuming perfect knowledge on the TO
--◇--	Lower EVM when compensating the impact of the TO with respect to PMI selection and channel estimation assuming perfect knowledge on the TO
-⊖-	Upper EVM when compensating the impact of the TO with respect to PMI selection and channel estimation using the DMRS-based TO estimation according to (4.22)
-∗-	Lower EVM when compensating the impact of the TO with respect to PMI selection and channel estimation using the DMRS-based TO estimation according to (4.22)

however, perfect knowledge on the TO cannot be assumed. Following the findings achieved in Section 4.3 of this thesis, the DMRS-based TO estimation error is biased due to the non-negligible impact of the channel phase difference in (4.22), such that

$$\tau_{\text{RMSE}} = \begin{cases} 1.9 \mu\text{s} & \text{for } \gamma_{\text{SNR}}^{\prime(m)} = -1 \text{ dB and MCS4} & (4.36a) \\ 0.9 \mu\text{s} & \text{for } \gamma_{\text{SNR}}^{\prime(m)} = 8 \text{ dB and MCS14} & (4.36b) \\ 0.3 \mu\text{s} & \text{for } \gamma_{\text{SNR}}^{\prime(m)} = 21 \text{ dB and MCS25} & (4.36c) \end{cases}$$

holds for the RMSE of the estimated TO, as depicted in Figure 4.9. The normalized magnitude of the residual channel estimation error decreases as the RMSE of the estimated TO decreases, as depicted in Figure 4.12, so does the gain when compensating the impact of the TO for channel estimation using the DMRS-based TO estimation and reads -1.8 dB, -0.9 dB and -0.2 dB for MCS4, MCS14 and MCS25, respectively, as denoted in Table 4.7. Regarding the fourth column of Table 4.7, it is important to point out that the gain for MCS25 experienced when making use of the suggested channel estimation scheme for unsynchronized CoMP transmission in conjunction with the DMRS-based TO estimation scheme (4.22) is equal to the gain if ideal knowledge on the TO is assumed.

The performance of the implicit feedback generation scheme and the suggested channel estimation scheme adapted for unsynchronized CoMP transmission in terms of SNR over bandwidth efficiency is discussed in Section 4.6 of this thesis.

4.6 Performance Evaluation

To demonstrate the performance of the suggested PMI selection and channel estimation scheme for unsynchronized IL single-layer CoMP transmission in TM10, numerical results at the link level are carried out. The assumed simulation parameters are summarized in Table 4.8 on page 219. As already mentioned in Section 2.10 and Section 3.4 of this thesis, the numerical results at the link level are carried out for MCS4, MCS14 and MCS25, where the performance is evaluated at 90% of the maximum bandwidth efficiency of the respective MCS denoted in (2.98a), (2.98b) and (2.98c), respectively.

The performance of the unsynchronized IL single-layer CoMP transmission in TM10 for the 4×2 MIMO antenna configuration using the IRC receiver (2.73) is provided for the case that the impact of the TO with respect to PMI selection and channel estimation is neglected and compensated, where in the latter case perfect knowledge on the TO and the DMRS-based TO estimation scheme (4.22) is considered. The respective results in terms of SNR over

Table 4.7. Comparison of the lower EVMs in Figure 4.14 (created by the author of this thesis).

	MCS4	MCS14	MCS25
Reference EVM at $\tau_{\text{TO}}^{(b)} = 0 \mu\text{s}$	-1.8 dB	-6.5 dB	-11.4 dB
Gain when neglecting the impact of the TO for channel estimation for $\tau_{\text{TO}}^{(b)} = 3 \mu\text{s}$	-3.1 dB	-3.9 dB	-6.1 dB
Gain when compensating the impact of the TO for channel estimation assuming perfect knowledge on the TO for $\tau_{\text{TO}}^{(b)} = 3 \mu\text{s}$	-0.2 dB	-0.2 dB	-0.2 dB
Gain when compensating the impact of the TO for channel estimation using the DMRS-based TO estimation according to (4.22) for $\tau_{\text{TO}}^{(b)} = 3 \mu\text{s}$	-1.8 dB	-0.9 dB	-0.2 dB

bandwidth efficiency are depicted in Figure 4.15 on page 220 for a TO equal to $2.3 \mu\text{s}$. A generalization on arbitrary values of the TO not exceeding $6.5 \mu\text{s}$ is provided in the further course of this section. Moreover, the performance in terms of SNR over bandwidth efficiency for synchronized IL single-layer CoMP transmission with the 4×2 MIMO antenna configuration provides the upper bound performance for IL transmission, as discussed in Section 3.4 of this thesis and is depicted in Figure 4.15. In addition, the reference performance for the lower bound in terms of SNR over bandwidth efficiency is represented by the IL single-layer transmission in TM9 for the 4×2 MIMO antenna configuration, as depicted in Figure 4.15. The unsynchronized IL single-layer CoMP transmission in TM10 when neglecting the impact of the TO with respect to channel estimation for the 2×2 MIMO antenna configuration is considered too, as depicted in Figure 4.15.

Analogously to Figure 4.15, the impact of the TO on the performance loss for the 4×2 MIMO antenna configuration in terms of TO over SNR caused by the practical limitations of unsynchronized IL single-layer CoMP transmission is evaluated at 90 % of the maximum bandwidth efficiency of the respective MCS and is depicted in Figure 4.17. The performance loss is provided for

- ignoring the impact of the TO with respect to PMI selection and channel estimation,
- ignoring the impact of the TO with respect to PMI selection and compensating the impact of the TO with respect to channel estimation according to Section 4.5 using the DMRS-based TO estimation scheme (4.22),
- compensating the impact of the TO with respect to PMI selection according to Section 4.4 of this thesis using the DMRS-based TO estimation scheme (4.22) and ignoring the impact of the TO with respect to channel estimation,
- compensating the impact of the TO with respect to PMI selection and channel estimation according to Section 4.4 and Section 4.5 of this thesis, respectively, using the DMRS-based TO estimation scheme (4.22) and
- compensating the impact of the TO with respect to PMI selection and channel estimation according to Section 4.4 and Section 4.5 of this thesis, respectively, assuming perfect knowledge on the TO.

The performance difference between synchronized IL single-layer CoMP transmission in TM10 and single-layer transmission in TM9 for the 4×2 MIMO antenna configuration is the same as in Section 4.2.2 of this thesis and is depicted by the dashed line in Figure 4.17 (a), Figure 4.17 (b) and Figure 4.17 (c) for MCS4, MCS14 and MCS25, respectively.

The necessity to compensate the impact of the TO with respect to PMI selection and channel estimation to maintain the advantages of single-layer CoMP transmission in TM10 in unsynchronized deployments has been identified in Section 4.2.2 and Section 4.2.3 of this thesis, respectively. Making use of the suggested PMI selection and channel estimation scheme for unsynchronized CoMP transmission, discussed in Section 4.4 and Section 4.5 of this thesis, respectively, in conjunction with the DMRS-based TO estimation scheme (4.22), the advantages of IL single-layer CoMP transmission in TM10 over IL single-layer transmission in TM9 can be maintained for the 4×2 MIMO antenna configuration for a TO up to approximately $2.6 \mu\text{s}$, $3.4 \mu\text{s}$ and $4.6 \mu\text{s}$ for MCS4, MCS14 and MCS25, as depicted in Figure 4.17 (a), Figure 4.17 (b) and Figure 4.17 (c), respectively. Regarding Figure 4.17 (a), it can be observed that making use of the suggested PMI selection scheme for unsynchronized CoMP transmission in conjunction with the DMRS-based TO estimation scheme (4.22) is not beneficial with respect to the performance loss in terms of TO over SNR for TOs not exceeding $1.8 \mu\text{s}$ irrespective of neglecting or compensating the impact of the TO with respect to channel estimation. Similar observations can be achieved in Figure 4.17 (b) for MCS14, too. Following the findings achieved in Section 4.4 and Section 4.5 of this thesis, the reason is that the suggested PMI feedback scheme rather than the suggested channel estimation scheme for unsynchronized CoMP transmission is susceptible for TO estimation errors for small TOs. For this reason, the performance loss in terms of TO over SNR at a TO equal to zero decreases as the index of the MCS increases, as depicted in Figure 4.17, as the operating range in terms of SNR increases, leading to a smaller RMSE of the estimated TO when making use of the DMRS-based TO estimation scheme (4.22). However, in total the advantages of unsynchronized single-layer CoMP transmission in TM10 over single-layer transmission in TM9 can be maintained for additional $0.6 \mu\text{s}$, $1.4 \mu\text{s}$ and $2.9 \mu\text{s}$ when besides compensating the impact of the TO with respect to channel estimation the impact of the TO with respect to PMI selection is compensated, as depicted in Figure 4.17 (a), Figure 4.17 (b) and Figure 4.17 (c) for MCS4, MCS14 and MCS25, respectively. Hence, the impact of the TO is compensated with respect to both, PMI selection and channel estimation.

The difference of the performance loss in terms of TO over SNR between the aforementioned two schemes in conjunction with the DMRS-based TO estimation scheme (4.22) and the assumption on perfect knowledge on the TO is denoted by ϵ_{MCS4} , ϵ_{MCS14} and ϵ_{MCS25} and reads 6.4 dB, 4.1 dB and 1.7 dB for MCS4, MCS14 and MCS25, respectively, as depicted in Figure 4.17. Obviously, $\epsilon_{\text{MCS4}} < \epsilon_{\text{MCS14}} < \epsilon_{\text{MCS25}}$ holds. Here again, the higher the index of the MCS, the higher the SNR operating range, the lower the RMSE of the estimated TO when making use of the DMRS-based TO estimation scheme (4.22) and, hence, the lower the difference of the performance loss in terms of SNR, as

depicted in Figure 4.17.

To discuss the impact of the TO on the achievable bandwidth efficiency for each considered MCS, the SNR over bandwidth efficiency depicted in Figure 4.15 is considered. Obviously, neglecting the impact of the TO with respect to PMI selection and channel estimation in unsynchronized IL single-layer CoMP transmission in TM10 for the 4×2 MIMO antenna configuration, in contrast to MCS25, the maximum bandwidth efficiency for MCS4 and MCS14 can be reached at the expense of a higher SNR, as depicted in Figure 4.15. The respective performance loss in case of MCS4 and MCS14 reads 3.7 dB and 4.9 dB, respectively, as depicted in Figure 4.15. In case of MCS25, the impact of the amplification of the equalized complex-valued modulation symbols carrying the codewords when neglecting the impact of the TO with respect to channel estimation, identified and discussed in Section 4.2.3 of this thesis, limits reliable signal detection and, as a result, reduces the maximum achievable bandwidth efficiency by approximately 0.24 bit/s/Hz for the 4×2 MIMO antenna configuration, as depicted in Figure 4.15. In all of the three cases for MCS4, MCS14 and MCS25 the advantages of IL single-layer CoMP transmission in TM10 for the 4×2 MIMO antenna configuration, aimed to mitigate the impact of inter-cell interference to improve the bandwidth efficiency in the cell-edge, vanish in unsynchronized deployments and perform even worse than IL single-layer transmission in TM9, as depicted in Figure 4.15.

An interesting observation comes out when comparing the SNR over bandwidth efficiency for unsynchronized IL single-layer transmission in TM10 for the 4×2 and the 2×2 MIMO antenna configuration, where in the former MIMO antenna configuration the impact of the TO with respect to both, PMI selection and channel estimation is neglected, while in the latter MIMO antenna configuration the impact of the TO with respect to channel estimation is neglected. Despite the limited beamforming gain of the 2×2 MIMO antenna configuration over the 4×2 MIMO antenna configuration, discussed in Section 2.4.3 and Appendix A of this thesis and verified in Section 2.10 of this thesis with numerical results at the link level for synchronized CoMP transmission, as well as the limited interference suppression capabilities of the LC-CCIMP scheme, discussed in Section 3.3.3 of this thesis and verified with numerical results in Section 3.4 of this thesis, making use of the 2×2 MIMO antenna configuration enables the UE to experience a higher bandwidth efficiency compared with using the 4×2 MIMO antenna configuration in this case, as depicted in Figure 4.15. Following the findings achieved in Section 4.2.2 and Section 4.2.3 of this thesis, the performance loss experienced by the UE when neglecting the impact of the TO with respect to channel estimation is negligible in comparison to the performance loss when neglecting the impact of the TO with respect to PMI selection for unsynchronized IL single-layer CoMP transmission in TM10 for MCS4 and MCS14 in conjunction with the 4×2 MIMO

antenna configuration at the considered TO equal to $2.3 \mu\text{s}$. As the 2×2 MIMO antenna configuration is robust against improper PMI selection, as discussed in Section 4.2.2 of this thesis, the gain of approximately 2.9 dB and 3.7 dB for MCS4 and MCS14, respectively, over the 4×2 MIMO antenna configuration is subject to the beamforming gain which can be maintained despite the TO equal to $2.3 \mu\text{s}$, as depicted in Figure 4.15. Furthermore, making use of MCS25 in conjunction with the 2×2 MIMO antenna configuration in unsynchronized IL single-layer CoMP transmission in TM10 enables the achieve the maximum bandwidth efficiency equal to 2.83 bit/s/Hz at a TO equal to $2.3 \mu\text{s}$, while the maximal bandwidth efficiency for the respective 4×2 MIMO antenna configuration saturates at 2.59 bit/s/Hz when neglecting the impact of the TO, as depicted in Figure 4.15. Unlike to MCS4 and MCS14, in case of MCS25 the performance loss experienced by the UE when neglecting the impact of the TO with respect to PMI selection is negligible in comparison to the performance loss when neglecting the impact of the TO with respect to channel estimation in unsynchronized IL single-layer CoMP transmission in TM10 in conjunction with the 4×2 MIMO antenna configuration at a TO equal to $2.3 \mu\text{s}$. Hence, the loss of the bandwidth efficiency of approximately 0.24 bit/s/Hz is subject to the higher code rate of the 4×2 MIMO antenna configuration compared with the code rate of the 2×2 MIMO antenna configuration, depicted and denoted in Figure 3.1 and Table B.3 on page 138 and 246, respectively, rather than the robustness against PMI selection.

Making use of the suggested PMI selection and channel estimation scheme for unsynchronized CoMP transmission discussed in Section 4.4 and Section 4.5 of this thesis, respectively, in conjunction with the DMRS-based TO estimation scheme (4.22), the PER and the EVM experienced at the considered TO equal to $2.3 \mu\text{s}$ can be the more reduced the higher the index of the MCS becomes. Consequently, a gain of 0.9 dB, 2.8 dB and 20.2 dB can be obtained when making use of the suggested TO compensation schemes compared with the case when neglecting the impact of the TO with respect to PMI selection and channel estimation in unsynchronized IL single-layer CoMP transmission in TM10 using the 4×2 MIMO antenna configuration for MCS4, MCS14 and MCS25, respectively, as depicted in Figure 4.15. Here gain, the higher the index of the MCS, the higher the SNR operating range, the higher the TO estimation accuracy and, thus, the higher the respective performance gain becomes. Hence, the gap to the synchronized IL single-layer CoMP transmission in TM10 with the 4×2 MIMO antenna configuration is reduced to 2.8 dB, 2.2 dB and 0.4 dB for MCS4, MCS14 and MCS25, respectively, as depicted in Figure 4.15.

To show that the limitations of the TO compensation with respect to both, PMI selection and channel estimation in unsynchronized IL single-layer CoMP transmission in TM10 are subject to the biased TO estimation error when making use of the DMRS-based TO estimation scheme (4.22) for the considered

TO equal to $2.3 \mu\text{s}$, the resulting SNR over bandwidth efficiency when making use of the PMI selection and channel estimation scheme for unsynchronized CoMP transmission, discussed in Section 4.4 and Section 4.5 of this thesis, respectively, in conjunction with the assumption on perfect knowledge on the TO is considered. In that case the PER is reduced to less than 0.01 while the EVM is equal to 0.2 dB close to the EVM experienced for synchronized CoMP transmission, such that the performance of approximately 0.2 dB close to the synchronized IL single-layer CoMP transmission in TM10 can be theoretically achieved for each MCS, as depicted in Figure 4.15. The residual gap of the aforementioned 0.2 dB is subject to the limitations caused by ISI which occur as the considered TO equal to $2.3 \mu\text{s}$ is larger than the difference of the length of the CP and the multipath spread of the mobile communication channel.

Table 4.8. Simulation Parameters (created by the author of this thesis).

Parameter	Value
General Parameters:	
Channel Bandwidth	$f_{\text{BW}}^{(m)} = 10 \text{ MHz}$
Channel Model	SCM-B
Transmission Mode	TM9 and TM10
Interference Profile	according to Section 2.8.3 with $\gamma_{\text{INR}}^{(m, \tilde{b}_1)} = 3.2 \text{ dB}$, $\gamma_{\text{INR}}^{(m, \tilde{b}_2)} = 1.3 \text{ dB}$
Timing Offset	Synchronized transmission with $\tau_{\text{TO}}^{(x_1)} = 0 \text{ }\mu\text{s}$ for $x_1 \in \{b_1, \tilde{b}_1, \tilde{b}_2\}$, Unsynchronized transmission with $\tau_{\text{TO}}^{(x_2)} \geq 0 \text{ }\mu\text{s}$ for $x_2 \in \{b'_1, b'_2\}$
CoMP Operating Set:	
Set of TPs the desired signal is transmitted from	$\mathbb{A}_1 = \mathbb{A}_1^{\text{data}} = \{\epsilon_{b_1}, \epsilon'_{b_1}, \epsilon'_{b_2}\}$ and $\mathbb{A}_1^{\text{CRS}} = \{\epsilon_{b_1}\}$
Set of TPs the interfering signal is transmitted from	$\mathbb{I}_1 = \{\epsilon_{\tilde{b}_1}, \epsilon_{\tilde{b}_2}\}$
Number of transmit AEs at the TPs	$N_{\text{T}}^{(x)} = 4 \vee N_{\text{T}}^{(x)} = 2$ for $x \in \{b_1, b'_1, b'_2, \tilde{b}_1, \tilde{b}_2\}$
MCS	4, 14 and 25 at TP $\epsilon_b \in \mathbb{A}_1^{\text{data}}$, random MCS selection at TPs $\epsilon_{\tilde{b}_1}$ and $\epsilon_{\tilde{b}_2}$
Channel Coding	Turbo Coding [3GP16d, Section 5]
UE:	
Channel Estimation	LSCE
Receiver	IRC
Channel Decoding	Turbo Decoding [Jun97, Section E.3]
Number of Receive AEs	$N_{\text{R}}^{(m)} = 2$
CSI Reporting	Subband PMI Feedback, LC-CCIMP scheme (Section 3.3.3)

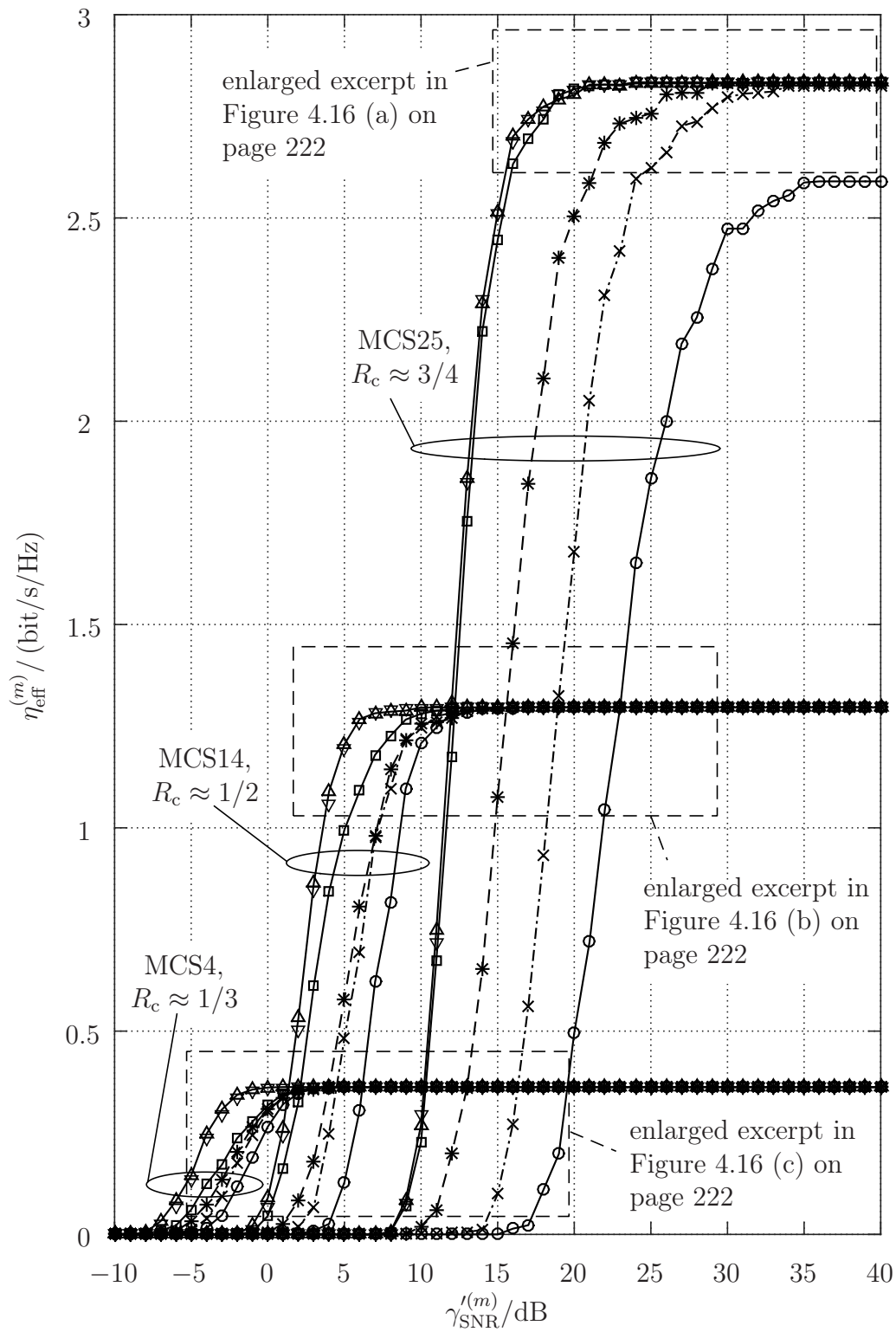


Figure 4.15. Performance of the TO compensation schemes for unsynchronized CoMP transmission (legend see Table 4.9; created by the author of this thesis).

Table 4.9. Legend for Figure 4.15.

—▲—	Synchronized IL single-layer CoMP transmission in TM10 with the $N_T^{(b)} \times N_R^{(1)} = 4 \times 2$ MIMO antenna configuration
—▼—	Unsynchronized IL single-layer CoMP transmission in TM10 with the $N_T^{(b)} \times N_R^{(1)} = 4 \times 2$ MIMO antenna configuration when compensating the impact of the TO $\tau_{TO}^{(b)} = 2.3 \mu\text{s}$ with respect to PMI selection according to Section 4.4 and channel estimation according to Section 4.5 of this thesis, assuming perfect knowledge on the TO
—■—	Unsynchronized IL single-layer CoMP transmission in TM10 with the $N_T^{(b)} \times N_R^{(1)} = 4 \times 2$ MIMO antenna configuration when compensating the impact of the TO $\tau_{TO}^{(b)} = 2.3 \mu\text{s}$ with respect to PMI selection according to Section 4.4 and channel estimation according to Section 4.5 of this thesis, using the DMRS-based TO estimation scheme (4.22)
—*—	IL single-layer transmission in TM9 with the $N_T^{(b)} \times N_R^{(1)} = 4 \times 2$ MIMO antenna configuration.
—×—	Unsynchronized IL single-layer CoMP transmission in TM10 with the $N_T^{(b)} \times N_R^{(1)} = 2 \times 2$ MIMO antenna configuration when neglecting the impact of the TO $\tau_{TO}^{(b)} = 2.3 \mu\text{s}$ with respect to channel estimation
—○—	Unsynchronized IL single-layer CoMP transmission in TM10 with the $N_T^{(b)} \times N_R^{(1)} = 4 \times 2$ MIMO antenna configuration when neglecting the impact of the TO $\tau_{TO}^{(b)} = 2.3 \mu\text{s}$ with respect to PMI selection and channel estimation

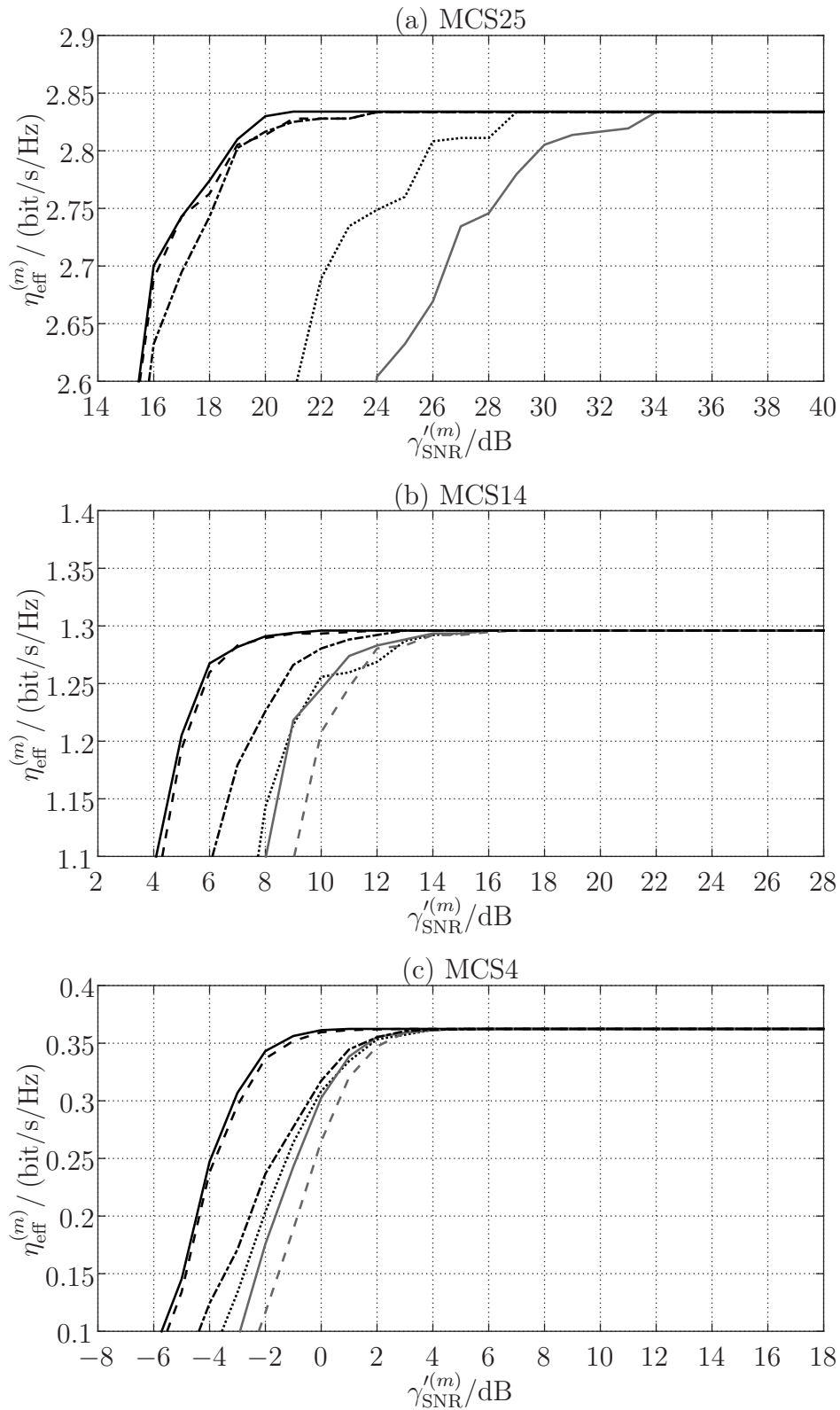


Figure 4.16. Enlarged view of Figure 4.15 for (a) MCS25, (b) MCS14 and (c) MCS4 (legend see Table 4.10; created by the author of this thesis).

Table 4.10. Legend for Figure 4.16.

—	Synchronized IL single-layer CoMP transmission in TM10 with the $N_T^{(b)} \times N_R^{(1)} = 4 \times 2$ MIMO antenna configuration
- - -	Unsynchronized IL single-layer CoMP transmission in TM10 with the $N_T^{(b)} \times N_R^{(1)} = 4 \times 2$ MIMO antenna configuration when compensating the impact of the TO $\tau_{TO}^{(b)} = 2.3 \mu\text{s}$ with respect to PMI selection according to Section 4.4 and channel estimation according to Section 4.5 of this thesis, assuming perfect knowledge on the TO
- - - -	Unsynchronized IL single-layer CoMP transmission in TM10 with the $N_T^{(b)} \times N_R^{(1)} = 4 \times 2$ MIMO antenna configuration when compensating the impact of the TO $\tau_{TO}^{(b)} = 2.3 \mu\text{s}$ with respect to PMI selection according to Section 4.4 and channel estimation according to Section 4.5 of this thesis, using the DMRS-based TO estimation scheme (4.22)
.....	IL single-layer transmission in TM9 with the $N_T^{(b)} \times N_R^{(1)} = 4 \times 2$ MIMO antenna configuration.
—	Unsynchronized IL single-layer CoMP transmission in TM10 with the $N_T^{(b)} \times N_R^{(1)} = 2 \times 2$ MIMO antenna configuration when neglecting the impact of the TO $\tau_{TO}^{(b)} = 2.3 \mu\text{s}$ with respect to channel estimation
—	Unsynchronized IL single-layer CoMP transmission in TM10 with the $N_T^{(b)} \times N_R^{(1)} = 4 \times 2$ MIMO antenna configuration when neglecting the impact of the TO $\tau_{TO}^{(b)} = 2.3 \mu\text{s}$ with respect to PMI selection and channel estimation

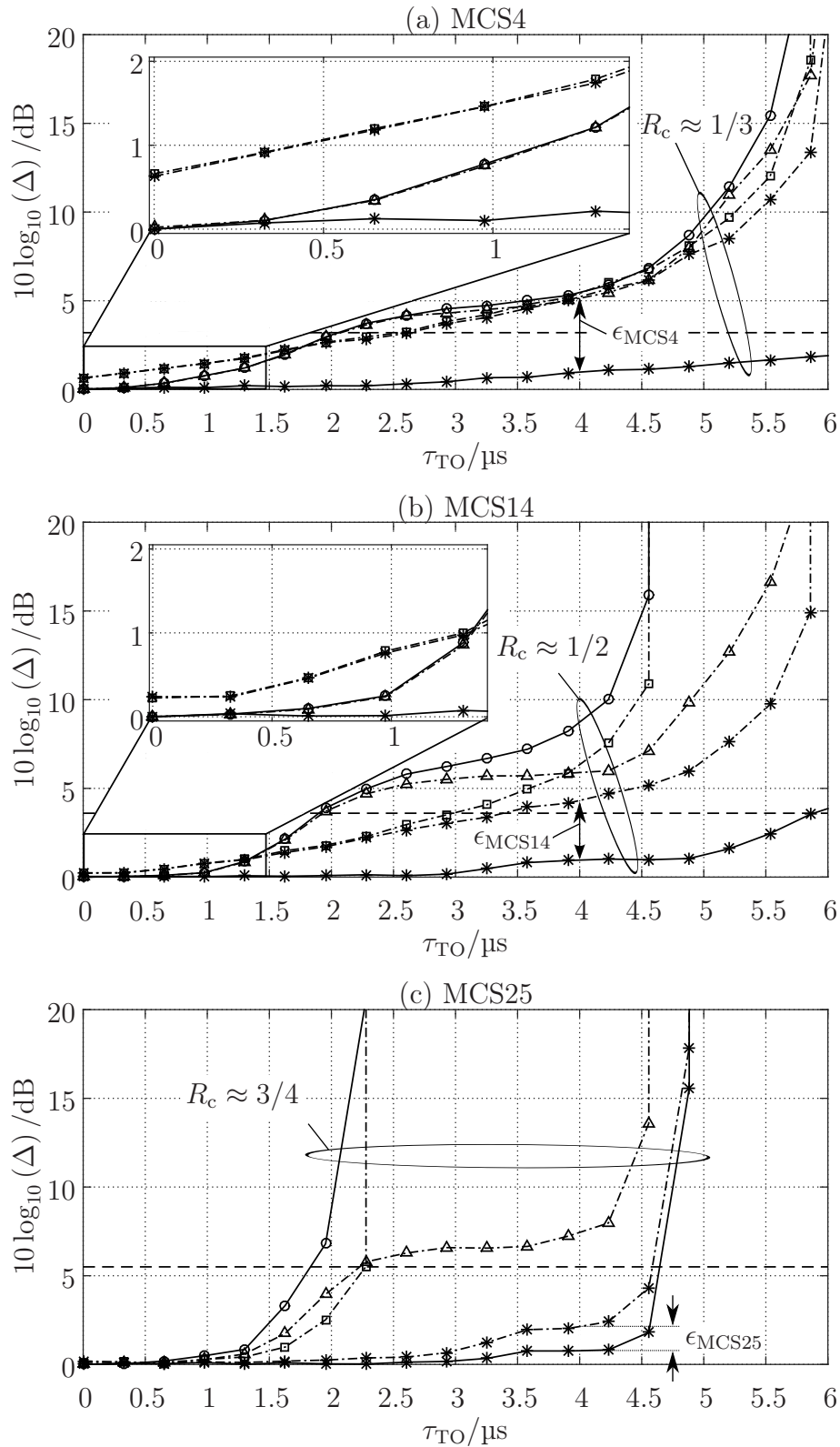


Figure 4.17. Impact of the TO on the performance for the 4×2 MIMO antenna configuration for (a) MCS4, (b) MCS14 and (c) MCS25 (legend see Table 4.11; created by the author of this thesis).

Table 4.11. Legend for Figure 4.17.

—○—	Ignore impact of the TO with respect to both, PMI selection and channel estimation in unsynchronized IL single-layer CoMP transmission in TM10
--▲--	Ignore the impact of the TO with respect to PMI selection and compensate the impact of the TO with respect to channel estimation according to Section 4.5 of this thesis, using the DMRS-based TO estimation scheme (4.22) in unsynchronized IL single-layer CoMP transmission in TM10
--■--	Compensate the impact of the TO with respect to PMI selection according to Section 4.4 of this thesis using the DMRS-based TO estimation scheme (4.22) and ignore the impact of the TO with respect to channel estimation in unsynchronized IL single-layer CoMP transmission in TM10
--*--	Compensate the impact of the TO with respect to PMI selection and channel estimation according to Section 4.4 and Section 4.5 of this thesis, respectively, using the DMRS-based TO estimation scheme (4.22) in unsynchronized IL single-layer CoMP transmission in TM10
—*—	Compensate the impact of the TO with respect to PMI selection and channel estimation according to Section 4.4 and Section 4.5 of this thesis, respectively, assuming perfect knowledge of the TO in unsynchronized IL single-layer CoMP transmission in TM10
-- --	Performance difference between synchronized IL single-layer CoMP transmission in TM10 and IL single-layer transmission in TM9

Chapter 5

Summary and Outlook

5.1 Summary

The present thesis aims at extending the state-of-the-art in terms of CoMP transmission in unsynchronized cellular LTE networks. To meet the ubiquitous connection with cell-edge-free experience, CoMP transmission is a key technique to improve the bandwidth efficiency in interference-limited cellular LTE networks. In the present thesis, the practical limitations of conventional non-CoMP transmission in interference-limited cellular LTE networks are discussed to motivate the necessity for cooperative implicit feedback generation in CoMP transmission. However, as the transmit signals in a practical implementation will reach the user at several and varying delays, unsynchronized CoMP transmission might experience large TOs, imposing a significant performance loss. In order to maintain the promised advantages of CoMP transmission, solutions enabling reliable cooperative implicit feedback generation and channel estimation in unsynchronized cellular LTE networks are provided. The content and the key findings achieved in the individual chapters of this thesis are summarized in the following.

Chapter 1 starts with a brief historical background, addressing the essential mathematical, physical and technological preconditions for modern wireless communication. Subsequently, the tremendous growth of subscribers and the related increase of inter-cell interference in conjunction with the driving forces behind 4G LTE systems evolving towards the continuously increasing bandwidth efficiency, are identified as challenging requirements. The overview of state-of-the-art interference mitigation techniques with respect to enhanced receivers, signal precoding and CoMP transmission has shown that the suggested schemes are investigated either independently or under strongly idealized system conditions, where the impact of inevitable varying delays is not sufficiently considered. Based on this, the scope and objective of this thesis are then defined.

In Chapter 2 the necessary physical layer aspects of LTE systems are provided to investigate the limitation of inter-cell interference on the performance in the downlink. In this context, the relationship between the transmission mode, the MIMO antenna configuration and the associated transmission of reference signals used for both, implicit feedback generation and receiver design to enable inter-cell interference mitigation, is discussed. To ensure reliable inter-cell interference mitigation and to maintain the beamforming gain of the 4×2 MIMO antenna configuration, the practical implementation of the IRC receiver in conjunction with the DMRS-based covariance matrix estimation is suggested, while implicit feedback generation is carried out by evaluating the CSI-RSs in TM9 to keep the code rate for each MCS low. By providing the reasons, the gap to the noise-limited cellular LTE network in terms of SNR over bandwidth efficiency is still large and cannot be further reduced with the aid of the aforementioned practical implementation of the IRC receiver.

In Chapter 3 cooperative feedback generation schemes for synchronized CoMP transmission are discussed with the aim of further reducing the impact of inter-cell interference at the cell-edge user. The concept and the related requirements for codebook-based cooperative interference mitigation signal precoding are discussed with the help of the example of a practical CoMP scenario in TM10. In this context the theoretically achievable gain in terms of SNR over bandwidth efficiency of the O-CCIMP scheme for synchronized CoMP transmission is determined and its complexity derived. To reduce the complexity of the O-CCIMP scheme, the implementation-friendly LC-CCIMP scheme for synchronized CoMP transmission is derived and its complexity analyzed. It is shown that the LC-CCIMP scheme performs close to the O-CCIMP scheme in terms of SNR over bandwidth efficiency and outperforms the non-CoMP scheme considerably, while keeping the complexity low. Therefore the investigation on cooperative interference mitigation signal precoding schemes operating in practical CoMP transmission cellular LTE networks, is limited to the LC-CCIMP scheme.

In Chapter 4 the necessary conditions to maintain reliable implicit feedback generation and channel estimation in practical CoMP transmission cellular LTE networks suffering from unsynchronized signal transmission are provided. In this context, the dominant limiting factors preventing CoMP transmission from achieving the expected performance are discussed. With analytical results it is shown that the presence of the TO introduces a phase offset on the transmit covariance matrix, leading to improper implicit feedback generation and, thus a reduced post-SNR of the equalized signal for each transmitter equipped with more than two transmit antenna elements. Moreover, the equalized signals get amplified, as derived analytically, leading to limited signal detection capabilities when the TO increases. To maintain the promised advantages of CoMP transmission in practical cellular LTE networks, a TO compensation

scheme to enable reliable implicit feedback generation and reliable channel estimation is suggested. Numerical results at the link level then show that the usage of the suggested TO compensation scheme is mandatory to maintain the promised advantages of CoMP transmission in practical cellular LTE networks suffering from unsynchronized signal transmission, while the aforementioned performance depends to a great extent on the TO estimation accuracy.

5.2 Outlook

The number of spatial layers the desired signal is transmitted on, has been set to one in this thesis. Extending CoMP transmission from JP-DPS to JP-JT provides the flexibility of spatial layer scheduling among the geometrically separated transmitters. Beside advanced signal precoding schemes, each layer can either be transmitted by an individual transmitter out of the CoMP cooperating set, all layers by the same set of transmitters or by a hybrid spatial layer scheduling scheme with the aim of increasing the SM gain at the cell-edge user and, therefore, the bandwidth efficiency. Therefore, coherent signal reception of the desired signals as well as reliable cooperative implicit feedback generation and reliable channel estimation (discussed in Chapter 4 of this thesis) are indispensable to assure the promised advantages of JP-JT CoMP transmission in practical cellular LTE networks.

In this thesis the investigation on aperiodic CSI feedback has been focused on PMI rather than CQI feedback. Despite the use of the suggested TO compensation schemes to enable reliable implicit feedback and reliable channel estimation, the impact of ISI imposes irreversible performance loss for single-tap signal equalization with the consequence that the achievable bandwidth efficiency for high indices of MCSs vanishes due to the high code rate and the related small error protection capabilities as the TO increases. A remedy for this limitation is the choice of a lower index of the MCS. Therefore, to maximize the bandwidth efficiency of unsynchronized CoMP transmission for the cell-edge user, the estimated TO needs to be considered as additional information for CQI selection.

Appendix A

Codebook and Characteristic Antenna Diagram

The relation between the PMI, the precoding vector, the maximum achievable antenna gain and the characteristic antenna diagram at the eNodeB $\epsilon_b \in \mathbb{E}$ is summarized in Table A.1 on page 233 for single-layer transmission. The PMI is denoted in the first column of Table A.1. The respective precoding vector associated with the PMI out of the set $\mathcal{S}_{\text{PMI},4}$ is defined in (2.33) and denoted in the second column of Table A.1. The maximum achievable antenna gain over an isotropic radiator [Mol05, Section 4.1] in logarithmic scale is denoted in the third column of Table A.1. Moreover, the equivalent characteristic antenna diagram in logarithmic scale for four horizontally placed transmit AEs with a spacing of a half of the wavelength [3GP06, Table A.1.3-3] is depicted in the fourth column of Table A.1 for the respective precoding vector. Calculating the antenna gain for the eNodeB $\epsilon_b \in \mathbb{E}$ equipped with four transmit AEs, ϱ_{TX} in (2.34) turns to

$$\varrho_{\text{TX}} = \left| \left(\begin{array}{c} 1 \\ \exp \left(-j2\pi \cdot \frac{d_{\text{TX}}^{(b)}}{\lambda_c} \cdot \cos(\phi) \right) \\ \exp \left(-j2\pi \cdot \frac{2d_{\text{TX}}^{(b)}}{\lambda_c} \cdot \cos(\phi) \right) \\ \exp \left(-j2\pi \cdot \frac{3d_{\text{TX}}^{(b)}}{\lambda_c} \cdot \cos(\phi) \right) \end{array} \right)^{\text{T}} \cdot \frac{1}{2} \begin{pmatrix} 1 \\ \nu_1 \\ \nu_2 \\ \nu_3 \end{pmatrix} \right|^2. \quad (\text{A.1})$$

For a transmit AE spacing $d_{\text{TX}}^{(b)}$ equal to a half of the wavelength [3GP06, Table A.1.3-3], the representation of the antenna gain at the eNodeB $\epsilon_b \in \mathbb{E}$

denoted in (A.1) can be further simplified to

$$\varrho_{\text{TX}} = \left| \begin{pmatrix} 1 \\ \exp(-j\pi \cos(\phi)) \\ \exp(-2j\pi \cos(\phi)) \\ \exp(-3j\pi \cos(\phi)) \end{pmatrix}^T \cdot \frac{1}{2} \begin{pmatrix} 1 \\ \nu_1 \\ \nu_2 \\ \nu_3 \end{pmatrix} \right|^2 = \frac{1}{4} \left| 1 + \sum_{i=1}^3 \nu_i \cdot \exp(-j \cdot i \cdot \cos(\phi)) \right|^2, \quad (\text{A.2})$$

where ν_1, \dots, ν_3 in (A.1) and (A.2) denotes the phase information of the respective precoding vector [3GP16f, Table 6.3.4.2.3-2]. For $\nu_i = 1, i = 1, \dots, 3$, the antenna gain in (A.2) for the precoding vector with PMI equal to zero reads

$$\varrho_{\text{TX}} \left(\phi, \underline{\mathbf{p}}^{(b)}[k, \ell] = \frac{1}{2} \begin{pmatrix} 1 \\ 1 \\ 1 \\ 1 \end{pmatrix} \right) = \frac{1}{4} \cdot \left| 1 + \sum_{i=1}^3 \exp(-j \cdot i \cdot \cos(\phi)) \right|^2. \quad (\text{A.3})$$

Making use of the triangle inequality for complex numbers [Bro+01, Section 1.4.2.1]

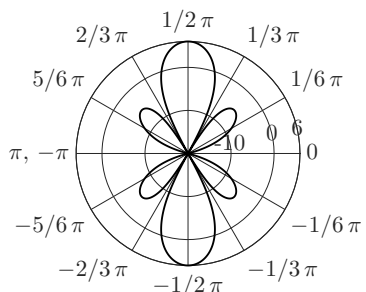
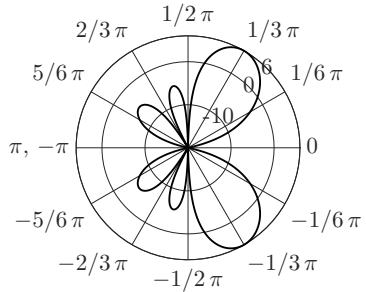
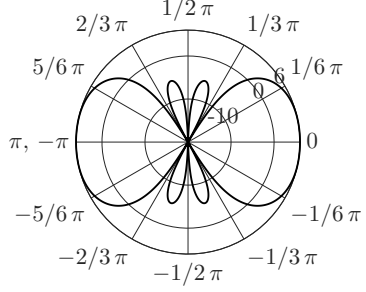
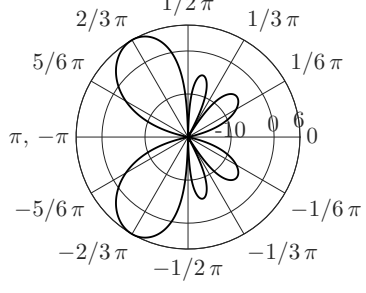
$$\frac{1}{4} \cdot \left| 1 + \sum_{i=1}^3 \exp(-j \cdot i \cdot \cos(\phi)) \right|^2 \leq \frac{1}{4} \cdot \left(1 + \sum_{i=1}^3 |\exp(-j \cdot i \cdot \cos(\phi))| \right)^2 = 4 \quad (\text{A.4})$$

holds. Hence, the inequality on left hand side of (A.4) is maximal when the argument of each exponential function is equal to zero [Bro+01, Section 14.5.2]. The argument of each exponential function of the inequality on the left hand side of (A.4) is equal to zero when the directional cosine $\cos \phi$ in the argument of each exponential function in (A.4) is equal to zero. As a result, the inequality on the left hand side of (A.4) is maximal for

$$\phi \in \left\{ \varphi \mid \varphi = \frac{2n+1}{2}\pi, n \in \mathbb{Z} \right\}. \quad (\text{A.5})$$

In that case, the expression in (A.4) is fulfilled with the equal sign. On the interval within $-\pi$ to π this is fulfilled for $\phi \in \{-\pi/2, \pi/2\}$. Obviously, for $\phi \in \{-\pi/2, \pi/2\}$ the antenna gain is maximal and reads 6.02 dBi over and isotropic radiator, as depicted in the characteristic diagram for the transmit antenna for the precoding vector with PMI equal to zero, provided in Table A.1. Valid values for the transmit direction providing the maximal antenna gain over an isotropic radiator can be determined analogously for precoding vectors with PMI equal to one up to PMI equal to fifteen.

Table A.1. Codebook and characteristic antenna diagram for signal transmission from four transmit AEs (created by the author of this thesis using [3GP16f, Table 6.3.4.2.3-2]).

Precoding matrix index	Precoding vector $\underline{\mathbf{p}}^{(b)} [k, \ell]$	Maximum antenna gain	Characteristic antenna diagram
0	$\frac{1}{2} \begin{pmatrix} 1 \\ 1 \\ 1 \\ 1 \end{pmatrix}$	6.02 dBi	
1	$\frac{1}{2} \begin{pmatrix} 1 \\ j \\ -1 \\ -j \end{pmatrix}$	6.02 dBi	
2	$\frac{1}{2} \begin{pmatrix} 1 \\ -1 \\ 1 \\ -1 \end{pmatrix}$	6.02 dBi	
3	$\frac{1}{2} \begin{pmatrix} 1 \\ -j \\ -1 \\ j \end{pmatrix}$	6.02 dBi	

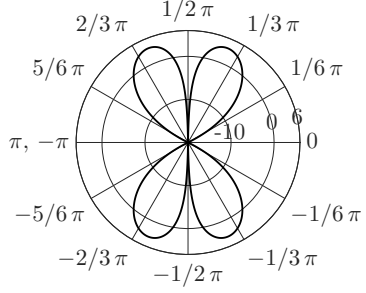
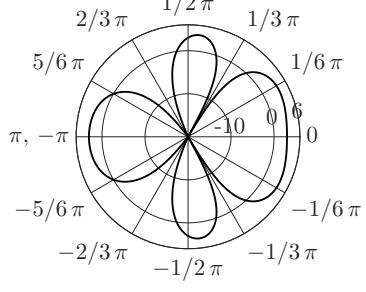
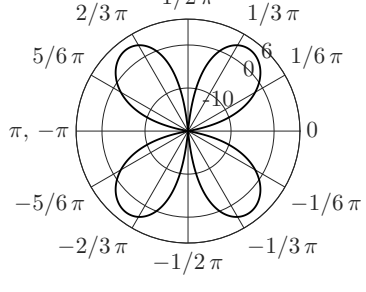
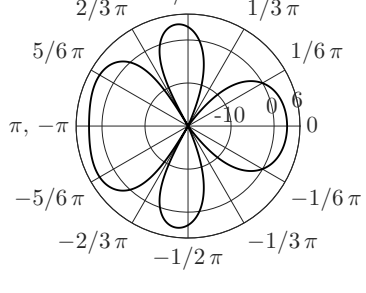
Continued on next page

Table A.1. Codebook and characteristic antenna diagram for signal transmission from four transmit AEs (*Continued from previous page*).

Precoding matrix index	Precoding vector $\underline{\mathbf{p}}^{(b)} [k, \ell]$	Maximum antenna gain	Characteristic antenna diagram
4	$\frac{1}{2} \begin{pmatrix} 1 \\ (1+j)/\sqrt{2} \\ j \\ (-1+j)/\sqrt{2} \end{pmatrix}$	6.02 dBi	
5	$\frac{1}{2} \begin{pmatrix} 1 \\ (-1+j)/\sqrt{2} \\ -j \\ (1+j)/\sqrt{2} \end{pmatrix}$	6.02 dBi	
6	$\frac{1}{2} \begin{pmatrix} 1 \\ (-1-j)/\sqrt{2} \\ j \\ (1-j)/\sqrt{2} \end{pmatrix}$	6.02 dBi	
7	$\frac{1}{2} \begin{pmatrix} 1 \\ (1-j)/\sqrt{2} \\ -j \\ (-1-j)/\sqrt{2} \end{pmatrix}$	6.02 dBi	

Continued on next page

Table A.1. Codebook and characteristic antenna diagram for signal transmission from four transmit AEs (*Continued from previous page*).

Precoding matrix index	Precoding vector $\underline{\mathbf{p}}^{(b)} [k, \ell]$	Maximum antenna gain	Characteristic antenna diagram
8	$\frac{1}{2} \begin{pmatrix} 1 \\ 1 \\ -1 \\ -1 \end{pmatrix}$	3.75 dBi	
9	$\frac{1}{2} \begin{pmatrix} 1 \\ j \\ 1 \\ j \end{pmatrix}$	3.75 dBi	
10	$\frac{1}{2} \begin{pmatrix} 1 \\ -1 \\ -1 \\ 1 \end{pmatrix}$	3.75 dBi	
11	$\frac{1}{2} \begin{pmatrix} 1 \\ -j \\ 1 \\ -j \end{pmatrix}$	3.75 dBi	

Continued on next page

Table A.1. Codebook and characteristic antenna diagram for signal transmission from four transmit AEs (*Continued from previous page*).

Precoding matrix index	Precoding vector $\underline{\mathbf{p}}^{(b)} [k, \ell]$	Maximum antenna gain	Characteristic antenna diagram
12	$\frac{1}{2} \begin{pmatrix} 1 \\ 1 \\ 1 \\ -1 \end{pmatrix}$	2.48 dBi	
13	$\frac{1}{2} \begin{pmatrix} 1 \\ 1 \\ -1 \\ 1 \end{pmatrix}$	2.48 dBi	
14	$\frac{1}{2} \begin{pmatrix} 1 \\ -1 \\ 1 \\ 1 \end{pmatrix}$	2.48 dBi	
15	$\frac{1}{2} \begin{pmatrix} 1 \\ -1 \\ -1 \\ -1 \end{pmatrix}$	2.48 dBi	

Appendix B

Derivation of the Code Rates

B.1 Introduction

The set $\mathcal{S}_{i, n_{\text{PRB}}, \text{TM}}^{(b, N_{\text{T}}^{(b)})}$ represents the physical time-frequency resources that can be used to transmit the precoded complex-valued modulation symbols in the i -th subframe and n_{PRB} -th PRB for $0 \leq i \leq 9$ and $0 \leq n_{\text{PRB}} < N_{\text{RB}}^{\text{DL}}$, respectively for signal transmission in the respective TM and $N_{\text{T}}^{(b)}$ transmit AEs at the eNodeB $\epsilon_b \in \mathbb{E}$. Let $\mathcal{S}_{i, n_{\text{PRB}}}$ denote the set of all physical time-frequency resources in the i -th subframe and n_{PRB} -th PRB for $0 \leq i \leq 9$ and $0 \leq n_{\text{PRB}} < N_{\text{RB}}^{\text{DL}}$, respectively, where the cardinality of $\mathcal{S}_{i, n_{\text{PRB}}}$ is equal to $N_{\text{RE}}^{\text{SF, PRB}}$ (2.6). The number of physical time-frequency resources that can be used to transmit the precoded complex-valued modulation symbols is reduced by the physical time-frequency resources for RS transmission in the respective TM. Moreover, the number of physical time-frequency resources that can be used to transmit the precoded complex-valued modulation symbols is further reduced by the physical time-frequency resources reserved for signal transmission on the

- PBCH,
- PCFICH,
- PDCCH and
- PHICH

as well as for the PSS and the SSS, which are altogether included in the set $\mathcal{S}_{i, n_{\text{PRB}}}^{\text{other}}$ for $0 \leq i \leq 9$ and $0 \leq n_{\text{PRB}} < N_{\text{RB}}^{\text{DL}}$. The cardinality of the set $\mathcal{S}_{i, n_{\text{PRB}}}^{\text{other}}$ is denoted by $N_{i, n_{\text{PRB}}}^{\text{other}}$. Detail information on the resource elements reserved for the PBCH, the PCFICH, the PDCCH and the PHICH can be found in [3GP16f, Section 6.6.4], [3GP16f, Section 6.7.4], [3GP16f, Section 6.8.4] and [3GP16f, Section 6.9.3], respectively. Moreover, detail information on the resource elements for the PSS and SSS can be found in [3GP16f, Section 6.11.1.2] and [3GP16f, Section 1.11.2.1], respectively.

The cardinality of the set $\mathcal{S}_{i, n_{\text{PRB}}, \text{TM}}^{(b, N_{\text{T}}^{(b)})}$ is provided in Table B.1 on page 239 for the first subframe. The first column of Table B.1 denotes the TM. The second column of Table B.1 denotes the number of eNodeBs that are considered for simultaneous transmission of the desired signal. The cardinality of $\mathcal{S}_{1, n_{\text{PRB}}, \text{TM}}^{(b, N_{\text{T}}^{(b)})}$ for the respective TM is denoted in the third and fourth column of Table B.1 for eNodeBs equipped with $N_{\text{T}}^{(b)}$ equal to two and four transmit AEs, respectively. Note that in case of desired signal transmission from more than one eNodeB, the choice of the physical layer cell identity influences the cardinality for $N_{\text{T}}^{(b)}$ equal to two and four transmit AEs. The derivation of the aforementioned set and the calculation of its cardinality is discussed in what follows.

B.2 Physical Time-Frequency Resources for Codeword Transmission

In case of TM6, channel estimation and CSI feedback generation is carried out by evaluating the CRSs [3GP16g, Section 7.2.3; 3GP16g, Section 7.2.4]. Hence, for the eNodeB $\epsilon_b \in \mathbb{E}$ equipped with $N_{\text{T}}^{(b)}$ equal to two and four transmit AEs

$$\mathcal{S}_{i, n_{\text{PRB}}, \text{TM6}}^{(b, N_{\text{T}}^{(b)})} = \mathcal{S}_{i, n_{\text{PRB}}} \setminus \mathcal{S}_{i, n_{\text{PRB}}}^{\text{other}} \setminus \left\{ \bigcup_{\pi_{\text{AP}} \in \mathcal{A}_{\text{CRS}} = \{0, \dots, (N_{\text{T}}^{(b)} - 1)\}} \mathcal{S}_{i, n_{\text{PRB}}, \text{CRS}}^{(b, \pi_{\text{AP}})} \right\} \quad (\text{B.1})$$

denotes the set of physical time-frequency resources that is used to transmit the precoded complex-valued modulation symbols carrying the codewords from the transmit AP0, \dots , AP $(N_{\text{T}}^{(b)} - 1)$ [3GP16f, Section 6.10.1] in the i -th subframe and n_{PRB} -th PRB for $0 \leq i \leq 9$ and $0 \leq n_{\text{PRB}} < N_{\text{sc}}^{\text{RB}}$. The physical time-frequency resources out of the set $\mathcal{S}_{i, n_{\text{PRB}}}^{\text{other}}$ as well as the physical time-frequency resources carrying the CRSs are excluded from the set $\mathcal{S}_{i, n_{\text{PRB}}}$ [3GP16f, Section 6.3.5]. Following the properties of the CRSs, discussed in Section 2.2.2 of this thesis, the cardinality of (B.1) reads

$$\left| \mathcal{S}_{i, n_{\text{PRB}}, \text{TM6}}^{(b, N_{\text{T}}^{(b)})} \right| = N_{\text{RE}}^{\text{SF, PRB}} - N_{i, n_{\text{PRB}}}^{\text{other}} - N_{\text{CRS}, N_{\text{T}}^{(b)}} \quad (\text{B.2})$$

for $0 \leq i \leq 9$ and $0 \leq n_{\text{PRB}} < N_{\text{sc}}^{\text{RB}}$, where $N_{\text{CRS}, N_{\text{T}}^{(b)}}$ is defined in (2.4), (2.5) and (2.10) for one, two and four transmit AEs at the eNodeB $\epsilon_b \in \mathbb{E}$, respectively. The cardinality (B.2) for the first subframe and n_{PRB} -th PRB with $0 \leq n_{\text{PRB}} < N_{\text{RB}}^{\text{DL}}$ is denoted in the third and fourth column of Table B.1 for the eNodeB $\epsilon_b \in \mathbb{E}$ equipped with $N_{\text{T}}^{(b)}$ equal to two and four transmit AEs, respectively.

Table B.1. Relation between the TM, the eNodeB configuration and the number of physical time-frequency resources (created by the author of this thesis).

TM	E	Cardinality of $\mathcal{S}_{1,n_{\text{PRB}},\text{TM}}^{(b,2)}$ for two transmit AEs at each eNodeB		Cardinality of $\mathcal{S}_{1,n_{\text{PRB}},\text{TM}}^{(b,4)}$ for four transmit AEs at each eNodeB	
		same cell-ID	different cell-ID	same cell-ID	different cell-ID
6	1	132		128	
8	1	120		116	
9	1	124		122	
10	1	124	-	122	-
10	2	124	118	122	116
10	3	124	112	122	110

In case of TM8, the eNodeB $\epsilon_b \in \mathbb{E}$ is transmitting in addition to the CRSs and complex-valued modulation symbols carrying the codewords the precoded DMRSs [3GP16g, Section 7.1]. Channel equalization is carried out by evaluating the precoded DMRSs [STB11, Section 8.2.2], whereas CSI feedback is carried out by evaluating the CRSs [3GP16g, Section 7.2.3; 3GP16g, Section 7.2.4]. Hence, for the eNodeB $\epsilon_b \in \mathbb{E}$ equipped with $N_T^{(b)}$ equal to two and four transmit AEs

$$\mathcal{S}_{i, n_{\text{PRB}}, \text{TM8}}^{(b, N_T^{(b)})} = \mathcal{S}_{i, n_{\text{PRB}}} \setminus \mathcal{S}_{i, n_{\text{PRB}}}^{\text{other}} \setminus \left\{ \bigcup_{\pi_{\text{AP}} \in \mathcal{A}_{\text{CRS}} = \{0, \dots, (N_T^{(b)} - 1)\}} \mathcal{S}_{i, n_{\text{PRB}}, \text{CRS}}^{(b, \pi_{\text{AP}})} \right\} \setminus \mathcal{S}_{i, n_{\text{PRB}}, \text{DMRS}}^{(b, 7)} \quad (\text{B.3})$$

denotes the set of physical time-frequency resources that is used to transmit the precoded complex-valued modulation symbols carrying the codewords from the transmit AP7 [3GP16f, Section 6.10.3] in the i -th subframe and n_{PRB} -th PRB for $0 \leq i \leq 9$ and $0 \leq n_{\text{PRB}} < N_{\text{sc}}^{\text{RB}}$. The physical time-frequency resources out of the set $\mathcal{S}_{i, n_{\text{PRB}}}^{\text{other}}$ as well as the physical time-frequency resources carrying the CRSs and the precoded DMRSs are excluded from the set $\mathcal{S}_{i, n_{\text{PRB}}}$ [3GP16f, Section 6.3.5]. Following the properties of the CRSs and the precoded DMRSs, discussed in Section 2.2.2 and Section 2.2.3 of this thesis, respectively, the cardinality of (B.3) reads

$$\left| \mathcal{S}_{i, n_{\text{PRB}}, \text{TM8}}^{(b, N_T^{(b)})} \right| = N_{\text{RE}}^{\text{SF, PRB}} - N_{i, n_{\text{PRB}}}^{\text{other}} - N_{\text{CRS}, N_T^{(b)}} - N_{\text{DMRS}} \quad (\text{B.4})$$

for $0 \leq i \leq 9$ and $0 \leq n_{\text{PRB}} < N_{\text{sc}}^{\text{RB}}$. The cardinality (B.4) for the first subframe and n_{PRB} -th PRB with $0 \leq n_{\text{PRB}} < N_{\text{RB}}^{\text{DL}}$ is denoted in the fifth and sixth column of Table B.1 for the eNodeB $\epsilon_b \in \mathbb{E}$ equipped with $N_T^{(b)}$ equal to two and four transmit AEs, respectively.

In case of TM9, the eNodeB $\epsilon_b \in \mathbb{E}$ is transmitting in addition to the CRSs, the precoded DMRSs and the precoded complex-valued modulation symbols carrying the codewords the CSI-RSs [3GP16g, Section 7.2.2]. Channel equalization is carried out by evaluating the precoded DMRSs [STB11, Section 8.2.2], whereas CSI feedback is carried out by evaluating the CSI-RSs [3GP16g, Section 7.2.3; 3GP16g, Section 7.2.4]. Hence, it is sufficient to limit the transmission of CRSs on the transmit AP0 [3GP16f, Section 6.10.1]. As a result, for

eNodeB $\epsilon_b \in \mathbb{E}$ equipped with $N_T^{(b)}$ equal to two and four transmit AEs

$$\mathcal{S}_{i, n_{\text{PRB}}, \text{TM9}}^{(b, N_T^{(b)})} = \mathcal{S}_{i, n_{\text{PRB}}} \setminus \left\{ \begin{array}{l} \mathcal{S}_{i, n_{\text{PRB}}}^{\text{other}} \\ \mathcal{S}_{i, n_{\text{PRB}}, \text{CRS}}^{(b, 0)} \\ \mathcal{S}_{i, n_{\text{PRB}}, \text{DMRS}}^{(b, 7)} \\ \bigcup_{\pi_{\text{AP}} \in \mathcal{A}_{\text{CSI-RS}} = \{15, \dots, (14 + N_T^{(b)})\}} \mathcal{S}_{i, n_{\text{PRB}}, \text{CSI-RS}}^{(b, \pi_{\text{AP}})} \end{array} \right\} \quad (\text{B.5})$$

denotes the set of physical time-frequency resources that is used to transmit the precoded complex-valued modulation symbols carrying the codewords from the transmit AP7 [3GP16f, Section 6.10.3] in the i -th subframe and n_{PRB} -th PRB for $0 \leq i \leq 9$ and $0 \leq n_{\text{PRB}} < N_{\text{sc}}^{\text{RB}}$ in TM9. As already mentioned in Section 2.2.4 of this thesis, the transmission of the CSI-RSs enables the UE $\mu_m \in \mathbb{U}$ to estimate the CSI for multiple eNodeBs, rather than just for one eNodeB $\epsilon_b \in \mathbb{E}$ [STB11, Section 29.1.2]. However, the physical time-frequency resources carrying the CSI-RSs at the interfering eNodeBs $\epsilon_{\tilde{b}} \in \mathbb{I}_m$ typically collide with the physical time-frequency resources used to transmit the precoded complex-valued modulation symbols at the eNodeB $\epsilon_b \in \mathbb{E}$ for $b \neq \tilde{b}$. The set of all physical time-frequency resources $\mathcal{S}_{i, n_{\text{PRB}}}$ on the right hand side of (B.5) is reduced by the physical time-frequency resources out of the set $\mathcal{S}_{i, n_{\text{PRB}}}^{\text{other}}$ as well as the physical time-frequency resources carrying the CRSs, the precoded DMRSs and, if scheduled, the CSIs-RSs [3GP16f, Section 6.3.5] in the i -th subframe and n_{PRB} -th PRB for $0 \leq i \leq 9$ and $0 \leq n_{\text{PRB}} < N_{\text{sc}}^{\text{RB}}$, respectively. The spacing for the CSI-RS is configurable in time-domain [3GP16f, Section 6.10.5.3]. To assess whether the eNodeB $\epsilon_b \in \mathbb{E}$ is transmitting the CSI-RSs in the i -th subframe, let $\left[\chi_{\text{CSI-RS}}^{(b, i)} \right]$ denote the IVERSON bracket [Bro+01, Section 5.1.2], defined as

$$\left[\chi_{\text{CSI-RS}}^{(b, i)} \right] = \begin{cases} 1 & \text{for } \bigcup_{\pi_{\text{AP}} \in \mathcal{A}_{\text{CSI-RS}} = \{15, \dots, (14 + N_T^{(b)})\}} \mathcal{S}_{i, n_{\text{PRB}}, \text{CSI-RS}}^{(b, \pi_{\text{AP}})} \neq \emptyset \\ 0 & \text{otherwise} \end{cases} \quad (\text{B.6})$$

for $0 \leq i \leq 9$ and $0 \leq n_{\text{PRB}} < N_{\text{sc}}^{\text{RB}}$. Making use of the IVERSON bracket in (B.6) and following the properties of the CRSs, the precoded DMRSs and the CSI-RSs, discussed in Section 2.2.2, Section 2.2.3 and Section 2.2.4 of this thesis, respectively, the cardinality of (B.5) can be calculated for the eNodeB

Appendix B Derivation of the Code Rates

$\epsilon_b \in \mathbb{E}$ equipped with $N_T^{(b)}$ equal to two and four transmit AEs according to

$$\left| \mathcal{S}_{i, n_{\text{PRB}}, \text{TM9}}^{(b, N_T^{(b)})} \right| = N_{\text{RE}}^{\text{SF, PRB}} - N_{i, n_{\text{PRB}}}^{\text{other}} - N_{\text{CRS}, 1} - N_{\text{DMRS}} - \left[\chi_{\text{CSI-RS}}^{(b, i)} \right] \cdot N_{\text{CSI-RS}, N_T^{(b)}} \quad (\text{B.7})$$

for $0 \leq i \leq 9$ and $0 \leq n_{\text{PRB}} < N_{\text{sc}}^{\text{RB}}$, where $N_{\text{CSI-RS}, N_T^{(b)}}$ is defined in (2.18) and (2.22) for $N_T^{(b)}$ equal to two and four transmit AEs at the eNodeB $\epsilon_b \in \mathbb{E}$, respectively. The cardinality in (B.7) for the first subframe and n_{PRB} -th PRB with $0 \leq n_{\text{PRB}} < N_{\text{RB}}^{\text{DL}}$ is denoted in the seventh and eighth column of Table B.2 for the eNodeB $\epsilon_b \in \mathbb{E}$ equipped with two and four transmit AEs, respectively. Moreover, it is assumed that the CSI-RSs are transmitted in the first subframe, such that the IVERSON bracket in (B.6) is equal to one in that case.

In case of TM10, the transmission of the CRSs, the precoded DMRSs and the CSI-RSs may be distributed over one or multiple eNodeBs $\epsilon_b \in \mathbb{E}$ [3GP16g, Section 7.1; 3GP13a, Section 5.1.4]. Moreover, channel equalization is carried out by evaluating the precoded DMRSs [STB11, Section 8.2.2], whereas CSI feedback is carried out by evaluating the CSI-RSs [3GP16g, Section 7.2.3; 3GP16g, Section 7.2.4]. Hence, as in TM9, it is sufficient to limit the transmission of CRSs on the transmit AP0 [3GP16f, Section 6.10.1]. Moreover, since TM10 the transmission of Zero Power (ZP) CSI-RSs is introduced [3GP16g, Section 7.2.6] to improve inter-cell interference estimation by the UE $\mu_m \in \mathbb{U}$ [Nag+13, Section II-A]. The ZP CSI-RSs have the same properties as the CSI-RSs, discussed in Section 2.2.4 of this thesis, with the difference that the transmit power of the ZP CSI-RSs is equal to zero [3GP16g, Section 7.2.6]. To enable reliable inter-cell interference estimation at the UE $\mu_m \in \mathbb{U}$, the interfering eNodeBs $\epsilon_{\tilde{b}} \in \mathbb{I}_m$ transmit the ZP CSI-RSs on the physical time-frequency resources which the eNodeBs $\epsilon_b \in \mathbb{A}_m^{\text{data}}$ use for CSI-RSs transmission, where $b \neq \tilde{b}$ holds [Nag+13, Section II-A]. The set of physical time-frequency resources that can be used to transmit the precoded complex-valued modulation symbols carrying the codewords for the eNodeBs $\epsilon_b \in \mathbb{E}$ equipped with $N_T^{(b)}$ two equal to two and four transmit AEs reads

$$\mathcal{S}_{i, n_{\text{PRB}}, \text{TM10}}^{(b, N_T^{(b)})} = \mathcal{S}_{i, n_{\text{PRB}}} \setminus \left\{ \begin{aligned} & \mathcal{S}_{i, n_{\text{PRB}}}^{\text{other}} \\ & \left\{ \bigcup_{\{b | \epsilon_b \in \mathbb{A}_m^{\text{CRS}}\}} \mathcal{S}_{i, n_{\text{PRB}}, \text{CRS}}^{(b, 0)} \right\} \\ & \left\{ \bigcup_{\{b | \epsilon_b \in \mathbb{A}_m^{\text{data}}\}} \mathcal{S}_{i, n_{\text{PRB}}, \text{DMRS}}^{(b, 7)} \right\} \end{aligned} \right.$$

$$\setminus \left\{ \bigcup_{\{b|\epsilon_b \in \mathbb{A}_m^{\text{data}}\}} \bigcup_{\pi_{\text{AP}} \in \mathcal{A}_{\text{CSI-RS}} = \{15, \dots, (14+N_T^{(b)})\}} \mathcal{S}_{i, n_{\text{PRB}}, \text{CSI-RS}}^{(b, \pi_{\text{AP}})} \right\} \quad (\text{B.8})$$

for $0 \leq i \leq 9$ and $0 \leq n_{\text{PRB}} < N_{\text{sc}}^{\text{RB}}$. Obviously, the set of all time-frequency resources $\mathcal{S}_{i, n_{\text{PRB}}}$ on the right hand side of (B.8) is reduced by the physical time-frequency resources out of the set $\mathcal{S}_{i, n_{\text{PRB}}}^{\text{other}}$ as well as the physical time-frequency resources used to transmit the CRSs at the eNodeBs $\epsilon_b \in \mathbb{A}_m^{\text{CRS}}$, the precoded DMRSs at the eNodeBs $\epsilon_b \in \mathbb{A}_m^{\text{data}}$ and, if scheduled, the CSI-RSs at the eNodeBs $\epsilon_b \in \mathbb{A}_m^{\text{data}}$ [3GP16f, Section 6.3.5] in the i -th subframe and n_{PRB} -th PRB for $0 \leq i \leq 9$ and $0 \leq n_{\text{PRB}} < N_{\text{sc}}^{\text{RB}}$. Following the properties of the CRSs, the precoded DMRSs and the CSI-RSs, discussed in Section 2.2.2, Section 2.2.3 and Section 2.2.4 of this thesis, respectively and making use of the IVERSON bracket in (B.6), the cardinality of the set defined in (B.8) can be calculated according to

$$\begin{aligned} \left| \mathcal{S}_{i, n_{\text{PRB}}, \text{TM10}}^{(b, N_T^{(b)})} \right| &= N_{\text{RE}}^{\text{SF, PRB}} - N_{i, n_{\text{PRB}}}^{\text{other}} - |\mathbb{A}_m^{\text{CRS}}| \cdot N_{\text{CRS}, 1} - N_{\text{DMRS}} \\ &\quad - \sum_{\{b|\epsilon_b \in \mathbb{A}_m^{\text{data}}\}} \left[\chi_{\text{CSI-RS}}^{(b, i)} \right] \cdot N_{\text{CSI-RS}, N_T^{(b)}} \end{aligned} \quad (\text{B.9})$$

for $0 \leq i \leq 9$, $0 \leq n_{\text{PRB}} < N_{\text{sc}}^{\text{RB}}$ and eNodeBs $\epsilon_b \in \mathbb{E}$, $\epsilon_{\bar{b}} \in \mathbb{I}_m$ equipped with $N_T^{(b)}$ equal to transmit AEs. Moreover, $|\mathbb{A}_m^{\text{CRS}}|$ denotes the cardinality of the set $\mathbb{A}_m^{\text{CRS}}$. The cardinality (B.9) for the eNodeBs equipped with two and four transmit AEs is denoted in the third and fourth column of Table B.1 for TM10, respectively, where the physical layer cell-identity for the eNodeBs out of the set \mathbb{E} , transmitting the desired signal to the UE $\mu_m \in \mathbb{U}$, can be either configured with the same or different physical layer cell-identities for each transmit antenna configuration. In this thesis, it is assumed that the eNodeBs $\epsilon_b \in \mathbb{A}_m^{\text{data}}$ transmit the CSIs-RSs in different subframes with to enable reliable CSI feedback at the UE $\mu_m \in \mathbb{U}$ in TM10. Furthermore, in this thesis it is assumed that the interfering eNodeBs $\epsilon_{\bar{b}} \in \mathbb{I}_m$ transmit the CSI-RSs on a subframe different to the subframe used for CSI-RSs transmission at each eNodeB $\epsilon_b \in \mathbb{A}_m^{\text{data}}$ in TM10. In case of same physical layer cell-identities among the eNodeBs $\epsilon_b \in \mathbb{E}$ [3GP13a, Section 5.1.2], it is assumed that the subset $\mathbb{A}_m^{\text{CRS}}$ consists of one eNodeB which transmit the CRSs to the UE $\mu_m \in \mathbb{U}$, while the eNodeBs within the subset $\mathbb{A}_m^{\text{data}}$ may be used to transmit the precoded complex-valued modulation symbols carrying the codewords, the precoded DMRSs and the CSI-RSs. In the other case of different physical layer cell-identities among the eNodeBs $\epsilon_b \in \mathbb{E}$ [3GP13a, Section 5.1.2] it is assumed that $\mathbb{A}_m^{\text{CRS}}$ equals to \mathbb{E} , such that each eNodeB $\epsilon_b \in \mathbb{E}$ is transmitting the CRSs

on orthogonal physical time-frequency resources, while the eNodeBs within the subset $\mathbb{A}_m^{\text{data}}$ may transmit the precoded complex-valued modulation symbols carrying the codewords, the precoded DMRSs and the CSI-RSs.

B.3 Numeric Results

The numerical results for the code rate R_c (2.42) for signal transmission in TM6, TM8 and TM9 are summarized in Table B.2 on page 245 for a channel bandwidth equal to 10 MHz. Moreover, the numerical result for the code rate R_c (2.42) for signal transmission in TM10 are summarized in Table B.3 on page 246 for a channel bandwidth equal to 10 MHz.

Regarding Table B.2, the first column denotes the index of the MCS with $0 \leq I_{\text{MCS}} \leq 28$ [3GP16g, Table 7.1.7.1-1]. The modulation mapping scheme for the respective MCS [3GP16g, Table 7.1.7.1-1] is denoted in the second column of Table B.2. The resulting code rate R_c (2.42) for TM6 when the eNodeB $\epsilon_b \in \mathbb{E}$ is equipped with $N_T^{(b)}$ equal to two and four transmit AEs is denoted in the third and fourth column of Table B.2, respectively. Furthermore, the resulting code rate R_c (2.42) for TM8 when the eNodeB $\epsilon_b \in \mathbb{E}$ is equipped with $N_T^{(b)}$ equal to two and four transmit AEs is denoted in the fifth and sixth column of Table B.2, respectively. Finally, the resulting code rate R_c (2.42) for TM9 when the eNodeB $\epsilon_b \in \mathbb{E}$ is equipped with $N_T^{(b)}$ equal to two and four transmit AEs is denoted in the seventh and eighth column of Table B.2, respectively.

Regarding Table B.3, the first column of Table B.3 denotes the index of the MCS with $0 \leq I_{\text{MCS}} \leq 28$. The modulation mapping scheme of the respective MCS is denoted in the second column of Table B.3. The resulting code rates for signal transmission in CoMP Scenarios 1, 2 and 3 for two TPs considered for signal transmission are denoted in the third and fourth column of Table B.3 for $N_T^{(b)}$ equal to two and four transmit AEs at each TP, respectively. The code rates for three TPs cooperating in CoMP Scenario 1, 2 and 3 are denoted in the fifth and sixth column of Table B.3 for $N_T^{(b)}$ equal to two and four transmit AEs at each TP, respectively. In case of CoMP Scenario 4, the code rates for two TPs considered for signal transmission are denoted in the seventh and eighth column of Table B.3 for $N_T^{(b)}$ equal to two and four transmit AEs at each TP, respectively, whereas the code rates for three TPs considered for signal transmission are denoted in the ninth and tenth column of Table B.3 for $N_T^{(b)}$ equal to two and four transmit AEs at each TP, respectively.

Table B.2. Relationship between MCS and code rate for TM6, TM8 and TM9 (created by the author of this thesis using [3GP16g, Table 7.1.7.1-1, Table 7.1.7.2.1-1]).

MCS index	Modulation Mapping Scheme	$\lceil R'_c \cdot 1024 \rceil$ for TM6 and		$\lceil R'_c \cdot 1024 \rceil$ for TM8 and		$\lceil R'_c \cdot 1024 \rceil$ for TM9 and	
		$N_T^{(b)}=2$	$N_T^{(b)}=4$	$N_T^{(b)}=2$	$N_T^{(b)}=4$	$N_T^{(b)}=2$	$N_T^{(b)}=4$
0	QPSK	110	113	121	125	117	119
1	QPSK	142	146	156	162	151	154
2	QPSK	174	180	192	198	185	189
3	QPSK	224	231	246	255	238	242
4	QPSK	283	292	312	323	302	307
5	QPSK	343	354	377	390	365	371
6	QPSK	403	415	443	458	429	436
7	QPSK	487	502	536	554	518	527
8	QPSK	547	564	601	622	582	591
9	QPSK	626	646	689	712	666	677
10	16 QAM	313	323	345	356	333	339
11	16 QAM	343	354	377	390	365	371
12	16 QAM	388	400	426	441	413	420
13	16 QAM	447	461	492	509	476	484
14	16 QAM	507	523	558	577	540	548
15	16 QAM	552	569	607	628	587	597
16	16 QAM	596	615	656	678	635	645
17	64 QAM	398	410	437	452	423	430
18	64 QAM	427	441	470	486	455	462
19	64 QAM	477	492	525	543	508	516
20	64 QAM	517	533	568	588	550	559
21	64 QAM	557	574	612	633	592	602
22	64 QAM	596	615	656	678	635	645
23	64 QAM	662	683	729	754	705	717
24	64 QAM	712	734	783	810	758	770
25	64 QAM	737	760	811	839	784	797
26	64 QAM	795	820	874	904	846	860
27	64 QAM	825	850	907	938	878	892
28	64 QAM	954	984	1049	1085	1015	1032

Table B.3. Relationship between the MCS, the modulation mapping scheme and the code rate for supported CoMP scenarios (created by the author of this thesis using [3GP16g, Table 7.1.7.1-1, Table 7.1.7.2.1-1; 3GP13a, Section 5.1.2]).

MCS Index	Modulation Mapping Scheme	CoMP Scenario 1,...,3				CoMP Scenario 4			
		$\lceil R'_c \cdot 1024 \rceil$ for $ \mathbb{E} = 2$ and $N_T^{(b)} = 2$		$\lceil R'_c \cdot 1024 \rceil$ for $ \mathbb{E} = 3$ and $N_T^{(b)} = 4$		$\lceil R'_c \cdot 1024 \rceil$ for $ \mathbb{E} = 2$ and $N_T^{(b)} = 2$		$\lceil R'_c \cdot 1024 \rceil$ for $ \mathbb{E} = 3$ and $N_T^{(b)} = 4$	
		$N_T^{(b)} = 2$	$N_T^{(b)} = 4$						
0	QPSK	123	125	129	132	117	119	117	119
1	QPSK	159	162	167	170	151	154	151	154
2	QPSK	195	198	205	209	185	189	185	189
3	QPSK	250	255	264	269	238	242	238	242
4	QPSK	317	323	334	340	302	307	302	307
5	QPSK	384	390	404	412	365	371	365	371
6	QPSK	450	458	474	483	429	436	429	436
7	QPSK	545	554	574	584	518	527	518	527
8	QPSK	611	622	644	656	582	591	582	591
9	QPSK	700	712	738	751	666	677	666	677
10	16 QAM	350	356	369	376	333	339	333	339
11	16 QAM	384	390	404	412	365	371	365	371
12	16 QAM	434	441	457	465	413	420	413	420
13	16 QAM	500	509	527	537	476	484	476	484
14	16 QAM	567	577	597	608	540	548	540	548

Continued on next page

Table B.3. Relationship between the MCS, the modulation mapping scheme and the code rate for supported CoMP scenarios
(Continued from previous page).

MCS Index	Modulation Mapping Scheme	CoMP Scenario 1,...,3				CoMP Scenario 4			
		$\lceil R'_c \cdot 1024 \rceil$ for $ \mathbb{E} = 2$ and		$\lceil R'_c \cdot 1024 \rceil$ for $ \mathbb{E} = 3$ and		$\lceil R'_c \cdot 1024 \rceil$ for $ \mathbb{E} = 2$ and		$\lceil R'_c \cdot 1024 \rceil$ for $ \mathbb{E} = 3$ and	
		$N_T^{(b)} = 2$	$N_T^{(b)} = 4$						
15	16 QAM	617	628	650	662	587	597	587	597
16	16 QAM	667	678	703	715	635	645	635	645
17	64 QAM	445	452	469	477	423	430	423	430
18	64 QAM	478	486	504	513	455	462	455	462
19	64 QAM	534	543	562	572	508	516	508	516
20	64 QAM	578	588	609	620	550	559	550	559
21	64 QAM	623	633	656	668	592	602	592	602
22	64 QAM	667	678	703	715	635	645	635	645
23	64 QAM	741	754	781	795	705	717	705	717
24	64 QAM	797	810	839	854	758	770	758	770
25	64 QAM	824	839	868	884	784	797	784	797
26	64 QAM	889	904	937	954	846	860	846	860
27	64 QAM	922	938	972	989	878	892	878	892
28	64 QAM	1067	1085	1124	1144	1015	1032	1015	1032

Appendix C

Complexity Analysis of the CCIMP Schemes

C.1 O-CCIMP Scheme

The complexity of the O-CCIMP scheme for subband PMI selection in terms of complex-valued additions and multiplications, denoted in (3.16) and (3.17), respectively, is derived in this section. As already mentioned in Section 3.3.4 of this thesis, the memory requirement is not considered in this thesis. Moreover, it is assumed that the arg max and the Hermitian operation does not contribute to the complexity.

Let $\Omega_{\text{O-CCIMP}}$ denote the complexity of the O-CCIMP scheme in terms of complex-valued additions and multiplications. As the set of precoding vectors maximizing the average post-SNR is found by performing a full-blown search to ensure that the global maximum of the average post-SNR is found, the average post-SNR needs to be calculated for $2^{N_{\text{T}}^{(b)}} \cdot \prod_{i=1}^{|\mathbb{I}_1|} (2^{N_{\text{T}}^{(\bar{b}_i)}} - 1)$ times. Hence, the complexity of the O-CCIMP scheme in terms of complex-valued additions and multiplications reads

$$\Omega_{\text{O-CCIMP}} = 2^{N_{\text{T}}^{(b)}} \cdot \prod_{i=1}^{|\mathbb{I}_1|} \left(2^{N_{\text{T}}^{(\bar{b}_i)}} \right) \cdot \Omega \left(\bar{\gamma}_{\text{post,O-CCIMP}}^{(1)} [w] \right), \quad (\text{C.1})$$

where $\Omega \left(\bar{\gamma}_{\text{post,O-CCIMP}}^{(1)} [w] \right)$ denotes the complexity in terms of complex-valued additions and multiplications to calculate the average post-SNR in the w -th subband for $0 \leq w < N_{\text{SB}}$. The complexity of the average post-SNR in (C.1) can be further decomposed into the sum of $2 \cdot N_{\text{symb}}^{\text{DL}} |\mathcal{S}_{\text{SB}}^{(w)}|$ numbers, where each summand represents the post-SNR in the (k, ℓ) -th RE, such that

$$\begin{aligned} \Omega \left(\bar{\gamma}_{\text{post,O-CCIMP}}^{(1)} [w] \right) &= \left(2N_{\text{symb}}^{\text{DL}} \left| \mathcal{S}_{\text{SB}}^{(w)} \right| - 1 \right) \cdot \Omega (\text{ADD}) + \\ &2N_{\text{symb}}^{\text{DL}} \left| \mathcal{S}_{\text{SB}}^{(w)} \right| \cdot \Omega \left(\gamma_{\text{post,O-CCIMP}}^{(1)} [k, \ell] \right) \end{aligned} \quad (\text{C.2})$$

holds, where $\gamma_{\text{post,O-CCIMP}}^{(1)} [k, \ell]$ denotes the post-SNR experienced by the UE $\mu_1 \in \mathbb{U}$ in the (k, ℓ) -th RE for a fix set of precoding vectors and reads

$$\gamma_{\text{post,O-CCIMP}}^{(1)} [k, \ell] = \left(\hat{\mathbf{H}}_{\text{CSI-RS}}^{(1,b)} [k, \ell] \underline{\mathbf{p}}^{(b)} [k, \ell] \right)^{\text{H}} \hat{\mathbf{R}}_{\Sigma, \text{CSI-RS}}^{(1)} [k, \ell] \hat{\mathbf{H}}_{\text{CSI-RS}}^{(1,b)} [k, \ell] \underline{\mathbf{p}}^{(b)} [k, \ell]. \quad (\text{C.3})$$

Following (C.2), $\Omega(\gamma_{\text{post,O-CCIMP}}^{(1)} [k, \ell])$ represents the complexity in terms of complex-valued additions and multiplications to calculate the post-SNR (C.3). For a fix set of precoding vectors, the post-SNR (C.3) can be computed by the product of the

- Hermitian representation of the matrix-vector product denoted by the CTF $\hat{\mathbf{H}}_{\text{CSI-RS}}^{(1,b)} [k, \ell]$ and the candidate precoding vector $\underline{\mathbf{p}}^{(b)} [k, \ell]$,
- inverse of the covariance matrix $\hat{\mathbf{R}}_{\Sigma, \text{CSI-RS}}^{(1)} [k, \ell]$ and the
- matrix-vector product of the aforementioned CTF and the candidate precoding vector,

such that

$$\Omega \left(\gamma_{\text{post,O-CCIMP}}^{(1)} [k, \ell] \right) = 3 \cdot \Omega(\underline{\mathbf{M}} \underline{\mathbf{v}}) + \Omega(\underline{\mathbf{M}}^{-1}) + \Omega \left(\hat{\mathbf{R}}_{\Sigma, \text{CSI-RS}}^{(1)} [k, \ell] \right) + \Omega(\underline{\mathbf{v}}_1^{\text{H}} \underline{\mathbf{v}}_2) \quad (\text{C.4})$$

holds, where $\Omega(\hat{\mathbf{R}}_{\Sigma, \text{CSI-RS}}^{(1)} [k, \ell])$ denotes the complexity in terms of complex-valued additions and multiplications to determine the covariance matrix. Following (2.84), the complexity to calculate the covariance matrix can be decomposed into the

- $|\mathbb{I}_1|$ -fold outer product of two vectors, where the first vector is represented by the matrix-vector product of the CTF $\hat{\mathbf{H}}_{\text{CSI-RS}}^{(1,b_i)} [k, \ell]$ and the candidate precoding vector $\underline{\mathbf{p}}_j^{(b_i)} [k, \ell]$, while the second one denotes the Hermitian representation of the matrix-vector product of the aforementioned CTF and candidate precoding vector,
- $(|\mathbb{I}_1| - 1)$ -fold addition of the outer product vectors plus the addition of the
- thermal noise power over the received bandwidth weighted with the $N_{\text{R}}^{(1)} \times N_{\text{R}}^{(1)}$ identity matrix.

Hence,

$$\Omega \left(\underline{\mathbf{R}}_{\Sigma, \text{CSI-RS}}^{(1)} [k, \ell] \right) = |\mathbb{I}_1| \cdot \left(2 \cdot \Omega(\underline{\mathbf{M}} \underline{\mathbf{v}}) + \Omega(\underline{\mathbf{v}} \underline{\mathbf{v}}^H) + \Omega(\underline{\mathbf{M}}_1 + \underline{\mathbf{M}}_2) \right) + \Omega \left(\alpha \mathbf{I}_{N_R^{(1)}} \right) \quad (\text{C.5})$$

holds.

Inserting (C.5) into (C.4), (C.4) into (C.2), (C.2) into (C.1) and assuming that the number of transmit AEs at each of the interfering TPs out of the set \mathbb{I}_1 is equal to the number of transmit AEs at the TPs out of the CoMP operating set, the complexity of the O-CCIMP scheme for subband PMI selection in (C.1) in terms of complex-valued additions and multiplications turns to

$$\begin{aligned} \Omega_{\text{O-CCIMP}} = & 2^{N_T^{(b)}} \cdot \left(2^{N_R^{(1)}} - 1 \right)^{|\mathbb{I}_1|} \cdot \left(2 N_{\text{symp}}^{\text{DL}} \left| \mathcal{S}_{\text{SB}}^{(w)} \right| \left(3 \cdot \Omega(\underline{\mathbf{M}} \underline{\mathbf{v}}) + \Omega(\underline{\mathbf{M}}^{-1}) + \Omega(\underline{\mathbf{v}}_1^H \underline{\mathbf{v}}_2) \right) + \right. \\ & \left. |\mathbb{I}_1| \cdot \left(2 \cdot \Omega(\underline{\mathbf{M}} \underline{\mathbf{v}}) + \Omega(\underline{\mathbf{v}} \underline{\mathbf{v}}^H) + \Omega(\underline{\mathbf{M}}_1 + \underline{\mathbf{M}}_2) \right) + \Omega \left(\alpha \mathbf{I}_{N_R^{(1)}} \right) + \right. \\ & \left. \left(2 N_{\text{symp}}^{\text{DL}} \left| \mathcal{S}_{\text{SB}}^{(w)} \right| - 1 \right) \cdot \Omega(\text{ADD}) \right). \end{aligned} \quad (\text{C.6})$$

Replacing the complexities of the linear algebra operations by the respective complexities summarized in the second column of Table 3.2 on page 155, the complexity of the O-CCIMP scheme for subband PMI selection in terms of complex-valued additions and multiplications reads

$$\Omega_{\text{O-CCIMP,ADD}} = 2^{N_T^{(b)}} \cdot \left(2^{N_T^{(b)}} - 1 \right)^{|\mathbb{I}_1|} \left(2 N_{\text{symp}}^{\text{DL}} \left| \mathcal{S}_{\text{SB}}^{(w)} \right| \left(N_R^{(1)} (1 + |\mathbb{I}_1|) \left(3 N_R^{(1)} - 2 \right) \right) \right) \quad (\text{C.7})$$

and

$$\Omega_{\text{O-CCIMP,MUL}} = 2^{N_T^{(b)}} \left(2^{N_T^{(b)}} - 1 \right)^{|\mathbb{I}_1|} \cdot 2 N_{\text{symp}}^{\text{DL}} \left| \mathcal{S}_{\text{SB}}^{(w)} \right| \left(N_R^{(1)} \left(|\mathbb{I}_1| N_R^{(1)} + \left(N_T^{(b)} (3 + 2 |\mathbb{I}_1|) + 2 \right) + 9 \right) \right), \quad (\text{C.8})$$

as denoted in (3.16) and (3.17), respectively.

C.2 LC-CCIMP Scheme

The complexity of the LC-CCIMP scheme for subband PMI selection in terms of complex-valued additions and multiplications, denoted in (3.18) and (3.19),

respectively, is derived in this section. As already mentioned in Section 3.3.4 of this thesis, the memory requirement is not considered in this thesis. Moreover, it is assumed that the $\arg \max$, the $\arg \min$ and the Hermitian operation does not contribute to the complexity.

Let $\Omega_{\text{LC-CCIMP}}$ denote the complexity of the LC-CCIMP scheme in terms of complex-valued additions and multiplications. As the precoding vectors $\underline{\mathbf{p}}^{(b)} [k, \ell]$ and $\underline{\mathbf{p}}^{(\tilde{b}_i)} [k, \ell]$ for $1 \leq i \leq |\mathbb{I}_1|$ can be computed iteratively, the complexity of the LC-CCIMP scheme turns to

$$\Omega_{\text{LC-CCIMP}} = \Omega \left(\underline{\mathbf{p}}^{(b)} [k, \ell] \Big|_{\text{LC-CCIMP}} \right) + \Omega (\text{ADD}) + \sum_{i=1}^{|\mathbb{I}_1|} \Omega \left(\underline{\mathbf{p}}^{(\tilde{b}_i)} [k, \ell] \Big|_{\text{LC-CCIMP}} \right), \quad (\text{C.9})$$

where $\Omega \left(\underline{\mathbf{p}}^{(b)} [k, \ell] \Big|_{\text{LC-CCIMP}} \right)$ denotes the complexity in terms of complex-valued additions and multiplications to determine the precoding vector maximizing the local average post-SNR $\bar{\gamma}_{\text{post,L C-CCIMP}}^{(1,b)} [w]$ in the w -th subband for $1 \leq w < N_{\text{SB}}$. Analogously, $\Omega \left(\underline{\mathbf{p}}^{(\tilde{b}_i)} [k, \ell] \Big|_{\text{LC-CCIMP}} \right)$ denotes the complexity in terms of complex-valued additions and multiplications to determine the precoding vector minimizing the local average post-SNR $\bar{\gamma}_{\text{post,L C-CCIMP}}^{(1,\tilde{b}_i)} [w]$ of the i -th interfering TP for $1 \leq i \leq |\mathbb{I}_1|$ in the w -th subband for $0 \leq w < N_{\text{SB}}$.

To determine the local average post-SNR $\bar{\gamma}_{\text{post,L C-CCIMP}}^{(1,b)} [w]$ in (3.9) - (3.10), the CTF $\hat{\underline{\mathbf{H}}}_{\text{CSI-RS}}^{(1,b)} [k, \ell]$ is multiplied with the candidate precoding vector $\underline{\mathbf{p}}_j^{(b)} [k, \ell]$ what results in a new complex-valued vector. This step is repeated with the Hermitian operation. The scalar product of the two vectors is calculated to obtain the squared Euclidean distance in (3.9).

Following (3.9) and (3.10), the scalar product is calculated $2 \cdot N_{\text{sy mb}}^{\text{DL}} |\mathcal{S}_{\text{SB}}^{(w)}|$ times, where the sum of the scalar products is weighted with the inverse of the thermal noise power over the received bandwidth. To obtain the precoding vector maximizing the average post-SNR $\bar{\gamma}_{\text{post,L C-CCIMP}}^{(1,b)} [w]$, the average post-SNR needs to be calculated for $2^{N_{\text{T}}^{(b)}}$ times, such that

$$\begin{aligned} \Omega \left(\underline{\mathbf{p}}^{(b)} [k, \ell] \Big|_{\text{LC-CCIMP}} \right) = & 2^{N_{\text{T}}^{(b)}} \cdot \left(2 N_{\text{sy mb}}^{\text{DL}} \left| \mathcal{S}_{\text{SB}}^{(w)} \right| \cdot \left(2 \cdot \Omega (\underline{\mathbf{M}} \underline{\mathbf{v}}) + \Omega (\underline{\mathbf{v}}_1^{\text{H}} \underline{\mathbf{v}}_2) \right) + 2 \cdot \Omega (\text{MUL}) + \right. \\ & \left. \left(2 N_{\text{sy mb}}^{\text{DL}} \left| \mathcal{S}_{\text{SB}}^{(w)} \right| - 1 \right) \cdot \Omega (\text{ADD}) \right) \end{aligned} \quad (\text{C.10})$$

holds.

Subsequently, the precoding vector $\underline{\mathbf{p}}^{(\tilde{b}_i)} [k, \ell]$ for each $1 \leq i \leq |\mathbb{I}_1|$ is calculated. It is to be noted that the covariance matrix (3.11d) used to calculate the

precoding vector $\underline{\mathbf{p}}^{(\tilde{b}_i)} [k, \ell]$ is extended iteratively, such that

$$\Omega \left(\underline{\mathbf{R}}_n^{(1)} [k, \ell] \right) = n \cdot \left(2 \cdot \Omega (\underline{\mathbf{M}} \underline{\mathbf{v}}) + \Omega (\underline{\mathbf{v}} \underline{\mathbf{v}}^H) + \Omega (\underline{\mathbf{M}}_1 + \underline{\mathbf{M}}_2) \right) + \Omega \left(\alpha \underline{\mathbf{I}}_{N_R^{(1)}} \right) \quad (\text{C.11})$$

holds for the complexity in terms of complex-valued additions and multiplications to calculate the covariance matrix $\underline{\mathbf{R}}_n^{(1)} [k, \ell]$. Making use of the Gaussian additivity formula [MV99, Section 2.6], the complexity in terms of complex-valued additions and multiplications to determine all of the $|\mathbb{I}_1|$ the covariance matrices in (3.11b) and (3.11c) reads

$$\begin{aligned} \sum_{i=1}^{|\mathbb{I}_1|} \Omega \left(\underline{\mathbf{R}}_{i-1}^{(1)} [k, \ell] \right) = \\ |\mathbb{I}_1| \cdot \Omega \left(\alpha \underline{\mathbf{I}}_{N_R^{(1)}} \right) + \underbrace{\sum_{i=1}^{|\mathbb{I}_1|} (i-1)}_{=|\mathbb{I}_1| \cdot (|\mathbb{I}_1| - 1) / 2} \cdot \left(2 \cdot \Omega (\underline{\mathbf{M}} \underline{\mathbf{v}}) + \Omega (\underline{\mathbf{v}} \underline{\mathbf{v}}^H) + \Omega (\underline{\mathbf{M}}_1 + \underline{\mathbf{M}}_2) \right). \end{aligned} \quad (\text{C.12})$$

Making use of (C.12) and following the assumption that the number of transmit AEs at each of the interfering TPs out of the set \mathbb{I}_1 is equal to the number of transmit AEs at the TPs out of the CoMP operating set, the complexity of $\sum_{i=1}^{|\mathbb{I}_1|} \Omega \left(\underline{\mathbf{p}}^{(\tilde{b}_i)} [k, \ell] \Big|_{\text{LC-CCIMP}} \right)$ in (C.9) reads

$$\begin{aligned} \sum_{i=1}^{|\mathbb{I}_1|} \Omega \left(\underline{\mathbf{p}}^{(\tilde{b}_i)} \Big|_{\text{LC-CCIMP}} \right) = \\ \left(2^{N_T^{(b)}} - 1 \right) \cdot \left(\left(2 N_{\text{symp}}^{\text{DL}} \left| \mathcal{S}_{\text{SB}}^{(w)} \right| - 1 \right) \cdot \Omega (\text{ADD}) + \right. \\ \left. 2 N_{\text{symp}}^{\text{DL}} \left| \mathcal{S}_{\text{SB}}^{(w)} \right| \cdot (|\mathbb{I}_1| \cdot (|\mathbb{I}_1| - 1)) \cdot \left(2 \cdot \Omega (\underline{\mathbf{M}} \underline{\mathbf{v}}) + \Omega (\underline{\mathbf{v}} \underline{\mathbf{v}}^H) + \Omega (\underline{\mathbf{M}}_1 + \underline{\mathbf{M}}_2) \right) \right) + \\ \left(2^{N_T^{(b)}} - 1 \right) \cdot \left(2 N_{\text{symp}}^{\text{DL}} \left| \mathcal{S}_{\text{SB}}^{(w)} \right| - 1 \right) \cdot |\mathbb{I}_1| \cdot \Omega (\text{ADD}) + \\ 2 N_{\text{symp}}^{\text{DL}} \left| \mathcal{S}_{\text{SB}}^{(w)} \right| \cdot \left(4 \cdot \Omega (\underline{\mathbf{M}} \underline{\mathbf{v}}) + 3 \cdot \Omega (\underline{\mathbf{M}}_1 \cdot \underline{\mathbf{M}}_2) + 2 \cdot \Omega (\underline{\mathbf{M}}^{-1}) + 2 \cdot \Omega (\underline{\mathbf{v}}_1^H \underline{\mathbf{v}}_2) \right. \\ \left. 2 \cdot \Omega \left(\alpha \underline{\mathbf{I}}_{N_R^{(1)}} \right) + \Omega (\underline{\mathbf{v}} \underline{\mathbf{v}}^H) + \Omega (\text{ADD}) + \Omega (\text{MUL}) \right). \end{aligned} \quad (\text{C.13})$$

Inserting (C.10) and (C.13) into (C.9) and replacing the complexities of the linear algebra operations by the respective complexities summarized in the second column of Table 3.2 on page 155, the complexity of the LC-CCIMP scheme for subband PMI selection in terms of complex-valued additions and

multiplications reads

$$\begin{aligned}
 \Omega_{\text{LC-CCIMP,ADD}} = & \\
 & 2 N_{\text{sy mb}}^{\text{DL}} \left| \mathcal{S}_{\text{SB}}^{(w)} \right| \left(|\mathbb{I}_1| \cdot \left(2^{N_{\text{T}}^{(b)}} - 1 \right) \cdot \left(N_{\text{R}}^{(1)} N_{\text{R}}^{(1)} \left(1 + 3 \cdot |\mathbb{I}_1| + 3 \cdot N_{\text{T}}^{(b)} \right) - \right. \\
 & \left. N_{\text{R}}^{(1)} \left(2 \cdot |\mathbb{I}_1| + 3 \cdot N_{\text{T}}^{(b)} \right) + 2 \right) + 2^{N_{\text{T}}^{(b)}} \cdot \left(2 \cdot N_{\text{R}}^{(1)} N_{\text{R}}^{(1)} - N_{\text{R}}^{(1)} + 1 \right) - 1 \Big) + \\
 & \left(1 - 2^{N_{\text{T}}^{(b)}} \right) (2 + |\mathbb{I}_1|)
 \end{aligned} \tag{C.14}$$

and

$$\begin{aligned}
 \Omega_{\text{LC-CCIMP,MUL}} = & \\
 & 2 N_{\text{sy mb}}^{\text{DL}} \left| \mathcal{S}_{\text{SB}}^{(w)} \right| \left(|\mathbb{I}_1| \cdot \left(2^{N_{\text{T}}^{(b)}} - 1 \right) \cdot \left(N_{\text{R}}^{(1)} N_{\text{R}}^{(1)} \left(|\mathbb{I}_1| + 3 \cdot N_{\text{T}}^{(b)} \right) + \right. \\
 & \left. 2 \cdot N_{\text{R}}^{(1)} \cdot \left(N_{\text{T}}^{(b)} \cdot (|\mathbb{I}_1| + 1) + 2 \right) + 19 \right) + 2^{N_{\text{T}}^{(b)}} \cdot N_{\text{R}}^{(1)} \cdot \left(2 \cdot N_{\text{T}}^{(b)} + 1 \right) \Big) + \\
 & 2^{(N_{\text{T}}^{(b)}+1)},
 \end{aligned} \tag{C.15}$$

as denoted in (3.18) and (3.19), respectively.

Appendix D

Timing Offset Estimation Accuracy in Flat Fading Channels

To demonstrate the dependency of the biased TO estimation error and the finite coherence bandwidth of the mobile communication channel, the PDP of the SCM-B denoted in [3GP06, Table A.1.3-1] is modified in that way that the power of all but the first tap is set to zero, such that the coherence bandwidth of the spectrally flat mobile communication channel approximates to infinity. As a direct consequence thereof, the channel phase difference denoted by $\angle(\underline{g}_{\nu, \text{DMRS}}^{(m,b)}[k_j, \ell_j]) - \angle(\underline{g}_{\nu, \text{DMRS}}^{(m,b)}[k_i, \ell_i])$ is equal to zero for any $k_i, k_j \in \mathcal{S}_{\text{SB}}^{(w)}$, such that the TO estimation is not affected by the channel phase difference for $0 \leq w < N_{\text{SB}}$ and $1 \leq \nu \leq N_{\text{R}}^{(m)}$. The resulting TO estimation accuracy in terms of TO over RMSE when evaluating the precoded DMRSs for k'_{Δ} equal to five is provided in Figure D.1 on page 256 for both, the 4×2 and the 2×2 MIMO antenna configuration. For the sake of better readability, the range of the SNR is selected between -10 dB and 40 dB with a step size of 10 dB. Similarly as for the SCM-B with finite coherence bandwidth (2.87), it can be observed that the RMSE decreases for both, the 4×2 and the 2×2 MIMO antenna configuration if the SNR increases, as long as the TO does not approximate to the TO which can be theoretically estimated, as depicted in Figure D.1. Analogously to the findings achieved in Section 4.3 in this thesis, the RMSE of the TO estimation for the 4×2 MIMO antenna configuration is smaller for a TO equal to zero than the RMSE of the TO estimation for the 2×2 MIMO antenna configuration, as depicted in Figure D.1. With increasing values of the TO, the DMRS-based TO estimation for the 2×2 MIMO antenna configuration provides lower values of the RMSE than the DMRS-based TO estimation for the 4×2 MIMO antenna configuration. The reason for the dependency of the TO estimation accuracy and the MIMO antenna configuration is provided in Section 4.3 of this thesis. In contrast to the biased TO estimation error caused by the non-negligible channel phase difference discussed in Section 4.3 of this thesis, the RMSE of the TO estimation approximates to zero as the coherence bandwidth of the mobile communication channel approximates

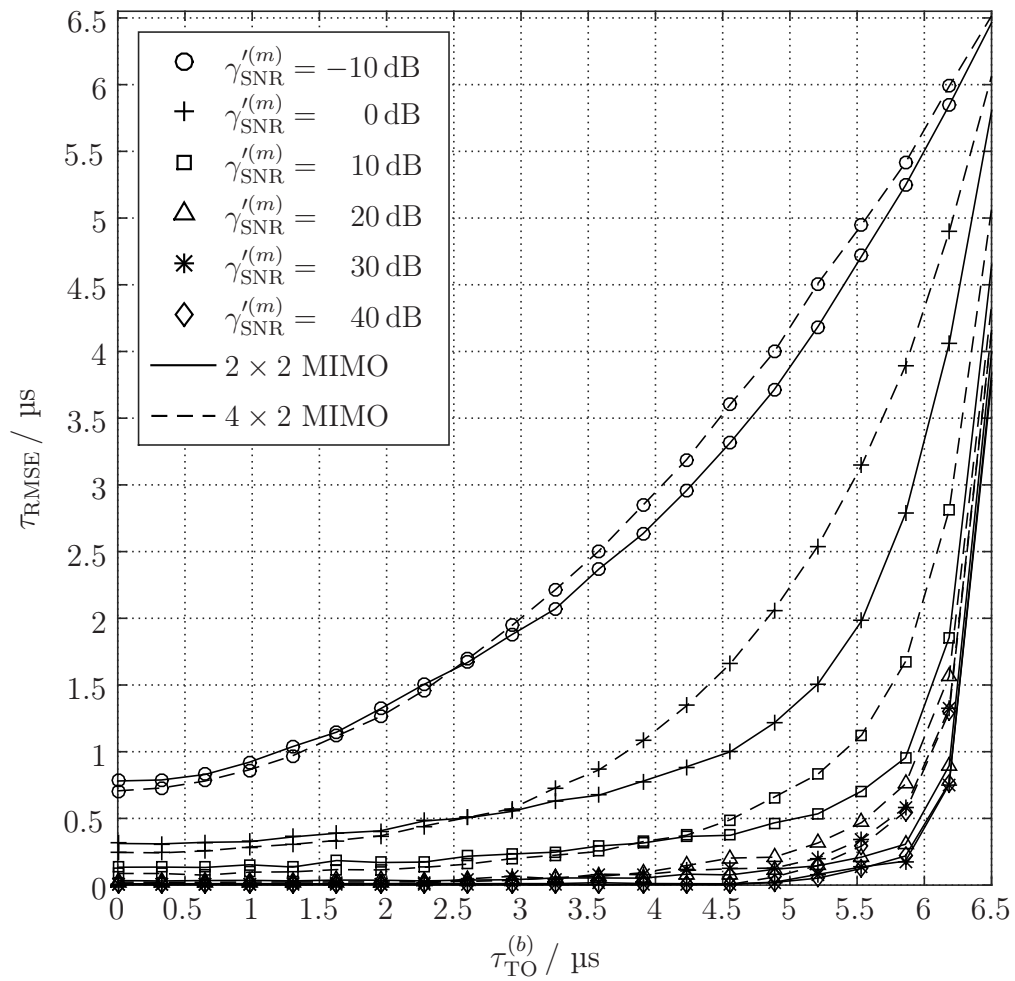


Figure D.1. Accuracy for DMRS-based TO estimation (created by the author of this thesis).

to infinity. Thus, it has been shown that the biased TO estimation error in Figure 4.9 can be attributed to the non-negligible channel phase difference of the SCM-B.

List of Frequently used Symbols

$\lceil \cdot \rceil$	Smallest integer greater than or equal to \cdot
$\lfloor \cdot \rfloor$	Largest integer smaller than or equal to \cdot
$(\cdot)^H$	Hermitian operation of \cdot
$(\cdot)^T$	Transpose operation of \cdot
$\mathbf{0}_{N_R^{(m)}}$	Null vector of dimension $N_R^{(m)} \times 1$
$\angle(\underline{z})$	Angle of $\underline{z} \in \mathbb{C}$
$*$	Linear convolution operation
\odot	SCHUR product of two matrices
$\mathbf{1}_{N_R^{(m)} \times 2}$	Matrix of ones of dimension $N_R^{(m)} \times 2$
$A_{64\text{QAM}}$	Scaling factor for 64 QAM symbols
\mathcal{A}_{CRS}	Set of transmit APs the CRSs are transmitted from
$\mathcal{A}_{\text{CSI-RS}}$	Set of transmit APs the CSI-RSs are transmitted from
$\mathcal{A}_{\text{DMRS}}$	Set of transmit APs the DMRSs are transmitted from
\mathbb{A}_m	Set of eNodeBs that simultaneously transmit the desired signal
$\mathbb{A}_m^{\text{CRS}}$	Subset of eNodeBs that simultaneously transmit the CRSs
$\mathbb{A}_m^{\text{data}}$	Subset of eNodeBs considered for simultaneous transmission of DMRSs, CSI-RSs and precoded complex-valued modulation symbols carrying the codewords
B_c	Coherence bandwidth
c_0	Speed of light with $c_0 \approx 3 \cdot 10^8$ m/s
$C_{\text{chan}}^{(m)}(k, \ell)$	Accumulated receive power of the desired signal
$C^{(m)}$	Accumulated average power of the desired signal
$C^{(m, \bar{b})}$	Average receive power of the interfering signal
$C^{(m, b)}$	Average receive power of the desired signal
\mathbb{C}	Set of complex values
$\underline{d}^{(b)}[k, \ell]$	Desired complex-valued modulation symbol
$d_{\text{TX}}^{(b)}$	Spacing among the physical transmit antennas
$\underline{d}^{(\bar{b})}[k, \ell]$	Interfering complex-valued modulation symbol

List of Frequently used Symbols

$\underline{\mathbf{d}}_{\text{prec}}^{(b)} [k, \ell]$	Precoded complex valued modulation symbol
$\underline{d}_{\zeta, \text{prec}}^{(b)} [k, \ell]$	ζ – th element of $\underline{\mathbf{d}}_{\text{prec}}^{(b)} [k, \ell]$
$\delta(t)$	DIRAC function
\mathbb{E}	Set of eNodeBs in the macro cellular deployed LTE network
$\underline{e}_{\nu}^{(m,b)}(t)$	Baseband representation of time-continuous desired receive signal at the output of the mobile communication channel
$\underline{e}_{\nu}^{(m)}(t)$	Baseband representation of time-continuous receive signals at the output of the mobile communication channel
$\underline{\mathbf{e}}(\phi)$	Steering vector
$\epsilon_{a_{\text{sync}}(m)}$	eNodeB the UE is assigned to with respect to synchronization
ϵ_{EVM}	Experienced EVM
$\eta_{\text{BW}, 90\%, x}^{(m)}$	90 % of $\eta_{\text{BW}, \text{max}, x}^{(m)}$
$\eta_{\text{BW}, \text{max}, x}^{(m)}$	Maximum bandwidth efficiency when using MCS with index x
$\eta_{\text{eff}}^{(m)}$	Experienced bandwidth efficiency
$\eta_{\text{IT}, \text{IL}}^{(m)}(k, \ell)$	IT bandwidth efficiency for IL transmission
$\eta_{\text{IT}, \text{loss}}^{(m)}(k, \ell)$	IT bandwidth efficiency loss
$\eta_{\text{IT}, \text{NL}}^{(m)}(k, \ell)$	IT bandwidth efficiency for NL transmission
$\mathbb{E} \{ \cdot \}$	Expectation of \cdot
$f_{\text{BW}}^{(m)}$	Channel bandwidth
f_c	Carrier frequency
F_m	Noise figure
f_s	Sampling frequency
f_{sc}	Subcarrier spacing
$G^{(m)}$	Geometry, experienced by the UE $\mu_m \in \mathbb{U}$
$\underline{\mathbf{g}}^{(m,b)} [k, \ell]$	Effective CTF between the UE $\mu_m \in \mathbb{U}$ and the eNodeB $\epsilon_b \in \mathbb{A}_m$
$\underline{\mathbf{g}}^{(m, \tilde{b})} [k, \ell]$	Effective CTF between the UE $\mu_m \in \mathbb{U}$ and the eNodeB $\epsilon_{\tilde{b}} \in \mathbb{I}_m$
$\underline{g}_{\nu}^{(m,b)} [k, \ell]$	ν – th element of $\underline{\mathbf{g}}^{(m,b)} [k, \ell]$
$\underline{g}_{\nu}^{(m, \tilde{b})} [k, \ell]$	ν – th element of $\underline{\mathbf{g}}^{(m, \tilde{b})} [k, \ell]$
$\underline{\mathcal{G}}^{(m)}$	Throughput experienced by the UE $\mu_m \in \mathbb{U}$
$\gamma_{\text{INR}}^{(m, \tilde{b}_i)}$	INR
$\underline{\mathbf{\Gamma}}^{(m)} [n_{\text{PRB}}]$	Transmit covariance matrix in absence of AWGN and ISI
$\overline{\gamma}_{\text{post}, \text{LC-CCIMP}}^{(1)} [w]$	Post-SNR of the desired signal for the LC-CCIMP scheme
$\overline{\gamma}_{\text{post}, \text{LC-CCIMP}}^{(1,b)} [w]$	Post-SNR of the desired signal for the LC-CCIMP scheme for NL signal transmission
$\gamma_{\text{post}}^{(m,b)} [k, \ell]$	Post-SNR of the desired signal
$\overline{\gamma}_{\text{post}, \text{LC-CCIMP}}^{(1, \tilde{b}_i)} [w]$	Post-SNR of the interfering signal for the LC-CCIMP scheme
$\overline{\gamma}_{\text{post}, \text{O-CCIMP}}^{(1)} [w]$	Post-SNR of the desired signal for the O-CCIMP scheme

$\overline{\gamma}_{\text{post}}^{(m,b)} [w]$	Average post-SNR of the desired signal in the w -th subband
$\underline{\Gamma}^{(m)} [n_{\text{PRB}}]$	Phase compensated representation of $\underline{\Gamma}^{(m)} [n_{\text{PRB}}]$
$\gamma_{\text{SNR}}^{(m)}$	SNR
$\gamma_{\text{SNR}}^{(m)}$	SNR in logarithmic scale
$\underline{H}^{(m,b)} [k, \ell]$	CTF between UE $\mu_m \in \mathbb{U}$ and eNodeB $\epsilon_b \in \mathbb{A}_m$ in case of MIMO
$\underline{h}^{(m,b)} [k, \ell]$	CTF between UE $\mu_m \in \mathbb{U}$ and eNodeB $\epsilon_b \in \mathbb{A}_m$ in case of SISO
$\underline{h}_{\nu, \zeta}^{(m,b)} (\tau, t)$	Channel response at the ν -th receive AE at UE $\mu_m \in \mathbb{U}$ at time t when transmitting a dirac impulse at time $t - \tau$ from the ζ -th transmit AE at eNodeB $\epsilon_b \in \mathbb{E}$
$\underline{H}^{(m, \tilde{b})} [k, \ell]$	CTF between UE $\mu_m \in \mathbb{U}$ and eNodeB $\epsilon_{\tilde{b}} \in \mathbb{I}_m$ in case of MIMO
$\underline{h}^{(m, \tilde{b})} [k, \ell]$	CTF between UE $\mu_m \in \mathbb{U}$ and eNodeB $\epsilon_{\tilde{b}} \in \mathbb{I}_m$ in case of SISO
$\underline{h}_{\nu, \zeta}^{(m,b)} [k, \ell]$	(ν, ζ) -th element of $\underline{h}^{(m,b)} [k, \ell]$
$I_{\text{chan}}^{(m)} (k, \ell)$	Accumulated receive power of the interfering signals
$I^{(m)}$	Accumulated average power of the interfering signals
\mathbb{I}_m	Set of eNodeBs that simultaneously transmit the interfering signal in the same frequency band to the UE $\mu_m \in \mathbb{U}$
I_{MCS}	Index of current MCS
$\underline{\mathbb{I}}_{ \mathbb{I}_m }$	Identity matrix of dimension $ \mathbb{I}_m \times \mathbb{I}_m $
$\underline{\mathbb{I}}_{N_{\text{R}}^{(m)}}$	Identity matrix of dimension $N_{\text{R}}^{(m)} \times N_{\text{R}}^{(m)}$
I_{TBS}	TBS index
$\Im \{ \cdot \}$	Imaginary component of \cdot
k_{B}	BOLTZMANN'S constant
λ_{c}	Wavelength of transmit signal
$\underline{\mathbf{m}}_{\text{E-IRC}} [k, \ell]$	Weight vector of the E-IRC receiver
$\underline{\mathbf{m}}_{\text{IRC}} [k, \ell]$	Weight vector of the IRC receiver
$\underline{\mathbf{m}}_{\text{IS}} [k, \ell]$	Weight vector of the IS receiver
$\underline{\mathbf{m}}_{\text{MMSE}} [k, \ell]$	Weight vector of the MMSE receiver
N_0	Spectral power density
$N_{\text{BS}}^{\text{max}}$	Maximum block size that can be interleaved using the turbo-code internal interleaver
N_{CB}	Total number of code blocks after code block segmentation
$N_{\text{cell}}^{(1)}$	Physical layer cell-identity group
$N_{\text{cell}}^{(2)}$	Physical layer identity within the physical layer cell-identity group
$N_{\text{cell}}^{\text{ID}}$	Physical layer cell-identity

List of Frequently used Symbols

$N_{CP,\ell}$	Number of samples for the CP when using sample interval T_S
N_{CRC24A}	Length of CRC when using the polynomial g_{CRC24A}
N_{CRC24B}	Length of CRC when using the polynomial g_{CRC24B}
$N_{CRS,N_T^{(b)}}$	Number of physical used to transmit the CRSs
$N_{CSI-RS,N_T^{(b)}}$	Number of physical resources used to transmit the CSI-RSs
N_{DMRS}	Number of physical resources used to transmit the DMRSs
N_{OFDM}	Number of samples for the OFDM symbol
$N_{i,n_{PRB}}^{other}$	Number of physical resources reserved for the PBCH, the PC-FICH, the PDCCH, the PHICH, the PSS and the SSS
N_{PRB}	Number of allocated PRBs
n_{PRB}	Physical resource block number
$N_R^{(m)}$	Number of receive antennas at the UE $\mu_m \in \mathbb{U}$
N_{RB}^{DL}	Downlink bandwidth configuration
$N_{RB}^{max, DL}$	Largest downlink bandwidth configuration
$N_{RB}^{min, DL}$	Smallest downlink bandwidth configuration
$N_{RE}^{SF, PRB}$	Number of REs in one subframe and PRB
N_{SB}	Number of subbands
N_{sc}^{RB}	Resource block size in frequency domain
N_{seg}	Number of bits after code block segmentation and code block CRC attachment
$n_{shift}(\ell)$	Accumulated number of samples of previous ℓ OFDM symbols and CPs
N_{symb}^{DL}	Number of OFDM symbols in a DL slot
$N_T^{(b)}$	Number of transmit antennas at the eNodeB $\epsilon_b \in \mathbb{A}_m$
$N_T^{(\bar{b})}$	Number of transmit antennas at the eNodeB $\epsilon_{\bar{b}} \in \mathbb{I}_m$
N_{TBS}	Number of bits in one TB
$\underline{n}^{(m)}[k, \ell]$	AWGN component in case of a single receive antenna
$\mathbf{n}^{(m)}[k, \ell]$	AWGN component in case of a multiple receive antenna
$\underline{n}_\nu^{(m)}[k, \ell]$	ν -th element of $\mathbf{n}^{(m)}[k, \ell]$
$\Omega(ADD)$	Complexity of adding two complex-valued scalars
$\Omega_{LC-CCIMP}$	Complexity of the LC-CCIMP scheme in terms of complex-valued additions and multiplications
$\Omega_{LC-CCIMP,ADD}$	Complexity of the LC-CCIMP scheme in terms of complex-valued additions
$\Omega_{LC-CCIMP,MUL}$	Complexity of the LC-CCIMP scheme in terms of complex-valued multiplications
$\Omega(MUL)$	Complexity of multiplying two complex-valued scalars
$\Omega_{O-CCIMP}$	Complexity of the O-CCIMP scheme in terms of complex-valued additions and multiplications

List of Frequently used Symbols

$\Omega_{\text{O-CCIMP,ADD}}$	Complexity of the O-CCIMP scheme in terms of complex-valued additions
$\Omega_{\text{O-CCIMP,MUL}}$	Complexity of the O-CCIMP scheme in terms of complex-valued multiplications
P_{B}	Probability of a block error
$P^{(b)}$	Transmit power at the eNodeB $\epsilon_b \in \mathbb{A}_m$
$\underline{p}^{(b)} [k, \ell]$	Precoding vector
$P_{\text{b,coded}}$	Probability of a coded bit error
$P^{(\tilde{b})}$	Transmit power at the eNodeB $\epsilon_{\tilde{b}} \in \mathbb{I}_m$
$P_{\text{b,uncoded}}$	Probability of a an uncoded bit error
$\underline{\Phi}^{(m,b)} [n_{\text{PRB}}]$	Matrix carrying the phase shift information
$\phi_{\Delta} (i, j)$	Phase offset
$\hat{\phi}_{\Delta} (i, j)$	Estimate of $\phi_{\Delta} (i, j)$
π_{AP}	Index of the AP
$p_{\text{PMI},N_{\text{T}}^{(b)}} \left(i \mid \tau_{\text{TO}}^{(b)} \right)$	Probability for PMI selection conditioned the TO
R_{c}	Code rate
R_{cell}	Radius of the cell
$\underline{r}^{(m)} [k, \ell]$	ν -th element of $\underline{\mathbf{r}}^{(m)} [k, \ell]$
$\underline{\mathbf{r}}^{(m)} [k, \ell]$	Receive signal in case of a multiple receive antenna at the UE
$\underline{r}_{\nu}^{(m)} [k, \ell]$	Receive signal in case of a single receive antenna at the UE
\mathbb{R}	Set of real values
\mathbb{R}_{+}	Set of real values greater than or equal to zero
$\hat{\underline{\mathbf{R}}}_{\Sigma, \text{CSI-RS}}^{(m)} [k, \ell]$	Estimated covariance matrix by exploiting the CSI-RSs and precoding vectors
$\hat{\underline{\mathbf{R}}}_{\Sigma, \text{DMRS}}^{(m)} [k, \ell]$	Estimated covariance matrix by exploiting the DMRSs
$\hat{\underline{\mathbf{R}}}_{\Sigma, \text{expl.}}^{(m)} [k, \ell]$	Estimated covariance matrix by exploiting the explicitly estimated effective channels
$\underline{\mathbf{R}}_{\Sigma}^{(m)} [k, \ell]$	Experienced covariance matrix
$\hat{\underline{\mathbf{R}}}_{\Sigma, \text{PDSCH}}^{(m)} [k, \ell]$	Estimated covariance matrix by exploiting the PDSCH
$\underline{\mathbf{R}}_{\text{T}}^{(m)}$	Transmit covariance matrix
$\Re \{ \cdot \}$	Real component of \cdot
$\rho^{(m,b)}$	Path-loss between the UE $\mu_m \in \mathbb{U}$ and the eNodeB $\epsilon_b \in \mathbb{A}_m$
$\rho^{(m,\tilde{b})}$	Path-loss between the UE $\mu_m \in \mathbb{U}$ and the eNodeB $\epsilon_{\tilde{b}} \in \mathbb{I}_m$
ϱ_{TX}	Antenna gain
$\mathcal{S}_{i, n_{\text{PRB}}}$	Set of available physical time-frequency resources
$\mathcal{S}_{i, n_{\text{PRB}}}^{\text{other}}$	Set of physical time-frequency resources used for the PBCH, PCFICH, PDCCH, PHICH, PSS, SSS
$\mathcal{S}_{i, n_{\text{PRB}}, \text{CRS}}^{(b, \pi_{\text{AP}})}$	Set of REs carrying the CRSs

List of Frequently used Symbols

$\mathcal{S}_{i, n_{\text{PRB}}, \text{CSI-RS}}^{(b, \pi_{\text{AP}})}$	Set of REs carrying the CSI-RSs
$\mathcal{S}_{i, n_{\text{PRB}}, \text{DMRS}}^{(b, \bar{\gamma})}$	Set of REs carrying the DMRSs
$\mathcal{S}_{k'_{\Delta}}^{(w)}$	Set of tuples with spacing k'_{Δ} in frequency direction
$\underline{s}_{\ell, \zeta}^{(b)}(t)$	Time-continuous OFDM baseband signal of the ℓ -th OFDM symbol and CP to be transmitted from the ζ -th transmit AP
$\mathcal{S}_{\text{PMI}, N_{\text{T}}^{(b)}}$	Set of PMIs in case of $N_{\text{T}}^{(b)}$ equal to two or four transmit AEs
$\mathcal{S}'^{(\tilde{b})}_{\text{PMI}, N_{\text{T}}^{(\tilde{b})}}$	Set of restricted PMIs
$\mathcal{S}_{\text{SB}}^{(w)}$	Set of subcarriers in the w -th subband
$\underline{s}_{\zeta}^{(b)}(t)$	Time-continuous OFDM baseband signal of one DL slot to be transmitted on the ζ -th transmit AP
σ_m^2	Thermal noise power over the received bandwidth
T_0	Environmental temperature
T_{frame}	Duration of one frame
T_{OFDM}	Duration of one OFDM symbol
T_s	Sample interval
T_{slot}	Duration of one slot
T_{subframe}	Duration of one subframe
$\tau_{\text{CIR}}(\cdot)$	Length of the CIR of \cdot
$\tau_{\text{CP}, \ell}$	Length of the CP of the ℓ -th OFDM symbol
τ_{DS}	Delay spread
$\hat{\tau}_{\text{TO}}^{(b)}$	Estimate of $\tau_{\text{TO}}^{(b)}$
τ_{MS}	Multipath spread
τ_{RMSE}	RMSE of the estimated TO
$\tau_{\text{TO}}^{(b)}$	Timing offset of the receive signal
\mathbb{U}	Set of UEs located in the cellular deployed LTE network which are operating in the same frequency band
$\mathbb{V}_{64\text{QAM}}$	Set of complex-valued modulation symbols following the 64 QAM modulation mapping scheme
$\mathbb{V}_{64\text{QAM}}^{(i)}$	Subset of complex-valued modulation symbols following the 64 QAM modulation mapping scheme
v_{shift}	Cell-specific frequency shift
$\left[\chi_{\text{CSI-RS}}^{(b, i)} \right]$	IVERSON bracket to assess whether the eNodeB is transmitting the CSI-RSs
$\Xi_{i, j}^{(m, b)} [n_{\text{PRB}}]$	Submatrix of $\underline{\mathbf{I}}^{(m)} [n_{\text{PRB}}]$
$\underline{y}_{\zeta}^{(b)} [k, \ell]$	Complex-valued symbol to be transmitted by the eNodeB $\epsilon_b \in \mathbb{E}$ from the ζ -th transmit AE

$\underline{z}_{\text{DIP}}$	Vector with DIP values ordered in descending order
$z_{\text{DIP},i}$	DIP of the interfering eNodeB $\epsilon_{\tilde{b}_i} \in \mathbb{I}_m$
\mathbb{Z}	Set of integer values

List of Acronyms

3G	3rd generation
3GPP	3rd Generation Partnership Project
4G	4th generation
AE	Antenna Element
AIPN	All Internet Protocol Network
AP	Antenna Port
ASLIC	Adaptive SLIC
AWGN	Additive White Gaussian Noise
BER	Bit Error Rate
BLER	Block Error Rate
BPSK	Binary Phase Shift Keying
C-RNTI	Cell - RNTI
CA	Carrier Aggregation
CB	Coordinated Beamforming
CCIMP	Codebook-Based Cooperative Interference Mitigation Precoding
CDD	Cyclic Delay Diversity
CFO	Carrier Frequency Offset
CIR	Channel Impulse Response
CoMP	Coordinated Multipoint
CP	Cyclic Prefix
CQI	Channel Quality Indication
CRC	Cyclic Redundancy Check
CRS	Cell Specific Reference Signal
CS	Coordinated Scheduling
CSI	Channel State Information
CTF	Channel Transfer Function
DC	Discrete Current
DF	Decorrelating Filter
DFT	Discrete Fourier Transform
DIP	Dominant Interferer Proportion

List of Acronyms

DL	Downlink
DMF	Decorrelating Matched Filter
DMRS	Demodulation Reference Signal
DPS	Dynamic Point Selection
E-IRC	Enhanced IRC
E-LMMSE-IRC	Enhanced Linear MMSE-IRC
eNodeB	Enhanced Node B
eNodeB-ID	eNodeB Identified
EPC	Evolved Packet Core
EPDCCH	Enhanced Physical Downlink Control Channel
EVM	Error Vector Magnitude
EWSD	<i>Elektronisches Wahlsystem Digital</i>
FDD	Frequency Division Duplex
HDV	High Definition Video
HOM	Higher Order Modulation
IA	Interference Alignment
IC	Interference Cancellation
ICI	Inter-Carrier Interference
IL	Interference Limited
IM	Interference Measurement
INR	Interference Noise Ratio
IRC	Interference Rejection Combining
IS	Interference Suppression
ISI	Inter-Symbol Interference
IT	Information Theoretic
JLSCE	Joint Least Square Channel Estimation
JP	Joint Processing
JT	Joint Transmission
LC-CCIMP	Low-Complexity CCIMP
LMMSE-IRC	Linear MMSE-IRC
LSCE	Least Square Channel Estimation
LTE	Long Term Evolution
MAC	Media Access Control
MAI	Multiple Access Interference
MBMS	Multimedia Broadcast Multicast Service
MBSFN	Multimedia Broadcast Service Single Frequency Network

MCS	Modulation and Coding Scheme
MF	Matched Filter
MIMO	Multiple-Input and Multiple-Output
ML	Maximum Likelihood
MMSE	Minimum Mean Square Error
MPDCCH	Machine Type Communication Physical Downlink Control Channel
MPEG	Moving Picture Experts Group
MRC	Maximum Ratio Combining
NAICS	Network-Assisted Interference Cancellation and Suppression
NL	Noise Limited
O-CCIMP	Optimal CCIMP
OFDM	Orthogonal Frequency Division Multiplexing
PBCH	Physical Broadcast Channel
PCFICH	Physical Control Format Indicator Channel
PDCCH	Physical Downlink Control Channel
PDCP	Packet Data Convergence Protocol
PDP	Power Delay Profile
PDSCH	Physical Downlink Shared Channel
PER	PMI Error Rate
PHICH	Physical Hybrid ARQ Indicator Channel
PHY	Physical
PMI	Precoding Matrix Index
PRB	Physical Resource Block
PRS	Positioning Reference Signal
PSS	Primary Synchronization Signal
QAM	Quadrature Amplitude Modulation
QCL	Quasi Co-Location
QoS	Quality of Service
QPSK	Quadrature Phase Shift Keying
RE	Resource Element
RFID	Radio Frequency Identification
RI	Rank Indicator
RLC	Radio Link Control
RMSE	Root-Mean-Square Error
RNC	Radio Network Controller
RNTI	Radio Network Temporary Identifier
RRC	Radio Resource Control

List of Acronyms

RRH	Remote Radio Head
RS	Reference Signal
RTT	Round-Trip Time
SCM	Spatial Channel Model
SCM-A	SCM Type A
SCM-B	SCM Type B
SCM-C	SCM Type C
SCM-D	SCM Type D
SCO	Sampling Clock Offset
SI	<i>Système International d'unités</i>
SISO	Single-Input and Single-Output
SLIC	Symbol Level IC
SM	Spatial Multiplexing
SNR	Signal to Noise Ratio
SRNC	Serving Resource Network Controller
SRS	Sounding Reference Signal
SSS	Secondary Synchronization Signal
TB	Transport Block
TBS	Transport Block Size
TDD	Time Division Duplex
TM	Transmission Mode
TO	Timing Offset
TP	Transmission Point
TS	Technical Specification
TTI	Transmission Time Interval
UE	User Equipment
UL	Uplink
ULA	Uniform Linear Array
UMTS	Universal Mobile Telecommunication System
WBAN	Wireless Body Area Networks
WLAN	Wireless Local Area Network
WMMSE-IRC	Widely Linear MMSE-IRC
WPAN	Wireless Person Area Networks
ZF	Zero Forcing
ZMCSCG	Zero Mean Circularly Symmetric Complex Gaussian
ZP	Zero Power

Bibliography

- [3GPa] 3GPP. *The Mobile Broadband Standard, LTE*. URL: <http://www.3gpp.org/technologies/keywords-acronyms/98-lte> (visited on 05/07/2016).
- [3GPb] 3GPP. *The Mobile Broadband Standard, LTE*. URL: <http://www.3gpp.org/specifications/releases/71-release-9> (visited on 05/07/2016).
- [3GPc] 3GPP. *The Mobile Broadband Standard, LTE*. URL: <http://www.3gpp.org/specifications/releases/70-release-10> (visited on 05/07/2016).
- [3GPd] 3GPP. *The Mobile Broadband Standard, LTE*. URL: <http://www.3gpp.org/specifications/releases/68-release-12> (visited on 05/07/2016).
- [3GPe] 3GPP. *The Mobile Broadband Standard, LTE*. URL: <http://www.3gpp.org/release-13> (visited on 05/07/2016).
- [3GPf] 3GPP. *The Mobile Broadband Standard, Start, Freeze and End dates*. URL: <http://www.3gpp.org/specifications/67-releases> (visited on 03/01/2016).
- [3GP06] 3GPP. *Technical Specification Group Radio Access Network; Physical layer aspects for evolved Universal Terrestrial Radio Access (UTRA) (Release 7)*. TR 25.814 V7.1.0. 3rd Generation Partnership Project, Sept. 2006.
- [3GP09a] 3GPP. *Technical Specification Group Radio Access Network; Evolved Universal Terrestrial Radio Access (E-UTRA); Physical Channels and Modulation (Release 8)*. TS 36.211 V8.9.0. 3rd Generation Partnership Project, Dec. 2009.
- [3GP09b] 3GPP. *Technical Specification Group Radio Access Network; Evolved Universal Terrestrial Radio Access (E-UTRA); Physical layer procedures (Release 8)*. TS 36.213 V8.8.0. 3rd Generation Partnership Project, Sept. 2009.

Bibliography

- [3GP09c] 3GPP. *Technical Specification Group Radio Access Network; Requirements for further advancements for Evolved Universal Terrestrial Radio Access (E-UTRA) (Release 8)*. TR 36.913 V8.0.1. 3rd Generation Partnership Project, Mar. 2009.
- [3GP10a] 3GPP. *Technical Specification Group Radio Access Network; Evolved Universal Terrestrial Radio Access (E-UTRA); Physical Channels and Modulation (Release 9)*. TS 36.211 V9.1.0. 3rd Generation Partnership Project, Mar. 2010.
- [3GP10b] 3GPP. *Technical Specification Group Radio Access Network; Evolved Universal Terrestrial Radio Access (E-UTRA); Physical layer procedures (Release 9)*. TS 36.213 V9.3.0. 3rd Generation Partnership Project, Sept. 2010.
- [3GP12] 3GPP. *Technical Specification Group Radio Access Network; Enhanced performance requirement for LTE User Equipment (UE) (Release 11)*. TR 36.829 V11.1.0. 3rd Generation Partnership Project, Dec. 2012.
- [3GP13a] 3GPP. *Technical Specification Group Radio Access Network; Coordinated multi-point operation for LTE physical layer aspects (Release 11)*. TR 36.819 V11.2.0. 3rd Generation Partnership Project, Sept. 2013.
- [3GP13b] 3GPP. *Technical Specification Group Radio Access Network; Evolved Universal Terrestrial Radio Access (E-UTRA); Physical Channels and Modulation (Release 10)*. TS 36.211 V.10.7.0. 3rd Generation Partnership Project, Feb. 2013.
- [3GP13c] 3GPP. *Technical Specification Group Radio Access Network; Small cell enhancements for E-UTRA and E-UTRAN - Physical layer aspects (Release 12)*. TR 36.872 V12.1.0. 3rd Generation Partnership Project, Dec. 2013.
- [3GP14a] 3GPP. *Overview of 3GPP Release 10*. Technical Report V0.2.1. 3rd Generation Partnership Project, June 2014.
- [3GP14b] 3GPP. *Overview of 3GPP Release 11*. Technical Report V0.2.0. 3rd Generation Partnership Project, Sept. 2014.
- [3GP14c] 3GPP. *Overview of 3GPP Release 8*. Technical Report V0.3.3. 3rd Generation Partnership Project, Sept. 2014.
- [3GP14d] 3GPP. *Overview of 3GPP Release 9*. Technical Report V0.3.4. 3rd Generation Partnership Project, Sept. 2014.
- [3GP14e] 3GPP. *Technical Specification Group Radio Access Network; Evolved Universal Terrestrial Radio Access (E-UTRA); Physical channels and modulation (Release 11)*. TS 36.211 V11.6.0. 3rd Generation Partnership Project, Sept. 2014.

- [3GP14f] 3GPP. *Technical Specification Group Radio Access Network; Study on Network-Assisted Interference Cancellation and Suppression (NAIC) for LTE (Release 12)*. TR 36.866 V12.0.1. 3rd Generation Partnership Project, Mar. 2014.
- [3GP15a] 3GPP. *Overview of 3GPP Release 12*. Technical Report V0.2.0. 3rd Generation Partnership Project, Sept. 2015.
- [3GP15b] 3GPP. *Release 13 analytical view version*. RP-151569. 3rd Generation Partnership Project, Sept. 2015.
- [3GP15c] 3GPP. *Technical Specification Group Radio Access Network; Evolved Universal Terrestrial Radio Access (E-UTRA); Physical channels and modulation (Release 12)*. TS 36.211 V12.8.0. 3rd Generation Partnership Project, Dec. 2015.
- [3GP15d] 3GPP. *Technical Specification Group Radio Access Network; Evolved Universal Terrestrial Radio Access (E-UTRA); Physical layer procedures (Release 10)*. TS 36.213 V10.13.0. 3rd Generation Partnership Project, June 2015.
- [3GP15e] 3GPP. *Technical Specification Group Radio Access Network; Study on Downlink Multiuser Superposition Transmission (MUST) for LTE (Release 13)*. TR 36.859 V13.0.0. 3rd Generation Partnership Project, Dec. 2015.
- [3GP15f] 3GPP. *Technical Specification Group Services and System Aspects; Vocabulary for 3GPP Specifications (Release 13)*. TR 21.905 V13.0.0. 3rd Generation Partnership Project, Dec. 2015.
- [3GP16a] 3GPP. *Technical Specification Group Radio Access Network; Evolved Universal Terrestrial Radio Access (E-UTRA) and Evolved Universal Terrestrial Radio Access Network (E-UTRAN); Overall description; Stage 2 (Release 13)*. TS 36.300 V13.3.0. 3rd Generation Partnership Project, Mar. 2016.
- [3GP16b] 3GPP. *Technical Specification Group Radio Access Network; Evolved Universal Terrestrial Radio Access (E-UTRA); Base Station (BS) radio transmission and reception (Release 13)*. TS 36.104 V13.3.0. 3rd Generation Partnership Project, Mar. 2016.
- [3GP16c] 3GPP. *Technical Specification Group Radio Access Network; Evolved Universal Terrestrial Radio Access (E-UTRA); Medium Access Control (MAC) protocol specification (Release 13)*. TS 36.321 V13.2.0. 3rd Generation Partnership Project, June 2016.
- [3GP16d] 3GPP. *Technical Specification Group Radio Access Network; Evolved Universal Terrestrial Radio Access (E-UTRA); Multiplexing and channel coding (Release 13)*. TS 36.212 V13.1.0. 3rd Generation Partnership Project, Mar. 2016.

Bibliography

- [3GP16e] 3GPP. *Technical Specification Group Radio Access Network; Evolved Universal Terrestrial Radio Access (E-UTRA); Packet Data Convergence Protocol (PDCP) specification (Release 13)*. TS 36.323 V13.2.1. 3rd Generation Partnership Project, June 2016.
- [3GP16f] 3GPP. *Technical Specification Group Radio Access Network; Evolved Universal Terrestrial Radio Access (E-UTRA); Physical channels and modulation (Release 13)*. TS 36.211 V13.1.0. 3rd Generation Partnership Project, Mar. 2016.
- [3GP16g] 3GPP. *Technical Specification Group Radio Access Network; Evolved Universal Terrestrial Radio Access (E-UTRA); Physical layer procedures (Release 13)*. TS 36.213 V13.1.1. 3rd Generation Partnership Project, Mar. 2016.
- [3GP16h] 3GPP. *Technical Specification Group Radio Access Network; Evolved Universal Terrestrial Radio Access (E-UTRA); Radio Frequency (RF) system scenarios (Release 13)*. TR 36.942 V13.0.0. 3rd Generation Partnership Project, Jan. 2016.
- [3GP16i] 3GPP. *Technical Specification Group Radio Access Network; Evolved Universal Terrestrial Radio Access (E-UTRA); Radio Link Control (RLC) protocol specification (Release 13)*. TS 36.322 V13.2.0. 3rd Generation Partnership Project, June 2016.
- [3GP16j] 3GPP. *Technical Specification Group Radio Access Network; Evolved Universal Terrestrial Radio Access (E-UTRA); User Equipment (UE) conformance specification Radio transmission and reception Part 1: Conformance Testing; (Release 13)*. TS 36.521 V13.1.0. 3rd Generation Partnership Project, Mar. 2016.
- [3GP16k] 3GPP. *Technical Specification Group Radio Access Network; Evolved Universal Terrestrial Radio Access (E-UTRA); User Equipment (UE) radio transmission and reception (Release 10)*. TS 36.101 V10.22.0. 3rd Generation Partnership Project, Mar. 2016.
- [3GP16l] 3GPP. *Technical Specification Group Radio Access Network; Evolved Universal Terrestrial Radio Access (E-UTRA); User Equipment (UE) radio transmission and reception (Release 11)*. TS 36.101 V11.16.0. 3rd Generation Partnership Project, Mar. 2016.
- [3GP16m] 3GPP. *Technical Specification Group Radio Access Network; Evolved Universal Terrestrial Radio Access (E-UTRA); User Equipment (UE) radio transmission and reception (Release 12)*. TS 36.101 V12.11.0. 3rd Generation Partnership Project, Mar. 2016.

- [3GP16n] 3GPP. *Technical Specification Group Radio Access Network; Evolved Universal Terrestrial Radio Access (E-UTRA); User Equipment (UE) radio transmission and reception (Release 13)*. TS 36.101 V13.3.0. 3rd Generation Partnership Project, Mar. 2016.
- [3GP16o] 3GPP. *Technical Specification Group Radio Access Network; Evolved Universal Terrestrial Radio Access (E-UTRA); User Equipment (UE) radio transmission and reception (Release 8)*. TS 36.101 V8.27.0. 3rd Generation Partnership Project, Mar. 2016.
- [3GP16p] 3GPP. *Technical Specification Group Radio Access Network; Evolved Universal Terrestrial Radio Access (E-UTRA); User Equipment (UE) radio transmission and reception (Release 9)*. TS 36.101 V9.24.0. 3rd Generation Partnership Project, Mar. 2016.
- [3GP16q] 3GPP. *Technical Specification Group Radio Access Network; Evolved Universal Terrestrial Radio Access Network (E-UTRAN); S1 Application Protocol (S1AP) (Release 13)*. TS 36.413 V13.2.0. 3rd Generation Partnership Project, Mar. 2016.
- [3GP16r] 3GPP. *Technical Specification Group Radio Access Network; Evolved Universal Terrestrial Radio Access Network (E-UTRAN); X2 application protocol (X2AP) (Release 13)*. TS 36.423 V13.3.0. 3rd Generation Partnership Project, Mar. 2016.
- [3GP16s] 3GPP. *Technical Specification Group Services and System Aspects; Telecommunication management; Performance Management (PM); Performance measurements Evolved Universal Terrestrial Radio Access Network (E-UTRAN) (Release 13)*. TS 32.425 V13.4.0. 3rd Generation Partnership Project, Mar. 2016.
- [3GP99a] 3GPP. *Technical Specification Group Services and System Aspects, Service aspects; Services and Service Capabilities*. TS 22.105 V.3.4.0. 3rd Generation Partnership Project, Apr. 1999.
- [3GP99b] *QoS Performance requirements for UMTS*. Agenda Item 6.3.3. Hampton Court, United Kingdom: 3GPP TSG-SA Working Group 1, May 1999.
- [Add+99] M. Addra, D. Castel, J. Dulongpont, and P. Genest. "Microelectronics in Mobile Communications: A Key Enabler". In: *IEEE Micro* 19.5 (Sept. 1999), pp. 62–70.

- [AGR10] I. F. Akyildiz, D. M. Gutierrez-Estevez, and E. C. Reyes. “The evolution to 4G cellular systems: LTE-Advanced”. In: *Physical Communication* 3.4 (Dec. 2010), pp. 217–244.
- [Agr10] G. P. Agrawal. *Fiber-Optic Communication Systems*. 4th ed. Hoboken, New Jersey, USA: John Wiley & Sons Inc., 2010.
- [Ann16] R. Annavajjala. “Low-Complexity Distributed Algorithms for Uplink CoMP in Heterogeneous LTE Networks”. In: *Journal of Communications and Networks* 18.2 (Apr. 2016), pp. 150–161.
- [Ast+09] D. Astely, E. Dahlman, A. Furuskär, Y. Jading, M. Lindström, and S. Parkvall. “LTE: The Evolution of Mobile Broadband”. In: *IEEE Communications Magazine* 47.4 (Apr. 2009), pp. 44–51.
- [AV10] I. F. Akyildiz and M. C. Vuran. *Wireless Sensor Networks*. 1st ed. Chichester, West Sussex, United Kingdom: John Wiley & Sons Inc., 2010.
- [Bai+10] Z. Bai, C. Spiegel, G. Bruck, P. Jung, M. Horvat, J. Berkmann, C. Drewes, and B. Gunzelmann. “Closed Loop Transmission with Precoding Selection in LTE/LTE-Advanced System”. In: *3rd International Symposium on Applied Sciences in Biomedical and Communication Technologies (ISABEL)*. Rome, Italy, Nov. 2010, pp. 1–5.
- [Bas+16] S. Bassoy, M. Jaber, M. A. Imran, and P. Xiao. “Load Aware Self-Organising User-Centric Dynamic CoMP Clustering for 5G Networks”. In: *IEEE Access* 4 (May 2016), pp. 2895–2906.
- [Bea+08] R. Beausoleil, P. Kuekes, G. Snider, S.-Y. Wang, and S. Williams. “Nanoelectronic and Nanophotonic Interconnect”. In: *Proceedings of the IEEE* 96.2 (Feb. 2008), pp. 230–247.
- [Bel56] “Nobel Prize in Physics Awarded to Transistor Inventors”. In: *The Bell System Technical Journal* 35.6 (Nov. 1956), pp. i–iv.
- [BL89] H. J. Bessai and W. Lorek. “Influence of Coding and Hardware Imperfections on the Bit Error Structure of Multilevel QAM Systems”. In: *IEEE Transactions on Communications* 37.6 (June 1989), pp. 626–634.
- [Bos98] M. Bossert. *Kanalcodierung*. 2nd. Stuttgart: Teubner, 1998.
- [Bra95] J. Bray. *The Communications Miracle: The Telecommunication Pioneers from Morse to the Information Superhighway*. New York, USA: Plenum Press, 1995.
- [Bro+01] I. N. Bronstein, K. A. Semendjajew, G. Musiol, and H. Mühlig. *Taschenbuch der Mathematik*. 5th ed. Thun und Frankfurt am Main: Verlag Harri Deutsch, 2001.

- [Bro86] *Brockhaus-Enzyklopädie: In 24 Bänden*. Vol. 19. Mannheim: F. A. Brockhaus-Verlag, 1986.
- [Che17] T. Chen. “Linear Receiver Design for Interfering Small Cell LTE Networks”. Bachelor’s Thesis. University of Duisburg-Essen, Feb. 2017.
- [CK13] A. Chien and V. Karamcheti. “Moore’s Law: The First Ending and a New Beginning”. In: *Computer* 46.12 (Dec. 2013), pp. 48–53.
- [Cor+01] T. H. Corman, C. E. Leiserson, R. L. Rivest, and C. Stein. *Introduction to Algorithms*. 2nd ed. Cambridge: The MIT Press, 2001.
- [Cox14] C. Cox. *An Introduction to LTE: LTE, LTE-Advanced, SAE, VoLTE and 4G Mobile Communications*. 2nd. Chichester, West Sussex, United Kingdom: John Wiley & Sons Inc., 2014.
- [CPP13] Y. Cheng, M. Pesavento, and A. Philipp. “Joint Network Optimization and Downlink Beamforming for CoMP Transmissions Using Mixed Integer Conic Programming”. In: *IEEE Transactions on Signal Processing* 61.16 (Aug. 2013), pp. 3972–3987.
- [CT07] T.-D. Chiueh and P.-Y. Tsai. *OFDM Baseband Receiver Design for Wireless Communications*. Singapore: John Wiley & Sons Inc., 2007.
- [CT12] T. M. Cover and J. A. Thomas. *Elements of Information Theory*. 2nd. Hoboken, New Jersey, USA: John Wiley & Sons Inc., 2012.
- [DPS14] E. Dahlman, S. Parkvall, and J. Sköld. *4G: LTE/LTE-Advanced for Mobile Broadband*. 2nd ed. Amsterdam, The Netherlands: Elsevier Ltd., 2014.
- [EDL14] A. R. Elsherif, Z. Ding, and X. Liu. “Dynamic MIMO Precoding for Femtocell Interference Mitigation”. In: *IEEE Transactions on Communications* 62.2 (Feb. 2014), pp. 648–666.
- [Ein31] A. Einstein. *Cosmic Religion with Other Opinions and Aphorisms*. New York, USA: Covici-Freide, 1931.
- [End07] J. Ender. *Radarverfahren und Methoden der Radar-Signalverarbeitung*. Vorlesungsskript. 2007.
- [Eri06] Ericsson. *LTE Channel Models for Concept Evaluation in RAN1*. R4-060101. Denver, USA: 3GPP, Feb. 2006.
- [Eri16] *Ericsson Mobility Report: On the pulse of the networked society*. Technical Report. Stockholm, Sweden: Ericsson, Feb. 2016.

Bibliography

- [GAH11] B. Ghimire, G. Auer, and H. Haas. “Busy Burst Enabled Coordinated Multipoint Network with Decentralized Control”. In: *IEEE Transactions on Wireless Communications* 10.10 (Oct. 2011), pp. 3310–3320.
- [Gei+12] S. Geirhofer, T. Ji, P. Gaal, A. Damnjanovic, J. Montojo, T. Luo, W. Chen, and K. Bhattad. *Cooperation and Operation of Macro Node and Remote Radio Head Deployments in Heterogeneous Networks*. US Patent App. 13/349,073. Aug. 2012.
- [Gho+11] A. Ghosh, J. Zhang, J. G. Andrews, and R. Muhamed. *Fundamentals of LTE*. Upper Saddle River, New Jersey, USA: Pearson Education, 2011.
- [Gla69] P. Glare, ed. *Oxford Latin dictionary. 2. Calcitro - Demitto*. Oxford, United Kingdom: Oxford University Press, Inc., 1969.
- [Gla71] P. Glare, ed. *Oxford Latin dictionary. 3. Demiurgus - Gorgoneus*. Oxford, United Kingdom: Oxford University Press, Inc., 1971.
- [HFK12] M. H. Hassan, Y. A. Fahmy, and M. M. Khairy. “Phase ambiguity mitigation for per-cell codebookbased limited feedback coordinated multi-point transmission systems”. In: *IET Communications* 6.15 (Oct. 2012), pp. 2378–2386.
- [HH03] B. Hassibi and B. M. Hochwald. “How Much Training is Needed in Multiple-Antenna Wireless Links?” In: *IEEE Transactions on Information Theory* 49.4 (Apr. 2003), pp. 951–963.
- [Him+10] N. Himayat, S. Talwar, A. Rao, and R. Soni. “Interference Management for 4G Cellular Standards”. In: *IEEE Communications Magazine* 48.8 (Aug. 2010), pp. 86–92.
- [HTR16] H. Holma, A. Toskala, and J. Reunanen, eds. *LTE Small Cell Optimization: 3GPP Evolution to Release 13*. Chichester, West Sussex, United Kingdom: John Wiley & Sons Inc., 2016.
- [Hua12] *Minutes for Ad Hoc for Geographically Non-co-located Antennas*. Technical Report R4-124984. Qingdao, China: Huawei HiSilicon, Aug. 2012.
- [Huq+15] K. M. S. Huq, S. Mumtaz, J. Bachmatiuk, J. Rodriguez, X. Wang, and R. L. Aguiar. “Green HetNet CoMP: Energy Efficiency Analysis and Optimization”. In: *IEEE Transactions on Vehicular Technology* 64.10 (Oct. 2015), pp. 4670–4683.
- [HW98] M.-H. Hsieh and C.-H. Wei. “Channel estimation for OFDM systems based on comb-type pilot arrangement in frequency selective fading channels”. In: *IEEE Transactions on Consumer Electronics* 44.1 (Feb. 1998), pp. 217–225.

- [HYA16] K. Hosseini, W. Yu, and R. S. Adve. “A Stochastic Analysis of Network MIMO Systems”. In: *IEEE Transactions on Signal Processing* 64.16 (Aug. 2016), pp. 4113–4126.
- [Int12a] *Investigation of UE Performance Degradation due to Frequency Offset Between Transmission Points*. Technical Report R4-126256. New Orleans, USA: Intel Corporation, Nov. 2012.
- [Int12b] *Investigation of UE Performance Degradation due to Timing Offset Between Transmission Points*. Technical Report R4-126255. New Orleans, USA: Intel Corporation, Nov. 2012.
- [Int12c] *Simulation and Discussion on the Timing Offset Between CRS and PDSCH*. Technical Report R4-125331. Santa Rosa, USA: Intel Corporation, Oct. 2012.
- [Irm+11] R. Irmer, H. Droste, P. Marsch, M. Grieger, G. Fettweis, S. Brueck, H.-P. Mayer, L. Thiele, and V. Jungnickel. “Coordinated Multipoint: Concepts, Performance, and Field Trial Results”. In: *IEEE Communications Magazine* 49.2 (Feb. 2011), pp. 102–111.
- [ITU96] *Information technology - generic coding of moving pictures and associated audio information: Video*. Technical Report H.262. International Telecommunication Union, Nov. 1996.
- [Jaf11] S. A. Jafar. “Interference Alignment - A New Look at Signal Dimensions in a Communication Network”. PhD thesis. California, USA: University of California, Irvine, 2011.
- [Jan+11] U. Jang, H. Son, J. Park, and S. Lee. “CoMP-CSB for ICI Nulling with User Selection”. In: *IEEE Transactions on Wireless Communications* 10.9 (Sept. 2011), pp. 2982–2993.
- [Jun97] P. Jung. *Analyse und Entwurf digitaler Mobilfunksysteme*. Stuttgart: B. G. Teubner Verlag, 1997.
- [Kam08] K.-D. Kammeyer. *Nachrichtenübertragung*. 4th ed. Wiesbaden: Vieweg+Teubner Verlag, 2008.
- [Kay98] S. M. Kay. *Fundamentals of Statistical Signal Processing: Detection Theory*. Upper Saddle River, New Jersey, USA: Prentice Hall PTR, 1998.
- [KF10] V. Kotzsch and G. Fettweis. “Interference Analysis in Time and Frequency Asynchronous Network MIMO OFDM Systems”. In: *IEEE Wireless Communication and Networking Conference (WCNC)*. Sydney, Australia, Apr. 2010, pp. 1–6.

Bibliography

- [KK09] R. Kreamer and M. D. Katz. *Short-Range Wireless Communications: Emerging Technologies and Applications*. Chichester, West Sussex, United Kingdom: John Wiley & Sons Inc., 2009.
- [Kle12] I. Kleiner. *Excursions in the History of Mathematics*. Boston, USA: Springer Science+Business Media, 2012.
- [KRF12] V. Kotzsch, W. Rave, and G. Fettweis. “Interference Cancellation and Suppression in Asynchronous Cooperating Base Station Systems”. In: *International ITG Workshop on Smart Antennas (WSA)*. Dresden, Germany, Mar. 2012, pp. 78–85.
- [Lan+15] Y.-Y. Lan, I.-W. Lai, C.-H. Lee, and T.-D. Chiueh. “Efficient Active Precoder Identification for Receivers With Inter-Cell Interference in Heterogeneous Networks”. In: *IEEE Transactions on Wireless Communications* 14.9 (Sept. 2015), pp. 5009–5021.
- [Lap05] P. A. Laplante, ed. *Comprehensive Dictionary of Electrical Engineering*. Boca Raton, Florida, USA: CRC Press, Taylor and Francis Group, 2005.
- [LC04] S. Lin and D. Costello. *Error Control Coding: Fundamentals and Applications*. Upper Saddle River, New Jersey, USA: Pearson Prentice Hall, 2004.
- [Lee+12a] D. Lee, H. Seo, B. Clerckx, E. Hardouin, D. Mazzarese, S. Nagata, and K. Sayan. “Coordinated Multipoint Transmission and Reception in LTE-Advanced: Deployment Scenarios and Operational Challenges”. In: *IEEE Communications Magazine* 50.2 (Feb. 2012), pp. 148–155.
- [Lee+12b] J. Lee, Y. Kim, H. Lee, B. L. Ng, D. Mazzarese, J. Liu, W. Xiao, and Y. Zhou. “Coordinated Multipoint Transmission and Reception in LTE-Advanced Systems”. In: *IEEE Communications Magazine* 50.11 (Nov. 2012), pp. 44–50.
- [Léo+12] Y. Léost, M. Abdi, R. Richter, and J. Michael. “Interference Rejection Combining in LTE Networks”. In: *Bell Labs Technical Journal* 17.1 (June 2012), pp. 25–49.
- [LG06] M. S. Lundstrom and J. Guo. *Nanoscale Transistors: Device Physics, Modeling and Simulation*. Boston, Massachusetts, USA: Springer Science+Business Media, Inc., 2006.
- [LL13] A. Liu and V. K. N. Lau. “Mixed-Timescale Precoding and Cache Control in Cached MIMO Interference Network”. In: *IEEE Transactions on Signal Processing* 61.24 (Dec. 2013), pp. 6320–6332.

- [LTY11] J. Lee, D. Toumpakaris, and W. Yu. “Interference Mitigation via Joint Detection”. In: *IEEE Journal on Selected Areas in Communications* 29.6 (June 2011), pp. 1172–1184.
- [Mac11] C. Mack. “Fifty Years of Moore’s Law”. In: *IEEE Transactions on Semiconductor Manufacturing* 24.2 (May 2011), pp. 202–207.
- [Mar+12] R. K. Martin, A. S. King, J. R. Pennington, R. Thomas, R. Lenahan, and C. Lawyer. “Modeling and Mitigating Noise and Nuisance Parameters in Received Signal Strength Positioning”. In: *IEEE Transactions on Signal Processing* 60.10 (Oct. 2012), pp. 5451–5463.
- [Mar08] D. A. Marcus. *Graph Theory: A Problem Oriented Approach*. Washington D.C., USA: The Mathematical Association of America Inc., 2008.
- [Max73] J. C. Maxwell. *A Treatise on Electricity and Magnetism*. Oxford, United Kingdom: Clarendon Press, 1873.
- [MDV13] M. Maso, M. Debbah, and L. Vangelista. “A Distributed Approach to Interference Alignment in OFDM-Based Two-Tiered Networks”. In: *IEEE Transactions on Vehicular Technology* 62.5 (June 2013), pp. 1935–1949.
- [Mol05] A. F. Molisch. *Wireless Communications*. New York, USA: IEEE Press, 2005.
- [Mol06] E. Mollick. “Establishing Moore’s Law”. In: *IEEE Annals of the History of Computing* 28.3 (July 2006), pp. 62–75.
- [Moo+13] S.-H. Moon, C. Lee, S.-R. Lee, and I. Lee. “Joint User Scheduling and Adaptive Intercell Interference Cancellation for MISO Downlink Cellular Systems”. In: *IEEE Transactions on Vehicular Technology* 62.1 (Jan. 2013), pp. 172–181.
- [Moo65] G. Moore. “The MOS transistor as an individual device and in integrated arrays”. In: *IRE International Convention Record*. Vol. 13. Mar. 1965, pp. 44–52.
- [MS09] C. Meinel and H. Sack. *Digitale Kommunikation: Vernetzen, Multimedia, Sicherheit*. Berlin, Germany: Springer, 2009.
- [MV99] K. Meyberg and P. Vachenauer. *Höhere Mathematik 1: Differential- und Integralrechnung Vektor- und Matrizenrechnung*. Vol. 5. Springer Berlin Heidelberg, 1999.
- [MW02] G. Merziger and T. Wirth. *Repetitorium der Höheren Mathematik*. 4th ed. Springe: Binomi Verlag, 2002.

Bibliography

- [Nag+13] S. Nagata, W. Xi, X. Yun, Y. Kishiyama, and L. Chen. “Interference Measurement Scheme for CoMP in LTE-Advanced Downlink”. In: *IEEE 77th Vehicular Technology Conference (VTC Spring)*. Dresden, Germany, June 2013, pp. 1–6.
- [Nok12] *Signaling Quasi Co-Location Between CRS and CSI-RS*. Technical Report R1-125257. New Orleans, USA: Nokia Siemens Networks, Nov. 2012.
- [OL07] J.-R. Ohm and H. D. Lücke, eds. *Signalübertragung - Grundlagen der digitalen und analogen Nachrichtenübertragungssysteme*. 10th ed. Berlin, Germany: Springer-Verlag Berlin, 2007.
- [Pap+11] A. Papadogiannis, H. J. Bang, D. Gesbert, and E. Hardouin. “Efficient Selective Feedback Design for Multicell Cooperative Networks”. In: *IEEE Transactions on Vehicular Technology* 60.1 (Jan. 2011), pp. 196–205.
- [Pat+13] E. Pateromichelakis, M. Shariat, A. Quddus, and R. Tafazolli. “On the Evolution of Multi-Cell Scheduling in 3GPP LTE / LTE-A”. In: *IEEE Communications Surveys Tutorials* 15.2 (2013), pp. 701–717.
- [PBT12] A. Papadogiannis, A. G. Burr, and M. Tao. “On the Maximum Achievable Sum-Rate of Interfering Two-Way Relay Channels”. In: *IEEE Communications Letters* 16.1 (Jan. 2012), pp. 72–75.
- [Per08] T. S. Perry. “Gordon Moore’s Next Act”. In: *IEEE Spectrum* 45.5 (May 2008), pp. 40–43.
- [Pra04] R. Prasad. *OFDM for Wireless Communications Systems*. Norwood, Massachusetts, USA: Artech House, 2004.
- [Pro01] J. G. Proakis. *Digital Communications*. 4th ed. New York, USA: McGraw-Hill, 2001.
- [Rei02] R. Reichwald. *Mobile Kommunikation: Wertschöpfung, Technologien, neue Dienste*. Wiesbaden: Gabler, 2002.
- [Ren15] R. Rennie, ed. *A Dictionary of Physics*. 7th ed. Oxford, United Kingdom: Oxford University Press, 2015.
- [Ros00] K. E. Rosengren. *Communication: An Introduction*. London, United Kingdom: SAGE Publications Ltd, 2000.
- [Ros13] P. Rost. “Robust and Efficient Multi-Cell Cooperation under Imperfect CSI and Limited Backhaul”. In: *IEEE Transactions on Wireless Communications* 12.4 (Apr. 2013), pp. 1910–1922.

- [Sal68] B. R. Saltzberg. “Intersymbol Interference Error Bounds with Application to Ideal Bandlimited Signaling”. In: *IEEE Transactions on Information Theory* 14.4 (July 1968), pp. 563–568.
- [Sch+13] K. Schuegraf, M. Abraham, A. Brand, M. Naik, and R. Thakur. “Semiconductor Logic Technology Innovation to Achieve Sub-10 nm Manufacturing”. In: *IEEE Journal of the Electron Devices Society* 1.3 (Mar. 2013), pp. 66–75.
- [Sha48] C. E. Shannon. “A mathematical theory of communication”. In: *The Bell System Technical Journal* 27.4 (Oct. 1948), pp. 623–656.
- [SI08] *The International System of Units (SI)*. Technical Report 8. Paris, France: Organisation Intergouvernementale de la Convention du Mètre, 2008.
- [Sie02] *System Overview EWSD*. Technical Report. Siemens AG, 2002.
- [SL05] H. Schulze and C. Lüders. *Theory and Applications of OFDM and CDMA Wideband Wireless Communication*. Chichester, West Sussex, United Kingdom: John Wiley & Sons Inc., 2005.
- [SM08] N. A. of Sciences and I. of Medicine. *Science, Evolution and Creationism*. Washington D.C., USA: The National Academics Press, 2008.
- [SN07] S. Sze and K. Ng. *Physics of Semiconductor Devices*. 3rd ed. Hoboken, New Jersey, USA: John Wiley & Sons Inc., 2007.
- [STB11] S. Sesia, I. Toufik, and M. Baker, eds. *LTE: The UMTS Long Term Evolution*. 2nd ed. Chichester, West Sussex, United Kingdom: John Wiley & Sons Inc., 2011.
- [Stü11] G. L. Stüber. *Principles of Mobile Communication*. 3rd ed. New York, USA: Springer, 2011.
- [TA11] G. Tietscher and S. Ache. *Continuing in the direction of LTE-Advanced: the latest test signals for LTE Rel. 9*. Technical Report. Rohde & Schwarz GmbH & Co KG, 2011.
- [Tan17] L. Tan. *A Generalized Framework of Linear Multivariable Control*. Oxford, United Kingdom: Elsevier Ltd., 2017.
- [TG11] H. R. Tanhaei and S. A. Ghorashi. “A Novel Channel Estimation Technique for OFDM Systems with Robustness against Timing Offset”. In: *IEEE Transactions on Consumer Electronics* 57.2 (May 2011), pp. 348–356.
- [Tru01] B. Truax. *Acoustic Communication*. 2nd ed. Westport, Connecticut, USA: Ablex Publishing, 2001.

- [TSS10] T. Toyserkani Arash, G. Ström Erik, and A. Svensson. “An Analytical Approximation to the Block Error Rate in Nakagami-m Non-Selective Block Fading Channels”. In: *IEEE Transactions on Wireless Communications* 9.5 (May 2010), pp. 1543–1546.
- [TV05] D. Tse and P. Viswanath. *Fundamentals of Wireless Communication*. Cambridge, United Kingdom: Cambridge University Press, 2005.
- [VA12] C. Voigt and J. Adamy. *Formelsammlung der Matrizenrechnung*. München: Oldenbourg Wissenschaftsverlag, 2012.
- [Wal01] B. Walke. *Mobilfunknetze und ihre Protokolle: Grundlagen, GSM, UMTS und andere zellulare Mobilfunknetze*. 3rd. Stuttgart: Teubner, 2001.
- [WD14] D. Warren and C. Dewar. *Understanding 5G: Perspectives on future technological advancements in mobile*. Technical Report. London, United Kingdom: GSMA Intelligence, Dec. 2014.
- [Wes13] S. Westwood. *Global State of LTE Report February 2013*. Technical Report. Open Signal, Feb. 2013.
- [Wol+98] P. W. Wolniansky, G. J. Foschini, G. D. Golden, and R. Valenzuela. “V-BLAST: An Architecture for Realizing Very High Data Rates Over the Rich-Scattering Wireless Channel”. In: *International Symposium on Signals, Systems, and Electronics (ISSSE)*. Pisa, Italy, Oct. 1998, pp. 295–300.
- [WSA03] B. Walke, P. Seidenberg, and M.-P. Althoff. *UMTS: The Fundamentals*. Chichester, West Sussex, United Kingdom: John Wiley & Sons Inc., 2003.
- [XRS16] D. Xu, P. Ren, and H. Song. “Precoder-and-receiver design scheme for multi-user coordinated multi-point in LTE-A and fifth generation systems”. In: *IET Communications* 10.3 (2016), pp. 292–299.
- [Yan+13] C. Yang, S. Han, X. Hou, and A. F. Molisch. “How Do We Design CoMP to Achieve its Promised Potential?” In: *IEEE Wireless Communications* 20.1 (Feb. 2013), pp. 67–74.
- [YKS13] W. Yu, T. Kwon, and C. Shin. “Multicell Coordination via Joint Scheduling, Beamforming, and Power Spectrum Adaptation”. In: *IEEE Transactions on Wireless Communications* 12.7 (July 2013), pp. 1–14.
- [ZF86] R. Zurmühl and S. Falk. *Matrizen und ihre Anwendungen für angewandte Mathematiker, Physiker und Ingenieure. Teil 2: Numerische Methoden*. 5th ed. Berlin: Springer-Verlag, 1986.

- [ZF92] R. Zurmühl and S. Falk. *Matritzen und ihre Anwendungen 1. Grundlagen. Für angewandte Mathematiker, Physiker und Ingenieure*. 6th ed. Berlin: Springer-Verlag, 1992.
- [Zha+07] H. Zhang, N. B. Mehta, A. F. Molisch, J. Zhang, and H. Dai. “On the Fundamentally Asynchronous Nature of Interference in Cooperative Base Station Systems”. In: *IEEE International Conference on Communications (ICC)*. Glasgow, Scotland, June 2007, pp. 6073–6078.
- [Zha+15a] H. Zhang, C. Jiang, J. Cheng, and V. C. M. Leung. “Cooperative Interference Mitigation and Handover Management for Heterogeneous Cloud Small Cell Networks”. In: *IEEE Wireless Communications* 22.3 (June 2015), pp. 92–99.
- [Zha+15b] H. Zhang, H. Liu, C. Jiang, X. Chu, A. Nallanathan, and X. Wen. “A Practical Semidynamic Clustering Scheme Using Affinity Propagation in Cooperative Picocells”. In: *IEEE Transactions on Vehicular Technology* 64.9 (Sept. 2015), pp. 4372–4377.
- [ZTE12] *Need for Quasi Co-Location Signaling for CSI-RS and CRS*. Technical Report R1-124824. ZTE, Nov. 2012.

Publications of the Author

- [Bad+12a] B. Badic, R. Balraj, T. Scholand, Z. Bai, and S. Iwelski. “Analysis of CQI prediction for MU-MIMO in LTE Systems”. In: *IEEE 75th Vehicular Technology Conference (VTC Spring)*. Yokohama, Japan, May 2012, pp. 1–5.
- [Bad+12b] B. Badic, B. Rajarajan, T. Scholand, Z. Bai, and S. Iwelski. “Impact of Feedback and User Pairing Schemes on Receiver Performance in MU-MIMO LTE Systems”. In: *IEEE Wireless Communications and Networking Conference (WCNC)*. Paris, France, Apr. 2012, pp. 399–403.
- [Bai+11a] Z. Bai, B. Badic, S. Iwelski, T. Scholand, R. Balraj, G. Bruck, and P. Jung. “On the Equivalence of MMSE and IRC Receiver in MU-MIMO Systems”. In: *IEEE Communications Letters* 15.12 (Dec. 2011), pp. 1288–1290.

- [Bai+11b] Z. Bai, S. Iwelski, G. Bruck, P. Jung, B. Badic, T. Scholand, and B. Rajarajan. “Receiver Performance-Complexity Tradeoff in LTE MU-MIMO Transmission”. In: *3rd International Congress on Ultra Modern Telecommunications and Control Systems and Workshops (ICUMT)*. Hungary, Budapest, Oct. 2011, pp. 1–7.
- [Bai+12] Z. Bai, B. Badic, S. Iwelski, R. Balraj, T. Scholand, G. Bruck, and P. Jung. “Interference Estimation for Multi-Layer MU-MIMO Transmission in LTE-Advanced Systems”. In: *IEEE 23rd International Symposium on Personal, Indoor and Mobile Radio Communications - (PIMRC)*. Sydney, Australia, Sept. 2012, pp. 1622–1626.
- [Bai+13a] Z. Bai, B. Badic, R. Balraj, S. Iwelski, T. Scholand, G. Bruck, and P. Jung. “Near Optimal Implicit Feedback Generation for Coordinated Multipoint Transmission”. In: *IEEE Communications Letters* 17.11 (Nov. 2013), pp. 2040–2043.
- [Bai+13c] Z. Bai, S. Iwelski, G. Bruck, P. Jung, B. Badic, T. Scholand, and R. Balraj. “Evaluation of Implicit Feedback in Coordinated Multipoint Transmission Beyond LTE-Advanced”. In: *IEEE 77th Vehicular Technology Conference (VTC Spring)*. Dresden, Germany, June 2013, pp. 1–5.
- [Bai+14a] Z. Bai, S. Iwelski, B. Badic, G. Bruck, and P. Jung. “Feedback Generation for Cell-Edge Transmission in Unsynchronized Coordinated Networks”. In: *Intel Technology Journal* 18.1 (Feb. 2014), pp. 122–140.
- [BIV10] T. Breddermann, S. Iwelski, and P. Vary. “Bad Parameter Indication for Error Concealment in Wireless Multimedia Communication”. In: *IEEE 72nd Vehicular Technology Conference Fall (VTC Fall)*. Ottawa, Canada, Sept. 2010, pp. 1–5.
- [Iwe+13c] S. Iwelski, Z. Bai, G. Bruck, P. Jung, B. Badic, T. Scholand, and R. Balraj. “Analysis of Interference-aware Receivers in Heterogeneous LTE Networks”. In: *IEEE/CIC International Conference on Communications in China (ICCC)*. Xi’an, China, Aug. 2013, pp. 314–320.
- [Iwe+14a] S. Iwelski, E. Majeed, Z. Bai, G. Bruck, and P. Jung. “Cooperative Implicit Feedback Generation in Interfering Heterogeneous LTE Networks”. In: *IFIP Wireless Days (WD)*. Rio de Janeiro, Brazil, Nov. 2014, pp. 1–6.

- [Iwe+14b] S. Iwelski, B. Badic, Z. Bai, R. Balraj, C.-H. Kuo, E. Majeed, T. Scholand, G. Bruck, and P. Jung. “Feedback Generation for CoMP Transmission in Unsynchronized Networks with Timing Offset”. In: *IEEE Communications Letters* 18.5 (May 2014), pp. 725–728.
- [Iwe+14e] S. Iwelski, Z. Bai, E. Majeed, G. Bruck, and P. Jung. “Impact of Antenna Configuration on Feedback Generation for non-ideal CoMP Transmission”. In: *IEEE 80th Vehicular Technology Conference (VTC Fall)*. Vancouver, Canada, Sept. 2014, pp. 1–5.
- [Iwe+14f] S. Iwelski, Z. Bai, E. Majeed, G. Bruck, and P. Jung. “On the Performance of CoMP Transmission in Unsynchronized Networks with Timing Offset”. In: *IEEE Wireless Communications and Networking Conference (WCNC)*. Istanbul, Turkey, Apr. 2014, pp. 571–576.
- [Iwe+14g] S. Iwelski, Z. Bai, E. Majeed, G. Bruck, and P. Jung. “Reliable Implicit Feedback Generation in Unsynchronized CoMP Transmission”. In: *IEEE 25th Annual International Symposium on Personal, Indoor, and Mobile Radio Communication (PIMRC)*. Washington D.C., USA, Sept. 2014, pp. 1–5.
- [Iwe+14h] S. Iwelski, Z. Bai, E. Majeed, G. Bruck, and P. Jung. “Robust FFT Window Replacement in non-ideal CoMP Networks with Timing Offset”. In: *IEEE 79th Vehicular Technology Conference (VTC Spring)*. Seoul, South Korea, May 2014, pp. 1–5.
- [Iwe+15a] S. Iwelski, E. Majeed, Z. Bai, G. Bruck, and P. Jung. “Cooperative Interference Mitigation in Heterogeneous LTE Networks”. In: *IEEE Wireless Communications and Networking Conference (WCNC)*. New Orleans, USA, Mar. 2015, pp. 135–140.
- [Iwe+15b] S. Iwelski, E. Majeed, Z. Bai, G. Bruck, and P. Jung. “Coordinated Interference Mitigation Precoding in Unsynchronized Small Cell LTE Networks”. In: *IEEE Global Communications Conference (GLOBECOM)*. San Diego, USA, Dec. 2015, pp. 1–7.
- [Iwe+15c] S. Iwelski, E. Majeed, Z. Bai, G. Bruck, and P. Jung. “Reliable Feedback Generation in Unsynchronized Joint-Processing CoMP Transmission Networks”. In: *IEEE 26th Annual International Symposium on Personal, Indoor, and Mobile Radio Communications (PIMRC)*, Hong Kong, China, Aug. 2015, pp. 921–926.

- [Iwe+16] S. Iwelski, E. Majeed, G. Bruck, and P. Jung. “On the Performance of Advanced Receivers in Unsynchronized Small Cell LTE Networks”. In: *IEEE International Conference on Communications (ICC)*. Kuala Lumpur, Malaysia, May 2016, pp. 1–7.
- [Maj+15] E. Majeed, S. Iwelski, Z. Bai, G. Bruck, and P. Jung. “Advanced Receiver Design for Interfering Small Cell Deployments in LTE Networks”. In: *IEEE Conference on Standards for Communications and Networking (CSCN)*. Tokyo, Japan, Oct. 2015, pp. 294–299.

Co-supervised Theses by the Author

- [Bao17] W. Bao. “Investigation of Channel Quality Index Feedback Schemes for LTE Networks”. Bachelor’s Thesis. University of Duisburg-Essen, Sept. 2017.
- [Fan14] Q. Fang. “Reliable CoMP Joint-Processing Joint-Transmission in Unsynchronized LTE Networks with Timing Offset”. Master’s Thesis. University of Duisburg-Essen, Dec. 2014.
- [Li18] M. Li. “Receiver Design for Spatial Multiplexing Signal Transmission in LTE Networks”. Master’s Thesis. University of Duisburg-Essen, Nov. 2018.
- [Lu13] W. Lu. “Investigation of Advanced Receivers for Heterogeneous Network Deployments in Long Term Evolution Advanced (LTE-A) Systems”. Master’s Thesis. University of Duisburg-Essen, May 2013.
- [Mos16] S. Mosleh. “Reliable Channel Quality Index Estimation in Unsynchronized CoMP Transmission LTE Networks”. Bachelor’s Thesis. University of Duisburg-Essen, Aug. 2016.
- [Tar13] K. Tarkunde. “Investigation of Coordinated Multipoint (CoMP) in Long Term Evolution Advanced (LTE-A) Systems to improve downlink communication for cell-edge user-equipments”. Master’s Thesis. University of Duisburg-Essen, Jan. 2013.
- [Teh13] H. Teh. “Feedback Optimization for Coordinated Multipoint Transmission in Beyond LTE-Advanced Systems”. Bachelor’s Thesis. University of Duisburg-Essen, Apr. 2013.

- [Wan16] S. Wang. “Cooperative Interference Mitigation Precoding in Next Generation Small Cell LTE Networks”. Bachelor’s Thesis. University of Duisburg-Essen, Feb. 2016.
- [Yau13] H. K. Yau. “Remote Communication between the iPhone and a Vehicle using Socket Communication”. Bachelor’s Thesis. University of Duisburg-Essen, May 2013.
- [Zho13] Q. Zhou. “Impact of Time and Frequency Synchronization on the Downlink Performance in Coordinated Multipoint Transmission in LTE-Advanced Systems”. Master’s Thesis. University of Duisburg-Essen, Oct. 2013.

Filed Patents of the Author

- [Bai+13b] Z. Bai, S. Iwelski, G. H. Bruck, P. Jung, B. Badic, T. Scholand, and R. Balraj. “Empfänger und Verfahren zum Detektieren eines Vorkodierten Signals”. DE Patent 102011054913. May 2, 2013.
- [Bai+14b] Z. Bai, S. Iwelski, G. H. Bruck, P. Jung, B. Badic, T. Scholand, and R. Balraj. “Empfänger mit mehrschicht-störungslöschung”. DE Patent 102013110672. Apr. 10, 2014.
- [Bai+14c] Z. Bai, S. Iwelski, G. H. Bruck, P. Jung, B. Badic, T. Scholand, and R. Balraj. “Receiver with Multi Layer Interference Cancellation”. US Patent 8,908,743. Dec. 9, 2014.
- [Bai+16] Z. Bai, S. Iwelski, G. H. Bruck, P. Jung, B. Badic, T. Scholand, and R. Balraj. “Receiver and Method for Detecting a Pre-coded Signal”. US Patent 9,231,675. Jan. 5, 2016.
- [Iwe+13a] S. Iwelski, Z. Bai, G. H. Bruck, P. Jung, B. Badic, T. Scholand, and R. Balraj. “Vorrichtung und Verfahren zum Bestimmen einer Vorcodiermatrix”. DE Patent 102013208486. Nov. 14, 2013.
- [Iwe+13b] S. Iwelski, Z. Bai, G. H. Bruck, P. Jung, B. Badic, T. Scholand, and R. Balraj. “Vorrichtung und Verfahren zum Decodieren eines Empfangenen Signals”. DE Patent 102013208363. Nov. 14, 2013.
- [Iwe+14c] S. Iwelski, Z. Bai, G. H. Bruck, P. Jung, B. Badic, T. Scholand, and R. Balraj. “Apparatus and Method for Decoding a Received Signal”. US Patent 8,842,782. Sept. 23, 2014.

Bibliography

- [Iwe+14d] S. Iwelski, Z. Bai, G. H. Bruck, P. Jung, B. Badic, T. Scholand, and R. Balraj. “Apparatus and Method for Determining a Precoding Matrix”. US Patent 8,781,027. July 15, 2014.